DTT - Divertor Tokamak Test facility - Interim Design Report

(Article begins on next page)

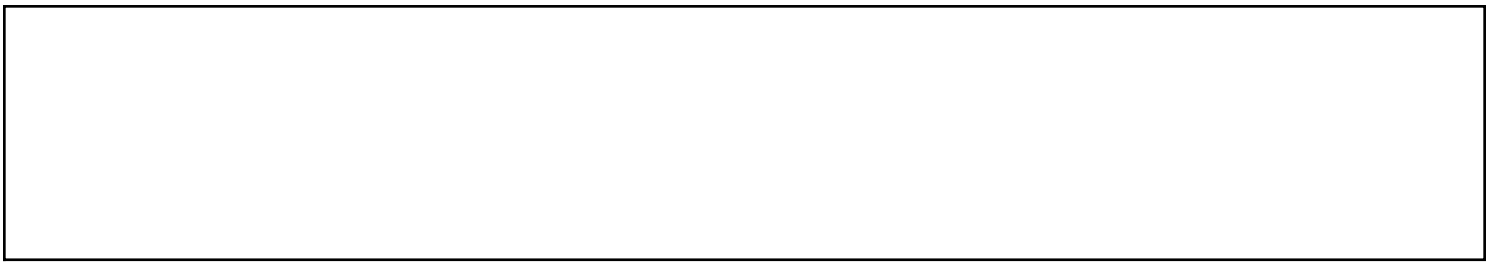

Member of EUROfusion

DTT

Divertor Tokamak Test facility

Interim Design Report

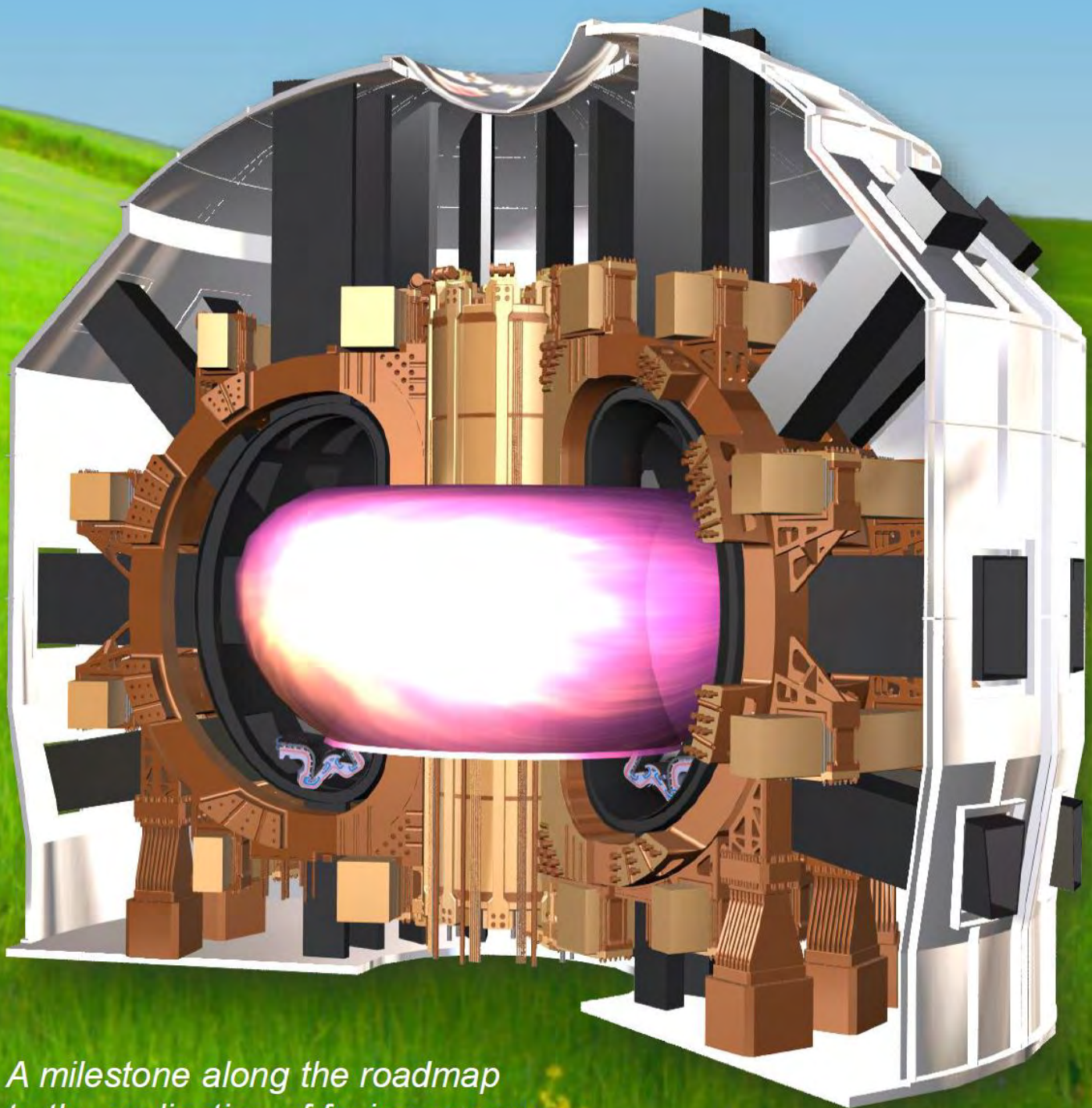

A milestone along the roadmap
to the realisation of fusion energy

DTT

Divertor Tokamak Test facility Interim Design Report

A milestone along the roadmap to the realisation of fusion energy

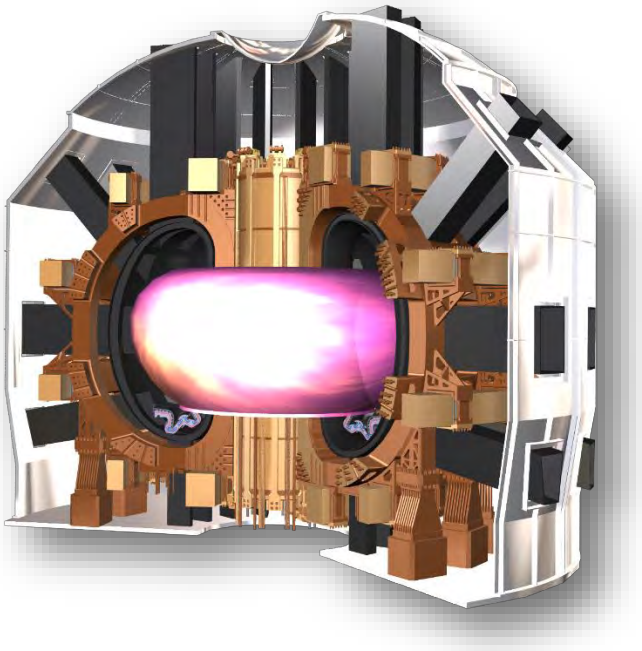

April 2019

Member of EUROfusion

DTT
Divertor Tokamak Test facility – Interim Design Report

Italian National Agency for New Technologies,
Energy and Sustainable Economic Development

Edited by Raffaele Martone (CREATE), Raffaele Albanese (CREATE), Flavio Crisanti (ENEA), Piero Martin (RFX) and Aldo Pizzuto (ENEA)

ISBN: 978-88-8286-378-4
Printed in April 2019 at ENEA Frascati Research Center,
Via Enrico Fermi 45, 00044 Frascati (Roma), Italy

Contributors

ENEA, Italy
L. Affinito
S. Almaviva
A. Anemona
M. Angelone
M.L. Apicella
A. Appi
G. Apruzzese
G. Artaserse
G. Barone
M. Baruzzo
P. Batistoni
F. Bombarda
L. Boncagni
P. Buratti
B. Caiffi
L. Caneve
M. Caponero
A. Cardinali
S. Ceccuzzi
C. Centioli
G. Claps
V. Cocilovo
A. Colangeli
F. Colao
G.M. Contessa
V. Corato
F. Cordella
F. Crisanti
A. Cucchiaro
O. D'Arcangelo
A. Della Corte
R. De Luca
L. Di Pace
A. Di Zenobio
G. Dose
C. Fiamozzi Zignani
D. Flammini
N. Fonnesu
A. Frattolillo
L. Gabellieri
G. Galatola
L. Giannini
E. Giovannozzi
M.T. Grieco
M. Guardati
M. Iafrati
I. Iovinella
A. Lampasi
C. Lanchi
V. Lazic
D. Liuzza
G. Maddaluno
S. Magagnino
A. Mancini
D. Marocco
E. Martelli
G. Mazzitelli
C. Mazzotta
G. Messina
C. Monti
L. Morici
F. Moro
L. Muzzi
D. Pacella
M. Pillon
C. Piron
A. Pizzuto
F. Pollastrone
G.M. Polli
M. Pospodarczyk
G. Ramogida
G.L. Ravera
R. Righetti
S. Roccella
G. Romanelli
A. Romano
R. Romano
A. Rydzy
S. Sandri
F. Starace
A.A. Tuccillo
O. Tudisco
S. Turtù
M. Vellucci
R. Villari
B. Viola
V. Vitale
G. Vlad
M. Zerbini
P. Zito
L. Zoboli
F. Zonca

ENEA - CNR - IFP, Italy
E. Alessi
B. Baiocchi
W. Bin
A. Bruschi
F. Causa
A. Cremona
F. Fanale
D. Farina
L. Figini
S. Garavaglia
G. Granucci
M. Lontano
A. Moro
A. Muraro
S. Nowak
E. Perelli
D. Ricci
S. Schmuck
C. Sozzi
M. Tardocchi
A. Uccello
B. William

ENEA - CREATE, Italy
R. Albanese
R. Ambrosino
M. Ariola
A. Castaldo
D. Coccorese
V. Coccorese
M. de Magistris
G. De Tommasi
G. Di Gironimo
R. Fresa
S. Grazioso
V.P. Loschiavo
R. Martone
D. Marzullo
M. Mattei
A. Mele
R. Mozzillo
F.P. Orsitto
A. Pironti
G. Rubinacci
A. Tarallo
S. Ventre
F. Villone

ENEA - Politecnico di Torino, Italy
R. Bonifetto
R. Maggiora
D. Milanesio
G.F. Nallo
L. Savoldi
F. Subba
R. Zanino
A. Zappatore

ENEA - RFX, Italy
P. Agostinetti
M. Agostini
M. Barbisan
T. Bolzonella
L. Carraro
C. Castaldo
R. Cavazzana
G. De Masi
A. Fassina
A. Ferro
L. Figini
P. Franz
L. Giacomelli
L. Giudicotti
F. Gnesotto
M. Gobbin
P. Innocente
A. Luchetta
G. Manduchi
L. Marrelli
P. Martin
E. Martines
M. Moressa
R. Pasqualotto
S. Peruzzo
L. Piron
M.E. Puiatti
P. Scarin
P. Sonato
G. Spizzo
M. Spolaore
D. Terranova
M. Valisa
M. Vallar
N. Vianello
P. Vincenzi
B. Zaniol
M. Zuin

ENEA - Università degli Studi della Tuscia, Italy
G. Calabrò
R. Lombroni
S. Minucci

ENEA - Università degli Studi di Milano-Bicocca, Italy
G. Gorini
M. Nocente

ENEA - Università degli Studi di Roma La Sapienza, Italy
A. De Santis
L. Maggiacomo
G. Mariano

INFN, Italy
M. Osipenko
M. Ripani
F. Murtas

IST, Universida de Lisboa, Portugal
R. Luis

Preface

After the release in 2015 of the project proposal ("DTT - Divertor Tokamak Test facility. Project Proposal", ISBN 978-88-8286-318-0, ENEA, 2015, also known as "Blue Book") and the publication of a dedicated Fusion Engineering and Design issue in 2017, many scientific, technical, managerial, logistic and financial activities have been performed by the DTT Team, its stakeholders and EUROfusion. As a result, the machine design has been upgraded and improved and the framework for the realization of the project has been better defined. This interim design report contains the state-of-the-art information about the project, which is still evolving. It will be then followed by the final design report in due time.

Following the guidelines described within the European Fusion Road Map, the DTT facility has been charged with the challenge to test the science of tokamak alternative divertor concepts under integrated physics and technical conditions that can reliably be extrapolated to DEMO. In a magnetic fusion device, the divertor is the system where energy and particles, transported out from the plasma through non-neutronic channels, are collected. In order to comply with the material, the power flowing to the divertor must be 10 MW/m^2. The baseline solution to the exhaust issue consists in a metal divertor operating in a plasma fully detached condition. However, as widely illustrated within the European Fusion Road Map, the baseline solution might not fit the needs of DEMO and of a future reactor. The plasma exhaust issue needs therefore to be solved with great urgency and strength in order not to cause delays to the development of fusion. In this effort a key aspect will be the availability of DTT scenarios, with high-performance core plasma properties consistent with relevant edge and SOL (Scrape-Off Layer) parameters. Testing the alternative divertor configurations in different scenarios will provide the whole set of information needed to choose the right solution for DEMO.

Succeeding the outcome of a dedicated European workshop, held in Frascati on July 2017, the DTT design has been deeply changed in order to increase its flexibility in line with suggestions of EUROfusion PEX Ad Hoc Group. The present design of the DTT facility is based on a superconducting tokamak with a double layer stainless steel vacuum vessel with major radius R=2.11 m, minor radius a=0.64 m and aspect ratio A=3.3, corresponding to a plasma volume of 28 m^3. The on-axis maximum toroidal field is B_T=6 T, and the maximum discharge duration allowed by the power supplies and the superconducting coils is 100 s. The maximum plasma current in the single null reference scenarios is I_p=5.5 MA, with an additional auxiliary power P_{Tot}=45 MW provided by a portfolio of ECRH, ICRH and negative ion beam injection. DTT vessel and magnet system are compatible with alternative divertor configurations like Double Null (5 MA peak current), Long Leg divertor plasma (5 MA), Negative Triangularity (5 MA), Snow Flake (4.5 MA), and Double super-X (3 MA). The objectives of DTT include the test of various divertor materials and the demonstration that a closed loop liquid metal heat removal system is viable in a tokamak at relevant edge and SOL parameters. Along the operation phase, flexibility will be ensured by the portfolio of heating systems, by the coil (external and in-vessel) and power supply systems, by several magnetic and non-magnetic actuators, by an advanced Disruption Mitigation System and by a choice of target plasma parameters (e.g. the Greenwald fraction is set as a target to 0.45), which allow for an ample exploration of the operational space in all directions. Real-time feedback control of the main quantities relevant for bulk and divertor plasma performance (e.g. MHD stability, fuelling, radiation level, transient events, plasma position, divertor magnetic topology) is implemented though an wide set of diagnostic and actuators which will exploit the recent strong progress on control science in the fusion community.

The DTT design and construction phase will take 7 years, and operation is expected to start at the end of 2025, with the assumption that the final design elements of the first divertor are fixed by the end of 2022. The first market survey on superconductive strands has already been launched in 2018, whereas the first call for tender will be released in 2019. The operations should then cover a period of more than 25 years, up to the initial phases of the DEMO realization. The present detailed planning of the construction activities is included in this document.

In the "Blue Book" the DTT cost was estimated to be about 500 M€, with half of the amount covered by a loan from the European Investment Bank, about 60 M€ already allocated by EUROfusion, a small fraction covered by International in-kind contribution and with remaining of the budget covered by Italian funds. An independent cost revision has been committed to a panel of fusion experts in fusion, based on the design features described in the "Blue Book". Although it was known that several very important and expensive items would have been changed, the independent cost revision was addressed with a key "Term of Reference" to provide indications of how to improve the design, while meeting the budget constraints. The panel carried out an analysis based on a statistical approach and considering also the design uncertainties. It provided useful advice and recommendations, in particular for magnets, vacuum vessel, and auxiliaries. These components underwent to significant simplifications in the present DTT design, leading to more efficient and considerably less expensive concepts. In the next future, the panel will upgrade the cost review working on the latest design described within this Interim Design Report.

After a public call launched by ENEA to all Italian regions to offer a site for the construction of DTT facility, nine excellent proposals were presented. The outcome of the selection was the ENEA site of Frascati, where the Frascati Tokamak (FT and FTU) successfully operated. The Frascati site, located in the outskirt of Rome, is one of the largest research area in Europe, where the labs of ENEA and other research institutions, namely those of the European Space Observatory, the National Institute for Nuclear Physics (INFN), the National Research Center (CNR), the National Institute for Astrophysics (INAF), and the campus of the University of Tor Vergata are located.

Presently, the DTT project team is composed by about 100 members, mainly coming from ENEA, CNR, Consorzio RFX, Consorzio CREATE and from Italian Universities. A smaller but growing number of contributors from foreign institutions are working on the project. The project is managed by an interim executive board of four members, supported by a number of interim task coordinators. More recently a large specific recruitment and training campaign has been launched for young personnel at various levels of competence. In the near future, a DTT consortium will be established to manage the construction and the operation phases of the device. The design integration is coordinated by a fortnightly "Technical Coordination Meeting", (TCM) where the different "Areas" responsible report the progresses and the problems. Around every three months a general Design Review Meeting (DRM) is called to deeply revise the progress of the full project or the final design of specific components. A Data Management System (DMS) based on advanced technology has been implemented and a reference living document, the Plant Integration Document (PID) has been prepared. Updated information is available at the web site http://www.dtt-project.enea.it/.

DTT is a strategic investment in several key areas of research and innovation, with significant implications on the energy and high-tech sectors. The project includes a strong collaboration with the Italian and European academic systems. In particular, in light of the DTT needs to employ highly qualified personnel during the next decades, synergies with a number of Universities have been established; aims of the agreements are the increase of their higher educational programs in technical and scientific fields of interest for DTT, as specialized courses as well as research topics in Master and PhD courses. EUROfusion has also dedicated, within its programme of support for education and training of a new generation of scientist and engineers in

view of DEMO, a number of positions of Engineering Grants specifically to DTT. The Italian Government has offered to the European fusion system the opportunity to get complementary funding for a dedicated exhaust facility located in Italy.

The occupational impact is expected to be significant, with at least 250 people involved for the operation (50 % professionals, 50 % support personnel), with a significant part provided by the international scientific community. In addition, a substantial number of on-site workers are expected during the construction, as well as large indirect occupational benefits and spin-off opportunities. The expected economic impact on the hosting territory is also significant and has been evaluated in the order of 2 billion Euro.

The main objective of this Report is to provide the DTT Team members and the international scientific community with a snapshot of the current status of the DTT Project. This report would also like to assess that the DTT scientific project is a crucial step in the frame of the European fusion development roadmap, playing a crucial role for the development of one of the most promising technologies for an alternative, safe and sustainable new energy source. The DTT Team believes that its mission, in agreement and in collaboration with the entire international scientific community, is an essential support for the improvement of knowledge in view of the realization of DEMO.

R. Albanese, F. Crisanti, P. Martin, R. Martone, A. Pizzuto.

April 2019

Contents

Acknowledgements

The DTT Team gratefully thanks:

- Italian MISE and MIUR, and Regione Lazio for their financial support;
- The European Commission for the consideration of the DTT project;
- EUROfusion General Assembly, PEX Ad Hoc Group, PM Unit, ITER Physics Department, and Work Package WPDTT1 for their useful contribution to the DTT initiative;
- Fusion for Energy, ITER Organization, ENI, MIT/PFSC, and CFS for useful discussions;
- The DTT Cost Revision Committee for its excellent analysis and useful suggestions;
- The Chinese Academy of Science for the joint cooperation on DTT and CFETR development;
- CEA (France), EPFL (Switzerland), IPPLM (Poland), IST (Portugal), KIT (Germany), and VR (Sweden), VTT (Finland) for their interest to contribute the PEX activities connected to the DTT project.

Chapter I

EXECUTIVE SUMMARY

I.1 Introduction

The goal of the research on nuclear fusion is to master the process which drives the stars and to reproduce it in a device on earth to generate safe, clean and CO_2-free electricity. DTT is a key player in this worldwide effort. To achieve this breathtaking goal the community tries to confine with magnetic field a hot, dense and stable plasma in a doughnut shaped container for times long enough. The struggle to achieve these conditions has driven most of the research in the last decades and has produced significant results. More recently, it has been realized that the fulfillment of an additional requirement may be on the critical path: the management of the energy extracted from the plasma. In a reactor, most of it will flow out isotropically through neutrons, which will be absorbed by appropriate blankets around the machine. However, a significant amount of thermal power will be lost by the plasma as radiation, convection and conduction. The latter two, in particular, originate very high and localized heat loads on the device first wall, and in particular on the divertor, which is the system that collects the energy flowing out from the plasma through charged particles.

The urgency for a research effort on the plasma exhaust issue and on the divertor is now broadly recognized in the international community, and in particular in the European Fusion Roadmap [I.1-I.2], as one of the main challenges in view of the construction of a demonstration plant (DEMO, the first nuclear fusion power plant able to provide power to the electric grid by the second half of this century). In ITER [I.3], the International Fusion experiment for magnetically confined plasma, presently under construction in

Cadarache, France, it is planned to test the standard baseline approach to the power exhaust issue with a metal divertor operating in a plasma fully detached condition, i.e. without contact between plasma and first wall of the vessel. This solution could be unsuitable for the operating conditions of DEMO and future reactors. Lacking alternative solutions, the problem of thermal loads on the divertor might be a showstopper for the realization of the reactor.

For these reasons, the European roadmap plans to bring an alternative exhaust strategy to a sufficient level of maturity to secure the DEMO Engineering Design to proceed even if the performance of the baseline divertor was not entirely satisfactory. For the alternative approaches the extrapolation from existing proof-of-principle devices to DEMO based on modelling alone is considered too large. As stated in the European Fusion Roadmap [I.1-I.2], the intermediate step for testing alternative concepts is the Divertor Test Tokamak (DTT) facility. This tokamak has to carry out a number of scaled divertor experiments, under integrated physics and technical conditions that can reliably be extrapolated to DEMO. DTT should therefore have the possibility of testing different divertor magnetic configurations and technologies, including liquid metal divertor targets, and other promising solutions to cope with the power exhaust problem.

The original DTT proposal was presented in 2015 [I.4] and described in detail in [I.5]. This Interim Design Report (IDR) presents the outcome of the Italian DTT design review, which led to an up-down symmetric tokamak with major radius of 2.11 m, minor radius of 0.64 m, toroidal field of 6 T, plasma current of 5.5 MA, and pulse duration of about 100 s. In particular, the IDR illustrates the rationale for the design choices, focusing on the main differences with respect to [I.4-I.5], namely for magnet system, plasma scenarios, vacuum vessel, in-vessel components, thermal shield, neutron shield, and additional heating system.

I.2 The Challenge of Power Exhaust

I.2.1 Magnetic fusion as an energy source

Nuclear fusion is the process that powers the sun and the stars, making life on Earth possible. It is called "fusion" since the energy is produced by combining light nuclei (hydrogen isotopes) at extremely high temperatures (15 million degrees Kelvin in the sun, more than 100 million degrees Kelvin in laboratory devices). In the fusion process, part of the reactants' mass is converted into kinetic energy of the reaction products (helium and a neutron for the deuterium-tritium reaction), which in turn can be transformed into electric energy within a standard steam turbine cycle.

Nuclear fusion is among the energy sources able to guarantee the world energy sustainability without CO_2 production. Fusion can effectively contribute to meet the quick growth of the global energy demand, expected to more than doubling by 2050, due to the combined effect of the increases of population and energy needs per person in developing countries.

Controlled nuclear fusion will provide a source of energy:

- Environment-friendly: the products of the most promising fusion reaction (Deuterium-Tritium, D-T) are just helium and neutrons. No long-term, radioactive wastes arise and, with a proper choice of materials for the reaction chamber, the radioactivity induced in structural components decays in a relatively short time, compared to the values in carbon-fired plants.

- Intrinsically safe: no chain-reaction is possible, since a very small amount of fuel is needed in the vacuum vessel; as a consequence, in case of damage, accident, or loss of control, fusion reactions and heat generation will very rapidly and automatically switch off.
- Sustainable: the fuel, deuterium and tritium (the latter produced from lithium inside the reactor), are widely available in nature and virtually unlimited (deuterium is abundant in sea water and lithium both in rocks and ocean water).
- CO_2-free: there is no production of greenhouse gases.

At the extremely high temperature needed to achieve fusion on Earth, the fuel is in the "plasma state", a particular condition where the atoms are fully ionized, i.e. split in ions and electrons. The containment of such a hot gas cannot be carried out by a conventional vessel. To solve this issue, two options are available.

The first, named "inertial fusion," consists in compressing and heating the fusion fuel in a very quick process, by means of a set of powerful laser beams; as a consequence, the nuclei are forced within distances so short that the fusion reactions are suitably triggered.

The second, named "magnetically confined fusion", uses a magnetic field to maintain the hot fuel “detached” from the wall. The plasma ions and electrons are trapped by the magnetic field, which limits the cross-field movements; however, charged particles can move freely along the parallel direction. If designed in such way to form nested magnetic flux surfaces, the magnetic field acts as a special container, preventing the charged particles from hitting to the surrounding material walls. Among the various magnetically confined configurations, the ''tokamak'' is able to provide the best performance (see Fig. I.1).

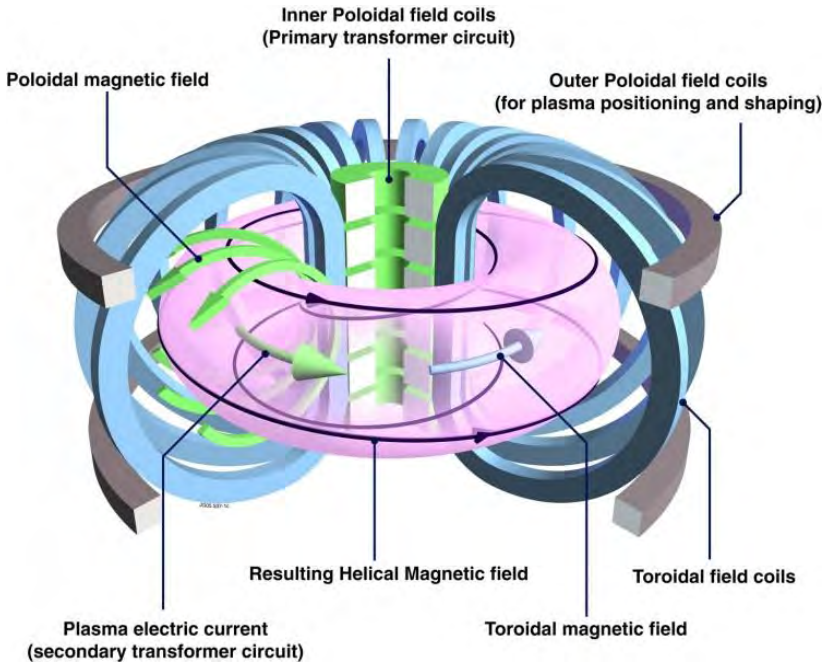

Figure I.1: The tokamak: magnetic field coils and the resulting field able to confine the plasma.

I.2.2 Power exhaust and scenario integration issues

In 2012 European Fusion Development Agreement (EFDA) published a document on the European Fusion Roadmap [I.1], revised by EUROfusion in 2018 [I.2]. These documents propose a strategic vision toward the generation of electrical power by a Demonstration Fusion Power Plant (DEMO), by 2050.

The roadmap elaborates eight critical strategic missions to tackle the main challenges to achieving this ambitious goal. In particular, mission n. 2 ("*Heat-exhaust system*") of the Road Map is aimed at carrying out alternative solutions to the problem of disposing the heat load.

The confinement in a tokamak reactor [I.6] is the result of magnetic field lines forming a set of closed, nested magnetic surfaces. At the edge of the plasma (Fig. I.2), a thin (order of few millimeters) region with open field lines appears (Scrape-Off Layer, SOL). In a steady state magnetically confined fusion plasma the power which is injected into the plasma through auxiliary heating systems plus that produced by fusion reactions needs to be extracted from the device. Charged particles, which escape with their energy the confinement magnetic field, flow out from the core plasma through the SOL and are eventually exhausted in a narrow region of the chamber called divertor. Charged particles (and their related energy) flowing out from the core plasma through the SOL are directed to the divertor plates towards the separatrix (the last closed magnetic surface). The heat flux parallel to the magnetic field, in the SOL region of ITER and DEMO, is expected to be comparable to that on the sun's surface.

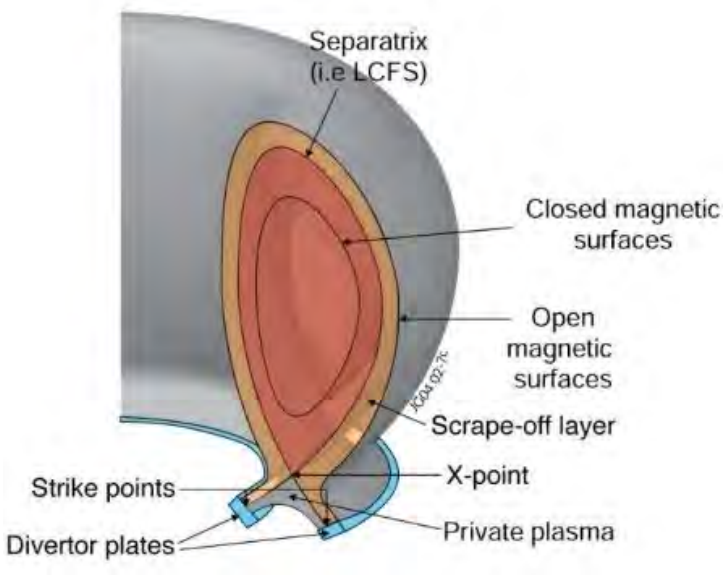

Figure I.2: Plasma edge: geometry of the Scrape-Off Layer (SOL) and of the divertor plates.

The strategy to cope with the problem of thermal loads on the divertor in DEMO and in future reactors relies upon several factors:

- development of plasma facing components able to cope with very large power fluxes (>10 MW/m^2) based on materials of reactor interest;
- selection of the divertor geometry and of the magnetic flux map such as to reduce the normal heat flux on the target, and therefore able to distribute the heat over a larger surface;
- removal of plasma energy before it reaches the target, via impurity radiation; this goal is pursued by increasing edge plasma density and injecting impurities (other substances than products and reagents) in the SOL region; in this way the fraction of the heating power impinging on the divertor is reduced up to a level compatible with the present available technology (about 10 MW/m^2);
- recycling of the particles released by the wall and increase of the density close to the plates, resulting in a "detachment" from the wall of the plasma; the temperature drops below the ionization threshold, the

particles become neutral and are not any more constrained by the magnetic field; consequently, no direct energy flow affects the divertor plates.

Any strategy for the solution of thermal loads problem must consider that:

- present experiments, where "detached" plasma conditions are obtained in small and medium size tokamaks, are characterized by conditions of the SOL region very different from those expected in ITER and DEMO;
- simulations with the available physics models for the study of SOL are presently not sufficiently reliable;
- stability of the detachment front has yet to be experimentally assessed for ITER and DEMO conditions;
- various problems might arise related to integration of this solution with the plasma core and the other reactor subsystems, e.g.:
    - impurity contamination of the core with consequent reduction in the efficiency of the confinement and in the general performance of the reactor;
    - compatibility of bulk plasma with the very high requested radiation fraction (> 90%);
    - compatibility with pumping of the particles;
    - monitoring of erosion, temperature, etc.

Moreover, a number of nuclear aspects must be taken into account, restricting the use of certain materials, e.g., requirements in terms of life expectancy of reactor components, the need of limiting the temperature in the divertor region to take vanishing the erosion rate.

I.3 DTT Role and Objectives

I.3.1 DTT role and objectives

The solution to adopt a conventional divertor (which will be tested in ITER) may not be suitable for extrapolation to DEMO. In order to mitigate the risk, alternative solutions must be developed. The DTT facility is designed to explore all the lines mentioned above in regimes – in particular as far as power loads are concerned – relevant for ITER and DEMO and where plasma core and edge properties are fully integrated.

While several alternatives, such as the cooled liquid Li limiter in FTU [I.7], the Super-X divertor in MAST-U [I.8] or the Snowflake divertor in TCV [I.9] are being investigated in presently operating tokamaks, the extrapolation from present devices to DEMO is considered not reliable [I.1-I.2].

DTT is part of the general European programme in fusion research, which includes many other R&D actions like experiments, modeling tools, and technological developments for liquid divertors. The specific role of the DTT facility is to bridge the gap between today's proof-of-principle experiments and the DEMO reactor. DTT should, in particular, have the capability to bring such solutions to a sufficient level of maturity and integration from both physics and technology points of view.

In this way, it will possible to integrate the knowledge about the concepts of a number of divertor presently under testing in existing machines, with the implementation requirements of DEMO.

The main objectives of DTT, as reported in a number of official European documents [I.2], can be summarized as follows:

- test whether the alternative divertor solutions (e.g., advanced divertor configurations or liquid metals) can be technically integrated and are able to withstand the strong thermal loads in the DEMO device if the fraction of radiated power turns out to be lower than expected;
- improve the experimental knowledge in the heat exhaust scientific area for parameter ranges that cannot be addressed by present devices.

In particular, it will be possible to assess whether:

- the alternative divertor magnetic configurations are viable in terms of the exhaust problems as well as of the plasma bulk performances;
- the alternative divertor magnetic configurations are viable in terms of poloidal coils constraint (i.e., currents, forces, etc.);
- the various possible divertor concepts are compatible with the technological constraints of DEMO;
- the divertors based on the use of liquid metals are compatible with the characteristics of the edge of a thermonuclear plasma;
- liquid metals are applicable to DEMO.

I.3.2 DTT in the European Fusion Roadmap

At the 21st General Assembly (GA) of EUROfusion on 11-12 April 2018 in Sofia, it was agreed:

- to finalise the description of the Key DTT Milestone: DTT ready for completion at low risk;
- to define a Key Power EXhaust (PEX) Milestone: readiness for decision on the PEX Divertor option to be tested on DTT;
- that the Program Manager, in contact with the STAC Chair and the PEX Ad Hoc Group (AHG) Chair, elaborates a proposal on the organisation of the EUROfusion follow-up of the DTT project and PEX programme;
- to earmark 60 M€ in FP9 for PEX on DTT;
- that whichever Key Milestones comes first (DTT or PEX), this will trigger the GA to make a decision on the most appropriate involvement of EUROfusion in DTT.

Afterwards, the PEX Ad Hoc Group, in contact with the DTT Executive Board, defined a set of common milestones [I.10]:

- COM.M1: DTT final design consistent with the requirements for testing alternate exhaust concepts based on the knowledge at the time;
- COM.M2: Decision on the first DTT divertor;
- COM.M3: Assessment of the interfaces and exhaust infrastructure and diagnostic opportunities in DTT.

I.4 Main Parameters

The relatively high toroidal field (B_T = 6 T) will give the possibility to achieve plasma performances (mainly measured by the ratio between power and major radius of about 15 MW/m), not far from those in DEMO. After the publication of the special issue of Fusion Engineering Design in November 2017 [I.5], the DTT Team has continued its activity to improve and refine the project, also in the light of some suggestions of EUROfusion. In addition, several technical and organizational activities to start the realization have been undertaken. The main topics addressed in this review activity include:

- Site selection: in April 2018 the final decision was to allocate the machine at the ENEA Research Center in Frascati (Rome);
- Cost revision: in March 2018 a Cost Revision Committee has been appointed to assess the construction costs and give robustness to the economic analysis of the project;
- Symmetrization: the DTT geometry is now up-down symmetric, so as to allow the introduction of an additional divertor and the realization of double-null configurations;
- Parameter assessment (Tab. I.I and Appendix A): the revision process led to a slight reduction of the major and minor radius (2.11 m and 0.64 m, respectively) and plasma current (5.5 MA) leaving the magnetic field unaltered (6.0 T);
- Additional review elements: a careful analysis was made taking into account nuclear, mechanical, thermal, and MHD issues, and leading to a revision of the main components and the various contributions to the additional heating; the maximum DD neutron yield estimated in H-mode high performance operations is $1.5 \cdot 10^{17}$ n/s with $1.5 \cdot 10^{15}$ n/s DT neutrons (i.e. 1%) from triton burn-up, which makes remote handling needed also in the first phase of operation;
- Management organization: a legal entity will be estabilished in 2019 so as to deal with the complex challenges of DTT construction and operation; meanwhile, an Interim Executive Board and an Interim Project Committee have been established for the general management of the project and the coordination of the various activities, respectively;
- DTT Interim Design Report: this “Green Book, available in web site [I.11], represents an updated version of the “Blue Book” [I.4].

TABLE I.I. MAIN DTT PARAMETERS FOR A SINGLE NULL CONFIGURATION

Parameter	Value
R (m)	2.11
a (m)	0.64
R/a	3.3
Volume (m^3)	29
q_{95}	3
I_p (MA)	5.5
B_T (T)	6.0
H_{98}	1.0
Pulse length @EOF (s)	90

I.5 Operational Programme

Fig. I.3 shows a schematic planning of the DTT operations. The first phase of the scientific program will aim at the realization and installation of the various components of the machine. In a subsequent phase the machine will reach the operative capability with a robust H-mode (i.e. operating regimes characterized by configurations of single-null divertor type, top performance and with all the additional power installed).

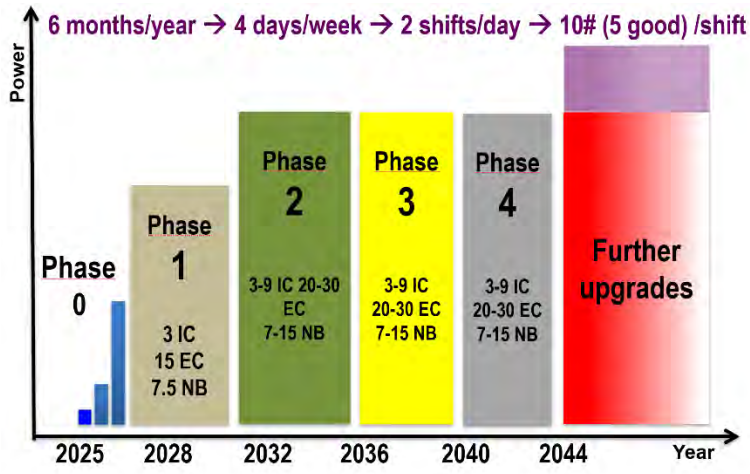

Figure I.3: Schematic planning of a possible DTT experimental program starting with single null plasmas., In Phases 1-2 the power is increased up to full performance. Phases 3-4 are devoted to alternative magnetic configurations and liquid metal divertors.

The next phases will be reserved to test a number of alternative divertor solutions, including new magnetic configurations and innovative technologies in the liquid metal.

The ambitious program of DTT is spread over a period of several years. During the initial plasma operations 3 MW of ICRH, 14.5 MW of ECRH, and 7.5 MW of NNBI will be available. Additional power, up to a total of 45 MW, will be afterwards installed, on the basis of the results of Phase 1 and the technologies available in the 2020's. The project foresees the testing of different magnetic configurations and divertor concepts; as an additional goal, also the solution based on the technology of liquid metal will be explored and optimized.

DTT will operate in parallel with ITER, likely before its high-performance operations. So, DTT could support and complement the ITER experimental program, paying attention to high priority issues like disruption avoidance/mitigation, R&D needs in plasma facing components, ELM pacing, and plasma control.

I.6 Plasma Performance

The DTT machine is able to host various configurations with the minimum plasma-wall clearance of 30 mm inboard. The plasma shape parameters for reference single null configuration are similar to those of the EU DEMO ($R/a \approx 3.3$, $k \approx 1.75$, $\langle\delta\rangle \approx 0.3$). The typical plasma parameters are shown in Tab. I.I and Fig. I.4 for the

standard and advanced configurations (mainly focused on X-Divertor and Snow Flake (SF) equilibria). In the DTT proposal [I.4], there was no mention about the DTT possibility to realize “long leg”, negative triangularity and Double Super-X (DSX) configurations, since the study of these configurations had been given a secondary priority. However, DTT will have the possibility to realize “long leg” configurations at I_p = 5 MA with a “standard” divertor geometry. A single null 5 MA plasma with negative triangularity and a DSX configuration will be feasible with I_p = 3 MA and $R_{Strike}/R_X \approx 1.5$, but these will require a dedicated divertor. With the use of the internal coils is possible to locally modify the poloidal magnetic field to obtain ideal SF, SF plus, SF minus and X-divertor configurations. The presence of the stabilizing passive plates outboard connected to the vacuum vessel via sidewalls allows good breakdown and vertical stability performance for all configurations except the DSX 3 MA plasma, where a modification of the in-vessel components would be needed.

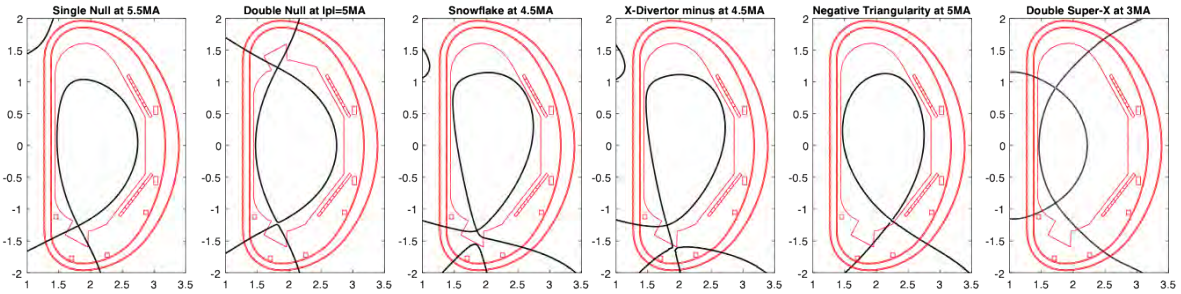

Figure I.4: Single Null (5.5 MA), Double Null (5 MA), Snow Flake (4.5 MA), X-Divertor (4.5 MA), Negative Triangularity (5 MA) and Double Super-X (3 MA) configurations at flat top. The DTT magnetic system is also compatible with a 5 MA long leg configuration. Negative Triangularity and Double Super-X require a dedicated divertor.

I.7 Basic Machine

I.7.1 Rationale of the design review

The design review process is carried out following the same requirements as in the original proposal. These include approximate preservation of non-dimensional DEMO parameters, integrated scenarios with solutions compatible with DEMO plasma performance and technological constraints, ratio of at least 15 MW/m between power crossing the separatrix and the major radius, possibility to test alternative magnetic configurations and liquid metal divertors.

The design review took also into account the conclusions of the DTT Workshop held at Frascati in June 2017, where various points had been examined to improve the proposal in the design review phase [I.12]. One feature is the flexibility of the machine, in order to be able to incorporate the best candidate divertor concept (e.g. conventional, snowflake, super-X, double null, liquid limiter), expected by about 2022. Up-down symmetry has been required to test double null configurations properly. Another important point is the additional power coupled to the plasma needed to guarantee significant results in view of DEMO.

Thus, the main aim of the first general DTT Design Review Meeting DRM-01, held in 2018, was the implementation of the changes indicated in the DTT Workshop, with the definition of an up-down symmetric

basic machine (Fig. I.5). The second general DRM-02 made a critical review of the activities discussed in a number of fortnight technical review meetings.

As an outcome of DRM-01 and DRM-02, the minor radius has also been reduced, with a minor increase in the aspect ratio, while the additional power coupled to the high-performance plasma is unchanged (45 MW). The remaining parameters have been obtained by means of 0-D simplified models usually adopted by system code tools (see Tab. I.I), achieving performance similar to the original proposal with increased flexibility at a fixed budget. The design solutions for the magnets and the vacuum vessel are also more effective than in the original proposal [I.4].

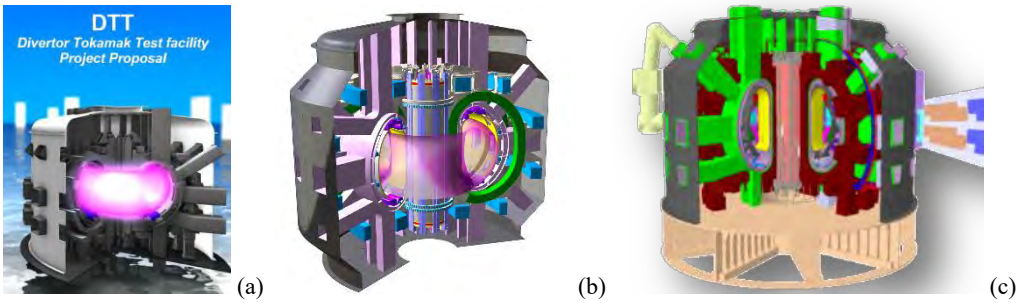

Figure I.5: DTT: a) original proposal (2015); b) outcome of DRM-01 (2018); c) outcome of DRM-02 (2019).

I.7.2 Radial build

The inboard radial build takes into account the inboard radius of the plasma (1.47 m), a minimum clearance of 30 mm between plasma and first wall, with 55 mm for the first wall structure and the in-vessel magnetic diagnostics. In the inboard side, the vacuum vessel is a structure with two shells of SS AISI 316 LN, each of them 15 mm thick, separated by a neutron shield of 90 mm with 65 mm of borated water and 25 mm of SS/B_4C/W/B_4C/SS sandwich. A 20 mm thick thermal shield operating at 80 K is located behind the vacuum vessel with a gap of 20 mm. The structure of the inner legs of the TF (toroidal field) coils spans from 820 to 1180 mm (whereas the winding pack spans from 908 to 1149 mm). Finally, the Central Solenoid (CS) consists of six identical modules wound in two layers, spanning from 437 to 759 mm. This radial build allows also for the insertion of an independent High Temperature Superconducting (HTS) coil. This additional solenoid might test this enabling technology for next generation fusion reactors and increase the flat top duration, raising the stored magnetic flux by about 1 Vs.

The radial build in the outboard is driven by the requirement on the ripple $(B_{max}-B_{min})/2B_0 < 0.5\%$. To achieve this, the winding pack of the outboard TF coil leg in the equatorial plane spans from 3721 to 3962 mm. This leaves a plenty of space in the outboard, where the first wall is located at a radius of 2.86 m, i.e. with a gap of 110 mm from the nominal single null plasma. This guatantees suitable flexibility for alternative plasma shapes. The vacuum vessel in the outboard has two 15 mm thick shells, with an inner radius of 3.17 m, leaving space to the in-vessel coils and the magnetic diagnostics. The cavity between the shells in which the borated water flows is larger than the inboard (200 mm).

I.7.3 Superconducting magnet system

To allow the DTT machine to investigate the wide range of different scenarios which are foreseen, the present Magnet System (Fig. I.6) is based on 18 Toroidal Field (TF) Nb_3Sn coils, operating at a peak field of 11.8 T and

a conductor operative current of 44.0 kA, a stack of 6 independently fed Central Solenoid (CS) modules, operating at 13.2 T and 29.9 kA, and 6 Poloidal Field (PF) coils, 2 of them reaching about 8.5 T and 35.0 kA (thus made of Nb_3Sn CICCs) and the other 4 working at lower fields and currents, relying on NbTi conductor technologies. The magnet system is fully symmetric with respect to the equatorial plane, with the PF coils designed to be identical in pairs.

The TF coils are now wounded in double pancakes and work in wedged condition, so a full set of Inner Inter-coil Structures (superbolts + pins) is foreseen to face the shear force between adjacent TF coils, whereas *ad-hoc* designed Outer Inter-coil Structures (OIS) give supports against the out-of-plane loads.

The present graded design of the CS allows for a saving of about 8 tons of expensive Nb_3Sn strand and enables the possibility of reaching the required high performance in terms of engineering current density and thus of magnetic flux (about $\pm$16.2 Vs).

The magnet system is compatible with a possible future upgrade, consisting in the insertion of an additional High Temperature Superconductor (HTS) coil inside the original CS bore at a later stage. This insert would give a modest and unnecessary increase (about $\pm$1 Vs) of the available flux, but it would achieve the technological target of demonstrating the feasibility of fusion magnetic confinement using HTS.

The PF system also includes six copper in-vessel coils; in particular:

- two in-vessel copper coils for radial and vertical stabilization and control;
- four in-vessel copper coils for magnetic control of SOL and strike point sweeping.

To pursue the aims of the program, particular attention has been devoted to the diagnostics and control issues, especially those relevant for plasma control in the divertor region, having in mind the requirement of a strong compatibility with the operating conditions in DEMO.

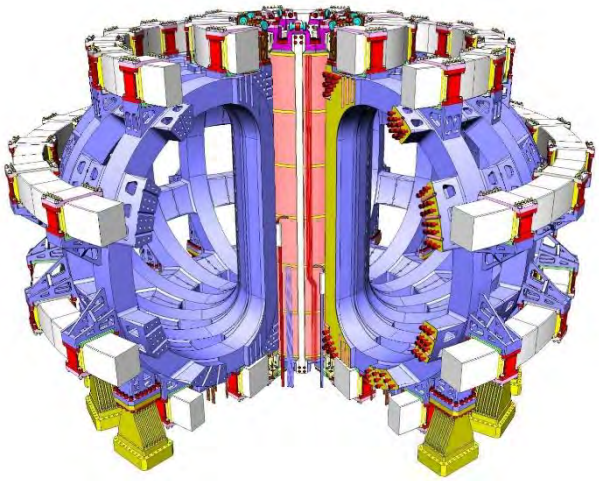

Figure I.6: The DTT superconducting magnet system, with 18 D-shaped TF coils, 6 PF coils, and a central stack of 6 CS modules.

I.7.4 Vacuum vessel and nuclear shield

The vacuum vessel, which was a single shell of INCONEL in the original proposal, has been modified into a double wall structure with ribs, having two shells of SS AISI 316 LN, each of them 15 mm thick and separated by a neutron shield in which borated water flows at 50-80 °C. The thickness of the neutron shield is 90 mm

inboard (with 25 mm of solid components) and 200 mm outboard. This neutron shield is designed for a DD neutron yield rate of $1.5 \cdot 10^{17}$ n/s (plus $1.5 \cdot 10^{15}$ n/s of 14 MeV neutron production due to triton burn-up) during the high-performance phase. This keeps the nuclear heating of the first TF coil layer below 1 mW/cm^3. The 18 sectors are joined by welding. The thickness of each shell is 15 mm while the 5 ports per sector have a 25 mm thick single shell. The elongation of the cross section of the vessel has been enhanced to reserve sufficient space to the divertor region. Fig. I.7 shows the vessel ports, dedicated to divertor remote handling, pumping, connections, heating and diagnostics.

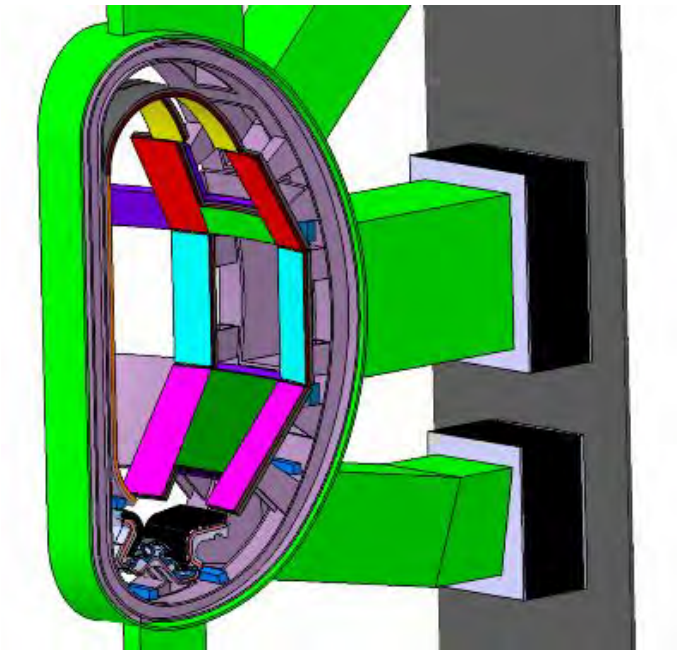

Figure I.7: A 20-degree sector of DTT, showing the double wall vacuum vessel in SS 316 LN, the single wall ports made of the same material, the first wall, the in-vessel coils, and part of the cryostat.

I.7.5 Additional heating system

DTT needs a significant amount of heating power for its size. In the initial phase 25 MW will be available, with the following heating mix: 15 MW of Electron-Cyclotron Radiofrequency Heating (ECRH) at 170 GHz with 16 gyrotrons, 3 MW of Ion-Cyclotron Radiofrequency Heating (ICRH) at 60-90 MHz, and 7.5 MW of Negative Neutral Beam Injection (NNBI) provided by a single tangential injector. The heating mix for the full performance of DTT will be decided at a later stage within the following ranges: 20-30 MW of ECRH, 3-9 MW of ICRH, and 7-15 MW of NNBI. The decision on the NNBI should be taken earlier since the insertion of an additional NNBI tangential injector has an impact on the design of the vacuum vessel.

Fig. I.8 shows the overall view of the NNBI system (based on 400 keV beam energy), the transmission lines of the ECRH system (to be realized in vacuum), and the different ICRH antenna concepts presently considered in the design, for which the final decision will be taken on the basis of the results of a set of experiments to be carried out in EAST.

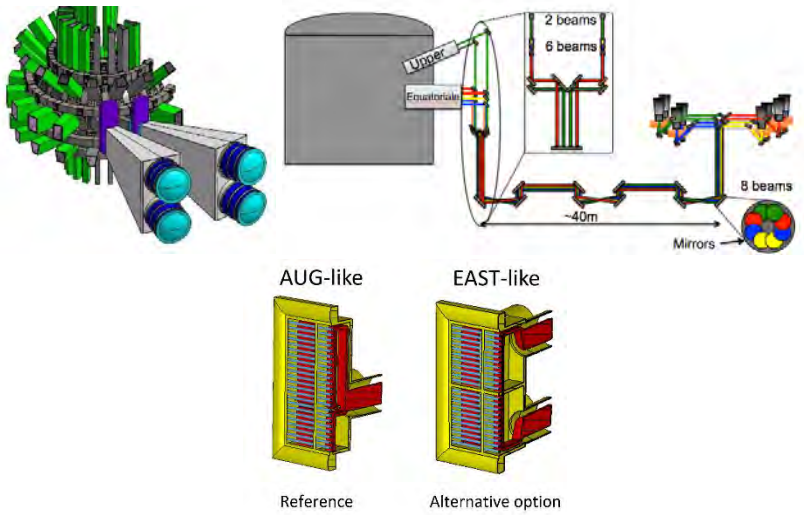

(a) *(b)* *(c)*

Figure I.8: System for heating: a) NNBI system; b) ECRH transmission lines; c) ICRH concepts considered for DTT.

I.7.6 In-vessel components

The main in-vessel components revisited in the design review include the first wall, the divertor, the in-vessel coils and the magnetic diagnostics. The design of other components (pumps, gas puffing systems, non-magnetic diagnostics) is ongoing.

The First Wall (FW) is designed with coaxial pipes [I.13]. Two alternative concepts are considered, one in CuCrZr and one in stainless steel, both coated with a 3 mm W layer deposited by plasma spray technique. It shall be compatible with the closed loop of liquid metal divertors and therefore be kept at a temperature above 200 °C.

As stated in Section I.3.3, if the PEX Key Milestone is achieved before DTT is ready for completion at low risk (around 2022-23), the optimal divertor configuration in view of DEMO will be identified on the basis of the outcome of the power exhaust studies together within EUROfusion,. In this case EUROfusion will contribute to the construction of the divertor, otherwise the EUROfusion contribution will be addressed to the additional heating. In the meanwhile, the baseline DTT design refers to an actively cooled conventional tungsten divertor, compatible with both SN and SF or XD configurations, segmented in 54 toroidal sectors or cassettes with inner and outer vertical target and a dome.

DTT is designed to test liquid metal divertors in a later phase. Two different techniques are being considered: capillary porous system and “boxes/pools” of liquid metal especially for Li for which evaporation is very important [I.7, I.14].

The in-vessel components also include:

- 2 independent n=0 copper coils and 2 stabilizing plates for vertical stabilization, fast radial control during breakdown and H-L transitions, and double null wobbling;
- 4 independent n=0 divertor coils for magnetic configuration control in the divertor region and strike point sweeping;
- a number of n>0 ELM/RWM coils.

I.7.7 Out-vessel components, auxiliaries, diagnostics and power supply system

The main out-vessel components revisited in the design review include port collars to reduce the nuclear heating, the thermal shield and the cryostat.

The DTT cryogenic system includes the following subsystems:

- A Warm Storage System (WSS) having sufficient capacity to store the whole helium inventory required for the cryogenic plant, where one of the vessels will be used for quench recovery;
- Liquid nitrogen storage tanks;
- A Warm Compression Station (WCS), including the Oil Removal System (ORS) and a full flow dryer;
- A Refrigeration Cold Box (RCB);
- An Auxiliary Cold Box with thermal dampers, connected to the RCB and to the tokamak by means of dedicated super-insulated cryogenic lines.

DTT is actively cooled. The cooling system of DTT, designed for a thermal power of more than 120 MW in a pulse of about 100 s, adopts a closed loop cooling water system, divided into 2 circuits: primary circuits (Divertor, First Wall, ECRH, ICRH, NBI, Electrical Power Supply and Cryoplant) filled with demineralized water and a secondary circuit filled with cooling water designed for working with pressure under 16 bar.

The power supply system has to feed 6 superconducting modules of the central solenoid, 6 poloidal field superconducting coils, 18 toroidal field superconducting coils designed for a current up to 45 kA, the in-vessel coils for plasma fast control and vertical stabilization, the ELM/RWM coils, the negative neutral beam injectors, the electron and ion cyclotron additional heating systems, and, finally, the auxiliary systems and services.

Diagnostics include mandatory systems for machine protection, safety (subject to regulatory standards), feedback control of relevant plasma parameters and a set of solutions to qualify in detail both divertor and core plasmas. To comply with the specific mission of DTT, the emphasis is on the diagnostics that evaluate the power exhaust channels and on those systems that allow keeping control of heat and particle disposal while preserving the integrity of the machine components and the quality of the plasma performance.

The experimental data and other signals (collected by the SCADA) will be handled and stored in the Historical Experiment Database (HED) using a software framework like MDSPlus. All the acquired data will be accessible via dedicated software interfaces, e.g. mimics will allow the real-time monitoring of the DTT plants.

The DTT Data Management System is based on a dedicated HW/SW infrastructure which allows the use of Virtual Machines thanks to the VMWare Technology. This infrastructure will host several DTT software services such as the Documentation Management System (DMS) based on the Alfresco SW platform, the Website, the Wiki pages, and the Indico collaboration tool.

I.8 Cost, Schedule and Licensing

The facility needs to be ready by 2025, in order to be able to bring at least one alternative divertor strategy to a suitable level of maturity around 2030 for a positive decision on DEMO. The nominal duration of the construction of DTT from the "green light" to the beginning of the initial operational phase is expected in about seven years.

The exploitation of DTT scientific program has been included in the European Road Map towards fusion energy. The realization of the facility has been submitted to European Fund for Strategic Investments (EFSI), to be considered for the funding of 50%, out of the whole investment, as part of the so-called "Juncker Plan". The DTT investment cost quoted on the basis of the Project Proposal [I.4] has been evaluated upon different bases: i) Direct experience in similar procurements; ii) Industry budgetary quotations; iii) Scaling from the cost of similar devices.

An independent cost revision has been committed to a panel composed by experts in fusion devices, considering the design features of the Project Proposal [I.4]. The panel made an excellent analysis, based on a statistical approach and considering also the design uncertainties. This proves a useful advice and recommendations, exploited when introducing the design changes discussed in two DTT Design Review Meetings. The Terms of Reference given to the Panel implied to carry out the cost revision based on the "Blue Book" [1.4]. These were given knowing that the Panel output could not be synchronized with the ongoing design review activity. This approach was followed on purpose in order to have from the Panel some important indications on the main actions needed to simplify the design so as to remain within the budget. In the near future, the Panel will analyze again the components that underwent to significant simplifications, leading to considerably less expensive concepts (including magnets and vacuum vessel).

The main milestones of the DTT project are reported in Appendix B. The first milestone (launch of market survey on SC strands) has already been met in 2018. A risk analysis is being carried out paying attention to the mitigating actions especially in case of delays and unexpected increases of costs.

The management of the project is planned to be carried out by means of a DTT Consortium. Negotiations with the potential partners are going ahead. Meanwhile, the activities are carried out by ENEA with the support of CNR, Consorzio CREATE, Consorzio RFX and several Italian Universities. The management is assigned to an Interim Executive Board and the activities are coordinated by an Interim Project Team (Appendix C).

The choice of the site took into account the mission of DTT as "European facility". In this perspective, significant elements for the selection of the site have been the accessibility and the scientific attractiveness for staff (scientists and engineers) that, coming from many European countries and beyond, will carry out the construction and promote experimentation.

The site, selected as a result of a Call for Interest addressed to the Italian Regions, is the ENEA Research Center in Frascati (Rome, Italy). The selected site is, indeed, compliant with the whole specifications of the location. Frascati is also a fairly attractive site from cultural and logistic standpoints.

Construction and operation of DTT will require the usual authorizations prescribed by national laws, i.e., the building and practicability permits, the anti-seismic certificate, the fire prevention certificate and the certificate related to environmental goods. In addition, DTT must undergo to the control of the national authorities for the purpose of the radiation protection, also referred to as nuclear safety. Pursuant to Italian law, the DTT licensing process for nuclear safety is that of a radiogenic machine classified in category A, certified with a specific decree from the Italian Minister of Economic Development. The Nuclear Safety permit has to be obtained before the beginning of the DTT nuclear operations, i.e. before the ionizing radiation production. The nuclear safety is strictly connected to the safety analysis and to the radiation protection and, in particular, it has to deal with the radiological environmental impact and the radioactive waste management. These arguments are therefore considered in the current approach, to set up the further developments and the technical documents to be attached to the license application.

I.9 Conclusions

After the design review, DTT is an up-down symmetric tokamak with a major radius of 2.11 m, a minor radius of 0.64 m, a toroidal field of 6 T, a plasma current of 5.5 MA, and a pulse duration of about 100 s. The power mix has been fixed in phase 1 when 25 MW will be coupled to the plasma with 15 MW of ECRH, 3 MW of ICRH, and 7 MW of NNBI. Instead, heating mix for the full performance of DTT will be decided at a later stage within the following ranges: 20-30 MW of ECRH, 3-9 MW of ICRH, and 7-15 MW of NNBI.

Substantial changes have been made also on the magnet system, the vacuum vessel, the neutron shield and the thermal shield, with a significant improvement of the efficiency.

I.10 References

[I.1] Fusion Electricity – A roadmap to the realisation of fusion energy, November 2012, *https://www.euro-fusion.org/wpcms/wp-content/uploads/2013/01/JG12.356-web.pdf*

[I.2] European Research Roadmap to the Realisation of Fusion Energy, November 2018, *https://www.euro-fusion.org/fileadmin/user_upload/EUROfusion/Documents/2018_Research_roadmap_long_version_01.pdf*

[I.3] *http://www.iter.org/*

[I.4] DTT Divertor Tokamak Test facility, Project Proposal, ENEA, 2015, ISBN:978-88-8286-318-0, http://fsn-fusphy.frascati.enea.it/DTT/downloads/Report/DTT_ProjectProposal_July2015.pdf

[I.5] Special Section of Fusion Engineering and Design, Vol. 122, 2017, pp. 253-294 and e1-e25

[I.6] Wesson J., "Tokamak", Oxford University Press 2011 – 4th Edition

[I.7] Mazzitelli G. et al., Nucl. Fusion, 51, 073006, 2011

[I.8] *http://www.ccfe.ac.uk/mast_upgrade_project.aspx*

[I.9] Reimerdes H., et al., Plasma Phys. Control. Fusion 55 (2013) 124027.

[I.10] Zohm H. for the PEX Group, Hold Points on the PEX Programme (towards a finalisation of the PEX phase 3 report), presented at the EUROfusion Bureau Meeting, Garching, October 5, 2018

[I.11] *http://www.dtt-project.enea.it/*

[I.12] Albanese R. et al., Design review for the Italian Divertor Tokamak Test facility, Fusion Engineering and Design, 2018, https://doi.org/10.1016/j.fusengdes.2018.12.016.

[I.13] Maviglia F. et al., "Thermal-hydraulic analysis for first wall and vacuum vessel thermal shield of Divertor Tokamak Test facility, presented at SOFT 2018, Giardini Naxos, Italy

[I.14] Nallo G.F. et al., "Modelling intrinsic impurity deposition on the I-DTT First Wall from a Liquid Metal divertor", presented at SOFT 2018, Giardini Naxos, Italy

Chapter II

ROLE AND OBJECTIVES

II.1 Introduction

The final goal to achieve electric energy from nuclear fusion processes in a magnetically confined plasma calls for an integrated approach to optimize confinement, stability, fueling and energy and particle exhaust. The former theme – i.e. managing the unavoidable exhaust of plasma energy and particles – has been kept for long at relatively lower priority in the fusion community. Since a few years – thanks to a growing amount of experimental and theoretical work – it has been recognized that ITER may not provide a viable solution to the exhaust issue, which needs therefore to be attacked with great urgency and strength in order not to cause delays to the development of fusion. The DTT experiment will provide a unique tool for the solution of that issues, fully integrated in the aforementioned approach.

In a steady state magnetically confined fusion plasma the power which is injected into the plasma through auxiliary heating systems plus that produced by fusion reactions needs to be extracted from the device. Energy in the neutron channel is isotropically collected in the blanket to be converted into electricity and to drive the tritium breeding process. Energy associated to charged particles, which escape the confinement magnetic field, is ultimately exhausted in a narrow region of the reaction chamber called the divertor. Given its purpose the divertor has by definition to withstand high power loads. In addition, the situation is worsened since its “wetted surface” - i.e. the fraction of its surface exposed to the power coming from the plasma – is much smaller than originally foreseen (see for example [II.1]). The wetted surface scales in fact as $\lambda_q \cdot R$, where R is the device major radius and λ_q is the scrape off layer (SOL) power flow decay length, so that the power

flux on the divertor plasma facing components is $q \propto P\, 2\pi\, R\, \lambda_q$, where P is the power leaving the plasma from the non-neutronic channel. A well-established empirical scaling shows that λ_q follows the law [II.2]:

$$\lambda_q(mm) = 1.35\, P_{SOL}^{-0.02} R^{0.04} B_p^{-0.94} \varepsilon^{0.42} \quad \text{(II.1)}$$

where P_{SOL} is the power in the scrape-off-layer, B_P the poloidal magnetic field and ε the aspect ratio. This means no dependence on machine size and a negative dependence on the plasma current.

If this scaling holds true in ITER conditions, then λ_q is expected to be of the order of 1 mm in that device. Considering the Q=10 scenario, with 500 MW of net fusion power (400 MW brought by neutrons and 100 MW lost through radiation and particles) the expected power exhausted on the divertor in a low radiation case is about 90 MW. This would bring a heat flux on the divertor of the order of 50 MWm^{-2}, a value far above the limit of present target materials.

The risk therefore exists that the divertor baseline strategy pursued in ITER, which relies on the existing experience with standard divertors in medium and large size devices, cannot be extrapolated to a fusion power plant. Hence, in parallel to the programme in support of the ITER baseline strategy, an aggressive programme on alternative solutions for the divertor is necessary, as it has also been recognized in the "European Research Roadmap to the Realisation of Fusion Energy" [II.3]. This program is based on three main thrusts:

a) Development of plasma facing components capable to withstand very large power fluxes, including the demonstration that a closed loop liquid metal heat removal system is viable in a tokamak at relevant edge and SOL parameters. At the moment, the technological limit for heat flux on present standard material is ~ 10-20 MWm^{-2}, which is unfortunately much lower than the expected heat fluxes in ITER.

b) Development of the physics understanding of the exhaust process – in particular through first principle models – finalized to the improvement of the divertor design. Aims of divertor studies are the study of modifications of its magnetic topology to decrease the divertor plates power flux by increasing the divertor "wetted" surface, and the exploitation of liquid metals as plasma facing components;

c) Development of plasma scenarios where plasma energy is removed by means of radiation before it reaches the plasma facing components while keeping optimized plasma core performance.

II.2 DTT Role and Objectives

The DTT facility is designed to explore all the three lines mentioned above in regimes – in particular as far as power loads are concerned – relevant for ITER and DEMO and where plasma core and edge properties are fully integrated. As described in detail in Chapter III, to integrate core and edge performance while meeting the budget constraints, a compact, high magnetic field approach based on the weak similarity scaling [II.4] has been chosen. This has led to the present design of the device, characterized by the following main parameters: minor radius a=0.64 m, major radius R=2.11 m, maximum plasma current 5.5 MA and on-axis toroidal magnetic field B=6 T, with an auxiliary power coupled to the plasma of 45 MW, provided by a portfolio of ECRH, ICRH and negative ion beam injection. Superconducting coils will allow for 100 s discharge duration.

These choices guarantee a value of the P_{sep}/R parameter (which is recognized as a key metric for the extent of the exhaust issue in a tokamak, with P_{sep} the power exiting through the separatrix) equal to 15 MW/m, i.e. similar to those foreseen for ITER and DEMO. At the same time, these design choices are compatible with significant plasma core performance that places DTT in a unique operational region, unexplored by present devices including JT-60SA. This makes DTT highly relevant also for a state-of-the-art integrated study of tokamak physics, as recommended also by the EUROfusion ad-hoc group on "Strategy for the Plasma Exhaust" (PEX AHG) [II.5].

The PEX AHG recognizes the need to start a program for risk mitigation actions in case showstoppers for the conventional divertor approach will be found in ITER. It also recommends in fact the development of core scenarios compatible with the conventional divertor and with alternative exhaust schemes.

Avoiding delay for DEMO and an electricity Pilot Plant based on alternative divertor schemes depends – quoting again the PEX AHG – by the ability to combine alternative exhaust schemes qualified in DTT with core scenarios developed through Medium Size Facilities, JT-60SA and ITER using the conventional divertor. The present DTT design, following the inputs from the EUROfusion experts in the 2017 Frascati Meeting, unifies for the first time in a single device both the edge and core scenarios, minimizing therefore the risk of integration of regimes explored in different devices with very different plasma parameters.

Key technical elements for allowing DTT to cope with these challenges are power availability, flexibility, control and accessibility.

The availability of 45 MW coupled to the plasma through different means (see chapter IX) in a high-field, high density, compact and superconducting device allows both for unprecedented combination of power loads on divertor and first wall materials and discharge duration and for tailoring plasma core performance in a variety of regimes, including high radiation ones.

Flexibility is a key choice for the device, both in the design phase and in the operation phase. The machine is in fact being designed flexible enough to accommodate the divertor identified within 2022/23 by EUROfusion as the most relevant for risk mitigation in DEMO and Pilot Power Plant. Up-down symmetry is ensured by the possibility of accommodating both lower and upper divertors, with symmetric divertor magnetic configurations. Negative triangularity configurations will also be available. Single-null, double null, up and down snow-flake, and super-X divertor configuration are all feasible in DTT thanks to the proper design of its mechanical layout and coil systems (see Chapter VII). In the operation phase, flexibility will be ensured in particular by the portfolio of heating systems, by the coil – both external and in-vessel- and power supply systems, by several magnetic and non-magnetic actuators, by an advanced disruption mitigation system and by a choice of target plasma parameters (e.g. the Greenwald fraction is set as a target to 0.45) that will allows for an ample exploration of the operational space in all directions (see Chapter III).

Real-time feedback control of the main quantities relevant for bulk and divertor plasma performance (e.g. MHD stability, fuelling, radiation level, transient events, plasma position, divertor magnetic topology) is implemented though an ample set of diagnostic and actuators which will exploit the recent strong progress on control science in the fusion community. On the topic of plasma control, as in many others, DTT can steward the tokamak fusion research by providing an agile device where open issues like for example disruption and runaway electron mitigation or ELM control can be studied in a relatively easy way, and which much less restrictions than in ITER.

Accessibility is provided by avoiding tritium operation, manned access to the vessel and a complete and reliable remote handling system (see Chapter IV). This, for example, will allow full replacement of both lower and upper divertors in reasonable time frames, so making DTT an effective divertor test facility.

II.3 Conclusions

The DTT facility will be charged with the challenge to test the physics and the technology of various alternative divertor concepts under integrated physics and technical conditions that can confidently be extrapolated to DEMO. The assessment of the alternative divertors will include also the conventional approach to put the expected benefits of the alternatives in perspective and to compare different approaches.

The assessment main objective will therefore that of demonstrating that an experimental alternative concept can be translated and engineered into a controllable exhaust solution for DEMO. This includes all the components of the divertor system: plasma facing components, diagnostics and actuators, ancillary systems, with the constraints that solutions need to be integrated with all other aspects and requirements of a power plant.

DTT will, thereby, close the gaps that exist between the power exhaust studies using alternative solutions that can be carried out in present day devices and DEMO, and will steward ITER for several aspects of tokamak physics and technology

II.4 References

[II.1] Loarte A., Neu G., Fusion Engineering and Design, Volume 122, November 2017, Pages 256-273
[II.2] Eich T. et al., Nuclear Fusion 53 (2013) 093031
[II.3] https://www.euro-fusion.org/eurofusion/roadmap/
[II.4] Special Section of Fusion Engineering and Design, Vol. 122, 2017, pp. 253-294 and e1-e25
[II.5] De Baar M. et al., “Report of the AHG on Strategy for the Plasma Exhaust-Phase 2”, 2016

Chapter III

PLASMA SCENARIOS AND PHYSICS BASIS

III.1 Introduction

The main objective of the Divertor Tokamak Test (DTT) facility is to host experiments aimed at studying solutions to handle power and particle exhaust in a tokamak and in particular in view of DEMO [III.1]. DTT fulfils the need of developing integrated and controllable exhaust solutions, which shall encompass plasma, plasma facing components (PFCs), control diagnostics and actuators. Experiments, theory and modelling will inform a strategy to mitigate the risk that conventional divertor might not be suitable for DEMO. The physics basis of viable alternative exhaust solutions has been summarized by the EUROfusion project WP-DTT1 [III.2]. The conceptual requirements at the base of DTT machine design remain as already in [III.3] and in [III.4]:

- specifications based on dimensionless parameters suitable for properly scale ITER-DEMO plasmas;
- capability of integrated scenarios (solutions to be compatible with plasma performance and technological constraints of DEMO);
- flexibility in the divertor region so as to allow testing different divertors;
- possibility to test alternative magnetic configurations (e.g. negative triangularity);
- assuring DEMO relevant ratio between power crossing the separatrix P_{sep} and major radius R, i.e. $P_{sep}/R \geq 15$ MW/m;
- possibility to test liquid metals on divertor;

The scaling process and consequent choice of machine parameters will be highlighted in the next paragraph III.2. Present status of engineering plasma scenarios will be reported in paragraph III.3**.** Plasma exhaust studies that have accompanied the DTT divertor design will be described in paragraph III.4.

Together with scientific and technical requirements a budget constraint of 500 M€ has been considered in conceiving DTT. Moreover, after the original proposal described in [III.3], the present intermediate report refers the ongoing design evolution, started after the EUROfusion DTT workshop held in Frascati in June 2017 [III.5], that aims at maximizing DTT flexibility while keeping the robustness of its scenarios and performances. The major change consists in the up-down symmetrisation of the machine, as shown in Fig. III.1, to improve its flexibility and allowing testing in the same machine more configurations: Single Null Divertor (SND); Double Null Divertor (DND), Snow Flake Divertor (SFD), X-Divertor (XD), Super-X Divertor (SXD), Double Super-X (DSX) and single null with Negative Triangularity (NT). Furthermore, additional heating power mix has been optimised and the design of the vacuum vessel, ports and remote handling systems has been updated considering application and testing of a liquid metal divertor.

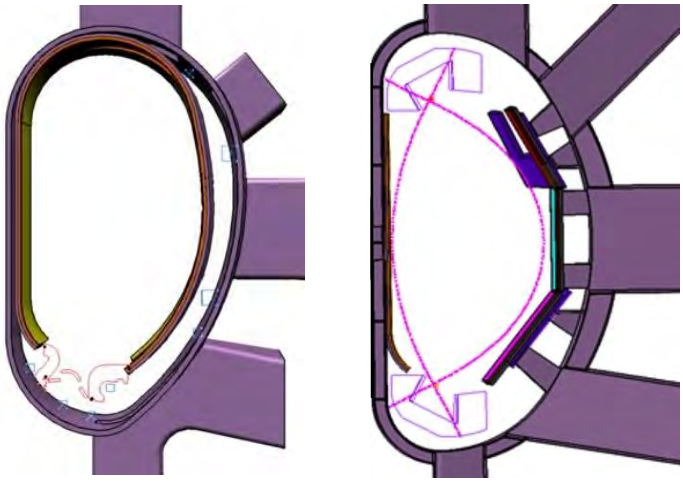

Figure III.1: DTT original single null design (left), symmetrised current version (right)

III.2 Physics Basis and Parameters

In the last two years DTT design has evolved maximising its flexibility to test different divertor solutions. This strengthens the capability to fulfil its mission, that remain unchanged [III.3]:

1. demonstrate a robust power handling solution that can be extrapolate to DEMO;
2. the solution must not degrade core and pedestal performance in a DEMO relevant plasma regime;
3. demonstrate that point 1 and 2 can be achieved integrating physics and technological aspects.

In this paragraph we will summarise the physics basis that originated DTT conceptual design and motivated the choice of main parameters referring to [III.3] and to [III.4] for details. Then we will highlight the differences, in present design from “Blue Book” resulting after iteration with international scientific community [III.5].

When scaling DTT down from ITER-DEMO, particular attention has been paid to preserve divertor and SOL regions parameters. A key parameter characterizing these two regions is P_{SEP}/R, that in DTT must then keep a value similar to the one expected in DEMO, i.e. $P_{SEP}/R \approx 15$MW/m. Previous works [III.6-III.7] have shown that "self-similarity scaled down experiment" can be approximated [III.6, III.8] by fitting five dimensionless parameters: $T=T_e/E_i$ (where E_i is a typical ionization energy), $\nu^*=L_d/\lambda_{ei}$, Δ_d/λ_0, ρ_i/Δ_d, β, where L_d is the divertor field line length, λ_{ei} is the electron-ion collisional mean free path, Δ_d is the SOL thickness, λ_0 is the neutrals mean free path, ρ_i is the ion Larmor radius, β is the plasma pressure normalised to the magnetic one. Some of these parameters are intrinsically linked with the divertor "topology" and this poses a first constraint for the DTT design: the necessity of having a very flexible divertor "region/configuration" to study and optimize the role played by the various topologically linked parameters.

Eventually, the machine dimension and bulk plasma performances should guarantee that exhaust solutions could be extrapolated to a reactor-graded plasma. Physics properties (bulk and edge) are completely determined by the dimensionless parameters ν^* (normalized collisionality), ρ^* (normalized Larmor radius), β and T [III.7, III.9]. However, it is not possible to simultaneously preserve all these quantities since the identical experiment will be obtained. To overcome this problem, while preserving main physics aspects of a reactor-like experiment (i.e. ITER, DEMO), DTT has been scaled down following the so called "weak scaling" described in [III.10]. Temperature, that rules the atomic physics in the SOL and divertor region must be preserved, as well as β that controls local magnetic topology. Between ν^* and ρ^* the similarity has been chosen for the former. Since preserving ρ^* would lead to unrealistic value of magnetic field, ρ^* is relaxed in a controlled way: $\rho_R^* = \rho_S^* R^{\varepsilon}$, where the subscripts *R* and *S* indicate respectively the "reactor" and the "scaled" device, ε is the "controlling" scaling parameter. This choice allows preserving the main physics properties in a scaled experiment dedicated to study the Power Exhaust. As already mentioned, overall cost of DTT must be within a fixed budget of 500 M€; the cost of a tokamak (without tritium and not including additional power) scales as the machine magnetic volume: $Cost \sim B^2R^3 \sim R^{2.75}$. DTT will not use tritium and it has been assumed that additional heating cost will not be higher than one third of the total cost, i.e. $Cost_{Heating} \approx 150$M€. Left side of Fig. III.2 shows the value of P/R versus R for three different values of the controlling parameter ε, as obtained by using the afore mentioned weak scaling.

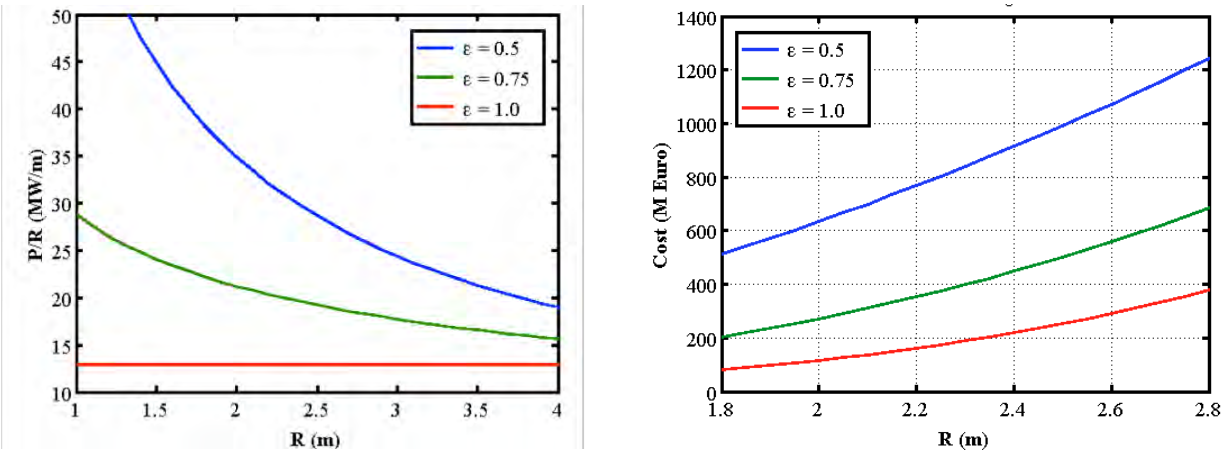

Figure III.2: Left-P/R scaling versus R for three different ε parameters: for ε=1 P/R is always too small; Right-Load Assembly device cost; for ε=0.5 the cost is always too high

Clearly, by increasing ε above a certain limit, P/R will remain below a reactor relevant value for all machine sizes; on the contrary for values too small of ε the needed additional heating power will increase stronger

than 1/R. Consequently, an intermediate ε = 0.75 value is an appropriate scaling controlling parameter. From the right side of Fig. III.2, where the machine cost versus major radius is reported for given ε, the maximum machine dimension can be deduced: the maximum machine radius cannot exceed 2.2 m to maintain the 350 M€ budget. Machine dimensions have to respect a minimum size to maintain the necessary flexibility in the divertor region, including remote handling capability, and actively cooled plasma facing components [III.3]. Finally, a pulse duration of up to 100 s has been assumed to allow plasma duration longer than any thermalization time. This process led to DTT parameters choice (Blue Book reference single null scenario) as summarised in the left column of Tab. III.I, all details can be found in [III.3] and [III.4].

TABLE III.I. BLUE BOOK AND REVIEWED DTT PARAMETERS

	Blue Book	**Reviewed**
R (m)	2.15	2.11
a (m)	0.7	0.64
I_P (MA)	6.0	5.5
B_T (T)	6.0	6
V (m^3)	33	28
$n_e(10^{20}m^{-3})$	1.7	1.8
n_e/n_G	0.45	0.42
P_{Tot} (MW)	45	45
τ_E (s) H_{98}=1)	0.47	0.43
T_e(keV)	6.2	6.1
β(%)	1.8	2.2
ν* (10^{-2})	2.4	2.6
ρ* (10^{-3})	3.7	2.9

Following the design review started after the EUROfusion DTT workshop held in Frascati in June 2017 [III.5] these parameters have been slightly modified. One of the major consequences of the machine up-down symmetrisation was indeed an increase of vertical dimension to host two divertors. The consequent volume increase has been compensated by a slight major radius reduction to avoid affecting budget constraint. Overall engineer optimisation, as well as poloidal coil best positioning and dimensioning, to achieve the envisaged variety of magnetic configurations (reference next paragraph), determined today parameters, summarised in the right column of Tab. III.I. It is worth noting that the data in Tab. III.I refer to the single null plasma volume. An estimate of overall DTT dimension would be better obtained referring to Vacuum Vessel dimensions (that contains the First Wall, Reference Chapter IV): R_{in} = 1.385 m; R_{out} = 3.14 m; a = 0.89 m; b = 1.85 m.

III.3 Plasma Scenarios

Promising experimental results on alternative configurations have been obtained in DIII-D [III.11], EAST [III.12], MAST [III.13], NSTX [III.14] and TCV [III.15-III.17]. The DTT device addresses the challenge of investigate alternative magnetic configurations including double null, snowflake, X-Divertor, negative triangularity and double super-X. The behaviour of such alternative configurations will be compared with the reference single null. The Super-X divertor concept seeks to maximize the major radius of the divertor targets

[III.18]. However, the maximum value is limited in DTT by the fixed position of the toroidal field coils. A Super-X configuration with a major radius of 2.11 m would have been incompatible with the budget constraint but possible Super-X configurations can be achieved with a reduction of the plasma major radius and plasma volume. Magnetic control issues of DTT SND and alternative scenarios are described in Chapter X.

III.3.1 Machine Configuration and Constraints

The last version of the DTT device has been designed with a major radius R_0= 2.11 m and an aspect ratio R/a = 3.3. Two stainless steel vessel shells of 1.5 cm have been assumed with two toroidally discontinuous stabilizing plates of 4 cm placed between the first wall and the in-vessel stabilizing coils, as illustrated in Fig. III.3. The main specifications considered for the design of the plasma scenario are hereafter summarized. They include constraints on the plasma, on the poloidal field (PF) coils, on the central solenoid (CS).

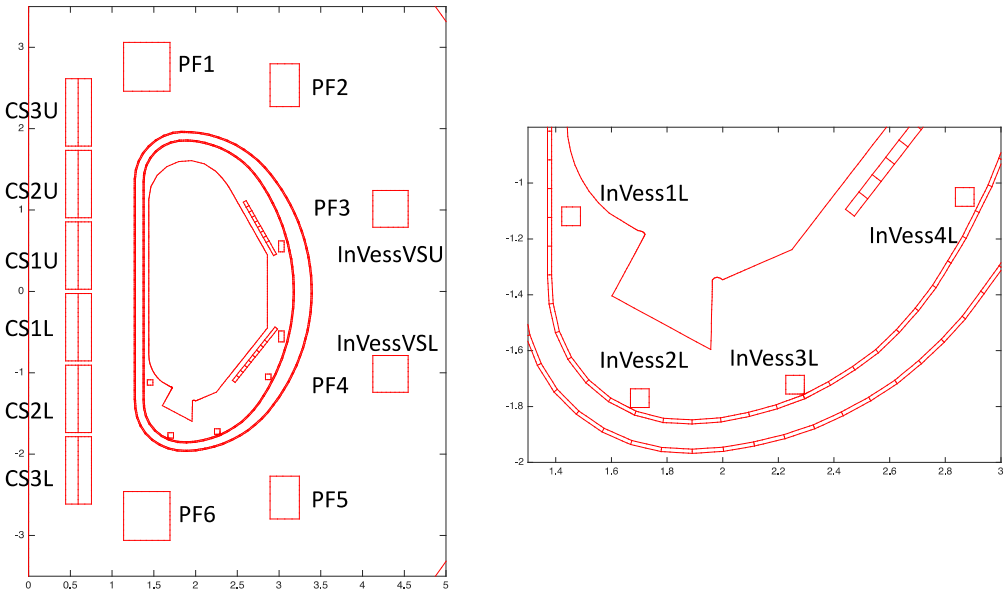

Figure III.3: Poloidal section of DTT device (Left) and divertor region (Right)

PF/CS coil currents

The DTT PF coils system, illustrated in Fig. III.3, is composed by six independent CS coils with a graded solution CS3U – CS2U – CS1U – CS1L – CS2L - CS3L; six independent PF coils PF1 – PF6, four independents lower divertor coils InVess1L – InVess4L and two independents in-vessel VS coils InVessVSU – InVessVSL.

TABLE III.II. PF COIL SYSTEM USED FOR MHD CALCULATIONS

	R [m]	Z [m]	DR [m]	DZ [m]	Turns
CS3U_H	0.518	2.200	0.150	0.828	88
CS3U_L	0.674	2.200	0.158	0.828	216
CS2U_H	0.518	1.320	0.150	0.828	88
CS2U_L	0.674	1.320	0.158	0.828	216
CS1U_H	0.518	0.440	0.150	0.828	88
CS1U_L	0.674	0.440	0.158	0.828	216
CS1L_H	0.518	-0.440	0.150	0.828	88
CS1L_L	0.674	-0.440	0.158	0.828	216
CS2L_H	0.518	-1.320	0.150	0.828	88
CS2L_L	0.674	-1.320	0.158	0.828	216
CS3L_H	0.518	-2.200	0.150	0.828	88
CS3L_L	0.674	-2.200	0.158	0.828	216
PF1	1.416	2.760	0.557	0.600	360
PF2	3.068	2.534	0.350	0.526	160
PF3	4.335	1.015	0.422	0.452	196
PF4	4.335	-1.015	0.422	0.452	196
PF5	3.068	-2.534	0.350	0.526	160
PF6	1.416	-2.760	0.557	0.600	360
InVessVSU	3.028	0.553	0.067	0.134	4
InVessVSL	3.028	-0.553	0.067	0.134	4
InVess1L	1.455	-1.119	0.067	0.067	2
InVess2L	1.702	-1.770	0.067	0.067	2
InVess3L	2.260	-1.722	0.067	0.067	2
InVess4L	2.870	-1.050	0.067	0.067	2

The PF coil system considered for the plasma scenarios is reported in Tab. III.II. A detailed description of the CS/PF coil system will be proposed in Chapter VII. Each CS module is composed by the interconnection of a high field and a low field sections having a different peak field. Minor differences with respect to Chapter VII are mainly related to the fact that the current is considered as uniformly distributed over the cross section including strands, void and jackets. The PF/CS coil positions and cross sections have been designed with an iterative procedure taking into account the above specifications as well as the geometrical constraints related to the locations of ports and TF coils. Table III.III reports voltage and current limits of the CS/PF coils.

TABLE III.III. VOLTAGE AND CURRENTS LIMITS (FOUR QUADRANTS)

	Isat (kA)	Vsat (V)
CS3U	29.9	600
CS2U	29.9	600
CS1U	29.9	600
CS1L	29.9	600
CS2L	29.9	600
CS3L	29.9	600
PF1	28.3	600
PF2	27.1	600
PF3	28.6	600
PF4	28.6	600
PF5	27.1	600
PF6	28.3	600
InVessVSU	25	200
InVessVSL	25	200
InVess1L	25	200
InVess2L	25	200
InVess3L	25	200
InVess4L	25	200

Magnetic field

The maximum magnetic field at the location of the CS coils shall not exceed 13.2 T in the high field section and 9.4 T in the low field section. The maximum magnetic field at the location of the PF coils changes as a function of the radial coordinate of the coils and it is fixed to:

- 5 T for PF3/4
- 4 T for PF2/5
- 8.5 T for PF1/6.

Vertical forces on the PF/CS coils

The maximum vertical force on the CS stack in DTT should not exceed 20 MN; the maximum separation force in the CS stack should not exceed 30 MN and the maximum vertical force on a single PF coil should not exceed 40 MN at the low field PF coils (PF2-PF5) and 30MN for PF1 and PF6.

The forces on the in-vessel coils are scaled from ITER [III.19], where the maximum force is 744 kN/m and the maximum current is 240 kA (up to 320 kA in short transients). Since in DTT we assume 100 kA, the maximum force should be reduced to 310 kN/m. Therefore, the limits of ±6 MN for the vertical force are taken for the coils connected to other structures (vacuum vessel or divertor) via rails or other means.

Plasma

The maximum plasma current is 5.5 MA, whereas the plasma shape parameters should be similar to the present European design of DEMO, with an aspect ratio R/a≈3.3, an elongation $k_{95\%} = 1.65 - 1.75$, and an average triangularity $\delta_{95\%} = 0.30$. The maximum values assumed in the nominal scenarios at full current for poloidal beta β_p and internal inductance l_i are 0.5 and 1.0, respectively. The minimum plasma-wall distance shall be 30 mm, considering that the power decay length at 5.5 MA is about 2 mm at the outboard midplane. The toroidal magnetic field ripple is limited to 0.4%, yielding R_0+a <2.75 m. The minimum grazing angle of the magnetic field at the strike points shall be 1.5 deg. The pulse length should be about 100 s, so as to overcome all thermal transients; this is guaranteed by a total available poloidal flux of about 43 Vs (CS swing of about 33 Vs and a PF contribution of about 10 Vs), not to mention the possible current drive contributions from the ECRH and the NBI system to be implemented at a later stage.

III.3.2 Single Null Scenario

Table III.IV shows the time evolution of the PF coil currents, along with the plasma geometrical and physical parameters that characterize the sequence of plasma shapes during a pulse. It defines the DTT reference Single Null scenario, obtained by using the CREATE-NL code [III.20] in combination with FIXFREE code [III.21].

As shown in Fig. III.4, a good magnetic field null, with a maximum field of 3 mT, during the plasma break-down (i.e., a large central hexapolar region even at low field) is guaranteed. At breakdown a toroidal electric field of 0.8 V/m for 100 ms has been imposed in the centre (R_C = 2.11 m, Z_C = 0.0 m).

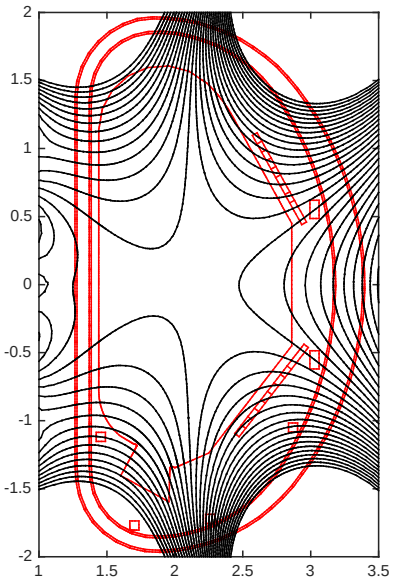

Figure III.4: Poloidal section of DTT magnetic map

The scenario has been designed so as to provide the necessary flux (~33 Vs) and to build-up the X-point configuration for the 5.5MA H-mode reference scenario. For this case, the discharge lasts around 73 s from the breakdown to the end of flat top with the X-point configuration sustained (at low and/or high beta) for ~ 60 s (much longer than the plasma resistive time). The central solenoid (CS) column is split in six different coils to allow the largest plasma shaping flexibility.

After the breakdown, the plasma current I_P rises up to 3.0 MA in Δt = 15 s; during this phase, the plasma evolves with a circular to elliptical shape, leaning on the inboard side of the first wall, where the tungsten thickness is planned to be increased by a factor of two. In this scenario the plasma remains limited for about 15 s achieving the X-point configuration with a plasma current of 3MA (XPF in Fig. III.5). Between t = 15 s and t = 22 s the plasma current ramps up to 4.3 MA increasing the plasma-wall distance in the high field side up to 30mm. Between t = 22 s and t = 27 s, the plasma shape reaches the reference values of triangularity $\delta_{95\%} = 0.3$ and elongation $k_{95\%} = 1.65$, the plasma current achieves its target value of 5.5 MA, while β_p remains very low.

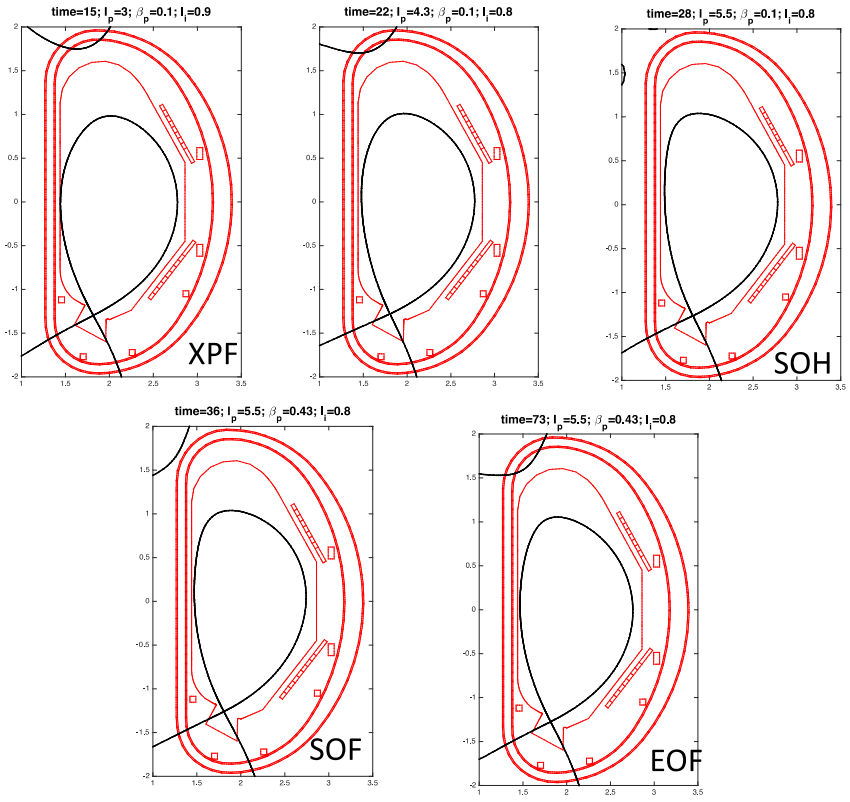

Figure III.5: Time evolution of plasma shapes and main plasma current parameters for SND scenario. XPF) X Point Formation; SOH) Start Of Heating; SOF) Start Of Flat Top; EOF) End of Flattop

The boundary flux Ψ_{SOF} at start of flat top (t = 27 s) is calculated assuming an Ejima coefficient C_{EJIMA} = 0.35, a premagnetization flux of Ψ_{Premag} = 16.2 Vs and a flux after the breakdown of Ψ_{BD} = 15.75 Vs [III.22]:

$$\Psi_{SOF} = \Psi_{BD} - (0.5\,\mu_0 R\, l_i I_p + C_{EJIMA}\,\mu_0 R\, I_p) = 4.86\ Vs \qquad \text{(III.1)}$$

where l_i is the internal inductance, R is the major radius and I_p is the plasma current.

At t = 28 s, full 45 MW additional heating is considered, causing an increase of the internal kinetic energy on a time scale longer than the plasma energy confinement time. After t = 36 s, all plasma physical parameters are assumed to remain nearly constant up to the end of the current plateau at t = 73 s. During the flat top with a plasma current of 5.5 MA and a toroidal field of 6 T, the plasma volume is 28 m^3, whereas the safety factor is q_{axis} = 1.0 at the magnetic axis, and q_{95} = 2.55 at 95% of the magnetic poloidal flux. The plasma shape evolution is illustrated in Fig. III.5 while the main parameters are reported in Tab. III.V.

At the end of flat top, the plasma is no longer heated and a controlled ramp-down phase similar to the JET tokamak follows, in which the plasma current decreases at the rate of 100 kA/s (up to 500 kA/s if needed in emergency cases) while keeping a single null configuration at low beta, low elongation, and controlled density (no more than 50% of Greenwald limit) till about 200 kA; then the plasma configuration becomes limited, leaning on the inboard wall, where the plasma current decreases to zero.

The present SND scenario has been designed without considering the current drive effect during the breakdown and flat-top phases. The scenario is compatible with a duty cycle considering 60 minutes between two pulses. The configurations satisfy the PF system limits reported in the Paragraph III.3.1 and keep a minimum distance of 30 mm between the plasma last closed surface and the first wall in the diverted phase, in order to minimize the interaction between the plasma and the main chamber.

Enough space has been allocated in the divertor region, to substantially vary the plasma divertor magnetic topology, to allow strike point sweeping and to have efficient pumping. In addition, the full divertor can be removed by remote handling to allow tests based on different divertor geometries and/or liquid metals.

TABLE III.IV. CURRENTS EVOLUTIONS OF THE SINGLE NULL SCENARIO

Time [s]	0	15	22	27	28	36	73
Ipl [MA]		3.00	4.30	5.50	5.50	5.50	5.50
Betapol		0.10	0.10	0.10	0.10	0.43	0.43
Li		0.90	0.80	0.80	0.80	0.80	0.80
Psb [Vs]		9.64	7.37	4.86	4.49	2.64	-3.04
CS3U [kA]	29.56	15.90	19.76	-3.97	-4.57	15.22	16.29
CS2U [kA]	29.90	6.26	2.13	22.67	21.46	9.03	-14.00
CS1U [kA]	29.90	8.01	-2.15	-21.58	-23.01	-23.26	-29.90
CS1L [kA]	29.90	2.82	-12.15	-23.21	-22.78	-21.20	-29.90
CS2L [kA]	29.90	5.97	0.03	-3.45	-4.63	-12.10	-28.50
CS3L [kA]	29.56	21.03	26.03	11.61	10.09	15.73	3.34
PF1 [kA]	4.06	14.01	14.63	12.84	12.22	4.43	5.63
PF2 [kA]	6.11	-6.23	-13.59	-19.22	-18.33	-13.53	-12.87
PF3 [kA]	0.01	-4.09	-4.30	-5.04	-4.90	-5.81	-10.71
PF4 [kA]	0.01	-5.21	-8.40	-9.93	-10.71	-15.70	-10.06
PF5 [kA]	6.11	-10.75	-14.78	-22.03	-21.23	-13.72	-23.00
PF6 [kA]	4.06	18.58	20.37	28.27	28.13	22.55	25.34

TABLE III.V. MAIN PARAMETERS OF THE SINGLE NULL SCENARIO

Time [s]	15	22	27	28	36	73
Ipl [MA]	3.00	4.30	5.50	5.50	5.50	5.50
Betapol	0.10	0.10	0.10	0.10	0.43	0.43
Li	0.90	0.80	0.80	0.80	0.80	0.80
Raxis - node [m]	2.13	2.16	2.14	2.14	2.14	2.17
Zaxis - node [m]	-0.03	-0.02	0.01	0.01	0.01	-0.01
R_XP- node [m]	1.81	1.81	1.80	1.80	1.80	1.82
Z_XP - node [m]	-1.30	-1.28	-1.26	-1.26	-1.26	-1.27
R [m]	2.11	2.13	2.13	2.13	2.11	2.11
a [m]	0.67	0.65	0.65	0.65	0.64	0.64
Btor_tot at Mag. Axis [T]	6.14	6.20	6.32	6.33	6.24	6.23
Btor0 at Major Radius [T]	6.07	6.11	6.29	6.29	6.13	6.05
q_95	4.35	3.07	2.52	2.49	2.53	2.54
elongation (k)	1.72	1.77	1.78	1.78	1.81	1.80
k_95	1.59	1.65	1.65	1.66	1.66	1.68
Triangularity (Delta)	0.28	0.37	0.46	0.44	0.42	0.39
Delta_95	0.19	0.26	0.32	0.32	0.31	0.29
Perimeter [m]	5.67	5.67	5.76	5.74	5.70	5.72
Volume [m^3]	28.69	28.37	28.86	28.72	27.88	28.50

III.3.3 Alternative Scenarios

DTT capabilities include various alternative configurations (ACs) such as ideal SFD, snowflake plus and minus (SFD^+ and SFD^-), XD, DND, NT and DSX plasmas (Fig. III.6 and Tab. III.VI).

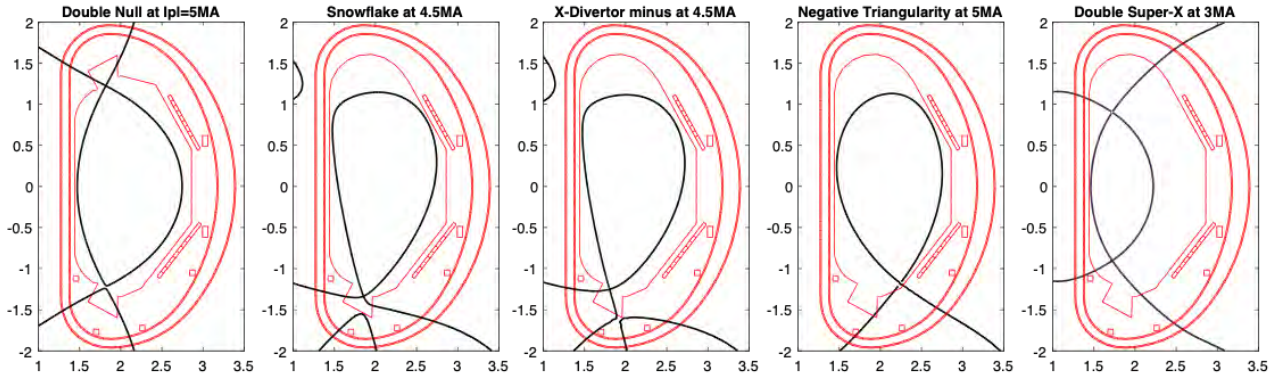

Figure III.6: DTT alternative configurations: DND, SFD⁺, XD, NT and DSX

TABLE III.VI. MAIN PARAMETERS OF THE ALTERNATIVE CONFIGURATIONS

	Double Null		**Snowflake**		**X-Divertor**		**Negative Triangularity**		**Double Super-X**	
Time [s]	SOF	EOF	SOF	EOF	SOF	EOF	SOF	EOF	SOF	EOF
Ipl [MA]	5.00	5.00	4.50	4.50	4.50	4.50	5.00	5.00	3.00	3.00
Betapol	0.43	0.43	0.43	0.43	0.43	0.43	0.43	0.43	0.43	0.43
Li	0.80	0.80	0.80	0.80	0.80	0.80	0.80	0.80	0.80	0.80
Boundary flux [Vs]	2.50	-4.65	3.23	-3.28	3.21	-3.08	2.60	-3.37	10.27	-3.65
Axis flux [Vs]	11.48	4.33	11.29	4.63	11.22	4.90	11.55	5.59	14.88	0.94
Raxis - node [m]	2.17	2.17	2.19	2.15	2.18	2.15	2.18	2.18	1.86	1.86
Zaxis - node [m]	0.00	0.00	0.22	0.22	0.20	0.22	0.14	0.19	0.00	0.00
Rbound - node [m]	1.82	1.82	1.85	1.79	1.80	1.77	2.24	2.24	1.71	1.71
Zbound - node [m]	1.23	1.23	-1.33	-1.30	-1.25	-1.27	-1.19	-1.19	-0.93	-0.93
R [m]	2.11	2.11	2.11	2.08	2.10	2.10	2.11	2.11	1.84	1.83
a [m]	0.64	0.63	0.63	0.62	0.62	0.62	0.64	0.64	0.39	0.39
Btor_tot at Mag. Axis [T]	6.19	6.19	6.16	6.24	6.20	6.19	6.20	6.19	6.93	6.96
Btor0 at Major Radius [T]	6.02	6.02	5.94	6.04	5.98	6.04	6.00	5.99	6.79	6.82
q_95	2.80	2.80	3.36	3.45	3.23	3.39	2.45	2.46	3.03	3.01
elongation (k)	1.92	1.92	1.95	2.00	1.90	1.96	1.81	1.81	2.38	2.38
k_95	1.71	1.72	1.74	1.79	1.73	1.78	1.68	1.68	2.07	2.06
Triangularity (Delta)	0.45	0.45	0.25	0.21	0.29	0.32	-0.13	-0.12	0.33	0.31
Delta_95	0.31	0.32	0.15	0.12	0.18	0.19	-0.11	-0.08	0.19	0.19
Perimeter [m]	5.81	5.79	6.05	6.03	5.86	5.93	5.66	5.68	4.15	4.14
Volume [m^3]	27.89	27.82	29.07	28.79	27.71	28.69	28.52	28.42	11.35	11.20

The double null configuration allows decreasing the inner wall heat load and split the average load between the upper and lower outboard targets with suitable plasma wobbling. However, the share is not guaranteed in the transient phases and therefore the outboard targets have to be designed considering the peak loads. The DTT PF coil system is able to sustain a high current (5 MA) double null configuration for a long flat top (more than 50 s).

The snowflake divertor concept seeks to decrease the poloidal field in the vicinity of the null point by introducing a second order null point [III.23]. This splits the separatrix around the null into six legs with two enclosing the confined plasma and four divertor legs. Since the exact SFD is only a point in the operational plane any real configuration is characterized by two nearby X-points [III.24]. The resulting configuration may have different topologies referred to snowflake plus (SFD^+) and snowflake minus (SFD^-) depending on whether the second x-point is located in the private or common flux region of the primary, active X-point, respectively. In DTT it will be possible to achieve SFD configuration in H-mode with a plasma current up to

4.5MA. A potentially undesirable consequence is an increase of the poloidal flux compression towards the target (in contrast to the XD). The lower poloidal field in the null point region leads to a longer connection length and divertor volume and is expected to generate large volumetric losses.

The X-divertor concept [III.25] seeks to flare the flux surfaces near the divertor targets. The flaring is obtained by decreasing the poloidal magnetic field and hence increasing the poloidal flux expansion at the target. In DTT the XD configuration is realized by a relaxation of the SFD configurations with a potential plasma current in H-mode of 4.5MA.

The Super-X divertor concept aims at increasing the total flux expansion towards the target. This is achieved by increasing the major radius of the divertor targets, Rt. The maximum value is usually limited by the toroidal field coils. Increasing Rt allows for an increase of the wetted area, without decreasing the grazing angle of the field lines at the target. It is worth to notice that the SFD^+ configurations illustrated in Fig. III.6 can also be regarded as Super-X configurations with a proper definition of the divertor plates. Under these premises and in agreement with the space available in the divertor region, the DTT up-down symmetric machine can achieve a Super-X plasma scenario at 4.5 MA with a flat top flux swing similar to the SFD case, a maximum toroidal flux expansion Rt/Rx ≈ 1.38 (Rx indicates the radial position X-point) and an outboard leg length leg_{out} ≈ 0.73 m. The possibility to achieve a Double Super-X at 3MA has been also investigated assuming a reduced plasma volume up to 11 m^3. However, this configuration requires a modification of the in-vessel components to reach acceptable vertical stability performances.

The PF coil system of DTT is also capable to sustain a significant plasma current up to 5MA with a negative triangularity of $\delta_{lower\ 95\%} = -0.16$ in the divertor region for a sufficiently long flat top. Due to the high radial coordinate of the X-point, this configuration, which slightly improves the magnetic flux expansion of the inner leg, can be tested in the first phase of the scientific programme at low current and/or in L-mode. In a second phase it can be tested for short periods also in H-mode with an alternative divertor and a slight modification of the first wall. Any configuration can be obtained via specific scenarios, or alternatively, during the flat top of a reference scenario (at full or reduced current) by means of a transition from SND to AC and vice versa. All these configurations satisfy current, field, vertical force and plasma-wall distance constraints.

III.3.4 In-Vessel Coils

The study of the divertor physics and technology is one of the main targets of the DTT device. Indeed, for optimizing the local magnetic configuration and consequently controlling various parameters related to the power exhaust (flux expansion, connection length, distance between null points, etc.), DTT will be equipped with a set of in-vessel coils capable to locally modify the magnetic field in the vicinity of the divertor target. Indeed, using these in-vessel coils, it will be possible to adjust a second null region in Snowflake-like configurations, obtaining a large area where poloidal magnetic field and its gradient are close to zero or defining XD-like configuration where the flux flaring at target can be largely varied. A first example of the flexibility of such a system is given by the possibility of moving from SFD^+ equilibrium at SOF, designed with only ex-vessel coils, (shown in Fig. III.6), to an ideal SFD and a SFD^- configurations, as shown in Fig. III.7. Table III.VII reports the currents imposed on InVess1L – InVess4L to obtain ideal SFD and SFD^- configurations.

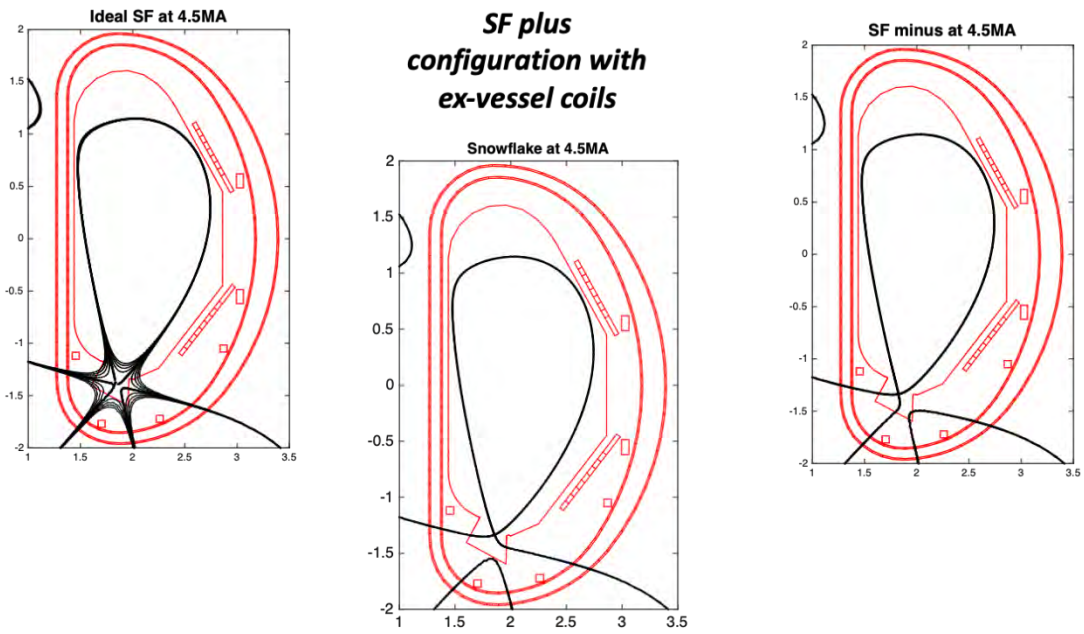

Figure III.7: Ideal SFD, SFD⁻ configurations obtained by means of in-vessel coils InVess1L-InVess4L

TABLE III.VII. CURRENTS IN IN-VESSEL COILS FOR IDEAL SF AND SF⁻ CONFIGURATIONS

	CURRENT [kA]	
	Ideal SFD	**SFD minus**
InVess1L	0	3.22
InVess2L	-20.54	-5.79
InVess3L	10.08	-6.56
InVess4L	0	-0.37

Figure III.8 shows a second example about the flexibility of such a system applied to a previous version of the machine geometry with R=2.15 m. The top left frame shows an XD like configuration. The presence of two nulls allows two regions (around the nulls) with a large flux expansion; these two regions are "connected" by a tight zone where the poloidal field increase bit forming a small "hill". The ex-vessel coils will allow varying the reciprocal position of the two nulls, from very far, up to overlap them; the in-vessel coils will allow modifying the topology of the zone connecting the two nulls.

The top right frame of Fig. III.8 shows an extreme case, where the in-vessel coils allows to go from the original XD like configuration (left frame) to a SFD like configuration, with a very large region with $B_p \approx 0$ and its gradient close to zero or even negative (see bottom right frame).

In-vessel coils in DTT are also used to implement feedback control strategies for the power exhaust, such as sweeping and wobbling. The details of the magnetic control issues in DTT are reported in Chapter X.

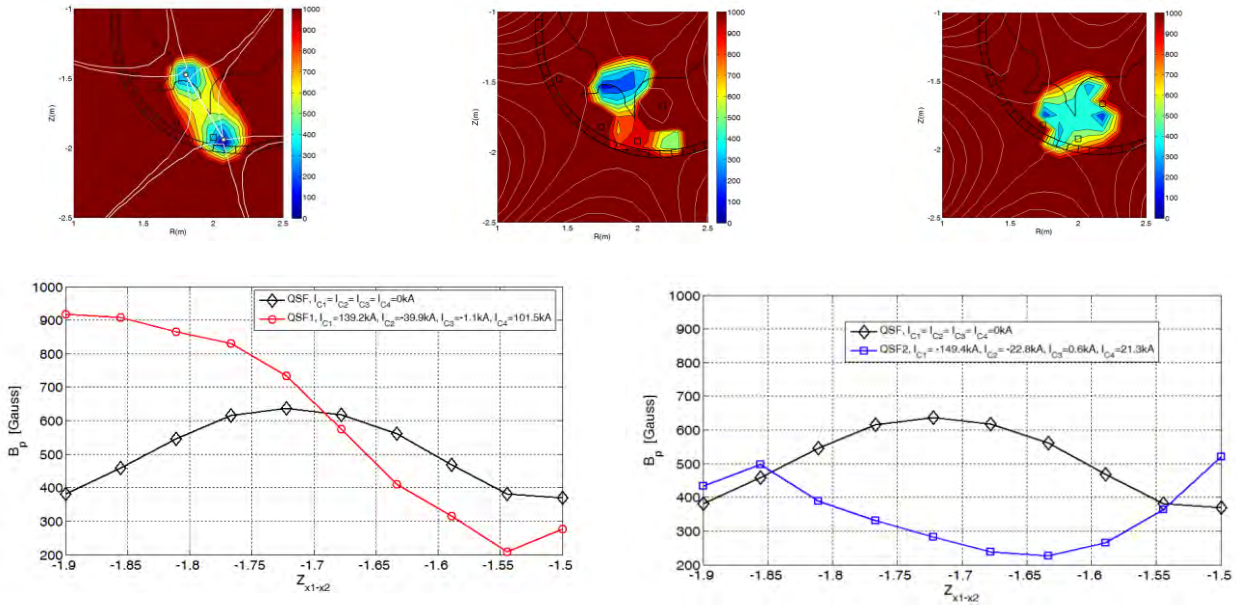

Figure III.8: Left two nulls configuration obtained by the ex-vessel coils; top center, the "hill" like filed reference configuration has been varied to a monotone slope like field configuration (left bottom); top left, the "hill" like filed reference configuration has been varied to a "mirrored" field configuration (right bottom)

III.3.5 Work in Progress

In this paragraph, we highlight briefly some of the ongoing analyses to improve DTT capability to reliably achieve the various expected scenarios. A first study is devoted to a possible increase of the radial coordinate of the X-point for SND and DND configurations in order to increase the space for the inner target and divertor cassette. Furthermore, in order to guarantee sufficient shape control performances during plasma transients, a possible increase of the plasma-wall clearance (currently fixed to 30 mm) is analysed. Finally, in order to improve the vertical stability performances of the plasma configurations, an increase of plasma major and minor radius is under investigation. This modification is then a viable solution to improve plasma vertical stability performances since, according to Fig. III.9, the radial shift would not violate the maximum constraint on ripple < 0.4%. A first DND configuration with R = 2.14 m and a = 0.65 m, maintaining the plasma current value to 5 MA, has been produced and it is shown in Fig. III.10. According to the results presented in Tab. III.VIII the increase of R, with the reduction of the distance between plasma and conducting structure, and the increase of a, with the reduction of k_{95} to 1.68, has led a consequent beneficial effect on plasma vertical stability performance.

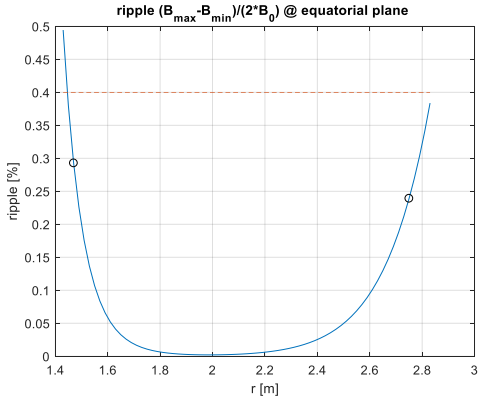

Figure III.9: Ripple behaviour on r coordinate

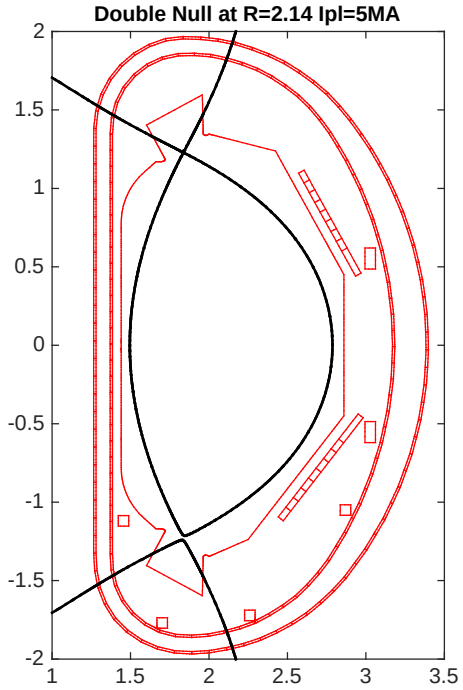

Figure III.10: DND configuration with R = 2.14m and a = 0.65

TABLE III.VIII. COMPARISON BETWEEN SHAPE PARAMETERS OF DND CONFIGURATIONS AT DIFFERENT MAJOR RADIUS

	Double Null	
	R = 2.11 m	**R = 2.14 m**
R [m]	2.11	2.14
a [m]	0.64	0.65
elongation (k)	1.92	1.89
k_95	1.71	1.68
Triangularity (Delta)	0.45	0.46
Delta_95	0.31	0.31

III.4 Plasma Exhaust and Divertor Studies

Given DTT goals, a significant effort is devoted to the study of the divertor physics and technology. Regarding the physics the main aim will be to find an optimal divertor magnetic configuration and to test liquid metal divertors at full plasma performances.

The estimation of the inter ELMs maximum power load on the DTT outer divertor target (usually the most loaded one), that probably can be expected to happen with SND configuration in attached regime, can be done by using the formula [III.26-III.27]

$$q(s^*) = \frac{q_0}{2} exp\left(\left(\frac{S}{2\lambda_q}\right)^2 - \frac{s^*}{\lambda_q F}\right) \cdot erfc\left(\frac{S}{2\lambda_q} - \frac{s^*}{S\,F}\right) \quad \text{(III.2)}$$

where q_0 is the peak heat flux density at the divertor entrance that is usually calculated by equating the integral of (III.2). over s* to $P_{div} = P_{sep}-P_{rad,SOL,}$ the power P_{sep} entering the separatrix minus the power radiated in the SOL, $P_{rad,SOL}$; λ_q is the power e-folding length at the outer midplane and S the width of the Gaussian, convoluted with the exponential profile, taking into account the diffusion in the Private Flux Region (PFR) of the power at the entrance of the divertor, while travelling along the divertor leg. Here F is the flux expansion factor calculated at the target, s* is the coordinate along the target surface in the poloidal cross section, with s*=0 at the outer strike point. The power e-folding length at the outer midplane can be evaluated by using the empirical scaling [III.26]

$$\lambda_q \sim 0.73\, B_T^{-0.8} q_{cyl}^{1.2} P_{SOL}^{0.1} \quad \text{(III.3)}$$

With $q_{cyl}=[2aB_T(1+k^2)]/(2\mu_0 I_P)$ and ε the inverse aspect ratio. S is dependent on local plasma parameters and on the divertor geometry: the final design of the divertor being not yet fixed, in a first approximation we can use for S the scaling found for the ASDEX-U divertor with tungsten PFCs [III.28], S [mm] ~$0.09\, n_{e,ped}[10^{19}$ m$^{-3}]/B_{pol}$ [T], with $B_{pol}= (\mu_0 I_p/2\pi a)\,((1+ k^2)/2)^{-0.5}$. It is worth noting that recently the proposed scaling of λ_q as $\propto B_p^{-1}$ has been questioned by both theoretical and numerical works [III.29] with λ_q becoming wider as soon as the perpendicular fall of length of electron heat channel becomes wider than the ion heat channel. It is not clear if, given the operational space explored by DTT this will be happening and presently work is in progress to tackle this problem through the use of the fluid code BOUT++ which has been able to reproduce this increase.

Starting from relation (III.2) it can be defined the integral power decay length λ_{int} given by $\lambda_{int} \approx \lambda_q + 1.64\, S$. Then by approximating the heat load profile at the target with a new exponential profile with λ_{int} instead of λ_q, the rough effect is to decrease the peak heat load by the ratio λ_q/λ_{int} which shows the additional effect of edge paramters and divertor geometry.

Using previous relations for the SND case without impurity seeding, with parameters reported in Table III.I (where P_{tot}= 40 MW was used), a flux expansion = 4, field lines grazing angles on targets of 3° and a conservative 2:1 ratio between outer and inner loads on divertor targets: on the outer target is it obtained an average specific power of about 25 MW/m^2 (within the first power decay length). This means that the heat load on the outer divertor target for SND configuration without impurities is not tolerable and that P_{tot} must be reduced to ≈ 16 MW or at least 50 % of the P_{plate} should be radiated. This shows that at full power DTT must operate in a high dissipative power fraction regime to reduce the power to the target to tolerable

thermo-mechanical values < 10 MW/m^2, while keeping a lower target temperature $T_{e,t}$ < 10 eV in order to reduce also the sputtering yield. That is the same operating condition expected for DEMO.

Generally speaking, in the radiative case, the amount of volumetric plasma cooling power density in presence of additional radiative species is given by [III.31]: $p_{cool}= n_e n_z L_z = n_e^2 c_z L_z$ with the cooling factor L_z depending on local electron density, temperature and the residence time τ of the charge state. Presently there is no clear statement that allows to define the ideal mixing ratio of impurities as a function of discharge parameters: this should consider not only the divertor condition but also the appropriate impurity compression, limiting in principle the leakage of impurities into the confined region which could negatively affect the plasma performance. It is worth remembering that examples have been found with a high radiative power fraction and no confinement degradation [III.32]: present understanding suggests that in these cases the degradation of pedestal pressure caused by enhanced impurity radiation in the confined region is largely compensated by a steepening of the core profiles of density and temperature [III.30]. Recent models [III.33] suggest that high B_T devices are favourite for impurity radiation with respect to lower field devices that require larger R to reach the same fusion power. Furthermore, Goldstone and co-authors [III.31] recently provided a scaling for the impurity concentration needed to reach a detached state $c_z \approx P_{sep}/[B_p(n_{sep}/n_G)^2]$ which shows a favourable scaling for DTT given the high current and the large separatrix Greenwald density fraction reached. As a final remark, DTT operation in ADC configurations as the Snowflake, could also provide the answer if in DEMO-relevant conditions the experimental observation obtained in L-Mode SFD configuration in TCV [III.34] hold, with radiation limited to the region between the two X-points without entering the confined region or the primary X-point. It is clear that modelling is required in order to provide reliable extrapolations of the foreseen radiative operational scenario in DTT, in particular to assess the relative advantages of the different configurations and to find the optimal operation conditions. The first results of the modelling done with the 2D edge fluid SOLEDGE-EIRENE [III.35-III.36] code are presented in the next paragraph.

The previous analysis is for an ideal toroidally continuous divertor targets: of course, the real divertor is composed by tiles with both finite poloidal and toroidal size. This can result in unavoidable tile misalignments, tolerances being not better than ± 0.3 mm, and therefore in possible overheating of tile edges, in particular the poloidal edges, the ones facing the toroidal direction (because of $B_T \gg B_p$). Shaping of the tile edges is therefore needed. This reduces the effective area available for heat load dissipation. For an initially cooled assembly the decrease of the effective area can be limited by using long toroidal size of the tiles: in an actively cooled structure this is strongly constrained by the need of optimizing the heat exchange with the coolant.

As for the central part of the divertor assembly, a dome will be inserted. Its presence is motivated by the need of providing a neutral pressure suitable for effective pumping and of limiting the backflow of neutrals towards the vacuum chamber, besides the one of protecting the underneath structures (coils, diagnostic etc.). The supporting structure of the dome will be semi-transparent to allow the transit of the neutrals created by the ion flux impinging on the vertical targets.

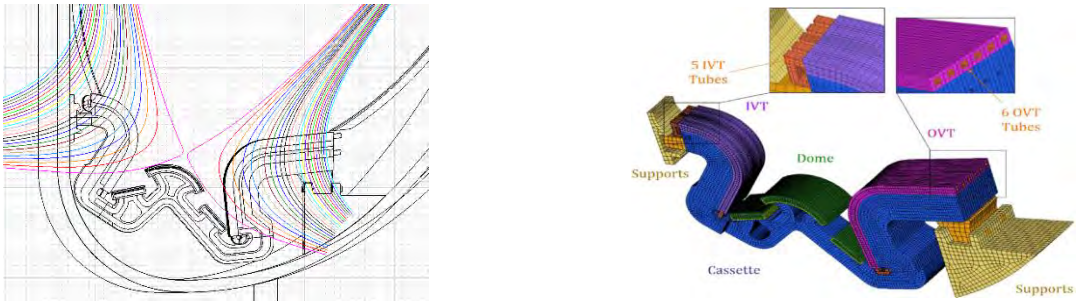

Figure III.11: Design of the reference initial divertor for the proposed DTT. The left one is a conceptual one. The right one is the first draft actual design.

Figure III.11 shows a sketch of the design of a proposed DTT divertor. It has been designed (Chapter IV) to allow experiments with a standard SND configuration and to perform quasi-Snowflake and X-Divertor experiments. This could allow testing the different magnetic topologies for a next divertor optimized for the most promising of them.

III.4.1 Fluid Modelling of DTT Divertor Configurations in Pure D and with Impurity Seeding

Fluid modelling of power exhaust has been done for the DTT tungsten divertor in SND and SFD+/SFD-, DND alternative divertor configurations (ADC). In the SFD cases this study has been done considering quasi ideal snowflake configurations, i.e. configurations with both x-points inside the divertor region and with a distance at mid-plane between separatrices smaller than the heat flux decay length. It is one of the targets of DTT to demonstrate that these configurations can be magnetically controlled during plasma ramp-up, H-mode transition, flat-up and ramp-down, this analysis does not consider these problems but want to highlight possible advantages of these configurations with a nearly optimized divertor geometry. Easier XD–like configurations with the second x-point out of the vessel, which can have some of the advantages of SFDs, will be analysed in future.

The main aims of the modelling are:

1) to find operating conditions compatible with divertor and wall;
2) to compare the SND configuration to the ADCs ones to assess the relative advantages;
3) to compare seeding gases (like neon and argon);
4) to start optimization of divertor geometry.

To provide answers to the first two points, the analysis moved along two directions at fixed separatrix density:

a) in a pure deuterium plasma, progressively reducing P_{SOL} from 40 MW till the achievement of detachment;
b) at the maximum P_{IN}= 45 MW finding the required argon or neon content to obtain a radiation power fraction of about 90% and to achieve detachment.

The two methods can indicate respectively either the amount of power to be lost inside the SOL by volume process or the degree of plasma contamination needed to achieve detachment. Higher allowed P_{SOL} or lower required amount of impurity content to operate in detached mode indicate a better capability of the divertor configuration to handle power exhaust.

Power scan has been performed at high separatrix density $n_{e,sep}$=1.0·1020 m^{-3} ($n/n_G \approx 0.8$), while seeding has been studied at medium and high separatrix density $n_{e,sep}$=0.5,1.0·1020 m^{-3} ($n/n_G \approx 0.4$) with a P_{SOL} reduced to 40 MW for neon seeding and 36 MW for argon seeding considering the difference to P_{IN}=45 MW radiated in the plasma core domain not considered in the modelling.

The same transport coefficients uniform on the computational domain were used in all cases with values D=0.35 m^2/s and χ=0.15 m^2/s. These values have been selected because in SND attached conditions they provide a radial decay of the quantity $n_e \times T_e^{3/2}$ of about 3 mm which can be considered an estimate of the upstream e-folding decay length of the power flowing channel on the outboard equator $\lambda_{q,u}$. This is an optimistic choice compared with the $\lambda_q \approx 2$ mm that can be obtained by the empirical relation [III.27] but it can be considered as a starting value also taking into account that values shorter than the poloidal gyroradius would raise concern on the validity of the fluid code results. Furthermore, while it can influence the absolute values at the targets it does not affect the comparison between divertor configurations and seeding gases.

To speed up the computation and avoid numerical instabilities drift were not included, although recent observations on ASDEX-U [III.37] suggest that fluid code simulation should retain also all the drifts, in order to properly account for the main ion flows. These flows have been suggested as a key ingredient to model the different impurity compression observed according to the radiative ion species.

Two fixed fluxes from core (Γ_c=0.15, 0.3·10^{22} s^{-1}) and gas-puffing (Γ_{puff}= 2.0, 3.0·10^{22} s^{-1}) were used to feed the density; the smallest fluxes were used for the medium density case and the highest for the high density one. The requested separatrix electron density was achieved using variable pumps albedo adjusted to match the requested $n_{e,sep}$. This method has been preferred against fixing the pumping speed mainly because it reduces the instabilities in the code and because pumping speed could partially be considered a free device design parameter while gas-puffing should be similar between divertor configurations.

A first insight of the differences between SND and ADCs configurations can be seen in Fig. III.12 where connection length, flux expansion and grazing angle are drawn for the configurations in function of the distance from the separatrix at the outer midplane. The figure shows the much higher connection length of SFD+/SFD- for $R-R_{sep} < \lambda_{q,u}$; for these configuration also the flux expansion is much higher beside the grazing angle is the same. This gives a preliminary indication of the potential advantage of SFDs in term of better spreading of power on divertor targets. In term of detachment achievement previous advantage could be partially mitigated by the worst closure of SFD divertor in respect of SND and DND ones (see divertor geometries in Fig. III.18).

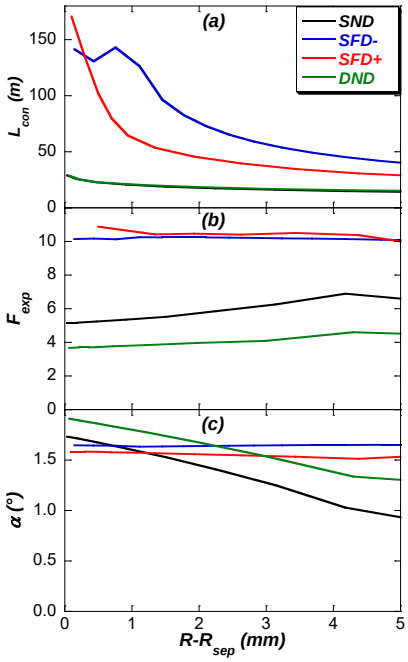

Figure III.12: Geometrical parameters: a) connection length; b) flux expansion at the outer target; c) grazing angles at outer target.

An example of electron density and temperature profiles at outer midplane is show in Fig. III.13 for the four divertor configurations at P_{SOL}=25 MW and the same $n_{e,sep}$. The figure shows that SFDs have higher density in the SOL and higher temperature at the separatrix, these differences are probably due to the longer connection lengths of these two configurations.

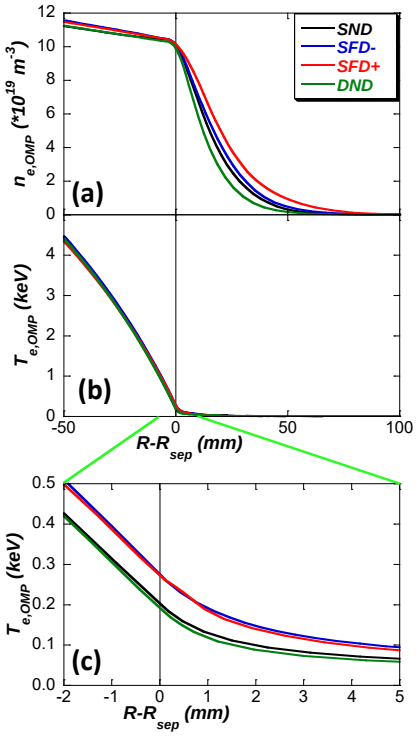

Figure III.13: Profiles at outer mid plane: a) electron density; b) electron temperature; c) zoom of temperature near separatrix.

Figure III.14 shows electron temperature and heat flux profiles at targets (for SFD- the worst two, SP_1 and SP_2 in this case) at various P_{SOL}. In the SND case the figure shows the movement of peak power away from separatrix at power close to detachment which is also observed experimentally, it also shown that more power is going to the outer strike point (also without drifts) due to the higher fraction of power crossing the separatrix in the outer region below the top stagnation point with respect the inner region, the difference is negligible in SFD case probably due to the different plasma shape. The figure clearly shows that detachment is possible at higher P_{SOL}≈15-20 MW in SFD- than in SND in which the power must be reduced to P_{SOL}≈10 MW which is in a relatively good agreement with the analytical result found in previous section. In general heat flux on targets is lower SFD- than SND, but when attached SFD- shows higher plasma temperature at targets. Not show in these plots is the non-optimal splitting of the power between the four strike points in SFD-, which could be improved reducing the distance between the primary and secondary separatrices from the 1 mm of the analysed case to a value much smaller than $\lambda_{q,u}$. A summary of power scan results is drawn in Figs. III.15 and III.16 (as before inner and outer target for SFD and DND are those with the worst heat fluxes). At the inner target SND provides the lowest T_e when it is attached but both SFDs detaches (T_e< 5 eV, yellow line in Fig. III.16) at higher power than others configurations. At outer target DND provides the lowest power when attached while SFD- detaches at higher power than others configurations. In general, considering all target SFD- seems to provide better results detaching on all targets at a power up to ≈20 MW which is about 50% higher than the SND threshold.

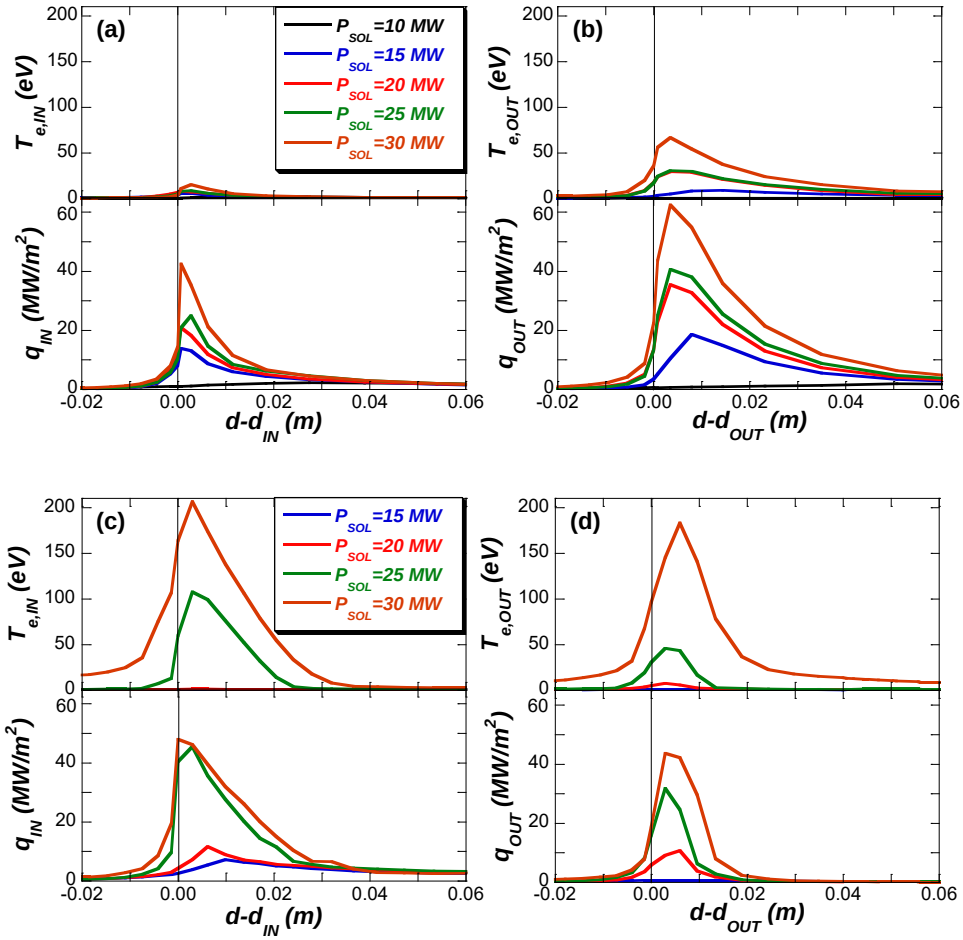

Figure III.14: Temperature and heat flux profiles at targets: a) SND inner target; b) SND outer target; c) SFD- inner target; d) SFD- outer target.

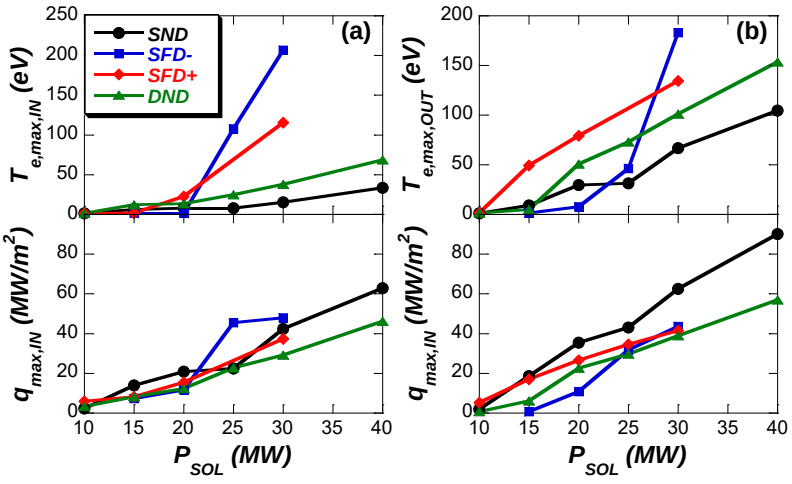

Figure III.15: Maximum electron temperature and heat flux at targets: a) Inner target; b) outer target

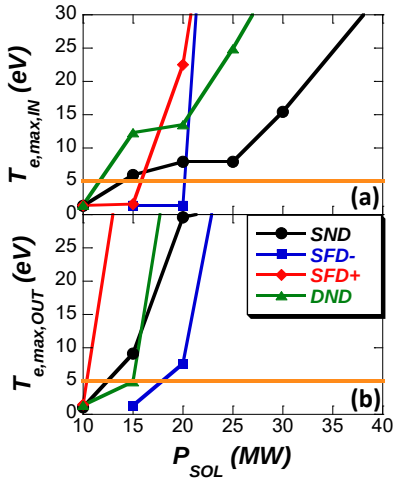

Figure III.16: Zoom of maximum electron temperature at targets: a) Inner target; b) outer target

Previous power scan in pure deuterium, shown that to achieve acceptable condition at the divertor in terms of low power load and detachment condition it is necessary to reduce P_{SOL} at a very low value also at high separatrix density. This shown that to operate at the DTT maximum input power it is necessary to radiate a high fraction (80-90% corresponding to 35-40 MW) of the input power. This can be achieved by seeding impurities. Since the dependence of the radiative loss function on plasma temperature differs among elements, the choice of impurity (single element or mix of several) may control the radiation distribution and balance core versus SOL radiation. Recent study of DEMO scenario found that argon can provide the right balance of core and SOL radiation [III.38], considering the smaller DTT power neon also could be a good solution. For this reason, modelling with neon and argon seeding was done both to compare configurations than seeding gases. Furthermore, the existence of an operation window at medium separatrix density was also searched.

Modelling with impurity requires the development of an operation scenario with an appropriate time sequence between heating power application and seeding by gas-puffing because different results can be obtained based on the time sequence. This is a results of the dependence of radiative cooling rate on plasma temperature, an example the radiative cooling rate for Ar and Ne assuming a corona equilibrium is shown in Fig. III.17, it is a strong function of the temperature for this reason the radiating effectiveness strongly depends on background plasma temperature, the same cooling can be obtained with a much smaller amount of seeding operating at the right plasma temperature. To achieve this result in the present modelling gas seeding injection was done on detached deuterium plasma before increasing P_{SOL}. The amount of gas-puffing seeding was then adjusted to reach the required radiation fraction while using for argon/neon the same pumps albedo required for a stationary deuterium content with the fixed D flux from core and gas-puffing previously described for the power scan in pure D. The same transport parameters used for deuterium have been used for impurities.

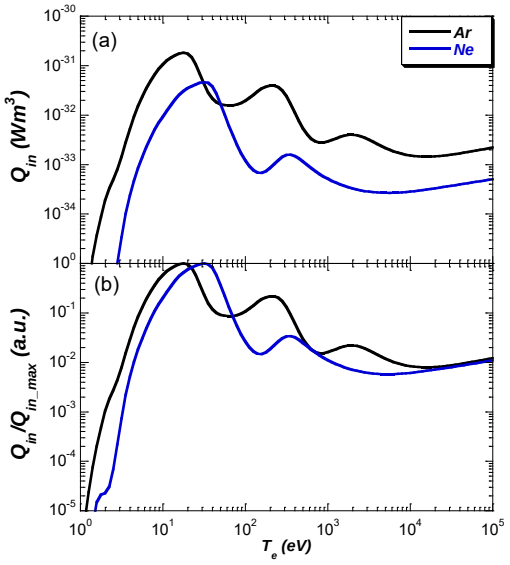

Figure III.17: Cooling rate versus electron temperature in corona equilibrium for argon and neon (from the ADAS database [III.39]). a) absolute values: b) normalized to the maximum.

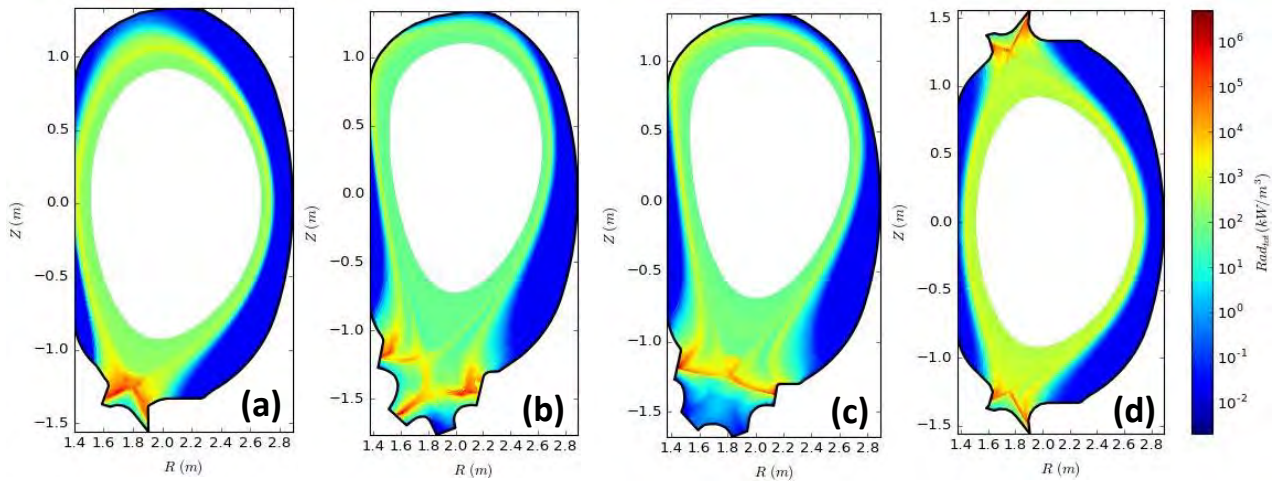

Figure III.18: Radiation distribution for Ar seeding with P_{SOL}=36 MW at $n_{e,sep}$=0.5·10^{20} m^{-3}: a) SND configuration; b) SFD- configuration; c) SFD+ configuration; d) DND configuration.

An example of total radiation distribution at maximum input power with argon seeding is drawn in Fig. III.18, in these cases a radiation fraction P_{rad}/P_{SOL}=90% has been obtained for all configurations with $n_{e,sep}$=0.5·10^{20} m^{-3} at P_{SOL}=36 MW. The figures show the advantage of the SFD- configuration in terms of a larger radiating volume. This allow the achievement of the same radiating fraction with a smaller amount of seeding entering in the core or a lower Z_{eff} at the separatrix (see Tab. III.IX).

At the high density of the previous power scan, the 90% radiation fraction can be achieved at very low impurity concentration (see Tab. III.IX). Also with neon seeding it is possible to achieve the same P_{rad}/P_{SOL} but at the lowest density this happens at the expenses of a much higher Z_{eff} at the separatrix (see Tab III.X) because of the lower radiating capability in the 0.1-1.0 keV range (see Fig. III.17). This is not the case at high density where neon seeding seems to provide similar or better operating conditions, this is due to the lower temperature present in the divertor region at high density that does not favour argon with respect to neon.

TABLE III.IX. Z_{EFF} AT SEPARATRIX TO ACHIEVE PRAD/PSOL=90% AT TWO DENSITY VALUES AND THE FOUR MAGNETIC CONFIGURATIONS WITH ARGON SEEDING

$n_{e,sep}$	SND	SFD-	SFD+	DND
$0.5 \cdot 10^{20}$	5.6	3.4	3.5	6.1
$1.0 \cdot 10^{20}$	2.3	1.5	1.7	2.3

TABLE III.X. Z_{EFF} AT SEPARATRIX TO ACHIEVE PRAD/PSOL=90% AT TWO DENSITY VALUES WITH NEON AND ARGON SEEDING.

$n_{e,sep}$	SND		SFD-	
	neon	argon	neon	argon
$0.5 \cdot 10^{20}$	7.3	5.6	6.2	3.4
$1.0 \cdot 10^{20}$	2.4	2.3	1.3	1.5

III.4.2 Liquid Metal Divertor

The study of liquid metals as plasma facing materials is part of the risk mitigation strategy as described in the European Research Roadmap to the Realisation of Fusion Energy [III.40].

Many experiments have been performed using liquid metals (LMs) in fusion-relevant devices [III.41-III.44], and many possible showstoppers have been overcome (i.e. tritium retention). Actually, lithium and tin are the best candidates in fusion devices; they have different operating temperature windows and scenarios. The experiments demonstrated the technological capability to handle liquid metals in a tokamak environment using the Capillary Porous system (CPS) technology [III.45] which has been adopted by the European strategy (see Fig. III.19).

Many codes are currently under developing to investigate liquid metal impurity production mechanisms and their impact on fusion relevant plasma. But, experiments in an integrated plasma scenario (H-mode and divertor configuration) are missing. For this reason, the Divertor Tokamak Test facility is designed to accomplish also the liquid metal divertor (LMD) test in harsh conditions.

In CPS case the considered DTT design strategy involves the liquid metal operating with negligible evaporation. In such conditions, the liquid metal behaviour does not differ from the solid metal. The advantages are the self-healing properties, allowing the surface replacement after the possible damage produced by a transient event (disruption, ELMs, VDEs). In addition, LMD are insensitive to neutron damage, therefore they can be considered as PFC with a long lifetime.

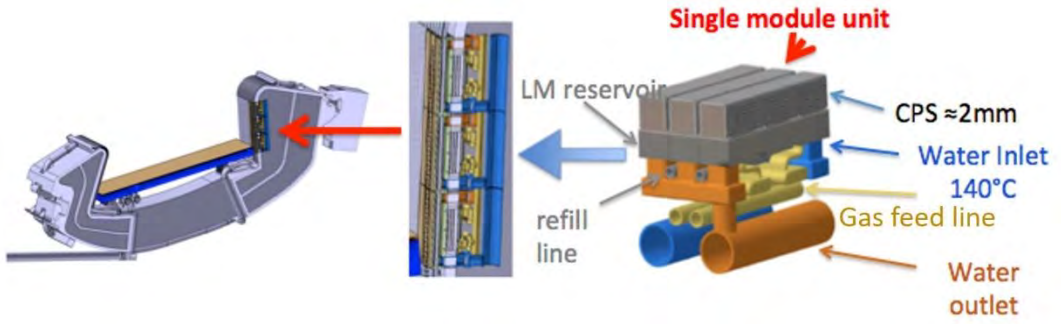

Figure III.19: Sketch of the DEMO divertor cassette (left)[III.46] with three CPS LMD modules installed on the outboard vertical target (middle); CAD of an LMD module (right)[III.47].

First simulations of a CPS LMD for DTT were performed by means of the COREDIV code for both Li and Sn targets [III.48]. The plasma species (fuel and metal plasma) were treated by means of a 2D multifluid transport approach based on Braginskii equations, whereas neutral species are treated by means of an analytical model. The code was modified by including 1D heat transfer in the target to take into account the temperature dependence of the evaporation source. This heat transfer model can approximately consider the target configuration, in terms of thickness of the LM-filled CPS and of the substrate. Results of COREDIV simulations suggest that LMD operation should be supported by additional impurity seeding (e.g. Kr) to reduce the target heat load, thereby avoiding excessive fuel dilution (in case of Li) or core plasma contamination (in case of Sn).

One possibility to reduce fuel dilution or core plasma contamination is to adopt a vapour-box configuration [III.49]. This consists in a series of boxes placed on top of the CPS target (or of an LM pool). The evaporated metal condenses on the walls, thereby reducing the net flux of metal atoms towards the core plasma. Based on pioneering work by Nagayama ([III.50]), Ono ([III.51]) and Goldston ([III.52]), an LM divertor of box-type has also been proposed for DTT [III.53]. The different “boxes” or chambers are defined in Fig. III.20. The IEC and OEC are the inner and outer evaporation chambers, respectively. They contain LM pools (or, alternatively, LM-filled CPSs) which receive the incoming plasma load. The choice of the width of the apertures follows from a trade-off. Indeed, the apertures should be kept as small as possible to avoid excessive vapour flux from the differential chambers, IDC and the ODC to the main plasma. Conversely, undesired production of impurities by sputtering would occur, should the separatrix end-up intersecting the aperture boundaries, because of, e.g., some accidental displacement of the plasma. A conservative width of 5 cm has therefore been selected for the apertures of the system. This value is based on an expected particle scrape-off width of ~1 cm close to the entrance of the plasma in the DCs, according to the model proposed by Goldston [III.54], and assuming an expansion factor f_{exp}~3. Two is the minimum number of chambers which is required for achieving the proposed concept of evaporation-radiation-condensation within a closed system with only a limited efflux of impurities (metal vapor) towards the main plasma.

The evaporated metal partly condenses on the actively cooled walls of the chambers, and partly crosses the aperture to reach the IDC and ODC, where further condensation occurs. The remaining amount of vapour escapes from the apertures at the top, towards the main plasma chamber (MC). In this way, a relatively large metal vapour density can be confined in the proximity of the divertor target, resulting in enhanced SOL plasma cooling due to ionization of metal atoms and radiation emission. According to preliminary estimates, this concept also has the potential of achieving a damping of the evaporated metal mass flow rate by a factor $\left(\frac{\dot{m}_{out}}{\dot{m}_{ev,pool}}\right) \sim 10^{-3}$ before it reaches the main plasma chamber [III.54].

To perform a preliminary evaluation of the performance of such a divertor, a self-consistent model has been proposed, which takes into account the most relevant phenomena characterizing the physics of such a system [III.55]. The divertor performance is evaluated by coupling:

- a 1D model of the SOL plasma, including interactions with the metal vapour in the energy balance;
- a 2D model for the walls, solving the heat conduction problem and allowing to take into account the active cooling, while providing the wall temperature which determines the condensation rates;
- a model for the metal vapour, accounting for evaporation, condensation, vapour flow through the apertures.

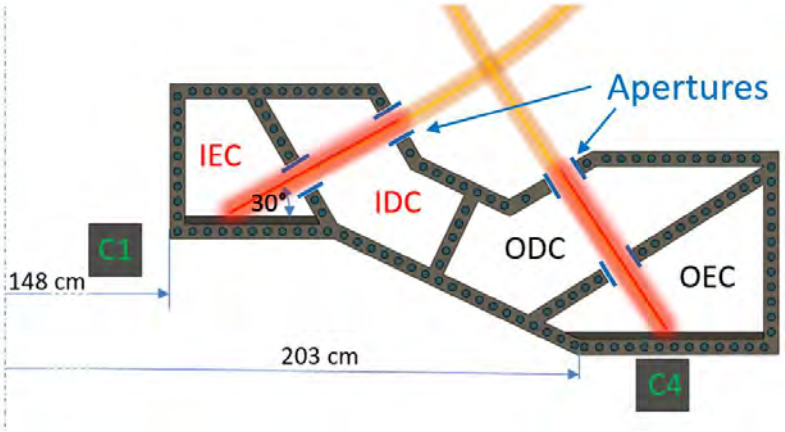

Figure III.20: Cross section of the DTT closed vapour box divertor geometry [III.55-III.56]. *Interaction regions between SOL plasma and metal vapour is highlighted in red.*

The model has shown that using Li leads to a vapour outflow of $\sim 0.5\ g/s$, whereas using Sn leads to an outflow which is a factor 10^{-3} less. Should further studies highlight the fact that this figure could still be unacceptably large; a new design could be conceived with a larger number of chambers. Operating temperatures of the pool for the two LMs are reported in Fig. III.21.

With two LMs the maximum temperature of the target is compatible with a W substrate [III.57] and significant difference between them is ultimately a consequence of the different temperature dependence of the evaporation rate. For Li, already at ~700˚C significant evaporation takes place, removing heat from the pool. The heat flux to the pool is also reduced due to plasma-vapour interactions. Instead for Sn there is a much less significant contribution of evaporation/condensation cooling as it is negligible plasma cooling due to plasma-vapour interactions, finally the box structure is capable of reducing the Sn vapour flow out towards the main plasma chamber by two orders of magnitude.

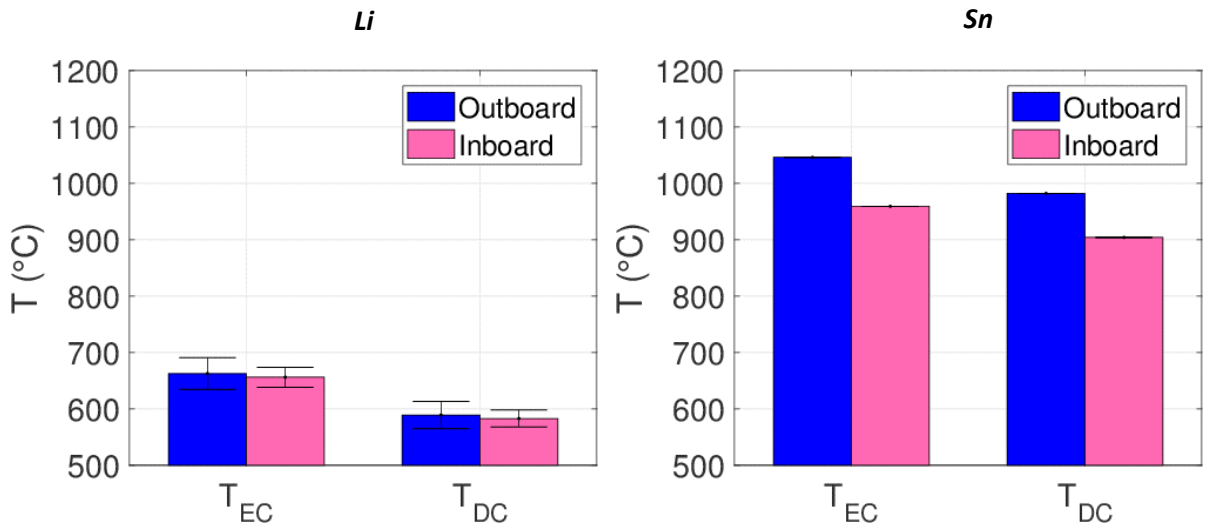

Figure III.21: Temperatures of the LM-vapour system within the various chambers for Li (left) and Sn (right). Error bars account for uncertainty on the particle dwell time of impurities in the plasma, τ (very small effect for Sn).

III.4.3 First Wall

The radiated power load on the DTT first wall (FW) in stationary condition has been estimated as a result of the SOLDGE2D-EIRENE modelling described in section III.4.1 and by using the Monte Carlo (MC) tool developed for radiation heat load calculation in DEMO during steady state and disruptions [III.57]. This MC tool allows the 1D radiated power profiles (W/m^3) to be turned into a 2D map of radiation density. A number of random points is generated uniformly inside the plasma and a rejection method is applied to obtain a density of points, in the poloidal cross-section of the plasma, distributed according to the given radiation profile. The volume variation with the major radius of toroidally-symmetric volume elements is considered by including a factor $2\pi R$. A search algorithm is finally applied to determine where the trajectories of photons originated at each point intersect the wall. The poloidal location of these intersections describes the heat distribution onto the wall. All the power input (45 MW) has been assumed to be radiated uniformly from the entire plasma or from an annular region ($0.75 < r/a < 1.0$) at the edge.

The resulting maximum value of the wall load is 0.5 MW/m^2, located on the outboard, for the former case, and 0.45 MW/m^2 for the latter one. To be pointed out that it was assumed that the wall absorbs all incident radiation, that is reflections have not been taken into account.

The two methods show a reasonable agreement: Fig. III.22 shows an example of the power load on inner and outer wall computed with SOLDGE2D-EIRENE and argon seeding at maximum input power.

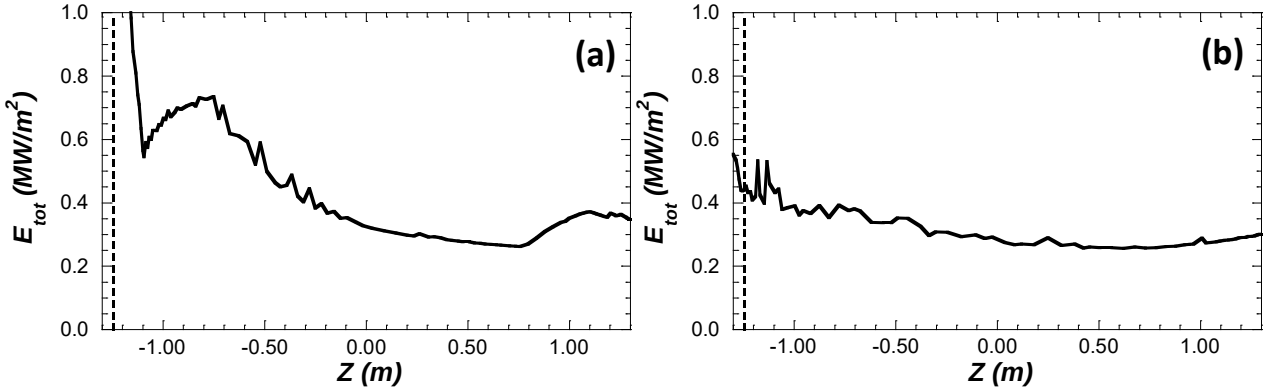

Figure III.22: Power load in stationary condition on the first wall, dashed line shows x-point position: a) inner wall; b) outer wall.

Simulations of inboard FW heat loads have been carried out during DTT start-up with plasma current linearly increasing during 15 s up to 3 MA. To be conservative only ohmic power losses have been considered with 1 V loop voltage, resulting in a linear increase of the SOL conducted power up to 3 MW. Following recent experimental evidences, suggesting the existence of a short near SOL energy e-folding length during start-up with the plasma leaning on the inboard wall, the value of this short energy e-folding length in DTT was estimated on the basis of the similarity of its scaling with the scaling for H-mode [III.58]. The latter in turn depends on the inverse of the poloidal magnetic field [III.59-III.60]. In DTT the estimated $\lambda_{q,omp}$ in H-mode being about 2 mm and taking into account the limited value of I_p at the start up as well as the mapping from outer to inner midplane, a $\lambda_{q,imp}$ = 5 mm has been assumed in the simulations; to be further conservative, all the power has been considered to flow to the inner wall with this short energy e-folding length. The maximum power load, reached at 15 s, resulted to be about 1.5 MW/m^2.

To be pointed out that in the TCV tokamak the power entering the near SOL was found to vanish for high collisionality [III.61], therefore for high density or low temperature, the latter being obtained during the start-up by impurity seeding [III.62]. In DTT, with a tungsten wall also high density could be used, if the case, the wall pumping being probably low.

III.4.4 Heat Load due to Edge Localized Modes

The impact of unmitigated type I Edge Localized Modes (ELMs) on divertor and on the FW has been analysed, based on the hypotheses holding for H-modes with low pedestal dimensionless collisionality (ν^*_{PED} ~ 6.3 x 10^{-2}), ELM energy W_{ELM} ~ 0.16 of the pedestal energy content $W_{PED,}$ with W_{PED}~0.4W_{TOT}, resulting in W_{ELM}~1.2 MJ. As for divertor loads, to be conservative all this energy was assumed to reach the divertor without losses to the FW. A broadening of the spatial deposition profile by a factor 4 with respect to the inter-ELM was assumed [III.63], with a factor 2 asymmetry in the in/out ELM energy deposition. Following experimental evidences [III.63] the ELM energy pulse at the divertor is expected to have a rise and decay phases so that only about 40% of this energy, corresponding to the quantity released during the rise phase, was assumed to contribute to material damage. A time deposition ~110 μs has been inferred from the correlation of the rise phase time with the transit time for pedestal ions to reach the divertor target = $2\pi Rq_{95}/c_{s,ped}$, with $c_{s,ped}$ the ionic sound velocity [III.64]. On the basis of these assumptions the damage factor

by one ELM for the inner divertor is expected to be about 10 $MJm^{-2}s^{-1/2}$, to be compared with the value 40-60 $MJm^{-2}s^{-1/2}$ quoted as limit for tolerable W damage.

III.5 Conclusions

The rationale driving the design of DTT has been summarised and the process of optimisation of its parameters, triggered by the workshop held in Frascati under the EUROfusion aegis in 2017, described. After this process DTT is now going to be built as an up-down symmetric tokamak with a major radius of 2.11 m, a minor radius of 0.64 m (in the reference single null scenario), a toroidal field of 6 T, a plasma current of 5.5 MA, and a pulse duration of ≈ 100 s. The present DTT device is able to achieve Single Null and alternative configurations such as double null, snowflake, X-divertor and single null with negative triangularity. However, being the alternative configurations more demanding on the PF/CS coils system, in terms of currents and vertical forces, a reduced plasma current has to be considered for their realisation. Moreover, the presence of the in-vessel divertor coils increases the machine flexibility giving the possibility to investigate different divertor solutions. These coils are also fundamental for the implementation of feedback control aid to tackle the power exhaust problem, such as the sweeping and the wobbling strategies described in Chapter 10.

The power exhaust modelling has shown the relevance of DTT in exploring solutions relevant for DEMO. Indeed, to provide acceptable heat fluxes at the targets as in DEMO, DTT must operate in a high dissipative radiative regime. In this regime, obtained by impurity seeding, the edge modelling has shown a clear advantage of Snow Flakes divertor configurations (in particular the SFD^{-}) in providing operation at maximum input power with plasma core contamination much smaller than in the Single Null case. DTT DEMO relevance does apply to the first wall too, which, for the first time, will experience power loads in the MW/m^2 range. Finally, simulations performed for DTT show that liquid metal can be a viable alternative solution in case of failure of standard solid targets. All these results motivated the special care taken in maximising DTT flexibility, to facilitate reaching its objectives, and providing in parallel a powerful tool to develop physics scenarios for DEMO. Indeed, the magnetic configuration flexibility, including the possibility of using liquid metal and the powerful additional heating mix are providing a unique tool where integrated physical and technological solution will be pursued. Completed this first stage, where the pace of machine design was dictating the modelling approach, a broader, systematic and integrated modelling approach is starting to design the scientific programme of DTT.

III.6 References

[III.1] Fusion Electricity – A roadmap to the realisation of fusion energy, November 2012 (http://users.eurofusion.org/iterphysicswiki/images/9/9b/EFDA_Fusion_Roadmap_2M8JBG_v1_0.pdf);

[III.2] WP-DTT1 Report on the "Development of Physics models for particle transport and power exhaust", Version 2.0, April 10, 2015, http://idm.euro-fusion.org/?uid=2MDHQT

[III.3] ENEA, "DTT Divertor Tokamak Test facility, Project Proposal", 2015, ISBN:978-88-8286-3180, and https://www.fsn-fusphy.enea.it/DTT_ProjectProposal_July2015.pdf

[III.4] "DTT. Divertor Tokamak Test facility", Fusion Eng. Des., Volume 122, Pages 253-394, e1-e26, Nov. 2017, http://www.sciencedirect.com/science/journal/09203796/122

[III.5] "Design review for the Italian Divertor Tokamak Test facility", https://doi.org/10.1016/j.fusengdes.2018.12.016
[III.6] Whyte D. G. Fusion Eng. Des. 87, 234 (2012);
[III.7] Lackner K., Fus. Scien. and Techn., 54, 989 (2008)
[III.8] Hutchinson I. H., Nucl. Fus., 36, 783 (1996)
[III.9] Kadomtsev B. B., Fiz. Plazmy, 1, 531 (1975)
[III.10] A. Pizzuto et al., Nucl. Fusion 50 (2010) 095005
[III.11] S.L. Allen et al, Fusion Energy Conf. San Diego,US, 2012
[III.12] G. Calabrò et al.,"EAST alternative magnetic configurations: Modelling and first experiments". Nuclear Fusion, 55 (2015) 083005
[III.13] A.W. Morris, IEEE Transactions on Plasma Science, 40 (2012) 6148288.
[III.14] V.A. Soukhanovskii et al, Phys. Plasmas 19 (2012) 082504.
[III.15] F. Piras, et al., Plasma Phys. Control. Fusion 51 (2009) 055009
[III.16] F. Piras, et al., Plasma Phys. Control. Fusion 52 (2010)124010
[III.17] R. Ambrosino, et al., Nucl. Fusion 54 (2014) 123008
[III.18] P.M. Valanju et al., " Super-X divertors and high power density fusion devices", Phys. Plasmas 16, 056110 (2009)
[III.19] X. Wang, F. Xie and H. Jin. "Electromagnetic Analysis of the ITER Upper VS Coil". Journal of Superconductivity and Novel Magnetism, 27 (4), pp. 1015-1019 (2014)
[III.20] R. Albanese, R. Ambrosino, M. Mattei, "CREATE-NL+: A robust control-oriented free boundary dynamic plasma equilibrium solver", Fusion Engineering and Design, 96-97, pp. 664-667(2015)
[III.21] F. Alladio and F. Crisanti, "Analysis of MHD equilibria by toroidal multipolar expansions", Nucl. Fusion 26 (1986) 1143.
[III.22] S. Ejima et al. "Volt second analysis of D-III discharges", Nuclear Fusion Vol. 22. No 10 (1982) 1313
[III.23] D.D. Ryutov, "Geometrical properties of a snowflake divertor", Phys. Plasmas 14 (2007) 064502.
[III.24] G. Calabrò et al., "Divertor configuration with two nearby poloidal field nulls: modelling and experiments for EAST and JET tokamaks" presented at 22nd International Conference on Plasma Surface Interactions in Controlled Fusion Devices, Rome, May 30 – June 03, 2016
[III.25] M. Kotschenreuther, et al., Phys. Plasmas 14 (2007) 72502
[III.26] Eich T, Leonard A, Pitts R, Fundamenski W, Goldston R, Gray T, Herrmann A, Kirk A, Kallenbach A, Kardaun O, Kukushkin A, LaBombard B, Maingi R, Makowski M, Scarabosio A, Sieglin B, Terry J, Thornton A, Team A and Contributors J 2013 *Scaling of the tokamak near the scrape-off layer H-mode power width and implications for ITER* Nucl Fusion 53 093031
[III.27] Eich T, Sieglin B, Scarabosio A, Fundamenski W, Goldston R, Herrmann A and Team *A Inter-ELM Power Decay Length for JET and ASDEX Upgrade: Measurement and Comparison with Heuristic Drift-Based Model* Phys Rev Lett 107 215001
[III.28] Sieglin B, Eich T, Scarabosio A, Arnoux G, Balboa I, Devaux S, Herrmann A, Hoppe F, Hölzl M, Kallenbach A, Lang P, Matthews G, Marsen S, Pamela S, Rack M, Wenninger R, the Team A and Contributors J 2013 *Power load studies in JET and ASDEX-Upgrade with full-W divertors Plasma* Phys Contr F 55 124039
[III.29] Chang C, Ku S, Loarte A, Parail V, Köchl F, Romanelli M, Maingi R, Ahn -W J, Gray T, Hughes J, LaBombard B, Leonard T, Makowski M and Terry J 2017 *Gyrokinetic projection of the divertor heat-flux width from present tokamaks to ITER* Nucl Fusion 57 116023
[III.30] Wischmeier M 2018 *The physics basis for a solution to the power and particle exhaust problem of a next step device* TH/P7-5
[III.31] Goldston R, Reinke M and Schwartz J 2017 *A new scaling for divertor detachment Plasma* Phys Contr F 59 055015
[III.32] Wischmeier M and team and contributors T 2015 *High density operation for reactor-relevant power exhaust* J Nucl Mater 463 22–9
[III.33] Reinke M 2017 *Heat flux mitigation by impurity seeding in high-field tokamaks* Nucl Fusion 57 034004
[III.34] Reimerdes H, Duval B, Harrison J, Labit B, Lipschultz B, Lunt T, Theiler C, Tsui C, Verhaegh K, Vijvers W, Boedo J, Calabro G, Crisanti F, Innocente P, Maurizio R, Pericoli V, Sheikh U, Spolare and Vianello N 2017 *TCV experiments towards the development of a plasma exhaust solution* Nucl Fusion 57 126007
[III.35] Bufferand, H., et al., 2015. *Numerical modelling for divertor design of the west device with a focus on plasma-wall nteractions*. Nuclear Fusion 55, 053025.
[III.36] D. Reiter, M. Baelmans, and P. Börner. *The EIRENE and B2-EIRENE codes*. Fusion science and technology, 47:172, 2005.
[III.37] E. Sytova et al. *Comparing N versus Ne as divertor radiators in ASDEX-upgrade and ITER* Nuclear Materials and Energy 2019 https://dx.doi.org/10.1016/j.nme.2019.02.019)
[III.38] R. Wenninger, et al., Nucl. Fusion 55 (2015) 063003.
[III.39] H. P. Summers, "The ADAS User Manual, version 2.6," 2004.
[III.40] European Research Roadmap to the Realisation of Fusion Energy, https://www.euro-fusion.org/fileadmin/user_upload/EUROfusion/Documents/2018_Research_roadmap_long_version_01.pdf
[III.41] T. W. Morgan, P. Rindt, G. G. van Eden, V. Kvon, M. A. Jaworski, and Lopes, *Liquid metals as a divertor plasma-facing material explored using the Pilot-PSI and Magnum-PSI linear devices Liquid metals as a divertor plasma-facing material explored using the Pilot-PSI and Magnum-PSI linear devices* Plasma Phys. Control. Fusion, vol. 60, no. 1, p. 14025 (11 pp.), 2018.
[III.42] S. V. Mirnov et al., *Li experiments on T-11M and T-10 in support of a steady-state tokamak concept with Li closed loop circulation*, Nucl. Fusion, vol. 51, no. 7, p. 073044 (9pp), 2011.
[III.43] M. Iafrati, G. Mazzitelli, M. L. Apicella, G. M. Apruzzese, J. P. S. Loureiro, I. Lyublinski, A. Vertkov, A. Berlov, G. Maddaluno, F. Crescenzi, A. Mancini, and FTU team, *Comparison between liquid lithium and liquid tin limiters in FTU*, 2017, O5.132 in the procedings from 44th EPS Conference on Plasma Physics in Belfast June 2017, [Online]. Available:http://ocs.ciemat.es/EPS2017PAP/pdf/O5.132.pdf

[III.44] R. Nygren and F. Tabares, *Liquid surfaces for fusion plasma facing components a critical review. part i: Physics and psi*, Nuclear Materials and Energy, vol. 9, pp. 6 21, 2016. [Online].
Available: http://www.sciencedirect.com/science/article/pii/S2352179115301307
[III.45] S. Mirnov and V. Evtikhin, *The tests of liquid metals (ga, li) as plasma facing components in t-3m and t-11m tokamaks*, Fusion Engineering and Design, vol. 81, no. 1, pp. 113 119, 2006, proceedings of the Seventh International Symposium on Fusion Nuclear Technology. [Online]. Available: http://www.sciencedirect.com/science/article/pii/S0920379605004874
[III.46] "DEMO_Divertor_2018_v3.0 (2N7KXG v3.0) (current)." [Online]. Available: https://idm.euro-fusion.org/?uid=2N7KXG.
[III.47] G. Mazzitelli et al., *Pre-conceptual design of liquid metal based plasma facing components* in joint Annual Meeting of WP JET2, PFC and DTT1-LMD, 19-22 Nov. 2018, Zagreb, Croatia, 2019.
[III.48] Zagorski, I. Ivanova-Stanik, V. Pericoli Ridolfini, M. Poradzinski, and F. Crisanti, "Integrated core-SOL-divertor modelling for DTT tokamak with liquid metal divertor targets," in Italy-Poland Meeting, Sept. 28, 2018.
[III.49] R. J. Goldston, A. Hakim, G. W. Hammett, M. A. Jaworski, and J. Schwartz, *Recent advances towards a lithium vapor box divertor*, Nucl. Mater. Energy, vol. 12, pp. 1118–1121, Aug. 2017.
[III.50] Y. Nagayama, "Liquid lithium divertor system for fusion reactor," Fusion Eng. Des., vol. 84, no. 7–11, pp. 1380–1383, 2009.
[III.51] M. Ono, M. A. Jaworski, R. Kaita, Y. Hirooka, D. Andruczyk, and T. K. Gray, *Active radiative liquid lithium divertor concept*, Fusion Eng. Des., vol. 89, no. 12, pp. 2838–2844, 2014.
[III.52] R. Goldston, E. D. Emdee, and J. Schwartz, *The lithium vapor box divertor* IAEA TM on Divertor Concepts, vol. 2016, no. T167. 2018.
[III.53] G. F. Nallo et al., *Modeling the lithium loop in a liquid metal pool-type divertor*, Fusion Eng. Des., vol. 125, pp. 206–215, Dec. 2017.
[III.54] R. J. Goldston, *Heuristic drift-based model of the power scrape-off width in low-gas-puff H-mode tokamaks*, Nucl. Fusion, vol. 52, no. 1, p. 013009 (7 pp), 2012.
[III.55] G. F. Nallo, G. Mazzitelli, L. Savoldi, F. Subba, and R. Zanino, *Self-consistent modelling of a liquid metal box-type divertor with application to the Divertor Tokamak Test (DTT) facility : Li vs . Sn*, Submitted to Nucl. Fus.
[III.56] R. Albanese, *DTT: a divertor tokamak test facility for the study of the power exhaust issues in view of DEMO*, Nucl. Fusion, vol. 57, no. 1, p. 016010, 2017.
[III.57] F. Subba et al., Plasma Phys. Control. Fusion 60 (2018) 035013.
[III.58] M. Kocan et al., Nucl. Fusion 55 (2015) 033019.
[III.59] Eich T. et al 2013 Nucl. Fusion 53 093013.
[III.60] R.J. Goldston 2012 Nucl. Fusion 52 013009.
[III.61] F. Nespoli et al., 2017 Nucl. Fusion 57 126029.
[III.62] F. Nespoli et al., Physics of Plasmas · December 2017 DOI: 10.1063/1.5023201.
[III.63] T. Eich et al., Journal of Nuclear Materials, 415 (2011) S856.
[III.64] A Loarte et al 2003 Plasma Phys. Control. Fusion 45 1549.

Chapter IV

MECHANICAL COMPONENTS

IV.1 Introduction

The major goal of the Divertor TOKAMAK Test facility (DTT) is to bring alternative divertor solutions to a sufficient readiness level to be adopted by EU-DEMO. To this end, the 2015 DTT baseline design [IV.1] is deeply revised to take into account new possible plasma configurations (i.e. Double Null -DN) involving, eventually, two divertors (upper and lower) and a symmetric configuration of the ex-vessel magnet system (Toroidal Field Coils and Poloidal Field Coils). In this chapter, the latest progresses, frozen at March 2019, related to the conceptual design of the main mechanical components of DTT device and the remote handling strategy are presented. The new design of Vacuum Vessel (VV) and Cryostat Vessel (CV) is mainly constrained by the space reserved for the magnetic coils and a new ports configuration. Concerning the VV, a double-wall structure made of AISI 316L(N) stainless steel is preferred over the previous single-shell Inconel structure [IV.2]. The shape of the Cryostat has to be compatible with the new ports configuration, which is now better detailed to consider remote maintenance systems, diagnostics and heating equipment.

Supports are also designed for the first wall, which is conveniently segmented in view of its remote installation/replacement. A preliminary conceptual design of the thermal shield is presented as well.

Divertor design strategy and, finally, remote handling system for main in-vessel components are also reported.

IV.2 Vacuum Vessel and Ports

The Vacuum Vessel (VV) is located inside the magnet system. It provides an enclosed, vacuum environment for the plasma and also acts as a first confinement barrier. VV is a stainless-steel torus vessel with a “D” shaped cross-section, delivered in several modules to be field welded. Its main components are: the main vessel, the port structures and the supporting system (Fig. IV.1).

The main functional requirements of the VV are listed as follows:

- it shall provide a boundary consistent with the generation and maintenance of a high-quality vacuum;
- it shall provide the first confinement barrier and withstand postulated accidents without losing confinement;
- it shall withstand the nuclear heating within the allowable temperature and stress limits;
- it shall support the in-vessel components and their loads under normal and off-normal operations;
- it shall maintain, together with the in-vessel components, a specified toroidal electrical resistance;
- it shall provide access ports or feedthroughs for in-vessel component, diagnostic, heating system, services and maintenance.

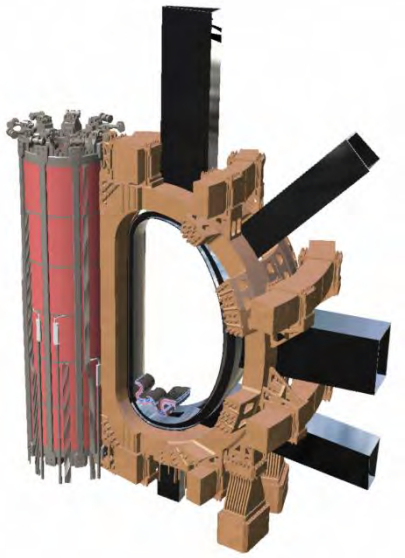

Figure IV.1: Isometric view of a Vacuum Vessel sector (in black) with schematic representation of magnets and divertor.

The design of the VV shall meet the following requirements:

- VV is a torus with “D” shaped cross-section;
- Each sector is 20° wide;
- Each sector must have several access ports for different purposes;
- At least one port per sector must be aligned with plasma center;
- Four sectors must allow the (de)commissioning of the outboard First Wall (FW) segments, the lower divertors and, eventually, of the upper divertors;
- All upper vertical ports (port#1 in Fig. IV.2) must allow for inboard FW segments (de)commissioning;

- Two ports in adjacent sectors must allow the installation of tangential negative neutral beam injectors (NNBI);
- The poloidal curvature of VV must consider the presence of the in-vessel coils;
- The location of the ports shall be defined taking into account the interface with Poloidal Field (PF) Coils, Toroidal Field (TF) coils and the inter-coil structure.

IV.2.1 Main vessel

The main vessel is a double-walled torus with "D" shaped cross-section, segmented as stated below (Fig. IV.2):

- 14 standard modules (20°) whose access ports are designed to satisfy requirements coming from diagnostic system, heating system, pumping system and Remote Handling system (see section IV.2.2);
- 1 NNBI module (80°) able to host two adjacent neutral beam injectors at the equatorial level.

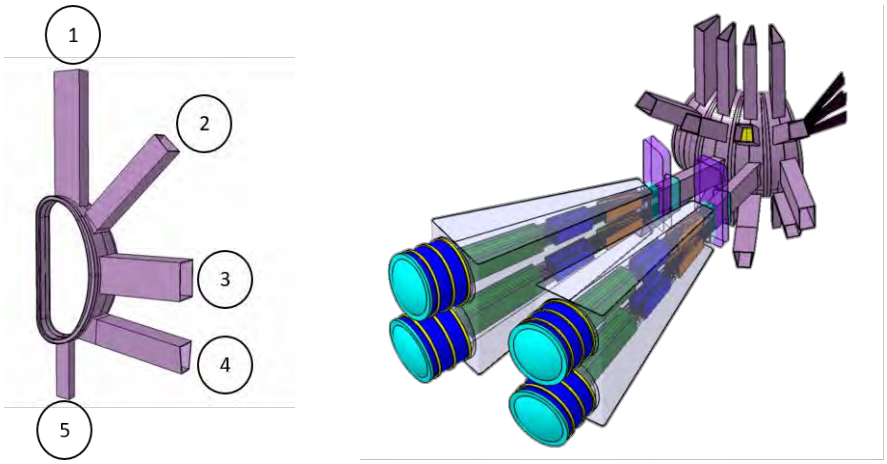

Figure IV.2: Standard and NNBI modules

The main vessel is an all-welded double wall structure. In the current configuration, the thickness of the inner and the outer shells is set equal to 15 mm.

The overall external dimensions of the VV are reported in Fig. IV.3. The maximum height is equal to 3940 mm, with a radius of 1265mm at the inboard side and of 3400 mm at the outboard side.

The material to be used for vacuum vessel has a significant influence on performance, fabrication characteristics, mechanical strength at operating temperature, chemistry properties, and cost. Compared with other possible candidates, AISI 316L(N) stainless steel has good mechanical properties, good chemistry properties, which are well-known (lot of companies can actually work with this material).

A set of internal ribs has been conceptually designed. The design has been driven by thermohydraulic and structural requirements. A nominal minimum clearance of 85 mm in operation conditions (VV warm and TFC cold) between VV and the magnetic coils has been granted to house properly the thermal shield. Tab. IV.I summarizes the main design parameters of the VV.

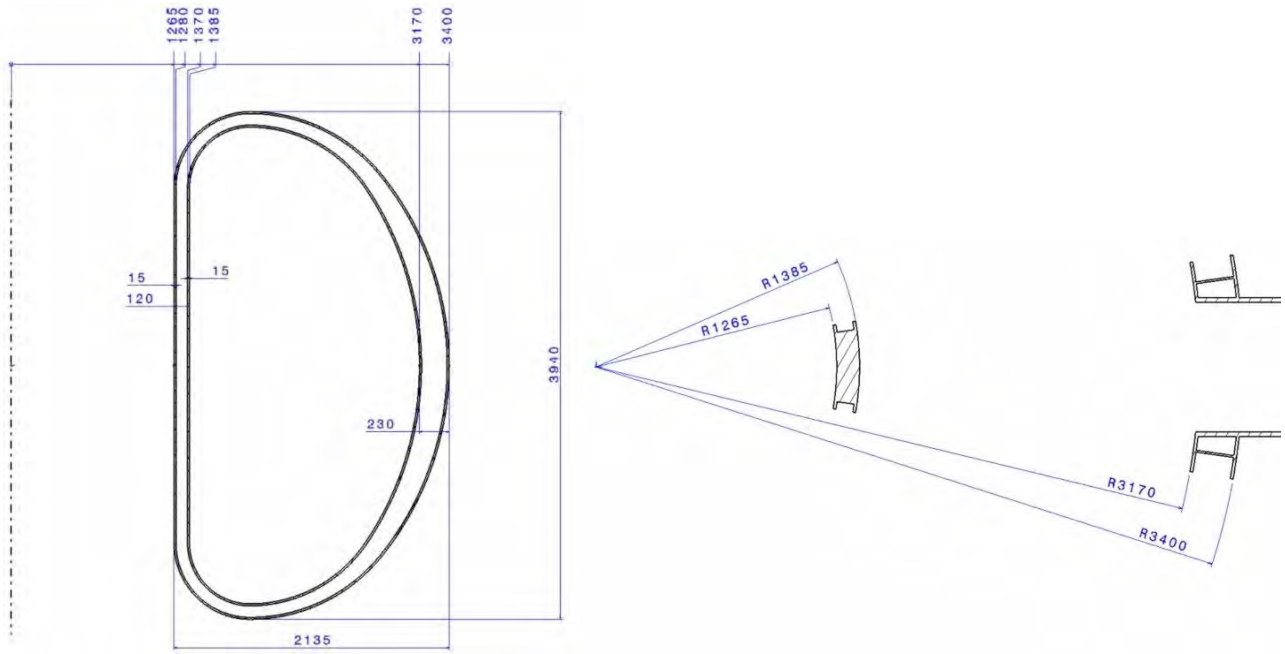

Figure IV.3: Overall dimensions (in mm) of main vessel poloidal section and radial build

TABLE IV.I. VV MAIN PARAMETERS

Shell Thickness (inboard)	15 mm
Shell Thickness (outboard)	15 mm
Ports Thickness	25 mm
Material	AISI 316-L(N)
Ribs thickness	10 mm
Torus outboard diameter	6800mm
Torus inboard diameter	2530mm
Weight of main vessel body	36900 kg
Torus height	3940mm
Volume of the shielding water	13.5 m^3
Volume of the VV – plasma side	75 m^3
Plasma Operating Temperature of the VV (max)	80°C
Baking temperature of the VV (max)	110°C
External surface of the vacuum vessel (holes subtracted)	111.5 m^2

IV.2.2 Access ports

The VV shall provide several openings for the plasma diagnostic systems, the vacuum system, the auxiliary heating system, the in-vessel Remote Handling (RH) maintenance system, etc. As mentioned, each 20° vessel standard module is equipped with 5 access ports conceived as single-walled structures welded to the main vessel. They have been numbered clockwise from top to bottom (Fig. IV.2). These ports are used for the

maintenance and the replacement of the in-vessel components (divertor cassette, first wall) and for the allocation of diagnostic and heating equipment. Their thickness has been provisionally determined in 25mm. The dimensions of access ports are shown in Fig. IV.4. Almost all the ports have space reservation for the cooling pipes of In-Vessel Components (i.e. FW and Divertor).

In particular: ports No.1 are mainly and provisionally devoted to the RH of the inboard segments of the First Wall and to the cooling pipes of the VV.

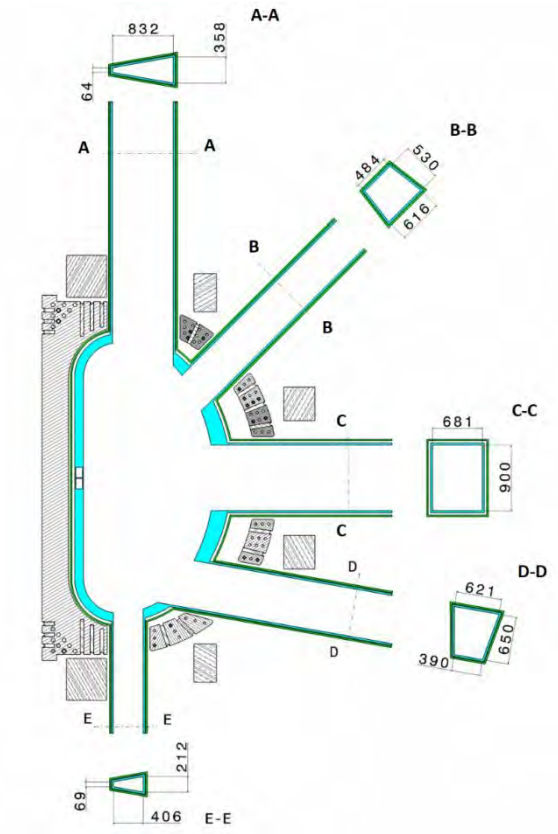

Figure IV.4: Dimensions of access ports of a standard 20° vessel module.

Ports No. 2 are aligned with plasma center in order to house proper the ECRH antenna and some diagnostics.

Ports No. 3 (equatorial ports) are mainly devoted to the diagnostic system, the ECH and ICRH antennas and the remote handling of the outboard segments of the FW (four ports dedicated). They are generally characterized by an opening shape relatively high and rather narrow. However, NNBI modules are quite different from the others, since their equatorial ports must accommodate the co-tangential unit of the NNBI system (Fig. IV.5). Since the beams are injected at 30-degrees relative to the poloidal plane, the available space for the port is reduced and the equatorial accessibility of the two adjacent sectors is compromised as well.

Ports No. 4 are aligned with a possible divertor exit path, in order to ease the access to divertor for remote maintenance or its (de)commissioning.

Ports No.5 are mainly devoted to diagnostics, pumping and fuelling.

The ports of the vacuum vessel are connected to the cryostat ports with bellows to be dimensioned based on loads and temperature ranges. It is understood that, proper port stubs shall be implemented to allow for the correct assembly of the port extensions.

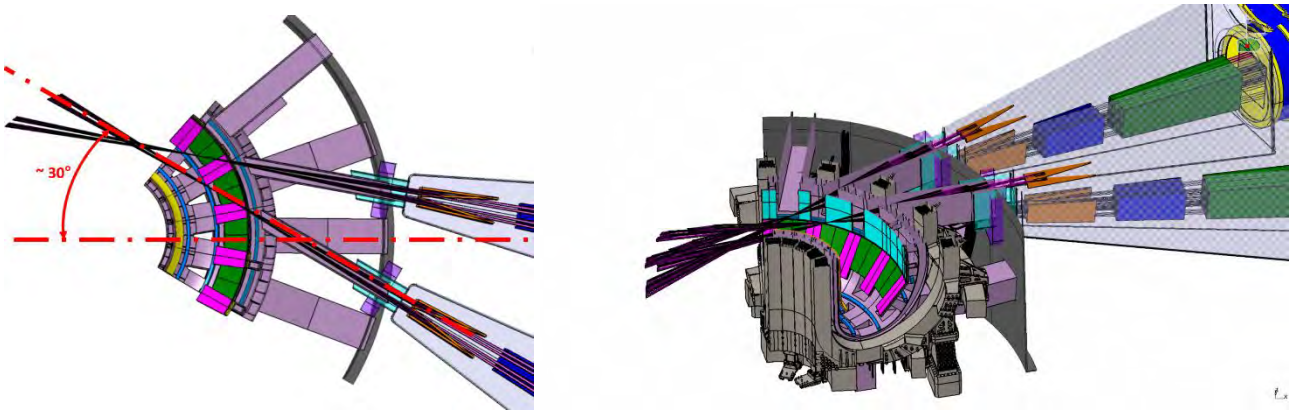

Figure IV.5: Equatorial port aimed at accommodating the co-tangential NNBI beam among the TF coils.

IV.2.3 Vacuum vessel supports

The VV is vertically supported through nine sliding supports resting directly on the ring pedestal. These sliding supports will be radially restrained against fast displacements taking place during seismic events or fast transients. However, they must be radially free to move during thermal expansion. The VV is also restrained vertically in the upward direction through a set of vertical links, located between the pedestal and the lower port. Additionally, the VV will be restrained in a toroidal plane for the position centering. The toroidal restraints will be made of special springs between the VV ports and pedestal ring. These toroidal supports shall maintain the horizontal relative position between the VV and the TF Coil. They can also reduce loads on the vertical supports and make sure that the two systems, VV and TFC, resonate in unison and maintain their relative displacement well below the allocated gap during a seismic event and/or VDE.

IV.2.4 Vacuum vessel cooling

The volume between the inner and the outer shells is designed to allow the circulation of the borated water, which acts as coolant and neutron streaming moderator, in order to reduce the nuclear heating density in the TF winding pack to acceptable limits.

The borated water is a 60°C saturated solution of 95% ^{10}B (B < 0.8 wt%). A requirement for the VV design is that the minimum temperature should be kept at 50 °C during normal experimental operations. The maximum temperature shall be kept below 80 °C to avoid issues related to corrosion effects of boric acid at high temperature.

The overall structure of the VV includes, besides the inner and outer shells, perforated poloidal and toroidal ribs, aimed at stiffening the structure and defining the flow path. The poloidal ribs have holes that ensure that borated water flows in the central part of the outboard sector (see Fig. IV.6). The toroidal ribs are distributed along the inboard sector and are characterized by holes that shall allow the distribution of the borated water in the VV. A preliminary design solution of the poloidal and toroidal ribs has been defined in order to avoid stagnant or recirculation areas in the flow path.

A fluid path of the borated water has been assumed: it flows in poloidal direction, going down in parallel in the two parts of the outboard sector, and going up through the inboard part as illustrated in Fig. IV.6.

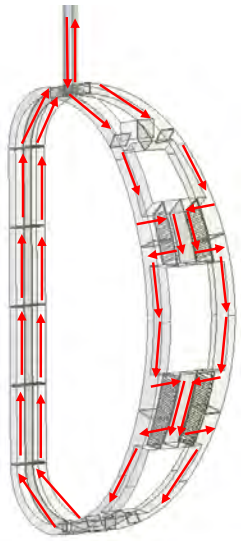

Figure IV.6: Flow path of borated water in one sector (20°) of the VV.

The inlet and outlet pipes (see Fig. IV.7) of the borated water are routed from the upper port: the first is linked to the outboard sector distributing the fluid in the two parts. The outlet pipe collects the borated water coming from the inboard part. It is assumed an inner diameter of 60 mm for the feeding pipes. The path of the VV water supply pipes inside the port is compatible with the space reserved to the FW supply pipe and remote handing FW modules as shown in Fig. IV.7.

Considering a neutron heating power of 80 kW and a DT less than 1°C between inlet and outlet, an overall mass flow rate of 20 kg/s has been considered.

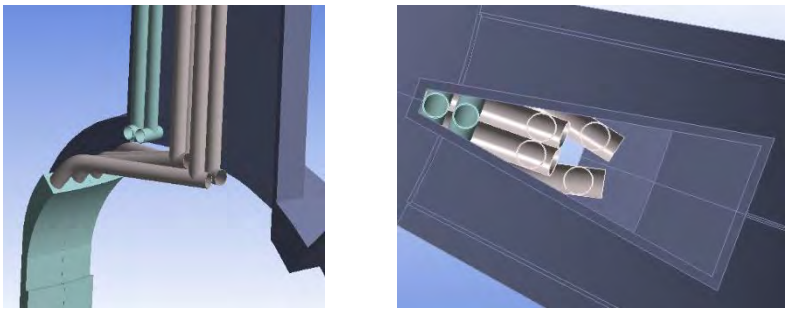

Figure IV.7: VV Feeding pipe arrangement in the upper port

CFD analyses will be carried out to investigate the steady-state flow distribution and pressure drop in the DTT VV under imposed coolant mass flow rate and to optimize the VV interspace design.

IV.2.5 Vacuum vessel mechanical analysis

A stress analysis on the main vessel was conducted in order to validate the thicknesses and the material provisionally defined and to identify possible critical areas.

The Vacuum Vessel is required to keep the ultra-high vacuum tight of less than 10^{-5} Pa and to satisfy target functions with various operational conditions.

Several load conditions and load combinations can occur during normal operation or accidental events. As first reference load case, the electromagnetic loads on metallic structures due to a Major Disruption with a 40 ms Current Quench has been considered as external forces applied to the vessel structures. Design analyses of the VV body is carried out in accordance with the criteria defined in ASME Sec. VIII div. 2.

Electromagnetic loads on the vacuum vessel due to the current quench in a plasma disruption

The evolution of the plasma during a disruptive event has been analyzed. The plasma evolution has been simulated with the CarMa0NL code [IV.3], able to self-consistently couple the 2D axisymmetric plasma and the 3D eddy current models. This analysis does not consider the effect of the halo currents on the 3D conducting structures. Specifically, the disruption scenario is defined by a linear decay of the plasma current starting from the reference equilibrium defined by I_p*=5.5 MA*, βp*=0.433* and l_i*=0.803*. The thermal quench has been modelled as a βp drop occurring in 0.2 ms, from the nominal value of βp to 10% of nominal value. It is assumed that the subsequent current quench occurs linearly in Δt_{CQ} = 40 ms.

The plasma equilibrium in the plasma region is solved on a second order triangular mesh (Fig. IV.8). The electromagnetic coupling of the two models associated to the plasma region and conductive 3D structures is made according coupling conditions fixed on a coupling surface in between the two regions. The 3D mesh of the conducting structure is reported in Fig. IV.9, whereas Fig. IV.10 illustrates some snapshots.

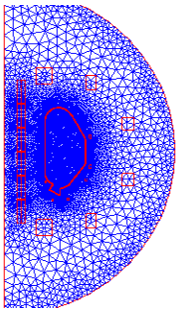

Figure IV.8: Triangular finite elements mesh used in the plasma region.

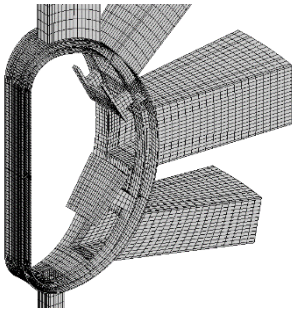

Figure IV.9: 3D mesh used in the disruption analysis.

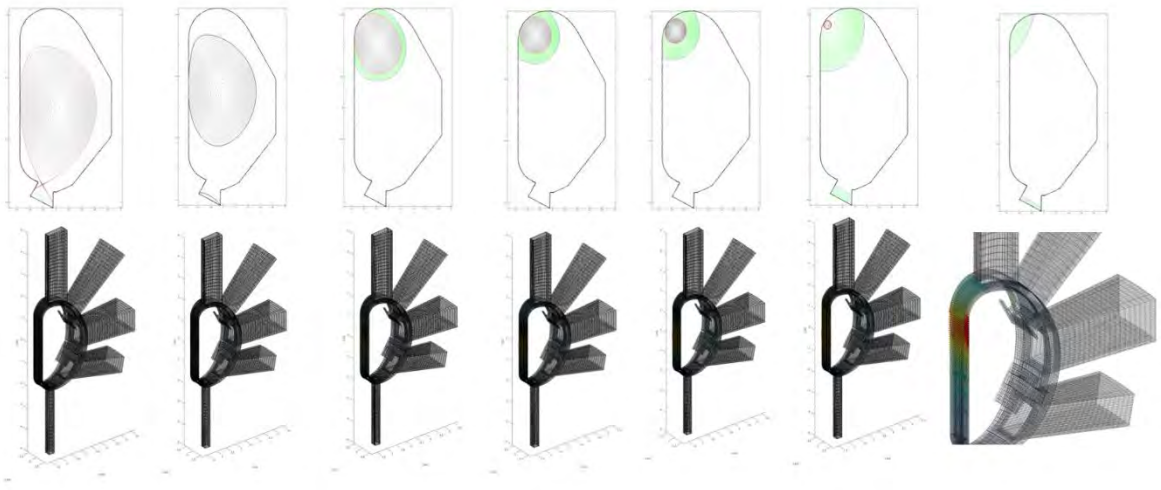

Figure IV.10: Some snapshots during the Major Disruption event

Simulation model

The standard module was used as reference for FEM analyses. The simulation model includes the main vessel, the port structures, the FW supports and the stabilizing plates (Fig. IV.11).

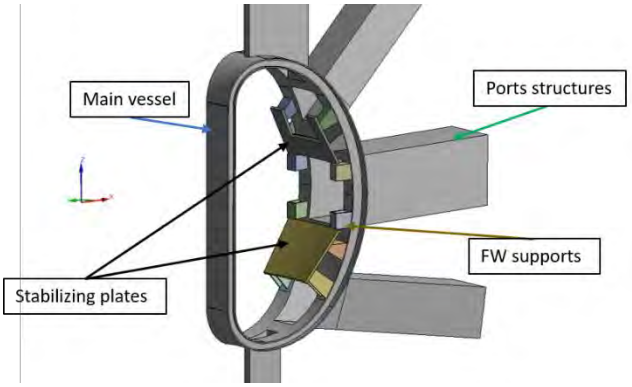

Figure IV.11: CAD model for structural FEA

The directions are named as follows:

- x is the radial direction
- y is the toroidal direction in the xz plane
- z is the vertical direction

The units used in this model are [mm, N].

A cyclic symmetry boundary condition was set on the left and right surfaces of a generic vessel sector. Since the main supports of the vacuum vessel have not been designed in enough detail, a displacement type constraint that limits the rotations in the xz plane but allows for deformations in radial direction has been applied to the lower port. The connections of the FW supporting structure with the stabilizing plates and the main vessel at the outboard side have been modelled as bonded contact regions.

The meshed FEM model consist of 56303 SHELL281 elements and 167982 nodes.

Material

As mentioned, AISI 316L(N) has been chosen as reference material. The material proprieties have been extracted from ASME B&PV Code - II.D.1, Table 2A. The design stress intensity for AISI 316L(N) at the design temperature at 80°C is 138MPa (see Tab. IV.II).

TABLE IV.II. AISI 316L(N) MATERIAL PROPERTIES

Material	AISI 316L(N)@80°C
Young's modulus	194 GPa
Poisson's ratio	0.266
Density	7860kg/m3
Sm (80°C)	138 MPa

Design criteria

The design criteria of vacuum vessel are based the ASME boiler and pressure vessel code section VIII. The electromagnetic loads on the vacuum vessel due to the current quench in a plasma disruption are considered as load category for normal allowable level (as defined in Section VIII, Div. 2) [IV.4].

The stress limits to be considered in the case of linear elastic analysis are the following:

- Primary membrane

$$P_m < S_m = 138\ MPa$$

- Primary membrane plus bending

$$P_m + P_b < 1.5\ S_m = 207\ MPa$$

Loads

The loads applied to the simulation model resulted from the EM analysis on the Vacuum Vessel during a Major Disruption with a 40ms Current Quench. Preliminarily, from the time history of the total EM forces two critical windows were identified between 10ms and 15ms and between 40ms and 50ms (Fig. IV.12). The time-varying nodal forces field was entirely transferred from the EM mesh to the structural mesh from 0ms to 60ms (i.e. 300 timesteps of 0.2ms each). The own weight of the VV has been considered as well.

Results

The analyses, conducted according to ASME rules, showed that the material and the thickness chosen for the main vessel are sufficient to withstand the current quench EM loads.

Figures IV.13 and IV.14 show, respectively, the resultant forces along the Z direction (for the whole torus, 18 sectors) from EM analyses and the Z reaction forces results in the structural FEM model.

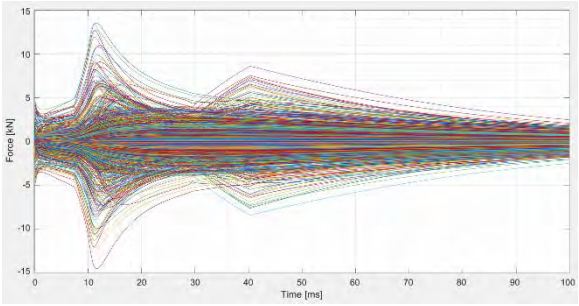

Figure IV.12: EM force time history: trend of EM nodal forces components (Fx, Fy, Fz) for all the nodes of the EM mesh.

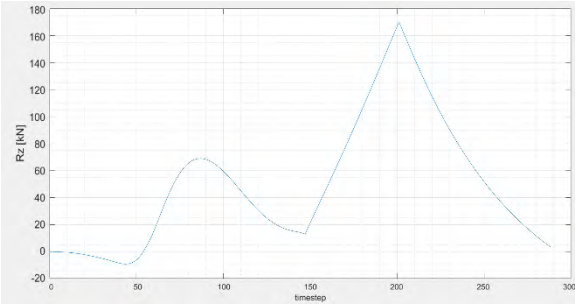

Figure IV.13. Resultant loads in Z direction, from EM analyses.

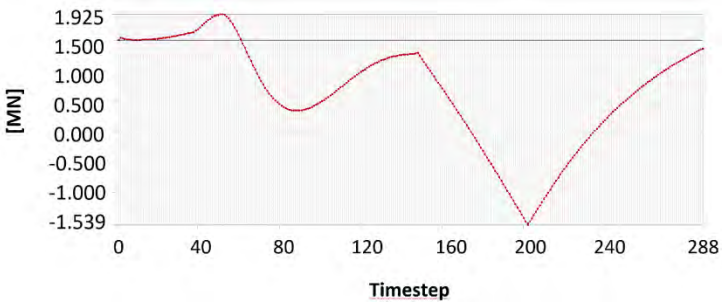

Figure IV.14: Reaction forces along Z direction.

Considering both the EM forces and the own weight of the whole torus (≈153000 kg – black line in Fig. IV.14 set at the reaction forces due to only own weight), the Z reaction forces validated the FEM model, both in terms of loads mapping from EM to structural mesh and in terms of boundary conditions.

Figure IV.15 shows the maximum values of the Von-Mises stresses in the 300-load step considered. The maximum absolute value is reached at about 15ms (i.e. timestep no. 75). A second local maximum is identified at 40,4ms (timestep no. 202), when the vertical EM forces resultant is the highest (see Fig. IV.13). It is worth noticing that the analysis did not considered any dynamic effect (inertial, dumping, etc.).

Table IV.III summarizes the resultant forces applied on the VV, FW supports and stabilizing plates in the latter critical instants.

The Von Mises Stress at 15ms and at 40.4ms are shown in Figs. IV.16 – IV.19. ASME rules are generally verified except for some local effects due to geometrical simplifications, which can be surely neglected.

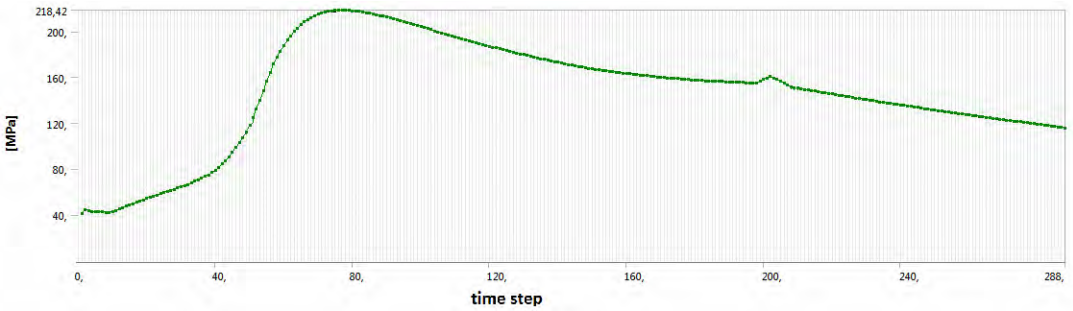

Figure IV.15: Evolution of max equivalent (Von-Mises) stress from 0 to 60 ms

TABLE IV.III. RESULTANT FORCES AT CRITICAL INSTANTS

Time	Force X [N]	Force Y [N]	Force Z [N]	Total Force [N]
15ms	-5.2615e6	-9889.6	56941	5.2931e5
40.4ms	-1.2937e6	3270.1	1.6087e5	1.3036e6

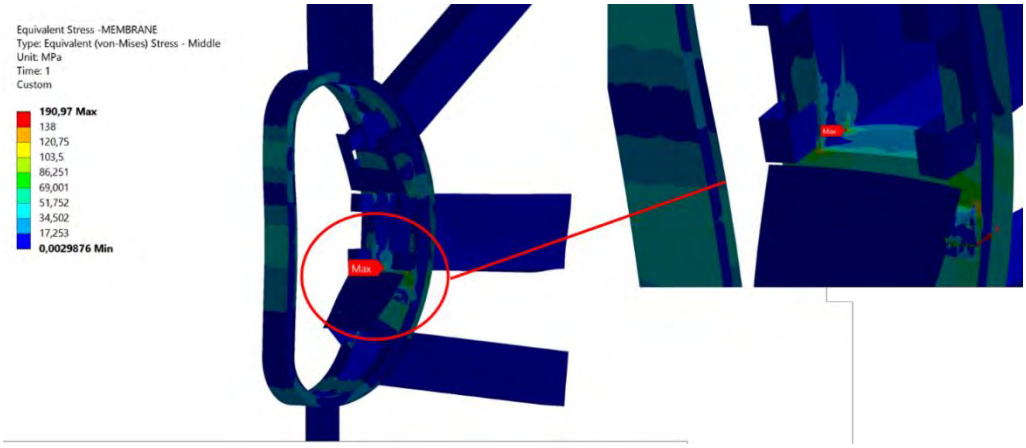

Figure IV.16: Primary membrane stress distribution at 15ms.

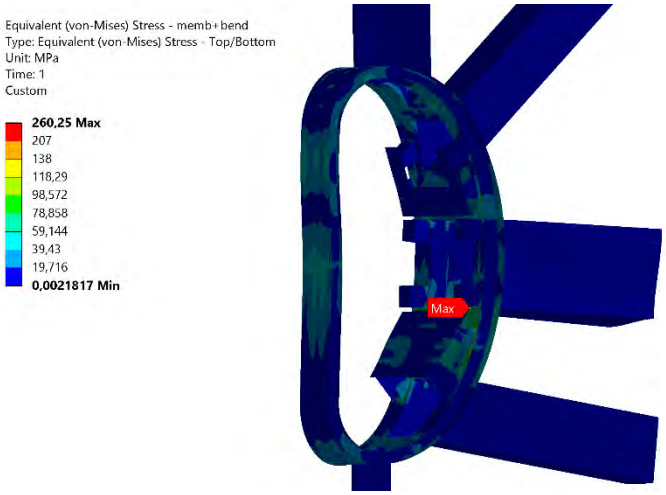

Figure IV.17: Primary membrane plus bending stress distribution at 15ms.

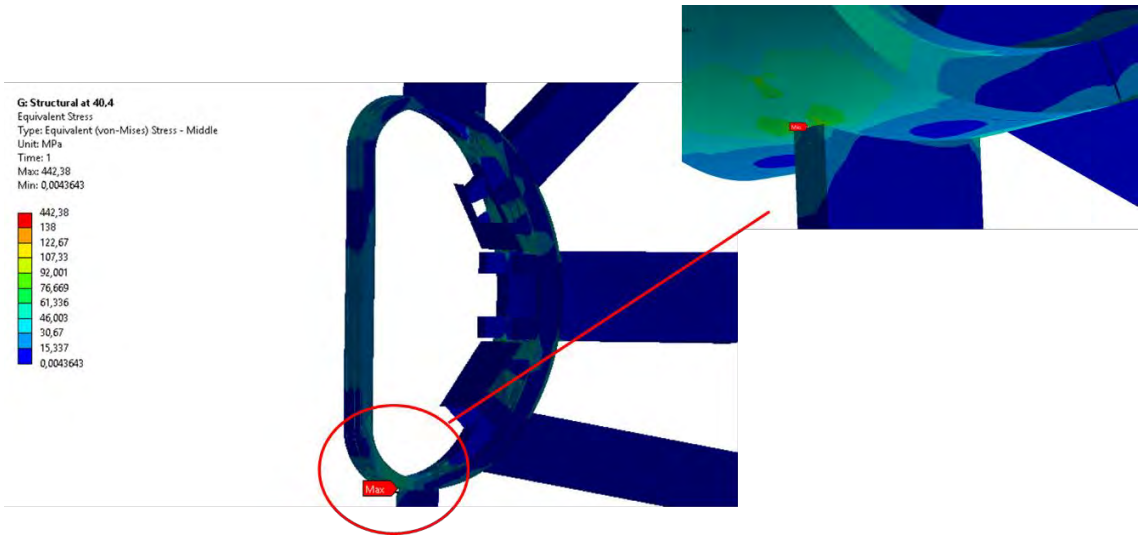

Figure IV.18: Primary membrane stress distribution at 40.4ms.

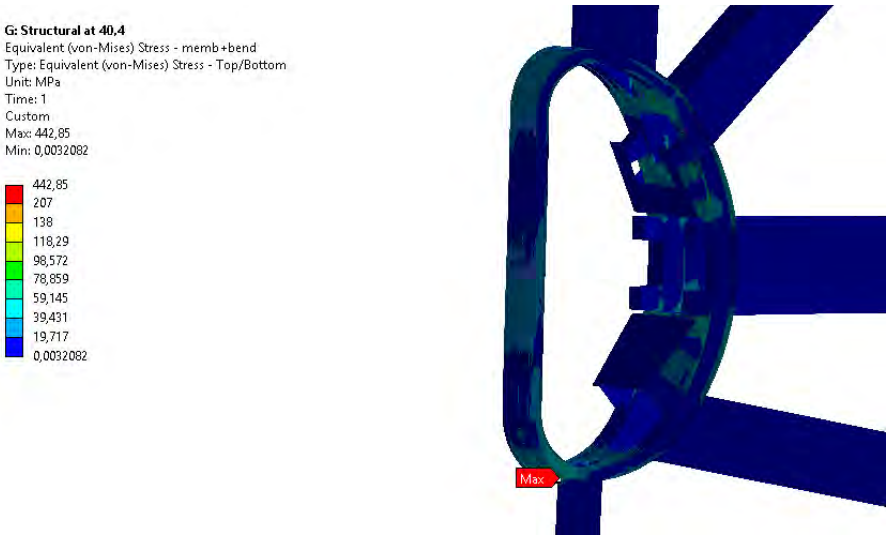

Figure IV.19: Primary membrane plus bending stress distribution at 40.4ms.

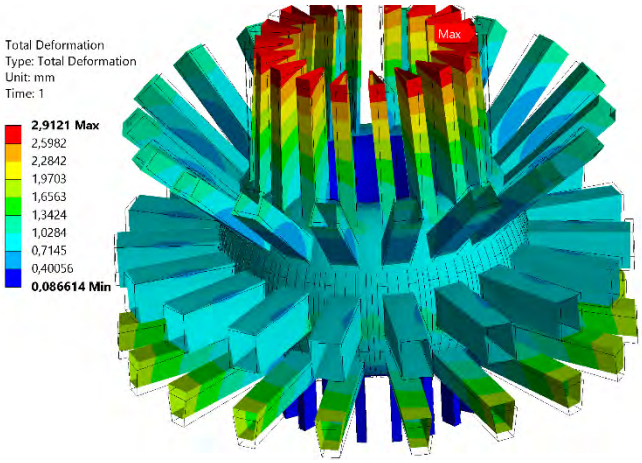

Figure IV.20: Vacuum Vessel total displacement at 15ms.

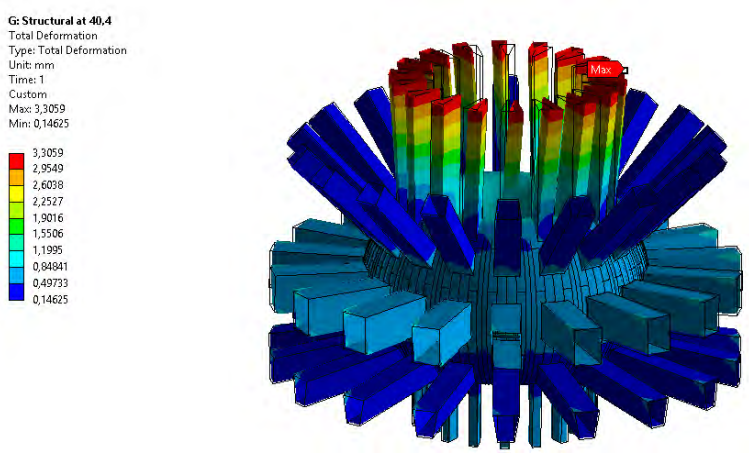

Figure IV.21: Vacuum Vessel total displacement at 40.4ms

The total displacement at 15 ms and 40.4 ms are shown in Figs. IV.20 and IV.21, respectively. Tab. IV.IV summarizes the maximum values of displacements components at critical instants.

TABLE IV.IV. DISPLACEMENTS AT CRITICAL INSTANTS

Time	Ux [mm]	Uy [mm]	Uz [mm]	Utot [mm]
15ms	-2.26	-1.76	1.83	2.91
40.4ms	2.44	2.43	1.17	3.31

IV.3 Cryostat

The Cryostat Vessel (CV) is a vacuum tight container, surrounding the entire Tokamak Basic Machine, which provides the vacuum for the superconducting magnets and forms part of the secondary confinement barrier. The vacuum environment is intended to avoid excessive thermal loads from being applied to the components that are being operated at cryogenic temperatures by gas conduction and convection. The CV provides ports and penetrations, with proper bellows, to the vacuum vessel (see Fig. IV.22).

The bellows compensate for differential movements; they have a rectangular rounded shape and are made of stainless steel materials.

CV must also provide openings for pipes connecting equipment outside the Cryostat to the corresponding elements inside the Cryostat (e.g. magnet feeders, water cooling pipes, instrumentation feedthroughs, CV pumping systems).

The design of the CV shall allow for safe man access inside the vessel during maintenance activities.

The design and construction of the CV shall ensure the required vacuum. The maximum allowable leak rate shall be consistent with achieving the global leak rate requirements for the Cryostat Vacuum boundary. The

maximum acceptable outgassing rate and the maximum allowable leak rate for DTT should be determined during the next design phases.

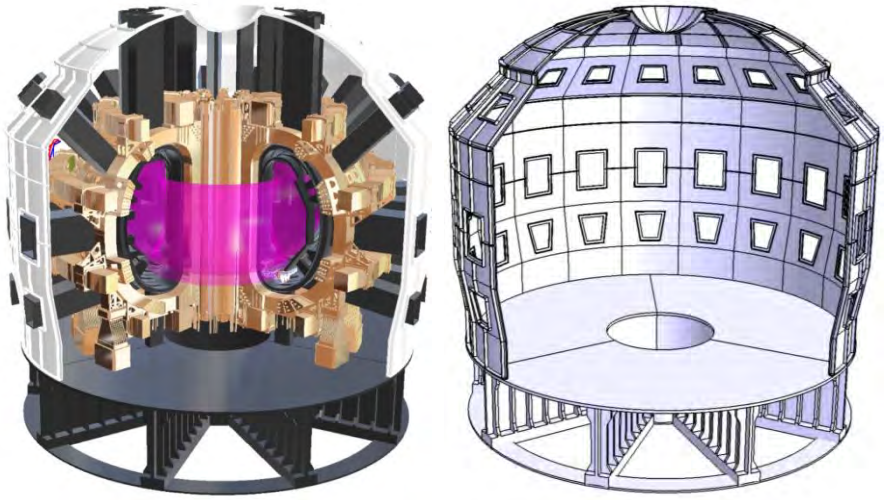

Figure IV.22: Pictorial view of DTT tokamak basic machine (left); 3D CAD model of DTT Cryostat (right).

The Cryostat has been preliminary designed according to the ASME section VIII-Div.2. The design principles are chiefly based on cost minimization and functionality. The cryostat consists of a single-wall cylindrical vessel with stiffness ribs, a basement made of welded plates and a tori-spherical top lid.

The top lid has a tori-spherical shape; its weight can be estimated in about 16 tons. The cylindrical section is conceived as composed by three sectors of about 120° that are bolted by flanges to top lid wall at top and to base plate at bottom. The vacuum tightness of CV is assured by non-structural welds between the bolted parts. Its maximum external diameter (~11.2 m) is determined by the dimension of the maximum diameter of the toroidal field coil with an additional small radial clearance of approximately 1m to facilitate the installation of components and to guarantee proper man access. The cylindrical section is about 7.5 m high; this dimension is determined by the size of components inside as well as to provide adequate vertical space for penetrations through the cryostat cylindrical shell needed to make the interconnections with external systems. The weight of cylindrical portion of the CV is about 66 tons. At the current conceptual stage, cryostat walls are dimensioned as 30mm thick with ribs 25 mm in thickness.

The CV is a fully-welded vessel made of AISI 304L(N) stainless-steel (Co<0.05 wt%, SA-240), providing a large number of penetrations for VV ports and several other horizontal penetrations for coolant pipes at upper and lower levels, as well as for other cryo and current magnets feeding lines. Furthermore, access penetrations for manned access for repair or inspection shall be included in the lower cylindrical portion of the CV and in the top lid (vertical entry).

The CV is supported by a fully welded stainless-steel basement (SA-240 304L(N) - Co<0.05 wt%), which mainly consists of welded plates with stiffness ribs in radial and toroidal directions. On the bottom the stiffening ribs are kept together by two ring plates on the maximum external diameter and at center. The central area of the CV basement has cylindrical shape to accommodate the feeding pipes of the systems inside the CV (see Fig. IV.23).

A preliminary dimensioning of the CV basement has been carried out. Starting from that the thicknesses of the basement top plate, bottom ring plates and radial stiffening ribs have been set to 80mm while the other

plates have 50mm of thickness. The major diameter of the basement is about 10.8m and its total height is set provisionally at about 2m, this dimension will be frozen when all CV penetrations are defined. It is understood that further FEM analyses shall be conducted to better define the steel thickness during more detailed design stages and when the CV load specification will be available. Moreover, the main dimension of the basement will be fixed once the layout of penetration for the in-vessel systems will be defined.

The CV basement has been conceived as divided in three toroidal sectors of 120° to allow for easily handling and transportation to the torus hall. The sectors are joined together through flanges and bolts.

The main parameters of CV are listed in Tab. IV.V.

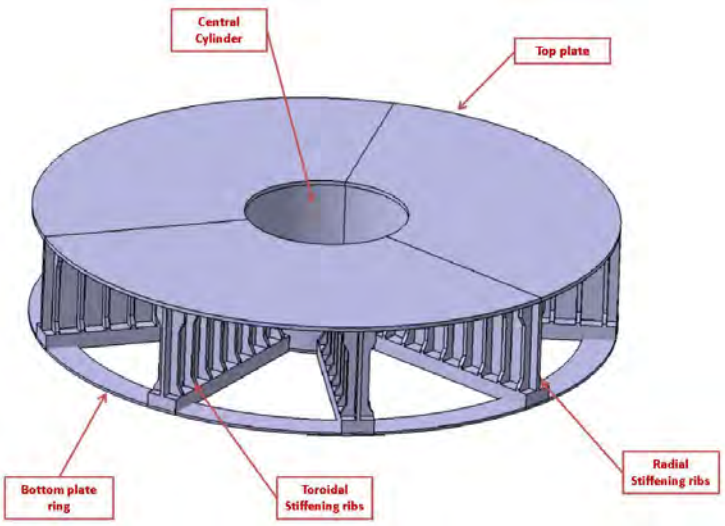

Figure IV.23: Cryostat steel basement

TABLE IV.V: MAIN PARAMETERS OF DTT CV

Major diameter at equatorial section	~11.2m
Diameter at top plate basement level	~10.8m
Maximum height including basement	~11m
Basement Height	~2m
Maximum height of top lid	~1.3m
Structural Material	SA-240 304LN - Co<0.05 wt%
Operational pressure	Vacuum, 10^{-3} Pa
Design temperature of cryostat wall	293 K
Vacuum tightness technology	Vacuum filling welds
Thickness of the Cryostat walls	30 mm
Thickness of the external ribs	25 mm
Estimated Mass of CV main cylinder	~66 tons
Estimated Mass of CV top lid	~16 tons
Estimated Mass of CV basement	~220 tons

IV.3.1 Structural analysis of Cryostat main cylinder and top lid

Structural FEM analyses in two different load conditions have been carried out to check the structural integrity of the CV main cylinder and top lid. Since the system load specification for the CV is not fully defined yet, the following load conditions have been considered:

- ***Normal Operation***: External ambient pressure 0.1 MPa (inside vacuum of 10^{-3} Pa) plus dead weight
- ***Accident Condition***: 0.15 MPa as CV internal pressure, in case of loss of fluid from the piping line plus external pressure of 0.1MPa and dead weight

The CV basement has been neglected in the analysis since those loads are not relevant for its dimensioning. The linear elastic analysis method has been adopted.

IV.3.2 FE model and boundary conditions

Starting from the CV CAD model a FE model of elementary sector of 20° has been developed (see Fig. IV.24). The mesh has SHELL181 element type, the material properties are related to SA-240 304 LN [IV.4].

Cyclic boundary conditions have been applied on the side edges of shell sector; the bottom flange of the cylindrical portion has been constrained against all rotation and translation. The coordinate system considered in the FEM model was cylindrical aligned to the origin of the machine.

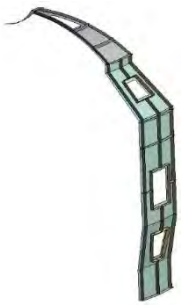

Figure IV.24: Shell model of 20° of CV

IV.3.3 Design criteria and results

The allowable stress in the case of SA-240 304LN at ambient temperature is 138 MPa [IV.4]. According to ASME section VIII-Div.2 the stress limits to be considered in the case of linear elastic analysis are the following:

- Primary membrane

$$P_m < S \ (138 \ MPa)$$

- Primary membrane plus bending

$$P_m + P_b < 1.5 \ S \ (207 \ MPa)$$

The results of the linear elastic analysis showed that the rules are met in all points of the CV both in Normal Operation and in Accident Condition. Values of stress above the limits are due to geometrical singularity points (see Figs. IV.25-IV.26).

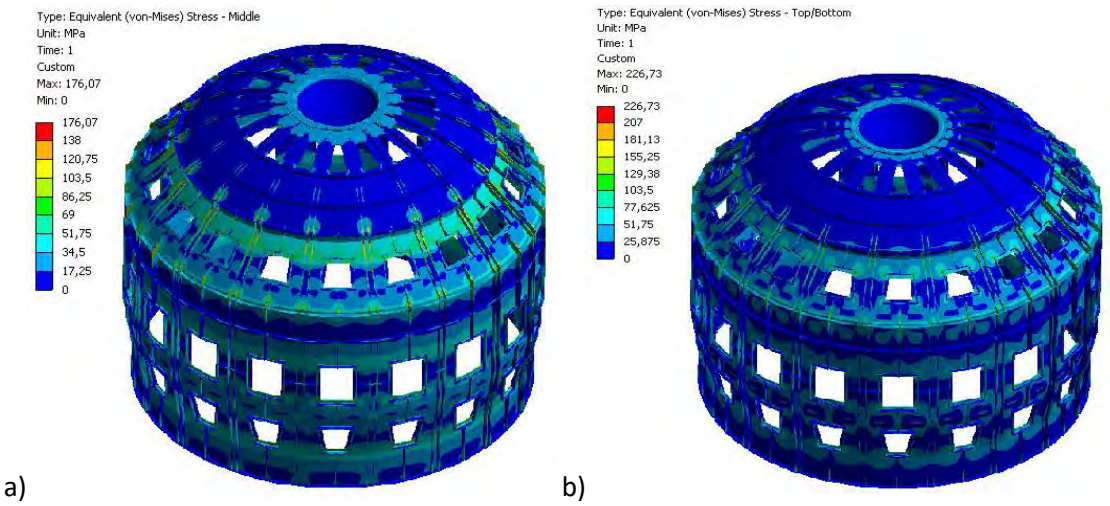

Figure IV.25: ***Normal Operation****: a) Primary membrane stress distribution; b) Primary membrane plus bending stress distribution.*

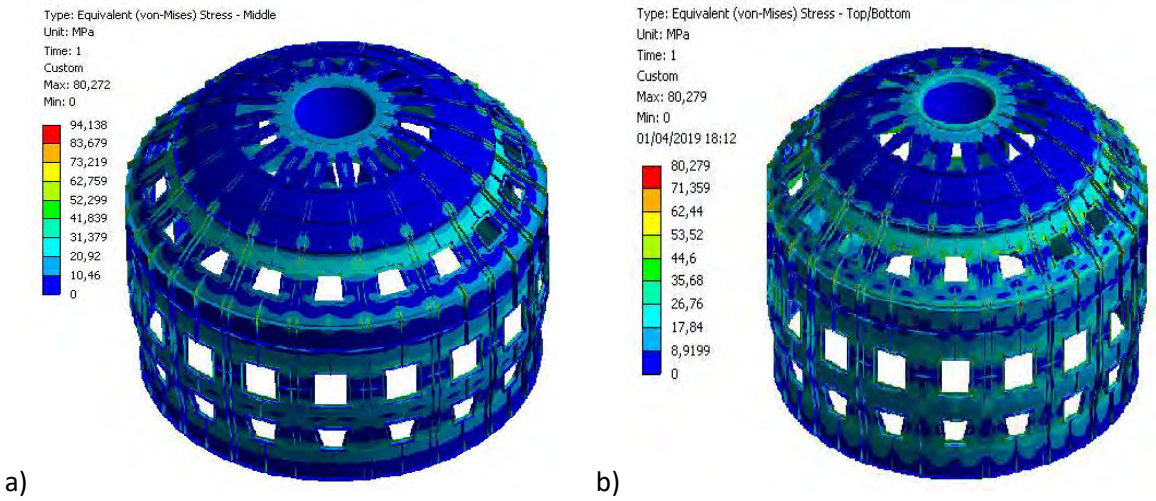

Figure IV.26: ***Accident Condition****: a) Primary Membrane stress distribution; b) Primary membrane plus bending stress distribution*

IV.4 Thermal Shield

The thermal shield (TS) in DTT (Fig. IV.27) is devoted to minimize the heat loads from the tokamak warm components, to the superconducting coils operating at 4.5 K. The TS is subdivided into three main regions covering respectively the vacuum vessel (VVTS), the ports (PTS) and the cryostat (CTS).

It is arranged, along the toroidal direction, in 18 electrically insulated segments (20 deg each), composed of several stainless-steel modules (AISI316L). Each module is made of a lower and upper sheet joined together by ribs along the two edges in the poloidal direction. The cooling is provided by helium gas (80 K and 1.8 MPa) flowing inside tubes welded to one sheet (Fig IV.28). The ribs are 10 deg spaced in the toroidal direction (half of vacuum vessel sector). The main geometrical parameters of the cooling module are reported in Tab.

IV.VI. It is worth noting that the TS module thickness is subject to change to 20 mm to increase the gap among the structures.

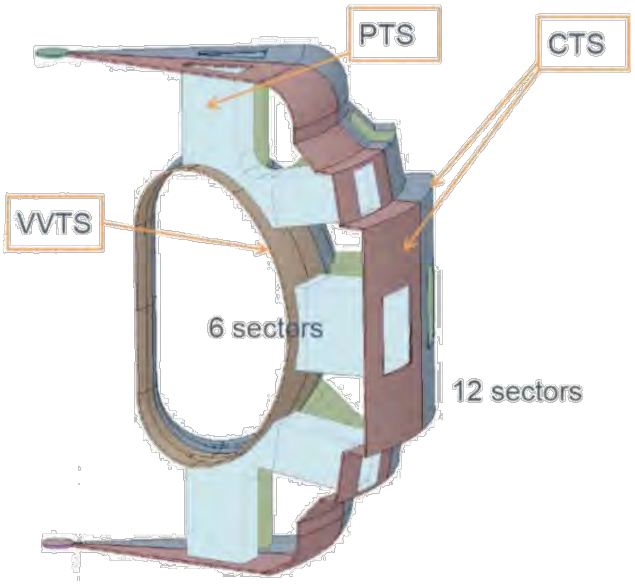

Figure IV.27: Schematic view of the DTT thermal shield

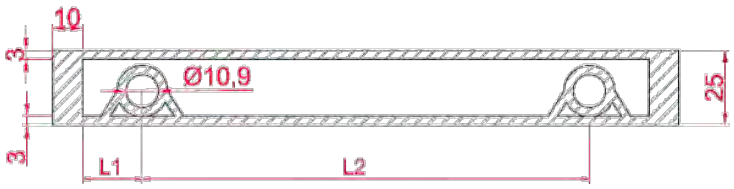

a)

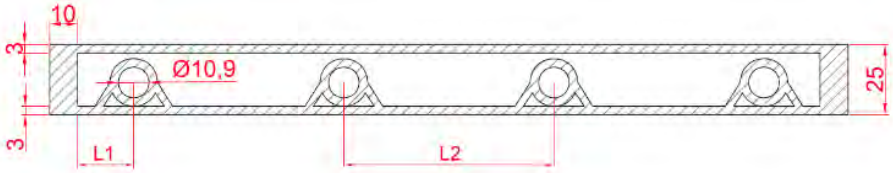

b)

Figure IV.28: TS module configurations with 2 (a) and 4 (b) cooling tubes

TABLE IV.VI: MAIN GEOMETRICAL PARAMETERS OF THE TS COOLING MODULE

Parameter	Value
Module thickness [mm]	25
Sheet thickness [mm]	3
Rib width [mm]	10
Tube inner diameter [mm]	10.9
Number of tubes per module	2 or 4

Using ANSYS mechanical code, 2-D analyses have been carried out for different configurations with two (Fig. IV.28 (a)) or four (Fig IV.28 (b)) tubes between two consecutive ribs. The distance between the ribs and the adjacent pipe center is indicated with L1, whereas the distances between two consecutive pipes is indicated with L2. The panel width (rib to rib distance) is defined by the poloidal position (being fixed the 10° toroidal sector).

Further, L1 has been chosen in such a way to keep the temperature difference between the average temperature on the panel surface facing to the coils and the helium bulk temperature, below 3 K. This said, with the assumption that the distance L2 is the same for the 4 tubes case, it follows that the geometry of the panels is univocally determined.

The flowing helium covers the following route inside the thermal shield cooling pipes: VVTS (inlet), PTS and CTS; with a bulk temperature of 70, 80 and 90 K, respectively. The helium pressure inside the pipes is set to 18 bar. Helium heat transfer coefficients for the three TS regions have been evaluated (see Tab. IV.VII) assuming a velocity of 22 m/s. Furthermore, the TS emissivity of the internal and external surfaces are assumed 0.3 and 0.15 respectively, while the VV and the coil emissivity is 0.15 and 1 respectively.

TABLE IV.VII: HEAT TRANSFER COEFFICIENT

Region	Temperature [K]	Heat transfer coefficient [W/(m²·K)]
VVTS	70	3543
PTS	80	3399
CTS	90	3267

A simulation of the VVTS inboard was executed for the two cooling tubes layout. In this case the VVTS is faced internally with the VV at 373.15 K and externally with the superconducting coils at 4.2 K. The internal distance between two ribs is 180 mm, (length of half a sector in the toroidal plane), while a distance of L1 equal to 20 mm was chosen to satisfy the above-mentioned temperature criterion. In the outboard zone, the distance between ribs is such that 4 pipes are necessary between the ports, while only 2 pipes should be placed laterally to the ports.

The 2D numerical simulations provide the heat flux for both the two and four tubes models, that are then multiplied for the associated areas to obtain the total power on the TS reported in Tab. IV.VIII. In the last column equivalent power at 4K is obtained using the standard efficiency considered for cryoplants (P4K=P70K T2/(T1 – T2) with T1=70 K and T2 =4.2K because the Helium for the TS cooling is extracted from the cryoplants at 70 K).

TABLE IV.VIII: POWER ON THERMAL SHIELD

Component	Area [m²]	Power [kW]	Equivalent Power at 4K [kW]
VVTS	96.47	8.56	0.535
PTS	272.48	24.06	1.504
CTS	266.26	10.92	0.682
Total		43.54	2.72

Therefore, 2.7 kW is the total power required by the cryogenic system for the TS cooling. The same procedure was applied to determine the total power on the coil system and the results are summarized in Tab. IV.IX.

TABLE IV.IX: POWER ON COILS

	Area [m^2]	Power [kW]
TF	146.91	0.09
PF	102.52	0.07
Total		*0.16*

The above results do not account for nuclear heating (neutron + gamma), which appears only during the plasma discharge. A potential helium leakage along the several kilometers of tubes represents a major hazard for the control and stability of the tokamak. Therefore, the associated risk needs to be carefully estimated and stringent requirements. A certain redundancy of the cooling tube shall be envisaged as well.

IV.5 First Wall

IV.5.1 First wall requirements

The DTT First Wall (FW) must satisfy the following external requirements:

- Compatibility with the closed loop experiment with the liquid lithium divertor. One of the experiments with the liquid lithium divertor foresees the possibility to recover the amount of metal evaporated from the divertor region by making it condensate without solidifying on the FW. A so-called “closed loop” takes place: the evaporated lithium flows back in liquid form along the FW surface towards the divertor region where it can evaporate again. The requirement for the FW is that for these dedicated experiments the minimum temperature of the plasma-facing surface must be above the melting point of lithium with margin. The value of 200°C has been chosen.
- Compatibility with the RH system. The FW modules must allow to be assembled and disassembled one by one.
- Compatibility with the electromagnetic loads. The fixing system of the FW modules onto the vacuum vessel must sustain the loads due to the Lorentz Force, both during nominal and undesired transients (e.g. breakdown, disruptions).
- Compatibility with the diagnostic system. The FW plasma-facing units and fixing system must accommodate a space for the placement of diagnostics. The reserved space for each magnetic diagnostic is 100 mm x100 mm x10 mm.
- Compatibility with DEMO. Materials with high and moderate activation, such as copper, must be avoided as structural material and reduced as much as possible for applications as functional material.

IV.5.2 Description of the FW layout

It was decided that the DTT FW should be an actively water-cooled component to withstand the thermal load, which is high particularly during the current ramp-up, and to allow temperature control of the surface compatible with different plasma scenarios and test campaigns.

The DTT FW will be divided in three main components: the inboard FW (IFW), the outboard FW (OFW) and the top FW (TFW). The first two components will operate in all the DTT scenarios, whereas the last will be replaced by an upper divertor for the double null scenarios. The IFW has a poloidal length of 2300 mm. It shows no upper baffle, which will be provided by the top FW/upper divertor. It is foreseen that the IFW will be used also as a limiter during the current ramp-up. The OFW and TFW have a poloidal length of 2250 mm and 1900 mm, respectively.

The FW components consist of plasma facing units (Unità Prima Parete or UPP in Italian) in which the heat load is dissipated. The UPPs are arranged in groups by the back structural supports (back-plate) to form the FW modules called MPP (Modulo di Prima Parete – in Italian). The back-plates provide connection to the VV and mechanical resistance to the electro-magnetic loads.

IV.5.3 Design specification of the DTT FW

The DTT FW must satisfy thermal, hydraulic and dimensional specifications. Regarding the thermal loads, the IFW will be designed to withstand the loads due to the current ramp-up which consists in a ramped load up to 1.5 MW/m^2 in 15 s. The outboard FW is designed for the steady state operation, which foresees a maximum load of 0.55 MW/m^2, whereas the TFW is designed for disruption loads. The maximum pressure of cooling water will be kept below 32 bar, while the flow velocity in the hydraulic water supply system must not be higher than 2.5 m/s. The water manifold will be placed at an upper position with respect to the plasma-facing unit modules, in order to allow outgassing of undesired bubbles from the region where thermal loads are applied. The radial dimension of the IFW in the straight portion of the components must not exceed 55 mm, so that the nominal tolerances between the plasma-facing surface and the separatrix will be satisfied. Moreover, the water system must not interfere with the allocated space for the upper divertor, though the DTT experiment will start with only a lower divertor.

IV.5.4 Design status

Inboard plasma facing unit

The inboard FW UPPs are designed to withstand the loads due to the ramp-up current. In any cases, During the flat-top phase, a temperature greater of at least 200 °C on the plasma facing surface should be assured for the Lithium divertor closed loop testing. Due to the poloidal inhomogeneities the minimum load expected during the single null standard scenarios is 0.2 MW/m^2. Due to the stringent dimensional requirements, a coaxial cooling pipe layout was chosen for the UPP. The cross section was optimized by means of thermo-mechanical analysis considering a thermal load ramped up to 1.5 MW/m^2 in 15 s followed by constant load of 0.2 MW/m^2 for 100s. To comply with the material requirement, stainless steel was preferred to copper as structural material. The stainless steel low thermal conductivity was taken to satisfy the requirement to low thermal load also with water bulk temperature close to the VV one. The inlet pressure was kept at 27 bar to allow the FW baking to 200°C. The water velocity of 3 m/s, in the swirled external circular crown, ensures

low pressure drop and suitable cooling time. As armor material, a 3 mm thick plasma-spray Tungsten layer was considered in the thermo-mechanical analysis.

Two different concepts were selected for the next step of manufacturing and testing of small mock-ups. For their different thermal behavior, they will be called capacitive (C) concept and thermal break (TB) concept.

Fig. IV.29 shows some geometrical parameters for both concepts: the cross section is referred to the straight part of the IFW. The external pipe diameters are 28/25mm, the inner pipe diameters are 19/16mm. between the two pipes there is a swirl tape 0.8mm thick with twist ratio 2. It can be noted that the width in the cross-section plane is greater in the TB case, than in the C case.

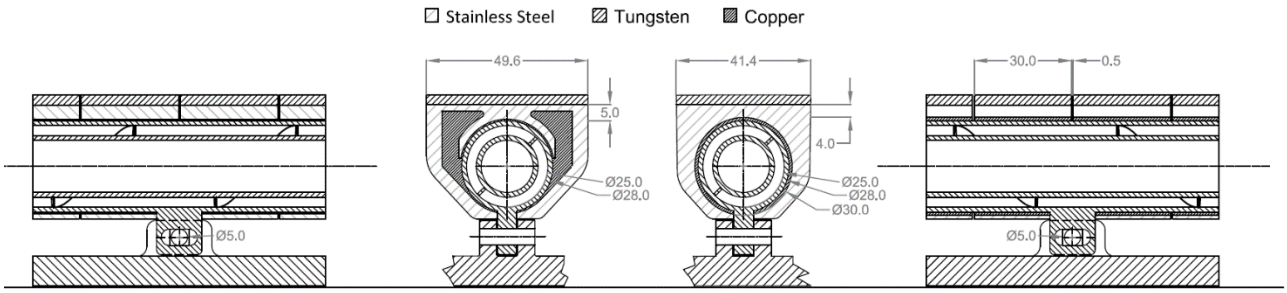

Figure IV.29: UPP design: thermal break concept on the left, capacitive concept on the right.

The water enters through the internal pipe and comes back from the external circular crown with, approximately, the same velocity. To mitigate the stress concentration at the junction between armor and substrate, a segmentation in the axial direction was obtained joining blocks of width of 30 mm with the coaxial pipe with 0.5 mm of gap between blocks.

In the analysis, the heat transfer coefficient as a function of the pipe inner surface temperature (T_{wall}) was calculated using the same thermal hydraulic correlations adopted at the ITER Organization. To meet the requirement of the plasma facing surface at 200 °C at low thermal load, the inlet water temperatures of 80°C and 120 °C were chosen for the C concept and TB concept, respectively.

AISI 316L (N) is the structural material of the pipe and was modelled as an elastic material. AISI 316L (N) and copper (Cu OFHC) are used for the blocks and, as functional materials, were modelled as plastic [IV.14].

In the C concept, the AISI of the block has the function to provide a heat tank able to preserve the pipe from the high incident heat flux during the ramp-up; only 1mm of Cu OFHC interlayer is used to provide, principally, a suitable substrate for the diffusion bonding, during the manufacturing process.

In the TB concept, a proper shape and thickness of AISI and copper in the cross section have the purpose of distributing the incident heat flux on the inner surface of the pipe up to obtain a flux expansion with a maximum wall heat flux less than the incident one. This leads to considerable advantages both for the thermal then mechanical behavior. The component here described could be further improved in terms of performance if the dimensional constraints will be relaxed.

Fig. IV.30 shows the temperature field at the end of the rump-up: the C concept exhibits a temperature greater than the TB concept of 36 °C. This difference is not small considering that, in TB concept, each pipe cools a greater surface.

Fig. IV.31 shows the plasma facing surface temperature after 100 s under 0.2 MW/m2 heat flux with results very close between the two designs and suitable for lithium liquefaction.

Fig. IV.32 shows the heat flux at the pipe inner surface, Wall Heat Flux (WHF), at the time in which the maximum occurs (17s). The WHF is the main responsible of the stress inside the pipe and then its minimizing is worthy. Also in term of WHF, it is observed a better behavior of the TB concept: the WHF is distributed on the surface decreasing the heat flux concentration on the top.

Two heat loads profiles were simulated to compare the performance of the two concepts (see Fig. IV.33): in case 1 (blue curve) the heat flux is increased linearly from 0 to 1.5 MW/m2 in 15 s, followed by a prompt decrease to 0.2 MW/m2 and it is kept constant until reaching the stationary conditions; in case 2 (red curve), when the heat flux reaches 1.5 MW/m^2 it is kept constant.

In Fig. IV.33 the blue curves show the results relating to case 1, while the red ones are related to case 2. The comparison in terms of temperature and wall heat flux (WHF) (see Fig. IV.34 and Fig. IV.35, respectively) shows that TB concept is preferable in steady state condition.

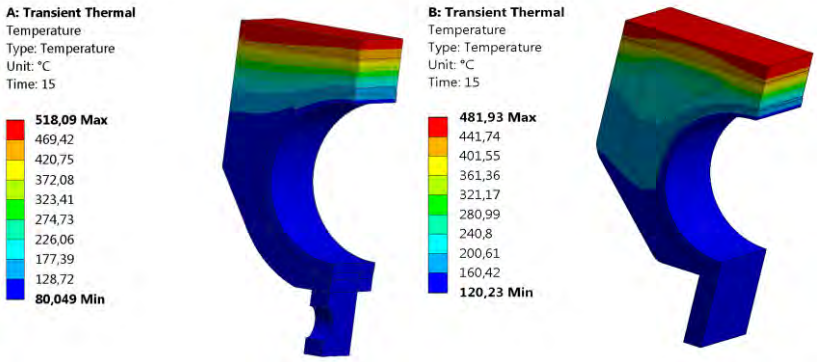

Figure IV.30: Temperature field at the end of the rump-up: the C concept on the left exhibits a temperature greater of 36 °C respect to the TB concept on the right.

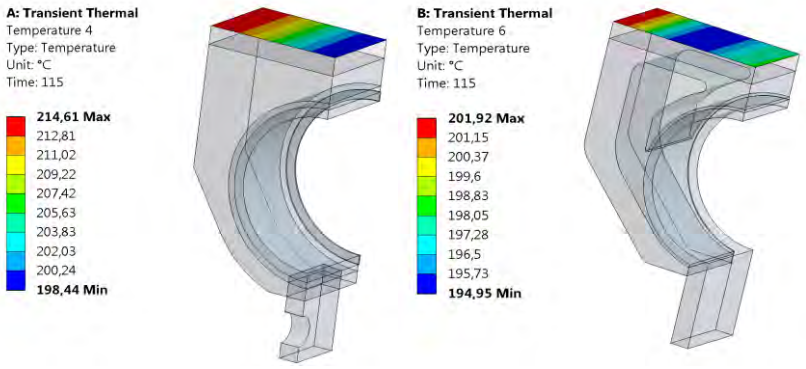

Figure IV.31: Plasma facing surface temperature after 100 s under low heat flux (0.2 MW/m2): C concept on the left and TB concept on the right

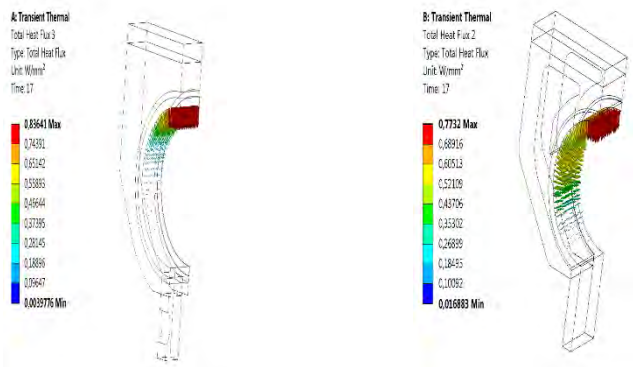

Figure IV.32: Wall heat flux: TB concept distributes the heat flux on the surface decreasing the heat flux concentration on the top.

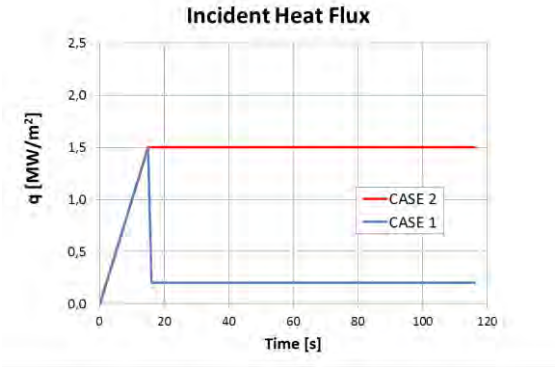

Figure IV.33: Two different load cases used for concept performance comparison

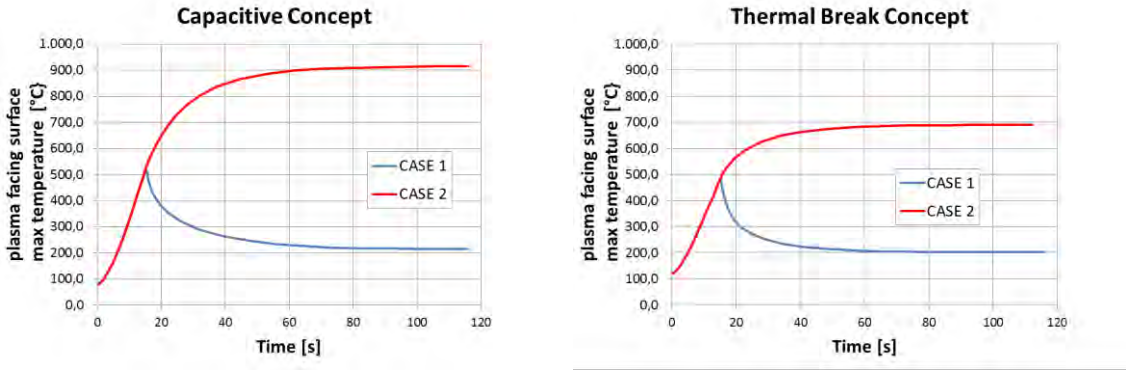

Figure IV.34: Comparison in term of surface temperature

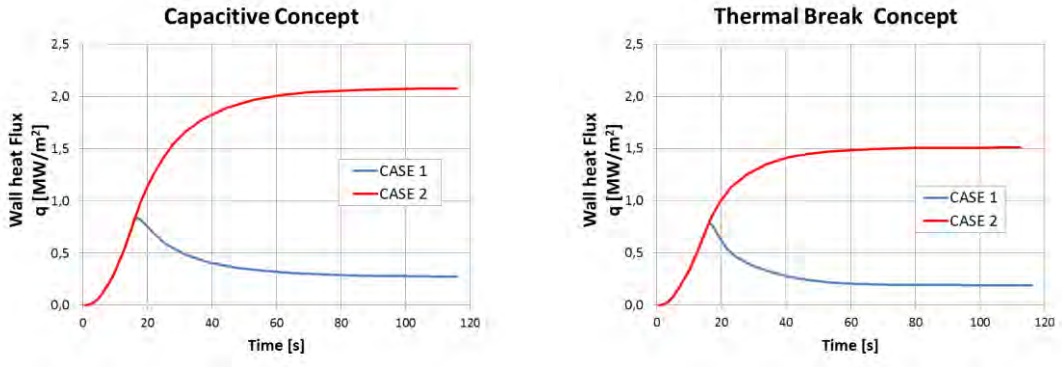

Figure IV.35: Comparison in term of wall heat flux

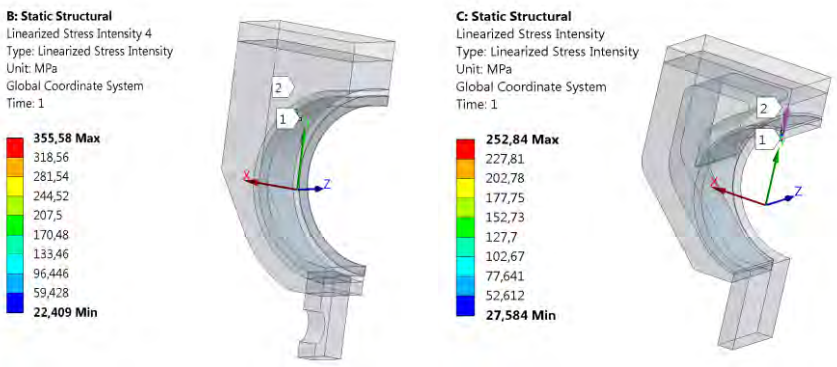

Figure IV.36: Linearized stress intensity

Table A.S03.5.1-1: S_m values versus temperature

T, °C	20	50	75	100	125	150	175	200	225	250	275	300	325	350
S_m, MPa	147	147	147	147	147	141	135	130	125	121	118	115	112	109

Figure IV.37: Sm value versus temperature as reported in [IV.14].

The mechanical results show (see Fig. IV.36) that 3Sm (=441MPa at 80 and 120 °C - see Fig. IV.37 from [IV.14]) criteria is verified by both concepts, ensuring that the membrane and bending stresses will shakedown after the first cycles of loading and unloading, thus ensuring that there will be no overall progressive deformation during the thermal-fatigue loading.

Inboard FW modules

The IFW consists of 36 modules, two for each of the 18 sectors. A single MPP of the inboard FW consists of 6 UPPs (5 for the thermal-break concept) and 5 back-plates. A sketch of an equatorial section of IFW module for TB and C design is shown in Fig. IV.38. The 5 equidistant back-plates are in the straight part of the IFW. The 6 equidistant forks are on each of the back-plate for the connection of the UPPs. The UPPs are joined by pin-bore coupling to the upper back-plate, while for the other 4 the connection is made by pin-slot coupling to allow free axial elongation. Each back-plate is fixed to the VV with four M8 insulated bolts, property class 12.9 with 80% of preloading removable from the front (plasma facing side). This solution ensures stress below the preloading stress in the case of disruptive electromagnetic loads obtained on the basis of preliminary conservative estimates.

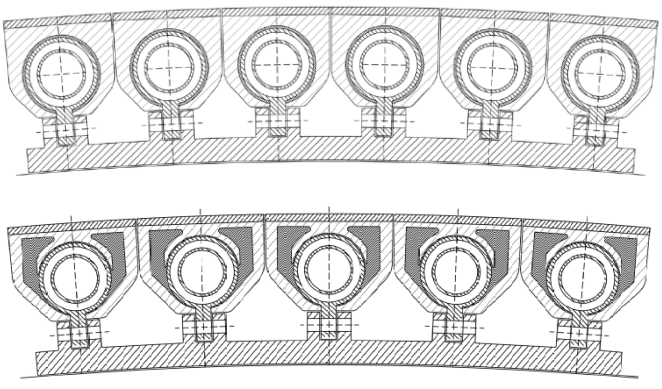

Figure IV.38: Sketch of an equatorial section of a module of inboard FW for C design (on the top) and TB design (on the bottom).

The TB design allows decreasing the pipes number to 5, with a 20% reduction of the mass flow rate. The total mass flow rate to the IFW is 150 kg/s in the case of 6 pipes per module or 120 kg/s for 5 pipes per module.

A thermo-mechanical analysis has been carried out on half-length of a C concept UPP with realistic constraints under a uniform constant thermal load of 0.5 MW/m^2. With a maximum temperature of 400 °C on the surface (see Fig. IV.39), a maximum radial displacement towards the inside of the VV of 0.3 mm (see Fig. IV.40) and an axial elongation of 0.9 mm relative to half-length of UPP (see Fig. IV.41) were computed.

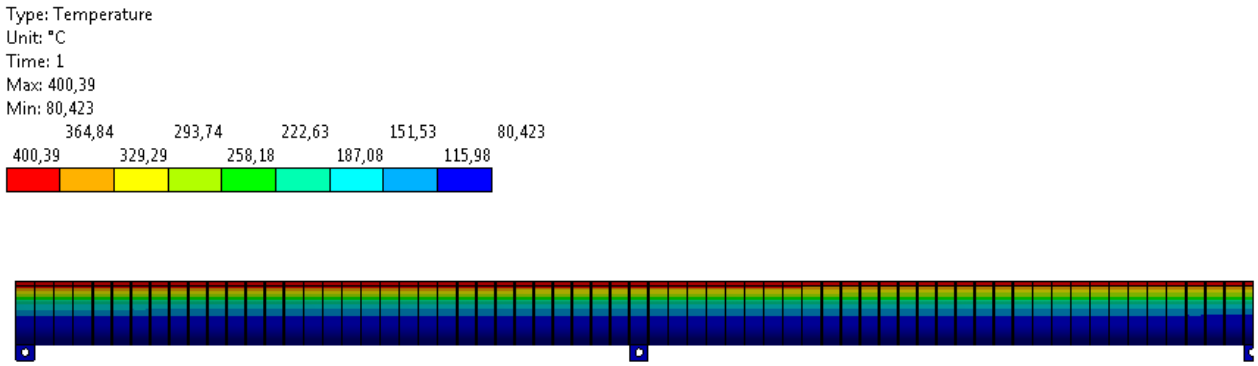

Figure IV.39: Temperature field on inboard UPP at 0.5 MW/m^2 steady state load condition

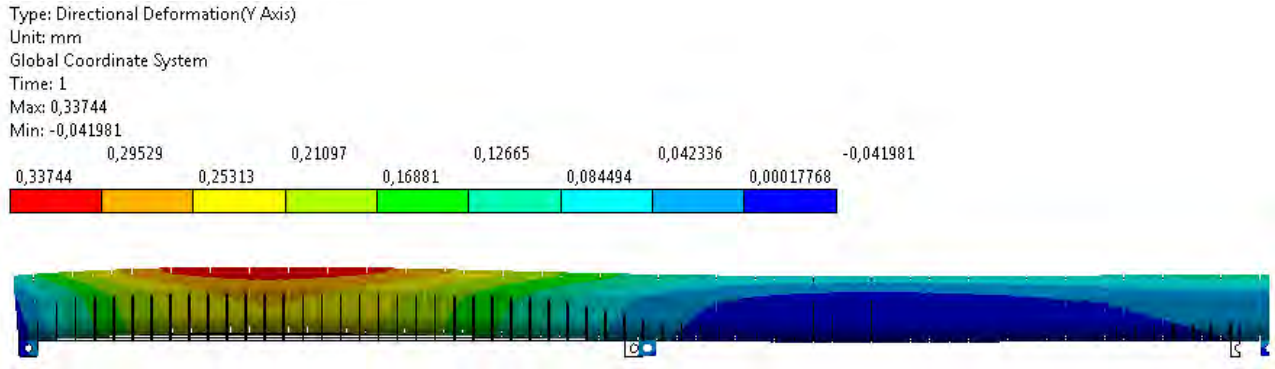

Figure IV.40: Radial displacement of inboard UPP at 0.5 MW/m^2 steady state load condition

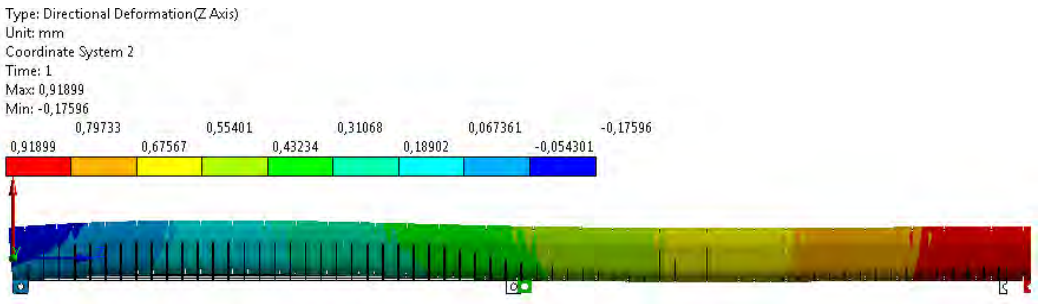

Figure IV.41: Axial elongation of inboard UPP at 0.5 MW/m^2 steady state load condition

FW supply pipes

Remote maintenance is a crucial requirement of the DTT FW. In this respect, the supply and return pipes of each FW module deserves specific attention in the design phase. One of the requirements considered in the

design was that each module could be dismounted without interfering with the adjacent one. Another requirement was that supply and return pipes do not interfere with the volume allocated for the upper divertor. Taking into account the requirements, the arrangement shown in Fig. IV.42 has been elaborated. It consists of a set of four pipes per port (two inlets and two outlets). In Fig. IV.42a the poloidal view shows that the pipes are compatible with the space allocated for the upper divertor. In Fig. IV.42b, the top view shows the four pipes (with an inner diameter of 70 mm) placed symmetrically with respect to the port symmetry plane. The idea is that the pipes are tees accessible from the bottom by a proper laser welding and cutting tool [IV.15-IV.17]. In case of remote maintenance of a module, the outermost pipe will be cut in proximity of the manifold first and then removed from the port, then innermost pipe will be cut and removed leaving the FW module with its manifold free to be extracted out of the vessel through the upper port. It is worth noting that the outward space of the port could be occupied during operation by any diagnostics or auxiliary systems provided these are removed before the remote FW maintenance activity. Conversely, the innermost space of the port can be used by the supply pipes of the VV cooling system and no restrictions can be put on them.

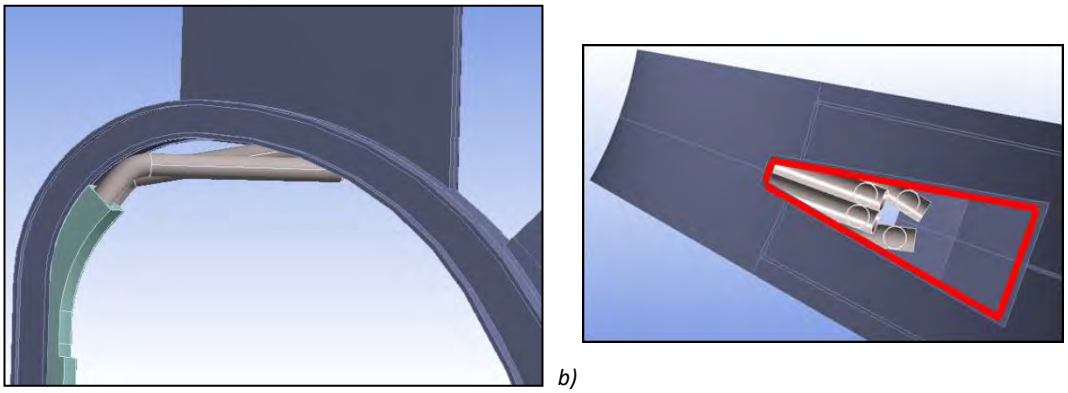

Figure IV.42: FW inlet and outlet pipe arrangement. In a) the poloidal view shows that pipes do not interfere with the volume allocated to the upper divertor. In b) the top view from port 1 shows the space occupied inside the port by the supply and return pipes.

Manufacturing and testing

Manufacturing of small mock-ups is going to be done. The blocks made in AISI will be filled with copper by casting. The coaxial pipe will be joined to the blocks by diffusion bonding or brazing process.

Each block will be covered with 3 mm of W by plasma spray deposition with interlayer to functional gradient of Cu and W to mitigate the stress to the junction. This kind of coating on AISI 316L (N) was manufactured and still under test in the high heat flux test facility of GLADIS in the Max-Planck institute in Garching. The first sample tested survived to 100 cycles with a surface temperature around 650°C, but the complete data analysis is ongoing. Metallographic analysis after the test campaign will give relevant indications for the design criteria of these components.

Final remarks

Both the concepts satisfy the requirements. The TB is better from a thermo-mechanical point of view and also from the hydraulic one, reducing the total mass flow rates of the FW cooling system. The C concept allows having water temperatures very close to those of VV, reducing the risk of local warming incompatible with the requirements for borated water. Furthermore, the C concept is made with a minimum amount of

copper and is constructively simpler and therefore economic and more DEMO relevant, avoiding the copper use.

In any case the choice must be subordinated to complete experimental campaigns that could constrain the maximum temperatures of the W plasma spray coating and of the junction with the steel to lower values than those reached with the capacitive concept during the ramp-up.

IV.6 Divertor

The main objective of the DTT project is to test alternative divertor design and configurations. Therefore, the machine is designed so as to be compatible with the actual single null (SN) configuration ("conventional" divertor) and the other alternative configurations described in Chapter III: X Divertor (XD), Super-X divertor (SXD), Snow Flake Divertor (SFD) or Double Null (DN). This flexibility feature is also apparent in the compatibility with the application and testing of a Liquid Metal Divertor, that implies specific requirements to the design of VV, ports and RH devices. The selection of the materials and magnetic configuration to be tested in the first experimental phase of DTT will be carried out together with the EUROfusion consortium on the base of the most promising Plasma Exhaust solutions identified for DEMO. Currently, a conventional divertor is integrated in the DTT conceptual design (Fig. IV.43). Moreover, up-down symmetric divertor design is considered in order to allow for testing of DN configuration (Fig. IV.44).

The main divertor mission is to exhaust the major part of the plasma ions thermal power in a region far from plasma core in order to control plasma pollution. Thus, the main high-level requirements to be considered in the design of DTT divertor shall be related to the power exhaust and vacuum pumping needs. After these, the divertor cassette design shall consider the following requirements:

- Incidence angle of plasma legs on divertor targets
- Thermal loads on the divertor targets
- Alignment between adjacent targets to avoid edge effects
- Interfacing system – FW, VV, ports
- Remote handling for divertor replacement

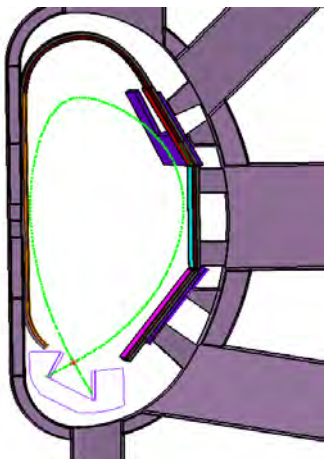

Figure IV.43: SN configuration

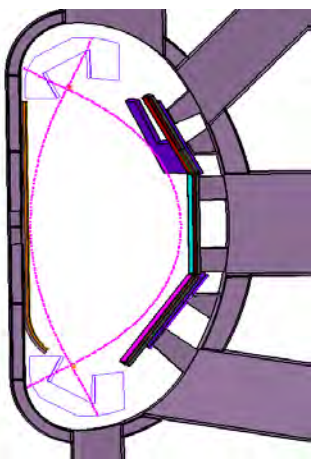

Figure IV.44: DN configuration

- Supports to transmit loads during normal operation, baking, major disruptions, seismic events
- Coolant supply
- Diagnostics

Based on such requirements, the DTT conventional divertor design started from the definition of a draft poloidal profile driven by the design inputs of the vertical targets in terms of distances and angles assumed as in Fig. IV.45.

The DTT divertor is segmented in 54 toroidal sectors or cassettes (3 divertor module per port; quasi-symmetric wrt the equatorial plane in the upper part for the DN configuration). Each divertor cassette comprises a cassette body, which supports the plasma facing components (PFCs), an inner (IVT) and outer vertical target (OVT) and a dome.

The IVT and OVT are designed including a set of W-shaped solid FAST-like [IV.5] [IV.6]. Since power exhaust solutions for DEMO are still under evaluation, present DTT divertor design should be compatible, as much as possible, with quite different topologies of power load. Within the old FAST proposal [IV.6] it was developed and designed a divertor (Fig. IV.46a) optimized for both the SN and the quasi Snow Flakes experiments, where the reciprocal position of the nulls can be varied with continuity. This divertor practically "consists" of two parts. There are two deep long necks (vertical targets - ITER style) where the strike angle (≈20°) and the neck "closure" have been optimized to maximize the radial local losses. On the top, the two "necks" are connected to a flat divertor zone by a blended part; both this part and the flat one have been designed to allow this large flexibility in the magnetic configuration, but remaining always with a power load lower than 15÷20MW/m^2.

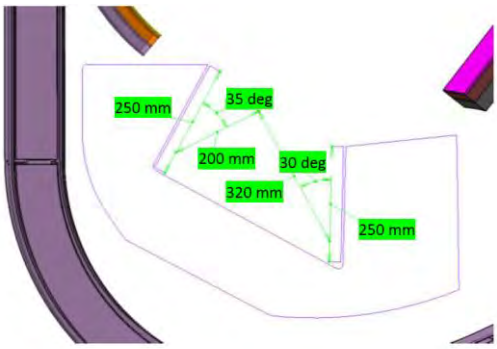

Figure IV.45: SN divertor - Inner and Outer vertical target design criteria.

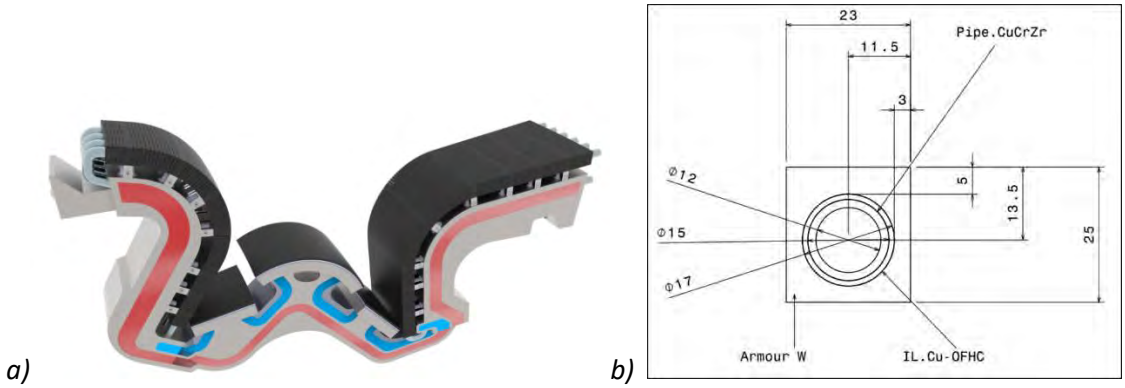

Figure IV.46: a) Design of a FAST-like divertor; b) Plasma facing units' configuration

The manufacturing concept of the solid ITER- like divertor provides, for the PFUs, Tungsten (W) mono-blocks, brazed on CuCrZr tube by means of a 'soft' Cu Oxygen-free high thermal conductivity (Cu-OFHC) inter-layer 1 mm thick (Fig. IV.46b).

Thermo-hydraulic analyses with this divertor concept, carried out using pressurized water (4MPa) flowing in the PFUs CuCrZr pipe at around 20 m/s, with an inlet temperature of 100°C, show that the surface temperature will never get higher than 1100 °C, and the interlayer will remain around 400°C. In the following activities for the design of a new divertor, different types of pipes should be also tested, alternatively to the CuCrZr pipes. Presently pipes realized by alloys of W and Cu have been realized and it planned to test their neutrons capability in fast fission reactors. In parallel, studies to analyze other types of materials based on Vanadium alloys are going ahead.

The Cassette Body is made of AISI 316L(N) and has the function to support the PFUs and to route the coolant. Structural analyses on the proposed cassette design have shown the capability to sustain forces and stresses connected even with the worst imaginable vertical disruption at the highest plasma current (5.5 MA). In the Cassette design and in the VV design a particular care has been dedicated to the support and the assembling aspects. Since the machine main purpose is to be a facility dedicated to test different divertor, the possibility to "easily" replace a divertor, with a new one completely different, must be taken in account from the very beginning of the full machine design (ports, coils, VV, support forces,…).

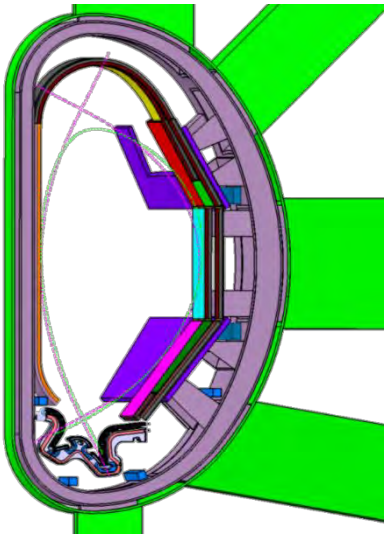

Figure IV.47: DTT first divertor – FAST geometry adapted to the last DTT design

In the present design the divertor is allocated towards the internal position, to allow high triangularity plasma and it is oriented so that SOL extensions over null point fit inside divertor legs. The size is primary chosen to allow a correct placement and removal from the plasma chamber.

Each divertor module will enter inside the vessel horizontally through a dedicated Port (No. 4) using an adequate rail system. Then it will be moved along toroidal direction inside VV until it reaches the position where it will be seated. Each module has a radial width of 0.85 m assuming the outer cover plate of cassette body normal to toroid axis and presents inclined targets and a dome tailored to separate the inner and outer zone, but, at the same time, allowing the necessary neutrals pumping. The estimated weight is about 200 kg.

Figure IV.47 shows the FAST divertor geometry adapted to the current DTT design. General interface requirements are met, but further work shall be performed to align the IVT and OVT positions according to the requirements presented above and to the dimensions shown in Fig. IV.36. Furthermore, cassette attachment to the VV shall be studied in detail considering alignment requirements, internal coil interfaces and RH issues.

IV.7 Remote Handling System

IV.7.1 DTT RM needs and requirements

After DTT shutdown, the expected activation rate on plasma-facing components is ~ 100 µSv/h; therefore, remote maintenance (RM) is mandatory. The basic requirements of DTT RM are listed as follows:

- RM schemes shall be flexible to adapt different divertors for different magnetic configurations;
- RM equipment shall be flexible to manage the replacement of first wall with “upper vertical targets” in case of double null magnetic configuration;
- RM equipment shall be flexible to manage different shapes of FW in case of super-X configuration;
- RM equipment shall be flexible to manage liquid metal divertor
- RM equipment should be able to sustain the diagnostics and heating system necessities;
- RM systems shall be flexible enough to work during scheduled maintenance and in case of failure;
- RM constraints shall drive the design of in-vessel components;
- RM systems shall guarantee feedback to RM operators. Force/torque sensors as well as cameras are needed to get sensory information. Virtual reality and physics-based simulators are needed.

The call for tender for DTT RM is expected to be in the 3rd quarter of 2020. However, RM is important since the beginning of the design of the machine, since it drives (among other factors) the design of the in-vessel components, VV ports and layout of the building. Furthermore, it is expected that DTT remote handling will operate also during the machine assembly phase (although absolutely not necessary), in order to test and validate remote handling strategies before real remote operations on the machine.

IV.7.2 DTT RM strategy

The DTT RM strategy is conceptually illustrated in Fig. IV.48.

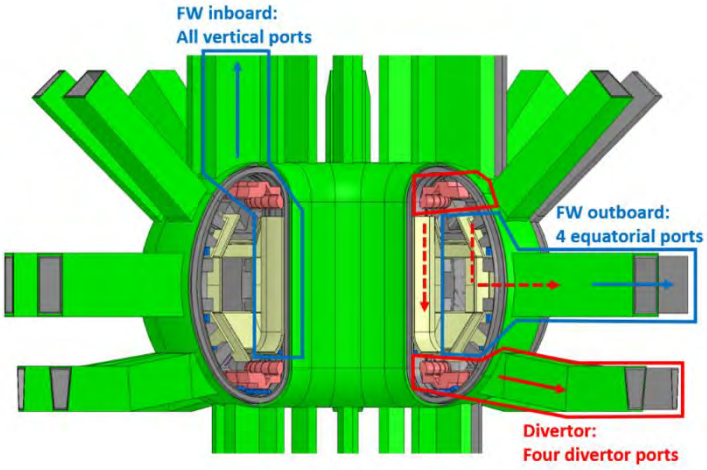

Figure IV.48: DTT RM Strategy (double null configuration).

The RM strategy foresees:

- RM of divertors (DIV) through four divertor ports;
- RM of outboard first wall (OFW) modules through four equatorial ports;
- RM of inboard first wall (IFW) modules through all the vertical ports.

In case of single null magnetic configuration, “upper vertical targets” are expected to replace the upper divertors; in this case, their RM is planned through the four equatorial ports.

IV.7.3 Divertor remote handling

Divertor remote handling systems should allow:

- Insertion/extraction of divertor cassettes and divertor diagnostics as well as their transportation from/to a transfer cask docked at divertor RM ports;
- Cutting, welding, alignment and inspection of cassette cooling pipes;
- Transportation of the divertors and their equipment from the vacuum vessel to a storage place.

The motion sequence for divertor replacement/installation through the divertor ports is illustrated in Fig. IV.49. The divertor cassettes will be installed through four RH ports (RH Sectors #01, #05, #10, #14). Each port is devoted to the installation of divertor cassettes in the sectors at its left side (for reducing the number of needed equipment). The RH ports and the sequence planned for installation of divertor cassettes are shown in Fig. IV.50.

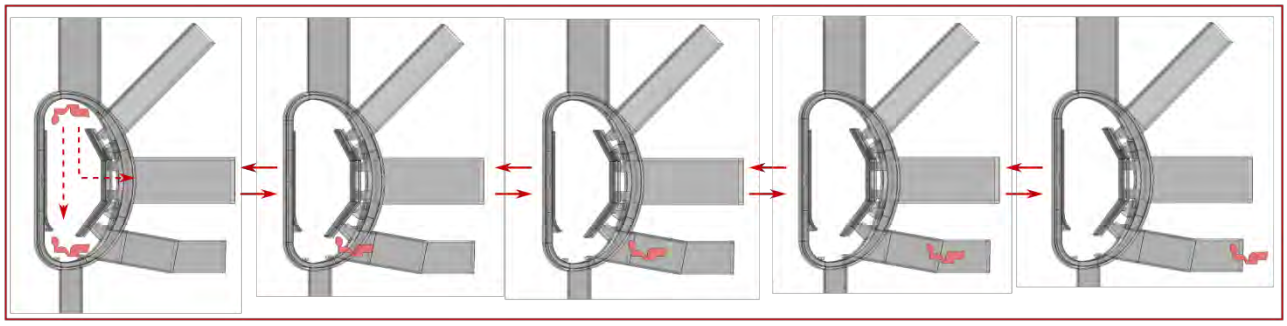

Figure IV.49: Motion sequence of divertor replacement/installation through the divertor port.

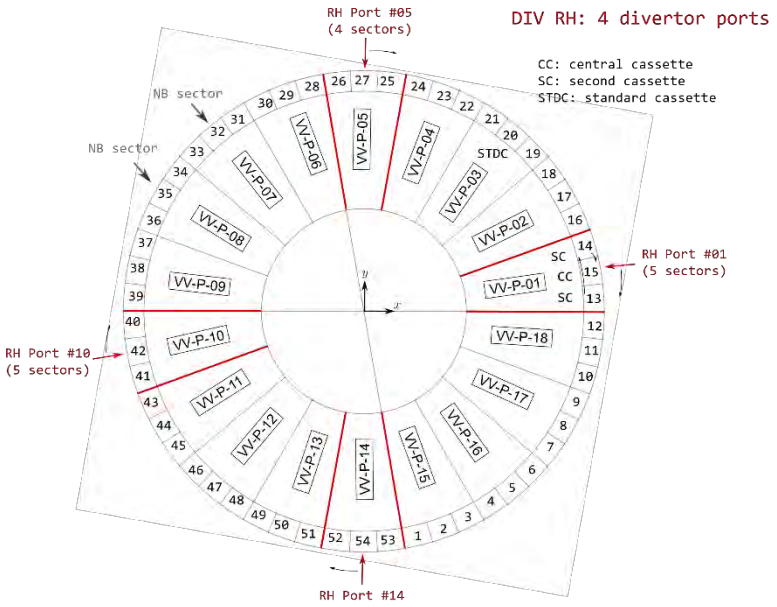

Figure IV.50: Remote handling ports with the sequence of installation from the divertor ports

Accordingly, the divertor RM needed equipment are listed in Tab. IV.X. The design of these components is driven by the previous experience on ITER divertor remote handling systems [IV.7].

TABLE IV.X: LIST OF PLANNED DIV RM EQUIPMENT

DIV RM Equipment	Function
Cassette multifunctional mover CMM (x1)	To provide transportation inside the RH ports
Cassette toroidal mover CTM (going only left, x1)	To provide transportation inside the vessel
Central cassette end effector CCEE (x1)	To allow installation/replacement of Central Cassette (CC)
Second cassette end effector-right SCEE-r (x1)	To allow installation/replacement of Second Cassette (SC)-right
Second cassette end effector-left SCEE-l (x1)	To allow installation/replacement of Second Cassette (SC)-left
Standard cassette end effector STDCEE (going only left, x1)	To allow installation/replacement of Standard Cassette End Effector (STDC)
General purpose manipulator	To allow manipulation of tooling
Tooling systems	To allow cassette fixation
Transfer cask (x1)	To allow ex-vessel transportation

IV.7.4 First wall remote handling

First wall remote handling systems shall allow:

- Insertion/extraction of first wall modules as well as their transportation to/from the vacuum vessel
- Bolting for fixing modules; dust removal; rescue operations; vacuum vessel inspection; in-vessel diagnostic maintenance
- Cutting, welding, alignment and inspection of first wall cooling pipes.

Currently, the outboard first wall (OFW) modules are expected to be installed/replaced through four equatorial ports of the RH sectors #01, #05, #10, #14. The massive inboard first wall (IFW) modules are expected to be installed/replaced through all the vertical ports. In case of single null magnetic configuration, the current strategy is to replace upper vertical targets through the equatorial ports.

The outboard first wall modules are segmented to be RH-compatible. As an example, the motion sequence for installation/replacement of the OFW low module is illustrated in Fig. IV.51. A similar sequence is expected for the other OFW modules.

The inboard first wall module (IFW) is segmented such that, for each sector, two long IFW modules are foreseen, and they have to be replaced through the vertical ports. The sequence of planned motion for IFW replacement is illustrated in Fig. IV.52. As we can see, the IFW module is first moved in radial direction, then rotated of 90 degrees, and then vertically lifted through the vertical ports.

Tab. IV.XI shows the list of planned RM equipment for first wall installation/replacement. The DTT Boom is briefly described in the next section. Joined to it, a master-slave servo-manipulator coupled to a suitable end-effector ensures reaching all the FW modules with the correct position and orientation. A task module is instead foreseen to carry out tools and to provide a first storage place for OFW. The FW gripper should be able to grasp/manipulate all the OFW modules and the IFW modules for the in-vessel motion before rotation and lifting. It should have a self-actuated gripping mechanism, and it needs to be coupled to the end-effector of the in-vessel manipulator. Its design is driven by the previous experience on ITER Blanket remote handling systems [IV.7]. The FW vertical lifter couples with the upper collector of IFW from one side, and with a vertical crane from the other side. It ensures both the in-vessel rotation of IFW and the vertical lifting through a twistlock gripping system [IV.9]. Its design is driven by the previous experience on DEMO Blanket vertical remote handling strategy and systems [IV.10].

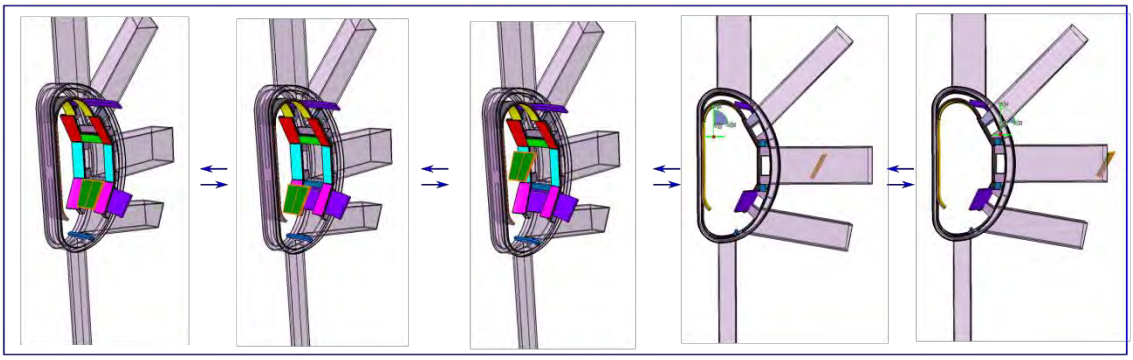

Figure IV.51: Motion sequence for the replacement/installation of one of the segments of the outboard first wall through the equatorial port.

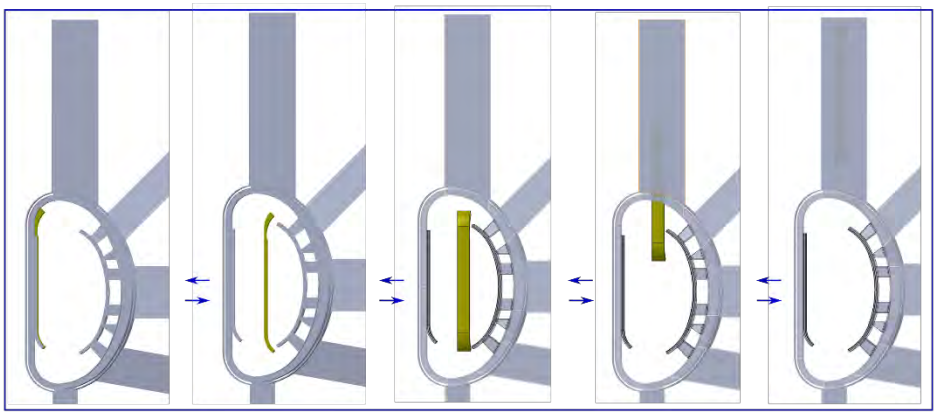

Figure IV.52: Motion sequence of the Inboard first wall replacement/installation through the upper ports.

TABLE IV.XI: LIST OF PLANNED FW RM EQUIPMENT

FW RM Equipment	Function
DTT Boom (x2)	To provide equatorial "rails" for manipulators and grippers handling the FW modules. Two booms (or hyper-redundant manipulators) are foreseen: one for transporting the manipulator, one for transporting the task module.
Master-slave servomanipulator	To ensure reachability (in position) of all FW modules; the slave manipulator has to be mounted on one DTT Boom, the master manipulator is in the control room.
Task module	To provide the tooling handling; to provide a temporary storing place for OFW modules
End-Effector	To ensure reachability (in orientation) of all FW modules. It has to be joined to the manipulator (or it can be directly part of it)
FW Gripper	To provide boltening/unboltening, gripping and manipulation of FW modules.
FW vertical lifter	To provide rotation and lifting of IFW
Crane	To allow vertical lifting and ex-vessel operations

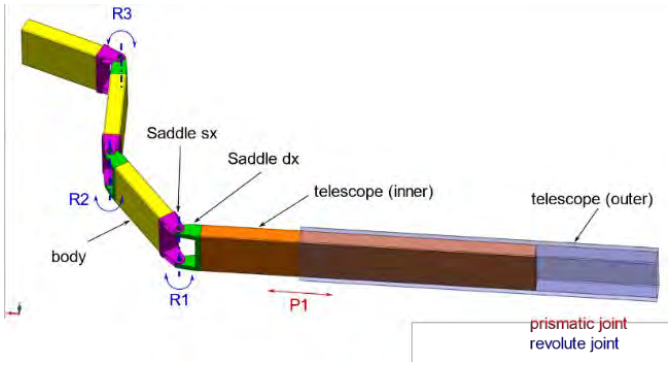

Figure IV.53: Conceptual design of the DTT Boom.

IV.7.5 DTT Boom

The concept design of the DTT Boom is shown in Fig. IV.53. It has the function of transporting manipulators, end-effectors and grippers for maintenance, as well as cameras and other sensors for inspection. One boom is deployed through the RH equatorial port #01, the other through the equatorial port #10. If necessary, supporting systems will be placed through the RH equatorial ports #05 and #14 (see Fig. IV.50).

DTT Boom current design is compliant with the DTT vacuum vessel, and it ensures reachability of all FW segments in half vessel with one manipulator. The current conceptual design foresees:

- A total of four joints (three revolute and one prismatic). In the current version, the DTT Boom has a planar design; however, additional joints for exploiting redundancy and ensuring out-of-plane motion (at the end of the boom, before the coupling with the manipulator) will be added in the final design. The stroke of the prismatic joint is set equal to 2000 mm;
- A total of one telescopic module and three revolute modules. The telescopic module is composed by an inner (orange component) and outer telescope (blue component), while each revolute module (of total length 1150 mm) is composed by three parts: main body (yellow component), saddle left (magenta component), saddle right (green component).
- Hollow rectangular cross-sections for the DTT boom components. The current dimensions (450 x 150 mm, with thickness equal to 2 mm) consider the compliance with the VV equatorial ports and are selected to provide a stiff behaviour of the manipulator (limited deflections). However, further studies will consider the internal disposition of electronics and cables.
- Aluminium material.
- Electrical actuators and harmonic drive gears

The design of the DTT Boom is driven by the previous experience on JET machine, and by software tools for modelling, simulation and vibration control of hyper-redundant flexible manipulators [IV.11].

IV.7.6 Pipe cutting/welding

Before removing (re-installing) the in-vessel components, remote cutting (welding) of pipes is necessary. The following considerations have been reached by the teams working on remote handling, pipes and components:

- One tool for both cutting/welding is preferred.
- In-bore tools are required.
- Laser technology should be preferred for accuracy reasons, and since it allows faster operations. With this respect, the laser and power sources should be ex-vessel, while a flexible optical fibre should be used to transmit the laser beam to the processing head.
- The maximum radius for designing bent pipes should allow the insertion of remote in-bore tools which can follow that radius [IV.12].

Regarding the tools to be used, off-the-shelf solutions developed for other reactors will be preferred [IV.12, IV.13].

IV.7.7 Control room

The control room is the core of the DTT remote maintenance system. It is composed by:

- Human-machine interfaces with force and visual feedback for testing and performing remote operations on in-vessel components.
- Virtual reality simulator for training of human operators.
- Supervisory system for all the remote handling equipment.

IV.8 Conclusions

The latest advancement (March 2019) in the conceptual design of the main mechanical components of DTT fusion reactor and remote maintenance related issues was presented here. In the last years, from the “Blue Book” to the present “Green Book”, important choices about shape, materials and dimensions, in particular of the VV, have been made in order to satisfy physical requirements and costs.

The structural analyses on VV and Cryostat Vessel have confirmed the robustness of the design.

At the end of 2019, the conceptual design phase with the first iteration of engineering analyses should be completed, in order to start more detailed analyses and virtual testing of almost all the designed parts. Call for tenders will be prepared at the end of 2020 and assigned in 2021.

For what concern the DTT remote maintenance, according to the scheduled planning, at the stage of publication of this “green book” we are in pre-conceptual phase: indeed, the RM strategy will be broadly accepted by the mid-2019. Then, the conceptual design is expected to be completed by end-2020, with the engineering design released by end-2021.

IV.9 References

[IV.1] Giuseppe Di Gironimo, Domenico Marzullo, Rocco Mozzillo, Andrea Tarallo, Fabio Villone (2017). The DTT device: First wall, vessel and cryostat structures. FUSION ENGINEERING AND DESIGN, vol. 122, p. 333-340, ISSN: 0920-3796, doi: 10.1016/j.fusengdes.2017.04.132

[IV.2] Mozzillo R, Tarallo A, Marzullo D, Bachmann C, Di Gironimo G, "Development of a master model concept for DEMO vacuum vessel", Fusion Engineering and Design, Volume 112, 15 November 2016, Pages 497-504, ISSN 0920-3796, http://dx.doi.org/10.1016/j.fusengdes.2016.06.009

[IV.3] Villone F. et al., Coupling of nonlinear axisymmetric plasma evolution with three-dimensional volumetric conductors, Plasma Physics and Controlled Fusion, 55 (2013) 095008.

[IV.4] ASME Boiler and Pressure Vessel Code.

[IV.5] Di Gironimo G. , Carfora D. , Esposito G. , Labate C. , Mozzillo R. , Renno F. , Lanzotti A. , Siuko M. Improving concept design of divertor support system for FAST tokamak using TRIZ theory and AHP approach, Fusion Eng. Des. 88 (2013), 3014-3020, DOI 10.1016/j. fusengdes. 2013.07.005.

[IV.6] Pericoli Ridolfini V, et al., Fus. Eng. and Des., 88 (2013) 1677

[IV.7] Esqué, Salvador, et al. "Progress in the design, R&D and procurement preparation of the ITER Divertor Remote Handling System." Fusion Engineering and Design 89.9-10 (2014): 2373-2377.

[IV.8] Noguchi, Y., et al. "Design progress of ITER blanket remote handling system towards manufacturing." Fusion Engineering and Design 136 (2018): 722-728.

[IV.9] BS 5237:1985 Specification for lifting twistlocks.

[IV.10] Coleman, M., et al. "Concept for a vertical maintenance remote handling system for multi module blanket segments in DEMO." Fusion Engineering and Design 89.9-10 (2014): 2347-2351.

[IV.11] Grazioso, S., et al. "Modeling and vibration control of flexible mechanical systems for DEMO remote maintenance: Results from the FlexARM project." Fusion Engineering and Design (2019).

[IV.12] Oka, Kiyoshi, et al. Development of pipe welding, cutting and inspection tools for the ITER blanket. No. JAERI-TECH--99-048. Japan Atomic Energy Research Inst., 1999.

[IV.13] Keogh, K., et al. "Laser cutting and welding tools for use in-bore on EU-DEMO service pipes." Fusion Engineering and Design 136 (2018): 461-466.

[IV.14] E. Rabaglino, 18th UIT Nat. Heat Transfer Conf., Como (Italy), 2000

[IV.15] Friconneau, J.-P., Alfille, J.-P., Cerdan, G., Damiani, C., David, O., Maisonnier, D., Palmer, J., Perrot, Y., Tesini, A., Wojtowicz, M.Overview of bore tools systems for divertor remote maintenance of ITER (2001) Fusion Engineering and Design, 58-59, pp. 481-486.

[IV.16] Friconneau, J.P., David, O., Martins, J.P., Palmer, J.D., Tesini, A. Assessment of a cooperative maintenance scheme for ITER divertor cooling pipes (2005) Fusion Engineering and Design, 75-79 (SUPPL.), pp. 531-535.

[IV.17] Hayashi, T., Sakurai, S., Takechi, M., Tsuru, D., Matsunaga, G. Remote handling tools for hydraulic connections of divertor cassettes in JT-60SA (2019) Fusion Engineering and Design

Chapter V

BUILDINGS AND LAYOUT

V.1 Introduction

The present section describes the site and torus hall layout and the assembly of the DTT facility, that, following the results of the call for interest launched by ENEA in 2017 [V.1] and concluded in April 2018 [V.2], will be hosted in the ENEA Frascati Research center.

Figure V.1 shows the map of the Frascati research center, where new buildings and renovations are highlighted. Main interventions are listed below and described in details in the following subsections:

- buildings for the additional heating system;
- cryogenic plant;
- sub-station for the HV 150kV grid transformers;
- area for the AC/DC converters;
- area for the secondary water-cooling system;
- DTT torus hall.

Respecting the original convention to put the height 0 at the basement of building F73, the one presently hosting FTU's converters, all the heights presented in this document are relative to it.

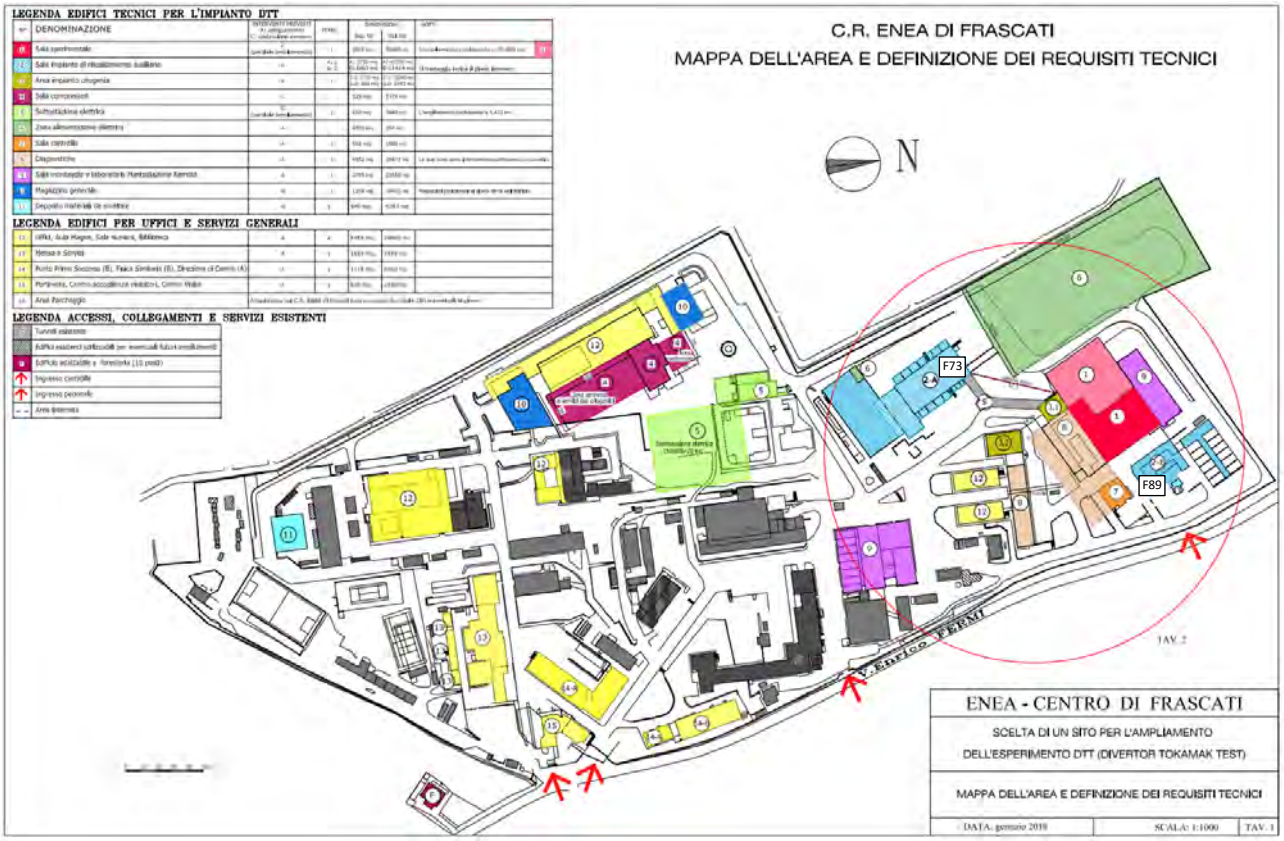

Figure V.1: Layout of the DTT site in ENEA Frascati research center.

V.2 Site and Buildings

V.2.1 Additional heating buildings

The buildings that will host the ECRH and ICRH systems will have to guarantee:

- Flexibility in the choice of future upgrade of the machine (from the initial installed power to the full power operation);
- A high level of accessibility to ease maintenance activities;
- Proximity to the torus hall but at an adequate distance (50 m for ECRH) in order to limit the effects of the stray field on the gyrotrons.

Two building configurations have been evaluated as shown in Fig. V.2a and V.2b. The two options are alternative: in the first, ICRH system (up to 3 modules, corresponding to 9 MW of power coupled to the plasma) is placed in building F73, and ECRH (up to 4 clusters of 8 gyrotrons each, for a total of 32 MW of installed power) in a new building that substitutes building F89. In the second, the two systems are reciprocally replaced.

In order to arrive to a decision between the two options, a panel of experts, composed of representatives of the Heating and Current Drive and of the Building and Layout groups, has been established. The suggestion of the panel, based on technical and economic considerations, has been to implement the first option. The advantages associated to this option are summarized as follows:

a. Use of existing corridors between building F73 and the DTT hall to connect ICRH;
b. Shorter transmission lines (TL) of ECRH than in the opposite case, with consequent higher efficiency and lower losses;
c. Minimization of the renovation works needed in building F73.

Since eenhancements in the heating power of DTT will be based on the results achieved after a few years of operations, if an increase of ECRH power would be preferred to that of ICRH, building F73 would be capable to host both, and the same corridor would be used by the transmission lines of the two systems to reach the DTT hall. In this respect, the panel of experts identified a couple of consequences:

- The modules of ICRH installed first will occupy the furthest part of building F73, since the cost and the complexity of the ICRH transmission line is lower than that of ECRH;
- A penetration for the fifth cluster of ECRH potentially positioned in building F73 should be already realized on the south wall of the DTT hall.

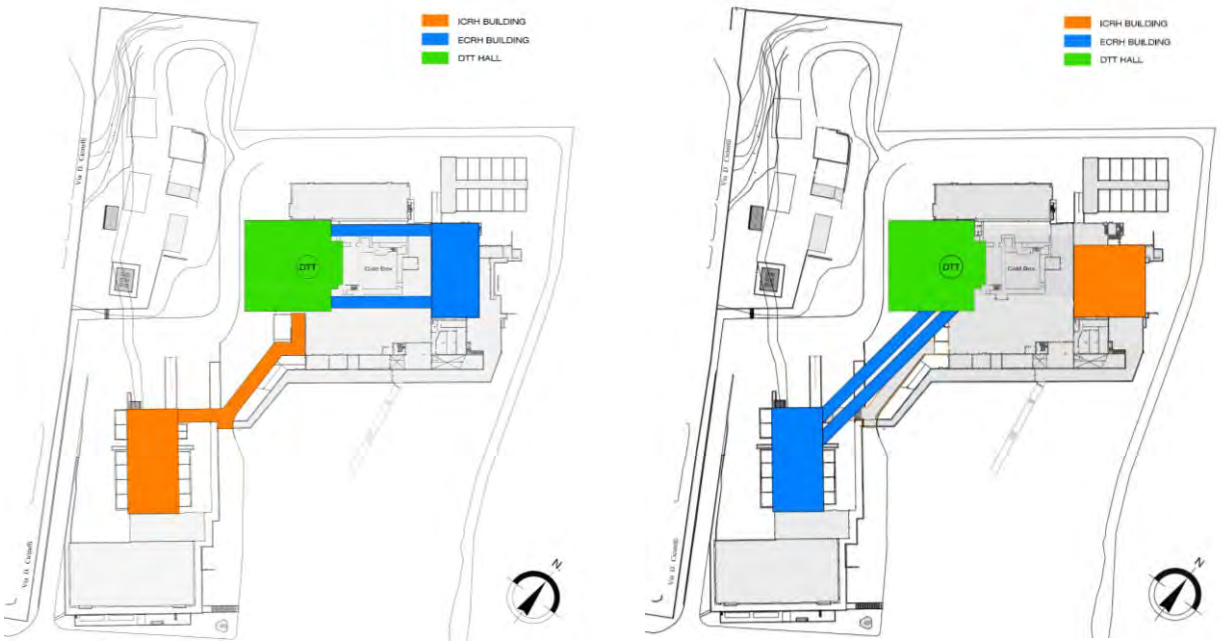

a) Reference option b) Alternative option

Figure V.2: Layout of the ECRH/ICRH systems in the DTT site.

Concerning the NBI system, the injectors will be placed in the DTT hall and directly connected to the cryostat, instead the High Voltage Deck (HVD) will occupy building F87 and the Acceleration Grid Power Supply (AGPS, to feed the acceleration grids), the Ion Source and Extraction Power Supply (ISEPS, to feed all the ion source loads) and the Ground Related Power Supply will be located in building F90 as shown in Fig. V.3.

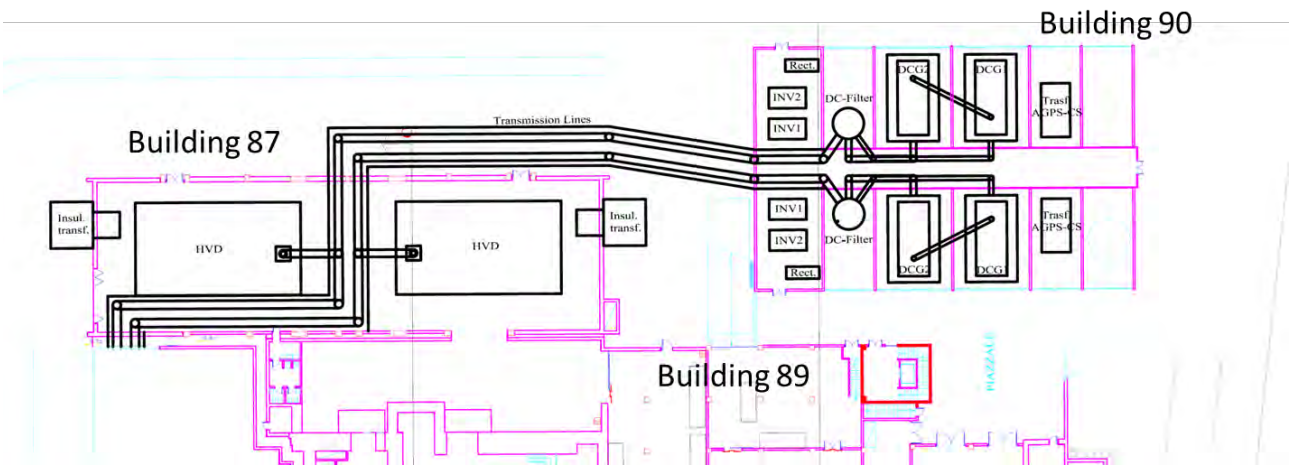

Figure V.3: Layout of the NBI power supply system in the DTT site.

V.2.2 Cryoplant layout

Figure V.4 shows the layout of the cryogenic plant system, devoted to provide the liquid Helium need to cool the superconducting coils. Section VI.2 presents the cryoplant system made of three main parts: the compressor hall, the He gas transfer line and the so-called cold box, where the He is liquified. Regarding the cold box, the requirement to be as close as possible to the DTT hall brought to the decision to place it in the FTU hall. This choice is valuable since the FTU hall is already equipped with a 100 tons crane able to support adequately the cold box components during the assembly. Moreover, it is adjacent to the DTT hall, but separated by a thick wall providing a significant neutron shielding and equipped with a reasonable number of penetrations. Also, the transfer line of the cold He to the superconducting magnets in the hall will be the shortest possible. Finally, the DTT cold box could reuse the liquid Nitrogen storage tanks, located in front of building F85, and the existing penetrations used for FTU.

Regarding the compressor hall, present layout foresees to place it in building F23 in front of the former FT building, as shown in Fig. V.4. Accordingly, large storage vessels, having sufficient capacity to store the whole helium inventory required for the cryogenic plant, plus one vessel for quench recovery, will be installed close to the compressors. The connection of the high pressure He gas to the cold box would be done in part by a dedicated pipeline, in part sharing the same corridor used for the transmission line of the ICRH system. It is worth noting that routing of pipelines is only indicative and that a more detailed analysis should be performed before closing the layout of the system.

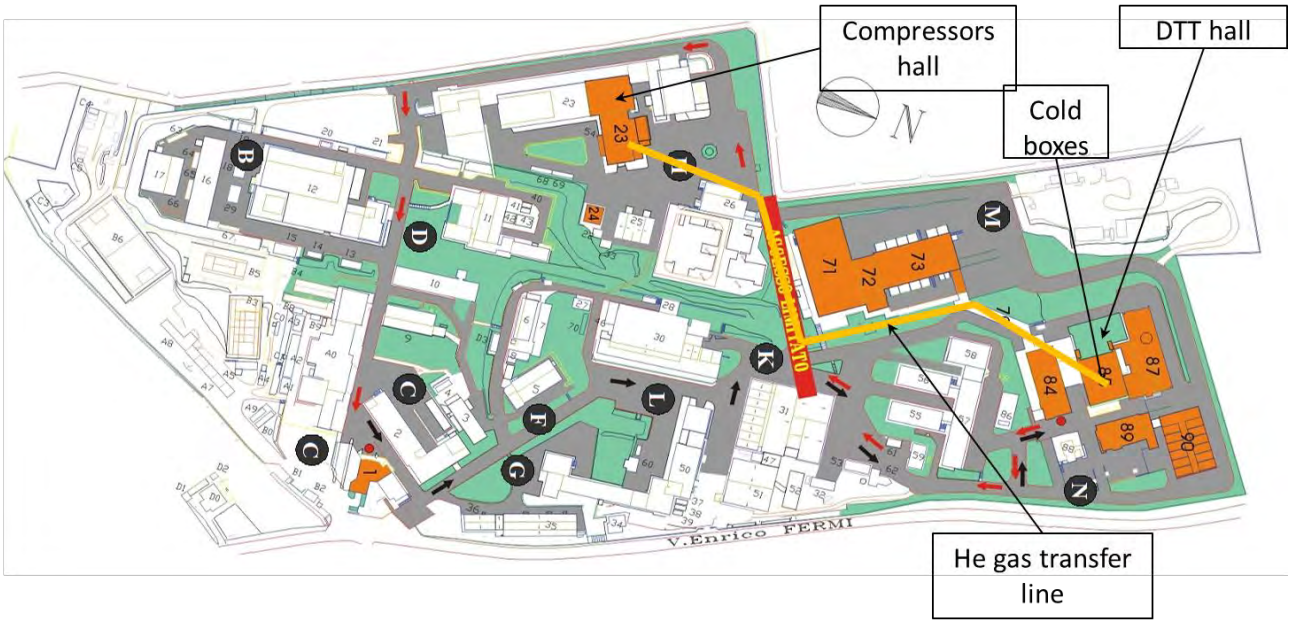

Figure V.4: Layout of the cryoplant system in the DTT site.

V.2.3 Sub-station for the HV 150kV grid transformers

Concerning the substation for the High Voltage 150 kV grid transformers, Fig. V.5 shows, highlighted in red, the area where the new electrical substation will be placed. Also the two main underground cables to feed the power supplies and converters area and the other sub-systems are depicted. It is worth noting that the path of the HV line to the electrical substation is not yet defined but, since it will be provided by the Lazio region authorities in the framework of the agreement for the DTT site, it is out of the scope of the present report.

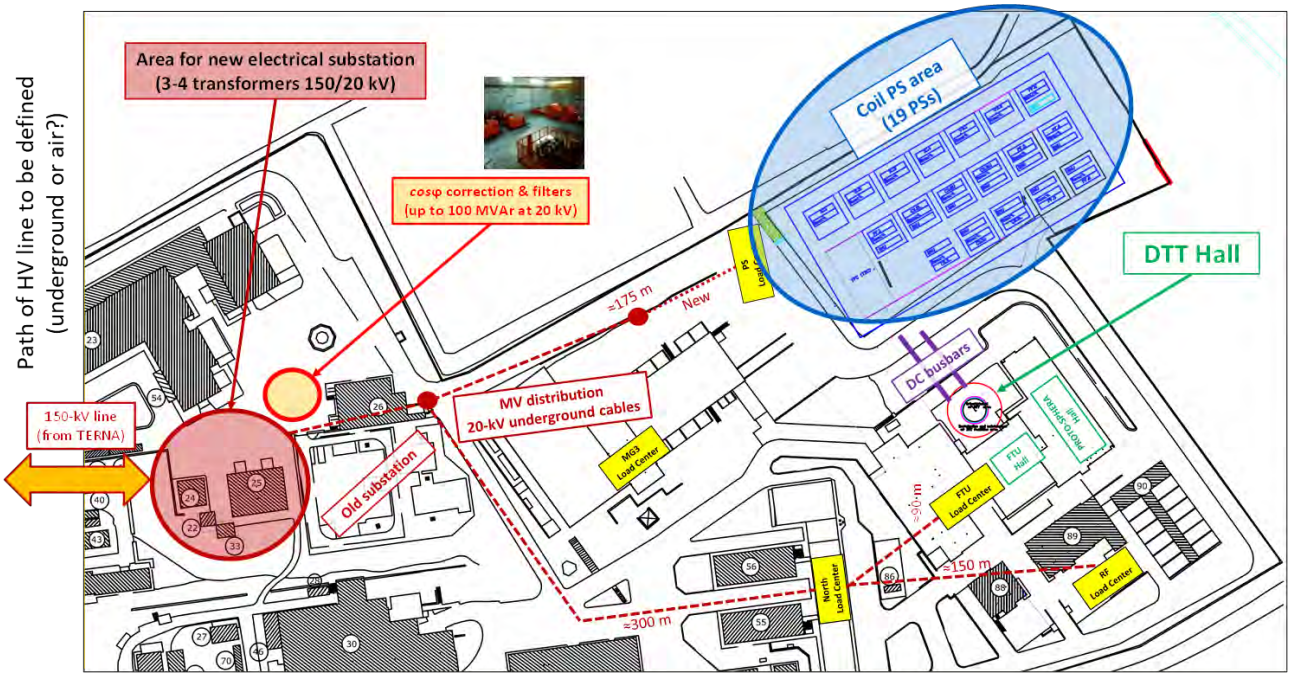

Figure V.5: Layout of the new electrical substation in the DTT site.

V.2.4 AC/DC converters layout

Figure V.6 shows the layout of the DC converters area, described in Section VIII and located in front of the DTT torus hall in an area presently not used in the ENEA Frascati research center. Up to forty-eight converters can be recognized with the grid necessary to bring the current to the magnets inside the hall. In Fig. V.6 the presence of an underground water pipeline is also reported. The presence of this water pipeline poses limitations to the excavation activity in the area needed to create the platforms. Therefore, a terracing that follows as much as possible the natural slope of the ground will be adopted. Each cluster of six converters will be accessible through a road network passable by trucks. Each cluster has a dedicated area 13 m x 13 m in which standard (40 feet) containers can be placed. The grid of busbars will gather in the middle and direct towards the torus hall entering from a side. The details of the busbars layout are still to be defined.

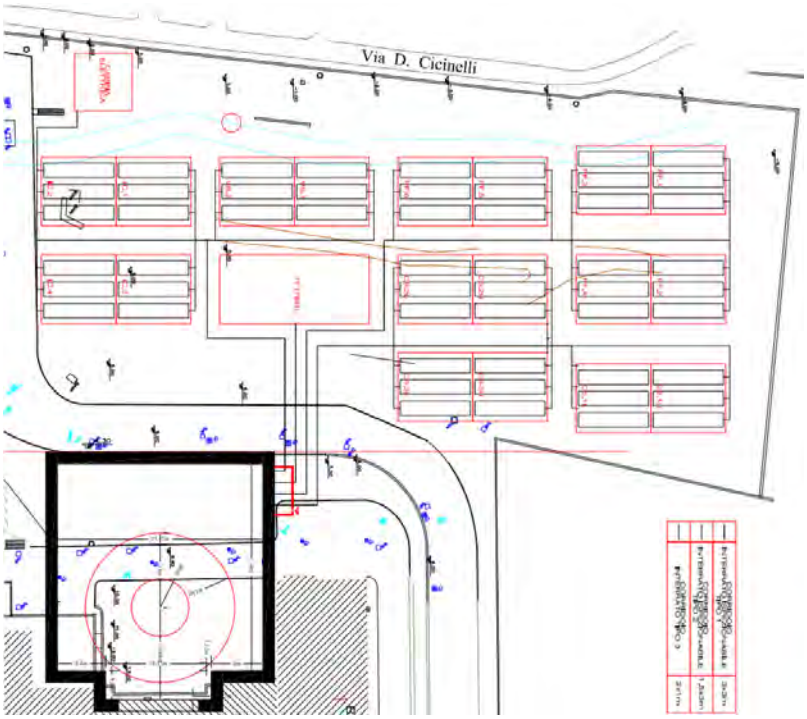

Figure V.6: Layout of the AC/DC converters.

V.2.5 Area for secondary water-cooling system

As reported in Section VI.3, the heat generated during the operations of DTT and in the dwell time between two shots, will be dissipated by a water-cooling system composed of two parts: a primary circuit in contact with the heat source and a secondary cooling circuit that will be common to each primary circuit. From this description it is apparent the necessity to locate the secondary loop in a position as much as possible barycentric with respect to the primary loops. Accordingly, Fig. V.7 shows the layout of the secondary loop in the DTT site. The pump room will be located in the basement of building F73, whereas the warm and cold tanks will be placed in the basement of building F71. Instead the chillers (14 m long, 2.5 m wide and 2.5 m high) needed to cool the water will occupy the area in between the two buildings. In Fig. V.7 the transfer lines to the different primary circuits to be cooled are also depicted. It can be noted that most of the heat sources are located on the right of the pump room, however the presence of the cryoplant compressor building on the left makes the present location a valid choice. It is worth noting that routing of pipelines is only indicative and that a more detailed analysis should be performed before closing the layout of the system.

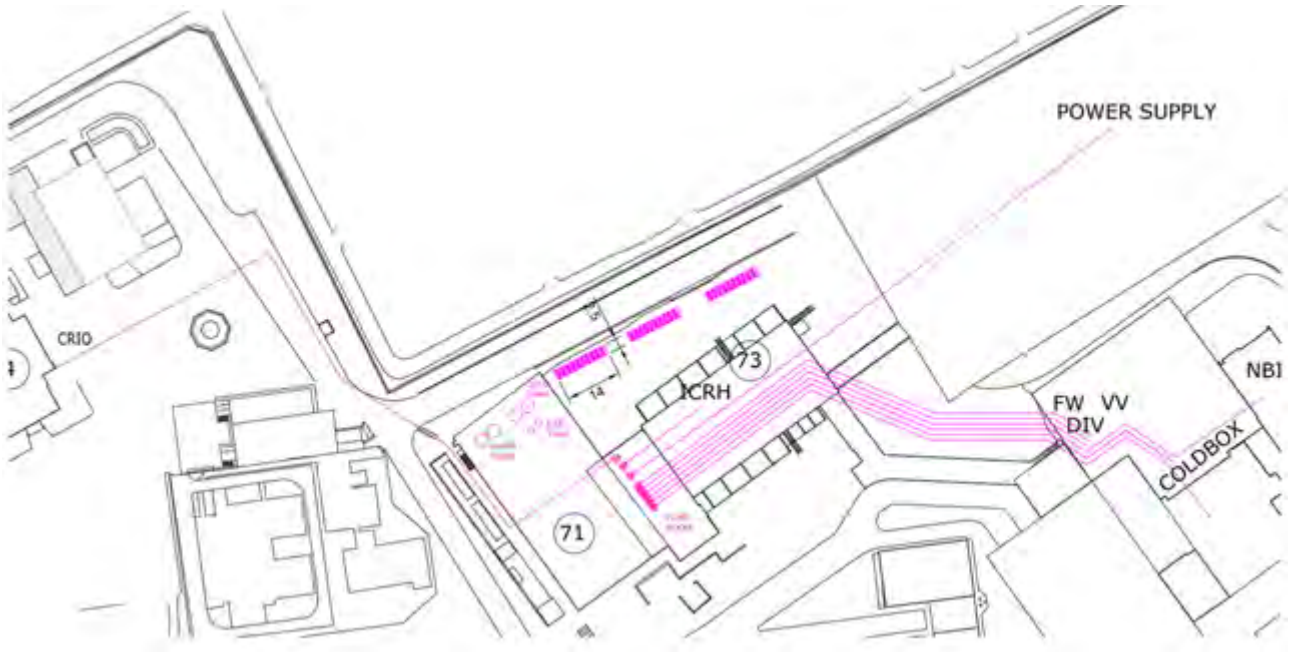

Figure V.7: Layout of the water-cooling system secondary loop.

V.3 Layout and Assembly in Tokamak Hall

The tokamak building, or torus hall, is one of the most critical components of DTT since it will provide the necessary shielding to the neutrons and radiation originating from the tokamak and because it will dictate the schedule of assembly operation of DTT. Having regard to the experience of other superconducting fusion machines, the layout of DTT tokamak building has been made in parallel with the assembly conceptual design. The following list of preliminary requirements has been identified:

- The DTT hall shall have concrete walls with a thickness of 2.2 m, as stated in Section XI;
- The DTT hall shall have a height compatible with the insertion from the top of the central solenoid whose height is about 6 m;
- The DTT machine will be placed at such a height that the lower lateral port of the cryostat is at +9.9 m (from the 0 of the site located at the basement of building F73), i.e. at the level of the FTU basement;
- The DTT hall shall have pre-assembly and testing areas where the sectors of the VV and the TF coils can be pre-assembled and tested before assembling in the final position;
- The DTT hall shall have a door large enough to let the largest PF coils (PF3/PF4 with about 9 m of external diameter) enter the hall, downloaded from the truck and inspected;
- The DTT hall shall have a crane with around 100-150 tons of max load.

According to the previous requirements, the torus hall has been presently designed to be 28 m tall, 35 m wide and 33m long in order to accommodate the machine and its ancillaries. Its basement will be at the same height of the facing road at 4.3 m from the 0 of the research center. To operate the machine a slab will be

created at height +9.9 m (level 0) as a continuation of the FTU basement, instead the basement (level -1 or ground level) will be 5.6 m below. The height of the building is compatible with a height of the machine of about 12 m and with a height of the CS around 6 m. The capability of the crane (100-150 tons) is derived by the assembly procedure that foresees pre-assembly modules made of 2 Vacuum Vessel sectors, 2 Toroidal Field coils and associated modules of thermal shield, intercoil structures and ports. The expected overall weight of the modules would be about 80 tons including the supporting structures. To allow the insertion of the coils in the pre-assembled VV sectors, the pre-assembly area should be equipped with a dedicated crane of about 30 tons. The assembly of DTT will start with the cryostat base on top of which the lower PF coils (PF6, PF5 and PF4) will be temporary positioned. Subsequently, modules made of 2 VV sectors and 2 TFC will be put on the cryostat base and welded together up to the completion of the toroidal shape. The upper PF coils (PF3, PF2 and PF1) will then be installed, followed by the central solenoid. In-vessel components and cryo- and water- distributions inside the cryostat will then be arranged in parallel and finally cryostat cylindrical section and cryostat top lid will be put in place. The arrangements of diagnostics and heating system ex-vessel will be done in parallel to the activities inside the vessel.

In Fig. V.8 a rendering image of the torus hall with the buildings of the ENEA Frascati research center in the background is shown. The building is the prolongation of the FTU building (the smallest one in the figure) where the cold box of the cryoplant will be placed. In this respect, a space reservation area colored in blue is represented. All machine services are supplied from the bottom and housed in the basement, while most of the heating and diagnostic systems are located in the lateral experimental hall. A volume (15 m tall, 5.5 m deep, and 17 m wide) is reserved for busbars (that will enter from that wall) and current lead boxes (from which the feeders for the superconducting magnets will originate). Another volume (4 m tall, 8 m deep and 16 m wide) in the basement of the DTT hall has been reserved for the matching unit of ICRH, and one for the heat exchangers of the primary water loop of first wall and divertor. However, both these two systems could be moved outside the main building and placed in the prolongation of the corridor hosting the transmission line of ICRH.

It can be noted that the layout shown in Fig. V.8 represents the DTT hall in a phase of advanced assembly of the machine in which the basement of FTU building is prolonged to cover almost all the DTT hall. However, in the initial assembly phase, half of the ground level in the DTT hall will be devoted to pre-assembly and testing of the VV and TFC sectors. Once the load assembly will be completed, the preassembly area shall be covered by a slab at height +9.9 m as shown in Fig. V.8. and Fig. V.9 shows a possible layout of DTT torus hall at level 0 after the assembly phase. Around the cryostat, the main components entering by the equatorial ports are sketched. The two negative neutral beam injectors are located in the lower part of the sketch (white triangles) and their support structure will be located in the basement. The red objects are the space reservations for the ICRH antennas, the cyan lines are the ECRH transmission lines in the hall, the yellow rectangles are the space reservation for remote handling, the purple rectangle is the Thomson scattering and the blue line is the cryogenic transfer line from the cold box, represented by the blue rectangle in the FTU hall on the left. Finally, it can be noted that the area above the pre-assembly zone has been prolonged at the ground level in order to host cabinets for diagnostics inside the hall. The reception area in front of the main door is left open to allow the loading or unloading of components even after the assembly phase.

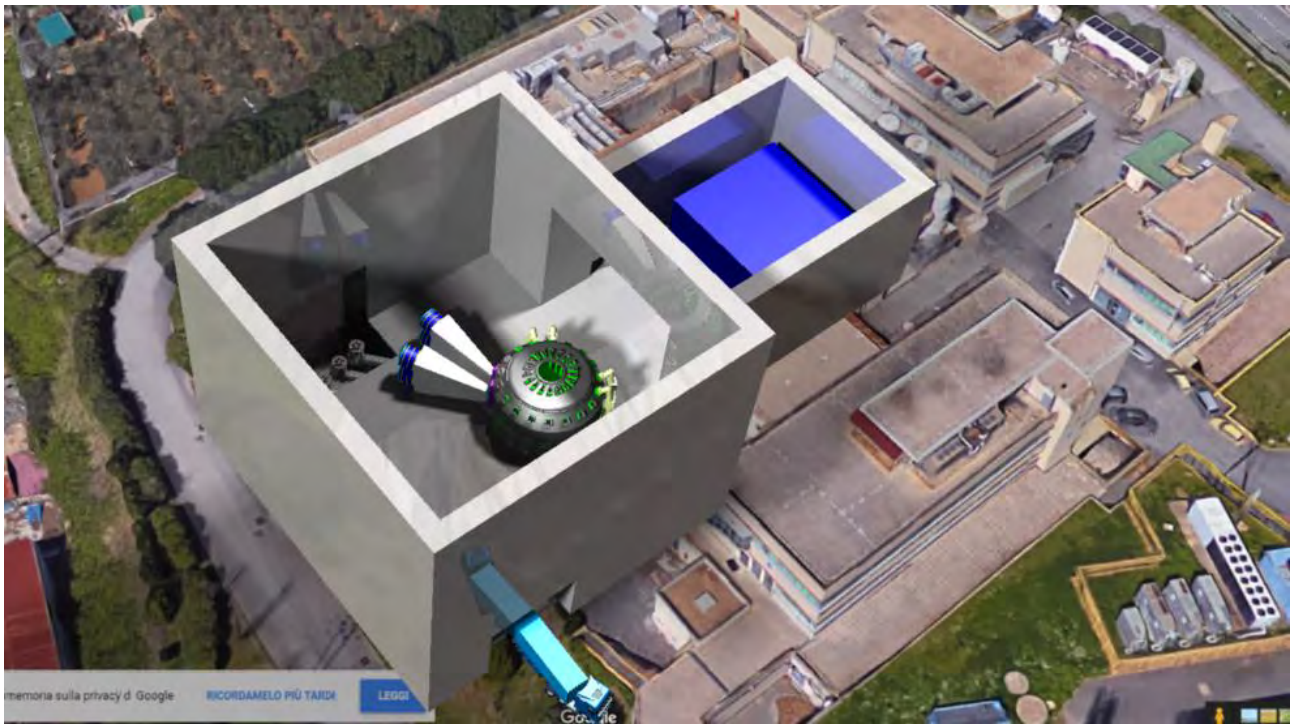

Figure V.8: Rendering image of the DTT conceptual layout in an advanced phase of the assembly.

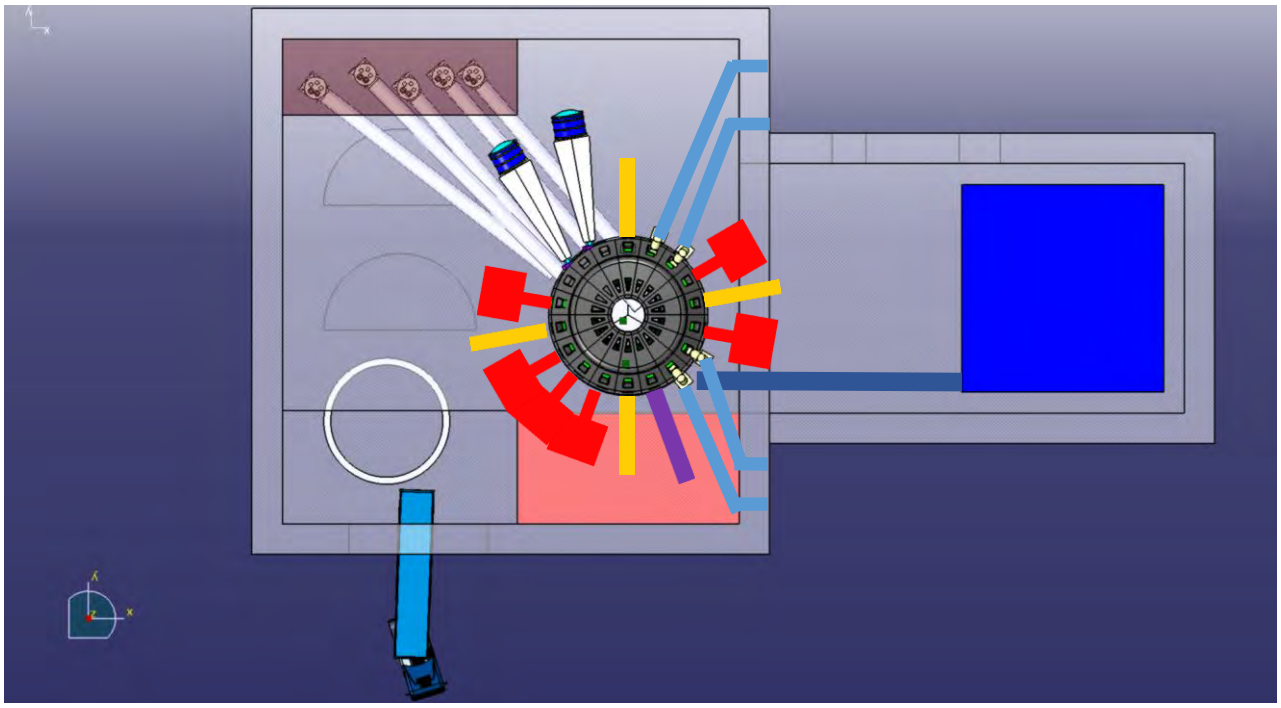

Figure V.9: Top view of the DTT torus hall at the end of assembly.

As already mentioned, the ground level will host the feeders for the superconducting magnets, the set of valve boxes to deliver the helium to the superconducting magnets, the structures supporting the magnets and the thermal shields, and the heat exchangers of the primary water-cooling system for first wall and divertor. Note also that the space between the cold box and the cryostat will be used for the temporary

storage of the components removed by remote handling that will be then moved outside the hall through the FTU main door located at level 0.

V.4 Conclusions

The layout of the DTT site and of the torus hall has been defined taking into consideration the assembly procedure. Also, components manufacturing and building constructions have been scheduled to start the integrated commissioning at the latest in June 2025 and to start first plasma within the end of 2025.

The building activities will start from the beginning of 2019, as described in Appendix B (see GANT chart ID #846 and following). As one can note, the first task is to complete the layout within third quarter of 2019, this will allow the completion of the design activities for the main buildings. Concerning the DTT torus hall, the construction activity will start in the fourth quarter of 2020 and should be completed in 21 months.

The assembly activities design, to be completed between the middle of 2020 and the middle of 2021, are described in the same Appendix (see GANT chart ID #904 and following). Assembly will start in 2022 with the arrival of the first components and in particular, the cryostat base will be positioned in middle of 2022. Assembly phase will span overall 4 years from the beginning of 2022 to the end of 2025.

V.5 References

[V.1] http://enerweb.casaccia.enea.it/enearegioni/UserFiles/Avviso_DTT.pdf

[V.2] http://www.enea.it/it/opportunita/inoltre-vi-segnaliamo/avviso-per-una-selezione-finalizzata-alla-scelta-di-un-sito-per-l2019insediamento-dell2019esperimento-dtt-divertor-tokamak-test/relazionefirmata.pdf

Chapter VI

AUXILIARIES

VI.1 Introduction

Several auxiliary systems are necessary in order to produce and control the plasma, to remove the fusion power for maintaining the fusion reactions and to ensure safety and plant protection.

The cryogenic system supplies supercritical He to the superconducting magnets and their structures, the current leads (HTS CL), and the thermal shields (TS) providing refrigeration for the various consumers and allowing different operation modes.

For safety operation the active water-cooling system will be able to handle large values of the input power over long plasma discharges.

VI.2 Cryogenic System

VI.2.1 Main duties of the cryogenic system

The DTT superconducting magnet system includes 18 Toroidal Field (TF) coils, 6 Central Solenoid (CS) modules and 6 Poloidal Field (PF) coils. All these superconducting coils will be supported by cold structures, located

inside a cryostat equipped with thermal shields (TS), which are actively cooled using pressurized helium at ~80 K. The coils and their related structures will be cooled by forced supercritical helium flow at ~ 4.5 K. The 30 High Temperature Superconducting current leads (HTS-CL), 6 for the TF coils, 12 for the CS modules and 12 for the PF coils, will operate between cryogenic and ambient temperatures, and will require cold helium flow at a temperature of ~ 50 K. Usually the cryogenic plant has also to provide the He cooling (below 4.5 K) for the dedicated divertor cryo-pumps. Also considering that the DTT divertor pump system should be applicable to DEMO, the choice to adopt Not Evaporable Getter (NEG) pumps is presently under investigation. The NEG pumps should be assisted by ionic pumps, for pumping out the noble gases, used in DTT for enhance the local radiation, but mainly present in DEMO as reaction "ashes" (He).

In case of a TF coil quench, all the TF coils will undergo a fast discharge, resulting in a large sudden energy release in the TF coils, with a rapid increase of both temperature and pressure. An adequate cold He (~ 15 - 20 K) mass flow rate must be released through quench relief valves in the Valve Box, to be collected in the quench line and stored in a dedicated quench recovery tank.

VI.2.2 DTT operation modes and preliminary estimate of heat loads

The cyclic operation, typical of a tokamak, results in significant variations of the heat load, that the cryogenic system must be able to handle. The DTT is expected to operate ~ 6 months per year, corresponding to ~ 100 experimental days per year (normal operation mode); about 4 months per year are anticipated to be dedicated for maintenance and adjustment, as well as for configuration changes and/or improvements, plus 1 month for cool down and 1 month for warm up.

In the latter two modes, the cryogenic system (and the related cryodistribution system) will have the duty of either cooling down or warming up progressively (~ 0.5 K/h) the different cryogenic components (TF, PF and CS coils and structures, TS, HTS-CL), preventing at the same time the onset of too large deviations from respective expected temperatures, that might induce considerable mechanical stresses and even hurt their integrity.

During experimental periods, the normal operation mode, which includes the Plasma Operation Mode (POS) and the dwell period (DWE), will last 4 days per week, about 10 hours a day (plus one hour at each end for pre- and post-experimental inspection). In the reference maximum performance scenario, plasma pulses will last ~ 100 s (including rump-up and ramp-down of the PF and CS coils and plasma initiation), with a stabilized plasma current flat-top of ~ 50 s, and will be repeated every 3600 s, with a total of 10 plasma pulses per day. Throughout the DWE period, between two successive plasma pulses, stationary heat loads include thermal radiation, the conduction across the support structures and the current leads, as well as the Joule heating in conductor joints and terminations. For the short duration of POS, additional large heat pulses are deposited into cold components, due to nuclear thermal heating, eddy current losses in the massive support structures, and AC losses induced in the conductors by electromagnetic variations. These additional loads are transferred through the cryodistribution to suitable thermal buffers inside the cryogenic system cold box. During the DWE phase, that follows each POS and features reduced heat loads, the cryogenic system must remove the part of additional heat stored in the cold components inside the DTT cryostat and in the thermal buffers, in order to recover the initial conditions to restart a new POS.

During idle periods of the coils, such as over nights and weekends, the cryogenic system has to operate in a Short Term Standby mode (STS), which may be characterized by somewhat reduced heat loads, except for the TS at 80 K. During STS the temperature of the superconducting coils could be slightly relaxed to 4.6 K, since there is no current feeding. The regeneration of the pumping system will be performed in STS mode

(possibly during night); this operation requires first warming up the NEG pumps, to their respective regeneration temperatures, followed by a temperature plateau long enough to ensure an adequate regeneration, and hence by a cool down phase. NEG pumps do not require cooling by the cryogenic system and are heated up independently. However they may need to operate at relatively high temperatures (from room temperature up to a few hundred degree Celsius, depending on the specific alloy), as well as to be regenerated at even higher temperatures, so they may contribute to the thermal radiation loads on surrounding cold components; this issue should be addressed in order to evaluate its impact on the cryogenic system requirements during STS operation.

As for maintenance, two scenarios, and two corresponding operating modes, are foreseen. In Short Term maintenance (STM) mode, tightly controlled access will be allowed for quick repairs or inspection; when in STM mode, the DTT VV is under vacuum and the magnets are kept cold, but not energized. In Long Term Maintenance (LTM) mode, access to the VV or to the cryostat will be allowed, if required, for maintenance or other operations to be performed on a longer timescale; in this mode the coils will be warm and, of course, not energized.

Baking and He Glow Discharge Conditioning (GDC) of the VV shall be carried out before each cool down of the DTT facility (i.e. with magnets still at room temperature), as well as once a month during normal operation, with the TF coils not yet energized but at low temperature. Each baking cycle could last up to a week, at the baking temperature, assumed to be limited to 110°C for the VV, as well as for the divertor targets, dome, and baffles. The first wall (FW), instead, could be heated up to 200 °C.

Some preliminary estimates of reference heat loads and operating temperatures during normal operation (including POS and DWE), the baking mode, and cool down/warm up phases are reported respectively in Tabs. VI.I, VI.II and VI.III. No calculation has been made, to date, concerning fast discharges of DTT; just to give an idea of the orders of magnitude of the relevant parameter, data from JT-60SA are reported in Tab. VI.IV [VI.1]. Further analyses are in progress, to provide robust values to be used during the tender phase of the cryogenic system.

TABLE VI.I REFERENCE HEAT LOADS AND OPERATING TEMPERATURES DURING NORMAL OPERATION

	During POS			During DWE		
System	**Heat load (kW)**	**Duration (s)**	**Inlet/outlet temperatures (K)**	**Heat load (kW)**	**Duration (s)**	**Inlet/outlet temperatures (K)**
TF + casing	~ 7.5 (nuclear heating) + 0.1 (radiation)	100	4.5/5.0	0.1 (radiation)	3500	4.5/5.0
PF + CS	1.6 (nuclear heating) + +0.7 (radiation and eddy currents)	100	4.5/5.0	0.1 (radiation)	3500	4.5/5.0
TF HTS-CL	6 × 1.5 = 9.0	100	50/300	6 × 1.6 = 9.0	3500	50/300
PF/CS HTS-CL	24 × 1.5= 36.0	300	50/300	0	3500	-
TS	1.1 (nuclear heating) ++ 43 (radiation)	100	80/100	43 (radiation)	3500	80/100

TABLE VI.II REFERENCE HEAT LOADS AND OPERATING TEMPERATURES DURING BAK

System	Heat load (kW)	Duration (days)	Inlet/outlet temperatures (K)
TF + casing	0.2 (radiation)	5	10/40
PF + CS	0.2 (radiation)	5	10/40
TF HTS-CL	0	5	
PF/CS HTS-CL	0	5	
TS	43 (radiation)	5	80/100

TABLE VI.III. AVERAGE HEAT LOADS DURING COOL DOWN AND WARM UP

Total mass (kg)	6×10^5
$\int_4^{300} c_p dT$ (J/kg)(*)	92.8×10^3
ΔT (K)	300
Total energy (J)	5.57×10^{10}
Time (days)	30
Time (s)	2.59×10^6
Average power (W)	2.15×10^4
Average cool down speed (K/s)	1.16×10^{-4}
Average cool down speed (K/h)	4.17×10^{-1}

(*) It is assumed that all the mass is made out of AISI 316 stainless steel

TABLE VI.IV. FAST DISCHARGE REFERENCE PARAMETERS FOR THE JT-60SA

Energy released in the TF coils (MJ)	Temperature rise	Pressure buildup	Released He mass flow rate	Total amount of He released to recovery tank
18.7	Up to 15÷20 K	Up to 2 MPa	Up to 1 kg/s	~ 200 kg

VI.2.3 Deployment of the main components of the DTT cryogenic system

The DTT cryogenic system will include the following systems:

- A Warm Storage System (WSS) – a set of large storage vessels having sufficient capacity to store the whole helium inventory required for the cryogenic plant; one of the vessels will be used for quench recovery.
- Liquid nitrogen storage tanks.

- A Warm Compression Station (WCS), including the Oil Removal System (ORS) and a full flow dryer.
- A Refrigeration Cold Box (RCB).
- An Auxiliary Cold Box with thermal dampers, connected to the RCB and to the tokamak by means of dedicated super-insulated cryogenic lines.

Figure VI.1 shows the deployment of the above components within the ENEA Frascati Centre. The cold boxes will be positioned in the cryogenic hall (presently hosting the FTU tokamak), located in close proximity to the DTT hall, to minimize the length of the cryogenic line. The liquid nitrogen storage tanks are already available and are located just outside of the cryogenic hall. The WCS will be placed at a distance of about 300 m from the cryogenic hall; to interconnect the WCS and the cold boxes inside the cryogenic building, the warm He gas pipes will be routed through an existing underground aisle. The WGS system will be located in close proximity of the WCS.

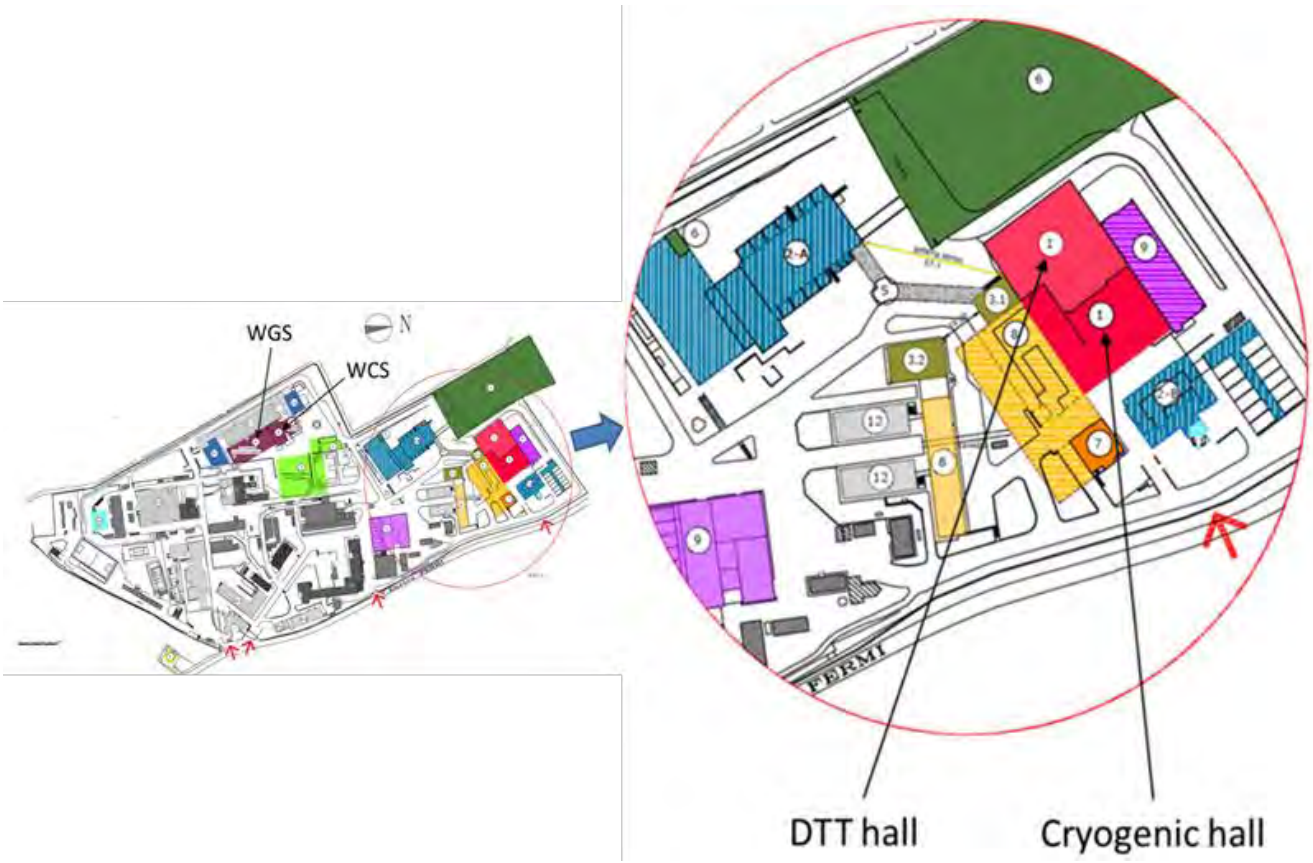

Figure VI.1: Deployment of the main components of the DTT cryogenic system

VI.2.4 Identification of a suitable conceptual design

Three different approaches are being considered, that need to be investigated and compared in terms of costs/benefits:

- A conceptual scheme similar to that of the JT-60SA cryogenic system [VI.2], featuring a single Claude refrigerating cycle providing refrigeration at 80 K for the TS, 50 K for the HTS-CL, 4.5 K for TF, PF and CS magnets, and 3.7 K, just in case, for the cryopump panels.

- In case of using NEG pumps, a scheme similar to that of the JT-60SA, but without the cooling loop at 3.7 K, is being considered. This is the reference option in view of DEMO, yielding a considerable simplification of the cryogenic system and perhaps in a significant reduction of both procurement and operating costs. Moreover, integration of the RCB and the ACB in a single cold box might be considered in this case as an option.
- A third conceptual scheme making use, within the same RCB, of two distinct refrigeration cycles, i.e. a reverse Bryton cycle to provide cooling for the TS at 80 K, and a Claude cycle for the other cryogenic users, is being considered as an option; such a conceptual scheme, combining those adopted for the JT-60SA and the EAST [VI.3-VI.4] cryogenic systems, may have the potential of decoupling the helium mass flow rates circulating through the thermal shields at 80 K (by means of the Reverse-Bryton cycle) from that feeding the Claude cycle to produce refrigeration at lower temperatures, perhaps reducing the refrigeration power at low temperatures (4.5 K or less).

VI.3 Water Cooling System

VI.3.1 Overview

In the DTT machine the specific power to heat the plasma is higher respect to the other Tokamaks with comparable dimensions. All heating systems (ICRH, ECRH, NBI) and cryogenic systems force DTT to become a machine cooled actively. Analyzing all thermal loads (see Tab. VI.V) applied to the machine during the plasma discharge the best solution to remove the largest part of the produced heat is a system based on pressurized water, except for the thermal shield and for the magnets cooled by liquid Helium.

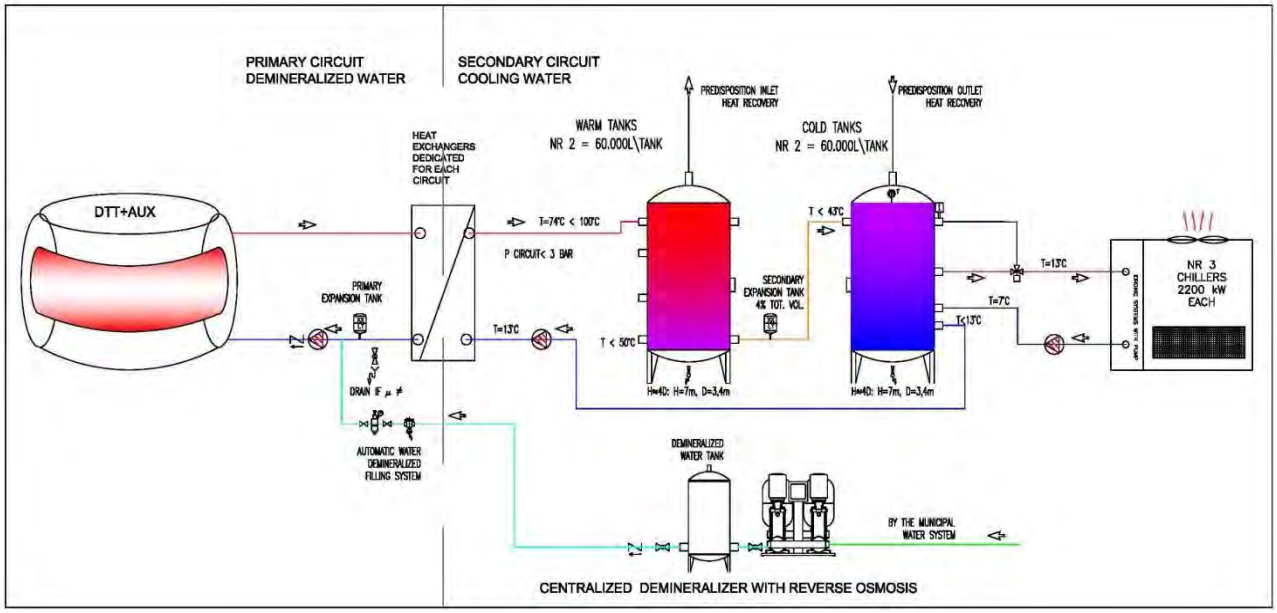

Figure VI.2: Conceptual Scheme of Cooling Water System during the plasma discharge

Having this in mind, the choice of the best cooling water system for DTT should be done considering the boundary conditions related to the site of ENEA Research Center of Frascati. ENEA is located on the slopes of

the hill with no rivers or lakes in the proximity. It is worth to consider also that the civil residents next to the research center would prevent the use of cooling wet towers because of the produced noise and steam. Moreover, the maximum water flow rate provided by the municipal aqueduct would not be enough to satisfy the cooling system requirements.

Eventually, the best viable solution is a cooling water system divided in two close loop circuits as shown in Fig. VI.2.

The primary cooling circuit is filled with demineralized water while the cooling of the vacuum vessel is carried out by borated water to provide maximum neutron shielding. To optimize the systems the demineralized water will be produced by a centralized demineralizer with reverse osmosis.

The primary cooling circuit transfers the thermal load, produced during the plasma operation, to the dedicated heat exchangers. All thermal loads are pumped in the secondary circuit using a classical cooling water, equipped with filter and chemically processed to avoid any deposition and for removal of corrosion products. The loop is closed by two types of tank for storage and by a set of chillers sized for this purpose.

VI.3.2 Primary cooling system parameters

DTT is a machine with a flat top of the pulse up to 50s and maximum dwell time for high performance of 3600s. During the plasma discharge some facility are thermally stressed for a defined duration as well as reported in Tab. VI.V.

The total thermal power produced during the plasma operation is around 127 MW, most of them is generated within 150 seconds, the largest part coming from the heating systems (Tab. VI.V). It is worth to note that the Cryoplant and the Toroidal Field Systems need to be cooled continuously. For standard operation all cooling equipment are designed (pipes, pumps, etc.) to operate at the temperature close to 60°C. During the baking phase or in the phase of divertor with metallic liquid the First Wall (FW) temperature could arise 200°C, with a saturation pressure over 14 Bar. The related cooling system has been designed to working in this temperature range. For this reason, the heat exchangers are sized to the maximum power, temperature and working pressure. Indeed, for the FW, divertor and vacuum vessel (during the baking) are foreseen shell-and-tube heat exchanger in stainless steel optimized for pressure over 16 Bar. The other circuit, where the pressure does not exceed 16 Bar, adopts plate heat exchangers in stainless steel. The last solution, thanks to the high heat exchange coefficient, saves installation space in the Torus Hall.

TABLE VI.V. INVENTORY OF THERMAL LOAD DURING THE PLASMA OPERATION

Facility	Dissipat. Thermal Power (kW)	Power Duration (S)	Primary System Inlet Cooling Temp. (°C)	Outlet Temp. Primary - Heat Exchanger (°C)	Drop Pres. System + Psat (BAR)	Dwell Time (S)	Volume Warm Tank(m^3)	Volume Cold Tank (m^3)
ECRH	40.000	50	15	40	7	3600	35	35
Power Supply	3.200	50	15	35	6	3600	2	2
ICRH	11.000	50	20	40	8	3600	12	11
TF Power Supply	245	Steady State	35	45	6	Steady State	1	2
CS	280	300	35	45	6	3600	1	1
VS	280	100	35	45	6	3600	1	1
SNU	1.200	10	35	45	6	3600	2	2
FDU	120	10	35	45	6	3600	1	1
PFC	500	150	35	45	6	3600	1	1
CRYOPLANT	3.000	Steady State	15	25	8	Steady State	5	20
COLDBOX for	30	Steady State	13	14	5	Steady State	1	1
NBI	23.000	50	15	35	14	3600	25	25
DIVERTOR	30.000	50	60	74	27	3600	35	20
FIRST WALL	15.000	50	67 (180 with Li Divertor)	74	27	3600	10	10
VACUM VESSEL	100	Steady State	60	74	27	Steady State	0	0
TOTAL	127.855			51			132	132
				Weighted Average Temp. (°C) According to Power				

VI.3.3 Secondary cooling system parameters

In order to minimize chilling power, electricity absorption and allocated space all cooling circuits are connected to the top of "Warm Tank" as it shown in Fig. VI.3, where the cooling waters, with different temperatures, are mixed. The heat stored in the "warm" tank has been calculated so that the temperature does not reach the boiling point as shown in Tab. VI.VI. In order to optimize the heat stratification, the warm tank is divided in 2 separated tanks of 60 m^3 volume each, 7 meters tall. From the bottom of the warm tank, the water lead to the top of two "cold tank", similar as volume to the "warm tank".

In the “cold tank”, during the dwell time, the chillers are cooling down the entire water volume getting the nominal temperature of 13°C (Fig. VI.3).

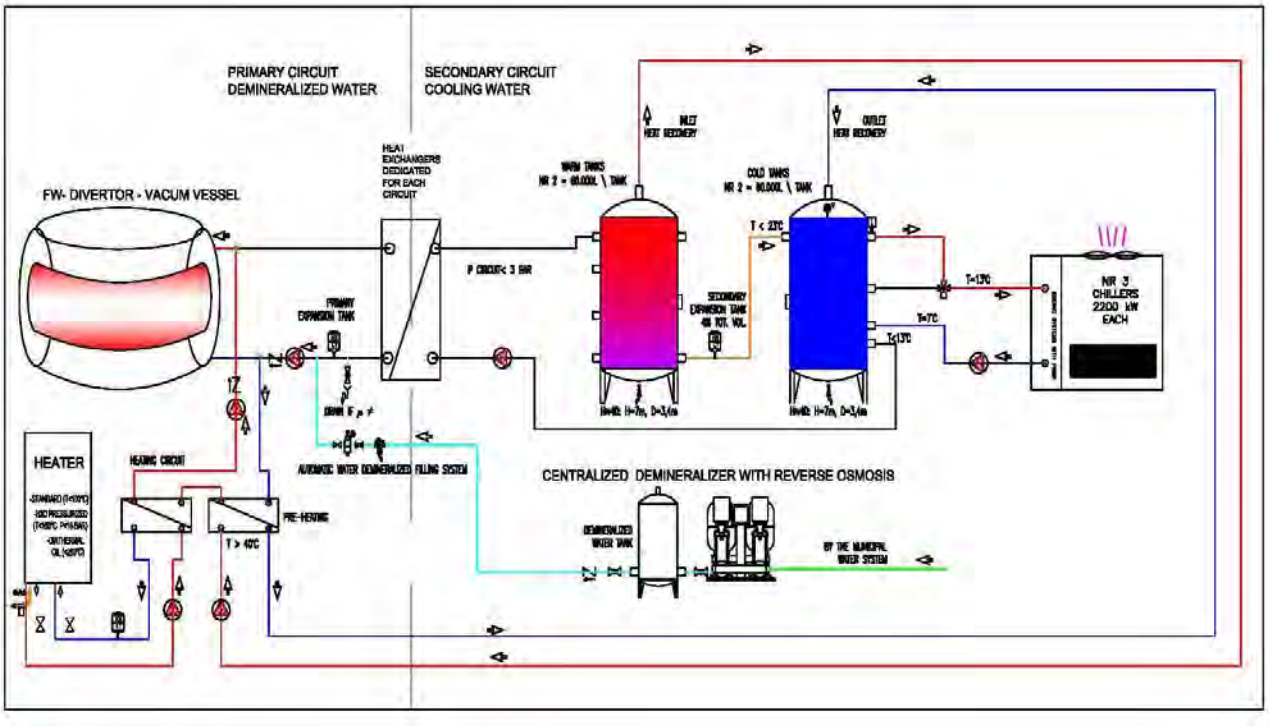

Figure VI.3: Cooling water loop during dwell time

TABLE VI.VI. INVENTORY OF THERMAL LOAD DURING THE PLASMA OPERATION

Volume warm tank (m3)	Volume cold tank (m3)		Flow-rate at full power (m3/h)	Maximum temperature arised in the warm tank(°C)	Power required supplied by chiller (kW)	Electric power absorbed by chiller (kW)	Minimum temperature arised in the cold tank(°C)
35	35	ECRH	1.376	28,7	556	192	15,0
2	2	Power Supply ECRH	138	34,1	44	15	15,0
12	11	ICRH	473	30,9	153	53	19,0
1	2	TF Power Supply	21	35,1	245	85	35,0
1	1	CS	24	55,1	23	8	35,0
1	1	VS	24	41,7	8	3	35,0
2	2	SNU	103	36,4	3	1	35,0
1	1	FDU	10	35,3	0	0	35,0
1	1	PFC	43	52,9	21	7	35,0
5	20	CRYOPLANT	258	15,1	3.000	1.038	15,1
1	1	COLDBOX for CRYOPLANT	13	12,0	30	10	12,0
25	25	NBI	989	26,0	319	111	15,0
35	20	DIVERTOR	1.843	70,2	417	144	52,3
10	10	FIRST WALL	1.843	84,9	208	72	67,0
132	132		7.158	43,8	5.028	1.740	26,1
				WEIGHTED AVERAGE OF TEMPERATURE (°C) HOT TANK			WEIGHTED AVERAGE OF TEMPERATURE (°C) COLD TANK

In order to save cooling energy, from the top of the warm tanks it could be drained the hot water to feed, as pre-heating, some circuit between the plasma operations (e.g. vacuum vessel).

VI.4 Fueling, Pumping, Baking System

VI.4.1 Fueling

The fuelling system can be identified as having the following main sub systems:

- Deuterium (and Hydrogen) plasma fuelling through valves and pellet injector, mainly positioned in the mid-plane;
- local neutral density control in front of the ICRH antennas;
- noble gas impurity injection in the main plasma and in the divertor region;
- massive gas injection in the main plasma region for disruption mitigation in different poloidal and toroidal location (solution still to be discussed).

The necessary feeding pipes distribution is presently under investigation, in order to best fuel (toroidally and poloidally) the plasma.

VI.4.2 Divertor pumping

By considering that the type of pump to be used in DTT should be also applicable to DEMO, the present strategy is to adopt for the high vacuum stage Not Evaporable Getter (NEG) pumps assisted by ionic pumps.

Besides the DEMO relevant this option has many advantages and overcome the drawbacks of cryogenic pumping systems: costs (investment and running costs), safety (explosion), availability (frequent regenerations) and reliability (high maintenance costs of cryogenic systems).

The amount of neutrals to be pumped as well as the total conductance of the pumping ducts is presently under evaluation, by fluid codes simulations and comparison with the ongoing worldwide experiments.

The pumping system is under study and development in collaboration with the European colleagues of KIT. It is planned to arrive at a final decision about the cryo-pumps use along summer 2019.

VI.4.3 Vacuum chamber pumping

The system for vessel evacuation could consist of pre-exhaust and main exhaust systems (turbo-molecular pumps). As a consequence of the proximity of the pumps to the tokamak, the pumps will need magnetic and radiation shielding. Magnetic shielding must assure allowable local field at TM pumps <3 mT (horizontal), <10 mT (vertical).

Each pump is connected, by a separate line, to the same pumping systems. The overall required number and pumping speed of the pumps will be calculated taking into account both required effective pumping speeds and conductance values.

VI.4.4 Baking system

Baking of the vessel is accomplished by drainage of the boron-water coolant and replacement by a flow of demineralized water. During the baking phase the vacuum vessel and the ports are heated to 383 K. As a consequence, the heat load on the Vacuum Vessel Thermal Shield (VVTS) and Port Thermal Shield (PTS)

increases considerably. In order to optimize the baking cleaning, this is foreseen to last up to a week. During the baking mode, the magnets and the HTS current leads are not operated. To avoid oversizing of the refrigerator particularly for the baking mode, the magnets are allowed to warm up a little and the outlet temperature of the TS is allowed to increase.

The in-vessel component baking (FW and divertor) is performed to 200 °C through water at proper temperature.

VI.5 Conclusions

Reference heat loads and operating temperatures during the POS and the STS phases have been evaluated, as well as the necessary cooling properties. Additional performances related either to maintenance operations mode or to Baking and He Glow Discharge Conditioning of the vacuum vessel has been defined. A preliminary layout of the cryogenic and of the water system within the ENEA Center is reported.

The main requirements of the cooling water are summarized as well as a conceptual scheme of the cooling system complete of a preliminary size of the components.

A detailed analysis is in progress to best determine the vacuum system requirements and to decide whether to use a cryogenic pumping system or to opt for an alternative system like the NEG pumps assisted by ionic pumps.

VI.6 References

[VI.1] F. Michel et al., Cryogenic requirements for the JT-60SA Tokamak, AIP Conference Proceedings 1434, 78 (2012), https://doi.org.10.1063/1.4706907

[VI.2] V. Lamaison et al., Conceptual design of the JT-60SA cryogenic system, AIP Conference Proceedings 1573, 337 (2014)

[VI.3] H. Bai et al., Cryogenics in EAST, Fus. Eng. Des. 81 (2006), 2597-2603

[VI.4] M. Zhuang et al., The cryogenic control system of EAST, Fus. Eng. Des. 87 (2012), 2007-2011

Chapter VII

SUPERCONDUCTING MAGNET SYSTEM

VII.1 Introduction

The DTT Magnet System is based on coils wound by superconducting Cable-In-Conduit conductors (CICCs), cooled down by forced flow of Supercritical Helium entering at 4.5 K. The main features of the coils have been already presented in year 2015 [VII.1-VII.2], and they have been more recently subjected to a partial review, leading to the design presented in this chapter. Some improvements have been implemented to obtain simplified manufacturing processes and, whenever possible, cost savings. As an example, in the present design the Central Solenoid (CS) is obtained by winding in layers different conductor unit lengths, so that the quantities of Nb_3Sn strand and of Stainless Steel (SS) are optimized, following the operative conditions. In the past reference the CS coil was made of pancake-wound coils, but the present graded design allows saving about 8 tons of expensive Nb_3Sn strand and, what is more important, it gives the possibility of reaching the required high performance in terms of engineering current density and thus of magnetic flux. Conversely, the Toroidal Field (TF) coils are now wound in Double Pancakes, whereas they were previously designed with a layer wound graded solution: in this case, the main driver for the change is that the cost saving, corresponding to the lower quantity of superconducting material, would have been lost because of the technical difficulties when winding a TF coil in layers. This solution, in fact, would have needed an additional R&D phase, being this not the “standard” technique for such D-shaped tokamak coils. On the other hand, it is worth mentioning that for a solenoid coil the layer winding technology is the standard one, already demonstrated within many different projects to be a reliable solution [VII.3–VII.5].

To allow the DTT machine to investigate the range of different plasma scenarios which are foreseen, the present Superconducting Magnet System, shown in Fig. VII.1, is composed of:

- 18 TF Nb_3Sn coils, operating at a peak field of 11.8 T and an operative current of 44 kA.
- a stack of 6 independently fed CS modules, operating at 13.2 T and 30 kA,
- 6 Poloidal Field (PF) coils, two of which reaching about 8.5 T and 30 kA (thus made of Nb_3Sn CICCs) and the other four working at lower fields and currents, thus relying on NbTi conductor technologies.

As the machine is fully symmetric with respect to the equatorial plane, the PF coils are designed to be identical in pairs.

The TF coils work in wedged condition. A full set of Inner Inter-coil Structures (IIS) withstands the shear force acting between adjacent TF coils, and *ad-hoc* designed Outer Inter-coil Structures (OIS) give support against the out-of-plane loads.

The 6 CS modules are identical, though working at slightly different operative conditions. They have been designed in such a way as to allow for the future addition of a High Temperature Superconducting (HTS) insert coil, which will have two main goals: to demonstrate the effectiveness of this technology for the next generation fusion reactors and to increase the coil performance, raising of about 1 Weber the magnetic flux over plasma. In this way, DTT will act also as a test bed for the future superconducting coils. It is worth noting that the goal of the DTT project is anyhow already achieved without this additional flux enhancement.

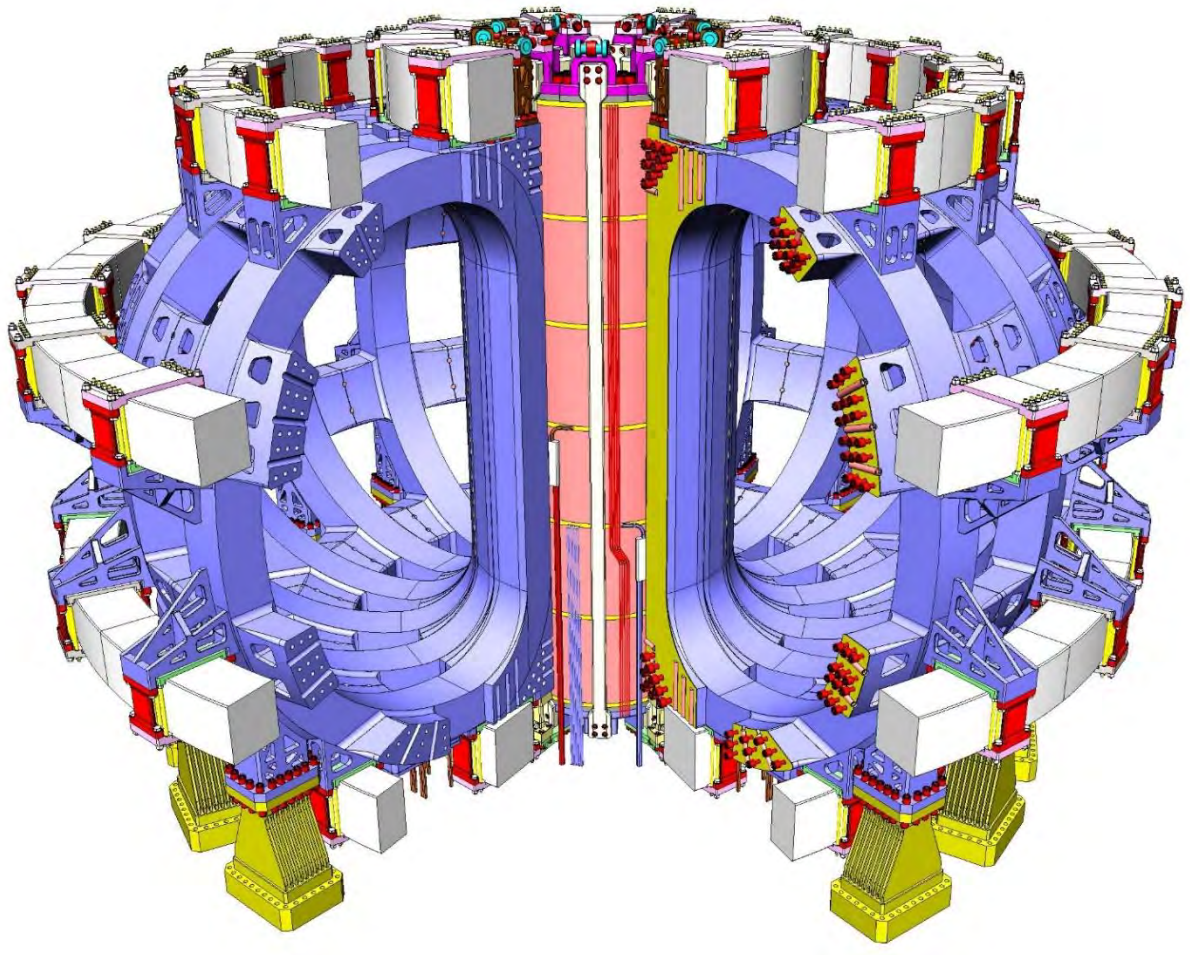

Figure VII.1: Artistic view of the DTT Superconducting Magnet System.

All components of the DTT Magnet System have been designed with the goal of providing sound and reliable solutions, that could be now detailed and then manufactured respecting all the main milestones of the tight schedule required by the project. Even though some aspects are still under investigation, the feasibility of all coils and their auxiliaries has been already demonstrated. As a risk mitigation measure, a design qualification campaign is being started during the preparation of the present report, aimed at confirming, by testing conductor and electrical joint samples, the quality of the design choices before starting the production phase.

VII.2 Toroidal Field Coils

As shown in Fig. VII.2, the Toroidal Field (TF) coils winding packs are constituted by 5 Double-Pancakes (DP), 2 “side” Double Pancakes (sDP) and 3 “regular” DPs (rDP), enclosed into a SS316LN casing for structural reinforcement. The conductor design is based on a 0.82 mm Nb_3Sn strand similar to what already produced for the ITER TF coils, but the requirements are slightly enhanced in terms of critical current densities (i.e. I_c > 285 A @ 12 T, 4.2 K and 0% applied strain, Cu/nonCu = 1). A direct check with many strand suppliers confirmed that this request is more than achievable: the strand procurement tender has been thus already launched. Even if more performing Nb_3Sn strand typologies are available on the market, the time and budget constraints of the project required to drop whenever possible an R&D phase: for this reason, it has been chosen to use a strand already deeply characterized in operative conditions similar to those of DTT, i.e. the ITER TF strand for which many suppliers could be put in competition.

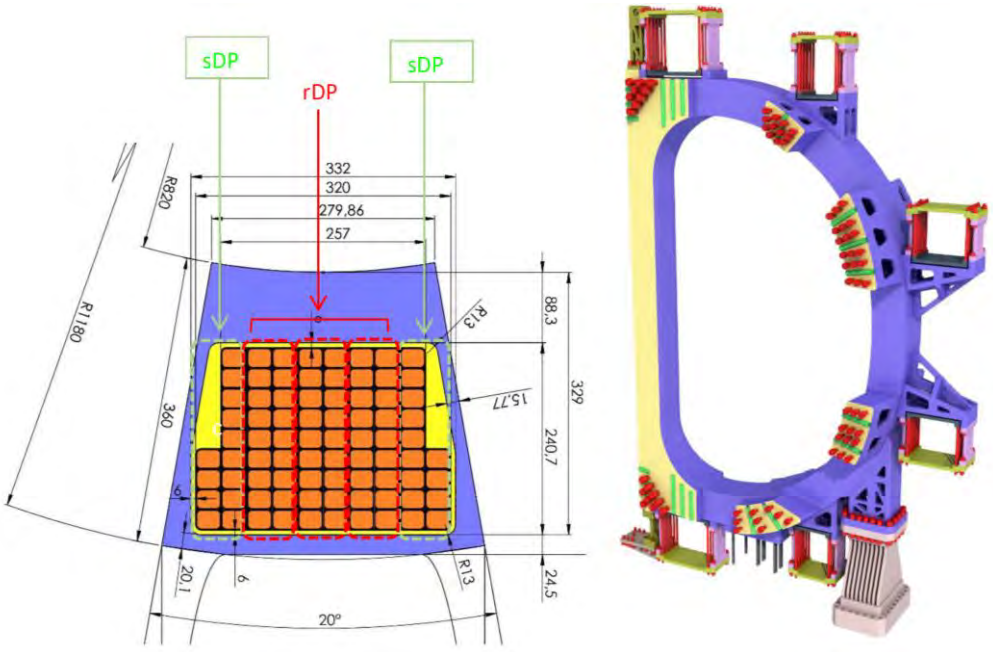

Figure VII.2: Cross section of the TF coil inner leg (left) and artistic view (right) of the TF case with details of IIS & OIS.

The magnets are fed in series at 44 kA, but they are grouped in 3 sets (6 coils each) for limiting the maximum voltage (presently it is about 1 kV at the single coil terminals) during the Safety Discharge. They reach a maximum magnetic field B_{peak}=11.8 T and, in these operative conditions, the estimated minimum temperature margin after the application of the Nuclear Load (estimated to reach about 1.3 mW/cm^3 at the first layer facing plasma) is 1.3 K (see following paragraph). The Nuclear Load is considered as the main heat

input to be taken into account being the AC losses negligible during the TF steady state, Being the neutron load on the SS case an important source of heating which could be then transferred to the WP, it has been decided to implement in the SS case a set of active cooling channels, whose final design is still under analysis to optimize their shape, number and distribution. The rectangular CIC conductors are obtained by rollers compaction of a round tube, performed after having inserted the superconducting cable into the jacket assembly. A wide set of conductors, all having features of which are relevant to the DTT magnets, have been already successfully tested in the framework of other projects [VII.6–VII.9] and taking advantage of such results the DTT TF coil design has been carried out. Some minor parameters may be finally defined, after the already mentioned qualification tests, which are planned at the SULTAN facility of the Swiss Plasma Center [VII.10], will be completed: for instance, is still open the possibility of choosing a very short cabling Twist Pitch sequence, as done for the ITER CS conductor [VII.11], or a combination of long Twist Pitch and low Void Fraction, as in [VII.9, VII.12], being both valid approaches to face the issue of the Nb_3Sn CICC performance degradation with loading cycles. For the time being, the second option is being considered for the analyses. In the following tables, the main parameters of the TF conductor (Tab. VII.I) and coil (Tab. VII.II) are summarized.

TABLE VII.I. TF CONDUCTOR CHARACTERISTICS

Nb_3Sn strand n.	486
Cu strand n.	162
Total strand n.	648
Nb_3Sn strand J_{SC} (A/mm^2)	1080
Nb_3Sn strand Cu/Non-Cu	1
Nb_3Sn Strand Cu RRR	>100
SS cable wrap thickness (mm)	0.05
Cable pattern$^+$	(1+2)x3x3x4x6
SS cable wrap overlap (%)	30
Ext. Cond. Dimension (mm)	29.5 x 23.3
Jacket thickness (mm)	2.0
Jacket material	316LN
Void Fraction (%)	26.4
Operative Current (kA)	43.96
Max magnetic Field (T)	11.8
Min Temperature Margin (K)	1.5

$^+$ = 1 out of 6 Last-but-one cabling stages is made entirely of Nb_3Sn strands

TABLE VII.II. TF COIL CHARACTERISTICS

Winding type	Double Pancakes
Double Pancake n.	5
Turns n.	80
Turn insulation thickness (mm)	1.0
DP insulation thickness (mm)	0.5
Ground insulation thickness (mm)	6.0
Insulation type	Fiber-glass/Epoxy*
Self-inductance (H)	0.041
Total Inductance (H, 18 coils)	2.07
Total Energy (GJ)	2.0
Safety Discharge parameters (s)	1.5 + 5
Hotspot temperature (K, all materials)	85
Maximum Voltage (kV, 1 coil)	1.0
Maximum Voltage (kV, 6 coils group)	6.1
Minimum Hydraulic Length (m)	47
Maximum Hydraulic Length (m)	108

* = the possibility of inserting some Kapton® insulation layers is still under discussion

The TF coils Inner Inter-coil Structures and Outer Inter-coil Structures have been designed (Fig. VII.2) in such a way as to ease the assembly activity and also to limit their cost, whilst working within the proper stress limits. So, a set of *superbolts + shear pins* has been placed at the ends of the TF straight leg, substituting the *pre-compression rings + shear keys* set considered in a previous version of the design, whereas 5 different typologies of OIS have been placed in the space between the various PF coils. After the mechanical analyses on these structures will be completed, in particular regarding all the fault conditions, their shape, positioning and number will be optimized.

Main Analyses Results

Structural Analyses

The Finite Element (FEM) analyses, performed for the Single Null (SN) reference scenario (see Chapter III for details), show that the stress levels estimated for ordinary operating conditions of the metallic components of the TF magnet system are within acceptable levels. Extremely localised peak stresses above admissible levels have been computed in the turn insulation of the TF winding pack (WP). However, more thorough 3-dimensional (3D) analyses are necessary to correctly quantify the consequences of these peaks.

All the results hereby reported derive from the combination of electromagnetic and structural analyses completed in ANSYS APDL®: 2-dimensional (2D) analyses with the model of the equatorial section of the TF coil inner leg were carried out to examine in detail the performance of the WP elements; 3D analyses to investigate the performance of the TF coil casing and inter-coil structures. As of today, the design of TF coils has been validated by static structural assessments. We utilize the static stress acceptance criteria expressed in [VII.13], and these criteria are valid only if primary stresses are correctly isolated from secondary stresses. Cooldown stress is classified as a secondary stress, therefore, the analyses hereby reported do not model it (i.e. the dimensions of all components are equal to those at 4 K conditions). It is however necessary to include the stress due to cooldown when fatigue performance is investigated. Such analyses are currently being performed. 2D analyses highlighted a peak stress intensity on one of the cable jackets equal to 898 MPa. This is indeed higher than the static stress limit for 316LN (i.e. 867 MPa). However, the stress linearization included in Fig. VII.3, shows that the primary stresses are still within acceptable levels. Detailed 3D analyses will confirm this aspect.

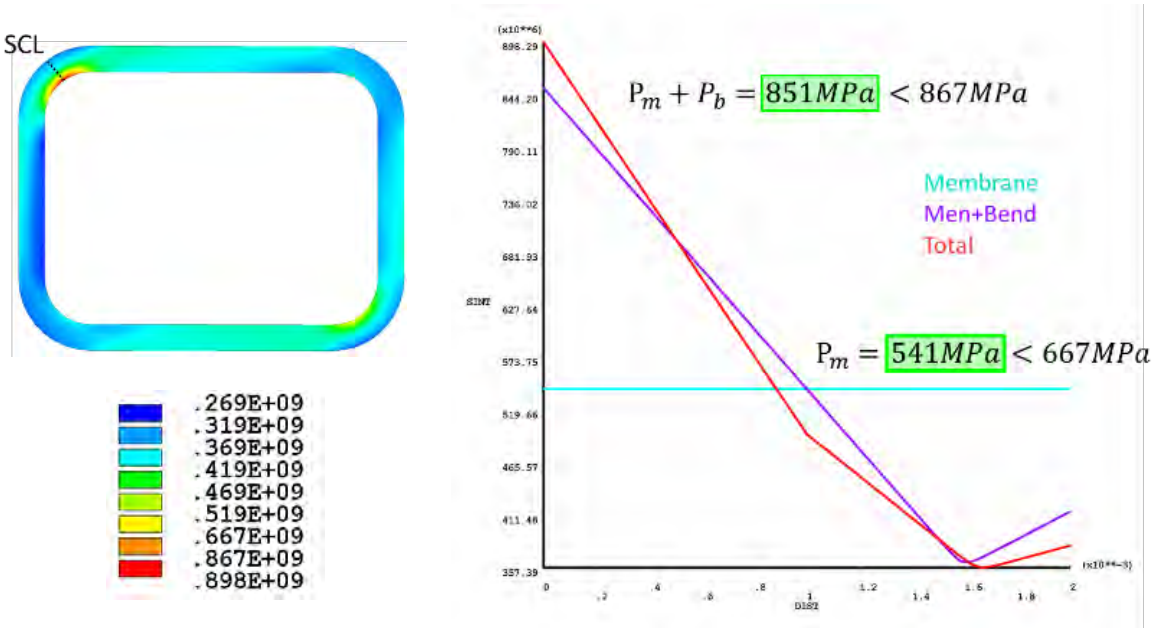

Figure VII.3: Stress linearization of the highest peak stress intensity [Pa] in the cable jackets of the TF WP.

Concerning the localised peak stress computed in the turn insulation material by the 2D analyses, we have reasons to believe it is due to numerical singularities and we therefore consider it not alarming. Moreover, we argue that the criterion applied [VII.13] is overly conservative and that further investigations are thus required.

On the other hand, beside verifying the acceptability of stress conditions on the casing structure, 3D analyses have allowed the validation of the proposal of employing a combination of superbolts and shear-pins to keep the wedging close. Details on these analyses will be given in a dedicated document in the next future; the main results can be briefly summarized in Fig. VII.4, showing that the computed stress is within acceptable limits (left) and that the wedge contact of the inner leg remains fully closed (right). The picture reports the outcome of the load-case related to the time t = 27 s of the Single Null scenario (i. e. the start of flat-top, see Chapter III). Indeed, we identified that moment as one of the most critical for the TF coil system in terms of out-of-plane loads.

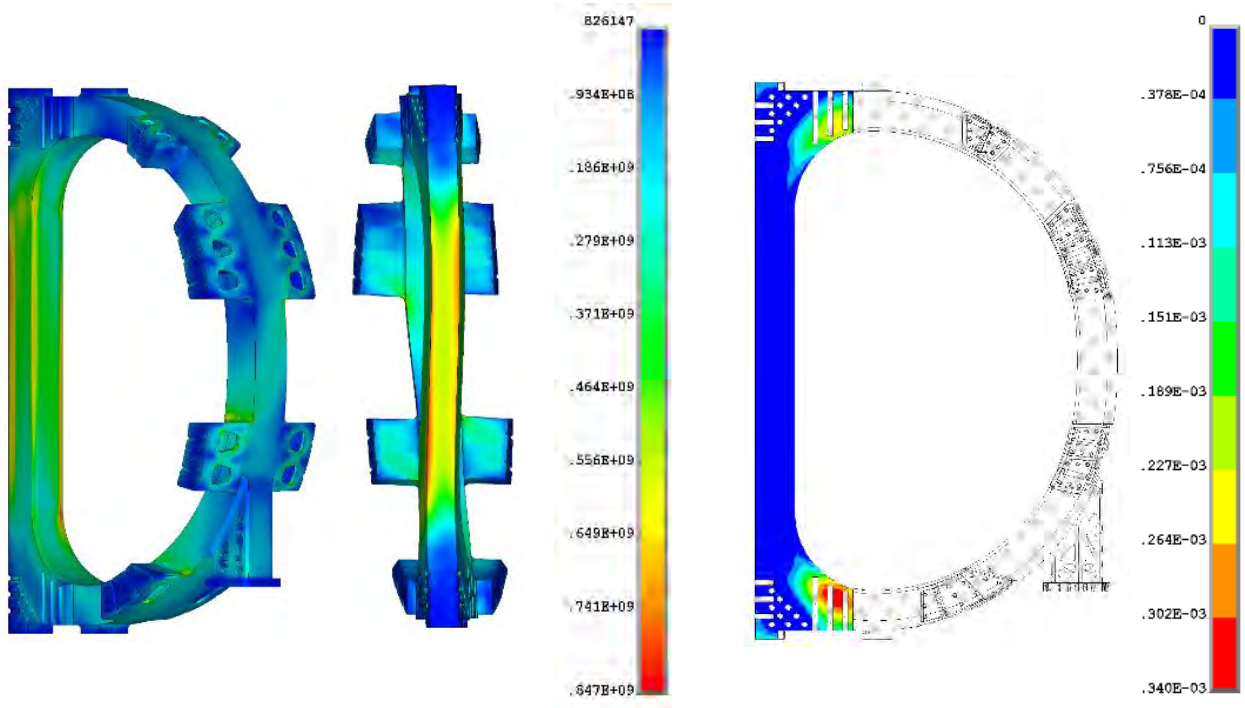

Figure VII.4: Computed stress intensity [Pa] in the TF casing structure (left) and gap opening [m] on the wedge (right) at 27 s in the SN scenario.

Thermal-Hydraulic Analyses

The thermal-hydraulic analyses of the DTT TF winding pack (WP) are carried out with the 4C code [VII.14], developed and qualified by means of suitable Verification and Validation procedure according to ASME standards [VII.15] and including predictive validation [VII.16] at Politecnico di Torino. The TF WP model developed in the 4C code includes all the 10 parallel cooling paths. The (turn-by-turn) counter-current flow in adjacent pancakes, due to the presence of a single inlet (at the innermost turn, at the bottom of the coil) for each double pancake, is accounted for. The main thermal-hydraulic parameters of the TF WP are shown in Tab. VII.III. The thermal coupling between neighbouring turns and pancakes is modelled considering the turn and double-pancake insulation as thermal resistances, increased by a factor ~5 (as calibrated on mock-ups of similarly wound coils [VII.17-VII.18]) to account for the multi-layer nature of the insulation, introducing uncertainties in the additional contact resistance.

TABLE VII.III. THERMAL-HYDRAULIC PARAMETERS OF THE TF WP

	sDP	**rDP**
Hydraulic length (m)	46.5	108.2
Pressure drop (bar)	0.4	1
Inlet/Outlet* temperature (K)	4.5/5.0	4.5/5.0
Inlet/Outlet pressure (bar)	6/5.6**	6/5
Mass flow rate (g/s)	2.5	2.6

** Maximum outlet temperature during a (periodic) plasma pulse.*

*** Suitable throttling valves should be installed at the sDP outlet to reduce the pressure to 5 bar.*

Inlet and outlet pressure (6 bar and 5 bar, respectively, for the long pancakes) and inlet temperature (4.5 K) are prescribed as boundary conditions for the simulation of the Single Null (SN) scenario. Only the nuclear heat load from the plasma is considered as driver: its poloidal and radial distribution is (conservatively) scaled proportionally to plasma current during the linear plasma ramp up and ramp down (with a duration of 27 s) and kept constant during the flat-top. For this analysis both static (radiative and conductive) heat load and the AC losses are neglected. The former is acting mainly on the coil casing, which is not considered in this simplified analysis (see below), and on the cooling circuit pipelines, for which a first estimation gives a value <1% of the nuclear heat load. The contribution of AC losses, being clearly a minor one for steady state coils, will be anyhow defined by further analyses. The nominal current (44 kA) and the corresponding magnetic field 3D distribution in the WP are constant during the entire plasma burn. The intrinsic strain on the Nb_3Sn strands, assumed equal to –0.65%, is considered uniform and constant.

The thermal coupling between WP and casing is neglected (considering the external WP surface adiabatic), and the casing is not modelled: similarly to what is being done for the EU-DEMO [VII.19], the casing cooling channels are being designed to remove most of the heat load deposited in the structures, so that the contribution of this heat load to the WP can be neglected (as a first approximation). The effect of fast transient events (e.g. plasma disruptions) inducing eddy currents in the structures, will also be analysed after the completion of the design of the case cooling channels.

The value of the minimum temperature margin, reached at the end of the flat-top of the plasma pulse (lasting about 60 s, with a repetition rate of 60 min) and computed at the effective magnetic field, is reported in Fig. VII.5 for different values of the peak nuclear heat load (located on the inboard leg), showing that the maximum acceptable heat load is 1 mW/cm^3 in order to meet the requirement of 1.5 K temperature margin. The current reference value of 1.3 mW/cm^3 would give a temperature margin of something more than 1.3 K.

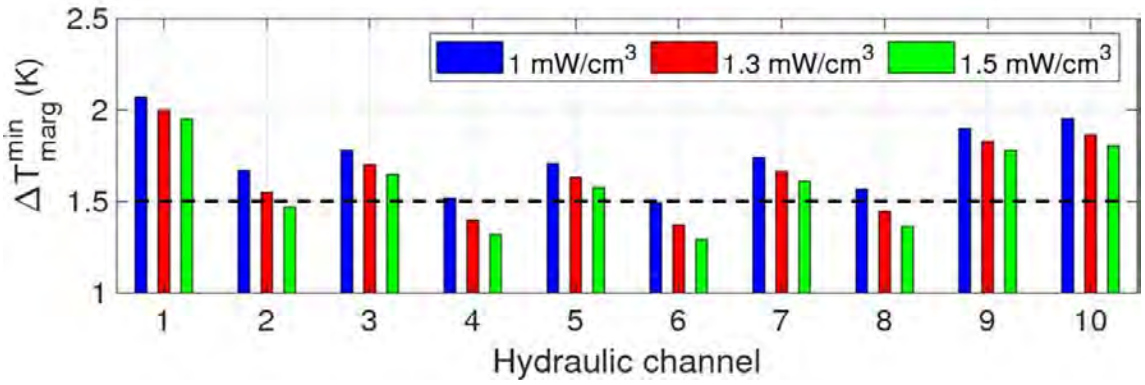

Figure VII.5: Minimum temperature margin in the TF WP computed for different peak nuclear heat loads (SN scenario).

A quench propagation analysis in the TF WP was also carried out, including a model of the supercritical He loop, initiating the normal zone at the time and location of the minimum temperature margin in channel #6. After the quench detection (0.15 V threshold with a validation time of 1.5 s), the current and magnetic field distribution are dumped exponentially (with a time constant of 5 s), accounting for the coupling losses (single time constant model, with $n\tau$ = 250 ms). Hot spot temperature and maximum pressure are well below the ITER acceptance limits, the former being about 85 K and the latter <11 bars (note that the cooling circuit is not modelled here, as its design has not been completed yet: WP inlet and outlet pressure are prescribed constant); for a direct comparison, quench tests in the JT-60SA TF coils (featuring a similar conductor, i.e.

without the central cooling channel) show a pressurization at the boundaries of ~ 7 bar [VII.20]. The quench does not propagate by conduction to adjacent pancakes and the possibility to adopt mass flow measurements as secondary quench detection system is highlighted.

VII.3 Central Solenoid

The Central Solenoid (CS) assembly consists of a 5.3 m high stack of six identical solenoids, named modules (CS3U to CS3L), with an axial pre-compression structure and a centring system. The weight of the CS system is transferred through its support to the TF coils structure (on 9 supports placed on alternated TF coil). The magnetic hoop forces during operation are reacted internally, within the winding, by the conductor jacket. As the 6 modules are independently fed, the CS serves not only to induce the current inside the plasma, but also to shape it. Each of the 6 modules is wound in layers, in order to maximize the coil engineering current density, and thus to guarantee the required flux swing. In the present design the pre-magnetization flux is 16.2 Vs, while total flux-swing due to CS (not accounting for additional heating) is 32.4 Vs with a flat-top flux swing of 5.7 Vs. As for the Cable-in-Conduit conductor (CICC) constituting the coil, a square and rectangular (for HF and LF, respectively) geometry is considered, with a constant thickness steel jacket, obtained by compaction of a round steel tube after cable insertion. The exact cable layout, either based on the very short twist pitch or on the long twist pitch and low void fraction configuration, will be established after qualification tests aimed to demonstrate a stable T_{cs} behaviour with electro-magnetic and thermal cycles, as well as acceptable AC losses behaviour.

TABLE VII.IV. MAIN FEATURES OF THE 6 IDENTICAL CS MODULES AND CONSTITUTING CONDUCTOR

	HF	**LF**
Operating current	29.9 kA	
Peak Field	13.2 T	9.4 T
S.c. wire features	0.82 mm diameter; Cu:nonCu = 1	
Ref. strand Ic(4.2K;12T;0%)	260.0 A	
Ref. strand Ic(6.3K;13T;-0.65%)	48.1 A	
# of superconducting wires in CICC	648	216
# of stabilizing Cu wires in CICC	0	192
Steel jacket material	316 LN	
Steel jacket thickness	6.1 mm	2.0 mm
CICC dimensions (non-insulated)	35.2 x 35.2 mm^2	17.4 x 28.3 mm^2
Turn insulation	1.2 mm (*glass-fiber + resin*)	
Ground insulation	6 mm (*glass-fiber + resin + Kapton*)	
G10 inter-module spacer thickness	40 mm	
# of layers x turns	4 x 22	8 x 27
Tot. module current	2.63 MA	6.46 MA
J_{ENG} (inside ground insulation)	21.1 A/mm^2	49.2 A/mm^2
CICC length	280 m (*in a single unit length*)	915 m (*made of 2 unit lengths*)
CS module inductance	73 mH	
CS module height	880 mm	
CS inner radius	437 mm	
CS outer radius	759 mm	

The coil design is the result of geometrical, electro-magnetic and mechanical considerations. The layer-wound coil is made of two sections, a high-field (HF) and a low-field (LF) grade, to be connected by an internal joint that will be manufactured in line, during winding, placed on top of each module and embedded within the 40 mm space separating vertically two adjacent modules. This separation space is designed to be filled by a slotted flange in G10 fiber composite insulator. Since the 915 m long LF CICC is made of two unit lengths, a second joint will be also manufactured in-line and embedded in the inter-module gap. The adopted embedded joint concept has been already developed and adopted in the past [VII.5, VII.21], but it will be qualified for the specific DTT CS requirements. In the two sub-coils the conductor operates at a peak magnetic field of 13.2 T and 9.4 T, respectively, and at a maximum current of 29.9 kA. The HF and LF CICCs feature 648 and 216 Nb_3Sn, 0.82 mm superconducting strands, respectively, and are characterized by a 6.1 mm and 2.0 mm thick SS316LN jacket, respectively. All coil layers are cooled in parallel, and the maximum hydraulic length among the different circuits is about 125 m: no pressure relief channel is thus foreseen in any of the CICCs. The main features of the CS module, and of the constituting conductor, are summarized in Tab. VII.IV.

Main Analyses Results

Structural Analyses

The fully detailed structural analyses of the DTT central solenoid are based on a 2D axisymmetric model. Indeed, the loads, the geometry and the boundary conditions that act on the poloidal system are axisymmetric. The first step of the analyses is the evaluation of the Lorentz force field generated by the superconducting cables during the plasma scenarios. In this case, the reference scenario is the Single Null, and the electromagnetic load is computed for seven characteristic instants. For the evaluations of the coil structure stress state the t = 0 s instant (i.e. the breakdown, see Chapter III) is taken into account, when the maximum operative current (29.9 kA) is applied to the CS modules. The structural model defined for the analyses includes all the mechanical components of the Winding Pack, and the mechanical contacts between the SC cables and the steel jacket, to allow the cable to bend into the jacket due to the action of the Lorentz force. The elements used to define the insulation material domains are oriented along the fiber winding directions. Main results of the analyses are shown in Fig. VII.6.

With this approach, it is possible to apply the safety criteria imposed on fragile materials. The structural analysis includes three calculation steps:

I) The application of preload compression, defined by a distributed pressure on the top of the magnet, of 25 MPa and the weights of the structures;
II) The cooldown effect, which causes the stresses due to the different thermal contractions of WP materials;
III) The energization of the six modules at the maximum operative current, with the load computed from the previous magneto-static analysis.

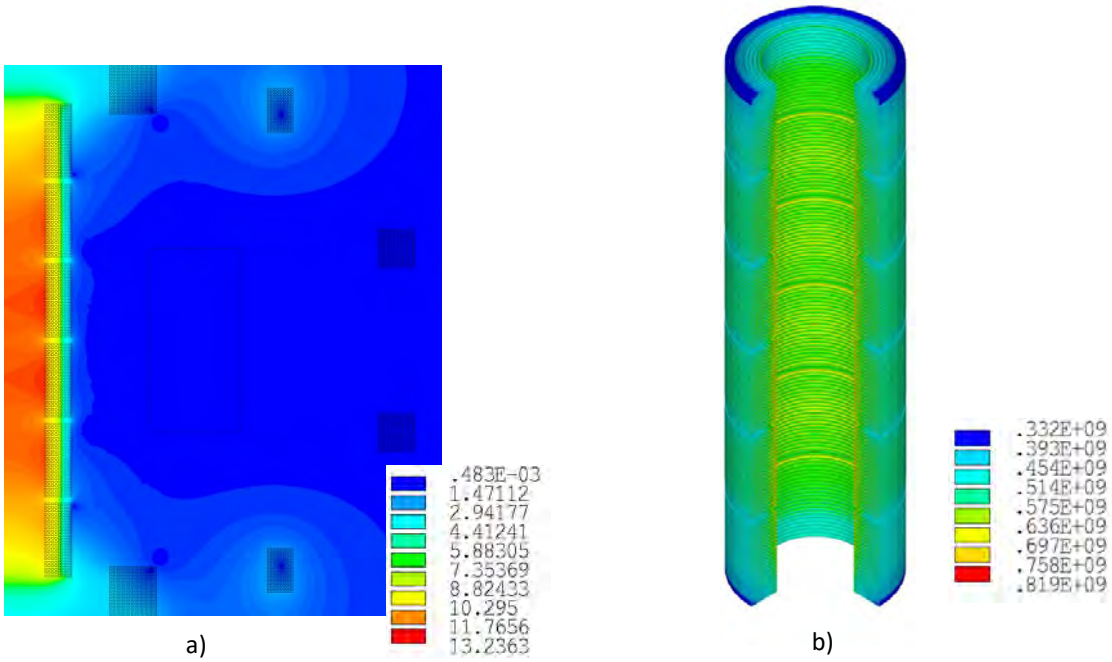

Figure VII.6: a) Plot of the magnetic field modulus on the poloidal system cross section. The 13.2 T peak value is located in the innermost HF cables; b) 3D expansion of the Stress Intensity equivalent stress for the six CS modules. The maximum stress is located in the innermost HF jacket corner.

The most stressed regions of the CS structure are located in the innermost HF cables (819 MPa), As shown In Fig. VII.7. The jacket corners cause a local increase of the stress flow in the steel. High, potentially critical stresses are concentrated there. In the corners where the allowable imposed by the design criteria are exceeded, further considerations are necessary.

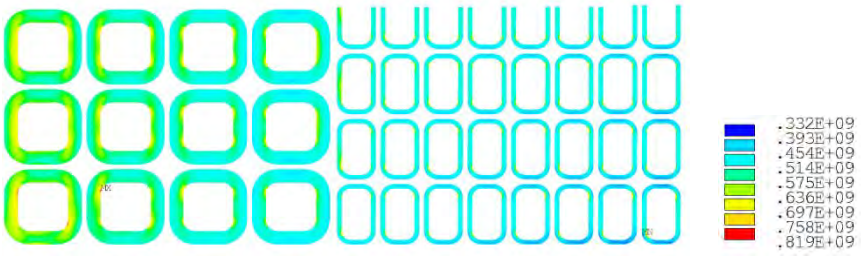

Figure VII.7: Stress intensity equivalent stress plot in the most stressed CS region.

The allowable limit of 867 MPa imposed by the design criteria [VII.13] for the primary membrane and primary bending stress summation in the SS316LN, is not exceeded in this structure even in localized peaks. For completeness, the linearization of the stress intensity is performed in the most stressed jacket corner, as in Fig. VII.8. A Stress Classification Line (SCL) is defined across the jacket thickness, in the neighborhood of the critical area. For the linearization the cooldown effect, classified as thermal secondary stress, is excluded.

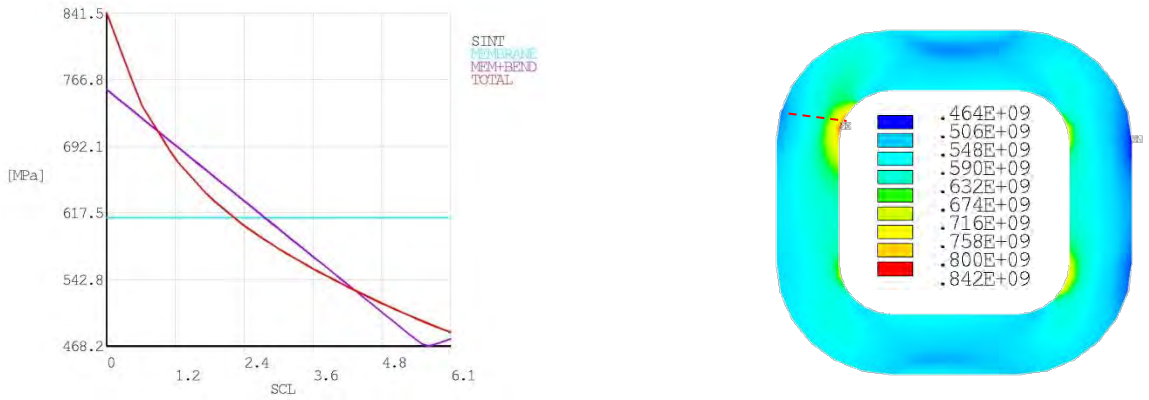

Figure VII.8: Linearization of the stress intensity equivalent stress. The primary membrane constant component is under the allowable limits of 667 MPa. The linear varying component, summation of the membrane and bending stress component, is in the safety region too, below the limit of 867 MPa.

The specifications required for static analyses are therefore satisfied by the current design of the CS. For the fatigue life assessment, the S-N approach is applied for the critical stress cycle of the solenoid (2 x 30.000 cycles have been taken in consideration for this assessment, as this coil reaches 2 times the maximum stress peak during each pulse). The study of the Lorentz forces behavior in the plasma scenario, has highlighted the time instants that characterize the point of minimum and maximum stress application. In particular, the start point of the critical stress cycle is t = -40 s, which corresponds to the start of the pre-magnetization phase where cooldown and preloads are applied, while the end point of the stress cycle is the t=0s instant, i.e. just before the breakdown when the applied electromagnetic loads are maximum. After the static analyses of these two time instants, the evaluation of the Goodman equivalent stress [VII.22] is performed, and compared with the SS316LN specific curve, as in Fig. VII.9.

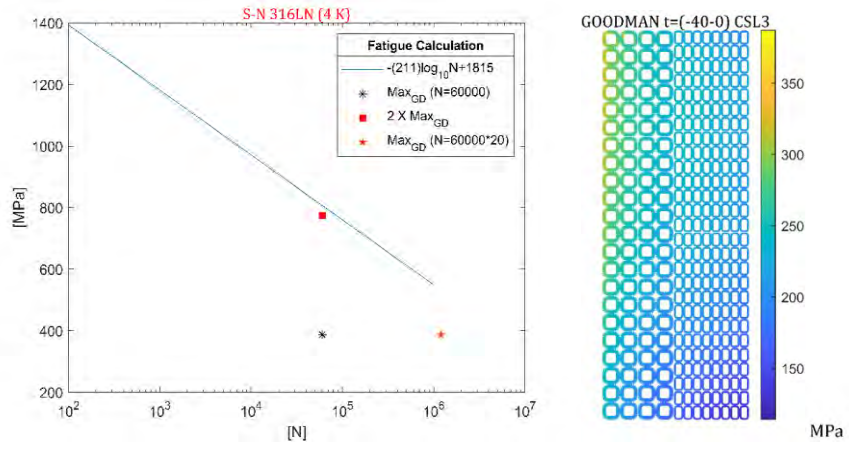

Figure VII.9: Plot of the Goodman equivalent stress for the most critical module (CSL3), and the S-N curve for the SS316LN steel. Both the fatigue criteria: 2σ_Goodman (at N°) eqv. Stress and σ_Goodman (at 20 N°), are below the safety region limit.

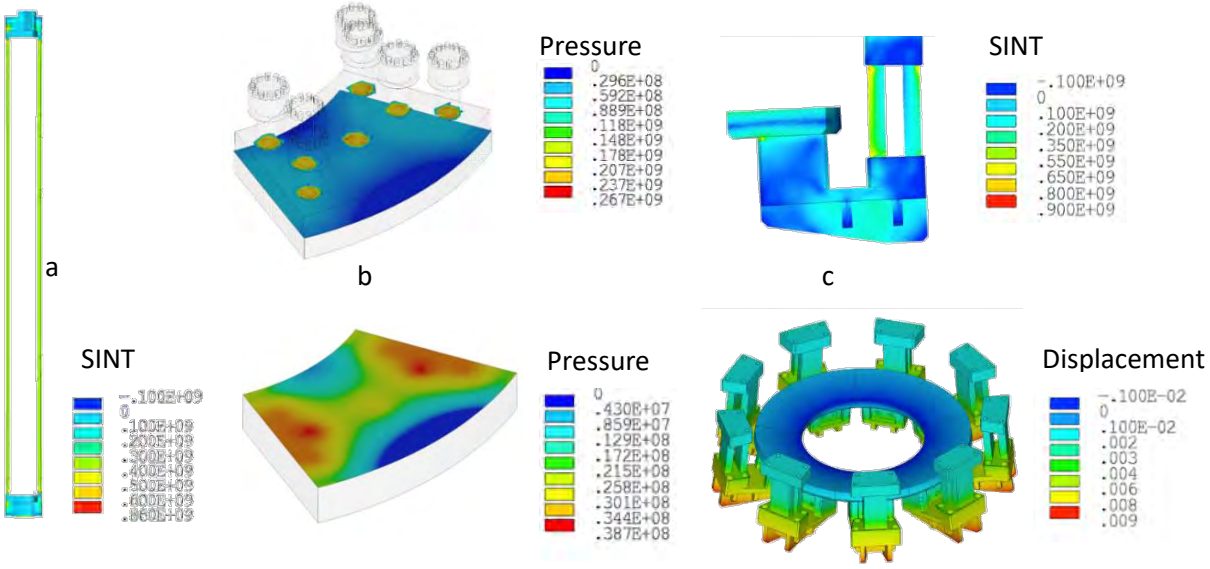

Figure VII.10: CS preload structure components: a) tie plates; b) distribution plate; the pre-load distribution is designed to make the localized load exerted by the superbolts (top) homogeneous. In this way the G10 plate (bottom) can receive and optimally transfer the pre-stress to the CS modules; c) support system; the CS support system must sustain the weight of the solenoid (~0.45 MN) and additional 15MN from the net vertical resultant action of the CS electromagnetic force.

During operation, the CS modules are subject to repulsion vertical forces. In particular, the maximum repulsion force is 28.45 MN, attained at t = 28 s of the Double Null (DN) scenario (being more demanding than the SN scenario for this aspect, see Chapter III). Therefore, a counteracting force of 25.48 MN must be exerted by the preload structure (see Fig. VII.10). Moreover, the different thermal contraction of materials during the cool-down partially erodes this counter-balancing preload, making it necessary to augment the preload force. A separate dedicated study, omitted here for the sake of brevity, is dedicated to quantify this effect: to compensate the opening gap, an additional force of 5 MN must be added to the pre-compression load. This approach has been also checked in the SN scenario, where minor preload force turned out to be necessary.

Thermal-hydraulic Analyses

A computation of the hotspot temperature ($T_{hotspot}$) reached by the conductor during a quench has been carried out, within a simplified adiabatic 0D model. Both HF and LF CICC are well within the acceptance criteria, with $T_{hotspot}$ below 250 K and 150 K, respectively considering that heat is absorbed by superconducting and copper wires only, or by all CICC components, including steel jacket and helium. For this computation, a quench detection delay time constant: τ_{delay} = 2 s has been considered, and a coil discharge time constant: $\tau_{discharge}$ = 4 s.

The thermal-hydraulic analysis of the DTT CS is performed with the 4C thermal-hydraulic code [VII.15]. The 4C model of the 6 modules of the CS (see Tab. VII.V), accounts for the 12 parallel hydraulic paths cooling the 12 layers; as for the TF coils, the (turn-by-turn) counter-current flow in adjacent layers is taken into account, as well as the thermal coupling among neighbouring turns and pancakes, modelled considering the turn insulation as a pure thermal resistance, increased by a factor ~5. The He inlets are located at the bottom of each module.

TABLE VII.V. THERMAL-HYDRAULIC PARAMETERS OF THE CS WP

	HF	LF
Hydraulic length(m)	~70.0	~110.0
Pressure drop (bar)	1	
Inlet/Outlet* temperature (K)	4.5/6.0	4.5/5.2
Inlet/Outlet pressure (bar)	6/5	
Mass flow rate (g/s)	4.0	2.0
Peak pressure (bar)	6.2	
Maximum temperature (K)	6.0	5.2

**maximum outlet temperature during a (periodic) plasma pulse.*

The magnetic field distribution accounts for radial and vertical variations (while it is uniform on each separate turn) and its evolution is followed during the entire SN pulse. The currents scenario in each module is also used as input for the analysis, while the intrinsic strain on the strands is considered uniform and constant at the assumed value of –0.65%. The plasma breakdown phase starting at t = 0 s, particularly demanding for the CS coil in terms of current variation rates, has been simulated as a field variation of 10% with respect to the peak, occurring during the first 150 ms.

Inlet and outlet pressure (6 bar and 5 bar, respectively) and inlet temperature (4.5 K) are prescribed as boundary conditions for the simulation of the scenario. Due to the different conductor sizes (between HF and LF grades) and to the different hydraulic lengths of each layer, the mass flow rates result to be in the range 3.5 ÷ 4 g/s for the HF layers (layer 4 and layer 1, respectively) and in the range 1.7 ÷ 2 g/s for the LF layers (layer 12 and layer 5, respectively). The external side of the winding pack of each module is considered adiabatic, thus neglecting the static (conductive and radiative) heat load and the thermal coupling between the modules. The nuclear heat load is also neglected (according to first estimations, it is few percent of the AC losses heat load), so that the only driver of the transient is the power generation in the strands due to the AC losses, in turn induced by the magnetic field variation. The AC losses, including both coupling and hysteresis losses, are computed according to [VII.23-VII.24]. A sensitivity analysis has been carried out, varying the conductor characteristic coupling time constant ($n\tau$) which is not already been measured, between 50 ms and 150 ms, while the effective filament diameter has been maintained at 15 µm.

The value of the minimum temperature margin in each module is reported in Fig. VII.11 and shows that for all cases analysed the minimum temperature margin never falls below the 1.0 K threshold.

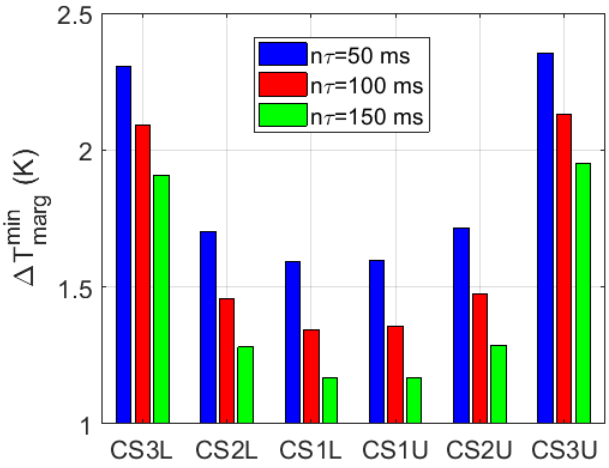

Figure VII.11: Minimum temperature margin in the CS modules calculated for different nτ values

In addition, the temperature margin has been studied for two different durations of the current ramp up and ramp down (namely 40 s and 60 s, to identify the most appropriate choice), for the nτ = 50 ms case. The result is reported in Fig. VII.12(a). Although the effect of the ramp rate in the range analysed is marginal, the ramp rate of 60 s will be retained in actual operation. It is to be noted that the minimum margin is in any case reached just before the breakdown, taking place at time *t* = 0 s in Fig. VIII.12(b), after which the current (and magnetic field) ramp down, causing a current sharing temperature increase, dominates on the operating temperature increase caused by the heat deposited by AC losses. The central modules experience a higher magnetic field in this phase so that their temperature margin is smaller but still above the acceptable threshold of 1.5 K. In all cases, the minimum temperature margin is reached at the innermost turn, where the magnetic field is maximum. The maximum re-cooling time after a plasma pulse is found in the most external LF layers (featuring the longest hydraulic length) and is ~ 1700 s, which is lower than the foreseen dwell time (3600 s).

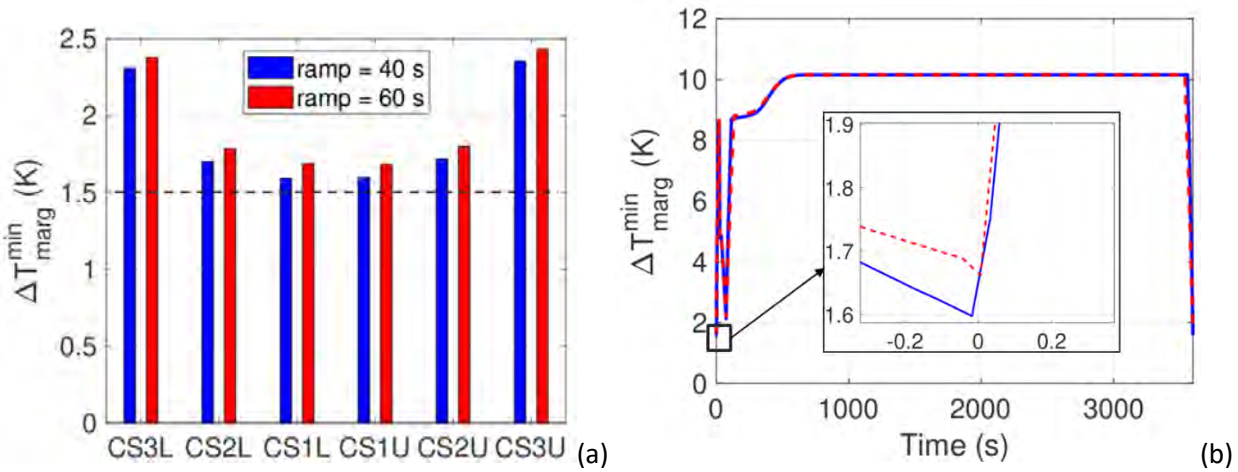

Figure VII.12: (a) Minimum temperature margin in the different CS modules and (b) its evolution in layer 1 of CS1L computed for different current charge and discharge ramp rates.

VII.4 Poloidal Field Coils

The 6 PF coils have been defined according to the requirements of the operational scenarios for DTT, in particular on the Single Null (SN) reference scenario. The perfect top-down symmetry of the DTT machine has been assured by designing the PF magnets to be identical in pairs, i.e. PF1/6, PF2/5 and PF3/4, as shown in Fig. VII.13.

PF 2/5 and PF 3/4 are wound using NbTi SC CIC conductor, with a B_{max} in the range 4 to 5 T. For the PF1/6 coils, the design has changed with respect to the 2015 reference [VII.1], as the updated requirements in performance for these coils increased the B_{max} to about 8.5 T, leading to the choice of Nb_3Sn for the PF1/6 CIC conductor.

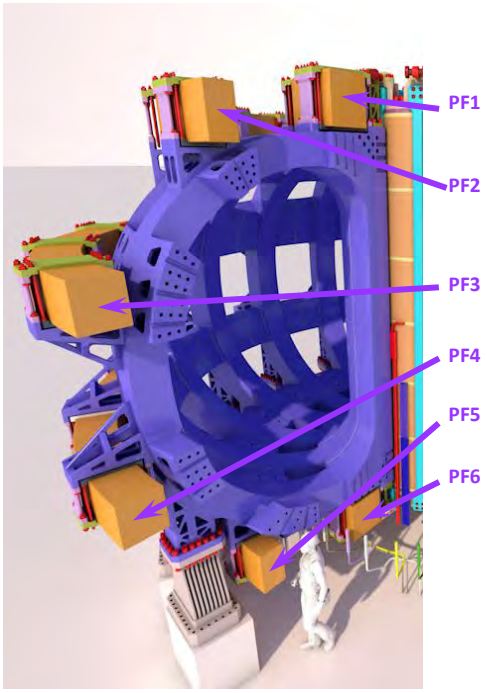

Figure VII.13: PF Coil System in DTT (artistic view).

The NbTi conductors for PF 2/5 and PF 3/4 are almost square CICCs, with a central channel for LHe pressure relief, due to the significant hydraulic length (192 m and 381 m, respectively). The two cables are identical in cabling pattern but differ in the number of NbTi vs Cu strands, in accordance with the operational scenario requirements. NbTi strand performance considered for the design is in line with what is already available in the market (reference Ic ~500 A @ 4.2K and 5T). PF2/5 and PF3/4 are wound in double pancakes (8 and 7 in number, respectively).

The Nb_3Sn CIC conductor for the PF1/6 is rectangular, with no central channel as the hydraulic length of 178 m seems to allow for a safe operation from first analyses. Also, the PF1/6 Nb_3Sn rectangular CIC conductor is obtained by rollers compaction of a round SS316LN jacket assembly where the SC cable has been previously inserted. As for TF and CS conductor, a wide range of conductors relevant to the DTT magnets and successfully tested [VII.8 - VII.11] have been considered for the design. After qualification tests carried out in the SULTAN test facility at the Swiss Plasma Center [VII.10] on conductor samples, minor features as

cabling Twist Pitch sequence and optimal Void Fraction to account for strain sensitivity of the Nb_3Sn strands will be adjusted. The Nb_3Sn strand used for the design is the same considered for the CS. PF1/6 coil are wound in 9 double pancakes. The present design of the PF coils is based on the SN reference scenario. Yet, DTT will operate at different scenarios, and an adjustment of the adopted margins in the PF coils may be required once all the scenarios will be detailed. In Tab. VII.VI the main PF coil characteristics are reported.

TABLE VII.VI. PF COIL CHARACTERISTICS

	PF1/6	**PF2/5**	**PF3/4**
Operative current [kA]	30	27.1	28.6
Peak field [T]	8.5	4	5
CIC ext. dim. [mm] (non-insulated)	24.8 x 28.6	28.0 x 29.3	28.0 x 29.3
Jacket thickness [mm]	4.2	3.8	3.8
Central Channel (OD/ID; [mm])	no	7/5	
# SC strands	180(Nb_3Sn)	162(NbTi)	324(NbTi)
# Cu strands	216	324	162
Inter-turn insulation (Kapton/Fiber glass) [mm]		1	
Total current [MA]	10.2	4.3	5.6
Winding type		double pancake	
Double Pancake Insulation (Kapton/Fiber glass) [mm]		1	
R centroid [mm]	1426	3049	4335
Z centroid [mm]	±2760	±2535	±1015
Coil inner radius [mm]	1157	2898	4124
Coil outer radius [mm]	1695	3200	4546
Coil height [mm]	569	517	452
Ground insulation (Kapton/Fiber glass) [mm]		5	
# turns (radial)	20	10	14
# turns (vertical)	18	16	14
N turns (total)	360	160	196
Hydraulic length [m]	178	192	380
Inductance [H]	0.4	0.3	0.7
Weight [t]	18	20	30

Main Analyses Results

Structural Analyses

The structural assessment of the Poloidal Field coils has been performed by means of full-detail Finite Element analyses. The PFCs will be operated in pulses, hence the evaluation of fatigue effects is paramount. As fatigue derives from periodic repetition of a specific stress cycle on the magnet in the real operative conditions, the structural analyses to be used for its investigation must include all primary and secondary sources of stress. Furthermore, the stresses are to be assessed against fatigue limits, for instance according to the Goodman criterion [VII.22], and not against the static ones (such as the Tresca criterion). The results shown here feature the application of cooldown and electromagnetic energisation, along with the weights of the coils. Fatigue calculations are on-going.

All the analyses have been performed in the Single Null reference plasma scenario (see Chapter III), for which the currents I(t) in each PFC are known at every instant. For each PFC couple (i.e. PF1/6, PF2/5, PF3/4) the coil subject to the highest module of the electromagnetic force has been identified, thus narrowing the analyses to three cases only.

Taking into account the presence of a ripple in the magnetic field caused by the number of the TF coils (TFC), two types of symmetry have been considered as modelling assumptions for the PFCs. The PF2/5 and 3/4 are closer to the TFC outboard profile, so there is a consistent ripple in the magnetic field, which reflects in a ripple of the magnetic forces. Given that the TFCs are 20° far apart, the ripple is 20-degree periodic, hence only a 20° cut-out of PF2/5 and 3/4 has been modelled. This will be called “cyclic symmetry” condition and translates to coupling constraints imposed on the nodes at the extremal sections of the cut-out. For the PF1/6 the ripple effect is almost negligible, therefore the magnetic forces are quasi-identical for each cross section of the coil, so these magnets have been modelled as axisymmetric structures for the moment, while full 3D analysis is on-going. To evaluate the electromagnetic loading, a magneto-static analysis has been performed for every instant of the Single Null scenario to calculate the magnetic field on each PFC, considering the contributions of all PFCs, TFCs, CS modules and of the plasma. For the PF1/6, modelled as axisymmetric structures, a separate axisymmetric magneto-static analysis has been carried out. The forces resulting from the interaction of the current in the PFCs and the magnetic field have been calculated (see Fig. VII.14), and the most loaded coils turned out to be the lower PFCs, namely the PFC 4 at t = 36 s, and the PFCs 5 and 6 at t = 27 s. Therefore, for these coils in these time points a full-detail FEM analysis has been performed. All these analyses are nonlinear, accounting for frictional contacts at the cable-jacket interface.

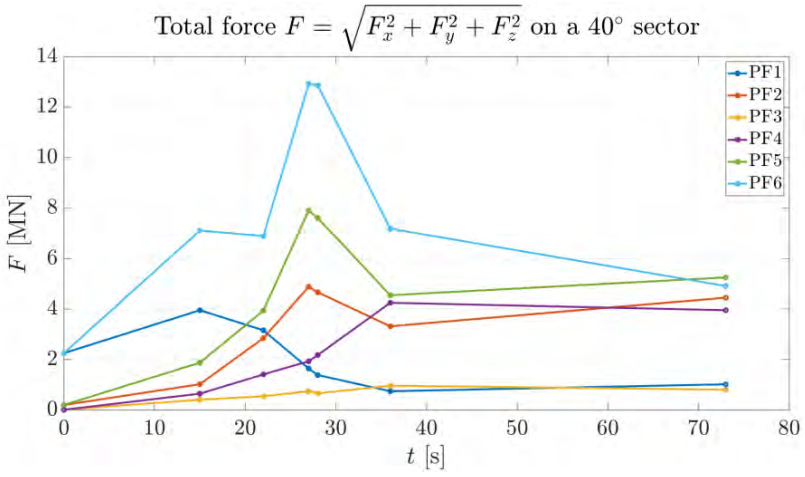

Figure VII.14: Total electromagnetic force on the PFCs [MN].

The main results from the simulations are hereby presented. The displacement field has a dominant radial component induced by the cooldown, and it is greater for the larger PFCs. The stress state of the jackets, measured in terms of the Stress Intensity (the maximum difference between the principal stresses), is shown in Fig. VII.15 and presents very localised peaks at the inner curvature fillets. The upper-left cable, i.e. the one closest to the above TFC, shows the highest peak stress. Given that the values of these peaks are positively below the static allowable values, it is expected that the analysed loading conditions will not raise significant fatigue issues, but analyses are underway to ascertain this.

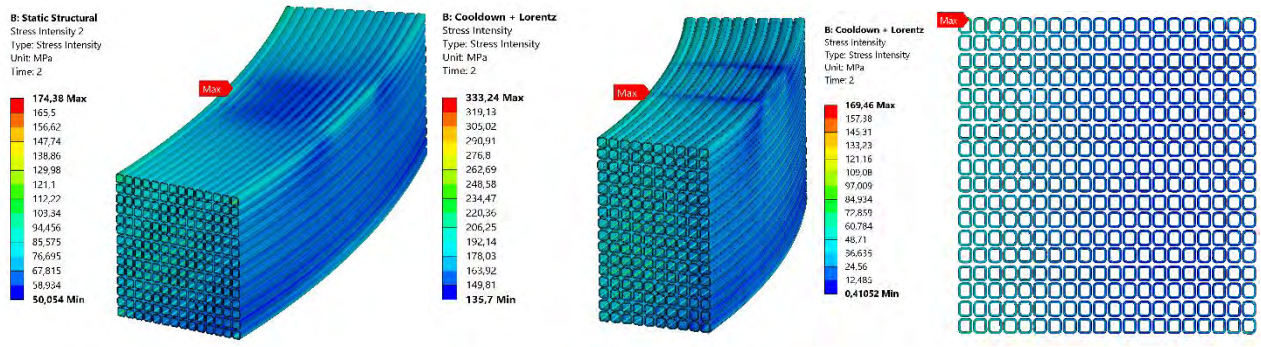

Figure VII.15: Stress Intensity on the jackets of PFCs (left to right) 4, 5, 6.

As for the insulation components (turn, double-pancake and ground insulation), the Stress Intensity shown in Fig. VII.16 attains peak values in correspondence of sharp edges, having not modelled curvature fillet radii for the sake of geometry defeaturing. As such, these stresses are regarded to be somewhat fictitious values, of little to no concern for the actual design. However, these values will be assessed against fatigue as well.

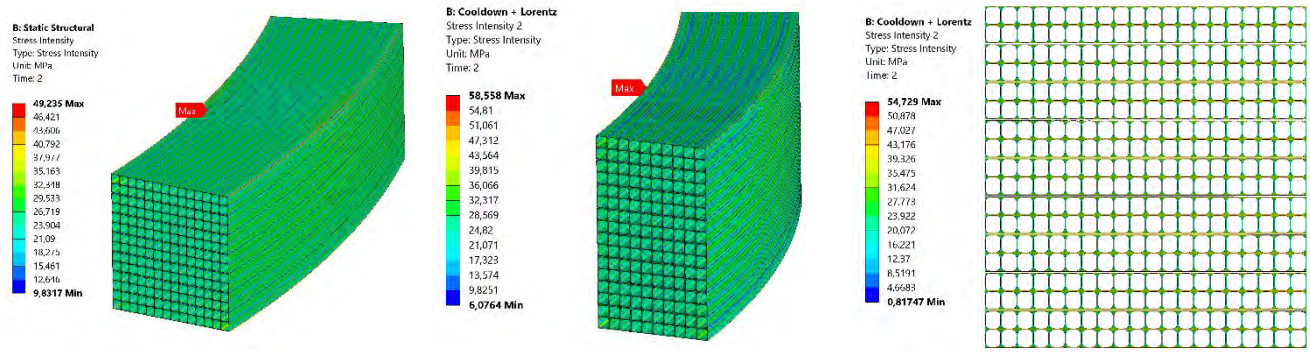

Figure VII.16: Stress Intensity on the turn insulation of PFCs (left to right) 4, 5, 6.

Thermal-Hydraulic Analyses

The thermal-hydraulic performance during the plasma flat-top (Single Null scenario) of the six PF coils has been analysed using the 4C code [VII.14]. The winding pack of each PF coil has been simulated individually. All the parallel cooling channels of each coil are modelled, taking into account the He flow and the thermal conduction in the solids (strands and jacket). The dynamics of the cooling circuit has been neglected because

no backflow is foreseen during normal operation. Therefore, constant boundary conditions have been imposed at the He inlets and outlets:

- Inlet pressure and temperature = 6 bar, 4.5 K;
- Outlet pressure = 5 bar.

The initial temperature is 4.5 K. The inter-turn and inter-pancake thermal coupling are taken into account. The ideal heat transfer would be given by the thermal resistance of the turn (and double pancake) insulation around each conductor. However, this ideal heat transfer is reduced by a factor ~5, as it was calibrated in other similar WP [VII.17].

The current and magnetic field evolutions are given as input to the analyses. Moreover, the radial and vertical (spatial) distribution of the magnetic field in the coils is also considered, assuming a uniform value for each turn. The heat deposition due to the AC losses is considered as driver of the simulation (the neutron load is assumed negligible for the PF with respect to AC losses): both coupling and hysteresis losses are taken into account. For the Nb_3Sn conductors, $n\tau$ = 50 ms has been considered, while $n\tau$ = 300 ms is assumed for the NbTi conductors. The hysteresis losses are modelled with the same parameters adopted for the CS modules.

The resulting mass flow rates in each PF coil are reported in Tab. VII.VII. The low mass flow rate in the Nb_3Sn coils does not lead to backflow during normal operation, but it could be an issue during quench, which thus needs to be further investigated. The NbTi coils have a much higher mass flow rate, even if their hydraulic length is longer, because their conductors are equipped with a low impedance central channel.

TABLE VII.VII. MASS FLOW RATE IN EACH PANCAKE AND LOCATION OF THE MINIMUM ΔT_{marg} FOR THE DIFFERENT COILS

	PF1	**PF2**	**PF3**	**PF4**	**PF5**	**PF6**
Mass flow rate (g/s/pancake)	1.2	10.7	7.1	7.1	10.7	1.2
Hydraulic channel (pancake) where min(ΔT_{marg}) is reached	1	9	14	8	7	9

Figure VII.17(a) shows the minimum temperature margin reached throughout a periodic pulse in each coil. All the minimum margins are above 2 K. The PF1 (Nb_3Sn) has a large margin because, to guarantee a perfect vertical symmetry of the machine needed to allow different configurations, it has been designed equal to PF6, which in the SN has to withstand higher current and magnetic fields with respect to PF1. The effect of the current ramp duration is negligible. This is because the minimum margin is reached at 73 s, i.e. at the end of the plasma flat-top (before the plasma current begins the ramp to zero), see Fig. VII.17(b).

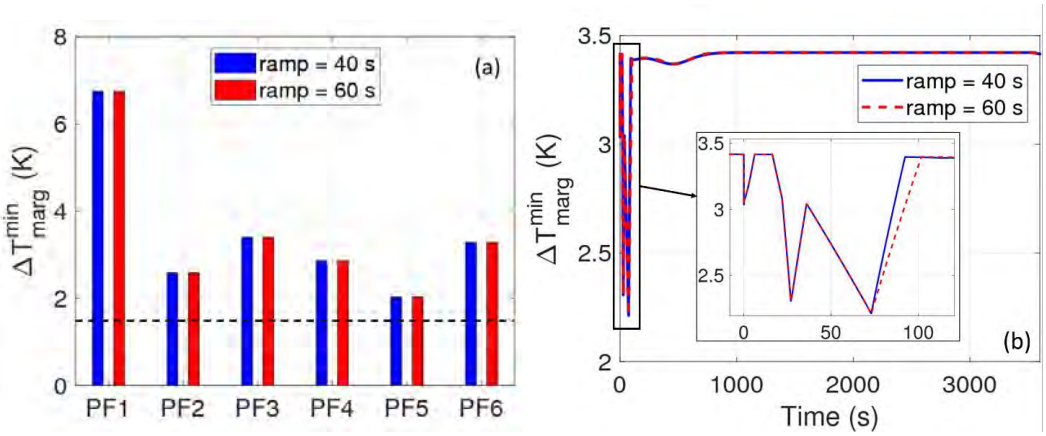

Figure VII.17: (a) Minimum temperature margin reached during a (SN) plasma pulse in each PF coil with current ramp of 40 s and 60 s. The 1.5 K threshold is also shown with a black dashed line. (b) Evolution of the temperature margin in PF5 during a (periodic) plasma pulse with current ramp of 40 s and 60 s. The zoom of the first seconds when the minimum margin is reached is also shown.

Preliminary conductor Hotspot temperature evaluation during quench by a simplified adiabatic 0D model is in agreement with the ITER acceptance criteria (250 K, assuming the heat is absorbed only by cable) for $T_{hotspot}$ of the PF (worst case PF1/6) CICC, with assumed quench validation time, τ_{delay}= 1.5 s, and assumed coil discharge time constant, $\tau_{discharge}$= 6 s.

More detailed analysis by the POLITO group is ongoing to estimate with more confidence the $T_{hotspot}$ thus to assessing max voltage during the discharge.

VII.5 Magnet System Electrical Modeling

A parametric electrical model has been developed for the simulation of the behavior of the DTT magnetic system. This electrical model is necessary in the magnet design phase for the calculation of the coil inductances and mutual inductances values and for the knowledge of the voltages on different coils during plasma scenarios. As their currents are pulsed, voltages on CS and PF coils are of particular interest.

The model has been developed in three steps:

- the magnets geometry is isolated from the whole system geometry imported in ANSYS Workbench®;
- the magnet geometry alone is imported in ANSYS Maxwell® 3D where a magneto-static study is completed to obtain mutual inductances matrix;
- mutual inductances matrix is imported in ANSYS Simplorer® where the lumped element model is developed for the simulation of the electrical circuit of interest.

TF coil system

From the model we calculated that the TF coils system, with an operative current of 44 kA and 80 turns, has a total energy of about 2 GJ with a total inductance of 2.07 H. The self-inductance of each TF coil is 41.4 mH. In Fig. VII.18 the whole TF system mutual inductances matrix is shown.

Inductance (H) _TF coil System																		
	TF01	TF02	TF03	TF04	TF05	TF06	TF07	TF08	TF09	TF10	TF11	TF12	TF13	TF14	TF15	TF16	TF17	TF18
TF01	4,14E-02	1,63E-02	7,94E-03	4,44E-03	2,72E-03	1,79E-03	1,28E-03	9,88E-04	8,42E-04	7,97E-04	8,42E-04	9,88E-04	1,28E-03	1,79E-03	2,71E-03	4,45E-03	7,95E-03	1,63E-02
TF02	1,63E-02	4,14E-02	1,63E-02	7,95E-03	4,45E-03	2,72E-03	1,79E-03	1,28E-03	9,89E-04	8,42E-04	7,97E-04	8,42E-04	9,88E-04	1,28E-03	1,79E-03	2,72E-03	4,45E-03	7,95E-03
TF03	7,94E-03	1,63E-02	4,14E-02	1,63E-02	7,95E-03	4,44E-03	2,72E-03	1,79E-03	1,28E-03	9,88E-04	8,42E-04	7,97E-04	8,41E-04	9,88E-04	1,28E-03	1,79E-03	2,72E-03	4,44E-03
TF04	4,44E-03	7,95E-03	1,63E-02	4,14E-02	1,63E-02	7,95E-03	4,45E-03	2,72E-03	1,79E-03	1,28E-03	9,89E-04	8,42E-04	7,96E-04	8,41E-04	9,88E-04	1,28E-03	1,79E-03	2,72E-03
TF05	2,72E-03	4,45E-03	7,95E-03	1,63E-02	4,14E-02	1,63E-02	7,95E-03	4,45E-03	2,72E-03	1,79E-03	1,28E-03	9,89E-04	8,42E-04	7,97E-04	8,42E-04	9,89E-04	1,28E-03	1,79E-03
TF06	1,79E-03	2,72E-03	4,44E-03	7,95E-03	1,63E-02	4,14E-02	1,63E-02	7,95E-03	4,45E-03	2,72E-03	1,79E-03	1,28E-03	9,88E-04	8,41E-04	7,96E-04	8,42E-04	9,89E-04	1,28E-03
TF07	1,28E-03	1,79E-03	2,72E-03	4,45E-03	7,95E-03	1,63E-02	4,14E-02	1,63E-02	7,95E-03	4,45E-03	2,72E-03	1,79E-03	1,28E-03	9,88E-04	8,42E-04	7,97E-04	8,42E-04	9,88E-04
TF08	9,88E-04	1,28E-03	1,79E-03	2,72E-03	4,45E-03	7,95E-03	1,63E-02	4,14E-02	1,63E-02	7,95E-03	4,45E-03	2,72E-03	1,79E-03	1,28E-03	9,88E-04	8,42E-04	7,97E-04	8,41E-04
TF09	8,42E-04	9,89E-04	1,28E-03	1,79E-03	2,72E-03	4,45E-03	7,95E-03	1,63E-02	4,14E-02	1,63E-02	7,95E-03	4,45E-03	2,72E-03	1,79E-03	1,28E-03	9,89E-04	8,42E-04	7,97E-04
TF10	7,97E-04	8,42E-04	9,88E-04	1,28E-03	1,79E-03	2,72E-03	4,45E-03	7,95E-03	1,63E-02	4,14E-02	1,63E-02	7,95E-03	4,44E-03	2,72E-03	1,79E-03	1,28E-03	9,89E-04	8,42E-04
TF11	8,42E-04	7,97E-04	8,42E-04	9,89E-04	1,28E-03	1,79E-03	2,72E-03	4,45E-03	7,95E-03	1,63E-02	4,14E-02	1,63E-02	7,95E-03	4,44E-03	2,72E-03	1,79E-03	1,28E-03	9,88E-04
TF12	9,88E-04	8,42E-04	7,97E-04	8,42E-04	9,89E-04	1,28E-03	1,79E-03	2,72E-03	4,45E-03	7,95E-03	1,63E-02	4,14E-02	1,63E-02	7,95E-03	4,44E-03	2,72E-03	1,79E-03	1,28E-03
TF13	1,28E-03	9,88E-04	8,41E-04	7,96E-04	8,42E-04	9,88E-04	1,28E-03	1,79E-03	2,72E-03	4,44E-03	7,95E-03	1,63E-02	4,14E-02	1,63E-02	7,94E-03	4,44E-03	2,72E-03	1,79E-03
TF14	1,79E-03	1,28E-03	9,88E-04	8,41E-04	7,97E-04	8,41E-04	9,88E-04	1,28E-03	1,79E-03	2,72E-03	4,44E-03	7,95E-03	1,63E-02	4,14E-02	1,63E-02	7,95E-03	4,45E-03	2,71E-03
TF15	2,71E-03	1,79E-03	1,28E-03	9,88E-04	8,42E-04	7,96E-04	8,42E-04	9,88E-04	1,28E-03	1,79E-03	2,72E-03	4,44E-03	7,94E-03	1,63E-02	4,14E-02	1,63E-02	7,95E-03	4,44E-03
TF16	4,45E-03	2,72E-03	1,79E-03	1,28E-03	9,89E-04	8,42E-04	7,97E-04	8,42E-04	9,89E-04	1,28E-03	1,79E-03	2,72E-03	4,44E-03	7,95E-03	1,63E-02	4,14E-02	1,63E-02	7,95E-03
TF17	7,95E-03	4,45E-03	2,72E-03	1,79E-03	1,28E-03	9,89E-04	8,42E-04	7,97E-04	8,42E-04	9,89E-04	1,28E-03	1,79E-03	2,72E-03	4,45E-03	7,95E-03	1,63E-02	4,14E-02	1,63E-02
TF18	1,63E-02	7,95E-03	4,44E-03	2,72E-03	1,79E-03	1,28E-03	9,88E-04	8,41E-04	7,97E-04	8,42E-04	9,88E-04	1,28E-03	1,79E-03	2,71E-03	4,44E-03	7,95E-03	1,63E-02	4,14E-02

Figure VII.18: TF coils system mutual inductances matrix.

The model has been validated against the TF coils system inductances calculated with the software OPERA 3D®, which gives the same results.

CS and PF coils with plasma current

While all CS coils have 304 turns and a maximum current of 29.9 kA, PF coils system is symmetric with respect to the plasma plane, with PF1, PF2 and PF3 having 360, 160 and 196 turns with 28.3 kA, 27.1 kA and 28.6 kA, respectively (during the SN reference scenario). In the model, a circular cross section coil, positioned at R = 2.11 m, simulates the plasma current. The calculated self-inductance of a single CS module coil is 73.1 mH, whereas the self-inductance of PF1/6 is 422 mH, of PF2/5 is 283 mH and of PF3/4 is 664 mH. In Fig. VII.19 the mutual inductances matrix of the whole system including plasma is shown. The value given in Fig. VII.19 for the self-inductance of the plasma has not a physical meaning, as it depends on the assumed geometry, but its numerical value is anyway essential, as it is employed in the mathematical model.

This electric model has been used for the calculation of voltages across CS and PF coils in operative plasma scenarios and in other relevant situations useful for the magnets and insulation design.

	CS_Lo1	CS_Lo2	CS_Lo3	CS_Up1	CS_Up2	CS_Up3	PF01	PF02	PF03	PF04	PF05	PF06	plasma
CS_Lo1	7,31E-02	1,99E-02	3,77E-03	1,99E-02	3,77E-03	1,23E-03	3,61E-03	4,19E-03	8,47E-03	9,72E-03	6,42E-03	7,67E-03	9,79E-05
CS_Lo2	1,99E-02	7,31E-02	1,99E-02	3,77E-03	1,23E-03	5,34E-04	1,93E-03	2,72E-03	6,76E-03	9,90E-03	9,25E-03	1,87E-02	6,30E-05
CS_Lo3	3,77E-03	1,99E-02	7,31E-02	1,23E-03	5,34E-04	2,78E-04	1,14E-03	1,81E-03	5,12E-03	8,94E-03	1,14E-02	4,53E-02	3,41E-05
CS_Up1	1,99E-02	3,77E-03	1,23E-03	7,31E-02	1,99E-02	3,77E-03	7,68E-03	6,42E-03	9,71E-03	8,47E-03	4,19E-03	3,61E-03	9,79E-05
CS_Up2	3,77E-03	1,23E-03	5,34E-04	1,99E-02	7,31E-02	1,99E-02	1,87E-02	9,25E-03	9,90E-03	6,76E-03	2,72E-03	1,93E-03	6,29E-05
CS_Up3	1,23E-03	5,34E-04	2,78E-04	3,77E-03	1,99E-02	7,31E-02	4,53E-02	1,14E-02	8,93E-03	5,12E-03	1,81E-03	1,14E-03	3,41E-05
PF01	3,61E-03	1,93E-03	1,14E-03	7,68E-03	1,87E-02	4,53E-02	4,22E-01	8,04E-02	5,17E-02	2,67E-02	8,69E-03	5,06E-03	1,32E-04
PF02	4,19E-03	2,72E-03	1,81E-03	6,42E-03	9,25E-03	1,14E-02	8,04E-02	2,83E-01	1,15E-01	5,27E-02	1,60E-02	8,69E-03	1,83E-04
PF03	8,47E-03	6,76E-03	5,12E-03	9,71E-03	9,90E-03	8,93E-03	5,17E-02	1,15E-01	6,64E-01	1,95E-01	5,27E-02	2,67E-02	3,96E-04
PF04	9,72E-03	9,90E-03	8,94E-03	8,47E-03	6,76E-03	5,12E-03	2,67E-02	5,27E-02	1,95E-01	6,64E-01	1,15E-01	5,17E-02	3,96E-04
PF05	6,42E-03	9,25E-03	1,14E-02	4,19E-03	2,72E-03	1,81E-03	8,69E-03	1,60E-02	5,27E-02	1,15E-01	2,83E-01	8,04E-02	1,83E-04
PF06	7,67E-03	1,87E-02	4,53E-02	3,61E-03	1,93E-03	1,14E-03	5,06E-03	8,69E-03	2,67E-02	5,17E-02	8,04E-02	4,21E-01	1,32E-04
plasma	9,79E-05	6,30E-05	3,41E-05	9,79E-05	6,29E-05	3,41E-05	1,32E-04	1,83E-04	3,96E-04	3,96E-04	1,83E-04	1,32E-04	4,77E-06

Figure VII.19: CS, PF and plasma system: mutual inductances matrix.

VII.6 Current Leads

Current leads (CL) are essential components of superconducting magnets. They are the part of the electrical connection between the power supply at room temperature and the magnet at cryogenic temperature. Main goal in the design of this component is to minimize the thermal load to be removed by the refrigeration system, being the heat load proportional to operational cost. Current leads manufacturing cost plays also a role in technologic design choices to be adopted. For the resistive part, the thermal load is proportional to the square of the current and it is quite independent of the electric conductor used, because thermal and electrical property are linked by the Wiedemann-Franz law [VII.24]. The only way to break this bond and improve the performances, is the use of high temperature superconductors (HTS).

To understand which solution is the best choice for DTT needs, a survey of the existing and successfully tested CL has been considered, with a current higher than 10 KA for tokamaks or however significant for the purpose [VII.25 – VII.30]. It is remarkable, compared to all the others, the number of CL, as well as the design performances, in ITER, JT60SA and W7X. For these projects, the resistive part of CL is cooled with a forced flow of helium at 50 K, in the shape of a heat exchanger consisting of a core with fins, made of copper. The HTS part is BSCCO (Bismuth Strontium Calcium Copper Oxide superconductors) in AgAu matrix. A pair of 20 kA CL for HZB (produced by EPFL-SPC, Switzerland) has the same cryogenic and similar HTS part, but a different copper exchanger, made of a multitude of thin wires. EAST and NHMFL chose the same HTS, but with liquid nitrogen as a coolant. In KSTAR the CL are made of brass thin wires, cooled with a bath of liquid helium at the cold end, exploiting the evaporation to cool the conductor up to the room temperature [VII.31]. The only ones produced with REBCO (Rare-Earth Barium Copper Oxide superconductors) and successfully operating, a pair of 12/18 kA CL cooled with liquid nitrogen, are those manufactured by the NCR Kurchatov Institute [VII.32].

At present, in DTT the use of nitrogen, which has the advantage of keeping constant the temperature on the warm side of the HTS, is kept aside for possible activation problems, to be further verified. The choice of superconductor has an impact on the total cost of CL of about 35-50%, so a not-trivial balance between the initial cost and the operating cost is necessary. In fact, the production cost of the ITER type is 4 times higher than the KSTAR type, whilst the operating cost of the KSTAR type is 3 times higher than the ITER type.

The widely differing operative conditions between the CL for TF and those for CS/PF lead to completely different design strategies. The destiny in the life of the CL for the TF coils is to stay almost indefinitely energized, so the choice of the ITER TF CL type is mandatory. The cost of a high-performance CL can be minimized by the use of REBCO as HTS, the cost of which is 5 times lower than that of BSCCO. This choice can be taken thanks to the current state of the art and facilitated by the peculiarity of DTT of having a short discharge time of the magnets in the event of a quench. A different strategy is needed for the CL of CS/PF, for which the duty cycle is less than 1/10 over a daily period. The amount of superconductor must be calibrated to the maximum current and, for DTT, this current is considerably high, say 702 kA, compared to other tokamaks (with proper scaling in size). In this case the choice of the KSTAR type seems to be the most appropriate, also as it allows to postpone the production of the power required in the peaks, along the idle time in the cycle, taking advantage of the accumulation of liquid helium and so mitigating the increase in the cost of the refrigeration system caused by low performance.

CL design is still on-going, and the final choices will be in agreement also with the cryogenic system requirements.

VII.7 Conclusions

The Superconducting Magnet System of DTT has been described in this chapter, highlighting its main features and principal changes with respect to what already presented in past works. Though some aspects are still to be investigated in more details, the illustrated conceptual design status proves to be sound and reliable. No major problems or killing factors have been found so far. Some components will enter the engineering and then tendering phases in the close future, whereas for others a longer period of study is necessary. In general, the progress of the design is respecting the overall project time schedule.

VII.8 References

[VII.1] ENEA, "DTT Divertor Tokamak Test facility, Project Proposal", 2015, ISBN:978-88-8286-318-0, and http://fsn-fusphy.frascati.enea.it/DTT_ProjectProposal_July2015.pdf

[VII.2] A. Di Zenobio et al., "DTT device: Conceptual design of the superconducting magnet system", Fusion Engineering and Design 122 (2017) 299–312

[VII.3] (a) I. R. Dixon, et al., "Electromagnetic Cycling and Strain Effects on Cable-in-Conduit Conductors With Variations in Cabling Design and Conduit Material Properties", IEEE Trans. Appl. Supercond. 19 (2009) 1462
(b) I. R. Dixon, et al., "Cable-in-Conduit Conductor Fabrication for the Series-Connected Hybrid Magnets", IEEE Trans. Appl. Supercond. 22 (2012) 4301004

[VII.4] S. A. J. Wiegers, et al., "Conceptual design of the 45 T hybrid magnet At the Nijmegen high field magnet laboratory", IEEE Trans. Appl. Supercond. 20-3 (June 2010) 688–691

[VII.5] V. Corato, et al., "Detailed design of the large-bore 8 T superconducting magnet for the NAFASSY test facility", Supercond. Sci. Technol. 28 (2015) 034005 (9pp)

[VII.6] A. della Corte et al., "Successful performances of the EU-AltTF sample, a large size Nb_3Sn cable-in-conduit conductor with rectangular geometry", Supercond. Sci. Technol. 23 (2010) 045028 (6pp)

[VII.7] L. Muzzi, et al., "Design, manufacture and test of an 80 kA-class Nb_3Sn cable-in-conduit conductor with rectangular geometry and distributed pressure relief channels", IEEE Trans. Appl. Supercond. 27-4 (June 2017), Art. ID 4800206

[VII.8] L. Muzzi, G. De Marzi, A. Di Zenobio, A. della Corte, "Cable-in-conduit conductors: lessons from the recent past for future developments with low and high temperature superconductors", Top. Rev. Supercond. Sci. Technol. 28(2015) 053001 (25pp)

[VII.9] K. Sedlak, et al., "Test of the MF-CICC conductor designed for the 12 T outsert coil of the HFML 45 T hybrid magnet", IEEE Trans. Appl. Supercond. 26-4 (June 2016), Art. ID 4300305A. Di Zenobio et al., "Joint Design for the EDIPO", IEEE Trans. Appl. Supercond. 18-2 (June 2008) 192–195

[VII.10] https://spc.epfl.ch/research/superconductivity/page-97675-en-html/

[VII.11] D. Bessette, et al., "Design of a Nb_3Sn CICC to withstand the 6000 electromagnetic cycles of the ITER central solenoid", IEEE Trans. Appl. Supercond. 23 (2015) 4200505

[VII.12] P. Bruzzone, et al., "Test results of a Nb_3Sn cable-in-conduit conductor with variable pitch sequence", IEEE Trans. Appl. Supercond. 19 (2009) 1448

[VII.13] F. Nunio, Support for mechanical structural analyses on TF system, EFDA_D_2KXW8H, 2015

[VII.14] L. Savoldi Richard, F. Casella, B. Fiori, and R. Zanino, "The 4C code for the cryogenic circuit conductor and coil modeling in ITER," Cryogenics, vol. 50, pp. 167–176, 2010

[VII.15] R. Bonifetto, A. Froio, L. Savoldi, R. Zanino, and A. Zappatore, "Verification of the 4C code for thermal-hydraulic transient modeling in superconducting magnets for nuclear fusion using the method of manufactured solutions," presented at the ASME V&V Symposium, 2018

[VII.16] R. Zanino, R. Bonifetto, A. Brighenti, T. Isono, H. Ozeki, and L. Savoldi, "Prediction, experimental results and analysis of the ITER TF Insert Coil quench propagation tests, using the 4C code," Superconductor Science and Technology, vol. 31, 2018, Art. ID 035004

[VII.17] L. Savoldi Richard, R. Bonifetto, Y. Chu, A. Kholia, S. H. Park, H. J. Lee, and R. Zanino, "4C code analysis of thermal-hydraulic transients in the KSTAR PF1 superconducting coil," Cryogenics, vol. 53, Jan. 2013, pp. 37–44

[VII.18] R. Bonifetto, L. Savoldi, and R. Zanino, "Thermal-hydraulic analysis of the JT-60SA Central Solenoid operation," to appear in IEEE Trans. Appl. Supercond. (2019)

[VII.19] A. Brighenti, R. Bonifetto, L. Savoldi, R. Zanino, and A. Zappatore, "Thermal-hydraulic analysis of the 2016 design of a DEMO TF magnet and CS WP," EFDA_D_2MS56X v2.0, 13/04/2018, unpublished document.

[VII.20] Y. Huang, W. Abdel Maksoud, L. Genini, D. Ciazynski, P. Decool, and A. Torre, “Quench tests analysis of the first JT-60SA Toroidal Field coils,” Fusion Engineering and Design, vol. 124, 2017, pp. 147–152
[VII.21] A. Di Zenobio et al., “Joint Design for the EDIPO”, IEEE Trans. Appl. Supercond. 18-2 (June 2008) 192–195
[VII.22] J. Feng, P. Titus, "Proposed Method for Evaluating Multiaxial Fatigue in ITER", Plasma Science and Fusion Center, Massachusetts Institute of Technology Cambridge, USA, PSFC/RR-07-4, July, 2007
[VII.23] N. Pompeo and L. Muzzi, arXiv:1101.5825
[VII.24] M.N. Wilson, “Superconducting Magnets”, Oxford University Press, 1983
[VII.25] P. Bauer, “Development of HTS Current Leads for the ITER Project” ITER Technical Report, 2018
[VII.26] R. Heller et al., “Experimental Results of a 70 kA high temperature superconductor current lead demonstrator for the ITER magnet system” IEEE Trans. Appl. Supercond., 2005
[VII.27] R. Heller et al., “Towards a 20kA high temperature superconductor current lead module using REBCO tapes”, Supercond. Sci. Technol. 31, 2018
[VII.28] S. Drotziger et al., “Investigation of HTS Current Leads UnderPulsed Operation for JT-60SA”,IEEE Trans. Appl. Supercond., 2012
[VII.29] R Wesche et al., “Results of the test of a pair of 20 kA HTS currents leads”, EUCAS, 2013
[VII.30] BI Yanfang et al., “HTS current leads for EAST tokamak project”, ICEC 20, Beijing, 2005
[VII.31] N. H. Song et al., “Development of KSTAR TF Coil Current Lead”, Transactions of the Korean Nuclear Society Spring Meeting Chuncheon, 2006
[VII.32] I.A. Kovalev et al., “Test results of 12/18 kA ReBCO coated conductor current leads”, Cryogenics, 2017

Chapter VIII

POWER SUPPLY SYSTEM

VIII.1 Introduction

The design of the Power Supply (PS) system of a new tokamak starts with many degrees of freedom and options involving many technical and economic aspects [VIII.1–VIII.3]. This is a stimulating and rare opportunity, but also a complex process requiring many successive iterations with all the other tokamak systems and external stakeholders, that may even lead to continuous modifications in the previous choices.

As the Frascati Research Center is presently hosting a tokamak (FTU) and many other research facilities, some electrical systems and supporting services are already available or can be updated. On the other hand, the existing buildings involve several design constraints in terms of space and layout.

This chapter presents the conceptual design of the DTT PS and electrical systems. The DTT PSs are designed to achieve single-null, double-null, snow-flake, super-X and other advanced magnetic configurations [VIII.4-VIII.5]. The overall optimization included the type of superconductors and the number of turns in each coil (see Chapter VII), looking for the best trade-off between the current per turn and the PS voltage.

In order to achieve the DTT power exhaust target levels, at least 45 MW of additional power shall be coupled to the plasma by mixing 3 different H&CD systems [VIII.6]: radiofrequency at ion and electron cyclotron resonance frequencies (ICRH and ECRH) and at most two negative neutral beam injectors (N-NBI). The optimal mixing composition will be identified after a first experimental phase coupling at least 25 MW from all the 3 systems (15 MW of ECRH, 3 MW of ICRH, 7.5 MW of N-NBI).

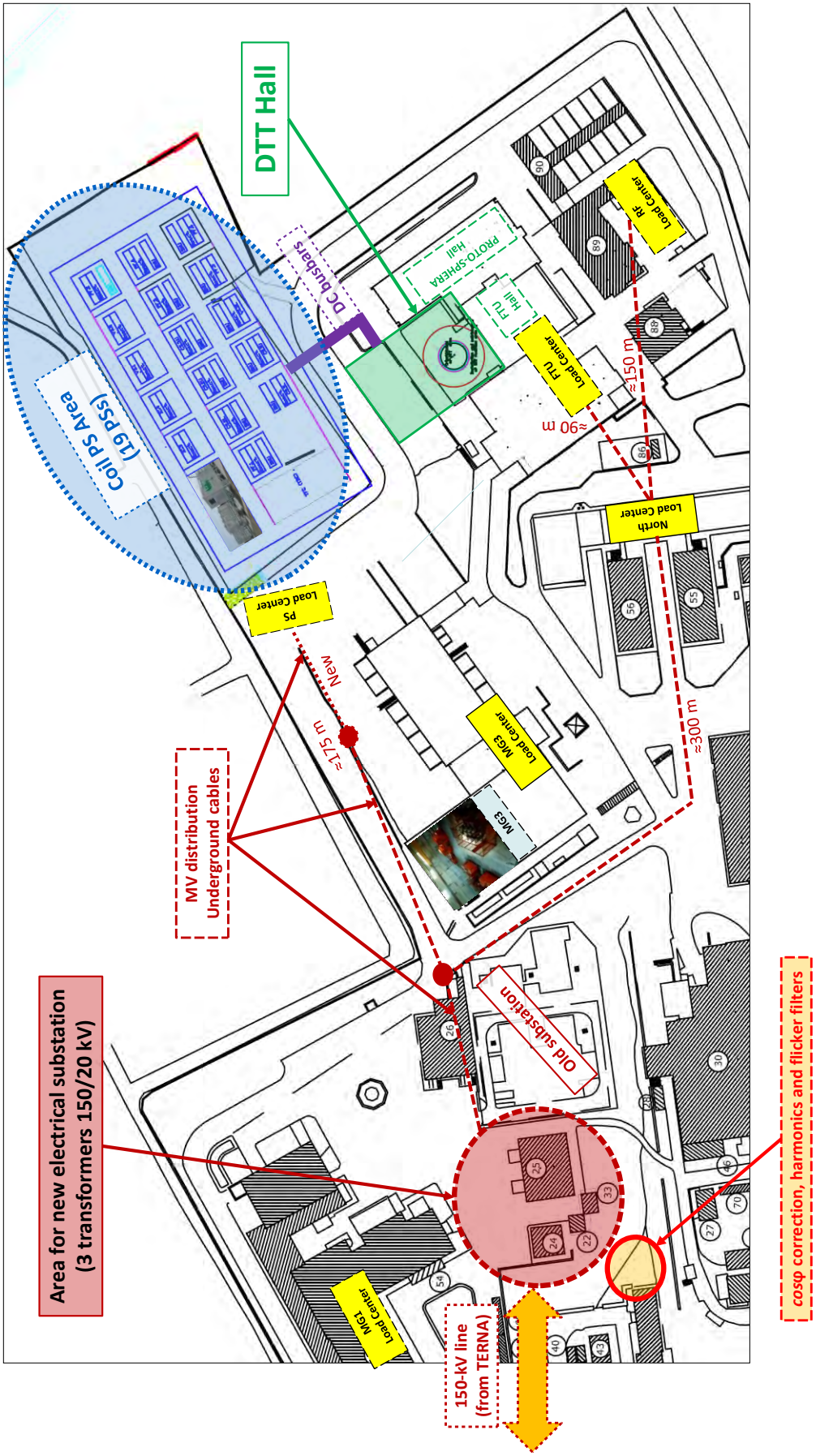

Figure VIII.1: Layout of the main electrical systems of the DTT site in the ENEA Center in Frascati. The access and the path of the HV line inside the center is to be defined with the transmission grid operator (Terna).

Even though DTT will be upgraded in successive phases, the distribution system, the input cables and the connection to the national grid must be sized for the maximum power demand in the final configuration.

The DTT PS system has to feed:

- 18 superconducting Toroidal Field Coils (TFCs), designed to operate with a current up to 44 kA;
- The Central Solenoid (CS), divided in 6 superconducting modules (CS3U, CS2U, CS1U, CS1L, CS2L, CS3L), each having an independent PS circuit;
- 6 superconducting Poloidal Field Coils (PFCs), classified as PF1, PF2, PF3, PF4, PF5, PF6;
- 2 in-vessel outboard copper coils for real-time Vertical Stabilization (VS) of the plasma;
- 4 in-vessel copper coils to shape the magnetic configuration close to the divertor;
- Further not-axisymmetric coils for plasma control (ELM, RWM, etc.), only partially considered in the present design;
- The electron cyclotron H&CD system (ECRH);
- The ion cyclotron H&CD system (ICRH);
- The neutral beam injectors (NBIs);
- All the auxiliary systems and services.

The design was carried out taking into account the following general design criteria: modularity, scalability, flexibility, efficiency, reliability, maintainability, cost reduction, safety.

The electrical system layout inside the DTT site with emphasis to the medium voltage (MV) distribution is sketched in Fig. VIII.1. As shown in the figure, the Coil PS Area contains 19 flat areas to place all the coil PS systems. The size of each flat area was fixed to 13 m x 13 m in order to contain up to 4 containers with a standard size of 40 feet. The Coil PS Area includes also the roads to transport and move the containers.

VIII.2 TFC Power Supply

VIII.2.1 Topology and requirements of the TFC circuit

The main requirements and constraints for the design of the TFC PS system are summarized in Tab. VIII.I. All the 18 coils are supplied in series to reduce the magnetic field toroidal ripple. The coils were divided in 3 sectors to limit the voltage across the coils in case of opening of the Fast Discharge Units (FDUs) [VIII.7-VIII.8].

As sketched in in Fig. VIII.2, the DTT Toroidal Field Coils (TFC) circuit consists of [VIII.9]:

- A TFC Base PS;
- A Crowbar Unit for the protection of the circuit [VIII.10];
- A DC busbar system;
- 3 FDUs;
- 6 current leads;
- 18 superconducting TFCs grouped in 3 coils sectors.

This chapter presents the systems/subsystems operating at ambient temperature, whereas the last two items, operating at cryogenic temperatures, are addressed in Chapter VII.

The area available for placing the entire TFC PS system including the 3 FDUs covers two sectors of the Coil PS Area in Fig. VIII.1, corresponding to a 13 m x 26 m area.

TABLE VIII.I. MAIN SPECIFICATIONS FOR THE DESIGN OF THE TFC PS SYSTEM

Characteristic	Value
Number of coils	18
Number of turns per coil	80
Total Inductance of the 18 coils	≈2 H
Self-Inductance of a single coil	41.4 mH
Total stored energy	≈2 GJ
Operating current	44 kA
Design margin for current	10%
Current including margin	≈48.5 kA
Time constant for TFC emergency discharge	5 s
Number of FDUs	3
Available area for the TFC PS and FDUs	13 m x 26 m
Dimensions of the busbar tunnel	2.84 m x 2.96 m

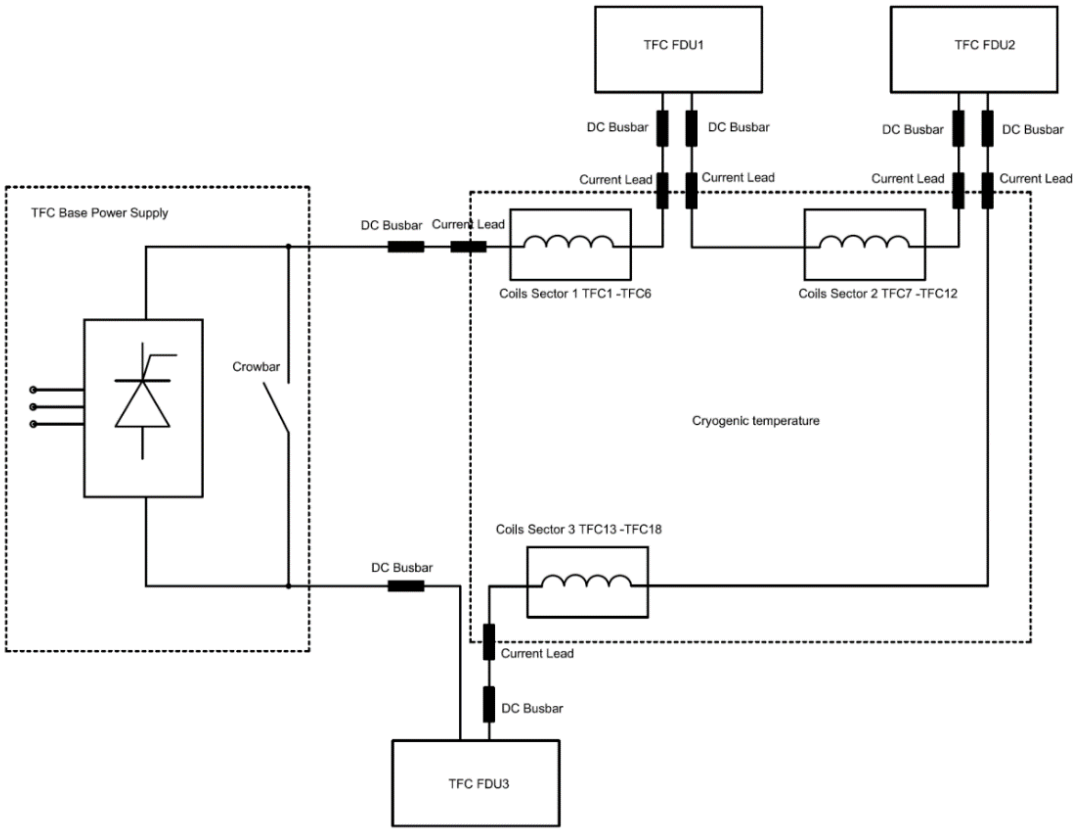

Figure VIII.2: Simplified electric scheme of the TFC circuit.

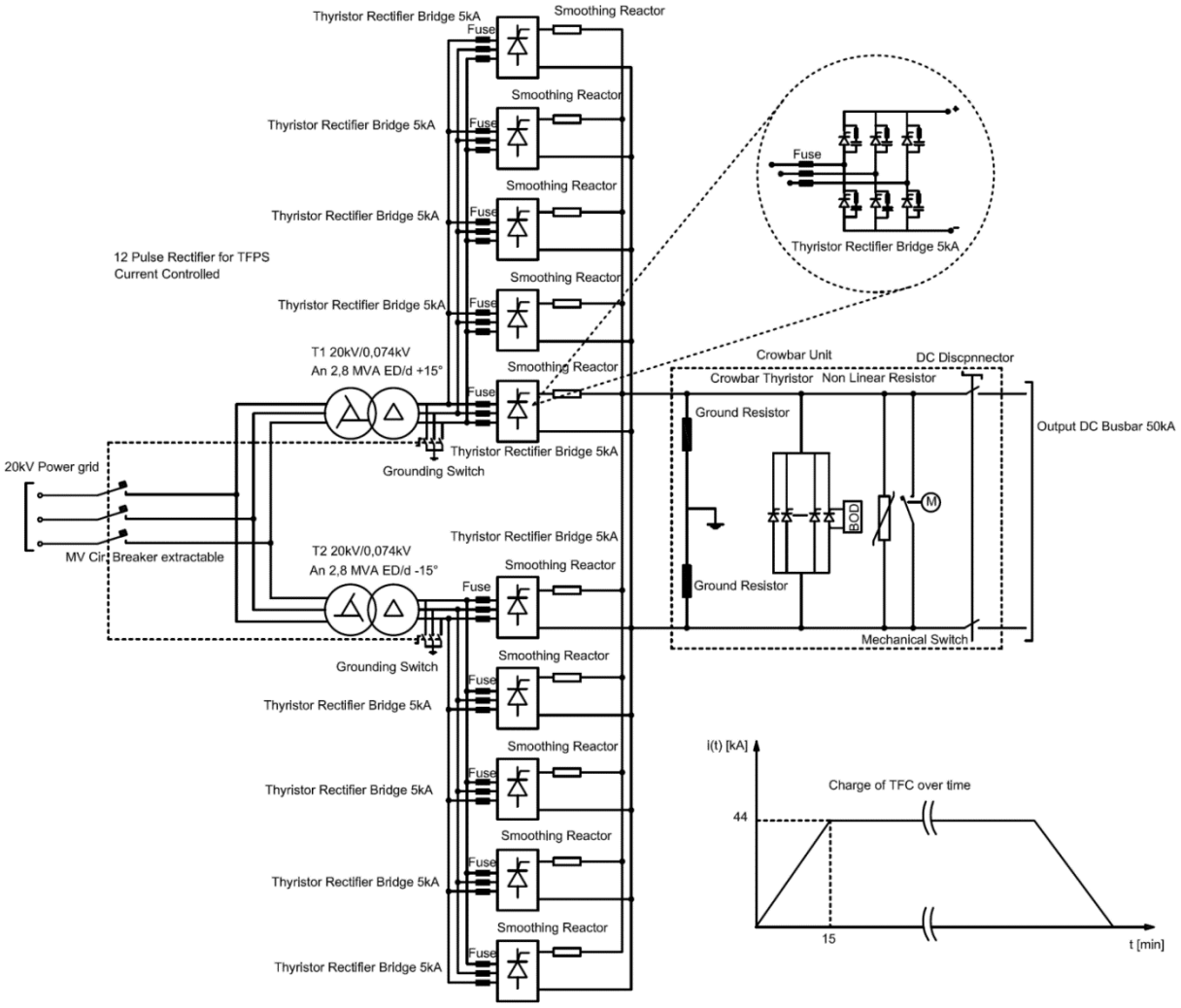

Figure VIII.3: Electric scheme of the TFC Base PS and crowbar protection unit. A typical current scenario generated by the Base PS is shown in the right bottom corner of the figure.

TABLE VIII.II. MAIN CHARACTERISTICS OF THE TFC BASE PS

Characteristic	Value
Quadrants	2
Global equivalent pulses	12
Number of converter transformers	2
Converter transformer windings	Extended delta/delta with ±15° phase shifting
Basic units	6-pulse thyristor rectifier bridges in parallel
Number of basic units	10
No-load DC current per unit	5 kA
No-load DC voltage per unit	±100 V
Smoothing reactors	10
Overcurrent protection	3 x 10 fuses

TABLE VIII.III. MAIN CHARACTERISTICS OF THE CROWBAR PROTECTION UNIT

Characteristic	Value
Type of operations	Unidirectional
Maximum current	48.5 kA
I^2t sustained through the crowbar	7.74 GA^2s
Number of operations without maintenance	2000

VIII.2.2 Design of the TFC Base PS and crowbar protection

A preliminary electric scheme of the TFC PS and crowbar is reported in Fig. VIII.3. The Base PS is a 2-quadrants 12-pulses AC/DC converter. Its main characteristics are summarized in Tab. VIII.II. The crowbar characteristics are summarized in Tab. VIII.III.

The Base PS shall be connected to the MV (20 kV) power distribution grid. The PS is protected on the MV side by an extractable AC circuit breaker, interlocked with two grounding switches (at secondary terminals of converter transformers). On the other side, the DC busbars are connected through a DC disconnector.

In order to keep a good power quality, a 12-pulse AC/DC topology was adopted instead of a classic 6-pulse rectifier. This technical solution allows to reduce the harmonics injected into the grid. In fact, the 12-pulse AC/DC converters inject only harmonic currents of h-order, where $h=12\cdot k\pm1$, $k=1,2,3\ldots$

A 12-pulse configuration is realized placing in parallel two 6-pulse converters and suppling them with two three-phase voltages shifted by 30°. The adoption of two converter transformers with resin insulation and extended delta/delta terminal connections achieves this shift, also ensuring that the distribution grid sees the same impedance in any operative condition.

The advantages of the adopted technical solution are summarized in the following:

- Reduced harmonic disturbances into the grid;
- Increased power quality;
- Increased power factor;
- Balancing in voltages and currents in any operative condition;
- Converter transformers with equal loads;
- Same short circuit power and impedance seen by power grid.

The crowbar system is a key protection device both for TFC PS and for the superconducting coils. Its function is to allow, in case of fault and/or quench, the freewheeling circulation of the current in the TFCs, in order to protect the TFC circuit against induced over-voltages.

The crowbar protection device is a hybrid-making-switch, consisting of the parallel of a static-switch, a mechanical switch and a varistor. The static switch is implemented by several thyristors in parallel and it is designed to be able to safely operate even if one thyristor or the mechanical switch is not operating. The mechanical switch takes some tens of milliseconds to close, limiting the conduction time of thyristors. The overvoltage protection is performed by a voltage transducer, a Break-Over-Diode (BOD) and a varistor assuring a fast intervention with a high redundancy protection level [VIII.10].

VIII.2.3 Design of the TFC Fast Discharge Units (FDUs)

The total magnetic energy stored in the superconducting TFCs can exceed 2 GJ. This energy is dangerous for the tokamak safety and must be rapidly extracted in case of a quench in the superconductors or of a fault in other systems as in the cryogenic system or in the TFC PS itself. The FDUs are protection systems for the safe and fast dissipation of this energy [VIII.7, VIII.8]. The protection is implemented by connecting a dump/discharge resistor in series to each TFC sector. Such resistor is actually divided in 2 identical units to limit the voltage to ground at insertion. The simplified scheme of a single FDU is shown in Fig. VIII.4, while the main characteristics of the TFC FDUs are summarized in Tab. VIII.IV.

The selected FDU scheme consists of:

- A DC hybrid circuit breaker, split in a mechanical By-Pass Switch (BPS) and a static circuit breaker.
- A dump/discharge resistor connected in parallel to the hybrid circuit breaker.
- A back-up protection made by a pyro-breaker.
- An earthing resistor.

The BPS is normally closed and the static circuit breaker is turned off during the DTT operations. When a FDU opening is requested, the static circuit breaker is turned on in order to limit the internal arc at the BPS opening. Afterwards, when all the 3 BPSs in the 3 FDUs are completely opened, the 3 static circuit breakers are turned off with a short and accurate response time [VIII.7, VIII.13 – VIII.16].

In addition to the elements shown in Fig. VIII.4, a proper voltage clamp mechanism is required in order to limit over-voltage peaks in transient due to derivative current on stray inductances.

TABLE VIII.IV. MAIN CHARACTERISTICS OF THE TFC FDUS

Characteristic	Value
Type of operations	Unidirectional
Number of FDUs	3
Operating current (including margin)	48.5 kA
Total magnetic to be dissipated	≈2 GJ
Time constant for TFC emergency discharge	5 s
Delay time	1.5 s
Nominal dump resistance for each FDU	0.138 Ω
Voltage applied to each coil sector at the discharge	≈6 kV
Nominal voltage applied to each coil at the discharge	≈1 kV
Coil voltage to ground at the discharge	≈3 kV

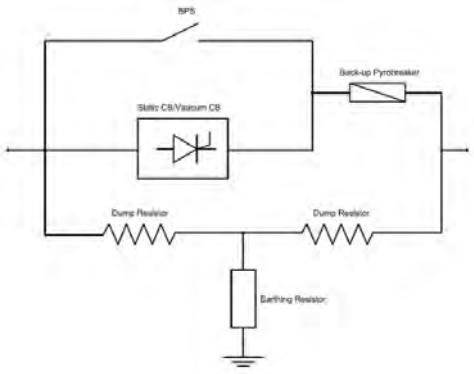

Figure VIII.4: Simplified scheme of a single FDU for the TFC circuit.

VIII.2.4 Size of the TFC DC busbars

The TFC DC busbars at ambient temperature are made in painted aluminium. The assumptions and the characteristics of the busbars are reported in Tab. VIII.V.

Figure VIII.5 shows a possible spatial disposition of the TFC busbars in their tunnel. As shown in Fig. VIII.5, the busbars lay in the horizontal direction, with the longer side of the cross section disposed vertically.

The electrodynamic strength was estimated, according to IEC Standard 60865-1 [VIII.11], as the maximum force normalized by the average distance between two fixed supports.

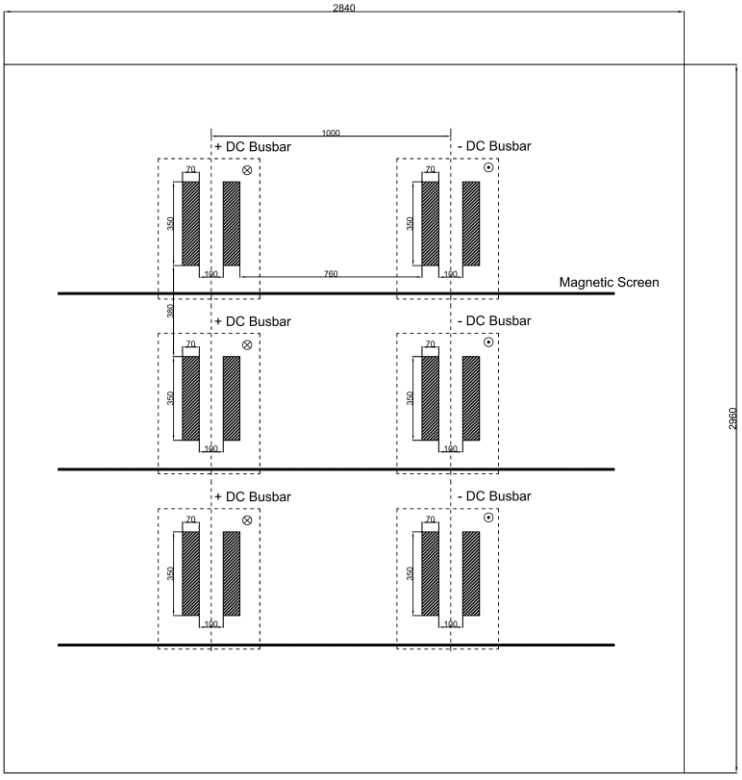

Figure VIII.5: TFC DC busbars as to be installed in their tunnel.

TABLE VIII.V. MAIN ASSUMPTIONS AND CHARACTERISTICS OF THE TFC BUSBARS

Characteristic	Value
Material	Aluminium
Air movement	Slight (up to 0.6 m/s)
Altitude	<1000 m
Maximum ambient temperature	35 °C
Irradiation coefficient	≈0.9
Solar radiation	0.7 kW/m^2
Maximum bar temperature	65 °C
Service	Continuous (days)
Current capacity	≈51 kA
Dimensions of the busbar tunnel	2.84 m x 2.96 m
Number of conductors per pole	2
Height	350 mm
Thickness	70 mm
Cross-section	24500 mm^2
Weight per conductor	66.15 kg/m
Current density	1.04 A/mm^2
Unitary voltage drop at 44 kA	51 mV/m
Unitary resistance	1.16 μΩ/m
Electrodynamic strength (IEC Standard 60865-1)	962.54 N/m
Distance between conductors in the same pole	100 mm
Distance between poles	760 mm
Distance between bars of different lines	380 mm
Magnetic screens	Between busbar rows
Inductance (considering magnetic screens)	0.46 μH/m
Estimated length per conductor	≈75 m

VIII.3 PFC Power Supply

VIII.3.1 Design models

The design moved from the reference scenarios defined in terms of time evolution of the coil currents to estimate successively the coil voltages, the Base PS voltages and the active and reactive powers [VIII.1, VIII.12]. Figure VIII.6 presents the currents and voltages in a reference single-null scenario with plasma at 5.5 MA. The current profiles of the in-vessel coils are not reported in Fig. VIII.6 as they actually depend on the real time plasma evolution. It is important to stress that the considered scenarios include a ramp-up time of

60 s for the coil currents, necessary to limit the superconductor heating, and a ramp-down time of 30 s, necessary to keep the plasma stable.

The DTT experiments are described by the scenario of the poloidal field coils (as in Fig. VIII.6) and plasma currents and by the inductance matrix containing the mutual inductances among the supplied (active) coils, the plasma and the "passive" elements of the tokamak. The entries in the main diagonal of the inductance matrix correspond to the self-inductance of each coil, listed in Chapter VII. The voltages across the coil terminals are obtained from the current scenario and the inductance matrix, as done for the voltage waveforms in Fig. VIII.6. These voltages are the average values in nominal conditions, while the instantaneous values depend on the actual disturbances and on the implemented control algorithms.

The actual voltages to be produced by the PS systems should account also for the voltage drops in the circuit (including DC bus bars, cryogenic transitions, connections, joints, parasitic effects and so on). In particular, the voltages at the plasma breakdown (zero time) are achieved by the support of a Switching Network Unit (SNU) [VIII.13 – VIII.16] in series between the PS and the coil. The SNU resistance and partition can be a degree of freedom in the PS design.

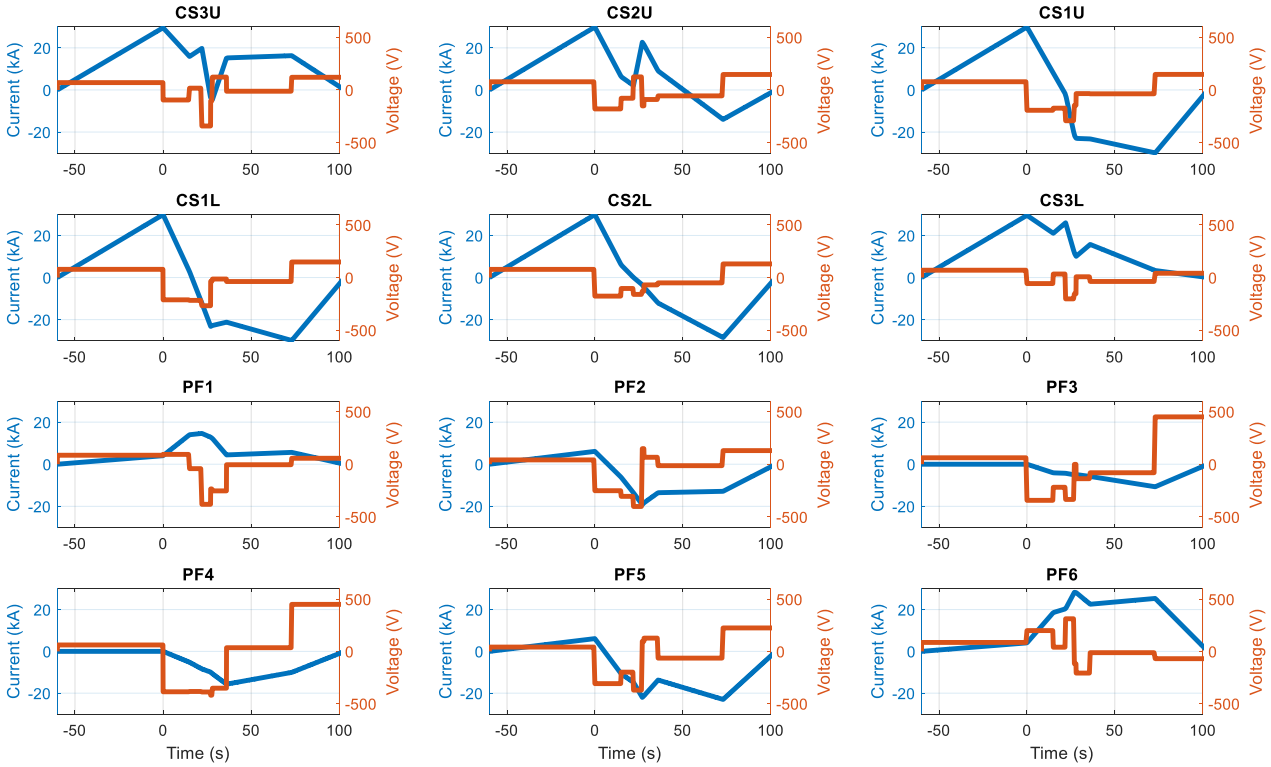

Figure VIII.6: Currents and voltages of the CS and PF coils during the reference single-null scenario with plasma at 5.5 MA, including the ramp-up and ramp-down phases of the PS currents. The voltage contribution of the SNUs at breakdown is not reported.

VIII.3.2 Ratings and topology of the poloidal coil PSs

With respect to [VIII.1], the CS and PF currents were increased to stay in the range ±30 kA. Slightly lower values were used in Chapter III for the PF coils, but a uniform design was preferred. The bars in Fig. VIII.7 summarize the maximum current and voltage amplitude needed for each CS and PF PS during the reference single-null, double-null and snow-flake scenarios, respectively.

The actual scheme for the coils PS was selected taking into account the final project requirements and budget. Also in order to reduce the costs, the PSs were grouped in 3 topologies [VIII.2] and the design was focused on modularity. Some considerations for the optimal selection of the PS topology are summarized in Tab. VIII.VI. The thyristor-bridge topology and the DC-link topology are sketched in Figs. VIII.8 and VIII.9.

The thyristor-bridge topology [VIII.1, VIII.3, VIII.9, VIII.17-VIII.19], sketched in Fig. VIII.8, was selected for the design of the TFC Base PS (see Fig. VIII.3) and for the in-vessel coils around the divertor (see Tab. VIII.VII). In particular for the TFC PS, the control can be slow (charge in minutes, flat-top for days). The resulting cosφ is low, but also the power and, as it is constant, the correction is simple.

The DC link with identical power in the input/output converters, mainly based on insulated gate bipolar transistors (IGBTs), is a configuration well explored for smaller converters and used in fusion only in limited cases [VIII.3, VIII.20-VIII.23]. The power quality at the input (reactive power, harmonics and so on) can be noticeably improved by using an Active Front End (AFE) to charge the DC link. This approach does not solve the problem of oversizing the electrical network. Therefore, the energy-conservation topology was selected for the CS and PF PSs. It features a low power demand at the input, a low impact on the external grid and a partial recovery of the energy delivered to the coils [VIII.24–VIII.26].

The main characteristics of the Base PSs for the CS, PF and in-vessel coils are summarized in Tab. VIII.VII.

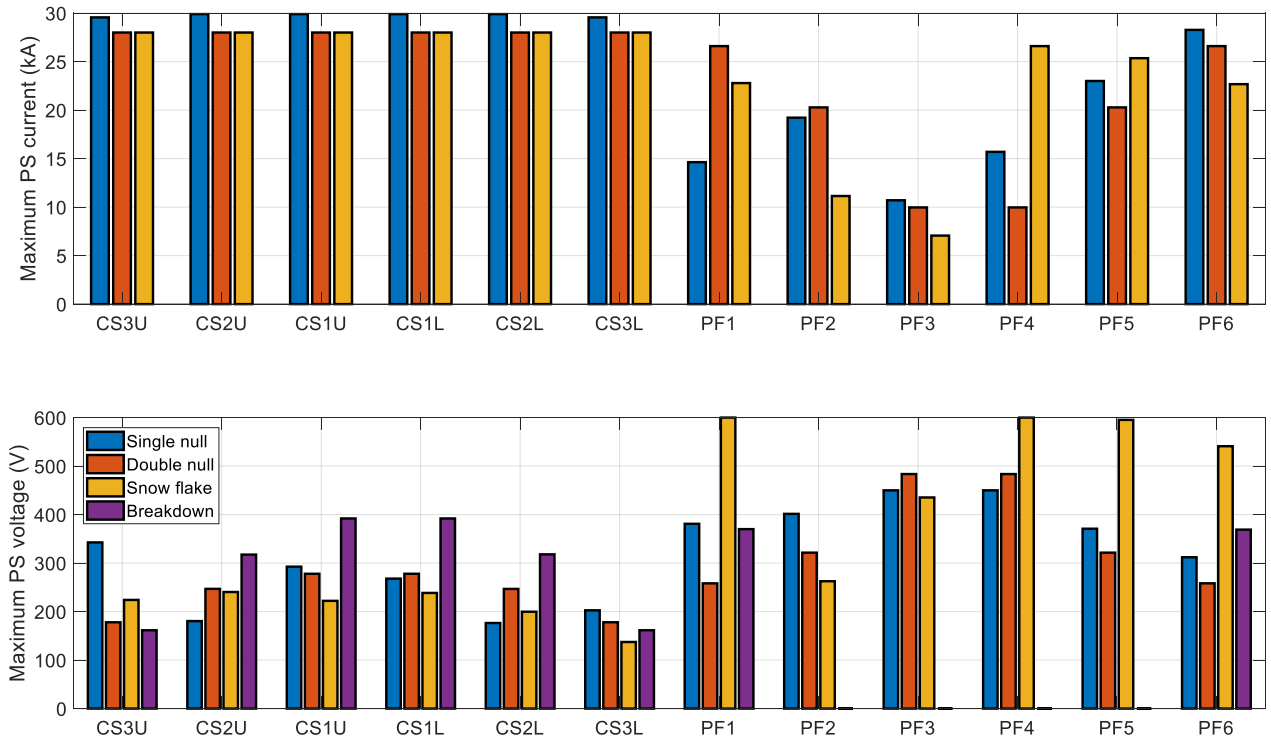

Figure VIII.7: Maximum currents and voltages required at the CS and PF PSs during different reference scenarios. The purple bars in the voltage plot refer to the maximum voltage contribution of the Base PS at the breakdown.

TABLE VIII.VI. SUMMARY OF MAIN ADVANTAGES AND DISADVANTAGES FOR EACH TOPOLOGY TO BE ADOPTED IN THE DTT COIL PSS

Topology	Advantages	Disadvantages
Thyristor bridges	Well known in fusion (proven reliability) Low "local" cost High power with less components	Slow (and complex) control Poor power quality (reactive power, harmonics, ...) Mandatory cosφ and harmonic correction Huge power from the external grid Ripple induced in magnetic sensors
DC link with same power in input/output converters	Fast control Dynamic compensation at breakdown High power quality (cosφ correction and harmonic filters are not necessary)	High cost DC link needs to be properly designed Huge power (backward power may be unacceptable for the grid) DC link to be discharged in case of fault
Energy-conservation converters (DC link with large energy storage)	Fast control and dynamic breakdown compensation Energy recovery (lower energy bill) Simpler distribution network (steady instead of pulsed) and protections Low upstream costs No oil in transformers (safety and pollution) Intrinsic modularity and possible upgrades	Less known technology Less know costs (but expected to decrease in next years) Internal energy losses in the supercapacitors Huge energy stored in supercapacitors Hundreds of supercapacitor modules Charger and DC link need to be properly designed

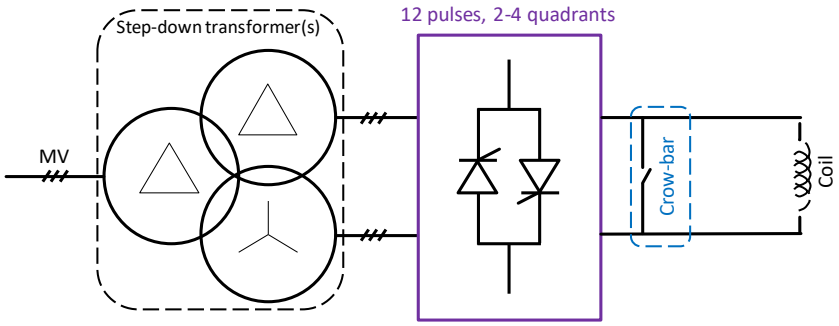

Figure VIII.8: Thyristor-bridge topology considered for the TF and IV PSs.

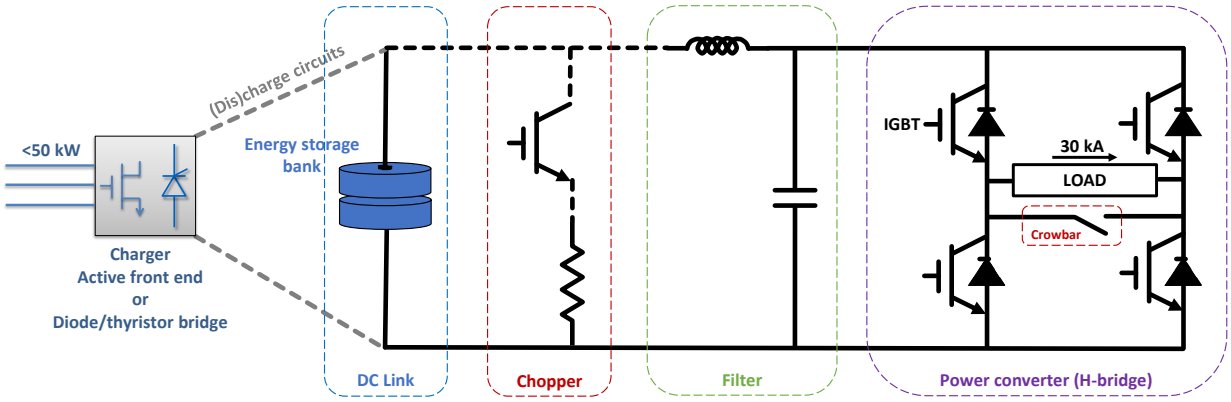

Figure VIII.9: Principles of energy-conservation converters: DC link with long-time energy storage capabilities and IGBT H-bridge at the output. The power at the input is very lower than that required at the output to supply the load.

VIII.3.3 Ratings and topology of CS and PF SNUs

The SNUs of the DTT CS and PF coils will be totally static (electronics). A good experience was accomplished with hybrid electromechanical-static switches in JT-60SA [VIII.13–VIII.16]. Nevertheless, such experience and the shorter operating time in DTT suggested to introduce a static SNU. This is implemented by the parallel of 24 Integrated Gate-Commutated Thyristors (IGCTs) in back-to-back configuration with their supporting circuits. The opening/closing time of this system is expected to be in the order of 100 μs [VIII.14–VIII.16].

The values of resistance available for the SNU operations are discrete. Based on the desired scenario, the actual resistors in parallel to the SNU can be connected/disconnected by selectors before each experiment.

The voltages requested at the breakdown are lower than in other tokamaks [VIII.3], even though a good loop electric field of 0.8 V/m is expected [VIII.4]. This is possible mainly because the current is not left uncontrolled to decay with the circuit time constant, but it is dynamically compensated by the Base PSs, and by exploiting the contribution of the VS PSs. Such capability, as the fine tuning of the breakdown voltages, is effectively available only using converters with fully-controlled commutation and accurate (static) SNUs. Moreover, the PSs can be used to compensate the variation of resistance with the temperature [VIII.14–VIII.15].

The fourth purple bar in the second subplot in Fig. VIII.7 displays the voltage, identical for all the configurations, necessary for the dynamic compensation at breakdown, namely the voltage variation to be covered around the value provided by the SNU.

In principle, the SNU support is useful in all the CS and PF coils. However, the simulations showed that the breakdown is more robust without SNUs in the coils with a weak contribution. For example, the SNU may be removed or left open in PF2-PF5. For this reason, the bars corresponding to these coils are absent in Fig. VIII.7.

Thanks to the back-to-back configuration, the SNU is able to open the current in both directions, so implementing also the function of Fast Discharge Unit (FDU). In order to introduces a further redundancy for safety, a sort of FDU was inserted in series to the SNU, as sketched in Fig. VIII.10. Such FDU only consists of a pyro-breaker with a fixed resistor. Therefore, the system has 3 levels of safety mechanisms in case of fault/quench:

1. In order to recover the energy stored in the coils, they are discharged by recharging the capacitors in the DC links;
2. If the previous method does not work or it is it too slow, the SNU IGCTs can be opened;
3. If also the second attempt fails, the pyro-breaker must be activated.

TABLE VIII.VII. MAIN CHARACTERISTICS OF THE BASE PSS FOR THE CS, PF AND IN-VESSEL COILS

Characteristic	CS/PF PSs	VS coil PSs	IV coil PSs	ELM/RWM PSs
Position	Ex-vessel	In-vessel equatorial	Around divertor	Non-axisymmetric
Load coil material	Superconducting	Copper	Copper	Copper
Number of PSs	12	2	4	To be defined
Number of quadrants	4	4	4 (2 possible)	4
Duty cycle and typical scenarios	<200 s / 3600 s	100 s / 3600 s	40 s / 3600 s	100 s / 3600 s
Ramps	Up 60 s, down 30 s	None	To be defined	None
Number of converter transformers	1 (also for more coils)	1	2	To be defined
Adopted topology	DC link storage H-bridge	DC link storage H-bridge	Thyristor bridge	DC link Same input power
Semiconductor technology	IGBT (IGCT)	IGBT	Thyristor	Silicon carbide
Energy stored in DC link per PS	>300 MJ	>100 MJ	None	To be defined
Charger	Diode or AFE	Diode or AFE	None	Diode/thyristor
Input power	<50 kW	<100 kW	>1 MW	<1 MW
Number of basic units	12	10	5	To be defined
Current	±30 kA	±25 kA	±25 kA	To be defined
No-load DC voltage	1000 V	200 V	200 V	To be defined
Worst-case DC voltage	600 V	200 V	200 V	To be defined
Control	Fast	Fast modulation	Slow	Fast
Controlled quantity	Current or voltage	Current or voltage	Current	Current
Supporting SNU	Static	None	None	None
Cooling	Raw water	Raw water	Demi water	Air

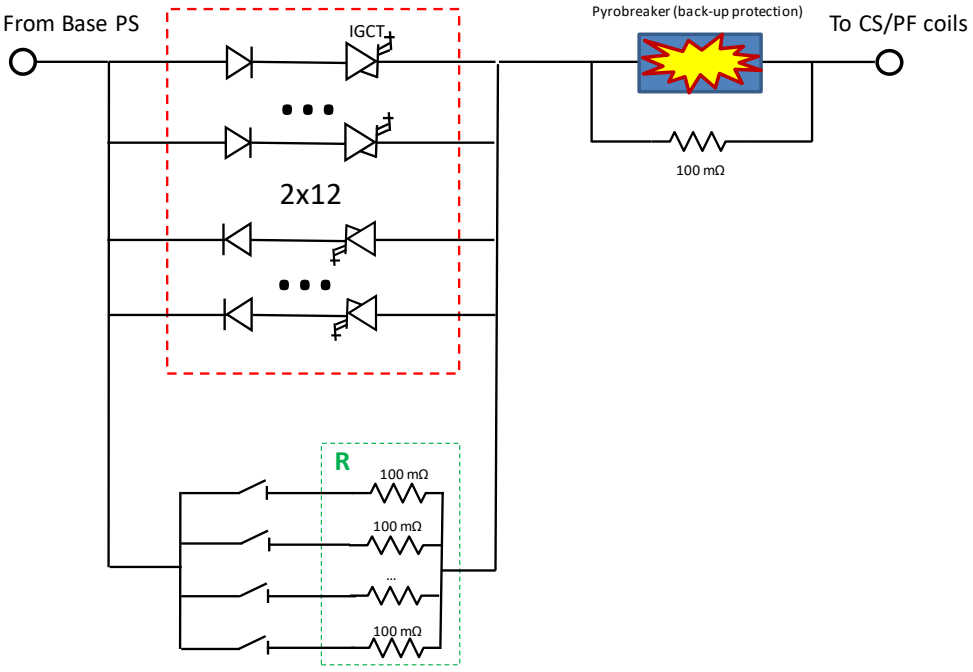

Figure VIII.10: Functional scheme of a DTT static SNU with an external FDU based only on a pyrobreaker.

VIII.4 Electrical Network

Even though DTT will be upgraded in successive phases, the electrical network must be sized for the maximum power in the final configuration. Therefore, the worst-case power demand from the grid and through the distribution network were estimated in the various design options, including the additional H&CD systems and the auxiliary services.

The ENEA Frascati Research Center is presently connected to a 150 kV line that can provide less than 10 MVA and cannot be upgraded also due to the presence of other loads on the same line. Moreover, the 3 FTU flywheels (MG1, MG2 and MG3) are sized to deliver energy for few seconds. Therefore, a new high-voltage line is necessary for DTT. The preliminary grid analyses indicated that the DTT power demand can be sustained only by the 400 kV transmission grid, having a strong node located at about 15 km from Frascati. In order to simplify the infrastructures and to limit the costs, the voltage is reduced to 150 kV immediately after the connection at 400 kV. A new 150 kV line will be fitted between the grid node and an electrical substation inside the ENEA Center. The old high voltage line and substation will be kept for the offices and to ensure an emergency backup in case of fault of the new systems.

The DTT loads, as in standard tokamaks, come from 3 general systems: auxiliary services, additional H&CD systems and coil PSs [VIII.3]. For the design purpose, they can be classified in two groups: steady-state (requiring a rather constant power) and pulsed (requiring power only during plasma operations, that are about 200 s for DTT including PS ramp-up and ramp-down). While the auxiliary and the H&CD loads clearly belong to the former and latter group respectively, the situation of the coil PSs is fuzzy and depends on the design choices.

Since the voltage drops produced by the pulsed loads are critical for the other ones, the DTT power is distributed through two separated sub-networks, classified as [VIII.27-VIII.28]:

1. Steady-state electrical network (SSEN).
2. Pulsed-power electrical network (PPEN).

Each of these networks will have specific 150 kV/20 kV transformers in the new electrical substation.

The resulting site layout and electrical distribution are sketched in Figs VIII.1 and VIII.11. The diagram in Fig. VIII.11 includes also the MG3 rotating machine, formerly used as flywheel, operating in DTT as synchronous condenser (compensator of reactive power). The electrical power is distributed through the 6 Load Centers shown in Fig. VIII.1. In particular, the PS Load Center is a new structure to host the transformers and switch for the distribution lines from the substation to the Coil PS Area.

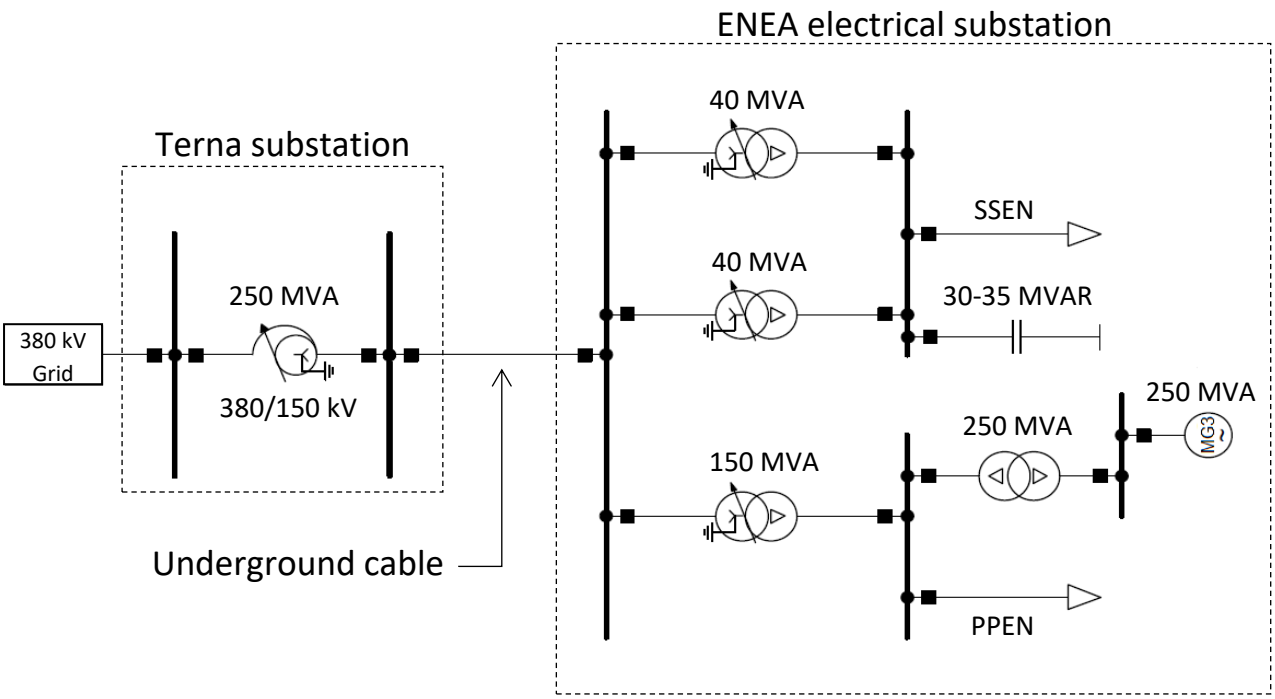

Figure VIII.11: Single-line diagram of the electrical network suppling the DTT facility. The new 150 kV line connects, after a path of about 15 km (mostly consisting in underground cables), a 380 kV Terna electrical substation to a new substation inside the ENEA Research Center in Frascati. Here, the distribution is split in the SSEN and PPEN subnetworks at 20 kV. The power factor of these networks is corrected by a capacitor bank and by a synchronous condenser, respectively.

Figure VIII.12 exemplifies the different contributions to the expected total DTT power for a typical scenario under some hypotheses on the PS implementation. This figure is thoroughly discussed in the following.

After a revision of the DTT electrical load list, the SSEN power was estimated to be about 60 MW. Due to the separation of the two electrical distribution networks, the simulations resulted in voltage drops within 3% in all the SSEN and a global cosφ>0.9 even with a limited power factor correction by capacitors.

The ECRH, ICRH and N-NBI PSs are connected to the 20 kV PPEN. The optimal mixing composition for the 3 different H&CD systems will be identified after a first experimental phase coupling at least 25 MW from all the 3 systems, as reported in Tab. VIII.VIII. This table also reports the maximum upgrade possible for each system in the successive phases, under the constrain that the total power coupled to plasma shall reach 45 MW to achieve the power exhaust target level.

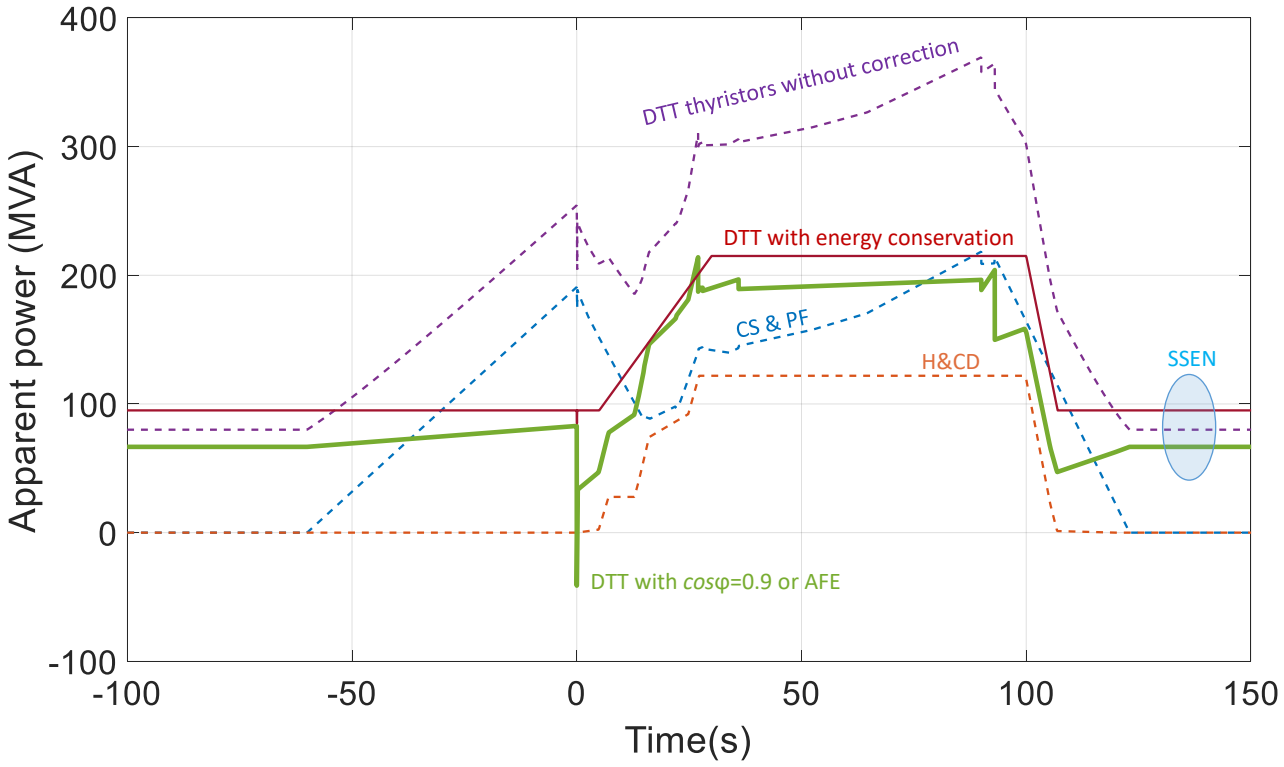

Figure VIII.12: Different contributions to the DTT expected total power demand from grid. Even if the curves refer to specific values and assumptions, the presented principles and the advantages of the energy-conservation topology are generally valid.

TABLE VIII.VIII. EXPECTED CHARACTERISTICS OF THE DTT H&CD SYSTEMS

H&CD system	Initial mix	Maximum expected upgrade	Wall-plug efficiency η	Power factor cosφ
ECRH	15 MW	30 MW	35-40%	0.9
ICRH	3 MW	9 MW	40%	0.9
N-NBI	7.5 MW	15 MW	40-45%	0.87

The H&CD electrical power S_{add} required to couple a specific power P_{plasma} to the plasma depends on the considered source. Table VIII.VIII summarizes the expected (target) wall-plug efficiency (η) and power factor (cosφ) of the H&CD systems, according to the model [VIII.1, VIII.3]:

$$P_{\text{plasma}} = \eta \cdot S_{\text{add}} \cdot \cos\varphi. \quad \text{(VIII.1)}$$

The H&CD scenario in Fig. VIII.13, assuming a H&CD mix with 25 MW of ECRH, 10 MW of ICRH and 10 MW of N-NBI, can be used as a reference case for the power calculations. The waveforms in Fig. VIII.13 were derived by simulations [VIII.6], without considering the possible fast and small power modulations. The H&CD power demand, represented by the dashed orange line in Fig. VIII.12, was derived directly from the scenario in Fig. VIII.13 by applying the η and cosφ data in Tab. VIII.VIII.

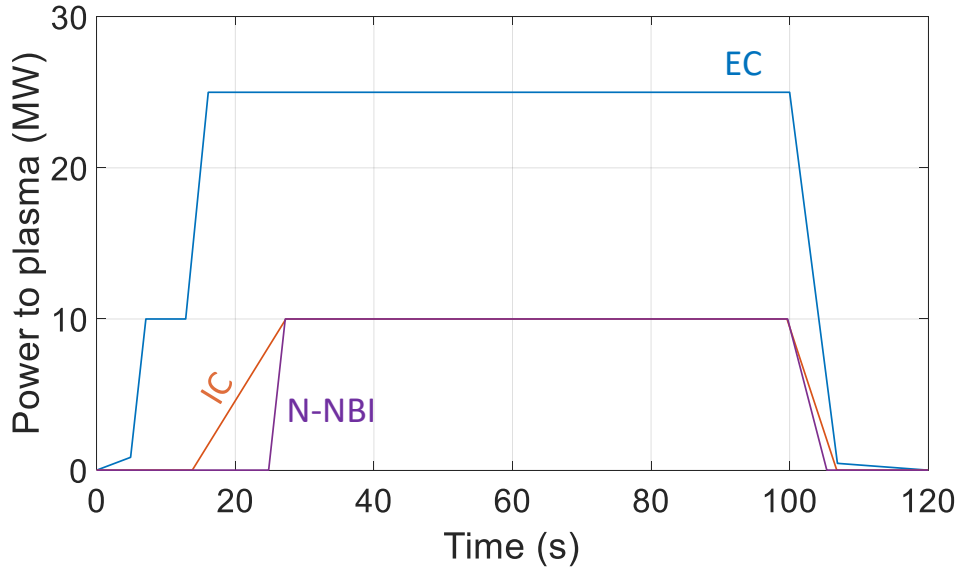

Figure VIII.13: Assumed scenarios for the 3 H&CD systems in the final DTT setup at full power.

The power of the CS and PF coils is very variable. The single-null scenario at 5.5 MA was used as reference for the power analyses. The global results are very similar for the double-null and snow-flake configurations, even though two relevant power peaks are present in the middle of the snow-flake scenario. Even when the power delivered to the coil is very low and the currents are lower than the rated values, the reactive power is relevant if the thyristor-bridge topology is adopted [VIII.1, VIII.3, VIII.27-VIII.28]. This leads to the dashed blue line in Fig. VIII.12.

The contributions of the dashed orange and blue lines in Fig. VIII.12, together with the auxiliary power, produce the total DTT power represented by the dashed purple line. The external transmission grid would not be able to handle this total power, mainly due to the large reactive power and the fast derivatives.

The reactive power issue can be solved by means of conventional correction techniques. For the national rules (that would be similar in other countries), the cosφ must be continuously corrected to 0.9, transforming the dashed purple line in Fig. VIII.12 in the solid green line. A further reduction of the cosφ can be achieved increasing the overall costs. The green line also approximates the total power if the AFE topology is adopted for all the coils, correcting the cosφ only for the H&CD contributions.

The power derivatives and peaks can be smoothed by means of an intermediate energy storage (energy-conservation converters). The solid red line in Fig. VIII.12 exemplifies the power profile when the coil PSs includes energy storage capabilities. In this case, the SSEN baseline is higher, due the powers requested by the chargers, but without problems for the cable and protection design. On the other hand, since the coil powers are managed only by the energy storage banks, the power profile is smoothed and the cosφ is not affected by the coil contribution. Accordingly, the performances are similar to those obtained with a large cosφ correction. The input power of the chargers can be even adapted to compensate the H&CD ramps, reducing their slopes. The resulting load is less critical for the external grid.

The solid red line in Fig. VIII.12 referring to the energy-conservation case is approximated to illustrate the phenomena, but Fig. VIII.14 contains a more realistic estimation of the total DTT power in a typical experimental scenario (with 45 MW of H&CD to the plasma). The difference between the SSEN power and the total power outside the pulse interval is due to the contributions of the cooling chillers that, thanks to the water tanks (see Chapter VI), are designed to operate only when the power demand is lower.

Of course, to ensure a safety margin and to allow future upgrades, the connection to the national transmission grid was requested for a power up to 300 MVA with the scenario represented by the red line in Fig. VIII.14, corresponding to worst-case assumptions also for the future upgrades.

Further simulations are being carried out to identify possible improvements and to assess the impact (voltage oscillations, flicker and so on) of the DTT facility on the transmission grid and the provisions required to cope with it.

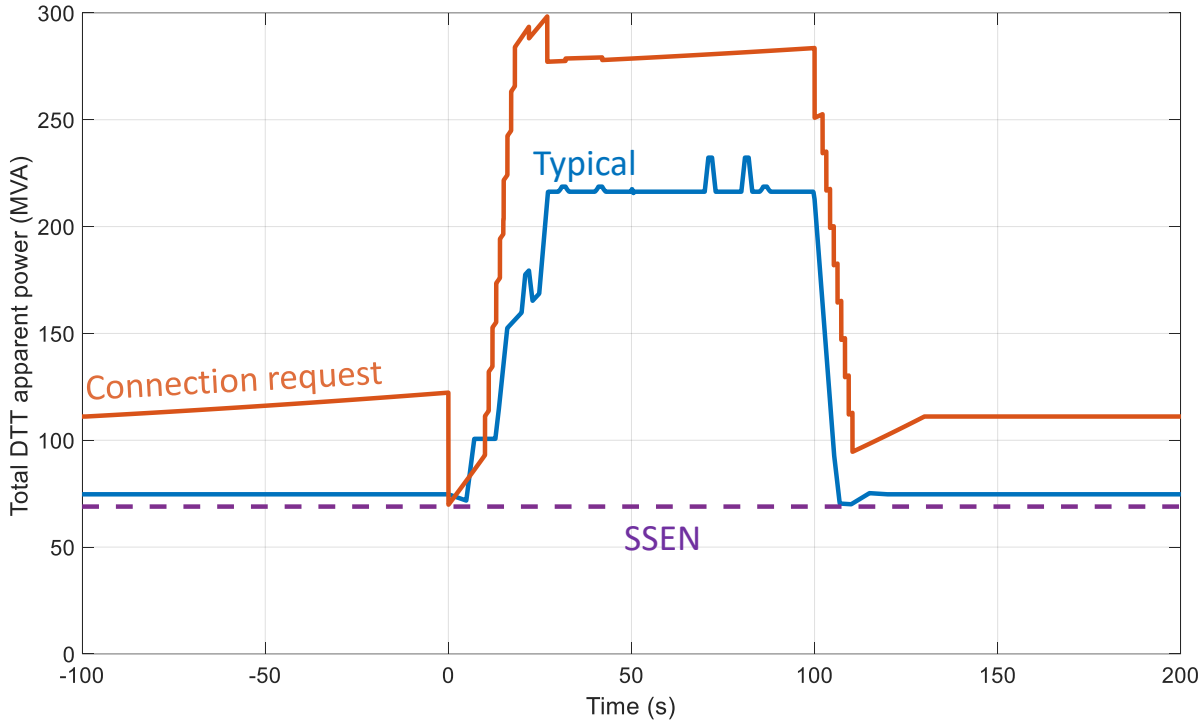

Figure VIII.14: Total power demand of the DTT facility during a typical scenario (blue line) and reference power profile used for the request of connection to the national grid (red line).

VIII.5 Conclusions

Many aspects and options must be taken into account in the electrical design of a new large fusion facility as DTT. Some considerations and results of this process were presented in this chapter.

Even though some parameters and interfaces of the PS system are still under definition, the general principles of the design are well established and only minor adjustments are expected with the project progresses. Nevertheless, further activities are foreseen to identify possible improvements and to adjust the parameters, also based on the available budget. The final engineering of the systems will be developed by the selected industrial supplier.

Some preliminary feasibility studies were carried out on the presented design, also taking account the experience of similar projects [VIII.3, VIII.9, VIII.20-VIII.21, VIII.23, VIII.27-VIII.28], resulting in a good level of confidence on the feasibility of the presented solutions in the time scale of the DTT project.

Two PS subsystems are expected to be particularly critical: the TFC FDUs and the energy-conservation converters. The DTT FDUs must open a current that is very higher than the previous realizations [VIII.7]. Moreover, the peak voltage is above the reapplied voltage sustainable by a single IGCT [VIII.13]. The voltage and the energy of the DC links in energy-conservation converters were never used in this kind of applications. The most critical activities, as the optimizations and verifications of the energy-conservation converters, are being analyzed with the support of other laboratories and specific prototypes will be developed in the next years.

The design of the PS system is expected to be completed in 2019. Afterwards, the Calls for Tender for the first DTT PS and electrical procurements will be launched. In order to complete the commissioning by 2025, most of these procurements must be launched and managed in parallel.

VIII.6 References

[VIII.1] A. Lampasi, P. Zito, F. Starace, P. Costa, G. Maffia, S. Minucci, E. Gaio, V. Toigo, L. Zanotto, S. Ciattaglia, "The DTT device: power supplies and electrical distribution system", Elsevier Fusion Engineering and Design, Volume 122, November 2017, Pages 356-364.

[VIII.2] A. Lampasi, A. De Santis, S. Minucci, F. Starace, P. Zito, "Conceptual design of the power supply systems for the Divertor Tokamak Test facility", Elsevier Fusion Engineering and Design, 2019.

[VIII.3] A. Lampasi, S. Minucci, "Survey of Electric Power Supplies Used in Nuclear Fusion Experiments", 17 IEEE International Conference on Environment and Electrical Engineering (EEEIC 2017), Milan, Italy, 6-9 June 2017.

[VIII.4] R. Albanese, F. Crisanti, P. Martin, A. Pizzuto, G. Mazzitelli, A.A. Tuccillo, R. Ambrosino, A. Appi, G. Di Gironimo, A. Di Zenobio, A. Frattolillo, G. Granucci, P. Innocente, A. Lampasi, R. Martone, G.M. Polli, G. Ramogida, P. Rossi, S. Sandri, M. Valisa, R. Villari, V. Vitale, "Design review for the Italian Divertor Tokamak Test facility", Elsevier Fusion Engineering and Design, 2019.

[VIII.5] G. Mazzitelli, R. Albanese, F. Crisanti, P. Martin, A. Pizzuto, A. Tuccillo, R. Ambrosino, A. Appi, G. Di Gironimo, A. Di Zenobio, A. Frattolillo, G. Granucci, P. Innocente, A. Lampasi, R. Martone, G. M. Polli, G. Ramogida, P. Rossi, S. Sandri, M. Valisa, R. Villari, V. Vitale, "Role of Italian DTT in the power exhaust implementation strategy", Elsevier Fusion Engineering and Design, 2019.

[VIII.6] G. Granucci et al., "The heating systems capability of DTT", 30th Symposium on Fusion Technology (SOFT), Giardini Naxos, Italy, 16-21 September 2018.

[VIII.7] A. Maistrello, E. Gaio, A. Ferro, M. Perna, C. Panizza, F. Soso, L. Novello, M. Matsukawa, K. Yamauchi, "Experimental qualification of the Hybrid Circuit Breaker developed for JT-60SA Quench Protection Circuits", IEEE Transactions on Applied Superconductivity, 2014, Volume: 24, Issue: 3.

[VIII.8] L. Novello, P. Cara, A. Coletti, E. Gaio, A. Maistrello, M. Matsukawa, G. Phillips, V. Tomarchio, K. Yamauchi, "Analysis of Maximum Voltage Transient of JT-60SA Toroidal Field Coils in Case of Fast Discharge", IEEE Transactions on Applied Superconductivity, vol. 26, no. 2, pp. 1-7, March 2016.

[VIII.9] L. Novello, O. Baulaigue, A. Coletti, N. Dumas, A. Ferro, E. Gaio, A. Lampasi, A. Maistrello, M. Matsukawa, K. Shimada, K. Yamauchi, P. Zito, "Present Status of the new Power Supply Systems of JT-60SA procured by EU", Elsevier Fusion Engineering and Design, Volumes 98-99, October 2015, Pages 1122-1126.

[VIII.10] P. Zito, A. Lampasi, O. Baulaigue, S. Gharafi, L. Novello, M. Matsukawa, K. Shimada, F. Fasce, M. Portesine, A. Dorronsoro, D. Vian, K. Celaya, B. Eikelboom, "Design and testing of Crowbar Protection System for the JT-60SA superconducting magnet power supplies", Elsevier Fusion Engineering and Design, Volume 124, November 2017, Pages 131-136.

[VIII.11] IEC 60865-1:2011, "Short-circuit currents - Calculation of effects - Part 1: Definitions and calculation methods", 2011.

[VIII.12] A. Lampasi, P. Zito, S. Minucci, F. Villone, "IPSE DIXIT: A User-Friendly Software Tool for the Design and Operation of Tokamak Power Supplies", 2017 IEEE 27th Symposium on Fusion Engineering (SOFE 2017), Shanghai, China, 4-8 June 2017.

[VIII.13] A. Lampasi, A. Coletti, L. Novello, M. Matsukawa, F. Burini, G. Taddia, S. Tenconi, "Final design of the Switching Network Units for the JT-60SA Central Solenoid", Elsevier Fusion Engineering and Design, 89 (2014), 342-348.

[VIII.14] A. Lampasi, P. Zito, A. Coletti, L. Novello, M. Matsukawa, K. Shimada, F. Burini, Y. Kuate Fone, G. Taddia, S. Tenconi, "First Switching Network Unit for the JT-60SA superconducting Central Solenoid", Elsevier Fusion Engineering and Design, Volumes 98-99, October 2015, Pages 1098-1102.

[VIII.15] A. Lampasi, P. Zito, L. Novello, M. Matsukawa, K. Shimada, F. Burini, G. Taddia, S. Tenconi, "Final tests of the four switching network units procured by the European Union for JT-60SA", Elsevier Fusion Engineering and Design, Volume 124, November 2017, Pages 163-168.

[VIII.16] A. Lampasi, F. Burini, G. Taddia, S. Tenconi, M. Matsukawa, K. Shimada, L. Novello, A. Jokinen, P. Zito, "Installation, Commissioning and Tests of Four Fast Switching Units of up to 20 kA for the JT-60SA Nuclear Fusion Experiment", Energies 2018, 11(4), 996.

[VIII.17] P. Zito, A. Lampasi, L. Novello, M. Matsukawa, K. Shimada, S. Hatakeyama, M. Portesine, A. Dorronsoro, D. Vian, K. Celaya, "Type Tests of JT-60SA Central Solenoid/Equilibrium Field (CS/EF) Super-Conducting Magnet Power Supplies", IEEE Transactions on Plasma Science, vol. 46, no. 5, pp. 1489-1496, May 2018.

[VIII.18] P. Zito, D. A. Lampasi, G. Maffia, G. Candela, "A Novel Digital Controller for 12-Pulse Back-to-Back AC/DC Converters in Nuclear Fusion Experiments", International Symposium on Power Electronics, Electrical Drives, Automation and Motion (SPEEDAM 2014), Ischia, Italy, 18-20 Jun. 2014.

[VIII.19] P. Zito, A. Lampasi, A. Coletti, L. Novello, M. Matsukawa, K. Shimada, D. Cinarelli, M. Portesine, A. Dorronsoro, D. Vian, "Design and realization of JT-60SA Fast Plasma Position Control (FPPC) Power Supplies", Elsevier Fusion Engineering and Design, Volumes 98-99, October 2015, Pages 1191-1196.

[VIII.20] D. Ganuza, D. Rendell, B. Arenal, J.M. de la Fuente, S.R. Shaw, V. Toigo, M. Zulaika, A. Arenal, JET EFDA contributors, "The design and manufacture of the enhanced radial field amplifier (ERFA) for the JET project", Fusion Engineering and Design 84 (2009) 810–814.

[VIII.21] A. Lampasi, G. Maffia, F. Alladio, L. Boncagni, F. Causa, E. Giovannozzi, L. A. Grosso, A. Mancuso, P. Micozzi, V. Piergotti, G. Rocchi, A. Sibio, B. Tilia, V. Zanza, "Progress of the Plasma Centerpost for the PROTO-SPHERA Spherical Tokamak", Energies 2016, 9(7), 508.

[VIII.22] E. Gaio, A. Ferro, L. Novello, M. Matsukawa, "Power Amplifiers Based on SiC Technology for MHD Mode Control in Fusion Experiments", IEEE Transactions on Plasma Science, no.99, pp.1-8.

[VIII.23] T. Rummel, T. Moennich, F. Fuellenbach, T. Murray, "Overview and status of commissioning of the Wendelstein 7-X magnet power supplies", IEEE Transactions on Plasma Science, Vol. 44, No. 9, September 2016.

[VIII.24] A. Lampasi, "Tokamak coil operations by energy-conservation converters and distributed energy storage", 30th Symposium on Fusion Technology (SOFT), Giardini Naxos, Italy, 16-21 September 2018.

[VIII.25] A. Lampasi, G. Taddia, S. Tenconi, F. Gherdovich, "Compact Power Supply with Integrated Energy Storage and Recovery Capabilities for Arbitrary Currents up to 2 kA", IEEE Transactions on Plasma Science, vol. 46, no. 10, pp. 3393-3400, Oct. 2018.

[VIII.26] A. Lampasi, S. Tenconi, G. Taddia, F. Gherdovich, L. Rinaldi, "A new generation of power supplies for pulsed loads", Elsevier Fusion Engineering and Design, 2019.

[VIII.27] C. Neumeyer, I. Benfatto, J. Hourtoule, J. Tao, A. Mankani, F. Milani, S. Nair, I. Suh, H. Tan, M. Wang, J. S. Oh, A. Roshal, "ITER power supply innovations and advances", IEEE 25th Symposium on Fusion Engineering (SOFE), San Francisco, CA, 2013, pp. 1-8.

[VIII.28] J. Hourtoule, C. Neumeyer, I. Suh, Y. Ding, L. Dong, C. Boyer, D. Cardoso Rodrigues, "ITER electrical distribution system", IEEE 25th Symposium on Fusion Engineering (SOFE), San Francisco, CA, 2013, pp. 1-5.

Chapter IX

HEATING AND CURRENT DRIVE

IX.1 Introduction

DTT has been conceived to tackle the exhaust issue in a DEMO relevant context. To fulfil this requirement a $P_{Sep}/R \approx 15$ MW/m is required, see Chapter III., that can be obtained with an additional power of 45 MW, coupled to the plasma by a mix of heating systems: Electron Cyclotron Resonance Heating (ECRH), Ion Cyclotron Resonance Heating (ICRH) and Negative Neutral Beam Injection (N-NBI). The full power required in DTT will be available in two steps, with the final power distribution (power mix) settled after the design and procurement of the first part. At the so called day-1 (the day-0 being the first commissioning of ohmic machine), the foreseen power is defined as that required to reach the H-mode in a 4 MA plasma, this request leads to 25 MW of additional power necessary and progressively available after one year from the machine start-up (day-0). The first experimental plasma (magnetic field 3T, plasma current up to 2 MA) is compatible with 8 MW of second harmonic ECRH, while for the injection of the rest of the power the magnetic field will be increased up to the 6T nominal value, with a plasma current of 4 MA. The day-1 additional power configuration will be therefore composed by 1 NNBI injector (7.5 MW at plasma), 2 ICRH antennas (1.5 MW of coupled power each antenna) and 2 ECRH clusters (8 MW installed from 8 gyrotron at 170 GHz for each cluster). During the procurement phase of the first step of the systems, the design of the final stage (45 MW) will be finalized and completed. This strategy will reduce the risk in the procurement of the DTT power systems, leaving enough time to verify, evaluate and modify the initial design. Three different options are

considered for the final power repartition, depending on the availability of the technical solutions and on the effective cost of each system.

The elemental power module, in each system, has been defined as follow:

- ECRH: Cluster of 8 gyrotrons for a total power of 8 MW installed;
- ICRH: Pair of antennas that deliver 1.5MW each, with shared transmitters;
- NNBI: one 400 keV beam injector able to deliver ≈7.5 MW to the plasma.

The configurations that have been selected, in term of power modules, are reported in Tab. IX.I.

TABLE IX.I. HEATING SYSTEMS MODULES AND RELATED POWER AT PLASMA FOR DIFFERENT CONFIGURATIONS

	ECRH Cluster	**ICRH Antennas**	**NNBI Injector**
Day-0	1 (7.2 MW)	0	0
Day-1	2 (14.4 MW)	2 (3 MW)	1 (7.5 MW)
Full Power Option a	4 (28.8 MW)	2 (3 MW)	2 (15 MW)
Full Power Option b	5 (36 MW)	2 (3 MW)	1 (7.5 MW)
Full Power Option c	4 (28.8 MW)	6 (9 MW)	1 (7.5 MW)

The three options (whose port allocation are shown in Fig. IX.1) for the full power configuration are all compatible with the defined layout of the heating buildings, the final choice will be based on technical solutions developed for ICRH system and consolidated costs. DTT will address the power exhaust issue in a ”integrated way”. Therefore, it is necessary, for the given divertor under study, to guarantee the plasma quality (in term of confinement and cleanliness) regardless of the divertor material/configuration performances (erosion, integrity, power handling). The selection of additional heating will be based therefore not only on the capability to inject a gross power in the plasma, but also on the functionality of a particular system to obtain an high plasma performances. Moreover, the coupling of sufficient additional power to the plasma must be guaranteed in the several different magnetic configurations expected to be used in DTT. A proper mix of the three systems allow to cover a wide list of physical tasks exploiting the peculiarities and the flexibility of each system. A representative list of tasks to be performed by DTT Additional Heating Systems is reported in Tab. IX.II.

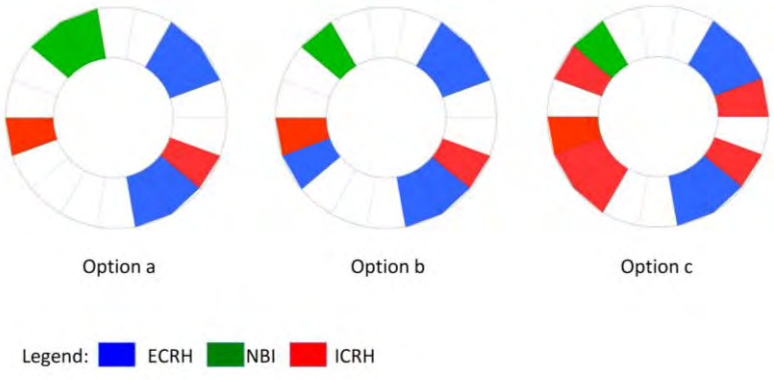

Figure IX.1: Possible equatorial ports allocation for the three full power configuration options.

TABLE IX.II. PHYSICAL REQUIREMENTS FOR DTT HEATING SYSTEMS

Task	EC	NBI	IC
Plasma Start up	x		
Current Ramp up	x	x	
H-mode access	x	x	x
Electron Heating	x	x	x
Ion Heating		x	x
Current Drive	x	x	
MHD Control	x		
Fast Particle Generation		x	x
Profiles Control	x		x
Impurity Accumulation	x	x	x
Momentum Injection and Control		x	
Transport Studies	x	x	
Isotopic Studies		x	
Diagnostics	x	x	
Wall Cleaning	x		x

IX.2 ICRH Heating

DTT ICRH system works in the frequency range 60-90 MHz, whose extreme frequencies locate the cyclotron resonances of ^{3}He and H minorities, respectively, at the DTT magnetic axis in the reference 6 T scenarios. The system can also support electron heating via mode conversion and wall conditioning through 2nd harmonic cyclotron heating of majority D ions. Other physical tasks, like generation of fast particles, density peaking, impurity accumulation and q-profile controls are possible, mostly after the upgrade to full power, while current drive is not foreseen.

The linear absorption of RF power by electrons, majority and minority ions has been investigated with TORIC [IX.1] for several fractions of the minority species. The reference single-null, B = 6 T, I_p = 5.5 MA scenario with the kinetic profiles computed with METIS [IX.2] in 2018 has been used as plasma target. Results are plotted in Fig. IX.2, showing that maximum absorption occurs at a fraction of the minority species of 6%. Relaxation and thermalisation processes due to collisions have been studied with the quasi-linear code SSQLFP [IX.3]. This analysis has been carried for values of the coupled power ranging from 3 to 15 MW: with a minority fraction of 3% and a power of 15 MW, the final power distribution is as follows:

- At 60 MHz: 55% to electrons, 41% to deuterium and 4% to helium 3;
- At 90 MHz: 60% to electrons, 38% to deuterium and 2% to hydrogen.

It allows the generation of a fast ion population with peak perpendicular energy up to 500 and 700 keV, respectively. Similar values, which are useful to study fast particle physics, can be achieved also with a

coupled power of 9 MW by varying minority concentrations. To accelerate ions up to 1 MeV, other approaches like the three-ions heating scheme or synergies with NBI are required, but they have not been assessed yet since they are secondary objectives for the ICRH system of DTT.

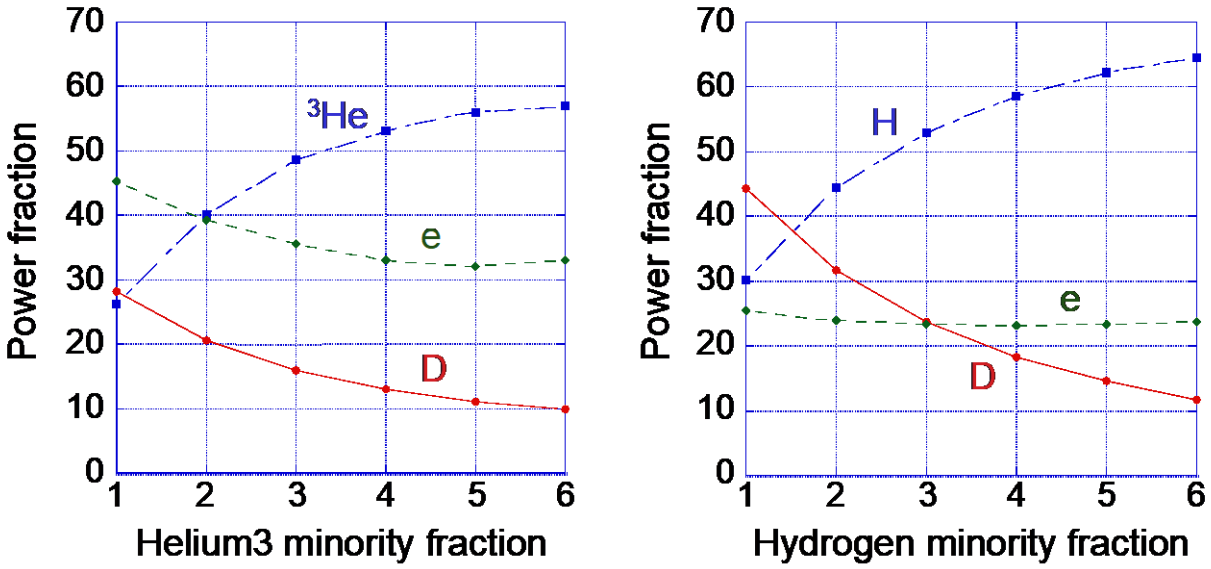

Figure IX.2: Fraction of power to various species vs. minority concentration for ^{3}He (left) and H (right) minority heating at 60 and 90 MHz respectively.

The ICRH system is conceived in modular units. Each module relies on a pair of antennas that are fed in parallel, through conjugate T or 3-db hybrid couplers [IX.4], to better cope with abrupt variations of the coupling due to edge-localized modes (ELM) or L-H transition. The system has to rely on standard technology and well-assessed solutions to meet the tight schedule of DTT construction. The state-of-the-art for power density handling capability of ICRH antennas is summarized in Fig. IX.2. By referring to the best achievements with ELMy H-mode plasmas shown in Fig. IX.3, a power density of 3.5 MW/m^2 has been envisaged for DTT. This choice leads to a coupled power of around 1.5 MW per antenna (i.e. 3 MW per module) for an equatorial port of 0.7 x 0.8 m^2. One module is scheduled for the initial phase of DTT and an upgrade with two more modules may be decided at a later stage.

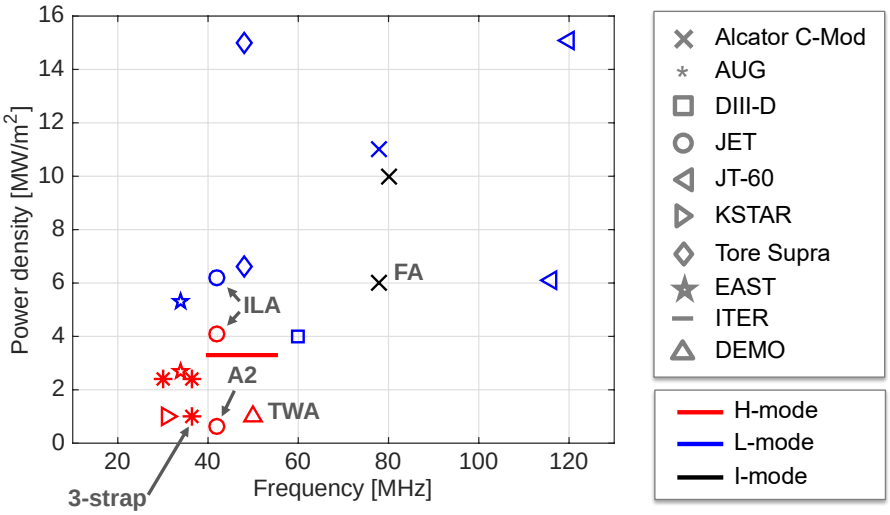

Figure IX.3: Power densities of ICRH antennas vs. frequency derived from literature and private communications.

Typical efficiencies for antenna coupling and transmission lines are 90% and 80%, respectively, entailing that the installed RF power per module has to be at least 4 MW. The transmitters have to provide this output power from 60 to 90 MHz in presence of a Voltage Standing Wave Ratio (VSWR) of 1.3, preferably 1.5, with periodic peaks up to 2.0 for 10 ms. Transmitters at ICRH frequencies consist in multi-stage amplifiers, whose end stage is a high-power grid tube placed in a suitable RF cavity equipped with tuning motors to vary the working frequency on a pulse-to-pulse basis. Two types of grid tubes are available: tetrode and diacrode, while cavities for the required frequency range are industrially unavailable and need a specific development. According to tube and cavity manufacturers, under aforementioned operational conditions and Continuous Wave (CW), a minimum output power of 2 MW and 1 MW can be expected for diacrode-based and tetrode-based transmitters, respectively. In the former case, the output level is almost constant vs. frequency, in the latter, higher power can be delivered only between 60 and 80 MHz, e.g. a power up to 2 MW for 30 s has been reached on a matched load. Accordingly, the ICRH system needs either 2 diacrode-based or 4 tetrode-based transmitters per module. The former solution is preferable because it reduces system cost and complexity, but the final decision will be taken after getting additional information from manufacturers. High voltage and auxiliary power supplies for the transmitters, as well as the hardware for commands, controls and data acquisition, and low-power RF units, rely on standard technology.

The Transmission Line (TL) is made of rigid coaxial cables based on the 9 3/16'' EIA standard or similar proprietary solutions like the RL 100-230 by Spinner used at JET. The External Conjugate-T (ECT) scheme is preferred as ELM-resilient matching network since it has been successfully tested at JET. Schemes based on 3-dB hybrid couplers are effective and simpler than ECT, but they would make the transmission line and matching system around 25% more expensive according to preliminary cost estimations. Moreover, they divert reflected power in excess toward a matched load rather than recirculating it toward the antenna, giving a slightly lower coupled power. The characteristic impedance Z_0 of the transmission line is 50 Ω from wave generators (output Z_0 = 50 Ω) to the Tee junction, while lower impedance is used from the junction to the antenna feeders to improve coupling. For the latter section, Z_0 = 30 Ω has been chosen as in the RF transmission line of JET because this value is expected to simplify component procurement. Water cooling of coaxial cables seems unnecessary from a preliminary analysis and decouplers are not foreseen, thus limiting TL cost. The latter choice prevents from doing ion-cyclotron current drive, which is not a physics requirement of the ICRH system of DTT at this stage. A schematic representation of the transmission line and its components is depicted in Fig. IX.4.

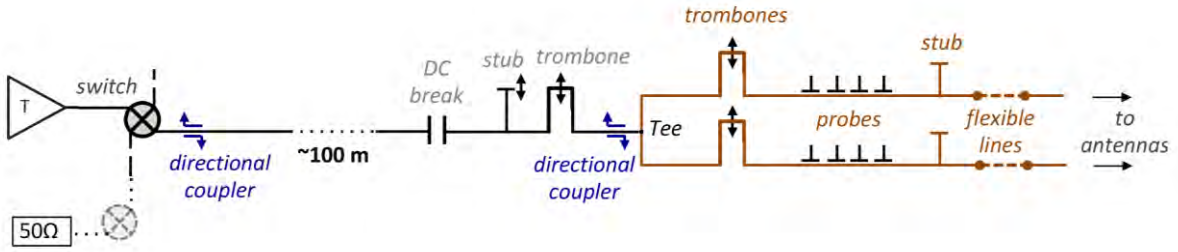

Figure IX.4: Transmission line and components from the transmitter (T) to the antenna feeders. Black and orange lines indicate Z_0 = 50 and 30 Ω, respectively.

Many antenna concepts, mostly based on existing couplers with documented performance, have been considered to identify the most suitable candidate for DTT. Several antenna designs have been optimised, in compliance with DTT constraints, running a time-domain commercial solver with some approximations like

flat geometry and seawater load in front of the antennas. The performances of optimized models have been simulated with TOPICA [IX.5] in the full-power single-null scenario of DTT, assuming a conservative value of decay length of 4 mm for the kinetic profiles in the scrape-off layer. Simulations showed that the movable antenna can couples 1.5 MW to the plasma, therefore the choice has to be restricted among movable launcher concepts. Due to the dimensions of DTT port, bumper tiles will be internally mounted on the First Wall (FW) with a remote handling system, so that, despite movable, the antenna cannot be smoothly plugged in. A distance of 3 cm from the Last Close Magnetic Surface (LCMS) has been considered. The heat load due to irradiation can be considered almost constant from the separatrix to the first wall and of the order of 0.5 MW/m^2. On the contrary, the decay length of the energy flux in the reference scenario is around 3 mm, so the fraction of heat load due to the energy flux is already negligible with the launcher pushed up to 1 cm from the LCMS. Nevertheless, some margin has been added due to phenomena like ELMs and runaway electrons, whose impact for a given antenna shift cannot be estimated yet. The power coupled to plasma depends on standoff voltage, whose value is still a topic of debate since different systems experienced different limits. A conservative value of 35 kV, compared to the 42 kV reached at JET and the design value of 45 kV for ITER, has been assumed for DTT.

The results of the following antenna candidates are reported in Fig. IX.5 along with launcher pictures:

- two folded straps and two feeders, similar to the 2-strap antenna of AUG [IX.6],
- two end-fed centre-grounded straps and four feeders, similar to the 2-strap antenna of EAST [IX.7],

The AUG-like antenna is the preferred choice because its two feeders imply a lower number of transmission lines than the EAST-like antenna and they simplify the connection to diacrode-based transmitters. On the other hand, cooling is troublesome, and this is the reason why the folded straps of existing systems are uncooled. Preliminary thermal simulations of strap heating in steady-state conditions due to RF losses and radiation from plasma suggest that four pipes may be required inside each conductor to avoid the embrittlement of strap material due to temperature increase. The EAST-like option, is thus considered in parallel as backup solution to face unexpected showstoppers coming from more detailed analyses or the choice of tetrode in place of diacrode as transmitter end-stage. The antenna front face will be shaped to match the plasma of the reference DTT scenario; a coupling deterioration in the case of different magnetic configuration is unavoidable and has not been quantified yet.

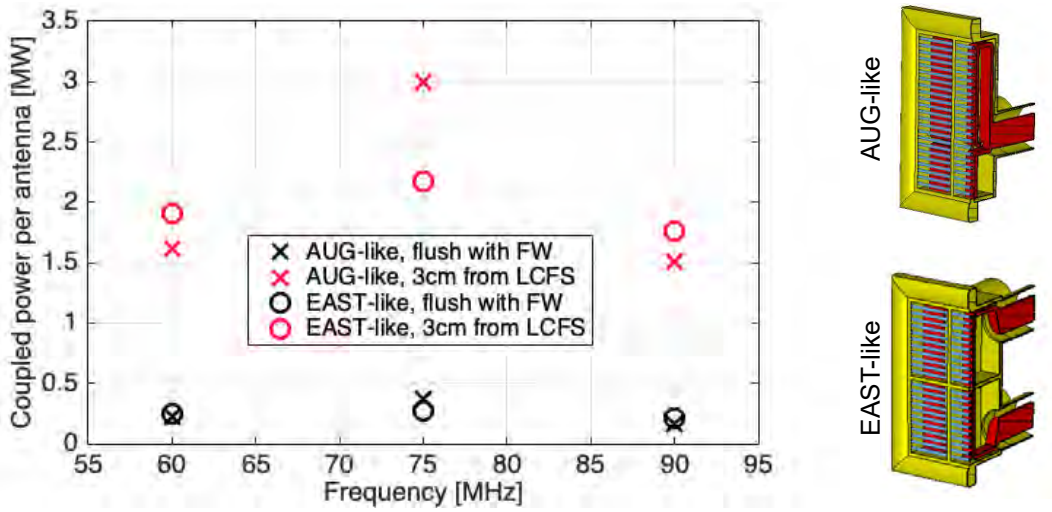

Figure IX.5: Power coupling capability of two antenna designs sketched aside, when they are flush with the First Wall (FW) or moved closer to the DTT full-power single-null plasma, assuming perfect matching and dipole phasing.

An innovative “equilibrium-resilient” antenna based on High Impedance Surfaces (HIS) would overcome some ICRH-specific issues like poor loading conditions and generation of high parallel electric fields. This concept has never been validated at high power. R&D activity, aimed at testing for the first time the power capability of such an antenna mock-up, is ongoing within a collaboration between ENEA and ASIPP. In case of successful validation, the HIS antenna concept would be adopted for DTT.

Concerning ion acceleration by parallel near E-fields, the RF potentials of both AUG-like and EAST-like antennas have been calculated, finding similar values, slightly higher than the reference AUG 2-strap antennas. The rather short decay lengths of DTT in the scrape-off layer should slightly alleviate this issue, however proper coating for antenna plasma-facing components, like boron, is mandatory to reduce the risk of contamination by ICRH-sputtered high-Z impurities, while screening techniques that prevent tungsten accumulation in the plasma core can provide further help.

Figure IX.6 shows two possible layouts of an ICRH module: the one is based on diacrodes and AUG-like antennas, the other on tetrodes and EAST-like antennas. In both cases, the realization can be accomplished during DTT construction timeline. The commissioning schedule of RF sources is tight but feasible, while risk mitigation strategies are considered for the development of vacuum feedthrough. Further would be added in case of upgrade of the system to a higher coupled power. Power supplies and transmitters will be installed in a single building that has to be selected yet between two options, whose distance from DTT hall is 85 m and 115 m, respectively. Coaxial cables will be arranged in a beam of tubes, allowing easy access for maintenance operations. The matching units will be placed right outside the DTT hall and each one will feed antennas ideally placed on opposite equatorial ports.

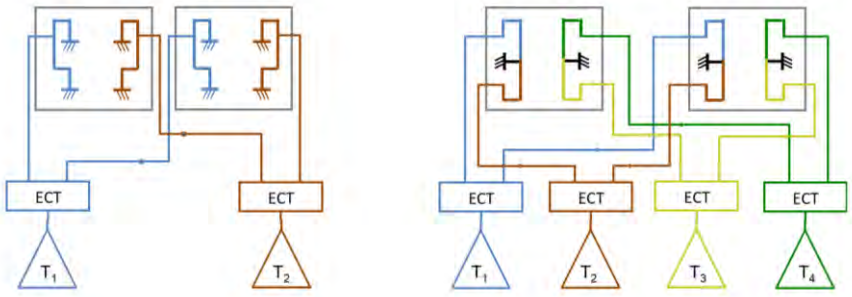

Figure IX.6: Layout of ICRH modules based on AUG-like (left) and EAST-like (right) antennas.

IX.3 ECRH Heating

The main guideline driving the ECRH project is to provide a compact and simplified design of the system, exploiting as far as possible the experience gained on the Electron Cyclotron systems of ITER [IX.8] and W7-X [IX.9-IX.10] and their mature technologies. The basic architecture consists of clusters of 8 gyrotrons fed by 4 Main high voltage Power Supplies (MPS) for the cathode and 8 for the Body Power Supply (BPS) plus the possible use of Anode Power Supplies (APS) in case of triode gyrotron. The 8 microwave beams are transmitted by an evacuated Quasi-Optical (QO) Multi-Beam Transmission Line (MBTL) and delivered to one DTT sector where 6 independent launching mirrors systems are located in one equatorial port (Port #3) and

2 are hosted in the corresponding upper port (Port #2). All the single launching lines are in principle identical with toroidal and poloidal steering angle capability. The upper port launcher is designed for real-time operations while the equatorial one could have less stringent requirements. The reference gyrotron adopted has requirements similar to those of the ITER tube, in order to minimize the risk and the cost of R&D. The gyrotron (1MW, 170GHz, 100s), based on depressed collector technology, should have an efficiency > 40% and a Gaussian output content > 95%. The overall coolant flow rate required is ~ 20 l/s per gyrotron. The magnetic field profile required by the gyrotron is maintained by a superconducting magnet based on cryogen-free technology, with a closed-cycle cryo-cooler and a cryo-compressor.

The power supplies are based on Solid State technology. One Main Power Supply, capable of 50-60 kV / 100 A, will feed two gyrotrons; a Body Power Supply for each tube with 30-40 kV / <1 A and eventually one Anode Power Supply is foreseen in case of triode gyrotron. Additional features are a power modulation capability up to 5 kHz and a real-time control of the gyrotron output power obtained through the anode and cathode voltage control to guarantee high reliability. The space necessary for 16 PSs is ~800 m^2 with a height of ~4 m and maximum weight foreseen of ~40 tons each.

The level of the Stray Magnetic Field (SMF) allowed by the gyrotron in both vertical and radial directions establishes the minimum distance among adjacent gyrotrons and their distance from the tokamak. The SMF has been calculated considering the contributions of plasma current I_P and of the currents in the central solenoid and in the six poloidal field coils. The requirements for gyrotron operation are $B_z < 1$ mT for the axial component and $B_R < 0.2$ mT for the radial component. The assessment of Bz and Br throughout the different phases of a reference DTT pulse (Single Null scenario with $I_P = 5.5$ MA) brings to a safe distance of about 50 m from the center of DTT tokamak and a mutual distance of 4.5 m among gyrotrons. Considering the distance requirement and the minimum space required for gyrotron hall that is ~ 24 m x 40 m x 15 m (height), the present proposal for the ECRH building is to modify the "F89" building increasing its dimensions (both area and height), as shown in Fig. IX.7.

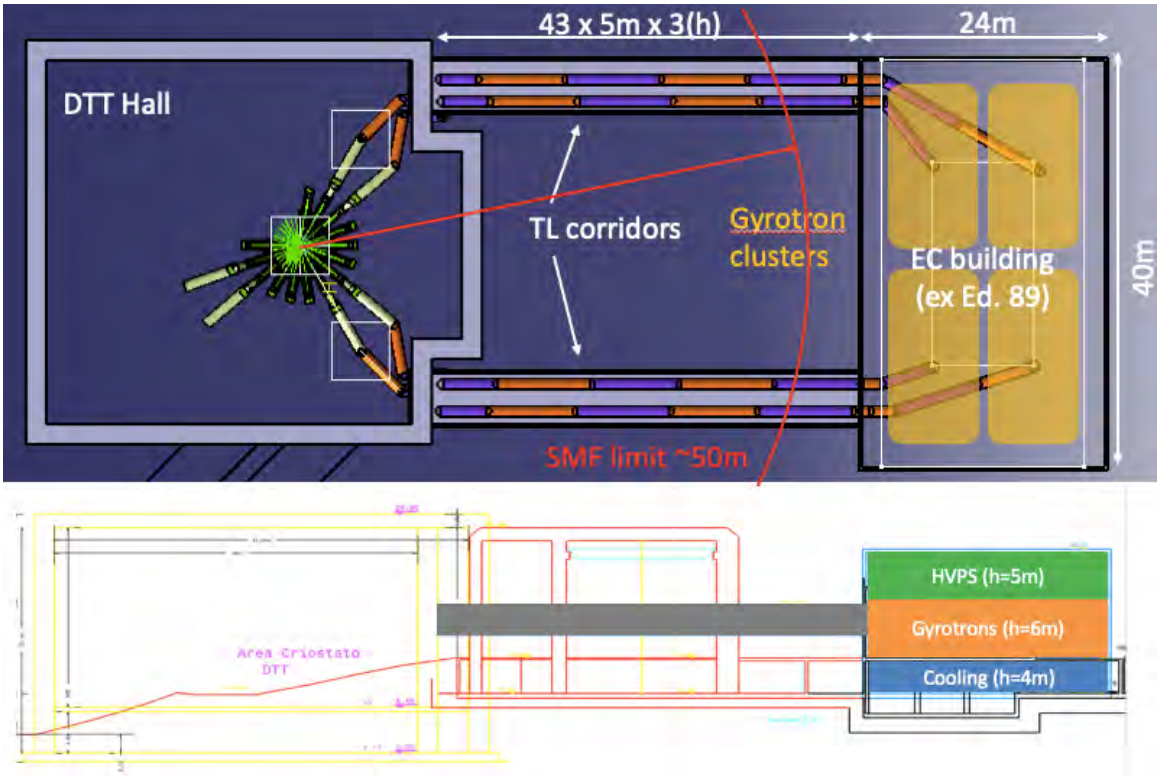

Figure IX.7: Preliminary CAD schematic layout for the EC system design.

The request is to have a three levels building with the cooling systems at level 0, the gyrotrons at level 1 and the Power Supplies at level 2. The EC building is connected to the DTT Hall through two 5 m x 3 m (height) straight corridors 43 m long hosting 2 MBTLs each one. The corridors are located ~5 m over the DTT equatorial level. In the present design the EC system is connected to the DTT sectors numbered 3, 4, 16 and 17 through port #2 and port #3. A further solution using sectors numbered 2, 3, 17 and 18 is under evaluation to improve the neutron shielding in crossing the DTT hall wall by the MBTLs (Fig. IX.7).

The target efficiency for the Transmission Line (TL) is > 90% with a power handling of 1 MW or more. Considering the large number of single beams (32÷40 accordingly to Tab. IX.I) the MBTL concept is envisaged, for its compact arrangement and simplicity, reduced required volumes and number of components. The design exploits QO propagation and is based on large confocal mirrors layout with up to 8 single beams (corresponding to one EC cluster) on the same optical surface. The single TL module consists of a straight path and a dogleg with a couple of planes and shaping mirrors for beams refocusing. The 8 beams of each EC cluster propagate alternatively crossing or parallel to each other between two MBTL modules. The present reference QO transmission line for each EC cluster consists of a shaping mirror after the Matching Optic Unit of the gyrotron, a polarizer mirror (to match the polarization at the entrance of the MBTL) and a mirror to reach the collector composed by 8 mirrors (one for each beam), that directs the beams towards the first large mirror of the MBTL. Large mirrors (MBTL units) transmit the beams into the tokamak hall where a splitter (i.e. a collection of 8 mirrors) separates the bundle into 8 single beams. Then, after reflection from a shaping mirror, two real-time controlled polarizers mirrors set the final polarization of the wave (see Fig. IX.8). The crossing of the back plate of the port is done using a short section of corrugated Wave-Guides (WG) (63.5 mm diameter) where a gate valve is placed to separate the vacuum of the machine from the MBTL. The WG realizes the input waist of the beam and is part of the launcher (Fig. IX.9).

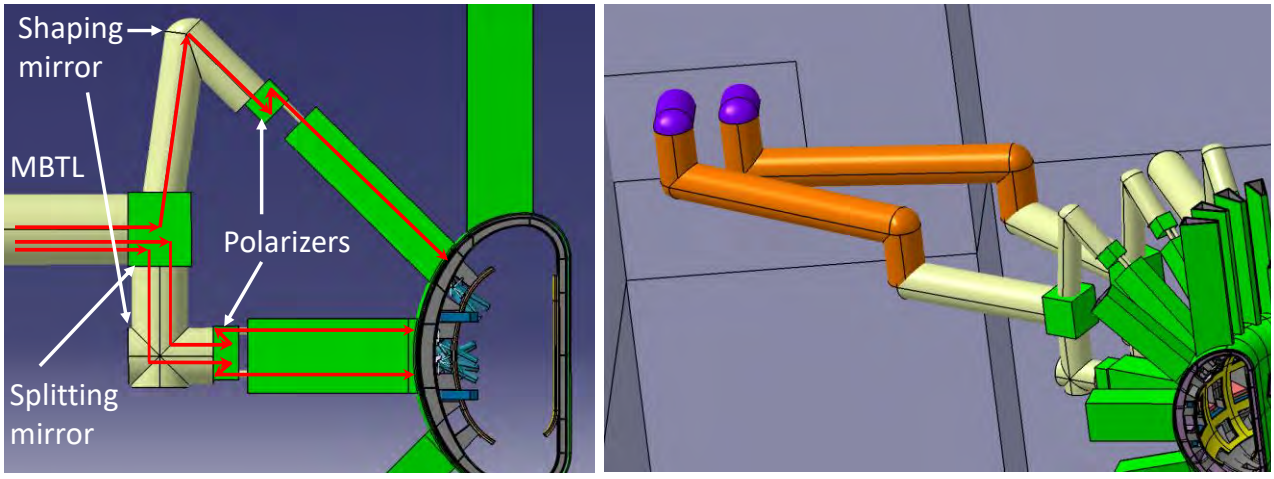

Figure IX.8: Preliminary TL schematic CAD design.

A study to validate the feasibility of the MBTL concept has been done considering a single circular focusing mirror with 8 overlapping beams organized on vertices of a regular heptagon and the eighth in the center. In designing the mirror, the guideline is to find a reasonable trade-off between the radius of a Multi Beam (MB) mirror and the distance between two focusing mirrors according to the system constraints, either technical or due to the building layout. At the present status of the design we have selected a distance of 10 m between two focusing mirrors: the minimum mirror diameter results therefore ~0.8 m. The total number of the TL mirrors depends clearly on the distance between the tokamak and the gyrotron hall but also on the number

of direction changes to be used in the routing. A preliminary loss calculation has been realized according to the routing proposed and summarized in Tab. IX.III.

TABLE IX.III. MBTL LOSSES PRELIMINARY ANALYSIS

Sector #	Confocal mirror	Plane mirror	Favourable polarization	Unfavourable polarization	Losses [%]	Losses [kW]
3	8	9	9	8	10.5	840
4	9	10	9	10	11.5	915
16	9	10	9	10	11.5	915
17	8	9	9	8	10.5	840
TOTAL	**34**	**38**	**36**	**36**		**3510**

The incident wave polarization on the mirror can be appropriately chosen to further decrease the power losses. In the ohmic case calculation the smallest loss contribution has been assigned to the MBTL path (supposing to maintain the same incident polarization along the mandatory straight MBTL path) whereas the contribution of other mirrors has been considered the largest one. Other loss contributions as beam truncation effects, mode conversion efficiency and misalignments will be object of future analysis. The mirror is supposed to be in aluminium to reduce cost and weight: the use of copper on the surface slightly decreases the losses since the ohmic absorption depends on the material resistivity. To minimize surface deformations due to thermal loads, the mirrors will be cooled. The 8 beams of each cluster will be connected to 8 independent launching mirrors, 6 in an equatorial port and 2 in an upper port of the same sector.

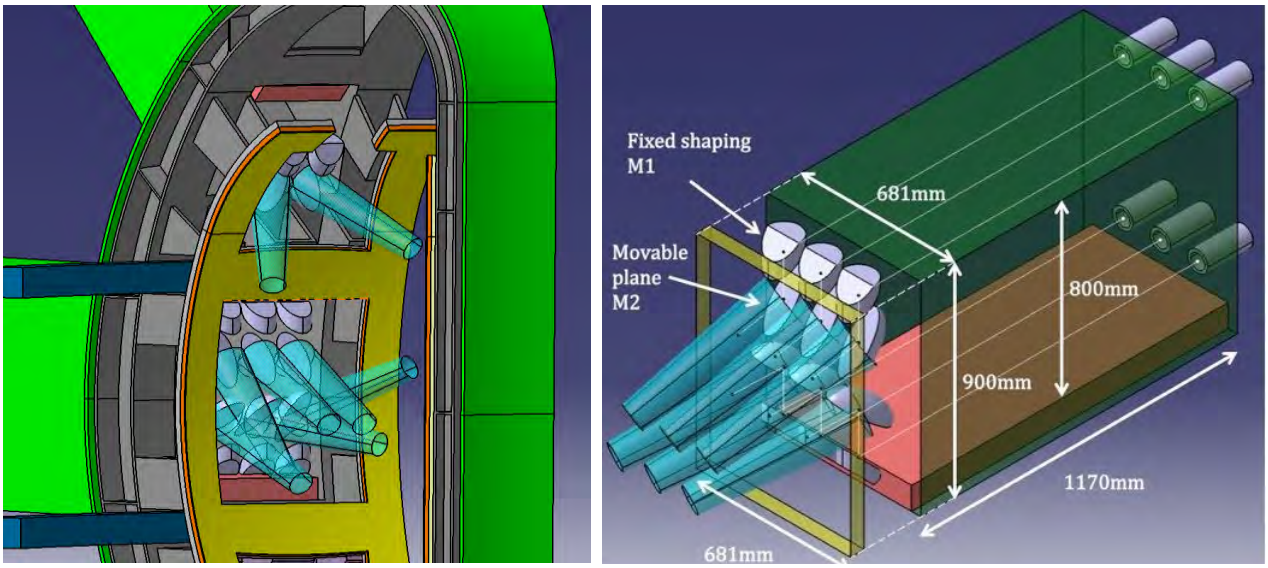

8

Figure IX.9: Preliminary CAD design of the EC launchers.

Both launchers are based on the front steering concept with two mirrors for each line, the first shaping (fixed) and the other one, faced to the plasma, plane and movable. The mirror dimensions are respectively 196 mm x 210 mm and 264 mm x 138 mm, compatible with a beam radius of 46 mm on the shaping mirror. The upper

launcher is real-time controlled, dedicated to the MHD activity and the equatorial launcher is also movable for main heating and other tasks (see Fig. IX.9). The design and the manufacturing of the launchers are under evaluation as well as the choice of the materials for the bulk (CuCrZr, Al and Mg alloys) and the coating (electroplating on all surfaces in contact with water for non-Cu materials). The mirrors are cooled with water (v_{H2O} ~ 1 m/s, channel width ~5-7 mm) and linear/rotary piezoelectric actuators are presently considered for their movement. The same plug-in structure is foreseen for all equatorial launchers and one similar for all the upper launchers to simplify design and construction phases and to increase the maintainability.

A first assessment of the EC wave absorption and Current Drive (CD) capabilities has been performed with the beam-tracing code GRAY [IX.11] on reference scenario calculated by the METIS code. For full-power scenario (B_T = 6 T, I_P = 5.5 MA, T_{e0} = 13 keV, n_{e0} = 2.1·10^{20} m^{-3}, Z_{eff} = 1.7) the results in terms of driven current are presented in Fig. IX.10 as a function of normalized toroidal radius ρ, for 170 GHz O-mode wave injection from the nominal position of the upper (R = 2.86 m, z = 0.97 m) and equatorial (R = 3.07 m, z = -0.08 m) launchers' steering mirrors (left and bottom-central mirror respectively). Complete absorption can be achieved in the full 0.2 < ρ < 0.8 range for both launchers. Maximum current drive, of the order of I_{CD}/P_0 ≈ 15-20 kA/MW, is achieved in the central region 0.2 < ρ < 0.4 for 15º ≤ |β| ≤ 20º. At mid radius, 0.4 < ρ < 0.6, maximum CD is obtained at larger toroidal angles, with small variations in the 20º ≤ |β| ≤ 30º range. Current Drive at the q = 3/2 and q = 2 rational surfaces (ρ = 0.75 and ρ = 0.88 respectively) for NTM control is better performed from the Upper Launcher (UL). At such outer radii CD from the UL is maximized already at |β| ≈ 10÷15º. The CD efficiency at the q = 3/2 and at q = 2 location is comparable for the two launchers (I_{CD}/P_0 ≈ 5 kA/MW at q = 3/2). However the upper launcher is preferable for NTM stabilization for two main reasons: the beam enters more perpendicular to the flux surfaces reducing refraction effects and the smaller toroidal angle and shorter distance between the launch point and the target allows for narrower current density profiles.

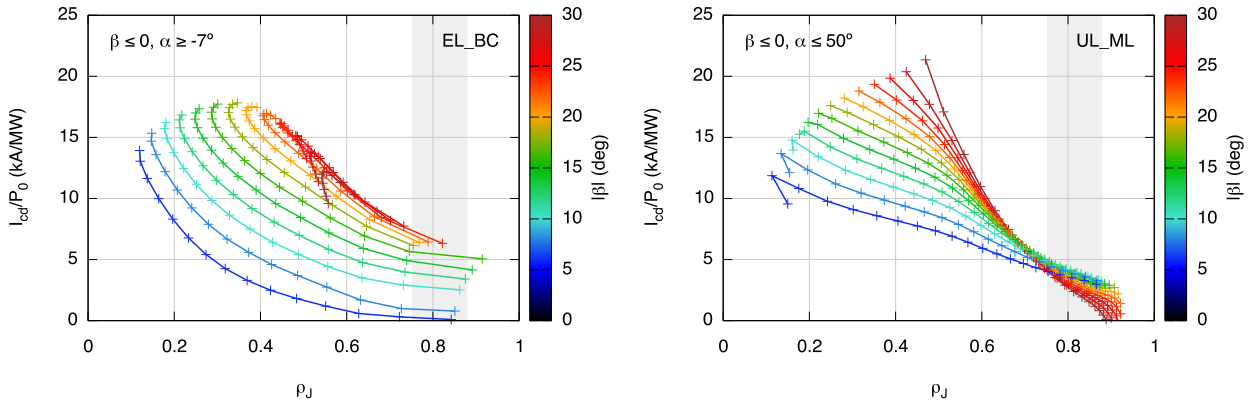

Figure IX.10: Total driven current I_{CD} with 170 GHz O-mode wave injection from the equatorial bottom (left) and upper (right) launchers, as a function of normalized driven current density profile location ρ_J. Color code identifies the toroidal injection angle β and the shaded region identifies the radial range between q=3/2 (ρ=0.75) and q=2 (ρ=0.88). Results are shown for the full-power reference scenario (B_T=6T, I_P=5.5MA, T_{e0}=13keV, n_{e0}=2.1 10^{20} m^{-3}, Z_{eff}=1.7).

A further task for the EC system is to assist plasma start-up. A preliminary assessment of the power required has been made by BKD0 [IX.12] code. The simulations show that with EC power at fundamental resonance (up to 2 MW) is possible to increase of a factor 4 the upper limit of the D_2 neutral pressure (ranging from 2.5 to 10 mPa) at E_{TOR} = 0.8 V/m which is envisaged on DTT using the Switching Network Unit (SNU).

IX.4 NBI Heating

IX.4.1 Beam particle energy and injection parameters

The primary goal of the Neutral Beam Injector (NBI) system is to reliably provide central plasma heating during the flat-top phase of the plasma discharge. The risk of shine-through of the neutral beam must be minimized and for this reason its use during early current ramp-up, late current ramp-down and low current scenarios must be carefully evaluated, to be accounted for in operation requirements. In addition to plasma heating, the NBI system can provide current drive capability.

An NBI system based on the acceleration of positive ions would inject efficiently particles into the plasma with energies in the order of 80-120 keV. This energy, given the high density expected for the DTT, would lead to a too peripheral power deposition. In order to heat particles in the core, a negative-ion-based NBI system at higher energies (E > 300 keV) is then proposed. Presently a 400 keV energy is considered as the most interesting value, representing a good compromise among costs, dimensions and performances. Moreover, the adoption of two acceleration stages would give the same voltage gap per acceleration stage (200 kV) of the ITER NBI [IX.13] thus allowing to exploit the advanced R&D carried out during the last years for the ITER NBI. This value (400 keV) will be considered as the reference one for the calculations described in the next paragraphs.

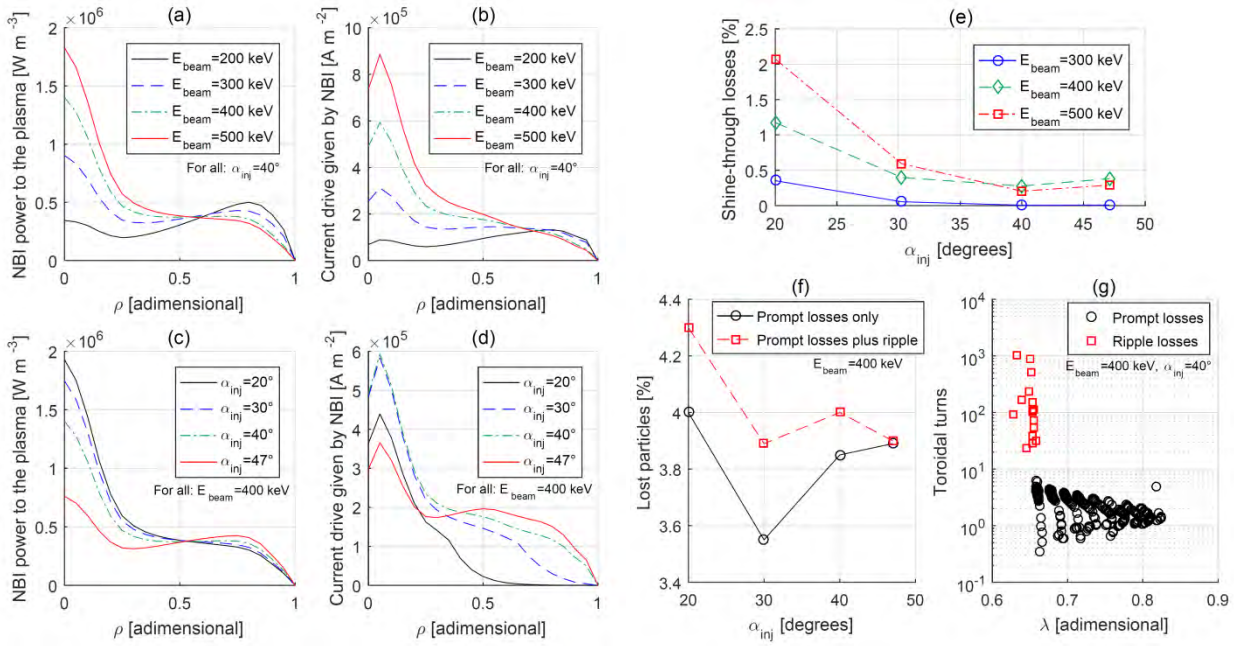

Figure IX.11: Main physics parameters leading the design, evaluated using the METIS and ORBIT codes: (a) NBI power released to the plasma as a function of beam energy E_{beam}, where ρ is the normalized toroidal flux (i.e. 0 means plasma core and 1 means last closed flux surface, i.e. plasma edge); (b) current drive released by the NBI as a function of E_{beam}; (c) NBI power as a function of injection angle α_{inj} at 400 keV; (d) current drive as a function of α_{inj} at 400 keV; (e) shine-through losses as a function of α_{inj} and E_{beam}; (f) fraction of prompt losses (black) and same quantity plus ripple losses (red) as a function of α_{inj}; (g) toroidal turns travelled by the particles before being lost, as a function of the pitch parameter λ. α_{inj} is defined as the angle between the beam axis and the radial direction at the first wall, as shown in Fig. IX.11a.

Evaluations with physics codes have been carried out to critically assess the choice of the most suitable beam

energy and injection angle. A set of simulations has been carried out using the fast tokamak simulator METIS, considering the reference single null scenario with two injectors [IX.14]. These simulations show that 400 keV beam energy allows central heating with enough beam penetration and suitable current drive (see Fig. IX.11a and b), while large injection angles give a wider heating distribution (see Fig. IX.11c and d) decreasing at the same time the shine-through losses (see Fig. IX.11e). The considered injection angle is the one evaluated at the first wall, as shown in Fig. IX.12a.

The losses of fast ions in presence of toroidal field magnetic ripple is another issue to face when designing a high-energy NBI system [IX.13]. The expected fraction of lost fast ions (monoenergetic and collisionless) has been calculated with the guiding-center ORBIT code [IX.15] using as input the single-null equilibrium for DTT (with ripple) and the initial fast ion positions calculated with METIS. The result is ~4% of losses for energy E_{beam} = 400 keV and tangency radius R_t = 1.77 m (corresponding to an injection angle α_{inj} ~ 40°), as shown in Fig. IX.11f. These losses can be divided in prompt losses (ions lost in less than 10 toroidal turns, black) and ripple losses (red trace, loss time > 10 turns). The contribution of ripple losses, which is due entirely to trapped particles, is rather modest (~0.5%) and decreases with the injection angle. To see this, one can plot the loss time, expressed in toroidal turns, as a function of the pitch parameter $\lambda = v_{//}/v$: while prompt losses are insensitive to pitch, ripple losses are localized at λ ~ 0.65, corresponding to particles injected with α_{inj} ~ 40° (see Fig. IX.11g). These results indicate that a resonance between trapped ion precession and ripple periodicity occurs. This is a collisionless mechanism that can determine the rapid loss of all high-energy, trapped ions [IX.16]: for this reason, for a beam energy of around 400 keV it is safer to design the beamline with an injection angle $\alpha_{inj} \geq 40°$. Given these results and the previous favorable shine-through evaluations, the energy of 400 keV seemed favorable and the injection angle was increased up to the mechanical limit (considering the presence of the toroidal field coils) of 42.4° of injection angle at the first wall (angle defined as in Fig. IX.12a). This angle corresponds to an angle of 30° measured with the radial direction at the vacuum vessel.

The physics evaluations have been carried out for the specific configuration of the single null; nevertheless, preliminary calculations with METIS have shown that the results are similar considering other configurations as double null and snowflakes. A physics validation of the alternative plasma scenarios is ongoing.

IX.4.2 Development of the injectors conceptual design

The conceptual design has been developed starting from the above physics requirements, and considering as main guidelines the maximization of flexibility, feasibility, RAMI and efficiency, and the minimization of cost and weight. The main components of the injector, shown in Fig. IX.12, are: a beam source (composed of an ion source and an accelerator), three Beam Line Components (BLC, i.e. a neutralizer, a residual ion dump and a calorimeter), an absolute gate valve and a duct to connect the injector to the vacuum vessel. As for the NBIs of JT60 [IX.17] and LHD [IX.18], a design with an air-insulated beam source is proposed, to reduce the vacuum volume, increase the source accessibility and avoid the need of a single large bushing to connect the Transmission Line to the vacuum vessel. A drawback of this solution is the required clearance between the ion source and the surrounding building structures (at least 2 m, to avoid electrical discharges). The DTT design differs from the Japanese scheme in the choice of the ion source: in fact, it is proposed to use the same Radio Frequency source concept adopted for ITER, developed by IPP Garching [IX.19]. BLC will be ITER-like too, while the vacuum vessel will be without large flanges (differently from ITER) to reduce cost and weight. Only small flanges are foreseen for pumping, diagnostics and BLC supplies, while the BLC maintenance is planned to be from behind, by removing the beam source. For the vacuum pumping, it is foreseen to have a hybrid system featuring both Non-Evaporable Getter (NEG) pumps and cryopumps.

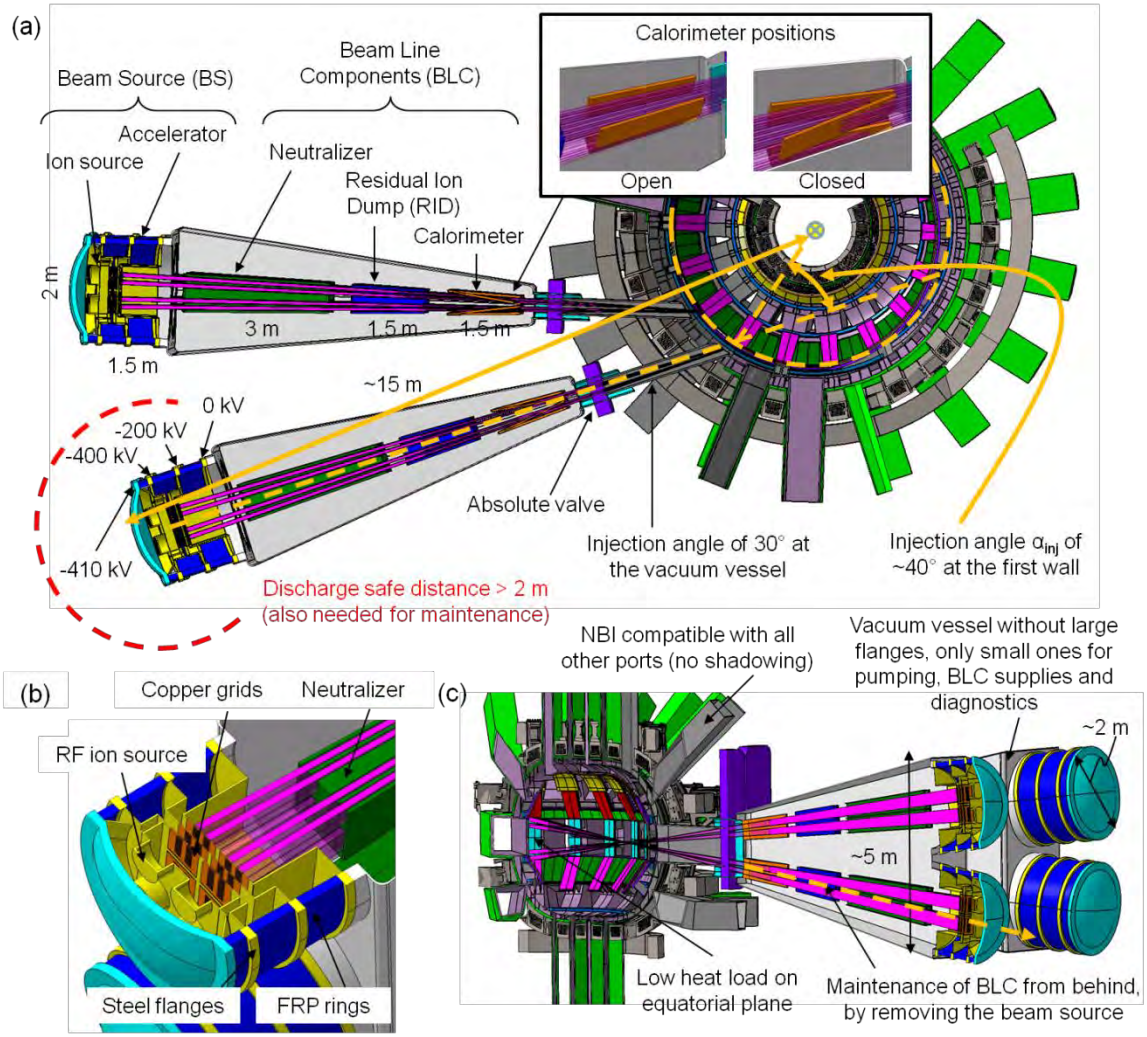

Figure IX.12: Conceptual design of the DTT NBI conceptual design with main dimensions: (a) view from top; (b) horizontal section view; (c) vertical section view.

The accelerator grids represent a critical component as they have a rather complex design, with very small cooling channels, apertures for the negative ions and grooves for the embedded magnets. They can be manufactured by means of copper electrodeposition on a milled base plate made of pure copper [IX.20]. As this is a complex manufacturing process, the possibility to manufacture the grids by additive manufacturing is currently being investigated. Another critical R&D program is proposed to develop and validate a manufacturing process for the Fiber-Reinforced Polymer (FRP) rings of the accelerator. In fact, these rings are quite large (diameter of 2 m and length of 0.5 m) and must fulfill several important functions, i.e. to maintain the electrical insulation between the acceleration stages, and to support the beam source while being perfectly leak tight and having a vacuum compatible surface on the internal side.

IX.4.3 Power Supplies

The NBI power supplies are composed of the following subsystems: Acceleration Grid Power Supply (AGPS, to feed the acceleration grids), Ion Source and Extraction Power Supply (ISEPS, to feed all the ion source

loads) and Ground Related Power Supply (GRPS, to feed the Residual Ion Dump and the correction coils to compensate the stray fields, if any).

The AGPS has to provide up to 400 kV on the two acceleration stages (200 kV each), with an output current up to about 60 A. A specific requirement for this application is the capability to switch-off the voltage generation in some tens of μs in case of grid voltage breakdown, to limit the energy delivered to the acceleration grids. For the AGPS, a solution similar to that adopted for the ITER NBI prototype, MITICA, could be envisaged [IX.21]. This would foresee one or two step-down transformers fed by Medium Voltage (MV) network, an AC/DC rectifier, a DC-link capacitor bank and two DC/AC inverters (instead of five installed in MITICA). Each inverter would fed a step-up transformer, to which is connected a High-Voltage (HV) full-bridge diode rectifier insulated with SF_6. These rectifiers are connected in series to provide the full voltage, and to a DC-filter tank containing HV resistors and capacitors to reduce the voltage ripple. Once filtered, the voltage is transmitted to the accelerator through a SF_6-insulated Transmission Line. This scheme is represented in Fig. IX.13.

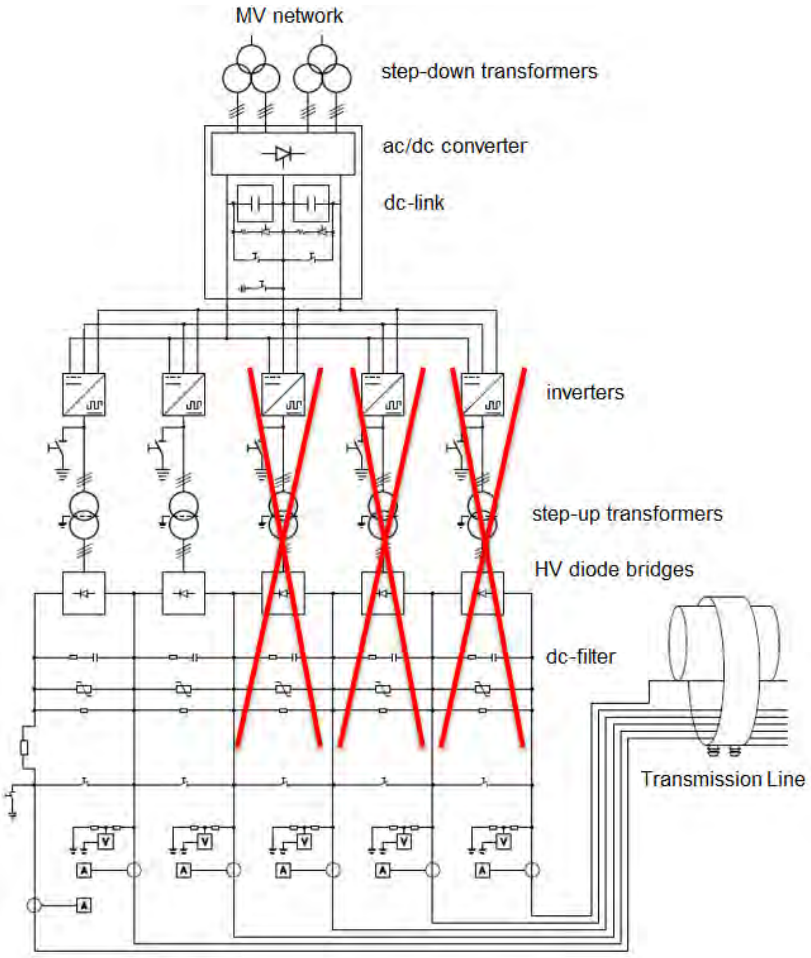

Figure IX.13: MITICA-like scheme of the DTT NBI Acceleration Grid Power Supply. Only two 200 kV generation stages are necessary for DTT. Crossed line are put over the components foreseen in MITICA but not needed for DTT.

The technology of the HV SF_6-insulated diodes bridges probably is not available in Europe, and this could represent an issue for the DTT application. In addition, possible improvements of the AGPS scheme adopted

in MITICA/ITER could be explored. In particular, the double conversion from AC to DC and vice-versa could be avoided, reducing the power losses. In addition, being the HV components in MITICA AGPS fully passive, there is no direct control on the DC-filter energy transferred to breakdowns and the voltage dynamics is limited by the step-up transformer frequency. The situation could be improved by adopting an alternative solution based on Modular Multilevel Converter (MMC) topology [IX.22].

The MMC scheme would include one or two step-up transformers, connected to MV network, feeding one AC/DC conversion stage composed of many air-insulated switching power modules connected in series. This HV conversion stage would fed directly the accelerator, providing the two required voltage steps and realizing also a fast voltage control. The MMC topology is largely adopted in HV DC transmission systems, due to its high efficiency, modularity and controllability, and it is available in Europe. Its main disadvantage is the increasing of building volume, due to the large clearances to be kept with respect to building walls. Verifications are in progress with industry to verify the compatibility with the present building area.

The main power supplies composing ISEPS are the Extraction Grid Power Supply (EGPS) and the RF Power Supply (RFPS). The first one feeds the two extraction grids of the NBI and could provide two different voltages to achieve the highest flexibility. The maximum output voltage is about 10 kV and the maximum current is about 70 A for each load. The RFPS is composed of four RF generators, each feeding a couple of RF drivers of the beam source with a maximum power in the order of 200 kW at 1 MHz, like in SPIDER (experiment dedicated to the ion source for ITER NBI) and MITICA. While in the Neutral Beam Test Facility (NBTF) the RF generators are tetrode-based auto-oscillators, for DTT a solid-state solution is advisable, mostly to avoid the multiple resonances due to the interference between matching network and generator, which cause frequency flips and reduced power transferred to the load, as recently found experimentally [IX.23]. Solid-state generators can be also more efficient, modular and redundant with respect to the tetrode-based solution. Industry seems interested in developing products for this promising market. Being the ion source referred to the AGPS potential, ISEPS shall be installed inside a High Voltage Deck (HVD) insulated in air for 400 kV with respect to the ground. The area of this HVD will be similar of that of SPIDER (143 m^2). ISEPS will feed the ion source loads through a set of feeders and RF lines contained in the inner conductor of the TL; the connection between the TL and the HVD is through an HV SF_6-air bushing. ISEPS will be fed through an insulating transformer, which could be connected to the HVD in air or through the TL. In the latter case, this transformer could be located outdoor, to save space in the buildings.

IX.5 Conclusions

The DTT Heating system will be based on consolidated technology as the main R&D effort will be devoted to the divertor design and construction. The additional power will be delivered to DTT with the highest reliability exploiting all the experience gained in the present and near future fusion device (ITER). The real step forward with respect to the present tokamak will be to transform experimental systems in robust and well controlled part of a tokamak plant, as it is for instance the poloidal magnetic field system. The ITER experience will be largely exploited by the use for the ERHC of the same 170 GHz / 1 MW gyrotron and in the NBI system that is a simplification of the MITICA injector. No development activity is foreseen in the main components of the systems apart the coupling. A major effort will be devoted in the coupling systems: a wide range ECRH front steering launcher and a movable ICRH antenna to cope with the various DTT scenarios. The goal for the DTT

heating system is to have the high reliability of the 45 MW necessary to perform the test of the divertor in reactor relevant conditions.

IX.6 References

[IX.1] M. Brambilla, Numerical simulation of ion cyclotron waves in tokamak plasmas, Plasma Phys. Control. Fusion 41 (1999), 1.

[IX.2] J.F. Artaud et al., Metis: a fast integrated tokamak modelling tool for scenario design, Nuclear Fusion 58 (2018) 105001.

[IX.3] M. Brambilla, Quasi-linear ion distribution function during ion cyclotron heating in tokamaks, Nuclear Fusion 34 (1994), 1121.

[IX.4] M Graham et al., Implementation of load resilient ion cyclotron resonant frequency (ICRF) systems to couple high levels of ICRF power to ELMy H-mode plasmas in JET, Plasma Phys. Control. Fusion 54 (2012), 074011.

[IX.5] V. Lancellotti et al., TOPICA: an accurate and efficient numerical tool for analysis and design of ICRF antennas, Nuclear Fusion 46 (2006), S476-S499.

[IX.6] J.-M. Noterdaeme et al., The ASDEX Upgrade ICRH antenna, Fusion Eng. Des. 24 (1994) 65-74.

[IX.7] Y.P. Zhao et al., EAST ion cyclotron resonance heating system for long pulse operation, Fusion Eng. Des. 89 (2014) 2642–2646.

[IX.8] M. Henderson et al., The targeted heating and current drive applications for the ITER electron cyclotron system, Physics of Plasmas 22 (2015) 021808.

[IX.9] V. Erckmann et al., Electron cyclotron heating for W7-X: physics and technology, Fusion Science and Technology 52 (2) (2007) 291-312.

[IX.10] H. Laqua et al., Overview of W7-X ECRH Results in OP1.2a, EPJ web of Conference 187 (2018) 01011.

[IX.11] D. Farina, A Quasi-Optical Beam-Tracing Code for Electron Cyclotron Absorption and Current Drive: GRAY, Fusion Science and Technology 52 (2) (2007) 154-160.

[IX.12] D. Ricci, Operational parameters for EC assisted start-up in ITER, Proceedings of 43° EPS (2016) ECA vol. 40A O5.130.

[IX.13] P. Agostinetti, et al., Detailed design optimization of the MITICA negative ion accelerator in view of the ITER NBI, Nucl. Fusion 56 (2016) 016015.

[IX.14] M. Vallar, et al., “Integrated physical assessment of DTT reference scenarios”, MFP-19 2nd Asia-Pacific Conference on Plasma Physics, 12-17,11.2018, Kanazawa, Japan

[IX.15] R. B. White, et al., in Fusion Energy Conference (Proc. 12th Int. Conf. Nice, France, 12-19 October 1988), vol. 2 (1988) 111.

[IX.16] R. B. White and M. S. Chance, Hamiltonian guiding center drift orbit calculation for plasmas of arbitrary cross section, The Physics of Fluids, vol. 27, no. 10 (1984), 2455-2467.

[IX.17] R. B. White, Chaos in trapped particle orbits, Phys. Rev. E, vol. 58 (1998) 1774-1779.

[IX.18] A. Kojima et al., Progress in long-pulse production of powerful negative ion beams for JT-60SA and ITER, Nucl. Fusion 55 (2015) 063006.

[IX.19] Y. Takeiri et al., High Performance of Neutral Beam Injectors for extension of LHD operational regime, Fusion Science and Technology 58 (2010) 482.

[IX.20] B. Heinemann et al., Latest achievements of the negative ion beam test facility ELISE, Fusion Eng. Des. (2018), Fusion Eng. Des., 136 (2018) 569.

[IX.21] P. Agostinetti, et al., Manufacturing and testing of grid prototypes for the ITER neutral beam injectors IEEE Trans. Plasma Sci. 42 (2014) 628.

[IX.22] V. Toigo, et al., Progress of the ITER NBI acceleration grid power supply reference design, Fusion Eng. Des., 88 (2013) 956.

[IX.23] F. Gasparini, et al., Investigation on stable operational regions for SPIDER RF oscillators, Fusion Eng. Des., in press.

Chapter X

DIAGNOSTICS, DATA ACQUISITION AND REAL TIME CONTROL

X.1 Introduction

In order to achieve its mission of finding viable solutions for the power exhaust issue in view of DEMO, DTT is to be equipped with diagnostic tools that can qualify the particle and heat fluxes through the plasma edge and control systems that may preserve both the integrity of the plasma facing components and the quality of the plasma performance. The broad range of measurements targeted on present day tokamaks is going to be largely relevant also for DTT. However, the overall duration of the plasma pulse around 100 seconds and the ten-fold increase of neutron flux, expected to be in the $10^{17}s^{-1}$ range (see Chapter X.3), will pose new challenges for achieving the desirable coverage with adequate space and time resolution [X.1]. The use of fibre optics in the port proximity, for instance, may be impaired and those instruments viewing the plasma with direct line-of-sights will have to be engineered in order to withstand high heat and neutron fluxes. Stray radiation from injected electron cyclotron waves will represent an additional source of heat for in-vessel diagnostics systems and therefore a constraint for the material selection of the in-vessel components.

Most of the mid-plane ports will be occupied by auxiliary heating and therefore multiple instruments will have to be integrated into a few accesses, sharing the space also with other technical equipment such as electrical cables and cooling fluids piping.

Pedestal and divertor regions are to be particularly addressed but an adequate diagnostic coverage of the main plasma is also necessary to assess the quality of the confinement and the divertor efficiency in compressing He and other impurities.

In this chapter, diagnostics, data acquisition and control infrastructure foreseen on DTT are described. Sensors, actuators, models and communication infrastructures are conceived in an integrated way in order to assure that the many interlaced functions of a complex fusion device, such as plasma control, machine-protection and safety, are fulfilled simultaneously.

Redundancy and/or possibility of maintenance my means of remote handling is foreseen for in-vessel diagnostics systems. DEMO relevant ways to control the plasma, that is with a minimal amount of direct measurements of the plasma parameters, will be experimented by relying more and more on physics and engineering models driven controls [X.2].

In section X.2, the set of diagnostics systems is described, mainly in terms of their functionalities and their main specifications. A set of fundamental diagnostics has been selected for both the development of the scientific basis of the experiment, the protection of the machine and the stable operation of the discharge under robust real time control. Section X.3 describes in more details some of the situations where feedback control will be necessary. The architecture of systems and subsystems used to collectively manage in an automated way the safe operation of the DTT device is implemented using a technology borrowed from the ITER experience and is described in section X.4.

X.2 Diagnostics

The main DTT diagnostics are listed in Tabs. X.I-X.VI grouped according to the parameters to be measured. A brief description of the most relevant diagnostic systems follows.

X.2.1 Magnetic probes

Magnetic probes inside the vessel must withstand large temperature excursions being located between the first wall and the vacuum vessel. A preliminary analysis has established that redundant sets of around 35 biaxial pick up coils poloidally distributed inside the vessel, in six toroidal positions, can measure the plasma current and its radial and vertical position with less than 1 % and 1 cm error respectively. The same sets are replicated by ex-vessel biaxial pick up coils that should withstand large thermal gradients in the cryostat. The ratio of outer to inner “equivalent area” (NA) factors of the pick up coils should be about 3. Biaxial coils of Mineral Insulated Cables (MIC) on Macor former appear to be suitable to fit the narrow space between first wall and vessel on the high field side, while ex-vessel pick up coils shall be based on coated Cu wire on a Torlon plastic former. More compact and higher bandwidth sensors based on Low-Temperature co-fired Ceramics (LTCC) technology will be adopted in order to measure dB/dt fluctuations. Non-integrated magnetic field and current measurements are also foreseen to calibrate standard probes, such as Radiation Hard Hall probes and optic fibre plasma current measurements. Halo and eddy currents in the vessel and first wall will be diagnosed using current shunts and Rogosky coils to be placed in the first wall support structures, in the divertor structures, with equi-spaced arrays in toroidal direction. The design and manufacturing of magnetic sensors for DTT will in any case benefit from recent developments for ITER [X.3-X.4] and RFX-mod2 [X.5].

X.2.2 Plasma equilibrium and shape

Besides the standard magnetic measurements (probes and saddle coils) several diagnostics will be integrated in equilibrium reconstruction models to evaluate equilibrium and plasma shape including non-integrated magnetic diagnostics, the interferometer–polarimeter, Motional Stark Effect, reflectometer and CCD cameras. Here we describe in particular the interferometer polarimeter and the reflectometer.

TABLE X.I. MAIN MAGNETIC DIAGNOSTICS OF DTT (IN RED THOSE NECESSARY FOR THE FIRST PLASMA)

MEASUREMENT	METHOD	FEATURES	ΔT & ΔS
		Magnetic diagnostics	
Magnetic Flux	Flux saddle and diamagnetic loop		0.1 ms
Magnetic Field and dB/dt	Pick up coils, Hall probes, polarimeter	MIC, LTCC Technology, about 35 per poloidal section, in 6 sections	0.1 ms, 0.5 μs for fluctuations
Halo /Hiro Currents	Rogowski coils, Resistive shunts		0.1 ms
Plasma Current	Pick up coils, optic fibre measurement		0.1 ms
Te Core	ECE: O1 covers the full radial profile, X2 covers the LFS up to the centre	O mode (O1: 130<f<250 GHZ) and 2nd harmonics, X mode (X2: 260<f<380) detectable	1-2 cm FW @ 1/e , 0.1 ms
	Thomson scattering	Extended spatial coverage at the pedestal	10 cm -3 cm, 50 ms
Ne Core	Thomson scattering		. 10 cm -3 cm, 50 ms
Real Time Ne Core	MIR Interferometer/ FIR polarimeter	Few chords MIR, high resolution FIR, Internal optics, QCL lasers	0.1 ms, 1 cm – 10 cm
Ti	Crystal spectrometer	Ar for Te< 5 keV, Kr otherwise	20 cm, 10 ms
	CXRS	Dα and/or impurities o edge diagnostic beam	50 ms
Fast Ions	NPA		5 ms
	CXRS	Dα	10 ms
Escaping Fast Ion	Scintillator probes /FILD		1 ms
Ion Flow Plasma Core	Crystal spectrometer	Tangential view	
	CXRS	Dα on main heating beam and/or impurities o edge diagnostic beam	10 ms
Runaway electrons	Synchrotron radiation,	Co- and counter current views	10 ms
	Cherenkov probes	In three positions	
	HXR / γ-Rays	TBD	

TABLE X.II. MAIN NEUTRON AND γ DIAGNOSTICS OF DTT (IN RED THOSE NECESSARY FOR THE FIRST PLASMA)

MEASUREMENT	METHOD	FEATURES	ΔT & ΔS
		Neutrons and γ	
Neutron Yield	Fission chambers		1 ms
	TOF & γ spectrometers	Neutron and γ cameras can be integrated	1 s /0.1 ms DAY 1
Neutron emission profile	Neutron γ Camera	From low to high neutron yield ($1.3 \cdot 10^{17}$ n/s).	10 ms

TABLE X.III. MAIN CORE RADIATION DIAGNOSTICS OF DTT (IN RED THOSE NECESSARY FOR THE FIRST PLASMA)

MEASUREMENT	METHOD	FEATURES	ΔT & ΔS
		Core Radiation	
ECE	ECE radiometer (ECE, Electron Cyclotron Current Drive		0.1 ms
SXR profiles	SXR tomography	Multiple cameras	0.1 ms
SXR profiles	SXR GEM camera	Tangential imaging, energy resolved camera	0.2 3cm, kHz
Bolometer array	Metal foil /AXUV tomography	Multiple cameras	2 cm, 3 ms

TABLE X.IV. MAIN DTT DIAGNOSTICS FOR CORE IMPURITIES AND DILUTION (IN RED THOSE NEEDED FOR THE FIRST PLASMA)

MEASUREMENT	METHOD	FEATURES	ΔT & ΔS
		Core impurities and dilution, besides Bolometry and SXR cameras	
Zeff	Interference filters 5235.5 A	Tangential chords and viewing dumps to avoid reflections	0.1 ms
	Low resolution spectrometer	$1/\lambda^2$, Tangential chords and viewing dumps	0.2 - 10 ms
Line emission	VUV survey spectrometer	100-1200 A, space resolved	10 ms , 5-10 cm
	Laser blow off	Target layers	Multipulse
	XUV spectrometer	10-340 A	10ms
	Crystal Spectrometer	1-6 A	10 ms

TABLE X.V. MAIN DIVERTOR DIAGNOSTICS FOR DTT (IN RED THOSE NECESSARY FOR THE FIRST PLASMA)

MEASUREMENT	METHOD	FEATURES	ΔT & ΔS
		Divertor diagnostics	
Divertor Te	Thomson Scattering	Injection from bottom	< 1 cm, 10 ms
Compression/Enrichment	Spectroscopy	Ar, He Lines ratio	1 cm , <10 ms
	Langmuir probes, Electrostatic sensors		2 mm, 1 ms
	Penning gauge spectroscopy.	Magnetic Field screened	10 ms
Neutrals	Fast baratron	On	ms
	RGA		100ms
	Filtered CCD cameras		10 ms, 2 mm
	NPA(TOF)	Energy lower limit around 5 eV	5 ms
Divertor detatchment	Visible Survey spectrometer	Imaging mode	2 mm in imaging mode
	VUV/VIS/NIR (NIR, Near InfraRed) spectrum	Lyman, Balmer & Paschen series	10 ms, > 1 cm
	Filtered CCD	3D imaging software development	2 mm, 10 ms
Divertor Ti	Spectrometer	Emission line Doppler broadening, Zeeman Splitting to be considered	1 ms
	Heterodyne Doppler		3mm

TABLE X.VI. MAIN DTT DIAGNOSTICS FOR PLASMA WALL INTERACTION AND DISRUPTIONS (IN RED THOSE NECESSARY FOR THE FIRST PLASMA)

MEASUREMENT	METHOD	FEATURES	ΔT & ΔS
		Plasma wall interactions and disruptions	
Wall temperature	IR camera	Impact of redeposition layers	
	instrumented tiles	Thermocouples, Langmuir probes, over three sectors	
Vessel deformation	Strain sensors/optical sensors	TBD	
Wall Hot Spots	CCD monitor	Pattern recognition	1 mm
Ri-deposition layers	Microbalance	Environment compatibility	100 ms
Composition and fuel	Samples	Steady /On robotic arms	
	LIBS	On robotic arm	During shutdown / In between shots

Interferometer-polarimeter

Two interferometer-polarimeter systems are foreseen: a few channels mid infrared (MIR) 10 μm, 5 μm CO2/CO toroidal system and a higher spatial resolution poloidal far infrared (FIR) one. The MIR vibration compensation scheme successful in both FTU and RFX-mod devices provides the reliable real time measurement of the chord averaged electron density [X.6]. To strength the real time measurement the systems can provide density measurement also from the Cotton-Mouton effect which is free from fringe jumps errors. The multi-chord FIR system measures the density and the plasma current profile (see Fig. X.1), the high number of channels and their distribution will provide enough resolution for a good equilibrium reconstruction. Optimal laser source solution for polarimeter measurements resilient to density gradients is the 100/50 μm one. Optically pumped CH_3OH 118 μm gas lasers are commercially available (e.g. at RFX-mod). Gas laser sources in the 50 μm range are yet unavailable but the so-called THz domain of QCL lasers is progressing. A conservative solution would be to use the CH3OH laser operated at 96.5 μm also for the vibration compensation, this make simpler the optical and detection systems while considering the DTT density regimes the additional noise due to the small differences between the two wavelengths will have a negligible effect on density resolution.

We are also evaluating the use of a Second Harmonic Interferometer based on a Continuous Wave Nd:YAG laser (1.06 microns), for the density feedback control, as DTT density variation is within a single fringe at this wavelength and the minimum detectable density would be about 5.1018 m^{-3}, low enough for the feedback requirements.

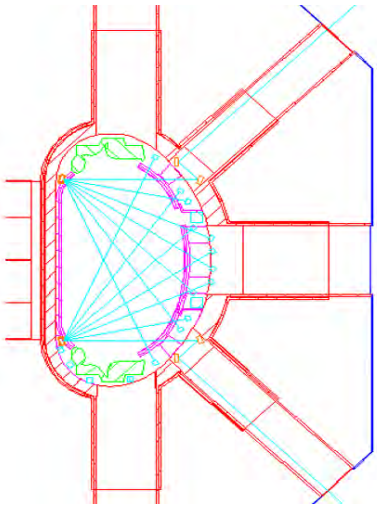

Figure X.1: Scheme for the interferometer-polarimeter topology of viewing chords

Reflectometer [X.7]

The frequency span of cut-off frequencies in DTT is quite large, considering high densities and two different working magnetic fields (3 T and 6 T), which suggest the use of the two frequency bands W (75-110 GHz) band D (110-170 GHz). The reflectometers can work both in X and O mode.

The maximum central and edge density measurable with such frequency ranges are:

- for 3 T, R-cut off, X mode, f = 170 GHz, $n_{max} = 3.5\times10^{20}$ m^{-3}

- for 3 T and 6 T, Plasma-cut off, O mode, f = 170 GHz, $n_{max} = 3.58\times10^{20}$ m^{-3}

In the 3 T scenario, we can operate with two different set-up: for low central density (below 1.8×10^{20} m^{-3}) the X-mode R cut-off covers the density range from about 0.1 to 1.8×10^{20} m^{-3}, that is almost the whole density profile. For higher density, the O-mode plasma cut-off allows spanning the density range from 0.7 to 3.6 $\times10^{20}$ m^{-3}. The L cut-off, at higher density, is always unaccessible due to the presence of the R cut-off in the plasma.

At 6 T the X mode right cut-off is only available for the very edge measurements (up to 0.9×10^{20} m^{-3}). The lower frequency band (75-110 GHz) can be used in X-mode L-cut-off for the plasma center at high density. Using part of the upper band till the cyclotron frequency at the edge (126 GHz), densities as high as 4.6×10^{20} m^{-3} can be measured. The minimum density measurable with X-mode L cut-off is about 2×10^{20} m^{-3}. The O-mode plasma cut off allows covering a larger range: 0.7 to 3.6 $\times10^{20}$ m^{-3}.

For lower densities, up to 1.5 $\times10^{20}$ m^{-3}, however, the possibility to use the lower band in O-mode (0.7 to 1.5 $\times10^{20}$ m^{-3}) and the upper band in X mode Right cut-off (0. to 0.9 $\times10^{20}$ m^{-3}) can be a solution.

X.2.3 Core kinetic profiles and fast particles

Several diagnostics are foreseen to document the kinetic content of the plasma core and the presence of non-Mawellian components in the particles energy distribution, the latter being particularly important for their possible impact on plasma wall interactions and impact on particle transport. Besides a Thomson Scattering system an ECE radiometer, charge exchange spectroscopy and a crystal spectrometer have been considered.

Thomson Scattering

For the measurements of Te and ne in the plasma core, the first choice is a conventional multipoint Thomson scattering (TS) system [X.8]. The laser source is a Nd:YAG (λ= 1064 nm), the scattering volumes are defined by fibre optic imaged onto the laser beam path and the scattered laser light is processed by filter polychromators employing Si APD (Avalanche Photo Diode) detectors. The possible geometries are: 1) the laser beam crosses vertically the plasma with entrance and exit on an upper and lower port. The scattering signal is collected from a large part of a vertical chord by partially recessed lens/mirror/fibre optic systems, located inside two or three diagnostic ports. 2) The laser beam enters the vacuum vessel from an equatorial diagnostic port crossing the plasma horizontally in the equatorial plane and the scattering signal is observed in a backward-like geometry by a collection optic system located in the same port, in an arrangement similar to that of the core TS System of ITER. Such systems can achieve a spatial resolution of ~ 3 cm along the laser beam and operate reliably at 25-50 Hz, in a range T_e > 50 eV, ne > 1019 m^{-3}. The final choice of the geometry and of the diagnostic ports will be dependent on the location of the scattering volume with the largest value of r/a. An alternative approach, based on the LIDAR TS concept, has also been considered for DTT. Based on the results of the JET LIDAR TS system, recent studies have shown that the advancements in the laser and detector technology could provide a spatial resolution of ~ 3 cm along the laser beam and a repetition time of 25-50 Hz using commercially available equipment. The LIDAR approach has many advantages with respect to a conventional system, mainly because the laser beam and the collection optics share the same diagnostic port, and because a single spectrometer and no fibre optics are required for measuring across the entire plasma, resulting in a significant reduction in costs and access issues. In the LIDAR scheme the laser beam crosses the plasma on the equatorial plane through an horizontal diagnostic port and is dumped on the inner wall while the scattered light is collected from the back, in a 180˚ scattering geometry, by a mirror/lens

system well recessed inside the diagnostic port and transmitted to the filter polychromator by a suitable optical relay system.

ECE radiometer

The ECE radiometer and Michelson interferometer provides the electron temperature profile with good space (1cm) and time (>200 kHz) resolution. Evaluations of the ECE radiation on a radial line of sight show that in DTT both 1st harmonics, O mode (O1: 130 < f < 250 GHz), and 2nd harmonics, X mode (X2: 260 <f < 380 GHz) spectral regions are detectable with radial resolution of 1 cm for the X2 and 2 cm for O1, respectively. The X2 has appropriate resolution for spatial detection of the MHD activity. O1 measurements in the High Field Side may be used for the characterization of the kinetic quantities in the pedestal. Extended spectra (1^{st} to 3^{rd} harmonics, 100-1000 GHz) detected with the Michelson interferometer provide information on the electron distribution function under intense electro heating. Advanced functions accessible with ECE measurements are turbulence measurements by a correlation system and imaging of MHD and ELMs dynamics through an array of radiometers. Moreover, oblique lines of sight collinear with ECCD (Electron Cyclotron Current Drive) provide an excellent option for closed-loop NTM detection and control.

Charge Exchange Recombination Spectroscopy

In the presence of a high energy (200- 400 keV) heating Neutral Beam Injector with a fan like distribution of beamlets, targeting isolated beamlets could enhance the spatial resolution of the charge exchange (Charge Exchange Recombination Spectroscopy, CXRS) processes [X.9]. However, the cross section drop of the charge exchange between deuterium and impurities at high energies (>150 keV) implies that one has to resort to the CX between beam and main plasma ions (DIIID and JET). Simulations show that significant Dα CX signal can be obtained from the plasma center, albeit large uncertainties on the passive contribution from the edge exist. A low power diagnostic beam of 50 to 80 keV and of about 4-6 Ampere of equivalent current could be used to qualify the pedestal. The presence of tungsten in the plasma facing components adds the extra complexity of a rich background spectrum [X.10].

Crystal Spectrometer

An alternative, passive method for yielding the ion temperature is provided by a high resolution, curved crystal spectrometer measuring the Doppler broadening of spectral emitted in the plasma core by highly ionized intrinsic or extrinsic impurities in the soft X-ray region (0.1 – 0.4 nm) [X.11-X.12]. As a by-product, the electron temperature, the impurity absolute density will also be measured. Plasma rotation is measurable too provided the toroidal angle of the LOS is sufficient. Depending on the emitting ion species a broad range of temperatures between 1 keV to over 20 keV and velocities above 104 m/s can be measured with time resolution around a few ms. Argon is extensively used for electron temperatures in the range 0.5 - 6 keV, Krypton is suitable for the highest temperatures. Good spatial resolution can be achieved adopting configurations with spherically bent crystals, or cylindrically bent crystals with slits [X.12]. These instruments have the advantage of the crystal acting as a mirror deflecting the radiation from the direct view of the plasma; the detector can thus be placed much further away, at a location where it can be conveniently screened. The new generation of solid-state detectors allows very high counting rates (up to 1 MHz per channel) and spatial resolution (<100 micron). Large detectors (sensitive area 100 x 300 mm) have been developed for KSTAR, NSTX and EAST and will be used on ITER. However, an ensemble of several smaller

detector strips could provide better coverage of the plasma emission region. Split detectors could be useful also for viewing different wavelength ranges with the same crystal. The crystal itself should not suffer from neutron exposure at the levels estimated for DTT.

X.2.4 Fast ions

Fast ion detection is important to establish the contribution of this components of the escaping particles to the overall power exhaust but also to evaluate their impact on the transport properties of impurities. For this purpose, DTT will rely on γ–ray detection and on edge scintillator probes [X.13], with a contribution from the Doppler shifted Balmer Alpha emitted by neutralized fast particles [X.14].

Collective Thomson Scattering

A Collective Thomson Scattering (CTS) system could provide a measurement of the distribution functions of both thermal and supra-thermal ions. It has been shown that CTS measurements with fast-ion D-alpha spectroscopy can provide 2D velocity space tomography, as shown in [X.15]. Simulations show that the frequency ranges ($\nu \lesssim 130$ GHz) and (240 GHz $\lesssim \nu \lesssim 270$ GHz) are potentially suitable as probing frequencies for CTS measurements in the DTT and that the top ECRH launcher is appropriate for the integration of the CTS lines. The criterion considered to select the frequency ranges is that the expected level of ECE signal detected on the line of sight of the launcher should be $\lesssim 1$ keV in a certain range of toroidal angles (in our case from 0° to ~20°, at least on one of the two toroidal directions). In this view, the procurement of at least one 170 GHz (dual-frequency or multi-frequency) gyrotron capable to emit power at a second frequency included in the range of interest is to be considered. Multi-frequency gyrotrons potentially suitable for both heating at 170 GHz and at a different frequency for CTS are already available on the market, see for instance [X.16]. Several components for the installation of a CTS system on DTT would be already available from the CTS diagnostic now installed on the FTU device, which is described in detail in [X.17-X.18].

X.2.5 Runaway electrons

HXR-γ detectors measuring radiation in the 10 MeV range measure the Bremsstrahlung radiation emitted by Runway Electrons [X.19]. HXR monitors, typically consist of an organic scintillator, most often C6F6, and primarily provide an alarm when a population of runaway electrons is born in the plasma [X.10]. The signal is proportional to the runaway electron current, although a quantitative relation between the two parameters is hard to establish. Four such detectors placed at the four cardinal points will be deployed. More detailed and quantitative information will be provided by HXR spectrometers based on an inorganic scintillator measuring the spectrum of the bremsstrahlung emission. Different plasma volumes can be observed associating the spectrometers with collimators. One can compare the experimental data with a synthetic diagnostic or alternatively one can attempt to derive the runaway distribution function directly from data and by adopting a suitable deconvolution method. Despite the uncertainties the deconvolution process can yet yield robust parameters such as the evolution as a function of time of the maximum energy of the runaway electron population, as well as the runaway electron current with ms time resolution. Experience with HXR spectrometers is much more recent compared to that of HXR monitors. Measurements have been demonstrated initially at compact tokamaks in Russia, such as Globus-M, and are now starting to be exploited at JET (UK) and in mid-size devices, including ASDEX Upgrade (Germany) and DIII-D (San Diego).

Cherenkov Probes

A Cherenkov probe diagnostic [X.20] inserted inside DTT's vessel will measure the fast electrons escaping the plasma [X.21-X.22]. The Cherenkov probe consists of a diamond detector coated with a thin Ti/Pt/Au interlayer to filter out visible and UV and a Mo layer to set an energy threshold for the electrons. A triple Cherenkov probe, with three different energy thresholds, located at the equatorial plane could perform an energy scan of the escaping electrons. Probes are coupled via optical fibres to photomultiplier placed outside the torus hall. Correlating the signals to those from other diagnostics (HXR, MHD activity, neutrons) allows to study the impact on RE of several mechanisms from MHD to kinetic. The phase difference between the signals of the two probes toroidally separated by 180° can be used to evaluate rotational effects of the plasma and to distinguish different MHD activities. Neutron induced noise such as due to nuclear reactions in the diamond detector and to scintillation processes in the optical fibres is to be carefully evaluated.

REIS

Runaway Electrons can be detected also by visible and near infrared cameras (spanning the wavelength range between 300 and 5000 nm) intercepting the forward emitted synchrotron radiation [X.23]. Similarly, VIS and NIR spectrometers can detect the same radiation and analyse their energy distribution so that using imaging and spectral analysis are collected together. Simultaneous observations in the two opposite toroidal directions can unmistakably identify the presence of RE as they develop in the plasma core. A REIS prototype was tested in FTU, AUG and TCV [X.24]. The REIS system will be integrated in the plasma monitor system and the spectrometer tools in order to improve the detection of hot spots or abnormal events in plasma discharges.

X.2.6 Neutron, gamma and Hard X-ray diagnostics

Neutron diagnostics will be ready at the DTT start-up to provide the basic information for the DTT operation in the early phase. These diagnostics tools feature well proved levels of affordability as they are based on long lasting experience gained in other tokamaks. No further studies are needed for their implementation and in some cases (e.g. fission chambers) detectors already available e.g. at FTU will be re-used.

A system of fission chambers moderated with polyethylene arranged at 120° toroidal angles will monitor DD neutrons. Furthermore, three groups of commercial diamond detectors [X.25-X.26] for the measurement of the burn-up neutrons (14 MeV) produced by the D-T reactions, about 1% of the neutron yield, will be used. Diamond detector can be covered with a layer of ^{6}LiF so to make them sensitive also to DD neutrons and perform simultaneous detection of total and 14 MeV neutron emission (already proven at JET) [X.21].

Activation foils will be used for total absolute neutron yield measurements and for 14 MeV neutron measurements using high threshold reaction materials. This requires a pneumatic system with 3-4 irradiation ends located inside the VV close to the plasma and a gamma-ray laboratory, reachable by the pneumatic system, where to perform spectrometry measurement using HPGe (High Pure Germanuim).

Calibration of the neutron monitors will be necessary, which can be attained against neutron activation of selected foils of suitable materials (e.g. In) however a dedicated calibration campaign (e.g. as performed for the JET-3 campaign) is to be envisaged at the DTT start-up. This requires a 252Cf neutron source and a 14 MeV neutron portable neutron generator.

The main role of the neutron/gamma camera is the reconstruction of the spatial neutron and gamma ray emissivity. One horizontal camera is envisaged, with the option of one/two vertical line of views, due to the limited access at the top of the machine in case the double null magnetic configuration is adopted.

The reference for this diagnostic is the JET neutron/gamma profile monitor. The instrument for DTT is made of about 10 lines of sights distributed on a horizontal camera. Each line-of-sight is associated to a suite of detectors: NE213 liquid scintillator for 2.5 MeV neutrons, a Bicron plastic scintillator for 14 MeV neutrons and a LaBr3 scintillator crystal for gamma-rays detection [X.27].

Other recently developed detectors such as two inorganic scintillator crystals called, CLYC and TLYC enriched with ^{7}Li and featuring good energy resolution and neutron gamma discrimination are also being considered for 2.5 MeV neutrons, since they can provide a good energy resolution. Solid states detectors are very compact and could be placed in front of the scintillators providing complementary information. However, their use strictly depends on the expected neutron fluxes. Among these detectors, artificial diamond and Silicon-carbide (SiC) detectors provide higher neutron hardness but their response to 2.5 neutrons needs to the investigated. The diagnostic for the so-called exploitation phase are intended for a more accurate and detailed analysis of DTT plasmas. They may require further R&D activities and include: Neutron spectrometer based on the Time Of Flight and HXR/Gamma (HXR, Hard X-Rays) ra (y spectrometers). These diagnostics requires a few dedicated lines of sight and although their implementation will happen at a later stage, their interface issues should be addressed from the beginning.

Calibration sources such as Am-Be neutron source and gamma-ray sources should be made available for in situ calibration. In particular, diamonds can be exploited to realize a neutron recoil detector, used to perform coincidence measurement of elastically scattered neutrons off a series of diamonds, where neutrons back scattered at large angle (→ 180°) are detected by plastic scintillators. The added value of these additional detectors is to add neutron spectroscopic capabilities to the camera.

X.2.7 Radiation and impurities

A large set of diagnostics will be devoted for the characterization of the impurity content of both the main plasma and divertor. Bolometry, Soft X-Rays detectors, short wavelength spectrometers plus effective charge monitors will be able to track the impurities content and their spatial distribution in the various experimental conditions.

Bolometry

Bolometry is essential for real-time control and optimization of the divertor power exhaust. On DTT a geometrical solution compatible with centimetre space resolution tomography has been studied based on 3 main heads, each hosting three fans covering the plasma core and three additional heads directed towards the divertor, as shown in Fig. X.2. The choice of detectors is oriented towards the radiation hard metal foils developed for ITER [X.28-X.29]. Faster and compact AXUV Silicon photodiodes tested on ASDEX Upgrade [X.30] and on C-mod [X.31] could be introduced for time resolved information, although their performance degrades strongly over time.

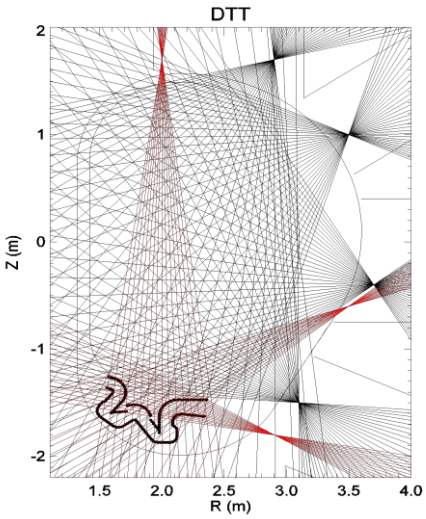

Figure X.2: Distribution of the bolometer arrays

Soft X-Ray radiation

Soft X-Ray tomography [X.32] is a powerful tool to diagnose both impurity accumulation and MHD activity in the hot plasma core, such as ELMs, sawtooth activity, or Fast Particles induced instabilities, e.g. Toroidal Alfven Eigenmodes. For DTT we envisage using the state-of-the-art system designed for shaped plasmas on ASDEX Upgrade (8 pinhole cameras installed with about 200 lines of sight. Silicon diodes screened by a curved Be filter 75 μm thick). The required bandwidth is 1MHz, in order to detect also high frequency MHD. New GEM detectors [X.33] are under consideration as they add the potential associated to photon counting and the additional advantage of measuring the energy of the photons. Such tools have been successfully adopted for standard tomography on a poloidal plane [X.34] and also for tangential imaging of the plasma [X.35] and are subject of ongoing developments. Soft X-ray and UV detectors based upon artificial diamond were already successfully tested at JET, they demonstrated good radiation hardness and fast response [X.24] and are proposed for DTT too [X.30].

Spectroscopy

The standard spectral range of interest for spectroscopic diagnostics is from visible to soft X-ray. Broad range, low resolution survey spectrometers, such as the SPRED [X.36], will be needed for monitoring the impurity contamination of the outer mid-radius plasma in the 10-30 nm spectral range. The pedestal region will require an even broader spectral range extending to at least 125 nm. The inner core can be effectively covered with grazing incidence and crystal type of spectrometers [X.11,X.37], which together allow monitoring the 0.1 to 35 nm range at varying spectral resolution with different gratings/crystals. An important requirement is that of absolute calibrations in both wavelength and luminosity in order to produce more quantitative estimates of the impurity content, hence of Zeff. These spectrometers, in general, view the plasma along single chords but spatial scans may be obtained on a shot-by-shot basis by tilting the instrument or exploiting the imaging capabilities of the instruments where possible. Therefore, the realization of multiple views to be obtained on a single discharge is going to require some R&D. A careful assessment of the background radiation sensitivity as well as of the neutron induced noise is also to be carried out.

Zeff

The measurement of the effective charge Zeff is based on the continuum radiation in the standard 523.5 nm region, collected by means of interference filters, 1 nm of bandwidth, and photomultipliers detectors [X.38]. Multiple LOS should be used and checked against local contamination from several possible elements such as: Ne I, Ar II, Xe II, Mo, W Fe. Observations along the toroidal direction are less affected by edge contamination. Spectrally resolved monitoring complements the filter measurements. Interference filter measurements are complemented by fitting the emission spectrum over a large wavelength range, between 350 and 900 nm, whereby the continuum is expected to display its $1/\lambda^2$ dependence; the stray light inside the spectrometer is to be carefully checked and evaluated by means of notch filters placed in front of the spectrometer.

X.2.8 Divertor diagnostics

Divertor and Plasma Wall Interaction diagnostics

In line with the experiment mission, a particular attention is to be devoted to the diagnostics of edge and divertor region, focussing on impurity level, thermal characterization of divertor strike points position and heat loads, plasma detachment, degree of enrichment of impurities and level of helium compression.

Charge exchange neutrals

Neutral particles play an important role at the edge of the plasma and in the divertor region hence in the exploitation phase of DTT two dedicated diagnostics are foreseen. Low energy escaping neutral particles will be detected by a time of flight (TOF) [X.39-X.40] neutral particle analyser (NPA) with a path of around 4 m. The energy distribution information will be complemented by the analysis of the shape of the D alpha emission line as detected by a high-resolution spectrometer. Coupling energy and density information yields the neutral pressure in the observed region.

Divertor Thomson Scattering

The measurement of Te and ne in the DTT divertor poses non-negligible challenges, mainly because of the

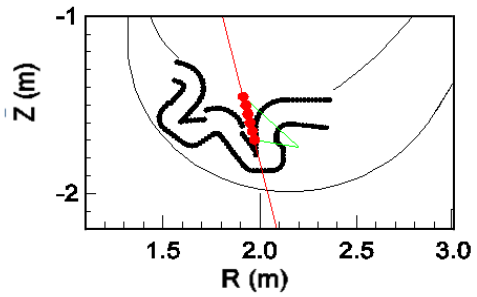

Figure X.3: Divertor Thomson Scattering Layout

low values of the plasma Te and ne to be measured (1 eV ≤ Te ≤ 10 eV, ne ~ 10^{19} m^{-3}). A conventional TS system, based on a Nd:YAG laser and a set of fibre optic and filter polychromators is considered [X.41]. Of

the two layouts discussed in the previous study, the solution in which both the laser beam and the collection optics accesses the divertor region from a lower port, is preferred. In this layout (see Fig. X.3) the laser enters the divertor from the lower-outboard side (thick red line) passing through the aperture between two adjacent divertor cassettes and is dumped on the inner side of the first wall. A width of the aperture of at least 20 mm is assumed, perhaps especially provided for the purpose. A beam dump is not required since the laser is sufficiently defocused when reaching the first wall. Red dots show the proposed scattering volumes, for which we can assume a minimum length of ~ 5 mm. Collection optics (in green) are placed behind the divertor plates, looking at the scattering volumes through the similar apertures. Preferably, both the laser relays and the collection optics should share the same mechanical support to improve alignment reliability. The fibre bundle can either be placed immediately behind the collection optics or outside the cryostat also depending on the expected impact of neutrons; in the latter case optical relays (typically in the form of a series of lenses) must be installed. The performance of this system would be further improved if the laser path could pass through the vessel crossing vertically the plasma from the lower to the upper port. This would add simplification of the laser alignment, reduction of stray light due to the fact that the beam will be dumped outside the vessel - and the possibility of laser multiple passages, improving either S/N ratio or spatial coverage. Viewing access to the divertor region is guaranteed from equatorial and middle-top ports. The X-point region is easily accessible from the side/lower port. Other LOS through the inner or outer divertor legs would benefit of intra-divertor accesses, which have not been defined at the moment, but constitute specific request that should be considered in the design phase of the divertor cassettes.

Divertor Spectroscopy

Emission spectroscopy will be used on DTT as a multi-purpose tool in the divertor plasma, particularly useful to characterize detachment states (deuterium Balmer or Paschen series), plasma position and in general the kinetics of impurities and main gas (from Doppler broadening and shift). Given the large magnetic field, both poloidal and toroidal, important Zeeman effects are expected. Two dimensional patterns of temperatures, ionization front and flows can be obtained by means of two-dimensional fast polarization interferometers [X.42]. As for other imaging systems, relays optics and detectors are to be positioned where they can be screened to neutrons. Viewing cameras with semi-tangential views of the divertor and equipped with Dα and Dγ filters will be used to evaluate the poloidal distribution of the neutral as done in AUG [X.43], under the assumption of toroidal symmetry. Divertor spectroscopy will cover the wavelength range between 10 and 125 nm as well as visible Near Infrared to monitor the main emitting species, including molecules.

Electrostatic Sensors

Embedded electrostatic sensors provide detailed localized information on poloidal profiles of main edge plasma parameters, in particular electron density, electron current, and, of paramount importance for the DTT scientific scope, heat load profiles on the divertor plates. With adequate time resolution and probe arrangement configuration, the fluctuation of the above-mentioned quantities can also be obtained for investigation of SOL turbulence and transport studies. The design of embedded electrostatic sensors needs to comply with the requirement of Remote Handling of divertor and first wall components. The incident angle of magnetic field line on the plasma facing surfaces has to be accounted for in the design of the electrode shape and position with respect to the component surface, in order to minimize the data interpretation uncertainty. The sensor sets to be installed have to take into account also the possible configurations for Langmuir probe operations (i.e. single, triple, Mirror Langmuir probe…). The aim is to collect plasma

parameter measurements with a time resolution suitable for evaluation of their background value as well as of their turbulence fluctuations. Possible interesting configurations so far considered are listed in Tab X.VII. More details can be found in [X.44]. Different measurement sets are planned to be developed along poloidal and toroidal arrays. Suitable power supplies have therefore to be accounted for biasing of embedded electrodes. It is proposed to equip two toroidal sectors with FW embedded electrostatic sensors, at a toroidal distance ≥ 45°, while three toroidal sectors are foreseen to be equipped with embedded sensors on the divertor. This solution is to respond to the need of redundancy, given the harsh environment expected in DTT. The poloidal resolution required for the adequate detection of the strike point footprint on the divertor plates is of of 2 mm. Examples of embedded sensors can be found in [X.45-X.50]. Toroidal ripple measurements require multiple poloidal arrays within the same poloidal sector. Regarding Resonant Magnetic Perturbations the toroidal separations of embedded sensors on the FW should be decided in agreement with the foreseen periodicity of the RMP experiments.

Thermocouples

Thermocouples (TC) represent the main thermal diagnostic for the divertor in particular to provide the power density deposited on the surface, bulk calorimetry, and surface temperature. It may be possible to instrument individual castellation with TCs based on Nicrosil–Nisil alloys (type N) and with tungsten-rhenium surface TCs with the possibility to crosscheck bulk calorimetry with power density. In preliminary tests, surface TCs proved to be a qualified diagnostic to accurately measure the heat flux during H-mode shots and to resolve heat flux profiles during strike point sweeps [X.51]. Poloidal arrays are recommended, which will be able to provide an accurate and high temporal resolution temperature and heat flux distribution profile. The spatial density of temperature sensors should be quite high to compensate for a possible lack of coverage of the IR cameras. A low spatial density of TCs can be embedded in the FW under the exposed surface to provide local temperatures relevant to the HFS and LFS and bulk calorimetry. Other TCs can be mounted on the FW cooling lines to measure coolant temperatures at the outlet and so determine coolant calorimetry and the power partitioning among FW elements. Coolant calorimetry TCs will not pass the coolant-vacuum barrier so increasing the system reliability. It is proposed to equip with TC two toroidal sectors ≥45° apart.

To prevent the Ettingshausen–Nernst effect TCs without ferromagnetic materials will be used, such as the Nicrosil–Nisil (type N) alloys. This TC type is also compatible with high radiation levels of neutron and gamma fluxes [X.1]. Maximum temperatures that can be measured are up to 1250° C using the Pyrosil or Nicrobell alloy for the TC armour [X.52].

Visible and Infrared Cameras

The wall and the divertor will be monitored by a set of visible cameras and infrared cameras.

Visible cameras are meant to serve as a general monitor system during the plasma discharge in particular with recognition capability of hot spots or abnormal events as well as imaging systems for visible light fluctuations i.e. to observe ELM fine-structure as in AUG and ELM precursors as on Alcator C-MOD. Two-dimensional imaging systems have been used on MAST to examine ELM filament structures.

IR cameras will be installed to monitor surface temperature of Plasma Facing Components (PFC's), in particular inner and outer targets, and therefore to evaluate the heat flux deposition on the divertor targets. For the latter purpose spatial resolution of at least 1 mm is necessary according to the multi-machine predicts

a power decay length predicts $\lambda_q \sim 2$ mm at the outboard mid-plane in DTT. The IR camera system should also be fast enough to resolve the local impact of ELM's, which are expected to broaden the plasma footprint.

TABLE X.VII. DIAGNOSTICS AND THEIR APPLICATIONS

Diagnostics	Diagnostic aims	measured quantities/ measure technique	position in the poloidal sector
Electrostatic embedded sensors	Magnetic configuration dynamics poloidal/toroidal profiles and fluctuations	Vf, ne, Te, flows/ single probe,triple probes, I-V characteristic),mirror probe,Ball-pen probe, Mach	First Wall LFS
	Magnetic configuration dynamics(i.e. start-up phase, ...)poloidal/toroidal profiles and fluctuations	Vf, ne, Te, flows/ single probe,triple probes, I-V characteristic),mirror probe,Ball-pen probe, Mach	First Wall HFS
	Heat load on strike points; monitoring of poloidal profiles at divertor	Vf, ne, Te, flows/ single probe,triple probes, I-V characteristic),mirror probe,Ball-pen probe, Mach	divertor and adjacent vertical plates
	Heat load on strike points	Vf, ne, Te, flows/ single probe,triple probes, I-V characteristic)	Liquid divertor
Thermocouples	During pulse operation and first wall conditioning: a) plasma studies from temperature, calorimetry, power densidty acquisition and calculation b) component protection	1) coolant calorimetry 2) local temperature + bulk calorimetry + power density (bulk TCs located at different distances from the heated surface)	First Wall LFS and First Wall HFS
	During pulse operation and first wall conditioning: a) plasma studies from temperature, calorimetry, power densidty acquisition and calculation b) component protection	1) coolant calorimetry 2) local temperature + bulk calorimetry + power density (bulk TCs located at different distances from the heated surface) 3) surface temperature + power density (surface TCs)	Divertor and adjacent vertical plates
	During pulse operation and first wall conditioning: a) temperature acquisition b) component protection	local temperature	Vacuum Vessel
	During pulse operation and first wall conditioning: a) plasma studies from temperature, calorimetry, power densidty acquisition and calculation b) component protection	1) coolant calorimetry 2) local temperature + bulk calorimetry + power density (bulk TCs located at different distances from the heated surface) 3) surface temperature + power density (surface TCs)	Liquid metal divertor
Fast insertable probes	Edge profiles; turbulence		Mid-plane LFS and divertor (X-point(s) proximity)

The IR temperatures images represent an efficient tool to assist the real time control of the divertor magnetic topology and of the detachment.

The measurement of the outer divertor heat load profile requires a particular attention since an underestimation of the temperature represents a real risk for the machine. Cross check with thermocouples will be important to validate IR measurements. Further complication is represented by reflections from the surrounding inner walls [X.53]. In addition, IR measurements require an accurate estimate of the emissivity factors of the IR emitting surfaces, which differ depending on the materials and their chemical and physical state. In this respect calibrated targets of known emissivity or the use of two wavelengths IR detectors can help discriminating the real temperatures of plasma facing components.

A wide-angle infrared could complement visible cameras for the detection of synchrotron radiation emitted by the runaway electrons created just after the thermal quench of a disruption.

Visible and infrared cameras have been organized on two sub-systems covering the vacuum chamber and the divertor respectively. Three or more wide angle visible cameras and infrared cameras will monitor the vacuum chamber using periscopes to relays the images outside the cryostat.

For the divertor several geometrical solutions are being considered in order to achieve the adequate space resolution, which use different ports for the LOS. The possibility to use spaces through the divertor structure for the LOS will be examined once the divertor design is delivered.

In situ PFC analysis

Laser Induced Background Spectroscopy (LIBS) with remote analysis capability and micro-destructive characteristics represents an ideal candidate to monitor the surface layer composition and the fuel gas content of the DTT plasma facing components. The feasibility of in-situ LIBS diagnostic of surface layer composition was demonstrated on FTU [X.54]. A LIBS system installed on a robotic arm could be used to probe the elemental composition of the various PFCs and of their fuel content during the machine maintenance periods.

X.2.9 Turbulence diagnostics

Several techniques are available to study the fluctuations properties of both core and edge plasmas and investigate phenomena like sawtooth oscillations [X.55] and Alfven eigenmodes [X.56], zonal flows and GAMs [X.57] as well as discriminating between ITG and TEM instabilities [X.42,X.58].

At the edge, besides the Langmuir probes, both embedded on PFC and installed on fast insertable systems, optical diagnostics such as Gas Puffing Imaging and Thermal Helium beams can be used to probe and image density and temperature fluctuations. These systems should be positioned both on the mid-plane region and in the X-point proximity. Injection of Li or Na high energy (tens of keV) beams provide highly space and time resolved density radial profiles [X.59].

Using Electron Cyclotron Emission Imaging (ECEI) [X.60], Edge-localized mode (ELM) growth and crash, followed by filaments propagation from the edge into the scrape-off layer, were observed in rich details.

In the core Beam Emission Spectroscopy [X.44], Phase Contrast Imaging [X.61] and Correlation Doppler Reflectometry (core and edge) [X.62-X.63] area available to study the degree of fluctuation level of density and temperature.

X.3 Real Time Control

X.3.1 Integration of diagnostics in the real time control system

The integration of the diagnostics in the real-time control system will be implemented along the following guidelines:

- Use of a common and standard (set of) technology for data acquisition and communication to reduce the integration effort.

- Define for each diagnostics the set of raw signals that may be involved in real-time control and their frequency and implement real-time data acquisition for them. Simplified version of the raw data processing algorithms will be implemented for real-time control in parallel with the diagnostics design to achieve the required computation speed even at the expense of measurement precision, within limits.

- Software framework for real-time control, like MARTe2, will be adopt since the early development stages and a running implementation tool will be made available on a simplified hardware platform in order to allow testing real-time data acquisition and communication schemes well in advance, proceeding in parallel with the definition of the actual control algorithms. The system can be used to support factory acceptance tests for diagnostics because it can be mounted on a standalone test system using the same approach of the ITER MiniCodac. Synthetic diagnostic and actuator models, even simplified, will be also implemented to test and develop real-time controllers.

- A source control or revision control software tool like GitLab [X.64] to record and manage changes to projects, files and documents across different teams will be adopted. GitLab allows also the continuous integration (CI) and continuous deployment of the new software: the software is validated by creating build-and-running automated tests. The goal is pushing code frequently, and having it tested, built, and deployed on some specific real-time target.

- A quality assurance standard like in [X.65] will be adopted.

- The network technology will be based the most updated and fast Gigabit Ethernet (GbE) available, with the possibility of having a shared reflective memory (star topology) between the controllers.

X.3.2 Control and data acquisition system

DTT shares data acquisition and control requirements with other long pulses fusion experiments such as ITER and JT-60 SA. Long lasting plasma discharges require an approach in data acquisition that is radically different from that taken so far in most current machines (with a plasma duration up to 1 minute); an approach where sensor and elaborated data are transferred to the experiment database during the discharge itself in order to allow the experimental team to have all the information necessary to take any necessary action in a timely manner.

The main technical implications of this new need are three: controllers need to be able to process real time data (from local or distributed sources) while at the same time be able to stream all the data out with a reasonable latency (<1s); data servers need to be able to collect the streaming data and update the database while users are concurrently accessing the existing pulse information; data visualization software need to be able to handle larger volume of data at the same time as new live visualization modes.

TABLE X.VIII. MAIN REAL TIME OBJECTIVES

	Diagnostics	Actuators	Control scheme
Plasma Current	Pick up coils	Magnetic Flux	PID
Axisymmetric equilibrium	Pick up coils /loops	PF coils	PID; Physics Model based
Electron Density	Interferometer/polarimeter	Gas valves/ Criopumps	PID
MHD / NTM, RWM	Pick-up coil, ECE ($\Delta\rho \leq 0.1$), SXR	ECE/Saddle coils, ECRH for NTM	PID; Physics Model
MHD / ELM control	Dα, Stored energy	Saddle coils, plasma shape, Vertical kicks, Pellets / RMP's	PID; Physics Model based
Plasma Detachment	IR Cameras / thermocouples / CCD cameras /spectroscopy /Thomson Scattering	Fast gas valves for D2 and impurities (placed near the strike points); Heating power?	PID; Physics model
Radiation/Enrichment factors	- Bolometer arrays, SXR arrays and VUV spectrometers for the core radiation; - Bolometer cameras, spectrometers in the divertor region;	Far-away valve acting on the core density In-vessel coils; Plasma Shaping and position; ECRH for heating	PID
Divertor Heat Flux	- Infrared cameras - Langmuir probes and thermocouples embedded in the divertor plates - Thomson scattering - Highspeed cameras equipped with suitable interference filters. - Magnetic measurements		
Disruption avoidance and mitigation system	- Shall accept data from all of the above controllers and diagnostics	Able to modify real-time control reference waveforms for the above controllers and trigger the DMS (Shattered Pellet) Injector, Massive Gas Injection)	Threshold triggered alarms, Machine learning algorithms, physics based models.

In addition to streamed data acquisition, the system must be able to use a subset of acquired signals for active control of the experiment. Real-time control systems for plasma discharge will impose different requirements that are less stringent on data throughput, but more demanding on data communication deadlines. As a consequence, a different communication bus will be defined for data used in real-time control, using an approach similar to the Synchronous Data Network (SDN) in ITER [X.66].

Plasma current, density, equilibrium, Beta, MHD control [Neoclassical Tearing Modes (NTM), Resistive Wall Modes (RWM), ELMs frequency and amplitude] and power exhaust control are some of the areas where feedback is to be applied (see Tab. X.VIII). As an example of the studies performed for DTT, in the following section a conceptual design for the DTT plasma shape control system is presented.

The design is developed on the basis of *engineering-oriented* models which enable a model-based design of the control systems. Simpler than *physics-oriented* simulation codes, such as transport codes [X.2, X.24, X.25], such linear models permit also to automate both the validation and deployment of the plasma axisymmetric magnetic control [X.67-X.70] but are also used to support the design and commissioning of the plasma

magnetic diagnostic [X.70, X.55] , as well as to run inter-shot simulations aimed at optimising the controller parameter.

X.3.3 Plasma magnetic control

Plasma magnetic control will be a crucial issue for the next generation devices due to the very stringent requirements both at flat-top and during plasma transients such as plasma initiation, L-H and H-L transitions, safe termination of discharges. Moreover, the presence of a nuclear environment causing a degradation of the magnetic sensors, the need of coordination between kinetic and magnetic control due to the increased role played by additional heating and the introduction of alternative magnetic configurations for the power exhaust problem, make this topic very challenging and fundamental for the proper machine operations.

Alternative divertor configurations (see Fig. X.4) represent the main DTT magnetic control issue. The next subsections discuss vertical stabilization, shape control and power exhaust control of DTT alternative configurations.

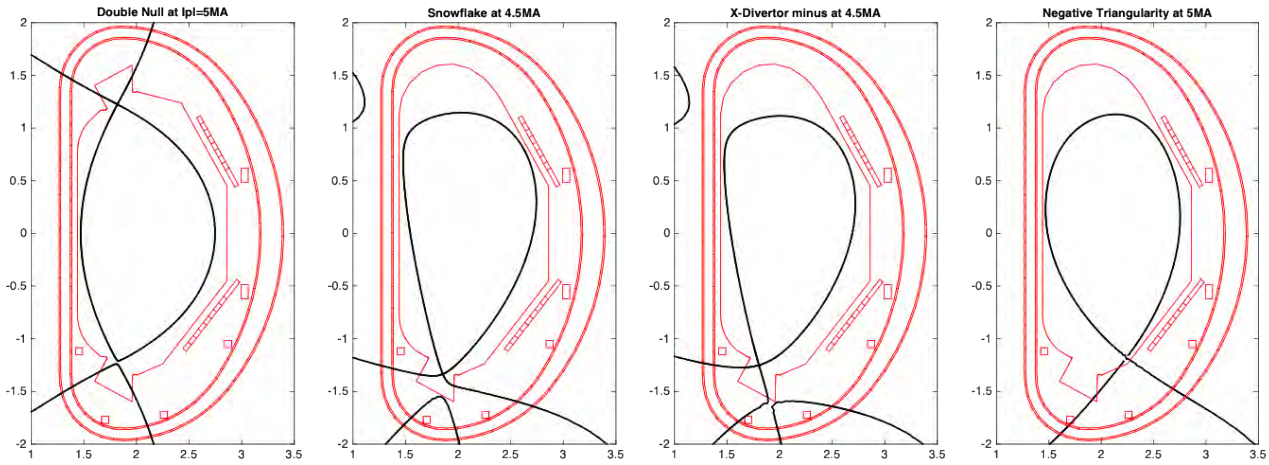

Figure X.4: DTT alternative configurations: double null, snowflake, X-divertor and single null with negative triangularity

X.3.4 Vertical stabilization

The need to design DEMO relevant highly elongated plasmas and the significant distance between the plasma and conductive structures due to DTT flexibility make the vertical stability control very challenging. DTT will be equipped with a pair of independent up-down symmetric in-vessel coils for vertical stability *InVessVSU-InVessVSL* and with two passive stabilizing plated of 40mm, as illustrated in Fig. X.5.

A preliminary vertical stability analysis has been carried out with 2D axisymmetric models. The definition of a detailed 3D model able to consider the non-toroidally continuous structures is in progress. In the meanwhile, to derive realistic values of plasma growth rate and stability margin, pessimistic and optimistic scenarios have been considered, with and without the upper plates. The passive stability parameters are reported in Tab. X.IX, where the in-vessel divertor coils are assumed open circuits. Table X.IX shows that the maximum growth rate for the DTT configurations is below 225 s^{-1} and a stability margin is always greater than the experimental lower bound of 0.3, even in the pessimistic 2D modelling of the plates.

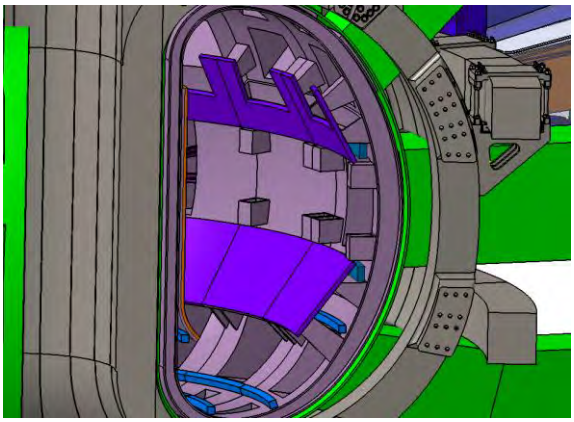

Figure X.5: DTT stabilizing plates and in-vessel coils

TABLE X.IX. PASSIVE VERTICAL STABILITY PARAMETERS

	K_95	li	R (m)	a (m)	Lower and equatorial plates		Toroidally continuous plates	
					Growth rate (s^{-1})	Stability margin	Growth rate (s^{-1})	Stability margin
SN	1,65	0.80	2.11	0.64	125	0.56	95	0.68
	1.61	1.00	2.12	0.64	144	0.52	102	0.65
SN_neg_triang	1.68	0.80	2.11	0.64	128	0.52	81	0.74
SF	1.74	0.80	2.11	0.63	224	0.34	125	0.54
XD	1.73	0.80	2.11	0.63	214	0.36	134	0.52
DN	1,71	0.80	2.11	0.64	187	0.37	149	0.43
	1,69	0.80	2.14	0.65	163	0.41	130	0.48

The assessment of the active vertical stability performance has been made in the case of a 1cm VDE in terms of best achievable performance. A constant voltage $\pm\alpha V_0$ has been imposed on the *InVessVSU-InVessVSL* with opposite signs, where V_0 is the minimum voltage able to stop the plasma vertical unstable mode for t→∞ and $\alpha \in R$ is a constant value fixed equal to 2. The results are reported in Tab. X.X, showing that the current and voltage requests for the in-vessel coils are always below the coil limits reported in Chapter III.

TABLE X.X. ACTIVE VERTICAL STABILITY PARAMETERS

	Z_max [cm]	Voltage [V]	Current [kA]	Power [MW]
SN	1.24	-83	-9.92	0.82
SN neg triang	1.24	-82	-9.10	0.74
DN (R=2.14m)	1.26	-78	-8.77	0.68
SF	1.27	-188.7	-12.28	2.32
XD	1.27	-174.99	-11.78	2.06

X.3.5 Plasma shape control

Plasma shape control of SN and DN configurations is a well-known problem in the plasma control community. A Multiple-Input, Multiple-Output (MIMO) strategy, based on the eXtreme Shape Control (XSC), is proposed for the feedback shape control of DTT SN and DN configurations integrated with the plasma current control

and the vertical stabilization (Fig. X.6). The XSC approach has been experimentally tested on JET and EAST and it is now proposed as reference control strategy for ITER [X.71-X.74].

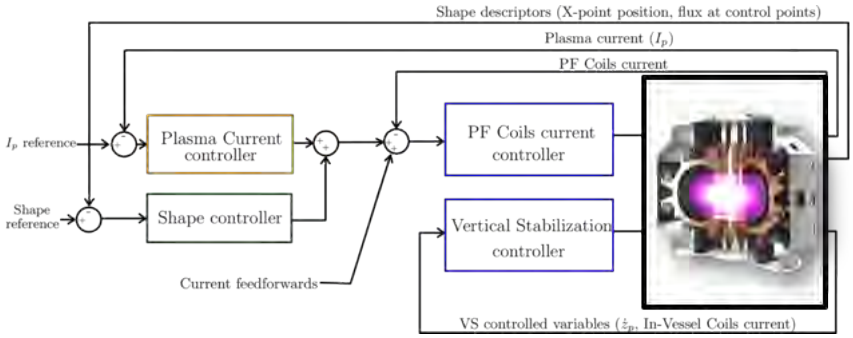

Figure X.6: Scheme of the shape, current and VS control plasma scenarios in DTT

The main problem for the plasma shape control of alternative configurations such as SF and XD is indeed related to the high sensitivity of these configurations with respect to plasma current variations. Figures X.7-X.9, show the effect on the DTT plasma configurations of:

- a big ELM (ΔWj=-1 MJ), simulated as a step in β_p and li, with $\Delta\beta_p=8\Delta Wj/(3\mu_0 R_0 Ip^2)$ and $\Delta li=-\Delta\beta_p$;
- a minor disruption modeled as $\Delta\beta_p=8\Delta Wj/(3\mu_0 R_0 Ip^2)$ and $\Delta\beta_p=\Delta li$.

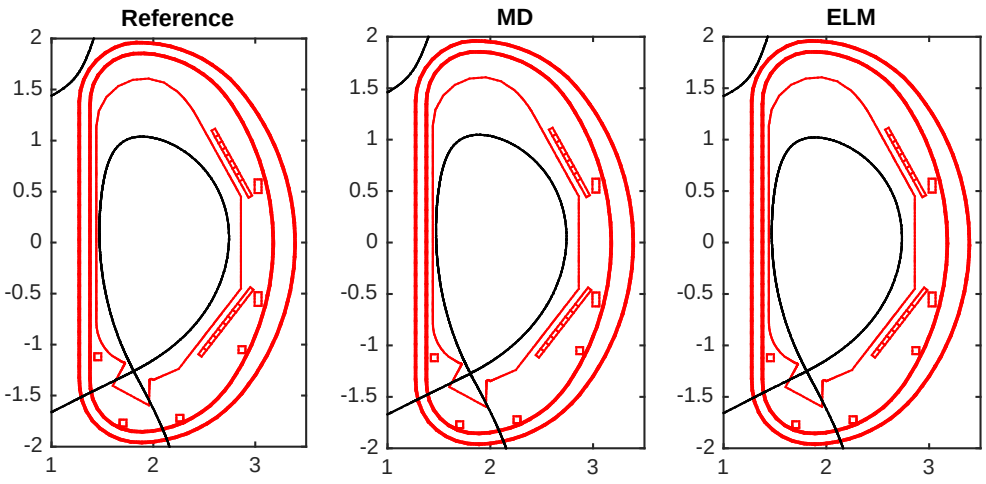

Figure X.7: MD and ELM effects on the flat top single null configuration

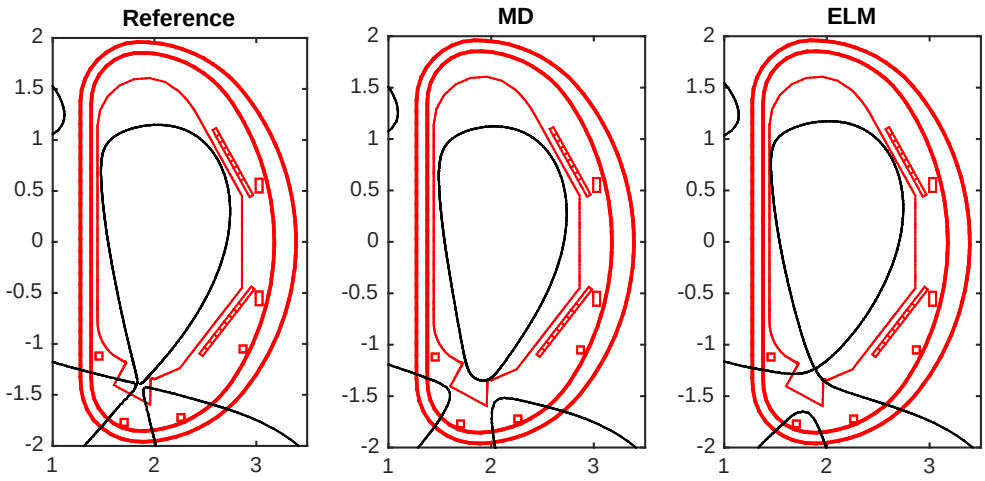

Figure X.8: MD and ELM effects on the flat top snowflake configuration

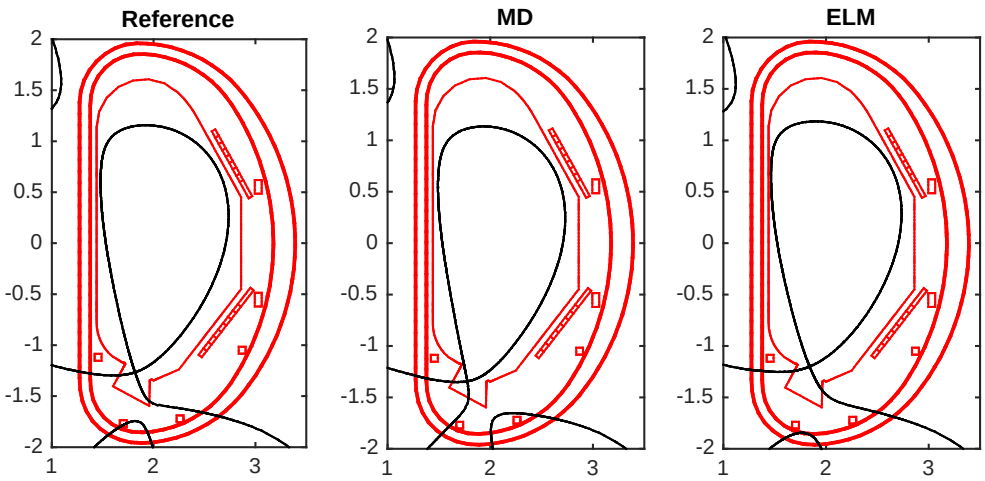

Figure X.9: MD and ELM effects on the flat top X-divertor configuration

Figures X.7-X.9 show that this set of disturbances causes a marginal variation of the SN plasma shape while the effect of the SF and XD is significant in the X-point region. This is an intrinsic problem of the SF configurations and it is related to the presence of a second order null point that flakes the flux surfaces in the divertor region. However, it can be reduced by increasing the distance between the X-points, that is the case of the XD configuration. It is important to underline that the sensitivity of the configurations to plasma current variations is independent on the feedback control strategy and it represents an alert on the possibility to design robust ideal-SF scenarios suggesting to move towards more robust solutions (XD) or to increase the space allocated for the X-point region.

X.3.6 Power exhaust control

DTT device will be equipped with four in-vessel divertor coils (InVess1L-InVess2L-InVess3L-InVess4L see Fig. X.10) able to locally modify the plasma flux surfaces of the alternative configurations, as described in Chapter 3.

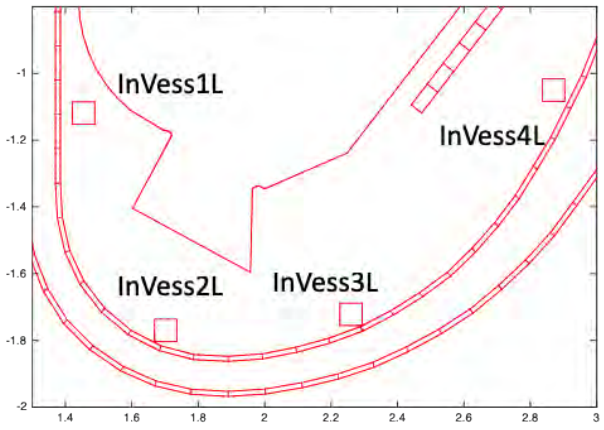

Figure X.10: DTT Invessel coils

The divertor coils, together with the VS coils *InVessVSU-InVessVSL,* will be also used in DTT to implement feedback control strategies aimed to reduce the power load on the divertor plates, such as sweeping and wobbling strategies.

The exhaust particles collected in the divertor region cause a localized thermal load around the *strike-points*, i.e. the intersections of the separatrix with the divertor. To spread this thermal load on a larger region, it is convenient to produce a periodical movement of the strike- points called "sweeping" [X.75-X.76]. In principle the strike-point sweeping should cause only a minor variation in the desired shape. The strike-point sweeping might also be imposed from ex-vessel coils only integrated in the plasma shape control system in order to perform thermal load spread without affecting too much the plasma shape. The drawback of this approach would be related to the maximum oscillation frequency that can be imposed to the strike-points due to the time constant of the vacuum vessel. The use of internal coils overcomes this problem imposing a local effect in the plasma X-point region.

Unlike the strike-point sweeping, in the "wobbling" technique the whole plasma is vertically displaced at a fixed period. It is usually applied to the DN configurations to periodically activate the upper and lower X-points. A wobbling strategy can be applied in DTT imposing a periodic voltage on *InVessVSU-InVessVSL* with opposite signs at the desired frequency.

X.3.7 MHD control

A provisional set up for Neoclassical Tearing Modes (NTM) and SawTooth (ST) control by means of the 170 GHz ECRH launching has been conceived by means of the codes GRAY (ECRH&ECCD) and SPECE (ECE) [X.77]. The system is based on 4 poloidally steerable 1 MW beams located in the upper port to minimize trapped electrons effects preserving the access to the HFS with Real Time capabilities. A toroidal steering between 10 and 15 degrees appears to be feasible. Several hardware specifications have been defined: cooling requirements, antenna concept, diamond window, focussing optics, plug-in supporting structure. Optimized current drive efficiency at accessible radial ranges is obtained from the Upper port and at the q=1, 3/2 and 2 surfaces has been estimated to be I_{cd}=9, 3.7 and 2.2 kA/MW respectively. The power and current drive radial localization Δρ along the accessible radial range is Δρ ≤ 0.1, which is promising for the NTM stabilization.

As to the Resistive Wall Modes, specific modelling of active mitigation for safety purposes has not been carried out yet for DTT as it was for JT60-SA [X.78], which will be important to define the need and the specifications of the internal correction coils.

X.3.8 ELM control

Vertical kicks, pellets and Resonant Magnetic Perturbations, have all been successful in some way to pace the ELM in a controlled manner in various experiments. In a different approach the pedestal region is maintained in a state of quasi relaxed situation where no ELMs are generated. The I-mode in C-mod [X.79], the Quiescent H Mode and Super H-mode [X.80] in DIII-D are such examples, all characterized by the presence of a continuous mode or broadband MHD spectrum. ELM-free plasma's in DIII-D are reached with sufficiently high ExB shear, which can be manipulated by means of the NBI torque and plasma shaping. The torque exerted by non-axisymmetric non-resonant magnetic perturbations has also been successful in reaching the QH mode with zero net NBI torque [X.82]. Injection of lithium, which modifies the edge density profile, has also led to ELM free regimes in DIII-D [X.81]. Lower Hybrid Current Drive has been successfully used on EAST to control ELMs [X.82], but its use it is not presently foreseen on DTT. Modelling of DTT scenarios is required

to establish which technique is the most appropriate to stabilize ELMs, depending also on the systems available for the purpose. The use of internal coils for RMP production is in fact still under discussion.

X.3.9 Control of disruption avoidance and mitigation systems

Given DTT level of plasma current and magnetic field the presence of a disruption mitigation system is mandatory in order to mitigate disruption thermal loads, electromagnetic forces and Runaway Electrons. The use of one (or more) Shattered Pellet Injectors as the main DMS actuators is presently under study, with the possible advantage of producing precious data for the ITER DMS before ITER high performance operation. Given a similar metallic wall and plasma actuators DTT would be an ideal test bed for ITER disruption avoidance strategies. The real-time system in charge of disruption avoidance and mitigation should be able to receive data from all of the diagnostics available in real-time, (among which pick up coils, bolometry, etc..), and to communicate new control references to the relevant actuators for discharge steering (plasma current controller, shape, heating and fuelling, other real-time controllers). Furthermore, such system should be connected to the disruption mitigation system via a low latency redundant network, in order to trigger mitigation actions when avoidance is not possible. Several types of algorithms are being used in present day tokamak devices in order to quantify the proximity to a disruption, from the use of thresholds on physics signals like the mode lock amplitude to machine learning algorithms, and with increasing complexity to physics based modelling capable of running in real-time. All of the above methods will be considered for DTT with a keener eye on the last two classes.

X.4 Instrumentation and Control System

X.4.1 DTT ICS architecture

DTT Instrumentation and Control System, DICS, is a combination of systems and subsystems that collectively allow automating the operation of the DTT device.

DTT ICS is composed of the following parts:

- The *central* control of DTT:
    - Central Command and Control System: CCCS, including control room mimics and computers, data storage and data processing computers, networks, and server to automate the managements of plant systems
    - Central Machine Protection Systems: CMPS
    - Central Occupational Safety Systems: COSS
- The *local* control of DTT plant: Plant System Controllers, organised in PSGs (Plant System Groups)
    - Implementing any locally required control, investment protection and occupational safety function.
- The *distributed* control of DTT experiment: Real Time Control Systems RTCS
- The interconnection among all parts of the ICS: the networks.

Segregation and Interrelation among Control, Protection and Safety

Control, Investment Protection and Safety functions typically have different requirements. Control functions tend to be the most complex of the three while Safety functions tend to have the highest criticality.

Safety functions also need to be developed following strict standards that imply use of specialised hardware and software together with thorough documentation.

Machine protection functions, depending on their criticality might also require adopting an approach similar to the safety ones. Unlike safety, no regulatory standard need to be followed, and is purely down to DTT management to weigh the cost benefit of each approach.

Because of these considerations, in most cases it is preferable to separate the I&C for 3 classes of functions.

DTT ICS implements a segregated central I&C layer with distinct CCCS CMPS and COSS.

The network interconnection is similarly organised with 3 groups of networks.

Plant System developers are instead left free to choose how and if to segregate functions with the sole constraint of providing 3 distinct interfaces for each of the three central I&C functions.

CCCS CMPS and COSS are not isolated systems (see Tab. X.XI). CCCS can trigger protection functions in CMPS. COSS will notify CMPS of initiating safety actions. Similarly, CMPS will notify CCCS of having started a machine protection action.

COSS is owner of the Long-Term Operation State of DTT and will make the information available to all central Systems. CMPS is owner of Pulse Operation State and will communicate it to the CCCS.

TABLE X.XI. I & C SYSTEMS CONNECTIONS

from\to	CCCS	CMPS	COSS
CCCS		can trigger	NC
CMPS	Provides Pulse state notifies protection actions		NC
COSS	Provides Long Term Op state	Provides Long Term Op state notifies protection actions	

X.4.2 Central Command & Control System (CCCS)

Central Command and Control functions

Central Command and control functions are those non-critical, non-real-time functions that allow coordinating the operation of plant systems. CCCS is the collection of systems that implement such functions. CCCS includes the mimics to manage the coordinated operation of DTT, terminals for DTT operations and plants management, servers to manage the plant database and perform automated sequences, mechanisms of communication to each plant systems.

Plant Distributed Database PDDB

This is the mechanism that allows conveying to CCCS information that is available within the Plant Systems. Using the same mechanism, the Central Systems can modify values and trigger actions within the Plant Systems.

It is an essential component of a SCADA system: whether one adopts EPICS or choses professional products like WINCC-OA, the chosen SCADA will provide a mechanism for distributing the field variables.

Central Operator Interfaces

CCCS includes a number of Operator Interfaces Screens that provide synoptic information about the DTT Plant and that allow coordination of the DTT machine operation (see Fig. X.11).

These synoptic screens will also provide, to a degree, navigation towards detail pages containing Plant System detail.

Whenever the Plant SCADA coincides with the Central SCADA, navigation down to all Plant details become possible without need to switch to different software. For this reason, the project shall encourage Plant System developers to all adopt the same solution.

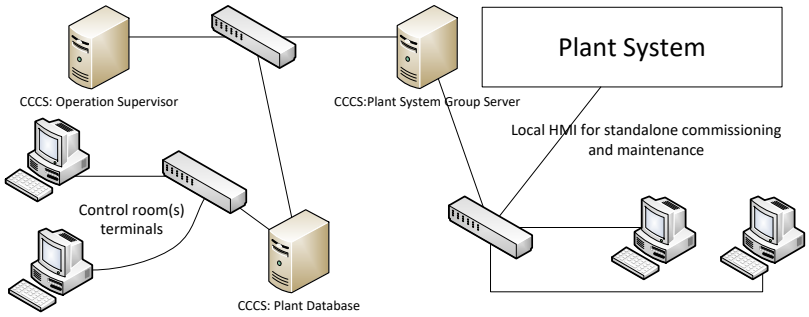

Figure X.11: Central operator Interfaces

Experiment management

Experiment management functions are those non-critical, non-real-time functions that allow managing information associated with an experiment. In particular, they provide the interface to edit Experiment Configuration, access to experimental data and check that experiment settings comply with operating Instructions.

One of the functions of CCCS is to provide the mechanisms to implement such functions, such as any required network and server infrastructure, an Operation Supervisor Software Framework, the Historical Experiment Database, the Experiment Configuration Editor.

Operation supervisor

CCCS Operation Supervisor is a central function that allows automatic coordination of the status of all Plant Systems.

The supervisor will assure the consistency of the machine status and of all of the plant systems, including coherence checks between CCCS and CMPS to avoid false protection system interventions.

The platform has not been chosen yet. The choice is between what will be natively available in the selected SCADA and what is been currently developed in ITER as part of the SUP CODAC services.

Historical Experiment database

Historical Experiment Database (HED) is a central function that allows maintaining a historical and coherent record of experiment data and parameters. The HED will contain a short-term database (at least one day of operation) and a long-term database to store the full lifetime of DTT. A remote data access portal will allow intercontinental remote access to experiment data. A uniform data access layer will be designed to allow uniform access to all DTT data.

HED will integrate in a single database scientific data produced by diagnostics systems and technical data collected by the SCADA.

The chosen platform to implement this function is MDS+. The platform has been chosen because of the proven track record over many years of use within the fusion community and because expert knowledge is available within the Italian fusion community.

The alternative would be switching to ITER DAN (Data Acquisition Network) which is currently under development. This choice main downside is that this platform will mature only when ITER will start serious operation which is later than DTT planned start of operation.

The integration between MDS+ and the chosen SCADA is an important objective of the DTT I&C prototype.

Plant System configuration

One of the most important functions of the CCCS is to manage the configuration of the DTT Plant.

To understand the task of CCCS, a clear distinction needs to be made between Experiment Configuration and Plant Configuration.

Plant Configuration is the sum of all the parameters that define the operation of a Plant System. Some of these parameters belong to the Experiment Configuration too, those whose value need to set as part of the preparation of an experiment. The remainder either has no impact to the experiment or need to be set independently of the experiment program to handle some specific issues of the plant.

During commissioning activities, the whole Plant System configuration will be handled using Operator Interfaces. During Experimental operation, the Operator Interface will allow access only to the parameters outside the Experiment Configuration Set.

The job to properly manage configuration is shared between the central SCADA that needs to guarantee the distinction between Experiment and Plant Configuration, and the Plant System that need to support these central functions.

DTT configuration will be managed by a combination of the central SCADA system and the Historical Experiment Database (MDS+). The integration of the two components and the detail definition of the Plant System configuration interface will decided as part of the development of the DTT I&C prototype.

CCCS experiment plans editor

Experiment Plans Editor is a collection of tools and services that, by interacting with the PDDB and the HED, implements a user friendly (human factor) interface to allow as much as possible, easy and error free, programming of the discharge. They include editing, comparing and verifying Experiment Plans and management of control room roles and workflows.

The technology used to implement this will either be the SCADA itself, or a custom web-based tool like Hieratika (prototype editor for ITER SUP).

X.4.3 Central Machine Protection System (CMPS)

Machine Protection functions are those critical, real-time functions that allow component failures (due to overloading or lifetime expiration) handling and minimisation (especially for those originating from operation unplanned events like disruptions), in order to ultimately mitigate the cost and schedule consequences.

This means being able to react to a component failure or risks of overload by shutting down part of the plant and eliminating or reducing the threat and start appropriate experiment termination strategies in order to minimise risks of damages and loss of experimental time.

Plant Systems are where the majority of the machine protection functions are implemented. CMPS main function is to coordinate the overall machine protection.

CMPS will:

- provide a set of servers to implement the critical global protection functions
- manage time clock and events distribution
- manage the Real Time Network RTN
- manage the Machine Protection Network MPN.

Real-time systems also contribute to the machine protection functions by distributing elaborated diagnostic data via the Real Time Network, implementing plasma termination scenarios and avoiding unsafe or risky (plasma) operational areas by tracking and avoiding the known limits.

Critical / non-critical protection functions

Critical protection functions are those functions necessary to avoid or ameliorate the consequences of a failure that will otherwise imply significant investment losses and or significant operation delays.

The implementation of these functions implies an appropriate quality-controlled process that extends to all of the components involved: sensors, actuators, electronics and communication media. Achieving this quality goal may be a costly or rather impossible, as functions where plasma control is the protection actuator.

For the above reason a distinction is made between critical protection functions and non-critical ones. The distinction is partially based on the investment and schedule risks and partially on the ultimately achievability of the quality goal. For those functions classified as critical, but where the quality process may not be applicable, the solution will be *defense-in-depth*: a combination of operation restrictions real-time controllers, limit avoidance and diversified real-time protection systems.

Central Machine Protection servers

CMPS servers implement the global critical protection functions (see Fig. X.12). The number of servers and their competence will be chosen such as to minimise their complexity.

A CMPS Server will typically deal with all protection functions associated with an actuator. In some cases, the Plant System self-protection system corresponds to the CMPS server itself.

Among the CMPS servers, one operates by coordinating all the others: the CMPS master server. Its function is: to make sure that systems are not able to operate if some CMPS servers are in alarms whenever appropriate, and to propagate a CMPS server alarm state to all the others.

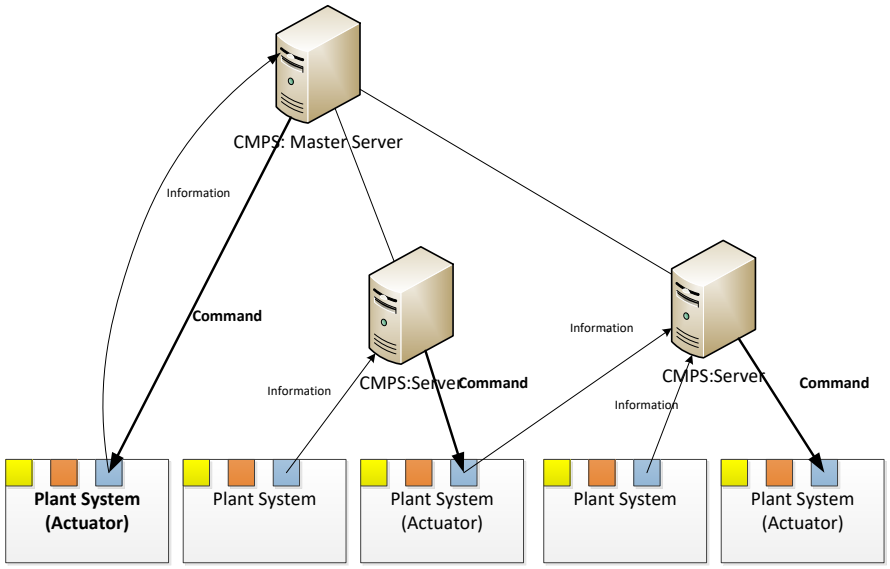

Figure X.12: Central Machine Protection Servers Scheme

Machine Protection technologies

Slow machine protection functions will be implemented using fail-safe or redundant fail-safe PLC hardware. Siemens for instance offers the F and FH series of PLCs.

Interconnection between Plant System MPS and CMPS will be implemented using a fail-safe network like Siemens Profi-safe.

User interface and top-level management of DTT CMPS will be handled using WINCC-OA. WINCC-OA provides the necessary assurances to be able to handle critical parameters and commands.

Fast machine protection will be handled using National-Instruments C-RIO hardware slave to a PLC. LabView will be used to configure the chassis and to connect the various I/O board to a fast logic solver VHDL component “FLS” that has been developed for the ITER project. This component has been developed following IEC61508 standard aiming at SIL2-SIL3.

X.4.4 Central Occupation Safety System (COSS)

Occupation Safety functions are those critical, real-time functions, that contribute to the mitigation of events that could result in harm to people within or in the proximity of the DTT facility. They include inhibit/control access to areas of potential safety hazards, interlock source of hazard (for instance high voltage) and react to unexpected/forced access to hazardous areas by removing danger.

Plant Systems are where the majority of the occupation safety functions are implemented. Plant Systems will implement control access mechanisms and communicate to the central safety functions the state of all protection mechanisms.

A candidate for the implementation of Central Safety is WINCC-OA.

X.4.5 Plant systems

Standard industrial control platform

A main PLC platform and a backup will be chosen as the preferred platform for the development of industrial control systems. Whenever a tender will be placed, some level of contractual pressure will be placed so that tenderers will adopt this platform. The main platform will be used for any in-house development, whenever PLCs are used. One of the initial tasks for DTT I&C team is to choose these platforms respecting the procurement rules.

Any in-house PLC software development will be based on a framework. UNICOS or ITER Industrial Control Library are candidate for such framework.

Standard Computer Platform

Linux has been chosen as DTT default development platform. This means that servers and client machine will be installed with this operating system. The choice of Linux distribution is still currently open. A candidate is clearly Red Hat Linux as it is aim to professional users. The downside is the cost of the support service that is needed to properly benefit from the platform.

A distinction will be made between Linux computer deployed in the CCCS and those deployed as part of Plant Systems. Central Linux installation will likely be standard distributions with standard kernels. Plant System installation will probably have a simplified kernel and a minimised Linux installation to maximise system availability and minimise vulnerabilities.

Similar consideration will hold for Real-Time Linux Systems where kernel parameter tuning is essential for performance.

DTT I&C team will select the Linux distribution and will prepare a specialised Linux distribution to be used for Plant System development. Development on the Linux platform will be based by default on the MARTe2 modular framework.

Data acquisition Hardware

PLC remote IO cards nowadays offer a price/performance ratio that is much more competitive than solutions based on PCI express. In addition, these devices are much more easily integrated in the field as they can be interfaced directly to most type of sensors. Galvanic isolation among channels groups is also easily available.

For applications where, simple algorithms and moderate performance are required (<1kHz) use of PLC and remote IO cards can be a very cost-effective solution especially considering the ease of installation and the availability of expertise in industry.

Where higher performance is required, National Instrument C-RIO used in combination with Linux PCs offers a very flexible solution to most problems because it allows offloading some processing to FPGA (Field Programmable Gate Array).

A platform for the high-performance diagnostics has not yet been identified.

Interface to CCCS

The majority of DTT Plant Systems will have an interface to the Central Control System.

There is not a mandatory requirement for the definition of the technology used to implement this interface. It is recommended that the designer adopt the most cost-effective solution for the plant design which provides some interfacing mechanism that is adequate for the desired integration.

There are instead a set of preferred solutions, in the sense that they help simplifying the task of the actual integration and later of the maintenance:

- Native interface to the chosen Supervisory Control and Data Acquisition (SCADA)
- OPC-UA
- RESTful

A Plant System with a different interface will be either integrated directly into the central SCADA technology or adapted to OPC-UA using some protocol adapter software.

X.4.6 Real time control

Real Time Control functions are those (mostly) non-critical, real-time functions that allow obtaining the required level of coordinated plasma operation.

Functions dedicated to complement machine protection or to implement complex/experimental plasma protections are also included. Many Diagnostic Plant Systems and many Plasma Actuator Plant Systems will contribute to this function.

The default platform for Real-Time development is Linux using the MARTe2 framework.

X.4.7 Networks

Command and Control Network

The network infrastructure will be based on Ethernet and will be subdivided into a number of network segments organised in such a way to segregate local traffic and implement a multi-level security. Such layers will regulate and secure communication between CCCS central layer and PSG server, control room terminals, remote participants.

Plant Systems will host their own field network segments which will be based on a mix of IP technology and some field-buses.

Data Acquisition Network

The Fast Data Acquisition Network is a tcp/Ip based network dedicated to the transfer of data acquired by Plant Systems to the Experiment Database. This network will be typically used when data rate exceeds 100 Hz. The nodes of this network will send the data to one or more MDS+ servers. No local storage of data will be allowed in the Plant Systems.

Real time network

RTN is the mechanism of communication among real-time systems (see Fig. X.13). Data is exchanged using a point to multipoint (MULTICAST) User Datagram Protocol (UDP) communication mechanism which offers predictable and repeatable data transfer latency in the presence of stationary traffic. Stationary data traffic means that all the nodes contribute to the network with fixed load, and periodic traffic patterns synchronised to the central timing system.

RTN is implemented using a managed switched multi-star network topology.

This infrastructure does not impose any particular technical hardware or software platform on the Plant System, naturally supporting different processing technologies (e.g. CPU and FPGA) and many operating systems.

This is the solution also adopted by ITER for the real-time network SDN.

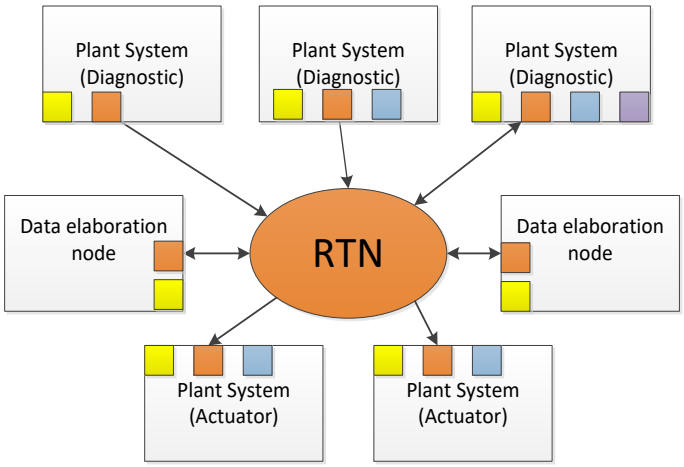

Figure X.13: Real Time Network Scheme

RTN Simulation Support

The real-time network will allow System in the loop tests by allowing a combination of Plant System to run together in a simulation where the inputs are synthetized artificially using real-time simulators.

Offline simulation tools will also be available to run Plant System real-time software on PC platforms as part of a Simulink closed loop simulation.

X.4.8 DTT I&C prototype

Central SCADA technology is currently under evaluation with a target decision for the end of 2019. The preferred option would be to adopt a scalable industrial product that had the ability to be integrated with other products.

Work is in progress to evaluate WINCC-OA, a Siemens product that derives from PVSS a CERN product. WINCC-OA stands for WINCC Open Architecture and is a scalable distributed SCADA system that runs on a number of platforms, including Linux. The Open Architecture part of the name means that the software is meant to be customised and expanded by integration of other products. This is the feature that is needed, and this is one of the reasons why the product has been selected for evaluation.

The other reason is that WINCC-OA has been adopted by ITER to manage all the critical systems: Machine Protection, Occupational Safety and Nuclear Safety. Additionally, WINCC-OA appears in some ITER Plant System, where either an interface between EPICS and the plant was too complex to develop o whether the number of process variables where too large to handle.

X.5 Conclusions

An overview of the complex system of diagnostics, control and data acquisition system that will have to be integrated on DTT has been given. Harsh environment, long discharges and ECE stray radiation will be the main challenges to face. The set of diagnostics will cover both core and edge plasma in order to properly document the exhaust parameters, such as heat loads, plasma detachment and particle compression at the divertor, and at the same time qualify the plasma performance. Real time control will be a key tool to assure that the discharge evolves along prescribed trajectories avoiding drifts towards regions of the parameters space at risk of disruption. The architecture of the instrumentation and control system that has to supervise and coordinate the machine operation and assure control, protection and safety has been defined. Technology behind will be based as much as possible on scalable industrial products with an eye on the choices made for ITER.

X.6 References

[X.1] Van Nieuwenhove and L. Vermeeren, “Irradiation effects on temperature sensors for ITER application,” Rev. Sci. Instrum., vol. 75, no. 1, pp. 75–83, Jan. 2004

[X.2] F. Felici, et al., Fusion Eng. Des. 89 (2014) 165–176.

[X.3] G. Vayakis, et al., J. Nucl. Mater. 417 (2011) 780–786.

[X.4] S. Peruzzo Fusion Engi. and Design 88(6-8):1302-1305 (2013)

[X.5] S. Peruzzo et al. Fus Eng and Des 123 (2017) 59-62

[X.6] P. Innocente, et al., Rev. Sci. Instrum. 63 (1992) 4996.

[X.7] T Estrada et al. Plasma and Fusion Research: Overview Articles Volume 7, 2502055 (2012)

[X.8] R Scannel et al., Journ of Instrum,12 (2017) C11010

[X.9] R. J. Fonck, R. J. Goldston, R. Kaita, *and* D. E. Post, *Appl. Phys. Lett*. **42**, 239 (1983)

[X.10] R. Neu, S. Brezinsek, M. Beurskens, *et al.,* 2013 IEEE 25th SOFE), DOI: 10.1109/SOFE.2013.6635302

[X.11] M. Bitter, S. von Goeler, R. Horton*, et al., Phys. Rev. Lett.* **42,** 304 (1979)

[X.12] R. Bartiromo, F. Bombarda, M. Leigheb, et al., Proc. Workshop on "Diagnostics for Contemporary Fusion Experiments (Varenna 1991)
[X.13] M. Garcia-Munoz et al., Rev. Sci. Instrum. 87, 11D829 (2016)
[X.14] W Weidbrink, Rev Sci. Instrum 81 (2010) 10D727
[X.15] Jacobsen A. S. et al 2016 Plasma Phys. Control. Fusion 58 042002
[X.16] Ikeda R. et al 2017 J. Infrared Milli. Terahz. Waves **38** 531
[X.17] Bin W. et al 2015 Fusion Eng. Des. **96**-**97** 733
[X.18] Bin W. et al 2016 Rev. Sci. Instrum. **87** 11E507
[X.19] M Nocente et al Review of Scientific Instruments **89**, 10I124 (2018
[X.20] L. Jakubowski et al., Radiation Measurements (2010).
[X.21] F. Causa et al., Nucl. Fusion 55 (2015) 123021
[X.22] F. Bagnato et al 2018 Plasma Phys. Control. Fusion 60 115010.
[X.23] JH Yu, EM Hollmann, et al. Physics of Plasmas, 20 (2013) 042113.
[X.24] B Esposito PL. Phys Contr. Fusion 2017 59 014044
[X.25] M. Rebai et al., Rev. Sci. Instrum., **87**, 11D823 (2016); doi: 10.1063/1.4960490
[X.26] M. Angelone, et al., Nucl. Instrum. Meth. In Phys. Res. A 595 (2008) 616
[X.27] D. Rigamonti et al., Rev. Sci. Instrum. 89, 10I116 (2018)
[X.28] L. Giannone et al, Plasma Phys. Contr. Fusion 47 (2005) 2123
[X.29] M. Angelone et al. Nucl. Instrum. Meth. In Phys. Res. A 623 (2010) 726
[X.30] M. Bernert, et al., Rev. Sci. Instrum. 85 (2014) 033503
[X.31] M.L. Reinke, I.H. Hutchinson, Rev. Sci. Instrum. 79 (2008) 10F306
[X.32] T Odstrcil > Review of Scientific Instruments 87 (2016) 123505, https://doi.org/10.1063/1.4971367
[X.33] F. Sauli, GEM: A new concept for electron amplification in gas detectors, Nucl. Instrum. Meth. A 386 (1997) 531
[X.34] D. Mazon et al 2017 JINST 12 C11034
[X.35] D Pacella et al Nuclear Instrum and Meth. A 720 (2013) 53
[X.36] R.J. Fonck, A.T. Ramsey and R.V. Yelle*, Appl. Opt.* **21** (1982) 2115
[X.37] J.L. Schwob, A.W. Wouters, S. Suckewer and M. Finkenthal, *Rev. Sci. Instrum*. **58** (1987) 1601
[X.38] K. Kadota, M. Otsuka, and J. Fujita, Nucl. Fusion 20, 209(1980)
[X.39] H Verbeek Journal of Physics E: Scientific Instruments, 19(11) 1986
[X.40] S. Costa Review of Scientific Instruments **66**, 330 (1995)
[X.41] O McCormack http://paduaresearch.cab.unipd.it/10679/1/mccormack_oisin_thesis.pdf
[X.42] J. Howard, JINST 10 (2015) P09023
[X.43] M Agostini et al Tb presented at the EPS Conf. - Milan, July 2019
[X.44] M. Spolaore, P. Agostinetti, M Agostini, M. Dalla Palma, G. Grenfell, M. Iafratia, E. Martines, S. Spagnolo, N. Vianello, M. Zuin "Working Group on Langmuir Thermocouples and Turbulence diagnostics for DTT: final report 2018" DTT-DIA-TEC-001 001, 13/02/2019
[X.45] Adamek, J., et al. "Electron temperature and heat load measurements in the COMPASS divertor using the new system of probes." Nuclear Fusion 57.11 (2017): 116017.
[X.46] Xu, J. C., et al. "Design of Langmuir probe diagnostic system for the upgraded lower tungsten divertor in EAST tokamak." Review of Scientific Instruments 89.10 (2018): 10J127
[X.47] Xu, J. C., et al. "Upgrade of Langmuir probe diagnostic in ITER-like tungsten mono-block divertor on experimental advanced superconducting tokamak." Review of Scientific Instruments 87.8 (2016): 083504
[X.48] Liu, J. B., et al. "In–out asymmetry of divertor particle flux in H-mode with edge localized modes on EAST." Nuclear Fusion 56.6 (2016): 066006.
[X.49] Kuang, A. Q., et al. "The flush-mounted rail Langmuir probe array designed for the Alcator C-Mod vertical target plate divertor." Review of Scientific Instruments 89.4 (2018): 043512.
[X.50] Chen, L., et al. "Thermal Analysis on Various Design Concepts of ITER Divertor Langmuir Probes." Fusion Science and Technology 73.4 (2018): 568-578.
[X.51] J. Ren Review of Scientific Instruments 89, 10J122 (2018); doi: 10.1063/1.5038677
[X.52] http://www.miccltd.com/temperature-measurement/mi-thermocouple-cable/thermocouple-sheath-nicrobell; http://www.temperature.com.au/portals/0/File/pdf/1362.pdf
[X.53] M.-H. Aumeunier et al. IEEE Transactions on Plasma Science, vol. 40, no. 3, 753-760, 20121
[X.54] G. Maddaluno, et al., Espoo Finland, 40th EPS Conference on Plasma Phys., vol. 37D, 2013, p. P5.102 http://ocs.ciemat.es/EPSAP/pdf/P5.102.pdf
[X.55] Park, H. K., et al Physical review letters 96.19 (2006): 195003.
[X.56] Conway G. et al. (2011) Phys Rev Lett 106 065001
[X.57] Classen, I. G. J., et al Review of Scientific Instruments 81.10 (2010): 10D929.
[X.58] A.R. Field Review of Scientific Instruments **80**, 073503 (2009)
[X.59] McCormick K and Team A Rev Sci Instrum 56 1063–5
[X.60] Tobias, B., et al. " Review of Scientific Instruments 81.10 (2010): 10D928
[X.61] Porkolab M, Rost C J et al. 2006 Ieee T Plasma Sci 34 229–34
[X.62] J. Schirmer Nucl. Fusion 46 (2006) S780–S791
[X.63] O. Grulke 'Transport studies for Wendelstein 7-X' preprint
[X.64] https://about.gitlab.com/
[X.65] https://vcis.f4e.europa.eu/marte2-docs/master/html/contributing/qa/qa.html

[X.66] H.K. Gulati, H. Dave, F. Di Maio, A. Wallander, Fusion Eng. Des. 85 (2010) 549
[X.67] D. Humphreys, et al., Fusion Eng. Des. 83 (2–3) (2008) 193–197
[X.68] G. De Tommasi, et al., IEEE Trans. Plasma Sci. 35 (3) (2007) 709–723
[X.69] T. Bellizio, et al., Fusion Eng. Des. 86 (2011) 1026–1029
[X.70] S. Peruzzo, et al., Fusion Eng. Des. 84 (2009) 1495–1498
[X.71] De Tommasi, G., Albanese, R., et al. (2007) IEEE Transactions on Plasma Science, 35 (3), pp. 709-723
[X.72] Albanese, R., Ambrosino, G., et al. (2005) Fusion Engineering and Design, 74 (1-4), pp. 627-632
[X.73] Ambrosino, G., Ariola, M., et al (2009) IEEE Transactions on Plasma Science, 37 (7 PART 2), pp. 1324-1331
[X.74] Albanese, R., Ambrosino, R. et al. A (2016) IEEE Conference on Control Applications, CCA 2016
[X.75] J. Wesson, The science of JET. Abingdon, Oxon: JET Joint Undertaking, 2000
[X.76] Ambrosino, G., Ariola, M. (2008) IEEE Transactions on Plasma Science, 36 (3 PART 2), pp. 834-840.
[X.77] E. Kolemen, J. Nucl. Mater. 463 (2015) 1186 (48693)
[X.78] S. Mastrostefano, P. Bettini, T. Bolzonella, M. Furno Palumbo, Y.Q. Liu, Matsunaga, R. Specogna, M. Takechi, F. Villone, Fusion Eng. Des. 96–97 (2015) 659
[X.79] L. Figini, et al., 43rd Conf. Plasma Phys Contr. Fusion, Leuven, Belgium, 2017 http://ocs.ciemat.es/EPS2016PAP/pdf/P4.072.pdf
[X.80] D.G. Whyte, et al., Nucl. Fusion 50 (2010) 105005
[X.81] T.H. Osborne, G.L. Jackson, Z. Yan, et al., Nucl. Fusion 55 (2015) 063018
[X.82] J. Li, H.Y. Guo, B.N. Wan, et al., Nat. Phys. 9 (2013) 817–821

Chapter XI

NEUTRONICS

XI.1 Introduction

A significant neutron production is expected in Deuterium-Deuterium (DD) operations of the DTT machine. Due to its high performances, the assessment of the radiation fluxes and nuclear loads is crucial in the design of the machine, in particular for proper shielding of superconducting coils and for the assessment of the neutron-induced radioactivity. The latter is mainly needed for the licensing process, for the definition of maintenance and decommissioning programs, and for radwaste management. For this purpose, three-dimensional neutron and gamma transport simulations have been performed using MCNP5 v1.60 Monte Carlo code [XI.1]. These analyses were mainly devoted to optimize the vacuum vessel shielding capability in order to reduce the nuclear heating on the superconductive magnets. To this end, owing to space constraints, a lot of effort has been made to study advanced shielding solutions aimed at guaranteeing sufficient protection of the magnets.

Additional shielding analyses were carried-out with MCNP5 and ADVANTG [XI.2] codes to optimize building design in order to fulfil the requirements in terms of dose limits and constraints outside the main bunker. Activation and shutdown dose-rate calculations were performed with FISPACT-II inventory code [XI.3] and Advanced D1S [XI.4] tool to assess the temporal evolution of the activity and dose-rate levels during different phases of DTT operations, inside and outside the cryostat.

XI.2 Neutron Yield and Irradiation History

The maximum DD neutron yield presently assumed in H-mode high performance operations is $1.5x10^{17}$ n/s with $1.5x10^{15}$ n/s Deuterium-Tritium (DT) high energy neutrons (i.e. 1%) from triton burn-up. The neutron yield rate has been evaluated on the basis of conservative mono-dimensional estimations and more accurate evaluations based on the latest plasma scenarios are in progress.

The neutron irradiation scenario during DTT lifetime is shown in Tab. XI.I. It is defined according to an optimistic 28-year experimental program, consisting in 6 months on and 6 months off operations. The number of pulses, their characteristics and the expected neutron emissivity depend on the plasma scenarios. According to such program, DTT is supposed to reach the maximum performance after 8 years of operations with an annual DD neutron yield of $1.53x10^{21}$ n/year (DT neutrons $1.53x10^{19}$).

The total DD neutron budget after 28 years of operation is $3.73x10^{22}$ (DT neutrons $1.53x10^{20}$), equivalent to $2.49x10^{5}$ s of operation at full power. This scenario is conservative for safety purposes and it has been used for shielding study, activation analyses and cumulated nuclear quantities.

TABLE XI.I. NEUTRON IRRADIATION HISTORY DURING DTT LIFETIME

Year	1	2	3	4	5	6	7	8	9 to 28
Maximum DD neutron yield rate (n/s)	$3.60{\cdot}10^{14}$	$2.70{\cdot}10^{15}$	$1.80{\cdot}10^{16}$	$4.30{\cdot}10^{16}$	$6.00{\cdot}10^{16}$	$9.30{\cdot}10^{16}$	$1.00{\cdot}10^{17}$	$1.10{\cdot}10^{17}$	$1.50{\cdot}10^{17}$
Annual DD neutron yield (n/year)	$9.00{\cdot}10^{18}$	$6.75{\cdot}10^{19}$	$4.50{\cdot}10^{20}$	$8.60{\cdot}10^{20}$	$1.20{\cdot}10^{21}$	$1.26{\cdot}10^{21}$	$1.35{\cdot}10^{21}$	$1.49{\cdot}10^{21}$	$1.53{\cdot}10^{21}$

XI.3 Neutronics Models

Two neutronics models were developed for the analyses (Fig. XI.1): a 20 deg full-sector detailed model for the nuclear loads, shielding study, activation and shutdown dose rate calculations inside and close to the cryostat, and a simplified 360 deg model with building, for the assessment of the radiation field inside and outside the DTT building and for air activation study.

The 20 deg model is a sector of the machine with reflecting boundaries to represent a 360 deg configuration. Some parts of this model have been converted from CAD into the equivalent MCNP representation using the CAD-to-MCNP interface provided in the SuperMC [XI.5] code. It includes: the Central Solenoid (CS), the Toroidal Field (TF) coil winding pack, case and ground insulator, the double wall Vacuum Vessel (VV), made of Stainless Steel (SS) filled with borated water (0.8% weight of B, enriched with 95% of ^{10}B) with an additional shield in the inboard side, the First Wall (FW), a CuCrZr[1]-water cooled duct with a tungsten armour. In Vessel

[1] It refers to the previous copper-based design, but preliminary studies have shown that the shielding results of the present analyses are valid even with the recent SS-based FW options (chapter IV).

Coils (IVC), Poloidal Field (PF) coils and Inter-Coil Structures (ICS) have been modelled as well. A simple representation of the divertor – ITER-like type in SN (Single Null) configuration – has been used: the divertor cassette is made with a 60%$_{vol}$ SS316L(N) and 40%$_{vol}$ water mixture and the 5 cm thick Plasma Facing Component (PFC) has been represented with a 71% W, 8.1% CuCrZr, 6.4% Cu and 14.5% water mixture. The five ports are almost empty, covered with a 1.5 cm thick SS plate only and they extend up to the cryostat. This produces a large amount of neutron streaming from the port. For this reason, 2 cm thick collars made of B_4C (Boron Carbide) compressed powder (2.3 g/cm^3 density) have been inserted in the equatorial ports to reduce the TF coil loads. The thermal shield between the VV and the TF is a double-wall structure (3 mm thick SS walls), separated by a 15 mm void shell and cooled by helium gas. The cryostat is made of SS304 steel. The VV has a different thickness and composition inboard (IB) and outboard (OB). The total thickness of the VV is 12 cm in IB (at the equatorial plane) and it is composed of a 1.5 cm thick front shell (SS), 6.5 cm of borated water and steel ribs, a 2.5 cm thick neutron shield and a 1.5 cm thick steel rear shell. The neutron shield is a B_4C–W–B_4C insert (more details are given in ection). The VV in OB (at the equatorial plane) is 23 cm thick and it is made of a 1.5 cm thick steel shell, 20 cm of borated water and steel ribs and a 1.5 cm thick steel rear shell. As the model does not include NBI, nor heating, diagnostic and auxiliary systems, additional studies were performed including a dummy port plug in all ports to make a preliminary estimation of port configuration effect.

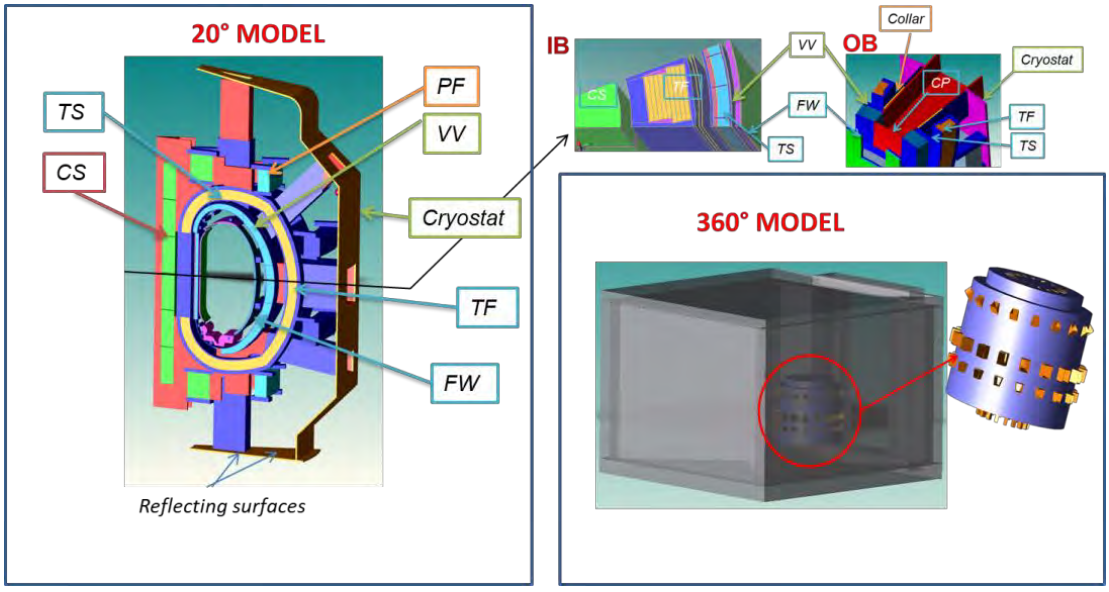

Figure XI.1: MCNP 20° model of DTT (left) and 360° model of DTT and building (right)

The 360 deg model has a simplified representation of the components inside cryostat and it is included inside the main building made of standard concrete. Neutron and gamma fluxes and effective dose outside bunker have been calculated by varying the concrete thickness to evaluate the shielding efficiency of the walls. It should be noted that waiting for a final design of the building that will host DTT facility, a conservative approach has been used, consisting in a reduced height than that presently considered (internal dimensions 35m x 33m x 23m instead of 35 m x 33 m x 28 m as in the present layout).

In both the models, the DD and DT neutron source distributions have been described according to a full current SN plasma scenario by a parametric representation using a dedicated subroutine included in MCNP.

The energy spectrum is that produced by a DD (2.45-MeV neutrons) and DT (14.1-MeV neutrons) plasma with a peak ion temperature of 11 keV.

XI.4 Shielding Design of the VV

The study of some advanced shielding solutions was necessary to guarantee sufficient protection of the magnets and to reduce the cryoplant capacity requirements, considering the challenging space constraints. In particular, the aim was to reduce the nuclear heating density to the superconducting coils below 1 mW/cm^3 with sufficient margin. In the present analyses a safety factor (SF) of 1.5 is assumed to consider the uncertainties related to design limitations, modelling approximations and nuclear data.

TABLE XI.II. NUCLEAR HEATING DENSITY IN TF COIL FIRST LAYER IN IB AT THE EQUATORIAL PLANE

VV thick. (cm)	Variant	Borated Water thickness (cm)	Nuclear heating density (mW/cm^3)		Ratio	Max Neutron yield rate @1mW/cm^3 (n/s)
			NO SF	SF=1.5		
12	(Ref) B-wat – Inner shield	6.5	0.84	1.26	-	1.19 x10^{17}
Impact of B in Water & Inner-shield						
12	Only VV shell - internal Void	0	5.23	**7.85**	6.23	1.91 x10^{16}
	Pure water - No inner shield	9	2.64	**3.96**	3.15	3.79 x10^{16}
	B-wat - No inner shield	9	1.17	**1.76**	1.39	8.55 x10^{16}
	Pure water - Inner shield	6.5	1.14	**1.71**	1.36	8.77 x10^{16} (8.44 x10^{16} In OB)
Impact of VV thickness						
12.5	Ref + 0.5 cm B-wat	7	0.78	**1.17**	0.93	1.28x10^{17}
13	Ref + 0.5 cm B-wat + 0.5 cm VV front shell	7	0.73	**1.10**	0.86	1.36x10^{17}
	Ref + 1 cm B-wat	7.5	0.72	**1.08**	0.86	1.39Ex10^{17}
13.5	Ref + 1.5 cm B-wat	8	0.67	**1.01**	0.79	1.49x10^{17}
14	Ref + 1.5 cm B-wat + 0.5 cm VV front shell	8	0.63	**0.95**	0.75	1.58x10^{17}

During the design evolution of the machine, more than 50 shielding configurations of the VV have been examined using water, borated water, Boron Carbide (B4C), W Carbide (WC) and/or Borated Steel (SSB) to reduce the TF nuclear heating. The nuclear heating density in the most critical zone, i.e. on the first layer of IB TF coil at the equatorial plane, for the most significant configurations is reported without and with a safety factor in Tab. XI.II. The neutron yield rate below which the nuclear heating density is less than 1 mW/cm^3 is also reported as well as the results with increased VV thickness. If the double-shell of the VV is empty, the maximum nuclear heating density results to be 5.3 mW/cm^3 (about 8 mW/cm^3 including SF=1.5), well above the design target, while the total TF heating is about 50 kW (~75 kW with SF). A double-wall VV filled with normal water only provides a nuclear heating density of 2.64 mW/cm^3 (3.96 mW/cm^3 with SF), much higher than 1 mW/cm^3. Even if the use of borated water (i.e. as in JT-60SA) provides a significant reduction, up to 1.17 mW/cm^3 (1.76 mW/cm^3 with SF), the design limit is not yet achieved.

Among all the examined feasible options, the best configuration consists in a combination of borated water and a 2.5 cm neutron shield of B_4C compacted powder and W inside a SS container. The best performing 12 cm thick VV radial layout consists of 1.5 cm of front steel shell, 6.5 mm of borated water (B 0.8 wt%, 95% B^{10} enriched) followed by a neutron shield insert of 0.1 cm of steel, 1 cm of B_4C powder, 0.5 cm of tungsten, 0.9 cm of B_4C powder, and 1.5 cm of rear steel shell. This option is the present reference configuration of the inboard vessel, resulting in a nuclear heating density of 0.84 mW/cm^3 (1.26 mW/cm^3 with SF). This value still exceeds the design target and an increase of 15 mm is required to provide nuclear heating density values below 1 mW/cm^3.

As the Boron content in water induces corrosion at high temperatures, the current strategy is to use borated water only during high performance plasma operations. On the basis of the results shown in Tab. XI.II, the machine might operate with pure water in several phases of DTT lifetime depending on the performances (i.e., when the neutron yield rate is lower than 8.44 x10^{16} n/s the nuclear heating in TF coil is below 1 mW/cm^3).

Figure XI.2 shows the poloidal profile along the first TF turn. The nuclear heating in OB is strongly affected by the port configuration. In the worst and not realistic case with empty ports the nuclear heating density is close to 1 mW/cm^3 at the side of port #2 (i.e. top-lateral port) and #3 (i.e. equatorial port). It should be noted that in port #3 a port collar of 2 cm of Boron Carbide has been inserted: without collar the nuclear heating density would increase of about 27 % (sector I). Even if collars could be useful in all ports to reduce the total nuclear heating in TF, in the present DTT design these are foreseen only in equatorial ports due to space constraints.

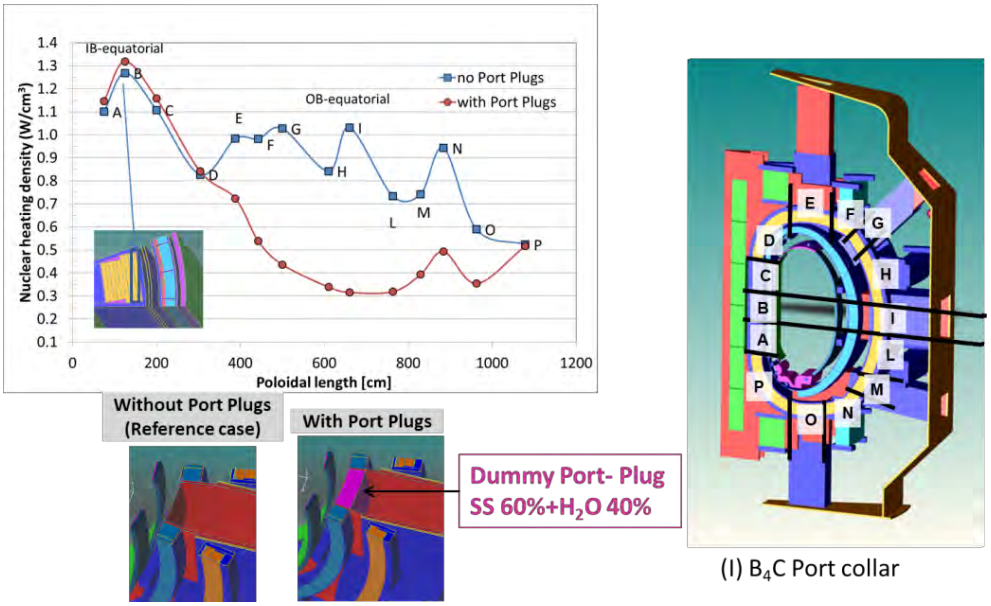

Figure XI.2: Poloidal distribution of the nuclear heating density in the First WP (Winding Pack) layer (with SF 1.5)

If all ports are plugged (i.e., with dummy port plug VV-shaped, made of SS 60% and water 40%), the nuclear heating density in outboard sectors shows a sensible reduction and in particular in sector I it decreases to 0.3 mW/cm^3. The total TF heating is 9.1 kW (13.7 kW with SF 1.5) with all ports empty and 5.8 kW (8.7 kW with SF 1.5) with dummy port plugs.

XI.5 Neutron and Gamma Fluxes

The three-dimensional neutrons and secondary gamma fluxes spatial distributions and radial profiles at the mid-plane in high performance phase (DD 1.5 x10^{17} n/s and 1% DT) inside cryostat are shown in Figs XI.3 and XI.4, respectively. The maximum neutron flux inside the plasma chamber is 1.1x10^{12} n·cm^{-2}s^{-1} corresponding to a cumulated neutron fluence at the end of life of 2.7x10^{17} n·cm^{-2}. The maximum gamma flux is 3x10^{11}γ·cm^{-2}s^{-1} and the total cumulated gamma fluence at of the end of life is 7.5 x10^{16} γ·cm^{-2}. The effect of streaming through the almost empty-ports is noteworthy.

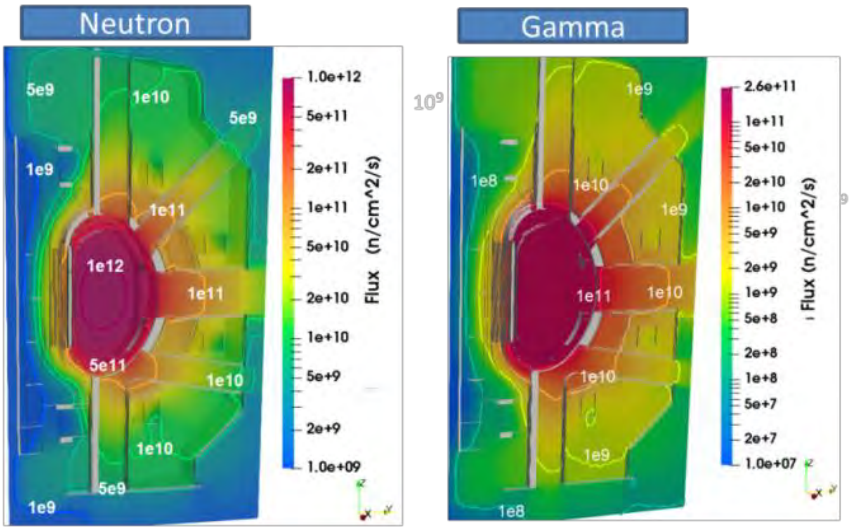

Figure XI.3: Maps of neutron (left) and gamma (right) fluxes inside cryostat in high performance phase.

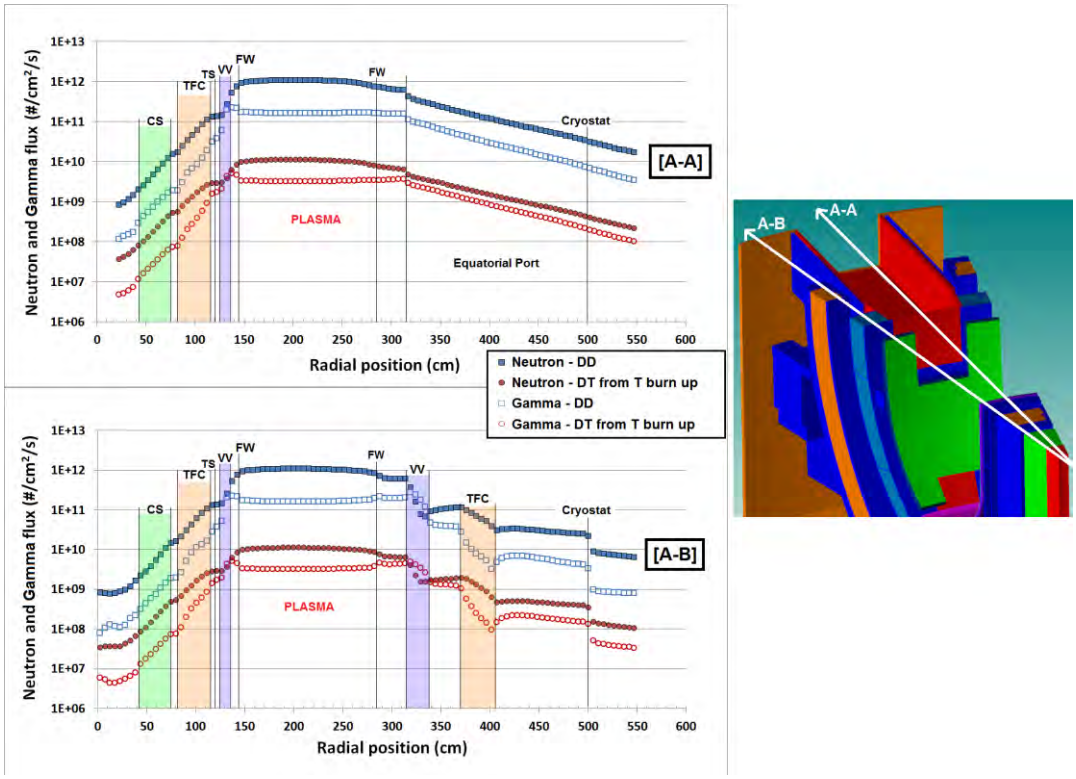

Figure XI.4: Central (A-A, top) and lateral (A-B, bottom) radial profiles of neutron and gamma fluxes.

At the mid-plane, inboard, the fluxes decrease of about three orders magnitude from plasma to CS. Outboard, 50 cm outside cryostat, the fluxes are about 1.5 and 2 orders of magnitude lower than in plasma chamber behind TF coil and along mid-port, respectively. The ratio between the gamma and neutron fluxes varies between 0.1 and 0.4 depending on the position; higher gamma contribution is found in borated water only. The contribution of DT neutrons to the total neutron flux is 1-5 %, while gammas coming from them represent 2-7 % of the total gamma flux. The fast neutron flux (E > 0.1 MeV) contribution is ~80% of the total in the components faced to the plasma and drops to ~10% in the cryostat. The contribution of neutrons with energy greater than 10 MeV is lower than 1%.

The spatial distributions of neutron and gamma fluxes inside the building are shown in Fig. XI.5. At the cryostat level the n flux is ~10^{10} n·cm^{-2}s^{-1}. At about 10 m far from the centre of the machine the neutron flux decreases below 5x10^{9} n·cm^{-2}s^{-1}. At the south wall the neutron and gamma fluxes are 3.3x10^{9} n·cm^{-2}s^{-1} and 6.8 x10^{8} γ·cm^{-2}s^{-1}. The maximum values close to the wall are 4.7x10^{9} n·cm^{-2}s^{-1} and 7.84 x10^{8}γ·cm^{-2}s^{-1} near the cold box hall.

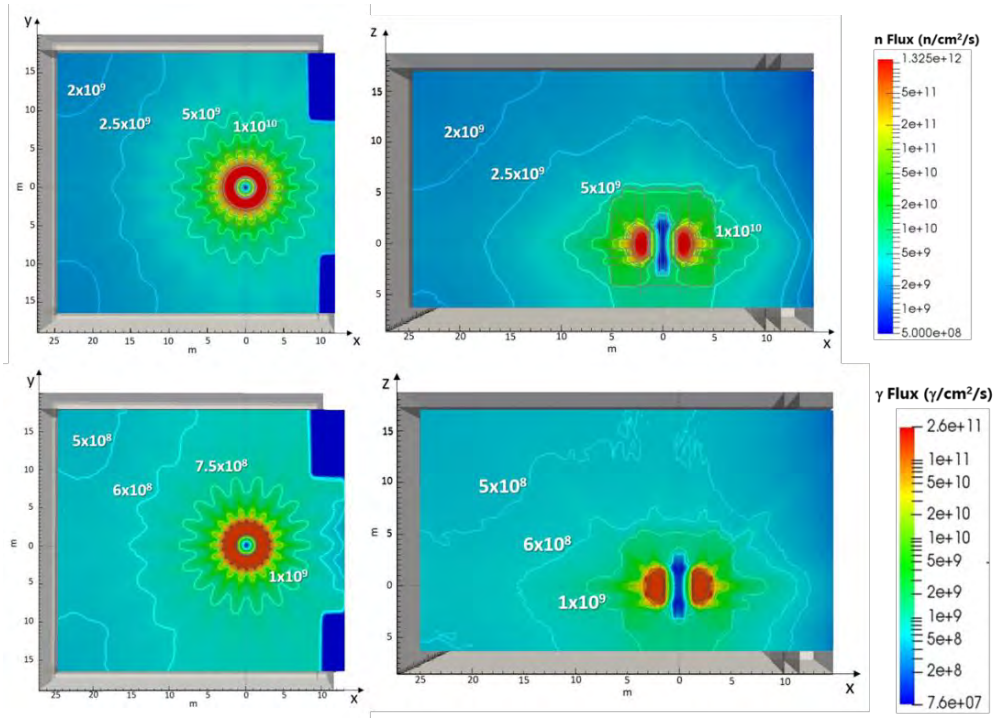

Figure XI.5: Maps of neutron (top) and gamma (bottom) fluxes inside the building during high performance phase.

XI.6 Nuclear Loads in DTT Components

During the high-performance phase, the maximum nuclear heating density in the FW is 34 mW/cm^3 on W and 9.5 mW/cm^3 on CuCrZr, in VV front shell it is 7.8 mW/cm^3 and it decreases to 1.7 mW/cm^3 in rear shell. In the thermal shield (TS) it is 1.34 mW/cm^3 and at the cryostat it is below 0.1 mW/cm^3. Nuclear heating in all machine components with and without dummy port plugs are reported in Tab. XI.III. The greatest loads are on FW, divertor and VV. The port plugs shield the outboard components, providing a significant reduction

of all the nuclear responses with respect to the configuration with empty ports. Conversely, due to backscattering effects, they slightly increase the loads on inboard components (max +13 % on the FW). It is worth stressing that both configurations represent two unrealistic and opposite cases. More accurate assessments will be performed including NBI and other heating, diagnostics and auxiliary systems.

TABLE XI.III. NUCLEAR HEATING IN ALL DTT COMPONENTS WITH AND WITHOUT DUMMY PORT PLUGS (NO SAFETY FACTOR)

		REF- No Port plug		Dummy PORT-PLUGS in all ports		
Component	**Sub-component**	**kW sub-component**	**kW Total**	**kW- sub-component**	**kW Total**	**Ratio Plug/No plug**
First wall*	W	7.3	**16.5**	8.5	**18.6**	1.13
	CuCrZr	9.2		10.1		
Vacuum vessel*	Shell + Ribs	14.4	**17.0**	15.3	**18.1**	1.06
	Neutron shield	2.6		2.7		
Thermal Shield			**1.4**		**0.9**	0.67
TF	SS-case	4.1		2.6		
	WP	4.7	**9.1**	3.0	**5.8**	0.63
	Insulator	0.3		0.2		
ICS			**1.9**		**0.8**	0.44
IVC			**6.0**		**6.0**	1.00
CS			**0.14**		**0.13**	0.91
PF			**1.6**		**0.4**	0.24
Divertor*	PFC	6.0	**10.7**	6.5	**11.5**	1.08
	Cassette	4.7		5.0		

** water is not included (i.e. for reference configuration: 60.4 kW in VV borated water, 7.9 kW in FW and 4.7 kW in divertor water)*

The maximum absorbed dose in the IVC and TF coil insulator at the end of life are ~1.2 MGy and ~90 kGy (without safety factor), respectively. Assuming a design limit of 10 MGy on epoxy resin, the maximum dose in the insulator at the end of operations is expected to be well below the limit recommended for the replacement.

The dpa and He-production on DTT components at the end of life are expected to be lower than $2x10^{-4}$ dpa and $4x10^{-4}$ appm, therefore the radiation damage is negligible and re-weldability is not compromised. Conversely, the conventional electronics might not withstand the expected radiation condition. The dose rate in silicon in the building is in the range $2x10^{-3} \div 1x10^{-2}$ Gy/s depending on the position, corresponding to a cumulated absorbed dose at the end of life of 0.5 ÷ 2.5 kGy. Considering the ITER limits on cumulated dose on critical electronics of 1 Gy and to non-critical electronics of 10 Gy, the critical (non-critical) electronics could withstand cumulative DTT irradiation of $1.5 \div 7.5\ x10^{19}$ n equivalent to 100-500 s at full power ($1.5 \div 7.5\ x10^{20}$ n equivalent to 1000-5000 s at full power for non-critical electronics). The conventional electronics should be frequently replaced, shielded or located outside the main building, otherwise the use of rad-hard electronics is recommended.

XI.7 Activation and Shutdown Dose Rate Assessment

Activation and shutdown dose rate analyses were performed using the 20 deg DTT model without port plug,

using the operational irradiation history reported in Tab. XI.I. The material compositions take into account the relevant impurities and, in particular, controlled Cobalt and Tantalum content is assumed for the structural steel (i.e. 500 wppm of Co and 100 wppm of Tantalum). A safety factor of 2 has been applied to all results for conservative purpose. The complete inventory was calculated during the whole DTT lifetime. The results in this chapter refer to three shutdown phases: between the second and third year (18 months scenario, 7.87 x10^{19} n), between the fourth and the fifth year (42 month scenario, 1.41x10^{21} n) and after 28 years (end-of-life, 3.73x10^{22} n) considering pulsed irradiation in the last period of operation for a proper assessment of the short-term activation. For each scenario and the results are provided for different cooling times (i.e. time after last irradiation). Figure XI.6 shows the temporal evolution of the contact dose rate of in-vessel components at the end of the three examined scenarios. After medium and high-performance plasma phases a not negligible activation at short-medium times after DTT shutdown is expected, especially for in-vessel components. The contact dose rate level at one day after the end of DTT operations is indeed > 200 mSv/h in tungsten (60mSv/h at the end of 42-months operations). At longer cooling times, higher induced radioactivity is observed in steel mainly due to nickel, cobalt, and tantalum activation (i.e. ~7 mSv/h in divertor cassette at one month after end-of-life shutdown). The outcome of the performed analyses highlights that a proper remote handling system is mandatory. The radioactivity level may require the preparation of a suitable temporary repository to store some of the dismounted activated components. However, within 50 years from the shutdown, the activity and contact dose of all components is expected to be as moderated as to be classified as low level waste. If alternative divertors are used, i.e. with targets made of a capillary porous system (CPS) filled with liquid metal, the plasma facing component is made of W-Li or W-Sn. Compared to a solid layer of W, in case of W-Li the effect on contact dose is marginal, but the tritium production from neutron interaction with Lithium increases (at shutdown after high performance phase the tritium production is 0.85ng/g_{comp}). The contact dose of the W-Sn compound does not differ significantly from the case of solid W for cooling times up to one month after shutdown. For longer cooling times it becomes higher than the latter, e.g., after one year from shutdown it is about one order of magnitude higher due to ^{125}Sb generated from ^{124}Sn, with a half-life of 2.76 y.

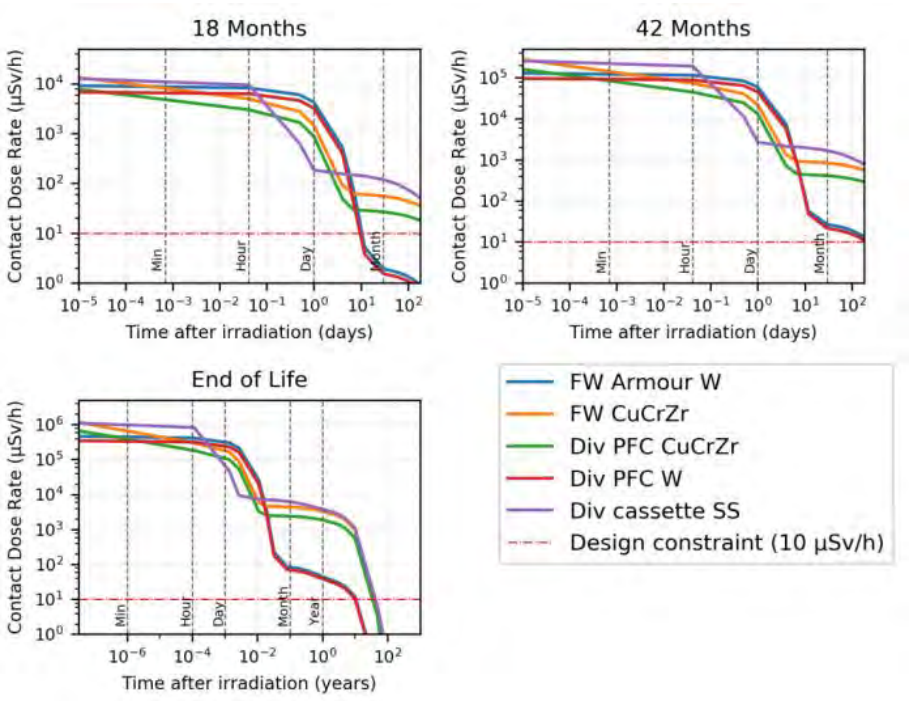

Figure XI.6: Contact dose rate in in-vessel components vs. cooling time after 18 months, 42 months and at end-of-life irradiation scenarios

Figure XI.7 shows the maps at one day and three-months of cooling time for the 18 months end-of-life scenarios. The shutdown dose rate versus time for the three scenarios is shown in Fig. XI.8, in several locations outside cryostat and close to cover plate.

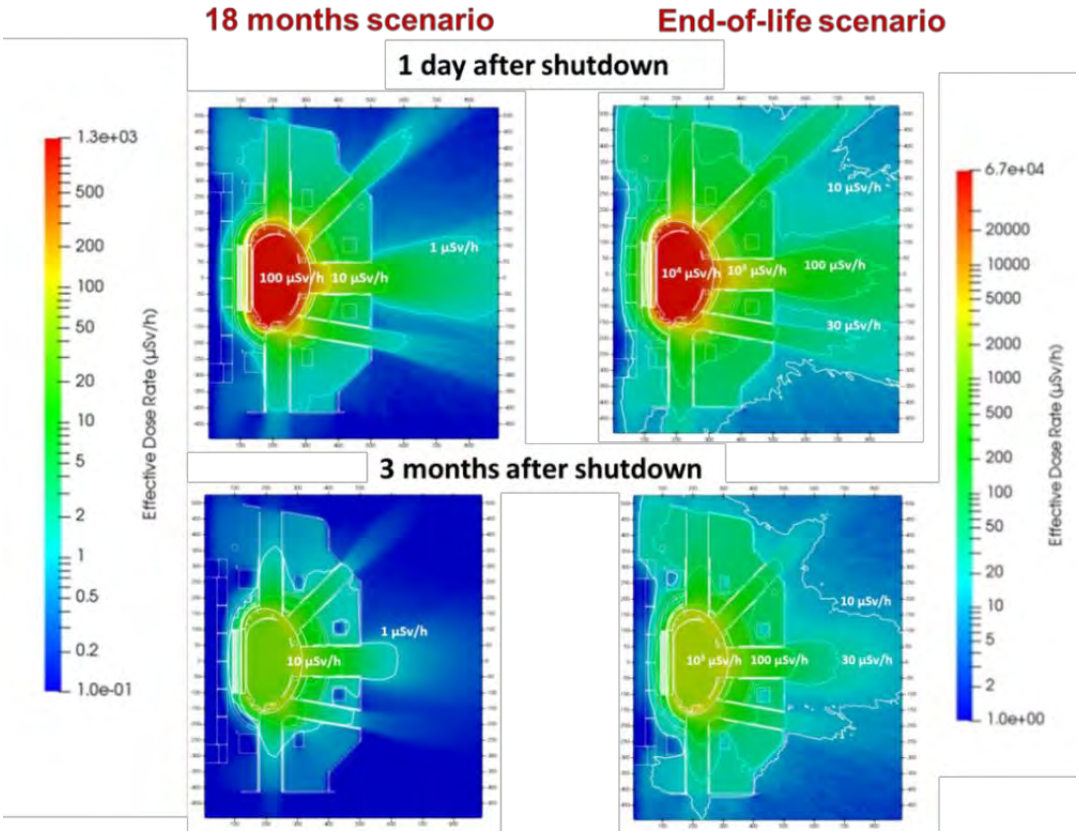

Figure XI.7: Shutdown dose rate after one day and three months at the end of 18 months of operations and at the DTT end-of-life.

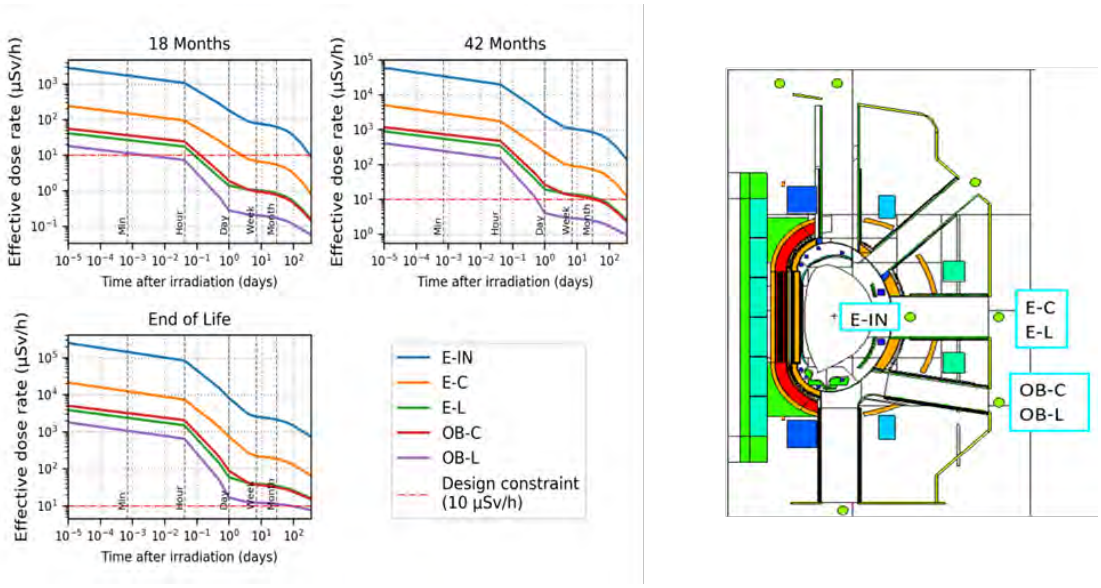

Figure XI.8: Shutdown dose rate vs. cooling time at some relevant positions inside and outside of the cryostat after18 months, 42 months and end-of-life scenarios. C and L refer to central lateral positions in toroidal direction, respectively.

At the end of the first phase, the dose level outside of the cryostat is sufficiently moderate to avoid access limitations to workers in the torus hall even at short cooling times. Conversely, in high performance phase, the shutdown dose rate level exceeds 100 μSv/h outside ports up to 3 m from the cryostat at one day after DTT shutdown. At one week from the shutdown the dose rate in front of the empty equatorial port is <10 μSv/h at the end of the first phase, ~100 μSv/h at the end of 42 months scenario and ~200 μSv/h at the end-of-life. The dose rate levels indicate that there is no need for remote handling outside cryostat, but during and at the end of high-performance phase the access to the torus hall should be controlled and maintenance operations accurately planned, to ensure that the annual exposure level will be well below 20 mSv to comply with Italian regulation as discussed in next chapter.

Neutrons induce also air-activation. ^{41}Ar produced by thermal neutron capture in ^{40}Ar, due to its high thermal cross section and relatively long half-life (about 1.8 h), is the main radionuclide responsible for environmental contamination. The average dose rate in the building at the end of high-performance phase is ~300 μSv/h and it drops to 0.1 μSV/h in about 1 day. The air change rate has been varied to study the effectiveness of ventilation (i.e. R from 0 to 5 air changes per hour). For example, considering one air change per hour (R=1) the dose rate is below 0.1 μSV/h after 5 hours. It should be anyway taken into account that the ventilation rate and the overall system should reduce the activated air released in the external environment that might imply an increase of the dose to the external workers and to the public.

XI.8 Building Requirements

In order to comply with the Italian limit for the annual effective dose to the public and non-radiation workers (1 mSv/y), specific design constraints of regulation practice have been adopted. In particular for non-exposed workers the assumed criterion is 300 μSv/y (i.e. 1/3 of the limit). For the public, Italian regulatory authority requires to respect an effective dose constraint of 10 μSv/y. The effective annual doses were calculated for distances up to 5 m outside the bunker wall and extrapolated up to 40 m using an exponential decay function, as shown in Fig. XI.9. For a 220 cm thick wall of ordinary concrete, the estimated dose rates both for exposed workers (155 μSv/y at 30 cm from the wall) and the public (0.4 μSv/y at the closest site boundary, 38 m away from the wall) are below the annual dose criteria. For lower thicknesses, the estimated dose rates exceed the targets.

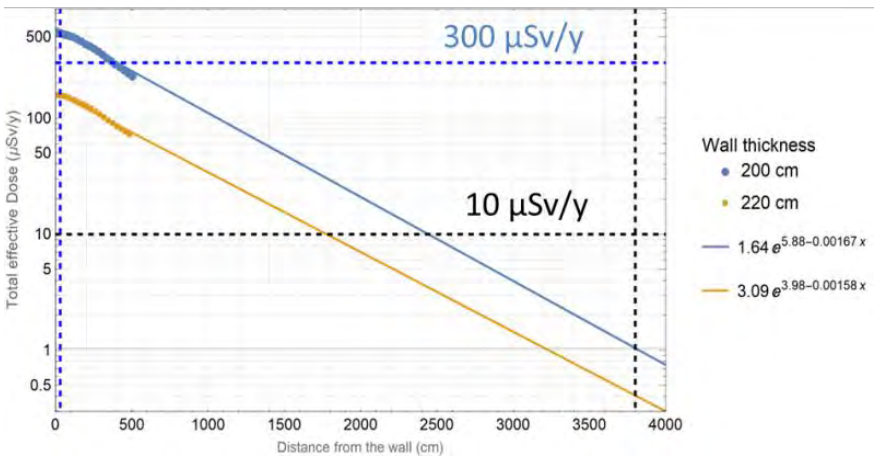

Figure XI.9: Annual effective dose rates (μSV/y) outside of the DTT building as a function of distance from the wall.

XI.9 Conclusions

Several neutronics analyses have been performed to support DTT design and licensing. The analyses were mainly devoted to optimize the vacuum vessel design, to reduce the nuclear heating on the superconductive magnets and to assess the temporal evolution of the activity and dose rate levels during different phases of DTT operations. Important outcomes for the design of crucial machine components as well as for planning of remote and manual maintenance, access to torus hall and management of activated components are provided.

Concerning the nuclear heating density on the TF coil, for $1.5x10^{17}$ n/s (+1% DT), the thickness of inboard VV configuration is not enough to guarantee that the TF coil nuclear heating density is below 1 mW/cm^3 with sufficient margin. Nevertheless, an increase of about 15 mm in VV thickness could comply with the required target. Boron in VV water is needed in high performance phase, but during the low-medium performance phase (i.e. up to 8.4 $x10^{16}$ n/s) the machine can operate with pure water. The port configurations have a significant impact on the nuclear responses and accurate analyses require a realistic description of the heating, diagnostics and auxiliary systems. Displacement damage and problems for re-weldability are not a concern for DTT components. However, high dose on silicon is expected and standard electronics should be regularly replaced, properly shielded or located outside DTT main building or radiation-hardened components need to be used. Concerning neutron induced activation, controlled Co and Ta contents are needed for structural steels inside the cryostat (i.e. 500 wppm for Co and 100 wppm for Ta). Inside the vessel high activation is expected, therefore in-vessel Remote Handling is mandatory and an ad-hoc temporary repository for dismounted activated components (e.g. Divertor) should be planned. Remote handling outside of the cryostat is not needed (access controlled) but accurate planning of maintenance, intervention and dismounting operations during and at the end of the high-performance phase is needed. A building wall made of 220 cm of concrete provides sufficient protection to workers and public. Analyses in progress are devoted to the accurate assessment of the neutron emissivity for different plasma scenarios, beams parameters and profiles and triton burn-up as well as neutron source generated in NBI. Update of the MCNP models following design evolution and including NBI, heating, diagnostics, building and penetrations is on-going. A sensitivity study is also underway to evaluate the effect of water chemical composition and density on nuclear loads. Additional related safety studies are in progress to assess: the T production, retention and contamination; the impact of impurity contents on shutdown dose rate, activation and dose rate during divertor replacement and transport; the release of effluent in environment and the estimation of Skyshine effect.

XI.10 References

[XI.1] X-5 Monte Carlo Team: MCNP - A General Monte Carlo N-Particle Transport Code, Version 5, LANL report LACP-03-0245 (2005).

[XI.2] S.W. Mosher et al., ADVANTG-An Automated Variance Reduction Parameter Generator, ORNL/TM-2013/416 Rev. 1, Oak Ridge National Laboratory, 2015

[XI.3] The FISPACT-II User Manual UKAEA-R(18)001 February 2018

[XI.4] R. Villari et al., "Shutdown dose rate assessment with the Advanced D1S method: Development, applications and validation", Fus Eng. Des., vol. 89, October 2014, Pages 2083-2087

[XI.5] Y. Wu, J. Song, H. Zheng, et al. CAD-Based Monte Carlo Program for Integrated Simulation of Nuclear System SuperMC, Annals of Nuclear Energy 82(2015) 161-168

Chapter XII

RADIATION, PROTECTION AND LICENSING

XII.1 Introduction

Construction and operation of DTT require the usual national civil authorizations, i.e. the building and practicability permits, and the certificates assessing the respect of the anti-seismic, fire prevention and environmental criteria. In addition, DTT must undergo to the control of the national authorities for the purpose of the radiation protection, also referred to as nuclear safety. Pursuant to Italian law, the DTT licensing process for nuclear safety is that of a radiogenic machine classified in category A. It is certified with a specific decree from the Minister of Economic Development (MISE, Ministero dello Sviluppo Economico). The Nuclear Safety permit has to be obtained before the beginning of the DTT nuclear operations, i.e. before the ionizing radiation production.

The nuclear safety is strictly connected to the safety analysis and to the radiation protection and, in particular, it has to deal with the radiological environmental impact and the radioactive waste management. These arguments are therefore considered in the current approach, to set up the further developments and the technical documents to be attached to the license application.

XII.2 Licensing Process

DTT will be classified, according to the Italian law [XII.1], as a radiogenic machine of category A as DTT will produce a neutronic flux greater than 10^7 n/s all over the solid angle averaged with time (in one year). A machine classified in category A, in order to operate, needs a licensing permit from the Ministry of Economic Development in agreement with the Ministry of Labor, the Ministry of Health, the Ministry of the Environment and the Ministry of Interior. The licensing procedure is summarized in Fig. XII.1. To obtain such a permit, a series of documentation needs to be prepared and sent by the DTT operator, with a formal application, to the Ministry of Economic Development (MISE). This will ask to other Ministries (Ministry of Labor, Ministry of Health, Ministry of the Environment and Ministry of Interior), to ISIN (National Inspectorate for Nuclear Safety and Radiation Protection) and to the Lazio Region (where DTT has to be installed) to review the documentation and to provide their formal opinion. All the above authorities (Ministries, ISIN and Lazio Region) are usually referred to as "regulatory authorities". Some of them make reference to internal technical organisms in order to provide a technical analysis and to define their opinion and prescriptions. The Ministry of Health makes reference to the INAIL (National Institute for Insurance against Accidents at Work) expert group. INAIL provides its own analysis to the reference Ministry that transmits the final opinion to the MISE. The Ministry of Interior asks a technical advice to the Firefighters Department that verifies the acceptability of the fire prevention systems foresee for the facility. The Lazio Region has its own technical commission devoted to the analysis of this kind of applications and provides its opinion after the commission involvement and final pronouncement.

The application for licensing to construct and operate DTT, according to the Italian law, must include at least the following information:

- general information, tax code and domicile of the applicant; in the case of companies: the company name, tax code and registered office;
- the type of practice to be carried out;
- the location of the premises and areas intended for the practice to be carried out;
- for each radiogenic machine: the acceleration type and the maximum energy of charged particles, maximum current and power, utilization factor (duty cycle), and the number of machines intended to be used;
- for radioactive materials: the total amount of radioactivity of radionuclides, distinguishing between unsealed sources and sealed sources, intended to be hold simultaneously and in relation to the calendar year;
- for all sources: the possible production of neutrons;
- methods of production and possible disposal of waste, with indication of the applicability or otherwise of the provisions referred to the Italian law;
- any recycling or reuse of materials.

It has to be accompanied by the following documentation, signed by a Qualified Expert for the part of his competence, also to demonstrate the suitability of the place where the practice will be carried out:

- description of the rooms and areas involved in the activity to be carried out, illustrated with drawings in plan and sections, indicating, for each room and area, the classification in radiological zones pursuant to Italian law, as well as the environments and the surrounding areas also outside the installation, indicating the intended use and any sources used, also by third parties;

- criteria followed for the purposes of identifying and classifying the areas and the classification of the personnel pursuant to Italian law;
- description of the operations to be carried out, the radiation sources and the equipment to be used, with reference to the various rooms and areas; description of the methods for handling the sources inside the installation; indication of compliance with the rules of good technique applicable in the design, construction and operation phase;
- identification and analysis of any scenarios involving potential exposures, and of specific intervention modalities in order to prevent exposures or limit their consequences on workers and on the population;
- production and management of radioactive waste and recycled or reused materials;
- programs for the construction or adaptation of the premises and areas intended for carrying out the activities, as well as the required tests;
- methods for decommissioning the installation;
- assessment of the doses for workers and for the reference groups of the population under normal operating conditions;
- the results of the preventive assessments of the spatial and temporal distribution of radioactive dispersed or released materials, as well as potential exposures relating to workers and target groups of the population in possible radiological emergencies;
- criteria and procedures for implementing the obligations pursuant to Italian law related to the attributions of the Qualified Expert and his communications to the employer;
- indication of how the other relevant obligations of the employer pursuant to Italian law are to be fulfilled, with particular reference to the content of the internal safety and protection regulations;
- indication of the ways in which the training in radioprotection of workers is intended to be assured and indication of their professional qualification.

The Ministry of Economic Development, once obtained the positive opinions from all the above Ministries and Organizations, will issue the licensing permit for construction and operation accompanied by specific prescriptions relevant to Design, Construction, Commissioning, Operation, Test & Maintenance and Decommissioning of DTT.

To begin the normal operations, after the commissioning phase, the DTT plant has to be included in the local emergency plan prepared by the Prefect.

Of course, a site that has already obtained licenses of the same type in the past, like the Frascati ENEA Research Center, is facilitated in terms of simplicity and speed up of the procedure. At the Frascati Center the experimental fusion machine named FTU was authorized with a category “A” permit that could be basically modified for the replacement with DTT. This is actually possible considering that, according to the Italian law, the two experimental fusion machines are considered of the same kind. As a consequence, the application will be related to the decommissioning of FTU machine, to the construction of new buildings and to the operation of DTT, and it will require a modification of the current FTU license. The modification is convenient also because, implying the existence of the activity that has to be modified, it does not make it mandatory to be implemented into a new emergency local plan (intervention plan) before to start the operation, with an evident speed-up of the procedure.

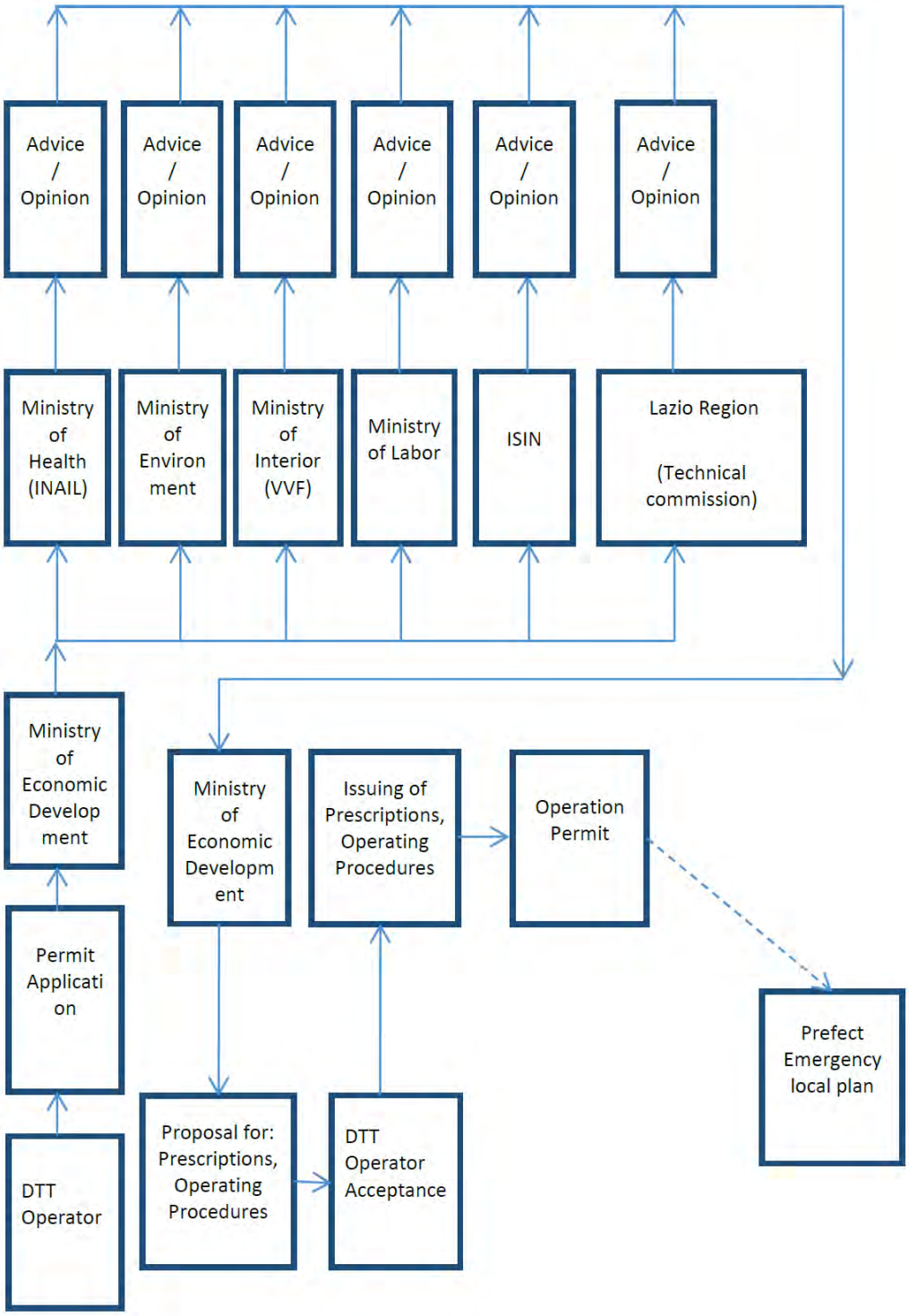

Figure XII.1: DTT Licensing Scheme

XII.3 Safety Analysis and Environmental Impact

The first step in the licensing process is the description of the plant, that needs to be prepared reporting the main parameters that define the operation domain (including the foreseeable extensions) for which the permit of operation is requested. The aspects to be stressed in this frame are those related to the risk agents and procedures that are likely to impact to the safety of the workers, of the population and of the environment. The safety analysis will start from the identification of the hazards (nuclear and conventional) present in the plant and their relevant characteristics (radiation flux, inventories and mobilization factor, etc.). From the nuclear safety point of view the main radioactive source terms foreseeable in DTT are:

- The neutron and gamma fluxes produced during the plasma operations inside the machine;
- The activated material of the primary Plasma Facing Components (PFCs);
- The Activated Corrosion Products (ACPs) in the cooling circuits;
- The activation of coolant in the primary cooling loops;
- The activated dust produced by plasma-wall interaction in the Vacuum Vessel (VV), particularly during the plasma transients and disruptions;
- The small amount of Tritium that can be found in the VV, in the cooling system components, in the pumps and in the fuel cycle system, due to the D-D reactions;
- The neutrons and gamma generated in the auxiliary systems, as the Neutral Beam Injection (NBI) systems and the calibration sources;
- The activated air inside the buildings.

All the above source terms could be evaluated by applying well known and published experimental results and simplified calculation rules, suitable of providing acceptable qualification and quantification of the needed input parameters to the safety analysis. However, advanced neutronic calculations and simulation codes will identify, characterize and quantify all the radioactive source terms, with higher accuracy.

The safety analysis will be developed for both normal operation and accidental situations. Considering the latter, a first extrapolation from the present experimental fusion machines (e.g. FTU and JET), shows that the radioactive inventories will be limited and very little mobilizable in accidental conditions. The main outcome of the analysis will be the development of the safety functions necessary to control neutron flux and radioactive inventories, in order to limit the doses to the workers and the releases to the environment in normal and accidental conditions. These indications will be mainly relevant to the control of the access to the classified areas, to the radiation monitoring definition and to the confinement of radioactive material. The systems implementing those safety functions will be considered critical and the relevant characteristics will be implemented during their entire life, including design, fabrication, assembling, commission, operation, test and maintenance.

The events, that in case of accident can imply some minor radioactive inventories, are the following:

- A complex event, composed by three unlikely contemporaneous accidents (a superconductor quench, a not properly discharge of the magnetic energy and an internal cryostat short cut);
- An important loss of cryogenic fluids in tokamak cryostat, that could determine an increase of the radioactivity within the main torus hall;

- A loss in the primary cooling circuit with the associated enthalpy.

Personnel at the DTT facility will be subjected to a number of non-radiological hazards as for other large industrial facilities. These include in particular: chemical risks, anoxia risk (due to the presence of items under vacuum, SF_6 insulator for NBI, CO_2 for fire suppression), magnetic and electromagnetic fields, and fire.

These hazards are addressed through the compliance with industrial safety regulations. Internal and external events, as well as the environmental conditions, will be considered for the safety analysis and for the design of the DTT safety systems. The external events are dependent on the specific site, typically they are: seismic events, flooding (considering natural and accidental ones), fire, loss of off-site power, explosions, other hazards associated with nearby installations and routes, extreme climatic conditions. The internal events are: plasma transients (disruptions and vertical displacement events) , fast discharge of magnetic energy, fire, loss of coolants, flooding, chemical risks, mechanical risks, electrical short cuts and arcs, explosion, pipe whipping.

The environmental conditions are identified for all the areas of the plant in normal and accidental conditions. Special attention will be given to the areas of the tokamak building for the complexity and severity of the environmental conditions and for the presence of systems important to safety.

The most important safety functions identified for DTT are: Shielding, Confinement, Access control to radiological zones and Monitoring system. A complete list of the safety functions will be identified during the systematic safety analysis of DTT.

The control system plays a very important role in this complex machine from the operation, scientific availability and protection/safety point of views.

It will be constituted of 3 main systems:

- control and data acquisition systems: devoted to the overall plant managing and monitoring, and to the acquisition and first elaboration of the experimental data;
- interlock systems: protect all the active systems and components, to maintain them inside their operating limits and conditions established for the correct functioning;
- safety control system: coordinates and monitors safety functions through the relevant safety systems, to bring and maintain the plant into a safe status from any abnormal event and to protect staff from any radiological risk (e.g. during the pulse). This system will be isolated as much as possible from the external world, to be better protected from cyber-attacks too. Any connection to the previous two systems should go just in the direction towards them.

XII.4 Radiation Protection

The radiation protection (or radiological protection, or radioprotection) is the collection of analyses and provisions needed to achieve proper operating conditions, prevention of accidents and mitigation of accident consequences, resulting in protection of workers, public and environment from undue radiation risks [XII.2].

Ionizing radiation can trigger both deterministic and stochastic health effects. The aim of radiation protection is to prevent reliably the deterministic effects of radiation and to reduce the risk of stochastic effects to a reasonably achievable level. The dose limit values are set so that deterministic effects are ruled out. In order

to keep the risk of stochastic damage from ionizing radiation as low as possible, three general principles have been set out in radiation protection for dealing with ionizing radiation: justification, optimization (or ALARA, As Low As Reasonably Achievable, principle) and dose limitation.

Adequate shielding, materials' specifications, classification of areas in radiological zoning as function of the dose rate, access control, work permits, radiation monitors, remote handling facilities, hot cell design, radiological waste management, and other specific procedures, are tools and practices to meet the ALARA criterion for the minimization of the radiation dose to the staff.

Radioprotection criteria and relevant practices are considered through the whole DTT life-cycle, from the design to the decommissioning.

XII.4.1 Limits and constraints

The operation of the DTT facility will be subject to the Italian regulatory limits. In designing DTT, Italian regulation, European directives and ICRP recommendations will be considered. In Tab. XII.I the Italian regulatory limits for people are shown along with project constraints that are more restrictive and more consistent with "best industry practice". In this context a limit is intended as a threshold, stated by law, that cannot be overcome, while a constraint is a reference value, stated by the designer, to be observed to guarantee the respect of limits or to organize the working activities according to the optimization principle [XII.3]. Personnel performing work requiring exposure to ionizing radiation will be designated as Radiation Workers (RW). All other personnel, including generic visitors, will be treated as Non-Radiation Workers (NRW). The annual whole-body effective dose limit for Radiation Workers is 20 mSv. This classification is broken down into two sub-categories according to the Italian regulation: category A RW and category B RW. The latter represents workers that are likely not to be exposed to an annual effective dose higher than 6 mSv, while the category A RW are those that are likely to overcome this limit.

Italian regulation indicates also equivalent dose limits for workers and population. The complete regulatory statement is as follows:

"the workers who, due to the work carried out on behalf of the company, are classified as exposed workers (RW), are likely to exceed one or more of the following values in a calendar year:

a. 1 mSv of effective dose;
b. 15 mSv of equivalent dose for the crystalline lens;
c. 50 mSv of equivalent dose for the skin, calculated on average on 1 cm2 of any skin, regardless of the exposed area;
d. 50 mSv of equivalent dose for hands, forearms, feet, ankles."

The project constraints defined by the designer to guarantee the respect of the regulatory limits, include administrative constraints that are normally used by the operating organization to prevent occupational doses exceeding regulatory limits but at the design stage provide a framework to satisfy a minimum level of radiation safety. In addition, well-designed administrative constraints improve the distribution of collective dose such that individual exposures are maintained ALARA. The annual project guideline for category A Radiation Workers is given here as 10 mSv/y, a half of the Italian regulatory limit of 20 mSv/y. During operation, if the annual administrative constraints were reached, workers would be deterred from further radiation exposure.

An administrative constraint is also given for acute exposures. The exposure per shift is an operational ALARA guideline that may also impact the design. The shift constraint controls the rate at which dose is received by

Radiation Workers (RW) and is not intended to be routinely reached. Here, it is defined as 0.2 mSv/shift, one hundredth of the annual dose limit. It is derived from a common practice at operating Nuclear Power Plants (NPPs) of scrutinizing work and requiring special authorization if it is estimated that a radiation worker would exceed one tenth of the annual limit in a single shift's work. DTT expected exposures permit the adoption of more conservative constraints, that is designed such that regularly planned activities can be performed without requiring workers to exceed this reference level in a single shift. Furthermore, the project constraints include a dose rate reference value which provides guidance for the application of an optimization process for the scheduled and not scheduled maintenance operations, with special reference to the remote handling approach.

The working activities performed in the DTT areas in general are not likely to expose people to specific equivalent doses, therefore workers classification, dosimetric control and protection will be based solely on the effective dose assessment and data. However particular operations could require potential radiation source to be manipulated or the workers to stay close to ionizing radiation sources imposing to consider the equivalent dose to specific organs or tissues.

TABLE XII.I. RADIOLOGICAL LIMITS AND CONSTRAINTS FOR DTT

Italian Regulation Effective Dose Limits	
Italian effective dose limit for annual individual exposure of a category A Rad Worker (RW)	20 mSv/y
Italian effective dose limit for annual individual exposure of a category B RW	6 mSv/y
Italian effective dose limit for annual individual exposure of a Non-Radiation	1 mSv/y
Project Constraints Proposed for DTT	
Individual cat. B RW effective dose constraint[(a)]	3 mSv/y
Annual individual cat. A RW effective dose constraint[(a)]	10 mSv/y
Annual individual Non-Radiation Worker effective dose[(b)]	0,3 mSv/y
Annual individual effective dose for population[(b)]	10 µSv/y
Recommended Individual effective dose for working shift[(c)]	0,2 mSv/shift
Collective worker dose target averaged over plant life time[(c)]	0,5 person-Sv/y
Dose rate constraint during scheduled and not scheduled maintenance[(c)]	100 µSv/h

(a) Limits divided by a safety factor of 2

(b) Recommended by the Italian Regulators (ISIN)

(c) Derived from Nuclear Fission Power Plants and ITER, safety projects and recommendations [XII.3, XII.4]

XII.4.2 Zone and personnel radiological classification

The accessibility of rooms and areas in the DTT facility depends on the anticipated hazard levels and the corresponding control required to ensure that the project guidelines are not exceeded.

Table XII.II presents the radiation access zone definitions and the corresponding conditions for access that will allow operation and maintenance of the facility to be safely performed within the framework of the adopted limits. Application of the access zone definitions at this stage of the design provides assurance that, during operation, programs for exposure control can be implemented for the facility as designed.

TABLE XII.II. CLASSIFICATION OF RADIATION ZONES

Zone (Area Classification)	**Access Limitations**	**Airborne / Total Dose Rate / Area Contamination Characteristics**
Zone A (Free Area)	Unlimited Access.	No airborne contamination. Dose rate < 0,5 µSv/h; No surface or airborne contamination and no reasonable possibility of cross-contamination.
Zone B (Supervised Area)	Limited Access for NRW Unlimited Access for RW	Total dose rate (internal + external) < 3 µSv/h; No loose contamination tolerated. May be subject to temporary surface or airborne cross-contamination, airborne should not exceed 1 DAC.
Zone C (Controlled Area)	Limited Access for all workers. Access requires planning and an appropriate level of approval	< 100 DAC and < 1 mSv/h; Airborne and loose surface contamination tolerated but must be identified and controlled. Airborne contamination should not exceed 100 DAC.
Zone D (Restricted Area)	These are restricted access area entry occurs only with a high level of approval from both an operational and a radiological safety view. These areas shall have physica barriers to prevent inadvertent personnel entry.	Airborne >100 DAC or external dose rate > 1 mSv/h; RED contamination control zones are only tolerated in Zone D. These areas have permanent or higher than AMBER levels of contamination.

DAC = Derived Air Concentration; unprotected exposure to 1 DAC = 10 µSv/h; 1 DAC HTO = $3{,}1 \times 10^5$ Bq/m^3

All areas of the DTT plant are zoned depending on the anticipated radiological hazard and conditions during short-term maintenance. The radiological hazard levels are expected to increase slowly with operation (see results in Chapter XI), however, the current application is intended to show that the access zones can be implemented consistently even during the most restrictive conditions. For example, initially the activated corrosion products (ACP) and tritium levels in the cooling system areas will be very low and the zoning for rooms affected by this system will initially be lower than those expected after some years of operation.

During activities/events that cause prohibitive radiation levels (e.g. plasma operation phase, in-vessel transport activities, etc.), areas that are otherwise accessible may be designated as 'restricted' for the duration of the activity, and physical access should be prevented. Such locations will be returned to be accessible only after a formal change control.

XII.4.3 Access control and work permit

The DTT facility shall have an Access and operation Control System (ACS) to control personnel occupancy in areas with radiation dose rates above the acceptable levels. The DTT ACS will be used to manage ingress and egress for areas that are alternatively access or exclusion areas. The system shall be designed to provide a warning, prevent access, or initiate mitigating action.

The ACS proposed for DTT will include the following main components: turnstiles high gate model, additional doors and fence, electronic locks, doors contacts, personal cards and intelligent card readers, emergency system (scram), patrol system, cameras, intercom system, signals (audible, visual and lights), computerized control system.

ACS has the main goal to control access to Zone D areas or areas restricted due to temporary activities or events. However, controlling access to zones B and C will require a combination of procedural and/or physical barriers, which will be integrated in the building design detail and the operating and maintenance procedures. The system will recognize the individual that is asking to access a specific area and will have the privilege to know his radiation work permit (RWP) content.

XII.4.4 Radiation monitoring system

The RAdiation MOnitoring System (RAMOS) shall cover the following safety functions:

- Health and radiological monitoring for workers;
- Area monitoring;
- Radioactivity-in-air monitoring;
- Scheduled and unscheduled controls and measurements;
- Radio-activation control and limitation.

The RAMOS proposed for DTT is composed by the following sub-systems:

- Fixed stations for area and environmental monitoring of gamma and neutron fields (RAMSES);
- Portable radiation monitoring equipment for controlling direct radiation and contamination;
- Effluent release measurement systems for radioactive gaseous release at the stacks;
- High resolution gamma spectrometer for analyzing the activated solid and liquid materials;

- Liquid scintillation counter for tritium contamination and waste control;
- Individual active dosimeters for controlling in real time workers and visitors exposure;
- Individual passive gamma and neutrons dosimeters for legal recording and assessment;
- Ambient passive gamma and neutrons dosimeters for environmental control;
- Calibration radioactive sealed sources.

The RAdiation Monitoring System for the Environment and Safety (RAMSES) for DTT comprises at least ten fixed monitoring stations and provides ambient dose equivalent, and ambient dose equivalent rate measurements in the working areas, as well as inside and outside the DTT perimeter. The fixed station network for area and environmental monitoring will be composed by gamma and neutron monitors, connected to rate-meters for the local display of the result and then to a data logger located in the radiation safety office.

The portable radiation monitors needed for DTT activities will be at least two Portable gamma monitors, two portable neutron monitors, two portable spectrometers. The effluent release measurement equipment will include tritium monitors for the DTT hall and air release at the stack monitors. About 20 individual active dosimeters are expected to be necessary for controlling in real time the exposure of visitors and external workers.

The permanent DTT staff potentially exposed to ionizing radiation will have personal passive dosimeters for gamma and neutrons radiation. The passive dosimeters will be rented from a qualified laboratory at the beginning of the DTT operation and will be used as a legal recording system of the individual radiation dose.

XII.5 Waste Management and Decommissioning

The radioactive waste is the waste that for legal and regulatory purposes contains, or is contaminated with, radionuclides at activity, quantity and/or concentration greater than the specific clearance levels as established by the reference regulatory body. In addition, the radioactive waste is radioactive material in gaseous, liquid or solid form for which no further use is foreseen. They are classified according to the Italian legislation [XII.5] into six categories:

0) exempted,
1) very low half-life,
2) very low activity,
3) low activity,
4) medium activity,
5) high activity.

DTT will produce radioactive wastes during operation and maintenance and during the dismantling phase. Pursuant the Italian law, the more critical of them are expected to be classified in the low or very low categories, however, the majority will be exempted radioactive waste. Their effective amount and characteristics will be determined by neutronic calculations, considering the operation plan of DTT (see Chapter XI).

A radwaste area is considered in the project; it will be classified as a radiation controlled zone with suitable characteristics, such as an access control, a ventilation system with appropriate filters, and a radiation monitoring system. This area will be devoted to the temporary storage of solid and liquid radioactive waste.

At the end of the operations DTT will be decommissioned. Decommissioning typically includes dismantling of the facility (or part thereof) to reduce the associated radiation risks, but a facility could be decommissioned without dismantling and the existing structures subsequently put to another use (after decontamination). The actual final destination of DTT has not yet been defined, however, administrative and technical actions will be taken at the end to allow the removal of some or all of the regulatory controls from the facility.

The decommissioning phase will be described in a specific plan including the decontamination and/or the removal of structures, systems and components, and the management of the residual radiation waste.

The decommissioning process will be resumed in the technical documents attached to the license application.

XII.6 Conclusions

The aspects considered in the current chapter are deemed to clarify what is the general process to be followed in Italy for obtaining the nuclear safety license for DTT. The specific approach to be applied to the radiation protection is also described and the involvement of workers and population in this frame is considered as the most important argument. The sensitive fields of the safety analysis and of the radioactive waste management are briefly discussed and the general approach to their solution is anticipated.

The preliminary analysis reported here does not highlight any criticality, however, the time required to complete the licensing process depends from different aspects (it could last from one to two years including the preparation of the application) and there is awareness that this could be the real challenge of this specific task.

XII.7 References

[XII.1] Decreto Legislativo del Governo 17 marzo 1995 n° 230 e successive modificazioni (dal D.Lgs. 26 maggio 2000, n.187; dal D.Lgs. 26 maggio 2000, n. 241; dal D.Lgs. 9 maggio 2001, n. 257; dal D.Lgs. 26 marzo 2001, n.151; dalla Legge 1 marzo 2002, n. 39 "Attuazione delle direttive 89/618/Euratom, 90/641/Euratom, 92/3/Euratom e 96/29/Euratom in materia di radiazioni ionizzanti.")

[XII.2] IAEA Safety Glossary – “Terminology Used in Nuclear Safety and Radiation Protection”, 2016 Revision

[XII.3] IAEA Safety Standards GSR Parts 1, 2 and 3 (2014) – “Radiation Protection and Safety of Radiation Sources: International Basic Safety Standards”

[XII.4] ITER Generic Site Safety Report, Volume VI, Occupational Safety (2006 and updates)

[XII.5] Decreto del Ministero dell’Ambiente 7 agosto 2015, GU n.191 del 19-8-2015

Appendix A

DTT REFERENCE PARAMETERS

Main parameters:

TABLE A.I. MACHINE PARAMETERS

R (m)/a(m)	2.11/0.64 SN – 2.14/0.65 DN
A	3.3 SN/DN
Vol (m^3)	≈28
Ip (MA)	5.5 SN – 5.0 DN
BT (T)	6 @ R0
Coil currents margins [% with respect to nominal]	+ 5% on TF and CS +10% on PF and in-vessel coils
Neutron production rate, Sn (n/s)	1.2-1.5 10^{17} DD + 1% DT
Maximum dwell time for high performance	3600
Nominal repetition time after disruption (s)	3600
Number of shots per day	5-10
Days of operation per year	100
Years of operation	25
Total number of shots	25000

TABLE A.II. ADDITIONAL POWER SYSTEMS

	ECRH [MW]	ICRH [MW]	NNBI [MW]
Phase-1	16	3	7.5
Phase-2	20-30	3-9	7.5-15

TABLE A.III. GEOMETRICAL PARAMETERS OF THE VV (INNER SIDE)

R_{max}	3.17 m
R_{min}	1.385 m
R_{mean}	2.28 m
a_{VV}	0.89 m
k_{VV}	2.07
Z_{top}	1.85 m
R_{top}	1.855 m

TABLE A.IV. GEOMETRICAL PARAMETERS OF THE VV (OUTER SIDE)

R_{max}	3.30 m
R_{min}	1.26 m
Z_{top}	1.97 m
R_{top}	1.855 m

Principal Cross Sections:

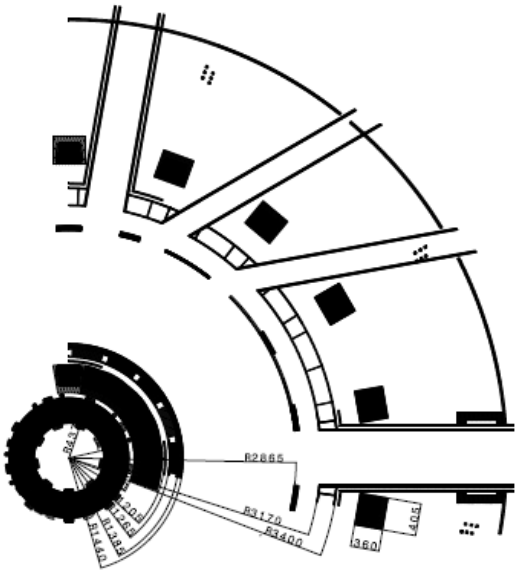

Figure A.1 DTT equatorial cross section

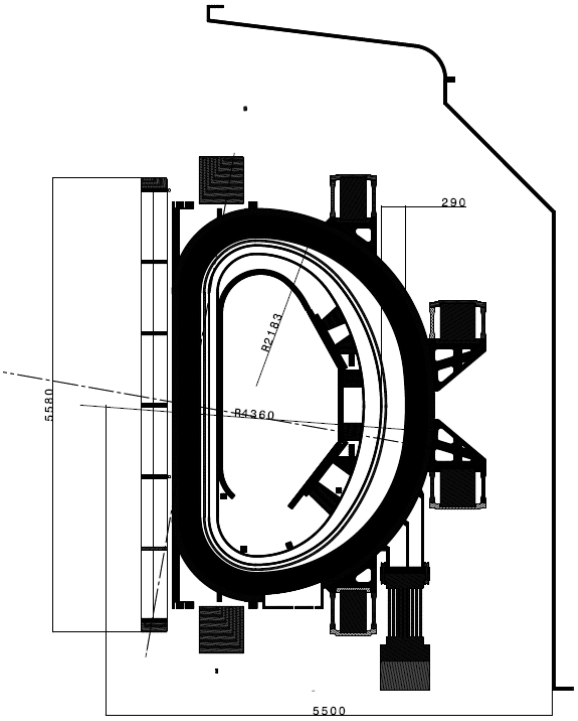

Figure A.2: DTT poloidal cross section (symmetry plane of a TF coil)

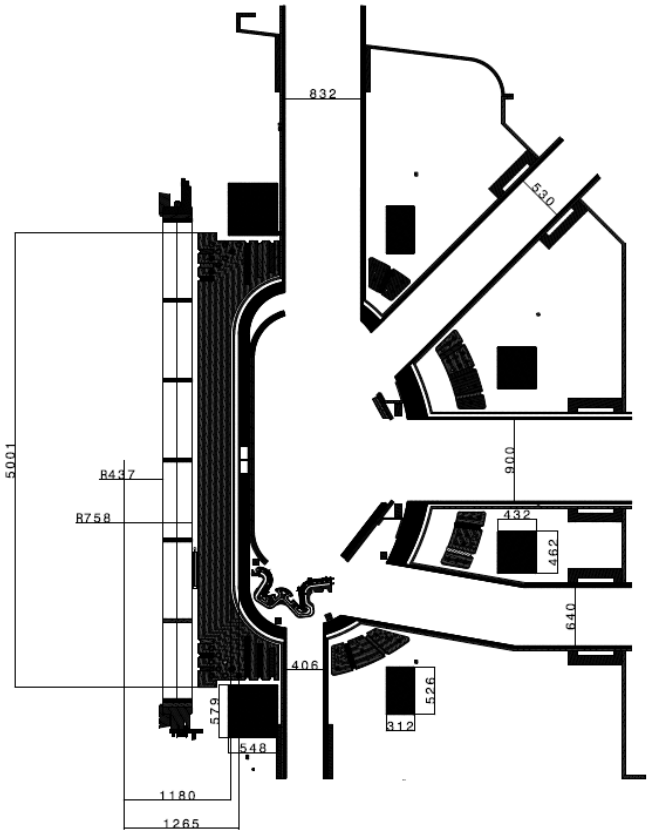

Figure A.3: DTT poloidal cross section (symmetry plane of vessel ports)

Operational states:

- **POS (Plasma Operation State)** i.e. from before initial magnetisation of CS up to after termination of plasma current;
- **STS (Short Term Standby)** i.e. plasma vacuum preparation, or overnight standby when for example the pumping system could be regenerated;
- **DWE (Dwell)** i.e. cooldown phase between a sequence of POS states (dwell time);
- **STM (Short Term Maintenance)** i.e. vessel evacuated, magnets cold but not energized, tightly controlled access for short term repairs or inspection;
- **LTM (Long Term Maintenance)** i.e. access available to vessel or cryostat if required, coils not energized and may be warm - ready for longer timescale maintenance.
- **BAK (Baking)** Vessel baking and He Glow Discharge Conditioning (GDC) shall be carried out before energizing the superconducting coils.
    - Vessel baking is limited to 110 °C (water without Boron is used).
    - Divertor targets, dome, baffles will be heated to 110 °C as the vessel is baked;
    - First wall will be heated up to 200 °C as the vessel is baked (TBC).

Daily Operation Scenario: DTT experimental time shall be 10 hours per day, plus one hour at each end for pre- and post-experimental inspection. The experiment shall be conducted by an operation team in two shifts. Regeneration of pumping system, wall conditioning, shall be carried out overnight by an operation team for the cryogenic system operating. The nominal repetition time is 3600 s for 50 s flat top.

Annual Operation Scenario: Annual operation shall consist of an experimental period and a maintenance period. Prior to shut down for maintenance, exhaust of tritium gas for less than one month and warming up of the superconducting coils for about one month are planned. The annual maintenance period is foreseen to last about 6 months, including warming up and cooling down periods. During the maintenance period, annual inspections of DTT facilities are planned according to safety regulations for electricity, high pressure gas, cranes etc. Maintenance and adjustment of heating systems and diagnostic systems an installations of new facilities or diagnostic systems will also be done. Between the warming up period and the cooling down period, inspection or repair of in-vessel components is planned using the remote handling systems. Work in the cryostat shall also be possible in the initial experimental phase before the radiation dose increases.

TABLE A.V. OPERATIONAL EVENTS

Nominal # of operation shots (up to)	= 100 x 10 x 25 = 25 000
TF Coil energisation (2 per month of operation)	= 2 x 6 x 25 = 300 + Fast discharge events
Magnet cooldown/warmup from RT	= 2 x 25 = 50
Vessel/In-vessel baking events	= 6 x 25 = 150
Vessel pump down from atmospheric	= 6 x 25 = 150
Cryostat pump down from atmospheric	= 2 x 25 = 50
Full current plasma disruptions	5-7% number of shots=1250-1750
Un-mitigated full current VDEs	2-3% number of shots=500-750
TF coil fast discharges	= 4 x 6 x 25 = 600

Heat loads:

TABLE A.VI. HEAT LOADS

System	Power To Be Removed (MW)	Duration (s)	Coolant Inlet Temperature (°C)	Delta T(°C)	Dwell Time (s)
ECRH + ICRH + NBI	77.2	50	15	25	3600
TF PS	0.2	Steady-state	35	10	0
CS PS	0.3	300	35	10	3600
In vessel PS	0.3	100	35	10	3600
SNU	1.2	10	35	10	3600
FDU	0.1	10	35	10	3600
PF PS	0.5	300	35	10	3600
CRYOPLANT	3.0	Steady-state	10-30	10	0
DIVERTOR	(ramp+const) 2-30	50-50	60	14	3600
FIRST WALL	(ramp+const) 3-15	50-50	60	14	3600
FIRST WALL (with Li divertor)	(ramp+const) 3-15	50-50	180 (with Li divertor)	20	3600
VV	0.1[1]	Steady-state	60	14	0

[1] VV is heated by neutrons and cooled by the VVTS

TABLE A.VII. HEAT LOADS ON THE CRYOGENIC SYSTEM IN NORMAL OPERATIONS

	During Shots			During Dwell Time		
System	**Power To Be Removed [kW]**	**Duration [s]**	**Inlet Temperature (ΔT) [K]**	**Power To Be Removed [kW]**	**Duration [s]**	**Inlet Temperature (ΔT) [K]**
TF + CASING	5.8-9.1[2] (NUCLEAR HEATING) + 0.1-0.3 (RADIATION) + CONDUCTION FROM GRAVITY SUPPORT (TBD[3])	100	4.5 (0.5)	0.1-0.3 (RADIATION) + CONDUCTION FROM GRAVITY SUPPORT (TBD[4])	3500	4.5 (0.5)
PF + CS	1.6+0.14[5] (NUCLEAR HEATING) + 0.1-0.3 (RADIATION)+ 0.2-0.6 (EDDY CURRENTS)	100	4.5 (0.5)	0.1-0.3 (RADIATION)	3500	4.5 (0.5)
HTS TF Current leads	6 x 1.5=9	STEADY-STATE	50 (250)	6 x 1.5=9	STEADY-STATE	50 (250)
HTS PF/CS Current leads	24 x 1.5=36	300	50 (250)	0	3500	0
Thermal shield	1.4[6] (NUCLEAR HEATING) + 42.0 (RADIATION)	100	80 (20)	42.0 (RADIATION)	3500	80 (20)
Feeders	0.1	STEADY-STATE	4.5 (0.5)	0.1	STEADY-STATE	4.5 (0.5)

[2] During 50 s flat-top, variation depends on ports closure
[3] It is estimated in the range 0.6-1.5 kW on the base of similar machines
[4] It is estimated in the range 0.6-1.5 kW on the base of similar machines
[5] During 50 s flat-top
[6] During 50 s flat-top

TABLE A.VIII. HEAT LOADS ON THE CRYOGENIC SYSTEM IN BAKING CONDITIONS

System	Power To Be Removed [Kw]	Duration [Days]	Inlet Temperature (Delta T) [K]
TF + CASING	0.1-0.3 (RADIATION) + CONDUCTION FROM GRAVITY SUPPORT (TBD[7])	5	10 (30)
PF + CS	0.1-0.3 (RADIATION)	5	10 (30)
HTS TF Current leads	0	5	-
HTS PF/CS Current leads	0	5	-
Thermal shield	42.0 (RADIATION)	5	80 (20)

TABLE A.IX. COOL-DOWN AND WARM-UP PARAMETERS

M_{tot} [kg]	6.00E+05
Integr(cap_316LN [J/kg K] *dT)_4-300K	92.8E+03
ΔT [K]	300
Energy [J]	5.57E+10
t [days]	30
t[s]	2.59E+06
P [W]	2.15E+04
cooldown-speed [K/s]	1.16E-04
cooldown-speed [K/h]	4.17E-01

Coil currents and parameters:

TABLE A.X. COIL CURRENTS AND PARAMETERS

System	Current [kA]	turns	Inductance	Max voltage [kV]
TF (18 modules with 3 circuit in series)	44	80	41.4 mH (1 module) / 2.1 H (18 modules)	1 (single module in operation – 3 (single module during test) – 6.5 (the series of 6 modules in operation)
PF (6 modules)	27-32	360 (PF1/6) 160 (PF2/5) 196 (PF3/4)	0.2-0.7 H (1 module)	3
CS (6 modules)	29.9	88 HF + 216 LF (1 module)	83 mH (1 module)	3.5 (at breakdown)
IVC-div (4 coils)	50	1	7 - 17 μH (1 coil)	100
IVC-VS (2 coils)	25	4	260 μH (1 coil)	0.2

[7] It is estimated in the range 0.6-1.5 kW on the base of similar machines

Appendix B

PLANNING

A detailed schedule has been worked out for all the planned DTT activities, starting from now, up to the integrated commissioning phase. Several milestones and check points have been inserted to best follow the project execution and control that any phase is concluded within the expected time.

The detailed schedule is reported in the GANTT chart shown in the following pages. The chart is made of 971 tasks, each linked to others through apposite relationships. The first column of the chart contains the ID of the task, the second shows eventual notes, the third includes a short description of the task, the fourth the duration, the fifth and sixth start and expected end, respectively. Finally, the seventh column reports the predecessors given by the relationships.

Presently, a risk analysis is under evaluation in order to mitigate and reduce as much as possible any problem that might come out along this planned schedule. It is indeed a very tight and ambitious planning. However, its feasibility has been carefully checked when compared with the actual timing of other similar (JT-60SA, MITICA, …) devices recently realized by the Italian fusion system.

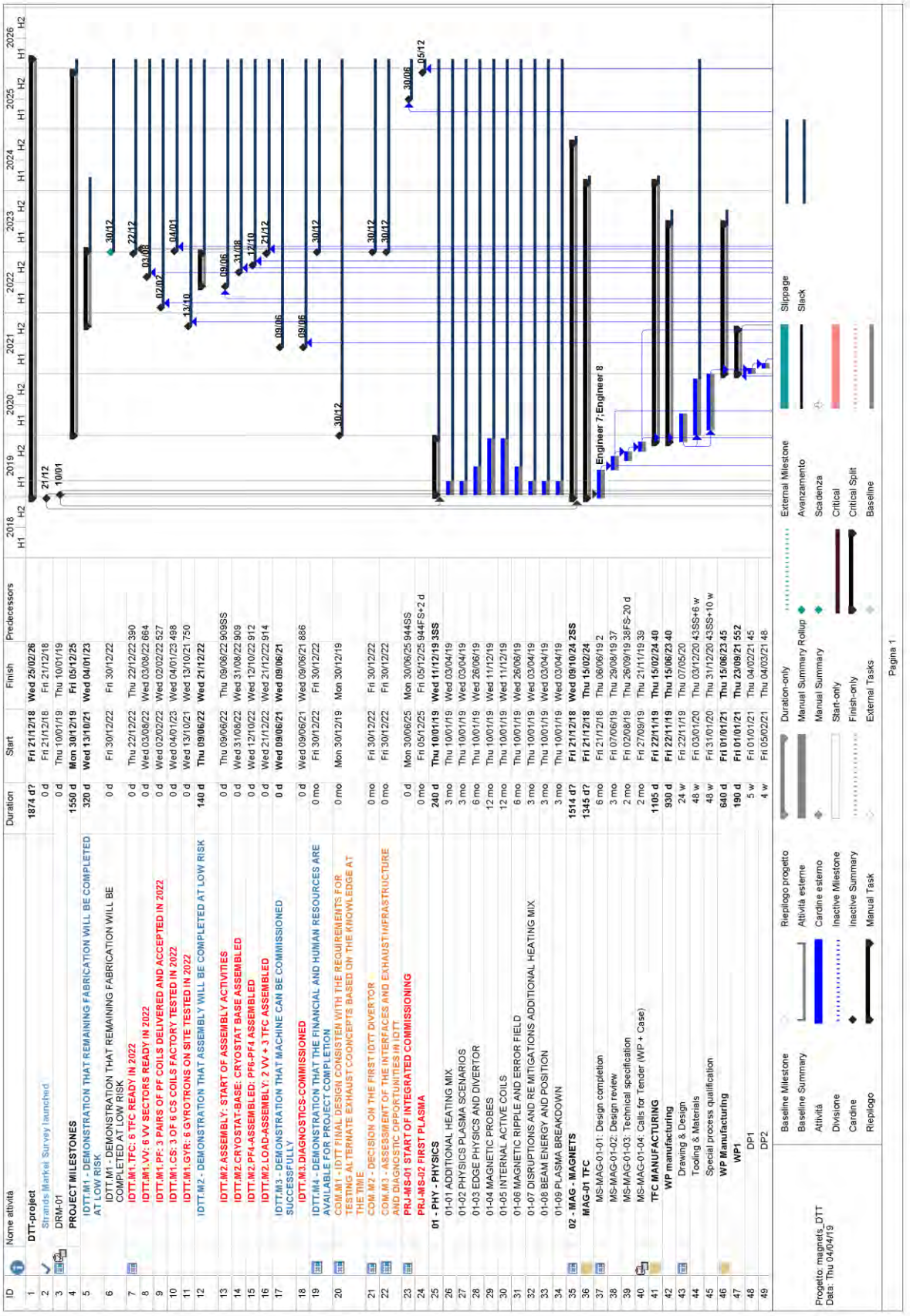
ID
Nome attività
Duration
Start
Finish
Predecessors
1 DTT-project 1874 d? Fri 21/12/18 Wed 25/02/26
2 Strands Market Survey Launched 0 d Fri 21/12/18 Fri 21/12/18
3 DRM-01 0 d Thu 10/01/19 Thu 10/01/19
4 PROJECT MILESTONES 1550 d Mon 30/12/19 Fri 05/12/25
5 IDTT.M1 - DEMONSTRATION THAT REMAINING FABRICATION WILL BE COMPLETED AT LOW RISK 320 d Wed 13/10/21 Wed 04/01/23
6 IDTT.M1 - DEMONSTRATION THAT REMAINING FABRICATION WILL BE COMPLETED AT LOW RISK 0 d Fri 30/12/22 Fri 30/12/22
7 IDTT.M1.TFC: 6 TFC READY IN 2022 0 d Thu 22/12/22 Thu 22/12/22 390
8 IDTT.M1.VV: 6 VV SECTORS READY IN 2022 0 d Wed 03/08/22 Wed 03/08/22 864
9 IDTT.M1.PF: 3 PAIRS OF PF COILS DELIVERED AND ACCEPTED IN 2022 0 d Wed 02/02/22 Wed 02/02/22 527
10 IDTT.M1.CS: 3 OF 6 CS COILS FACTORY TESTED IN 2022 0 d Wed 04/01/23 Wed 04/01/23 498
11 IDTT.M1.GYR: 6 GYROTRONS ON SITE TESTED IN 2022 0 d Wed 13/10/21 Wed 13/10/21 750
12 IDTT.M2 - DEMONSTRATION THAT ASSEMBLY WILL BE COMPLETED AT LOW RISK 140 d Thu 09/06/22 Wed 21/12/22
13 IDTT.M2.ASSEMBLY: START OF ASSEMBLY ACTIVITIES 0 d Thu 09/06/22 Thu 09/06/22 909SS
14 IDTT.M2.CRYOSTAT-BASE: CRYOSTAT BASE ASSEMBLED 0 d Wed 31/08/22 Wed 31/08/22 909
15 IDTT.M2.PF4-ASSEMBLED: PF6-PF4 ASSEMBLED 0 d Wed 12/10/22 Wed 12/10/22 912
16 IDTT.M2.LOAD-ASSEMBLY: 2 VV + 3 TFC ASSEMBLED 0 d Wed 21/12/22 Wed 21/12/22 914
17 IDTT.M3 - DEMONSTRATION THAT MACHINE CAN BE COMMISSIONED SUCCESSFULLY 0 d Wed 09/06/21 Wed 09/06/21
18 IDTT.M3.DIAGNOSTICS-COMMISSIONED 0 d Wed 09/06/21 Wed 09/06/21 886
19 IDTT.M4 - DEMONSTRATION THAT THE FINANCIAL AND HUMAN RESOURCES ARE AVAILABLE FOR PROJECT COMPLETION 0 mo Fri 30/12/22 Fri 30/12/22
20 COM.M1 - IDTT FINAL DESIGN CONSISTEN WITH THE REQUIREMENTS FOR TESTING ALTERNATE EXHAUST CONCEPTS BASED ON THE KNOWLEDGE AT THE TIME 0 mo Mon 30/12/19 Mon 30/12/19
21 COM.M2 - DECISION ON THE FIRST IDTT DIVERTOR 0 mo Fri 30/12/22 Fri 30/12/22
22 COM.M3 - ASSESSMENT OF THE INTERFACES AND EXHAUST INFRASTRUCTURE AND DIAGNOSTIC OPPORTUNITIES IN IDTT 0 mo Fri 30/12/22 Fri 30/12/22
23 PRJ-MS-01 START OF INTEGRATED COMMISSIONING 0 d Mon 30/06/25 Mon 30/06/25 944SS
24 PRJ-MS-02 FIRST PLASMA 0 mo Fri 05/12/25 Fri 05/12/25 944FS+2 d
25 01 - PHY - PHYSICS 240 d Thu 10/01/19 Wed 11/12/19 3SS
26 01-01 ADDITIONAL HEATING MIX 3 mo Thu 10/01/19 Wed 03/04/19
27 01-02 PHYSICS PLASMA SCENARIOS 3 mo Thu 10/01/19 Wed 03/04/19
28 01-03 EDGE PHYSICS AND DIVERTOR 6 mo Thu 10/01/19 Wed 26/06/19
29 01-04 MAGNETIC PROBES 12 mo Thu 10/01/19 Wed 11/12/19
30 01-05 INTERNAL ACTIVE COILS 12 mo Thu 10/01/19 Wed 11/12/19
31 01-06 MAGNETIC RIPPLE AND ERROR FIELD 6 mo Thu 10/01/19 Wed 26/06/19
32 01-07 DISRUPTIONS AND RE MITIGATIONS ADDITIONAL HEATING MIX 3 mo Thu 10/01/19 Wed 03/04/19
33 01-08 BEAM ENERGY AND POSITION 3 mo Thu 10/01/19 Wed 03/04/19
34 01-09 PLASMA BREAKDOWN 3 mo Thu 10/01/19 Wed 03/04/19
35 02 - MAG - MAGNETS 1514 d? Fri 21/12/18 Wed 09/10/24 2SS
36 MAG-01 TFC 1345 d? Fri 21/12/18 Thu 15/02/24
37 MS-MAG-01-01: Design completion 6 mo Fri 21/12/18 Thu 06/06/19 2
38 MS-MAG-01-02: Design review 3 mo Fri 07/06/19 Thu 29/08/19 37
39 MS-MAG-01-03: Technical specification 2 mo Fri 02/08/19 Thu 26/09/19 38FS-20 d
40 MS-MAG-01-04: Calls for Tender (WP + Case) 2 mo Fri 27/09/19 Thu 21/11/19 39
41 TFC MANUFACTURING 1105 d Fri 22/11/19 Thu 15/02/24 40
42 WP manufacturing 930 d Fri 22/11/19 Thu 15/06/23 40
43 Drawing & Design 24 w Fri 22/11/19 Thu 07/05/20
44 Tooling & Materials 48 w Fri 03/01/20 Thu 03/12/20 43SS+6 w
45 Special process qualification 48 w Fri 31/01/20 Thu 31/12/20 43SS+10 w
46 WP Manufacturing 640 d Fri 01/01/21 Thu 15/06/23 45
47 WP1 190 d Fri 01/01/21 Thu 23/09/21 552
48 DP1 5 w Fri 01/01/21 Thu 04/02/21 45
49 DP2 4 w Fri 05/02/21 Thu 04/03/21 48
2018
2019
2020
2021
2022
2023
2024
2025
2026
H1
H2
21/12
10/01
30/12
09/06
02/02
03/08
22/12
04/01
13/10
31/08
12/10
21/12
09/06
30/12
30/12
30/12
30/12
30/06
05/12
Engineer 7,Engineer 8
Baseline Milestone
Baseline Summary
Attività
Divisione
Cardine
Riepilogo
Riepilogo progetto
Attività esterne
Cardine esterno
Inactive Milestone
Inactive Summary
Manual Task
Duration-only
Manual Summary Rollup
Manual Summary
Start-only
Finish-only
External Tasks
External Milestone
Avanzamento
Scadenza
Critical
Critical Split
Baseline
Slippage
Slack
Progetto: magnets_DTT
Data: Thu 04/04/19
Pagina 1

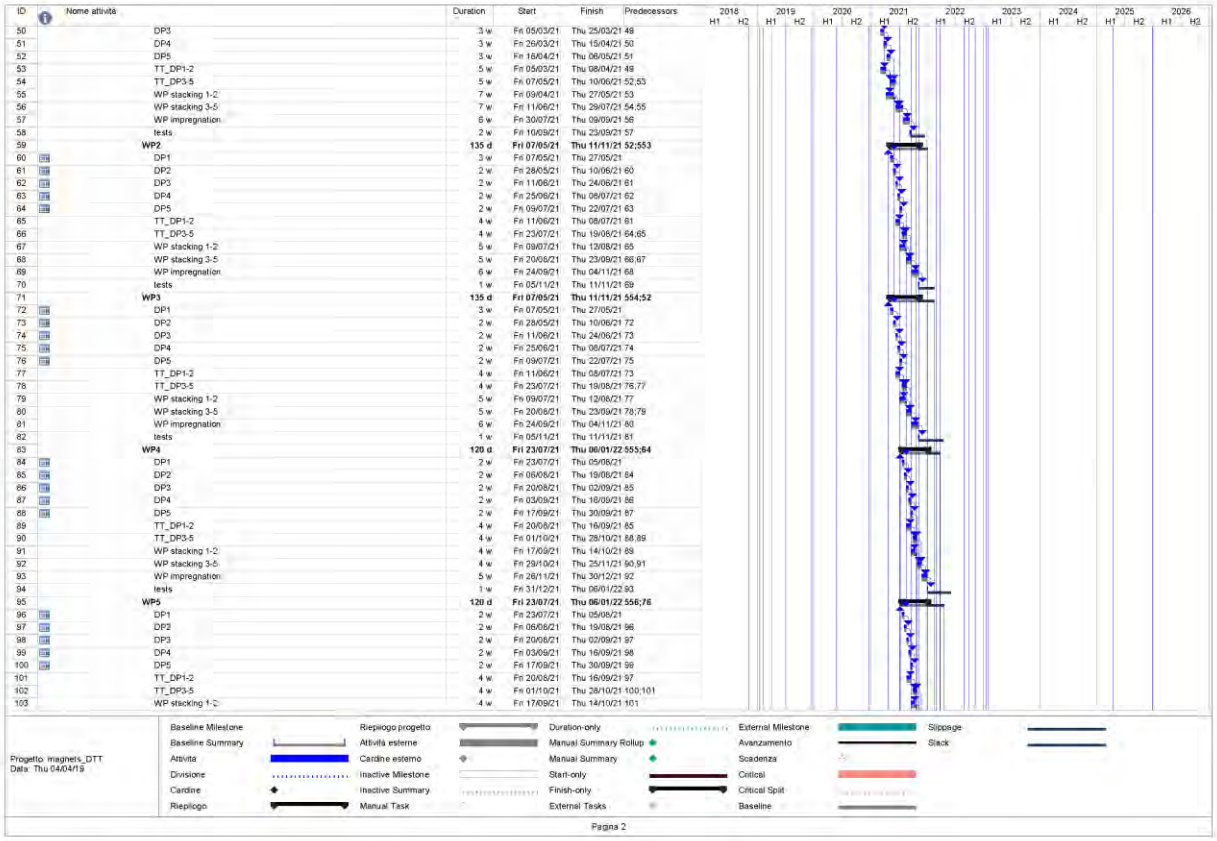
ID
Nome attività
Duration
Start
Finish
Predecessors
2018
2019
2020
2021
2022
2023
2024
2025
2026
H1 H2
50 DP3 3 w Fri 05/03/21 Thu 25/03/21 48
51 DP4 3 w Fri 26/03/21 Thu 15/04/21 50
52 DP5 3 w Fri 16/04/21 Thu 06/05/21 51
53 TT_DP1-2 5 w Fri 05/03/21 Thu 08/04/21 49
54 TT_DP3-5 5 w Fri 07/05/21 Thu 10/06/21 52;53
55 WP stacking 1-2 7 w Fri 09/04/21 Thu 27/05/21 53
56 WP stacking 3-5 7 w Fri 11/06/21 Thu 29/07/21 54,55
57 WP impregnation 6 w Fri 30/07/21 Thu 09/09/21 56
58 tests 2 w Fri 10/09/21 Thu 23/09/21 57
59 WP2 135 d Fri 07/05/21 Thu 11/11/21 52;553
60 DP1 3 w Fri 07/05/21 Thu 27/05/21
61 DP2 2 w Fri 28/05/21 Thu 10/06/21 60
62 DP3 2 w Fri 11/06/21 Thu 24/06/21 61
63 DP4 2 w Fri 25/06/21 Thu 08/07/21 62
64 DP5 2 w Fri 09/07/21 Thu 22/07/21 63
65 TT_DP1-2 4 w Fri 11/06/21 Thu 08/07/21 61
66 TT_DP3-5 4 w Fri 23/07/21 Thu 19/08/21 64,65
67 WP stacking 1-2 5 w Fri 09/07/21 Thu 12/08/21 65
68 WP stacking 3-5 5 w Fri 20/08/21 Thu 23/09/21 66,67
69 WP impregnation 6 w Fri 24/09/21 Thu 04/11/21 68
70 tests 1 w Fri 05/11/21 Thu 11/11/21 69
71 WP3 135 d Fri 07/05/21 Thu 11/11/21 554;52
72 DP1 3 w Fri 07/05/21 Thu 27/05/21
73 DP2 2 w Fri 28/05/21 Thu 10/06/21 72
74 DP3 2 w Fri 11/06/21 Thu 24/06/21 73
75 DP4 2 w Fri 25/06/21 Thu 08/07/21 74
76 DP5 2 w Fri 09/07/21 Thu 22/07/21 75
77 TT_DP1-2 4 w Fri 11/06/21 Thu 08/07/21 73
78 TT_DP3-5 4 w Fri 23/07/21 Thu 19/08/21 76,77
79 WP stacking 1-2 5 w Fri 09/07/21 Thu 12/08/21 77
80 WP stacking 3-5 5 w Fri 20/08/21 Thu 23/09/21 78;79
81 WP impregnation 6 w Fri 24/09/21 Thu 04/11/21 80
82 tests 1 w Fri 05/11/21 Thu 11/11/21 81
83 WP4 120 d Fri 23/07/21 Thu 06/01/22 555;84
84 DP1 2 w Fri 23/07/21 Thu 05/08/21
85 DP2 2 w Fri 06/08/21 Thu 19/08/21 84
86 DP3 2 w Fri 20/08/21 Thu 02/09/21 85
87 DP4 2 w Fri 03/09/21 Thu 16/09/21 86
88 DP5 2 w Fri 17/09/21 Thu 30/09/21 87
89 TT_DP1-2 4 w Fri 20/08/21 Thu 16/09/21 85
90 TT_DP3-5 4 w Fri 01/10/21 Thu 28/10/21 88,89
91 WP stacking 1-2 4 w Fri 17/09/21 Thu 14/10/21 89
92 WP stacking 3-5 4 w Fri 29/10/21 Thu 25/11/21 90,91
93 WP impregnation 5 w Fri 26/11/21 Thu 30/12/21 92
94 tests 1 w Fri 31/12/21 Thu 06/01/22 93
95 WP5 120 d Fri 23/07/21 Thu 06/01/22 556;76
96 DP1 2 w Fri 23/07/21 Thu 05/08/21
97 DP2 2 w Fri 06/08/21 Thu 19/08/21 96
98 DP3 2 w Fri 20/08/21 Thu 02/09/21 97
99 DP4 2 w Fri 03/09/21 Thu 16/09/21 98
100 DP5 2 w Fri 17/09/21 Thu 30/09/21 99
101 TT_DP1-2 4 w Fri 20/08/21 Thu 16/09/21 97
102 TT_DP3-5 4 w Fri 01/10/21 Thu 28/10/21 100;101
103 WP stacking 1-2 4 w Fri 17/09/21 Thu 14/10/21 101
Baseline Milestone
Baseline Summary
Attività
Divisione
Cardine
Riepilogo
Riepilogo progetto
Attività esterne
Cardine esterno
Inactive Milestone
Inactive Summary
Manual Task
Duration-only
Manual Summary Rollup
Manual Summary
Start-only
Finish-only
External Tasks
External Milestone
Avanzamento
Scadenza
Critical
Critical Split
Baseline
Slippage
Slack
Progetto: magnets_DTT
Data: Thu 04/04/19
Pagina 2

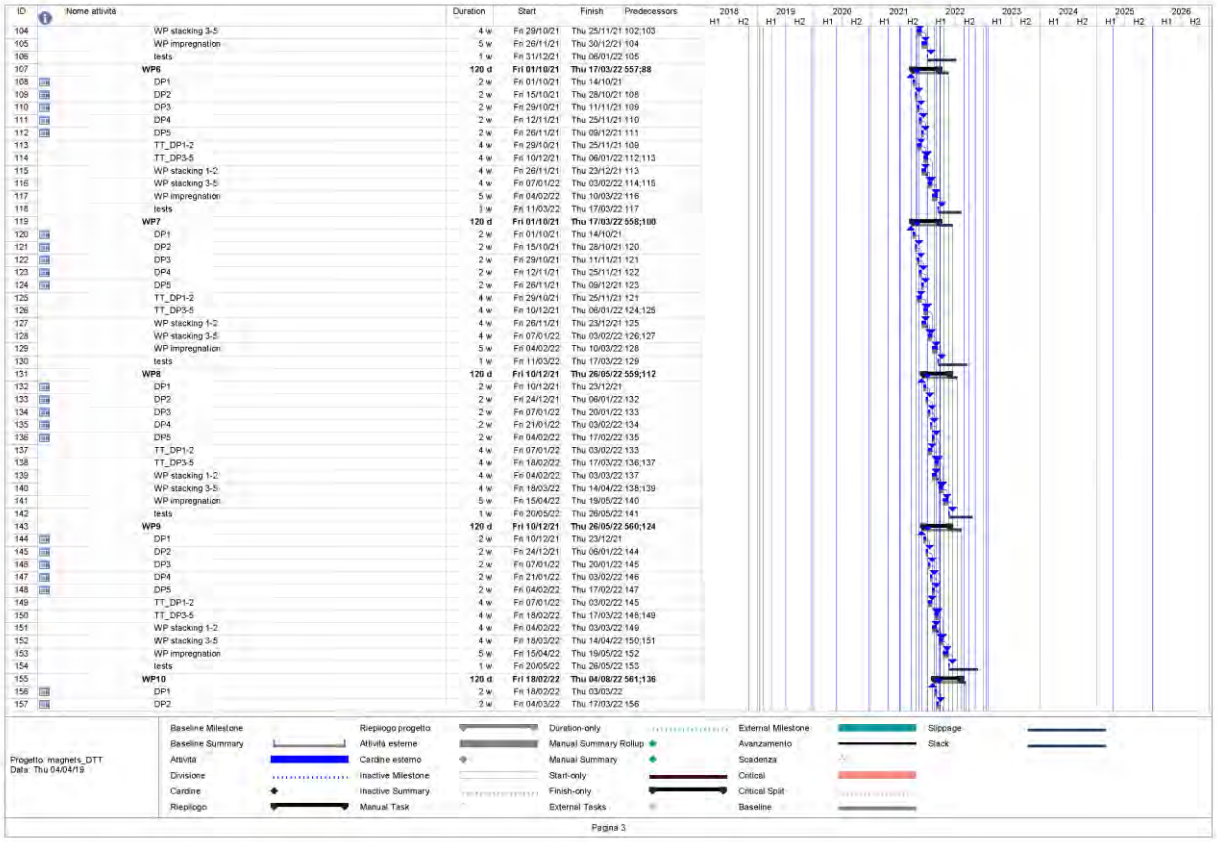
ID
Nome attività
Duration
Start
Finish
Predecessors
2018
2019
2020
2021
2022
2023
2024
2025
2026
H1 H2
104 WP stacking 3-5 4 w Fri 29/10/21 Thu 25/11/21 102;103
105 WP impregnation 5 w Fri 26/11/21 Thu 30/12/21 104
106 tests 1 w Fri 31/12/21 Thu 06/01/22 105
107 WP6 120 d Fri 01/10/21 Thu 17/03/22 557;88
108 DP1 2 w Fri 01/10/21 Thu 14/10/21
109 DP2 2 w Fri 15/10/21 Thu 28/10/21 108
110 DP3 2 w Fri 29/10/21 Thu 11/11/21 109
111 DP4 2 w Fri 12/11/21 Thu 25/11/21 110
112 DP5 2 w Fri 26/11/21 Thu 09/12/21 111
113 TT_DP1-2 4 w Fri 29/10/21 Thu 25/11/21 109
114 TT_DP3-5 4 w Fri 10/12/21 Thu 06/01/22 112;113
115 WP stacking 1-2 4 w Fri 26/11/21 Thu 23/12/21 113
116 WP stacking 3-5 4 w Fri 07/01/22 Thu 03/02/22 114;115
117 WP impregnation 5 w Fri 04/02/22 Thu 10/03/22 116
118 tests 1 w Fri 11/03/22 Thu 17/03/22 117
119 WP7 120 d Fri 01/10/21 Thu 17/03/22 558;100
120 DP1 2 w Fri 01/10/21 Thu 14/10/21
121 DP2 2 w Fri 15/10/21 Thu 28/10/21 120
122 DP3 2 w Fri 29/10/21 Thu 11/11/21 121
123 DP4 2 w Fri 12/11/21 Thu 25/11/21 122
124 DP5 2 w Fri 26/11/21 Thu 09/12/21 123
125 TT_DP1-2 4 w Fri 29/10/21 Thu 25/11/21 121
126 TT_DP3-5 4 w Fri 10/12/21 Thu 06/01/22 124,125
127 WP stacking 1-2 4 w Fri 26/11/21 Thu 23/12/21 125
128 WP stacking 3-5 4 w Fri 07/01/22 Thu 03/02/22 126,127
129 WP impregnation 5 w Fri 04/02/22 Thu 10/03/22 128
130 tests 1 w Fri 11/03/22 Thu 17/03/22 129
131 WP8 120 d Fri 10/12/21 Thu 26/05/22 559;112
132 DP1 2 w Fri 10/12/21 Thu 23/12/21
133 DP2 2 w Fri 24/12/21 Thu 06/01/22 132
134 DP3 2 w Fri 07/01/22 Thu 20/01/22 133
135 DP4 2 w Fri 21/01/22 Thu 03/02/22 134
136 DP5 2 w Fri 04/02/22 Thu 17/02/22 135
137 TT_DP1-2 4 w Fri 07/01/22 Thu 03/02/22 133
138 TT_DP3-5 4 w Fri 18/02/22 Thu 17/03/22 136,137
139 WP stacking 1-2 4 w Fri 04/02/22 Thu 03/03/22 137
140 WP stacking 3-5 4 w Fri 18/03/22 Thu 14/04/22 138,139
141 WP impregnation 5 w Fri 15/04/22 Thu 19/05/22 140
142 tests 1 w Fri 20/05/22 Thu 26/05/22 141
143 WP9 120 d Fri 10/12/21 Thu 26/05/22 560;124
144 DP1 2 w Fri 10/12/21 Thu 23/12/21
145 DP2 2 w Fri 24/12/21 Thu 06/01/22 144
146 DP3 2 w Fri 07/01/22 Thu 20/01/22 145
147 DP4 2 w Fri 21/01/22 Thu 03/02/22 146
148 DP5 2 w Fri 04/02/22 Thu 17/02/22 147
149 TT_DP1-2 4 w Fri 07/01/22 Thu 03/02/22 145
150 TT_DP3-5 4 w Fri 18/02/22 Thu 17/03/22 148,149
151 WP stacking 1-2 4 w Fri 04/02/22 Thu 03/03/22 149
152 WP stacking 3-5 4 w Fri 18/03/22 Thu 14/04/22 150,151
153 WP impregnation 5 w Fri 15/04/22 Thu 19/05/22 152
154 tests 1 w Fri 20/05/22 Thu 26/05/22 153
155 WP10 120 d Fri 18/02/22 Thu 04/08/22 561;136
156 DP1 2 w Fri 18/02/22 Thu 03/03/22
157 DP2 2 w Fri 04/03/22 Thu 17/03/22 156
Baseline Milestone
Baseline Summary
Attività
Divisione
Cardine
Riepilogo
Riepilogo progetto
Attività esterne
Cardine esterno
Inactive Milestone
Inactive Summary
Manual Task
Duration-only
Manual Summary Rollup
Manual Summary
Start-only
Finish-only
External Tasks
External Milestone
Avanzamento
Scadenza
Critical
Critical Split
Baseline
Slippage
Slack
Progetto: magnets_DTT
Data: Thu 04/04/19
Pagina 3

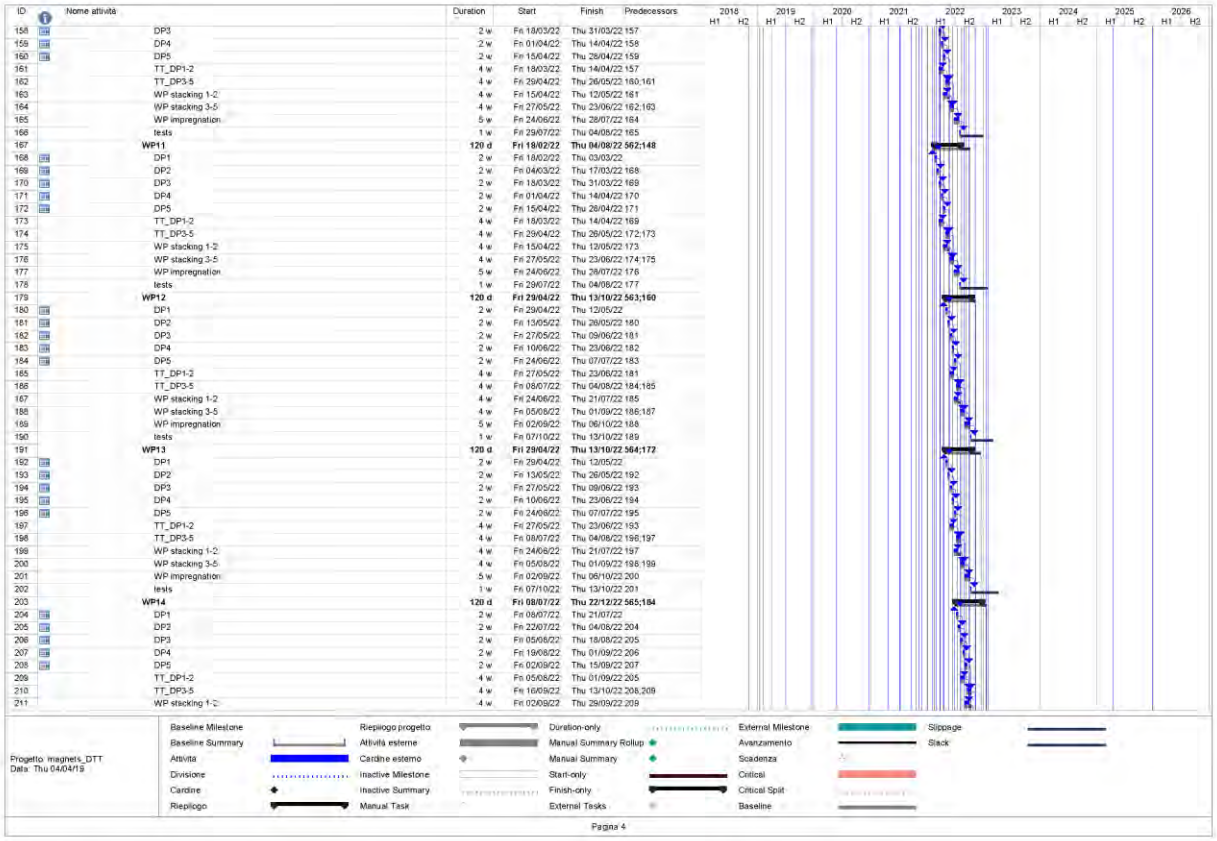
ID
Nome attività
Duration
Start
Finish
Predecessors
2018
2019
2020
2021
2022
2023
2024
2025
2026
H1 H2
158 DP3 2 w Fri 18/03/22 Thu 31/03/22 157
159 DP4 2 w Fri 01/04/22 Thu 14/04/22 158
160 DP5 2 w Fri 15/04/22 Thu 28/04/22 159
161 TT_DP1-2 4 w Fri 18/03/22 Thu 14/04/22 157
162 TT_DP3-5 4 w Fri 29/04/22 Thu 26/05/22 160,161
163 WP stacking 1-2 4 w Fri 15/04/22 Thu 12/05/22 161
164 WP stacking 3-5 4 w Fri 27/05/22 Thu 23/06/22 162,163
165 WP impregnation 5 w Fri 24/06/22 Thu 28/07/22 164
166 tests 1 w Fri 29/07/22 Thu 04/08/22 165
167 WP11 120 d Fri 18/02/22 Thu 04/08/22 562;148
168 DP1 2 w Fri 18/02/22 Thu 03/03/22
169 DP2 2 w Fri 04/03/22 Thu 17/03/22 168
170 DP3 2 w Fri 18/03/22 Thu 31/03/22 169
171 DP4 2 w Fri 01/04/22 Thu 14/04/22 170
172 DP5 2 w Fri 15/04/22 Thu 28/04/22 171
173 TT_DP1-2 4 w Fri 18/03/22 Thu 14/04/22 169
174 TT_DP3-5 4 w Fri 29/04/22 Thu 26/05/22 172;173
175 WP stacking 1-2 4 w Fri 15/04/22 Thu 12/05/22 173
176 WP stacking 3-5 4 w Fri 27/05/22 Thu 23/06/22 174;175
177 WP impregnation 5 w Fri 24/06/22 Thu 28/07/22 176
178 tests 1 w Fri 29/07/22 Thu 04/08/22 177
179 WP12 120 d Fri 29/04/22 Thu 13/10/22 563;160
180 DP1 2 w Fri 29/04/22 Thu 12/05/22
181 DP2 2 w Fri 13/05/22 Thu 26/05/22 180
182 DP3 2 w Fri 27/05/22 Thu 09/06/22 181
183 DP4 2 w Fri 10/06/22 Thu 23/06/22 182
184 DP5 2 w Fri 24/06/22 Thu 07/07/22 183
185 TT_DP1-2 4 w Fri 27/05/22 Thu 23/06/22 181
186 TT_DP3-5 4 w Fri 08/07/22 Thu 04/08/22 184,185
187 WP stacking 1-2 4 w Fri 24/06/22 Thu 21/07/22 185
188 WP stacking 3-5 4 w Fri 05/08/22 Thu 01/09/22 186,187
189 WP impregnation 5 w Fri 02/09/22 Thu 06/10/22 188
190 tests 1 w Fri 07/10/22 Thu 13/10/22 189
191 WP13 120 d Fri 29/04/22 Thu 13/10/22 564;172
192 DP1 2 w Fri 29/04/22 Thu 12/05/22
193 DP2 2 w Fri 13/05/22 Thu 26/05/22 192
194 DP3 2 w Fri 27/05/22 Thu 09/06/22 193
195 DP4 2 w Fri 10/06/22 Thu 23/06/22 194
196 DP5 2 w Fri 24/06/22 Thu 07/07/22 195
197 TT_DP1-2 4 w Fri 27/05/22 Thu 23/06/22 193
198 TT_DP3-5 4 w Fri 08/07/22 Thu 04/08/22 196,197
199 WP stacking 1-2 4 w Fri 24/06/22 Thu 21/07/22 197
200 WP stacking 3-5 4 w Fri 05/08/22 Thu 01/09/22 198,199
201 WP impregnation 5 w Fri 02/09/22 Thu 06/10/22 200
202 tests 1 w Fri 07/10/22 Thu 13/10/22 201
203 WP14 120 d Fri 08/07/22 Thu 22/12/22 565;184
204 DP1 2 w Fri 08/07/22 Thu 21/07/22
205 DP2 2 w Fri 22/07/22 Thu 04/08/22 204
206 DP3 2 w Fri 05/08/22 Thu 18/08/22 205
207 DP4 2 w Fri 19/08/22 Thu 01/09/22 206
208 DP5 2 w Fri 02/09/22 Thu 15/09/22 207
209 TT_DP1-2 4 w Fri 05/08/22 Thu 01/09/22 205
210 TT_DP3-5 4 w Fri 16/09/22 Thu 13/10/22 208,209
211 WP stacking 1-2 4 w Fri 02/09/22 Thu 29/09/22 209
Progetto: Imagnets_DTT
Data: Thu 04/04/19
Baseline Milestone
Baseline Summary
Attività
Divisione
Cardine
Riepilogo
Riepilogo progetto
Attività esterne
Cardine esterno
Inactive Milestone
Inactive Summary
Manual Task
Duration-only
Manual Summary Rollup
Manual Summary
Start-only
Finish-only
External Tasks
External Milestone
Avanzamento
Scadenza
Critical
Critical Split
Baseline
Slippage
Slack
Pagina 4

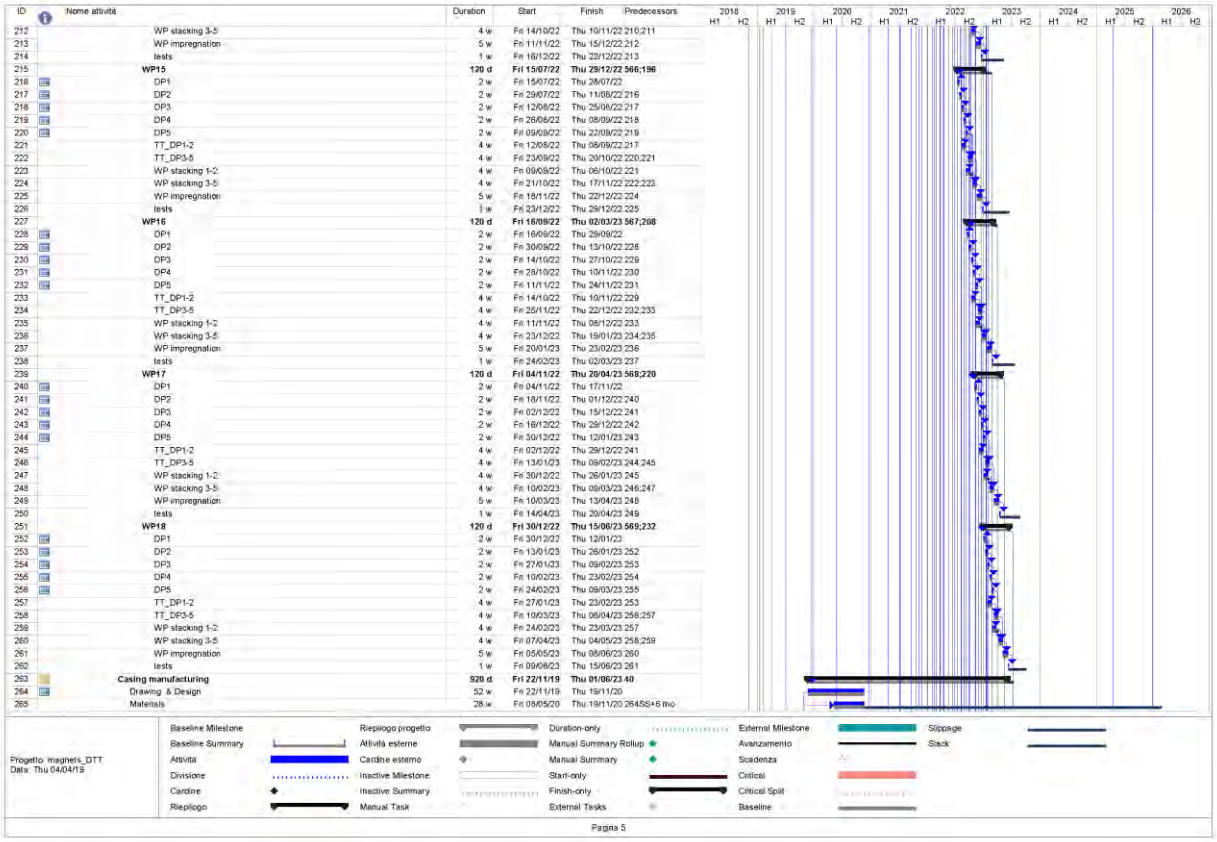
ID
Nome attività
Duration
Start
Finish
Predecessors
2018
2019
2020
2021
2022
2023
2024
2025
2026
H1 H2
212 WP stacking 3-5 4 w Fri 14/10/22 Thu 10/11/22 210,211
213 WP impregnation 5 w Fri 11/11/22 Thu 15/12/22 212
214 tests 1 w Fri 16/12/22 Thu 22/12/22 213
215 WP15 120 d Fri 15/07/22 Thu 29/12/22 566;196
216 DP1 2 w Fri 15/07/22 Thu 28/07/22
217 DP2 2 w Fri 29/07/22 Thu 11/08/22 216
218 DP3 2 w Fri 12/08/22 Thu 25/08/22 217
219 DP4 2 w Fri 26/08/22 Thu 08/09/22 218
220 DP5 2 w Fri 09/09/22 Thu 22/09/22 219
221 TT_DP1-2 4 w Fri 12/08/22 Thu 08/09/22 217
222 TT_DP3-5 4 w Fri 23/09/22 Thu 20/10/22 220,221
223 WP stacking 1-2 4 w Fri 09/09/22 Thu 06/10/22 221
224 WP stacking 3-5 4 w Fri 21/10/22 Thu 17/11/22 222,223
225 WP impregnation 5 w Fri 18/11/22 Thu 22/12/22 224
226 tests 1 w Fri 23/12/22 Thu 29/12/22 225
227 WP16 120 d Fri 16/09/22 Thu 02/03/23 567;208
228 DP1 2 w Fri 16/09/22 Thu 29/09/22
229 DP2 2 w Fri 30/09/22 Thu 13/10/22 228
230 DP3 2 w Fri 14/10/22 Thu 27/10/22 229
231 DP4 2 w Fri 28/10/22 Thu 10/11/22 230
232 DP5 2 w Fri 11/11/22 Thu 24/11/22 231
233 TT_DP1-2 4 w Fri 14/10/22 Thu 10/11/22 229
234 TT_DP3-5 4 w Fri 25/11/22 Thu 22/12/22 232,233
235 WP stacking 1-2 4 w Fri 11/11/22 Thu 08/12/22 233
236 WP stacking 3-5 4 w Fri 23/12/22 Thu 19/01/23 234,235
237 WP impregnation 5 w Fri 20/01/23 Thu 23/02/23 236
238 tests 1 w Fri 24/02/23 Thu 02/03/23 237
239 WP17 120 d Fri 04/11/22 Thu 20/04/23 568;220
240 DP1 2 w Fri 04/11/22 Thu 17/11/22
241 DP2 2 w Fri 18/11/22 Thu 01/12/22 240
242 DP3 2 w Fri 02/12/22 Thu 15/12/22 241
243 DP4 2 w Fri 16/12/22 Thu 29/12/22 242
244 DP5 2 w Fri 30/12/22 Thu 12/01/23 243
245 TT_DP1-2 4 w Fri 02/12/22 Thu 29/12/22 241
246 TT_DP3-5 4 w Fri 13/01/23 Thu 09/02/23 244,245
247 WP stacking 1-2 4 w Fri 30/12/22 Thu 26/01/23 245
248 WP stacking 3-5 4 w Fri 10/02/23 Thu 09/03/23 246,247
249 WP impregnation 5 w Fri 10/03/23 Thu 13/04/23 248
250 tests 1 w Fri 14/04/23 Thu 20/04/23 249
251 WP18 120 d Fri 30/12/22 Thu 15/06/23 569;232
252 DP1 2 w Fri 30/12/22 Thu 12/01/23
253 DP2 2 w Fri 13/01/23 Thu 26/01/23 252
254 DP3 2 w Fri 27/01/23 Thu 09/02/23 253
255 DP4 2 w Fri 10/02/23 Thu 23/02/23 254
256 DP5 2 w Fri 24/02/23 Thu 09/03/23 255
257 TT_DP1-2 4 w Fri 27/01/23 Thu 23/02/23 253
258 TT_DP3-5 4 w Fri 10/03/23 Thu 06/04/23 256,257
259 WP stacking 1-2 4 w Fri 24/02/23 Thu 23/03/23 257
260 WP stacking 3-5 4 w Fri 07/04/23 Thu 04/05/23 258,259
261 WP impregnation 5 w Fri 05/05/23 Thu 08/06/23 260
262 tests 1 w Fri 09/06/23 Thu 15/06/23 261
263 Casing manufacturing 926 d Fri 22/11/19 Thu 01/06/23 40
264 Drawing & Design 52 w Fri 22/11/19 Thu 19/11/20
265 Materials 28 w Fri 08/05/20 Thu 19/11/20 264SS+6 mo
Progetto: Imagnets_DTT
Data: Thu 04/04/19
Baseline Milestone
Baseline Summary
Attività
Divisione
Cardine
Riepilogo
Riepilogo progetto
Attività esterne
Cardine esterno
Inactive Milestone
Inactive Summary
Manual Task
Duration-only
Manual Summary Rollup
Manual Summary
Start-only
Finish-only
External Tasks
External Milestone
Avanzamento
Scadenza
Critical
Critical Split
Baseline
Slippage
Slack
Pagina 5

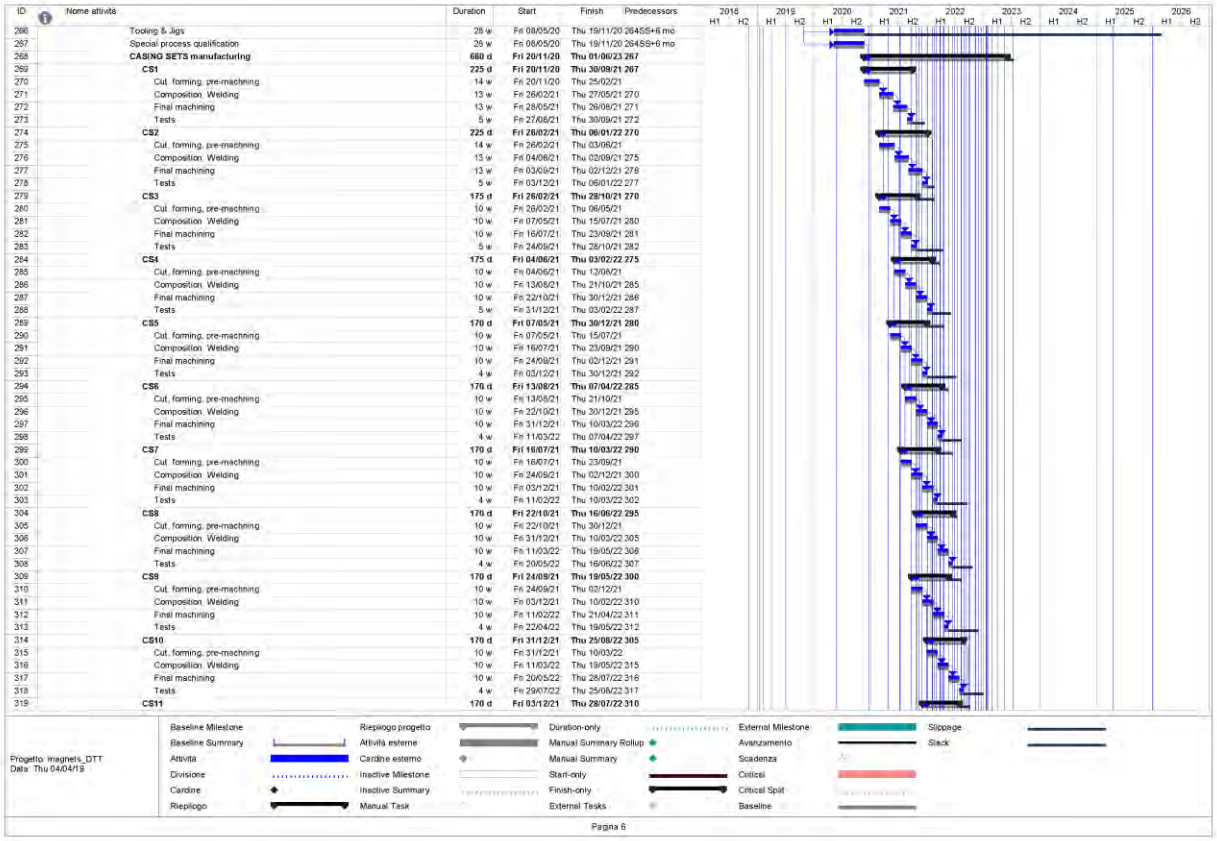
ID
Nome attività
Duration
Start
Finish
Predecessors
2018
2019
2020
2021
2022
2023
2024
2025
2026
H1 H2
286 Tooling & Jigs 28 w Fri 08/05/20 Thu 19/11/20 264SS+6 mo
287 Special process qualification 28 w Fri 08/05/20 Thu 19/11/20 264SS+6 mo
288 CASING SETS manufacturing 680 d Fri 20/11/20 Thu 01/06/23 267
289 CS1 225 d Fri 20/11/20 Thu 30/09/21 267
290 Cut, forming, pre-machining 14 w Fri 20/11/20 Thu 25/02/21
291 Composition: Welding 13 w Fri 26/02/21 Thu 27/05/21 270
292 Final machining 13 w Fri 28/05/21 Thu 26/08/21 271
293 Tests 5 w Fri 27/08/21 Thu 30/09/21 272
294 CS2 225 d Fri 26/02/21 Thu 06/01/22 270
295 Cut, forming, pre-machining 14 w Fri 26/02/21 Thu 03/06/21
296 Composition: Welding 13 w Fri 04/06/21 Thu 02/09/21 275
297 Final machining 13 w Fri 03/09/21 Thu 02/12/21 276
298 Tests 5 w Fri 03/12/21 Thu 06/01/22 277
299 CS3 175 d Fri 26/02/21 Thu 28/10/21 270
300 Cut, forming, pre-machining 10 w Fri 26/02/21 Thu 06/05/21
301 Composition: Welding 10 w Fri 07/05/21 Thu 15/07/21 280
302 Final machining 10 w Fri 16/07/21 Thu 23/09/21 281
303 Tests 5 w Fri 24/09/21 Thu 28/10/21 282
304 CS4 175 d Fri 04/06/21 Thu 03/02/22 275
305 Cut, forming, pre-machining 10 w Fri 04/06/21 Thu 12/08/21
306 Composition: Welding 10 w Fri 13/08/21 Thu 21/10/21 285
307 Final machining 10 w Fri 22/10/21 Thu 30/12/21 286
308 Tests 5 w Fri 31/12/21 Thu 03/02/22 287
309 CS5 170 d Fri 07/05/21 Thu 30/12/21 280
310 Cut, forming, pre-machining 10 w Fri 07/05/21 Thu 15/07/21
311 Composition: Welding 10 w Fri 16/07/21 Thu 23/09/21 290
312 Final machining 10 w Fri 24/09/21 Thu 02/12/21 291
313 Tests 4 w Fri 03/12/21 Thu 30/12/21 292
314 CS6 170 d Fri 13/08/21 Thu 07/04/22 285
315 Cut, forming, pre-machining 10 w Fri 13/08/21 Thu 21/10/21
316 Composition: Welding 10 w Fri 22/10/21 Thu 30/12/21 295
317 Final machining 10 w Fri 31/12/21 Thu 10/03/22 296
318 Tests 4 w Fri 11/03/22 Thu 07/04/22 297
319 CS7 170 d Fri 16/07/21 Thu 10/03/22 290
320 Cut, forming, pre-machining 10 w Fri 16/07/21 Thu 23/09/21
321 Composition: Welding 10 w Fri 24/09/21 Thu 02/12/21 300
322 Final machining 10 w Fri 03/12/21 Thu 10/02/22 301
323 Tests 4 w Fri 11/02/22 Thu 10/03/22 302
324 CS8 170 d Fri 22/10/21 Thu 16/06/22 295
325 Cut, forming, pre-machining 10 w Fri 22/10/21 Thu 30/12/21
326 Composition: Welding 10 w Fri 31/12/21 Thu 10/03/22 305
327 Final machining 10 w Fri 11/03/22 Thu 19/05/22 306
328 Tests 4 w Fri 20/05/22 Thu 16/06/22 307
329 CS9 170 d Fri 24/09/21 Thu 19/05/22 300
330 Cut, forming, pre-machining 10 w Fri 24/09/21 Thu 03/12/21
331 Composition: Welding 10 w Fri 03/12/21 Thu 10/02/22 310
332 Final machining 10 w Fri 11/02/22 Thu 21/04/22 311
333 Tests 4 w Fri 22/04/22 Thu 19/05/22 312
334 CS10 170 d Fri 31/12/21 Thu 25/08/22 305
335 Cut, forming, pre-machining 10 w Fri 31/12/21 Thu 10/03/22
336 Composition: Welding 10 w Fri 11/03/22 Thu 19/05/22 315
337 Final machining 10 w Fri 20/05/22 Thu 28/07/22 316
338 Tests 4 w Fri 29/07/22 Thu 25/08/22 317
339 CS11 170 d Fri 03/12/21 Thu 28/07/22 310
Baseline Milestone
Baseline Summary
Attività
Divisione
Cardine
Riepilogo
Riepilogo progetto
Attività esterne
Cardine esterno
Inactive Milestone
Inactive Summary
Manual Task
Duration-only
Manual Summary Rollup
Manual Summary
Start-only
Finish-only
External Tasks
External Milestone
Avanzamento
Scadenza
Critical
Critical Split
Baseline
Slippage
Slack
Progetto: Imagnets_DTT
Data: Thu 04/04/19
Pagina 6

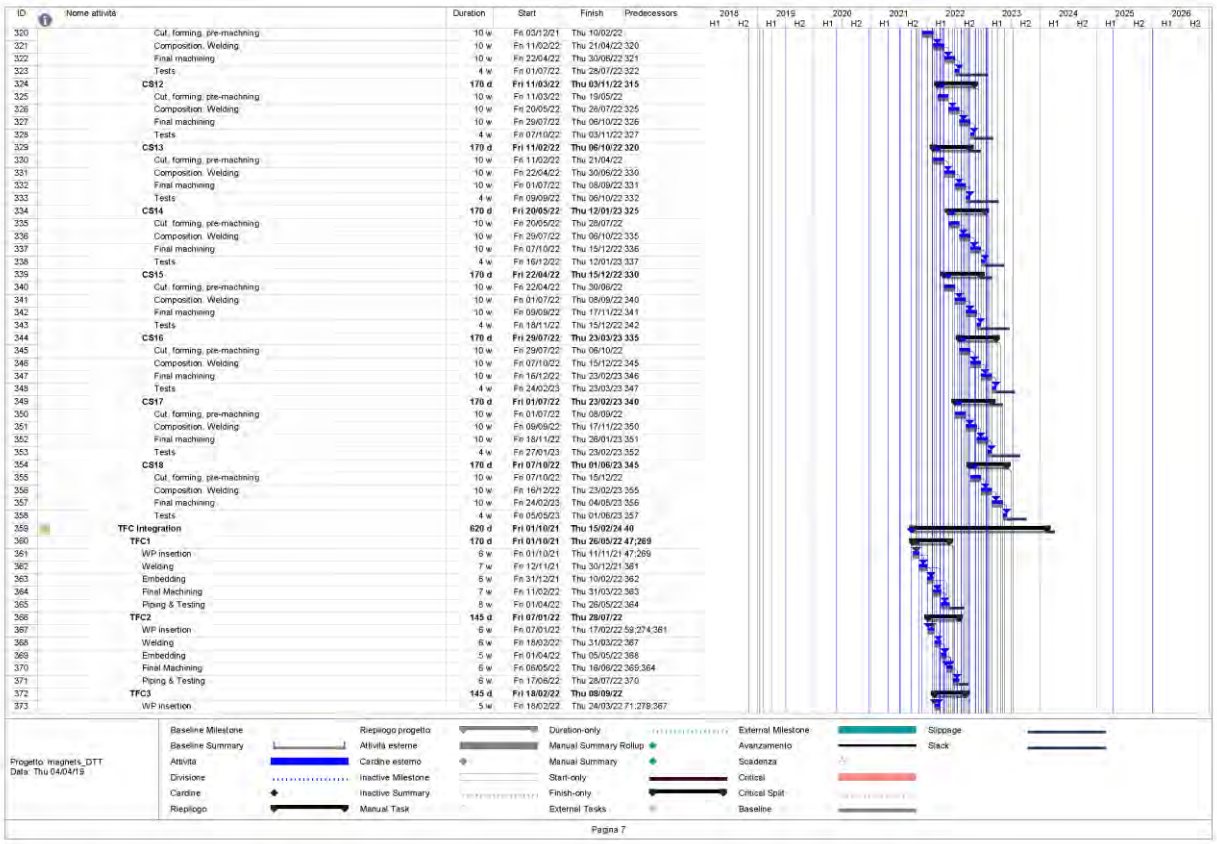
ID
Nome attività
Duration
Start
Finish
Predecessors
2018
2019
2020
2021
2022
2023
2024
2025
2026
H1 H2
320 Cut, forming, pre-machining 10 w Fri 03/12/21 Thu 10/02/22
321 Composition: Welding 10 w Fri 11/02/22 Thu 21/04/22 320
322 Final machining 10 w Fri 22/04/22 Thu 30/06/22 321
323 Tests 4 w Fri 01/07/22 Thu 28/07/22 322
324 CS12 170 d Fri 11/03/22 Thu 03/11/22 315
325 Cut, forming, pre-machining 10 w Fri 11/03/22 Thu 19/05/22
326 Composition: Welding 10 w Fri 20/05/22 Thu 28/07/22 325
327 Final machining 10 w Fri 29/07/22 Thu 06/10/22 326
328 Tests 4 w Fri 07/10/22 Thu 03/11/22 327
329 CS13 170 d Fri 11/02/22 Thu 06/10/22 320
330 Cut, forming, pre-machining 10 w Fri 11/02/22 Thu 21/04/22
331 Composition: Welding 10 w Fri 22/04/22 Thu 30/06/22 330
332 Final machining 10 w Fri 01/07/22 Thu 08/09/22 331
333 Tests 4 w Fri 09/09/22 Thu 06/10/22 332
334 CS14 170 d Fri 20/05/22 Thu 12/01/23 325
335 Cut, forming, pre-machining 10 w Fri 20/05/22 Thu 28/07/22
336 Composition: Welding 10 w Fri 29/07/22 Thu 06/10/22 335
337 Final machining 10 w Fri 07/10/22 Thu 15/12/22 336
338 Tests 4 w Fri 16/12/22 Thu 12/01/23 337
339 CS15 170 d Fri 22/04/22 Thu 15/12/22 330
340 Cut, forming, pre-machining 10 w Fri 22/04/22 Thu 30/06/22
341 Composition: Welding 10 w Fri 01/07/22 Thu 08/09/22 340
342 Final machining 10 w Fri 09/09/22 Thu 17/11/22 341
343 Tests 4 w Fri 18/11/22 Thu 15/12/22 342
344 CS16 170 d Fri 29/07/22 Thu 23/03/23 335
345 Cut, forming, pre-machining 10 w Fri 29/07/22 Thu 06/10/22
346 Composition: Welding 10 w Fri 07/10/22 Thu 15/12/22 345
347 Final machining 10 w Fri 16/12/22 Thu 23/02/23 346
348 Tests 4 w Fri 24/02/23 Thu 23/03/23 347
349 CS17 170 d Fri 01/07/22 Thu 23/02/23 340
350 Cut, forming, pre-machining 10 w Fri 01/07/22 Thu 08/09/22
351 Composition: Welding 10 w Fri 09/09/22 Thu 17/11/22 350
352 Final machining 10 w Fri 18/11/22 Thu 26/01/23 351
353 Tests 4 w Fri 27/01/23 Thu 23/02/23 352
354 CS18 170 d Fri 07/10/22 Thu 01/06/23 345
355 Cut, forming, pre-machining 10 w Fri 07/10/22 Thu 15/12/22
356 Composition: Welding 10 w Fri 16/12/22 Thu 23/02/23 355
357 Final machining 10 w Fri 24/02/23 Thu 04/05/23 356
358 Tests 4 w Fri 05/05/23 Thu 01/06/23 357
359 TFC Integration 620 d Fri 01/10/21 Thu 15/02/24 40
360 TFC1 170 d Fri 01/10/21 Thu 26/05/22 47;269
361 WP insertion 6 w Fri 01/10/21 Thu 11/11/21 47;269
362 Welding 7 w Fri 12/11/21 Thu 30/12/21 361
363 Embedding 5 w Fri 31/12/21 Thu 10/02/22 362
364 Final Machining 7 w Fri 11/02/22 Thu 31/03/22 363
365 Piping & Testing 8 w Fri 01/04/22 Thu 26/05/22 364
366 TFC2 145 d Fri 07/01/22 Thu 28/07/22
367 WP insertion 6 w Fri 07/01/22 Thu 17/02/22 59;274;361
368 Welding 6 w Fri 18/02/22 Thu 31/03/22 367
369 Embedding 5 w Fri 01/04/22 Thu 05/05/22 368
370 Final Machining 6 w Fri 06/05/22 Thu 16/06/22 369;364
371 Piping & Testing 6 w Fri 17/06/22 Thu 28/07/22 370
372 TFC3 145 d Fri 18/02/22 Thu 08/09/22
373 WP insertion 5 w Fri 18/02/22 Thu 24/03/22 71;278;367
Baseline Milestone
Baseline Summary
Attività
Divisione
Cardine
Riepilogo
Riepilogo progetto
Attività esterne
Cardine esterno
Inactive Milestone
Inactive Summary
Manual Task
Duration-only
Manual Summary Rollup
Manual Summary
Start-only
Finish-only
External Tasks
External Milestone
Avanzamento
Scadenza
Critical
Critical Split
Baseline
Slippage
Slack
Progetto: Imagnets_DTT
Data: Thu 04/04/19
Pagina 7

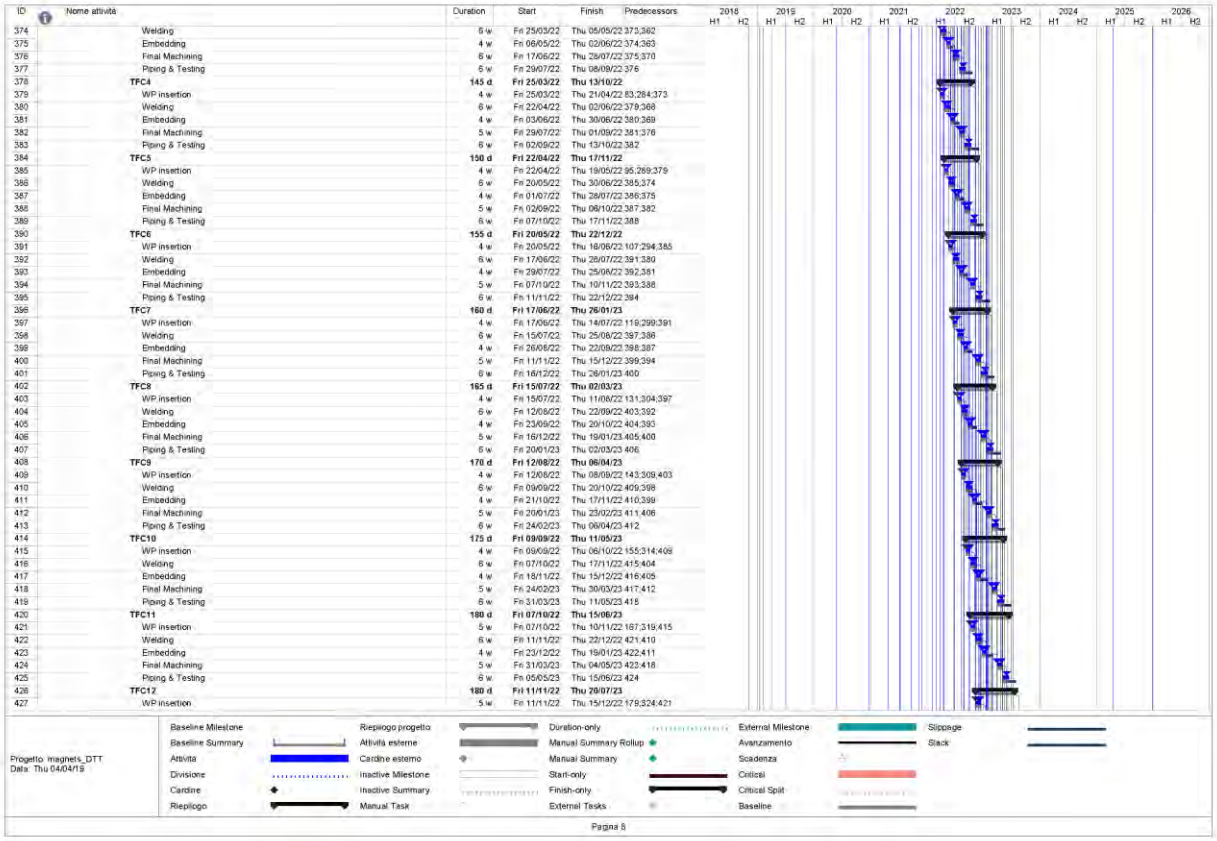
ID
Nome attività
Duration
Start
Finish
Predecessors
2018
2019
2020
2021
2022
2023
2024
2025
2026
H1 H2
374 Welding 6 w Fri 25/03/22 Thu 05/05/22 373;382
375 Embedding 4 w Fri 06/05/22 Thu 02/06/22 374;383
376 Final Machining 6 w Fri 17/06/22 Thu 28/07/22 375;370
377 Piping & Testing 6 w Fri 29/07/22 Thu 08/09/22 376
378 TFC4 145 d Fri 25/03/22 Thu 13/10/22
379 WP insertion 4 w Fri 25/03/22 Thu 21/04/22 83;284;373
380 Welding 6 w Fri 22/04/22 Thu 02/06/22 379;368
381 Embedding 4 w Fri 03/06/22 Thu 30/06/22 380;369
382 Final Machining 5 w Fri 29/07/22 Thu 01/09/22 381;376
383 Piping & Testing 6 w Fri 02/09/22 Thu 13/10/22 382
384 TFC5 150 d Fri 22/04/22 Thu 17/11/22
385 WP insertion 4 w Fri 22/04/22 Thu 19/05/22 95;269;379
386 Welding 6 w Fri 20/05/22 Thu 30/06/22 385;374
387 Embedding 4 w Fri 01/07/22 Thu 28/07/22 386;375
388 Final Machining 5 w Fri 02/09/22 Thu 06/10/22 387;382
389 Piping & Testing 6 w Fri 07/10/22 Thu 17/11/22 388
390 TFC6 155 d Fri 20/05/22 Thu 22/12/22
391 WP insertion 4 w Fri 20/05/22 Thu 16/06/22 107;294;385
392 Welding 6 w Fri 17/06/22 Thu 28/07/22 391;380
393 Embedding 4 w Fri 29/07/22 Thu 25/08/22 392;381
394 Final Machining 5 w Fri 07/10/22 Thu 10/11/22 393;388
395 Piping & Testing 6 w Fri 11/11/22 Thu 22/12/22 394
396 TFC7 160 d Fri 17/06/22 Thu 26/01/23
397 WP insertion 4 w Fri 17/06/22 Thu 14/07/22 119;299;391
398 Welding 6 w Fri 15/07/22 Thu 25/08/22 397;386
399 Embedding 4 w Fri 26/08/22 Thu 22/09/22 398;387
400 Final Machining 5 w Fri 11/11/22 Thu 15/12/22 399;394
401 Piping & Testing 6 w Fri 16/12/22 Thu 26/01/23 400
402 TFC8 165 d Fri 15/07/22 Thu 02/03/23
403 WP insertion 4 w Fri 15/07/22 Thu 11/08/22 131;304;397
404 Welding 6 w Fri 12/08/22 Thu 22/09/22 403;392
405 Embedding 4 w Fri 23/09/22 Thu 20/10/22 404;393
406 Final Machining 5 w Fri 16/12/22 Thu 19/01/23 405;400
407 Piping & Testing 6 w Fri 20/01/23 Thu 02/03/23 406
408 TFC9 170 d Fri 12/08/22 Thu 06/04/23
409 WP insertion 4 w Fri 12/08/22 Thu 08/09/22 143;309;403
410 Welding 6 w Fri 09/09/22 Thu 20/10/22 409;398
411 Embedding 4 w Fri 21/10/22 Thu 17/11/22 410;399
412 Final Machining 5 w Fri 20/01/23 Thu 23/02/23 411;406
413 Piping & Testing 6 w Fri 24/02/23 Thu 06/04/23 412
414 TFC10 175 d Fri 09/09/22 Thu 11/05/23
415 WP insertion 4 w Fri 09/09/22 Thu 06/10/22 155;314;408
416 Welding 6 w Fri 07/10/22 Thu 17/11/22 415;404
417 Embedding 4 w Fri 18/11/22 Thu 15/12/22 416;405
418 Final Machining 5 w Fri 24/02/23 Thu 30/03/23 417;412
419 Piping & Testing 6 w Fri 31/03/23 Thu 11/05/23 418
420 TFC11 180 d Fri 07/10/22 Thu 15/06/23
421 WP insertion 5 w Fri 07/10/22 Thu 10/11/22 187;319;415
422 Welding 6 w Fri 11/11/22 Thu 22/12/22 421;410
423 Embedding 4 w Fri 23/12/22 Thu 19/01/23 422;411
424 Final Machining 5 w Fri 31/03/23 Thu 04/05/23 423;418
425 Piping & Testing 6 w Fri 05/05/23 Thu 15/06/23 424
426 TFC12 180 d Fri 11/11/22 Thu 20/07/23
427 WP insertion 5 w Fri 11/11/22 Thu 15/12/22 179;324;421
Baseline Milestone
Baseline Summary
Attività
Divisione
Cardine
Riepilogo
Riepilogo progetto
Attività esterne
Cardine esterno
Inactive Milestone
Inactive Summary
Manual Task
Duration-only
Manual Summary Rollup
Manual Summary
Start-only
Finish-only
External Tasks
External Milestone
Avanzamento
Scadenza
Critical
Critical Split
Baseline
Slippage
Slack
Progetto: Magnets_DTT
Data: Thu 04/04/19
Pagina 8

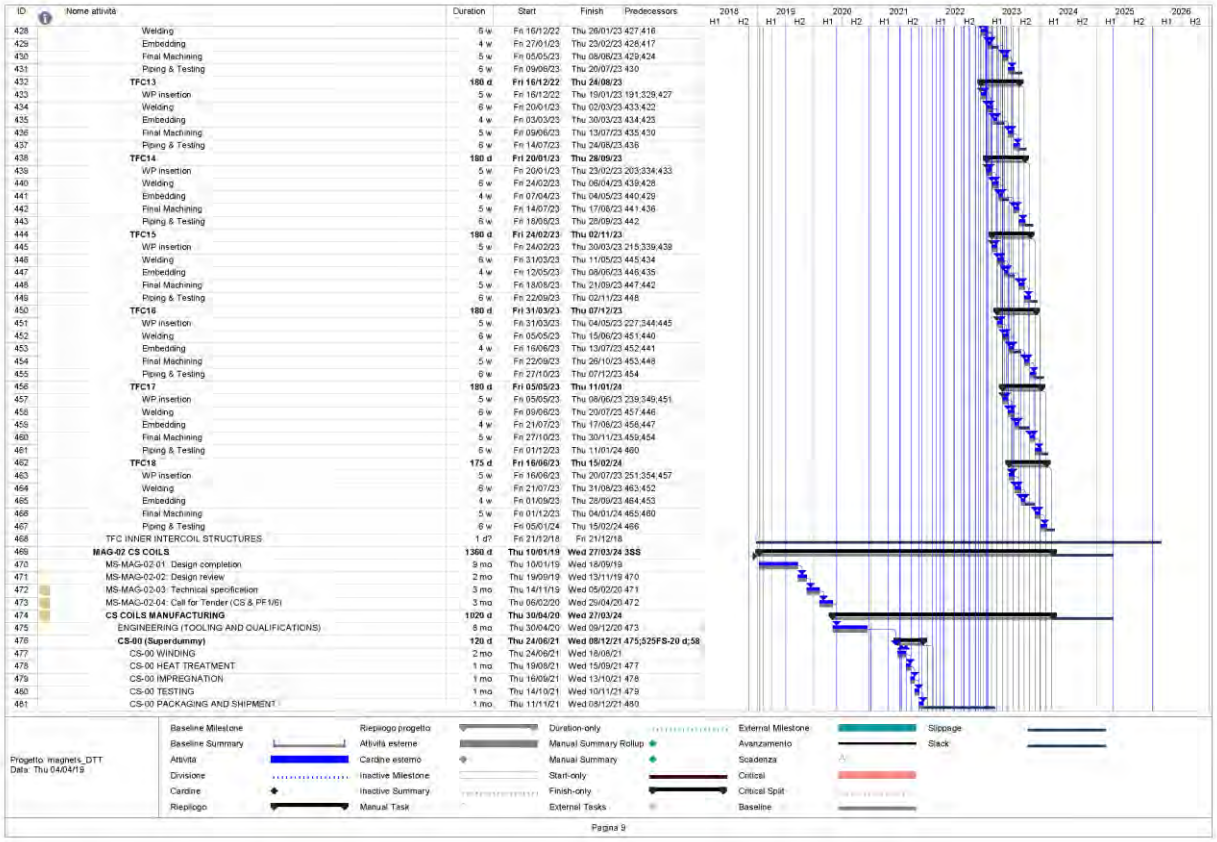
ID
Nome attività
Duration
Start
Finish
Predecessors
2018
2019
2020
2021
2022
2023
2024
2025
2026
H1 H2
428 Welding 6 w Fri 16/12/22 Thu 26/01/23 427;416
429 Embedding 4 w Fri 27/01/23 Thu 23/02/23 428;417
430 Final Machining 5 w Fri 05/05/23 Thu 08/06/23 429;424
431 Piping & Testing 6 w Fri 09/06/23 Thu 20/07/23 430
432 TFC13 180 d Fri 16/12/22 Thu 24/08/23
433 WP insertion 5 w Fri 16/12/22 Thu 19/01/23 191;329;427
434 Welding 6 w Fri 20/01/23 Thu 02/03/23 433;422
435 Embedding 4 w Fri 03/03/23 Thu 30/03/23 434;423
436 Final Machining 5 w Fri 09/06/23 Thu 13/07/23 435;430
437 Piping & Testing 6 w Fri 14/07/23 Thu 24/08/23 436
438 TFC14 180 d Fri 20/01/23 Thu 28/09/23
439 WP insertion 5 w Fri 20/01/23 Thu 23/02/23 203;334;433
440 Welding 6 w Fri 24/02/23 Thu 06/04/23 439;426
441 Embedding 4 w Fri 07/04/23 Thu 04/05/23 440;429
442 Final Machining 5 w Fri 14/07/23 Thu 17/08/23 441;436
443 Piping & Testing 6 w Fri 18/08/23 Thu 28/09/23 442
444 TFC15 180 d Fri 24/02/23 Thu 02/11/23
445 WP insertion 5 w Fri 24/02/23 Thu 30/03/23 215;339;439
446 Welding 6 w Fri 31/03/23 Thu 11/05/23 445;434
447 Embedding 4 w Fri 12/05/23 Thu 08/06/23 446;435
448 Final Machining 5 w Fri 18/08/23 Thu 21/09/23 447;442
449 Piping & Testing 6 w Fri 22/09/23 Thu 02/11/23 448
450 TFC16 180 d Fri 31/03/23 Thu 07/12/23
451 WP insertion 5 w Fri 31/03/23 Thu 04/05/23 227;344;445
452 Welding 6 w Fri 05/05/23 Thu 15/06/23 451;440
453 Embedding 4 w Fri 16/06/23 Thu 13/07/23 452;441
454 Final Machining 5 w Fri 22/09/23 Thu 26/10/23 453;448
455 Piping & Testing 6 w Fri 27/10/23 Thu 07/12/23 454
456 TFC17 180 d Fri 05/05/23 Thu 11/01/24
457 WP insertion 5 w Fri 05/05/23 Thu 08/06/23 239;349;451
458 Welding 6 w Fri 09/06/23 Thu 20/07/23 457;446
459 Embedding 4 w Fri 21/07/23 Thu 17/08/23 458;447
460 Final Machining 5 w Fri 27/10/23 Thu 30/11/23 459;454
461 Piping & Testing 6 w Fri 01/12/23 Thu 11/01/24 460
462 TFC18 175 d Fri 16/06/23 Thu 15/02/24
463 WP insertion 5 w Fri 16/06/23 Thu 20/07/23 251;354;457
464 Welding 6 w Fri 21/07/23 Thu 31/08/23 463;452
465 Embedding 4 w Fri 01/09/23 Thu 28/09/23 464;453
466 Final Machining 5 w Fri 01/12/23 Thu 04/01/24 465;460
467 Piping & Testing 6 w Fri 05/01/24 Thu 15/02/24 466
468 TFC INNER INTERCOIL STRUCTURES 1 d? Fri 21/12/18 Fri 21/12/18
469 MAG-02 CS COILS 1360 d Thu 10/01/19 Wed 27/03/24 3SS
470 MS-MAG-02-01: Design completion 9 mo Thu 10/01/19 Wed 18/09/19
471 MS-MAG-02-02: Design review 2 mo Thu 19/09/19 Wed 13/11/19 470
472 MS-MAG-02-03: Technical specification 3 mo Thu 14/11/19 Wed 05/02/20 471
473 MS-MAG-02-04: Call for Tender (CS & PFUS) 3 mo Thu 06/02/20 Wed 29/04/20 472
474 CS COILS MANUFACTURING 1020 d Thu 30/04/20 Wed 27/03/24
475 ENGINEERING (TOOLING AND QUALIFICATIONS) 8 mo Thu 30/04/20 Wed 09/12/20 473
476 CS-00 (Superdummy) 120 d Thu 24/06/21 Wed 08/12/21 475;525FS-20 d;58
477 CS-00 WINDING 2 mo Thu 24/06/21 Wed 18/08/21
478 CS-00 HEAT TREATMENT 1 mo Thu 19/08/21 Wed 15/09/21 477
479 CS-00 IMPREGNATION 1 mo Thu 16/09/21 Wed 13/10/21 478
480 CS-00 TESTING 1 mo Thu 14/10/21 Wed 10/11/21 479
481 CS-00 PACKAGING AND SHIPMENT 1 mo Thu 11/11/21 Wed 08/12/21 480
Baseline Milestone
Baseline Summary
Attività
Divisione
Cardine
Riepilogo
Riepilogo progetto
Attività esterne
Cardine esterno
Inactive Milestone
Inactive Summary
Manual Task
Duration-only
Manual Summary Rollup
Manual Summary
Start-only
Finish-only
External Tasks
External Milestone
Avanzamento
Scadenza
Critical
Critical Split
Baseline
Slippage
Slack
Progetto: Magnets_DTT
Data: Thu 04/04/19
Pagina 9

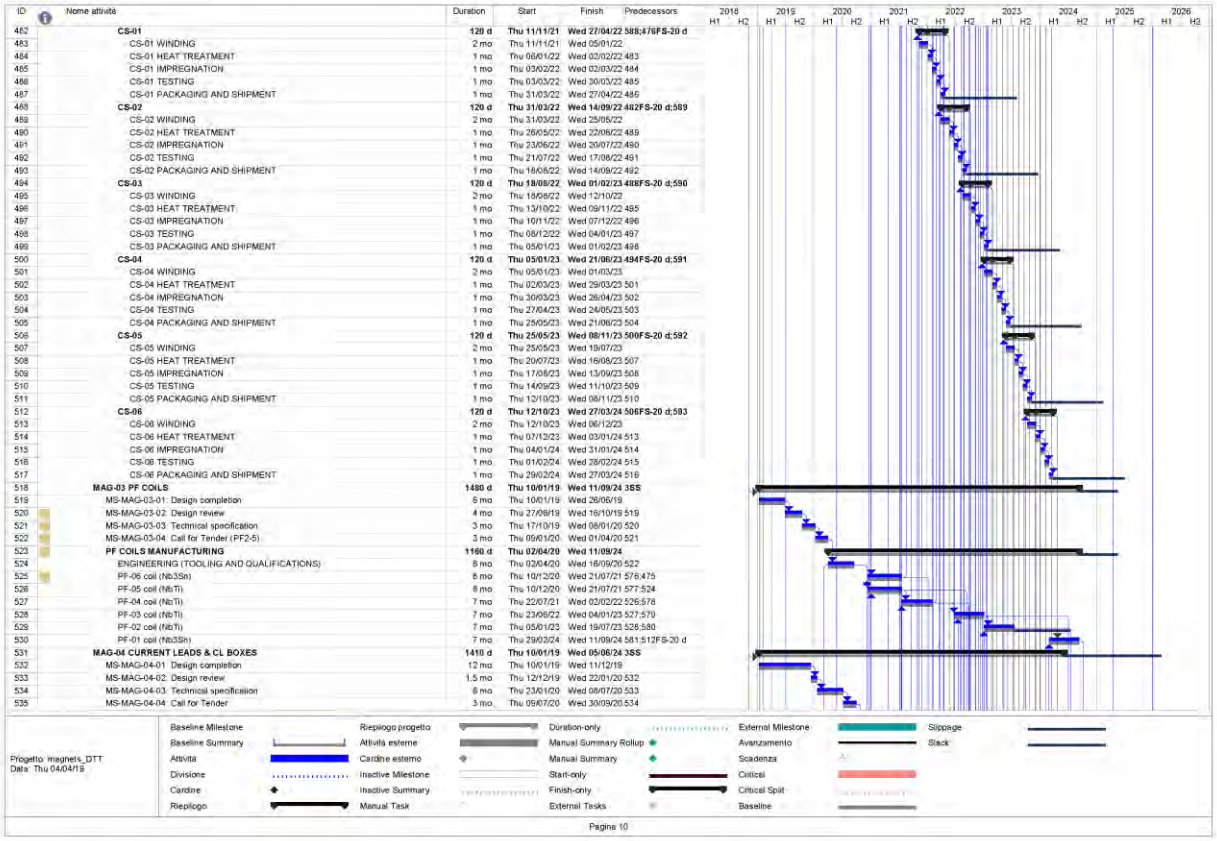
ID
Nome attività
Duration
Start
Finish
Predecessors
2018
2019
2020
2021
2022
2023
2024
2025
2026
482 CS-01 120 d Thu 11/11/21 Wed 27/04/22 588;476FS-20 d
483 CS-01 WINDING 2 mo Thu 11/11/21 Wed 05/01/22
484 CS-01 HEAT TREATMENT 1 mo Thu 06/01/22 Wed 02/02/22 483
485 CS-01 IMPREGNATION 1 mo Thu 03/02/22 Wed 02/03/22 484
486 CS-01 TESTING 1 mo Thu 03/03/22 Wed 30/03/22 485
487 CS-01 PACKAGING AND SHIPMENT 1 mo Thu 31/03/22 Wed 27/04/22 486
488 CS-02 120 d Thu 31/03/22 Wed 14/09/22 482FS-20 d;589
489 CS-02 WINDING 2 mo Thu 31/03/22 Wed 25/05/22
490 CS-02 HEAT TREATMENT 1 mo Thu 26/05/22 Wed 22/06/22 489
491 CS-02 IMPREGNATION 1 mo Thu 23/06/22 Wed 20/07/22 490
492 CS-02 TESTING 1 mo Thu 21/07/22 Wed 17/08/22 491
493 CS-02 PACKAGING AND SHIPMENT 1 mo Thu 18/08/22 Wed 14/09/22 492
494 CS-03 120 d Thu 18/08/22 Wed 01/02/23 488FS-20 d;590
495 CS-03 WINDING 2 mo Thu 18/08/22 Wed 12/10/22
496 CS-03 HEAT TREATMENT 1 mo Thu 13/10/22 Wed 09/11/22 495
497 CS-03 IMPREGNATION 1 mo Thu 10/11/22 Wed 07/12/22 496
498 CS-03 TESTING 1 mo Thu 08/12/22 Wed 04/01/23 497
499 CS-03 PACKAGING AND SHIPMENT 1 mo Thu 05/01/23 Wed 01/02/23 498
500 CS-04 120 d Thu 05/01/23 Wed 21/06/23 494FS-20 d;591
501 CS-04 WINDING 2 mo Thu 05/01/23 Wed 01/03/23
502 CS-04 HEAT TREATMENT 1 mo Thu 02/03/23 Wed 29/03/23 501
503 CS-04 IMPREGNATION 1 mo Thu 30/03/23 Wed 26/04/23 502
504 CS-04 TESTING 1 mo Thu 27/04/23 Wed 24/05/23 503
505 CS-04 PACKAGING AND SHIPMENT 1 mo Thu 25/05/23 Wed 21/06/23 504
506 CS-05 120 d Thu 25/05/23 Wed 08/11/23 500FS-20 d;592
507 CS-05 WINDING 2 mo Thu 25/05/23 Wed 19/07/23
508 CS-05 HEAT TREATMENT 1 mo Thu 20/07/23 Wed 16/08/23 507
509 CS-05 IMPREGNATION 1 mo Thu 17/08/23 Wed 13/09/23 508
510 CS-05 TESTING 1 mo Thu 14/09/23 Wed 11/10/23 509
511 CS-05 PACKAGING AND SHIPMENT 1 mo Thu 12/10/23 Wed 08/11/23 510
512 CS-06 120 d Thu 12/10/23 Wed 27/03/24 506FS-20 d;593
513 CS-06 WINDING 2 mo Thu 12/10/23 Wed 06/12/23
514 CS-06 HEAT TREATMENT 1 mo Thu 07/12/23 Wed 03/01/24 513
515 CS-06 IMPREGNATION 1 mo Thu 04/01/24 Wed 31/01/24 514
516 CS-06 TESTING 1 mo Thu 01/02/24 Wed 28/02/24 515
517 CS-06 PACKAGING AND SHIPMENT 1 mo Thu 29/02/24 Wed 27/03/24 516
518 MAG-03 PF COILS 1480 d Thu 10/01/19 Wed 11/09/24 3SS
519 MS-MAG-03-01: Design completion 6 mo Thu 10/01/19 Wed 26/06/19
520 MS-MAG-03-02: Design review 4 mo Thu 27/06/19 Wed 16/10/19 519
521 MS-MAG-03-03: Technical specification 3 mo Thu 17/10/19 Wed 08/01/20 520
522 MS-MAG-03-04: Call for Tender (PF2-5) 3 mo Thu 09/01/20 Wed 01/04/20 521
523 PF COILS MANUFACTURING 1160 d Thu 02/04/20 Wed 11/09/24
524 ENGINEERING (TOOLING AND QUALIFICATIONS) 6 mo Thu 02/04/20 Wed 16/09/20 522
525 PF-06 coil (Nb3Sn) 6 mo Thu 10/12/20 Wed 21/07/21 576;475
526 PF-05 coil (NbTi) 6 mo Thu 10/12/20 Wed 21/07/21 577;524
527 PF-04 coil (NbTi) 7 mo Thu 22/07/21 Wed 02/02/22 526;578
528 PF-03 coil (NbTi) 7 mo Thu 23/06/22 Wed 04/01/23 527;579
529 PF-02 coil (NbTi) 7 mo Thu 05/01/23 Wed 19/07/23 528;580
530 PF-01 coil (Nb3Sn) 7 mo Thu 29/02/24 Wed 11/09/24 581;512FS-20 d
531 MAG-04 CURRENT LEADS & CL BOXES 1410 d Thu 10/01/19 Wed 05/06/24 3SS
532 MS-MAG-04-01: Design completion 12 mo Thu 10/01/19 Wed 11/12/19
533 MS-MAG-04-02: Design review 1.5 mo Thu 12/12/19 Wed 22/01/20 532
534 MS-MAG-04-03: Technical specification 6 mo Thu 23/01/20 Wed 08/07/20 533
535 MS-MAG-04-04: Call for Tender 3 mo Thu 09/07/20 Wed 30/09/20 534
Baseline Milestone
Baseline Summary
Attività
Divisione
Cardine
Riepilogo
Riepilogo progetto
Attività esterne
Cardine esterno
Inactive Milestone
Inactive Summary
Manual Task
Duration-only
Manual Summary Rollup
Manual Summary
Start-only
Finish-only
External Tasks
External Milestone
Avanzamento
Scadenza
Critical
Critical Split
Baseline
Slippage
Slack
Progetto: Imagnets_DTT
Data: Thu 04/04/19
Pagina 10

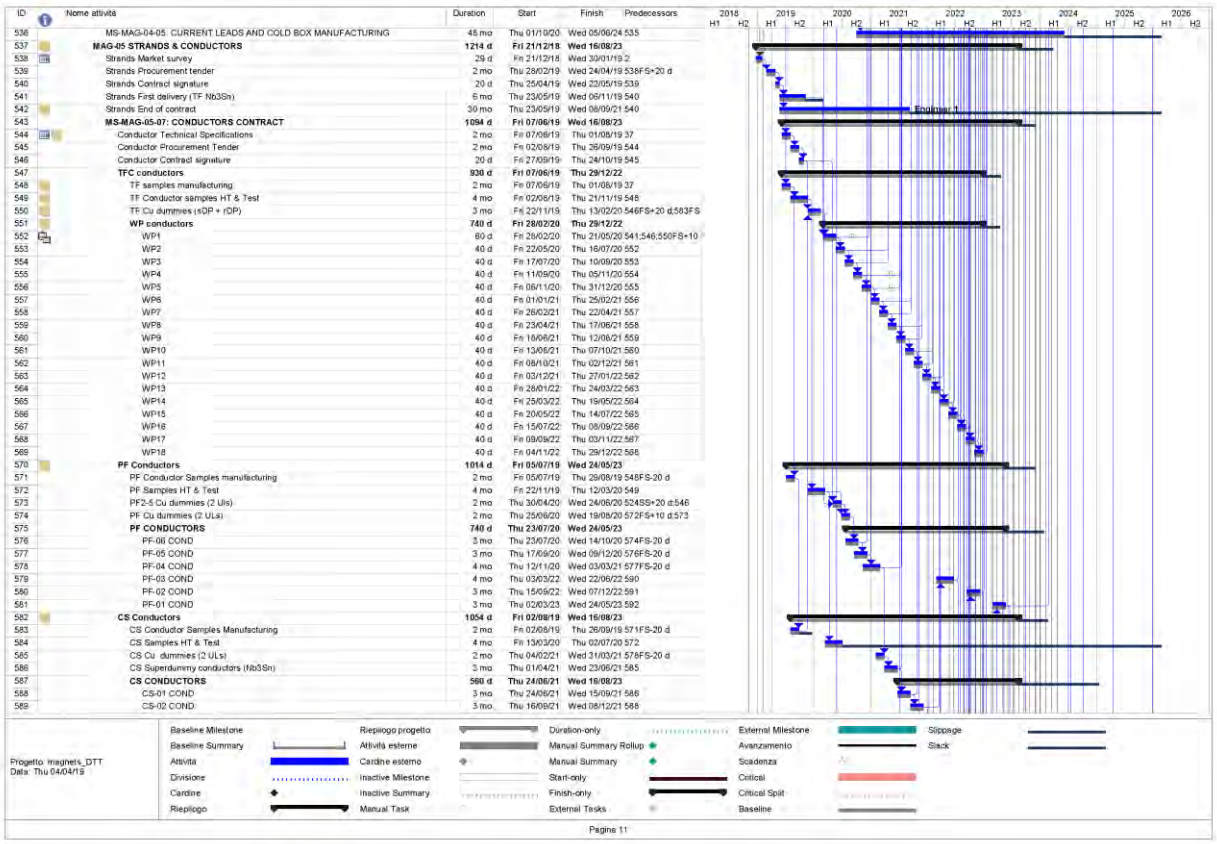
ID
Nome attività
Duration
Start
Finish
Predecessors
2018
2019
2020
2021
2022
2023
2024
2025
2026
536 MS-MAG-04-05: CURRENT LEADS AND COLD BOX MANUFACTURING 48 mo Thu 01/10/20 Wed 05/06/24 535
537 MAG-05 STRANDS & CONDUCTORS 1214 d Fri 21/12/18 Wed 16/08/23
538 Strands Market survey 29 d Fri 21/12/18 Wed 30/01/19 2
539 Strands Procurement tender 2 mo Thu 28/02/19 Wed 24/04/19 538FS+20 d
540 Strands Contract signature 20 d Thu 25/04/19 Wed 22/05/19 539
541 Strands First delivery (TF Nb3Sn) 6 mo Thu 23/05/19 Wed 06/11/19 540
542 Strands End of contract 30 mo Thu 23/05/19 Wed 08/09/21 540
543 MS-MAG-05-07: CONDUCTORS CONTRACT 1094 d Fri 07/06/19 Wed 16/08/23
544 Conductor Technical Specifications 2 mo Fri 07/06/19 Thu 01/08/19 37
545 Conductor Procurement Tender 2 mo Fri 02/08/19 Thu 26/09/19 544
546 Conductor Contract signature 20 d Fri 27/09/19 Thu 24/10/19 545
547 TFC conductors 930 d Fri 07/06/19 Thu 29/12/22
548 TF samples manufacturing 2 mo Fri 07/06/19 Thu 01/08/19 37
549 TF Conductor samples HT & Test 4 mo Fri 02/08/19 Thu 21/11/19 548
550 TF Cu dummies (sDP + rDP) 3 mo Fri 22/11/19 Thu 13/02/20 546FS+20 d;563FS
551 WP conductors 740 d Fri 28/02/20 Thu 29/12/22
552 WP1 60 d Fri 28/02/20 Thu 21/05/20 541;546;550FS+10
553 WP2 40 d Fri 22/05/20 Thu 16/07/20 552
554 WP3 40 d Fri 17/07/20 Thu 10/09/20 553
555 WP4 40 d Fri 11/09/20 Thu 05/11/20 554
556 WP5 40 d Fri 06/11/20 Thu 31/12/20 555
557 WP6 40 d Fri 01/01/21 Thu 25/02/21 556
558 WP7 40 d Fri 26/02/21 Thu 22/04/21 557
559 WP8 40 d Fri 23/04/21 Thu 17/06/21 558
560 WP9 40 d Fri 18/06/21 Thu 12/08/21 559
561 WP10 40 d Fri 13/08/21 Thu 07/10/21 560
562 WP11 40 d Fri 08/10/21 Thu 02/12/21 561
563 WP12 40 d Fri 03/12/21 Thu 27/01/22 562
564 WP13 40 d Fri 28/01/22 Thu 24/03/22 563
565 WP14 40 d Fri 25/03/22 Thu 19/05/22 564
566 WP15 40 d Fri 20/05/22 Thu 14/07/22 565
567 WP16 40 d Fri 15/07/22 Thu 08/09/22 566
568 WP17 40 d Fri 09/09/22 Thu 03/11/22 567
569 WP18 40 d Fri 04/11/22 Thu 29/12/22 568
570 PF Conductors 1014 d Fri 05/07/19 Wed 24/05/23
571 PF Conductor Samples manufacturing 2 mo Fri 05/07/19 Thu 29/08/19 548FS-20 d
572 PF Samples HT & Test 4 mo Fri 22/11/19 Thu 12/03/20 549
573 PF2-5 Cu dummies (2 Uls) 2 mo Thu 30/04/20 Wed 24/06/20 524SS+20 d;546
574 PF Cu dummies (2 ULs) 2 mo Thu 25/06/20 Wed 19/08/20 572FS+10 d;573
575 PF CONDUCTORS 740 d Thu 23/07/20 Wed 24/05/23
576 PF-06 COND 3 mo Thu 23/07/20 Wed 14/10/20 574FS-20 d
577 PF-05 COND 3 mo Thu 17/09/20 Wed 09/12/20 576FS-20 d
578 PF-04 COND 4 mo Thu 12/11/20 Wed 03/03/21 577FS-20 d
579 PF-03 COND 4 mo Thu 03/03/22 Wed 22/06/22 590
580 PF-02 COND 3 mo Thu 15/09/22 Wed 07/12/22 591
581 PF-01 COND 3 mo Thu 02/03/23 Wed 24/05/23 592
582 CS Conductors 1054 d Fri 02/08/19 Wed 16/08/23
583 CS Conductor Samples Manufacturing 2 mo Fri 02/08/19 Thu 26/09/19 571FS-20 d
584 CS Samples HT & Test 4 mo Fri 13/03/20 Thu 02/07/20 572
585 CS Cu dummies (2 ULs) 2 mo Thu 04/02/21 Wed 31/03/21 578FS-20 d
586 CS Superdummy conductors (Nb3Sn) 3 mo Thu 01/04/21 Wed 23/06/21 585
587 CS CONDUCTORS 560 d Thu 24/06/21 Wed 16/08/23
588 CS-01 COND 3 mo Thu 24/06/21 Wed 15/09/21 586
589 CS-02 COND 3 mo Thu 16/09/21 Wed 08/12/21 588
Baseline Milestone
Baseline Summary
Attività
Divisione
Cardine
Riepilogo
Riepilogo progetto
Attività esterne
Cardine esterno
Inactive Milestone
Inactive Summary
Manual Task
Duration-only
Manual Summary Rollup
Manual Summary
Start-only
Finish-only
External Tasks
External Milestone
Avanzamento
Scadenza
Critical
Critical Split
Baseline
Slippage
Slack
Progetto: Imagnets_DTT
Data: Thu 04/04/19
Pagina 11

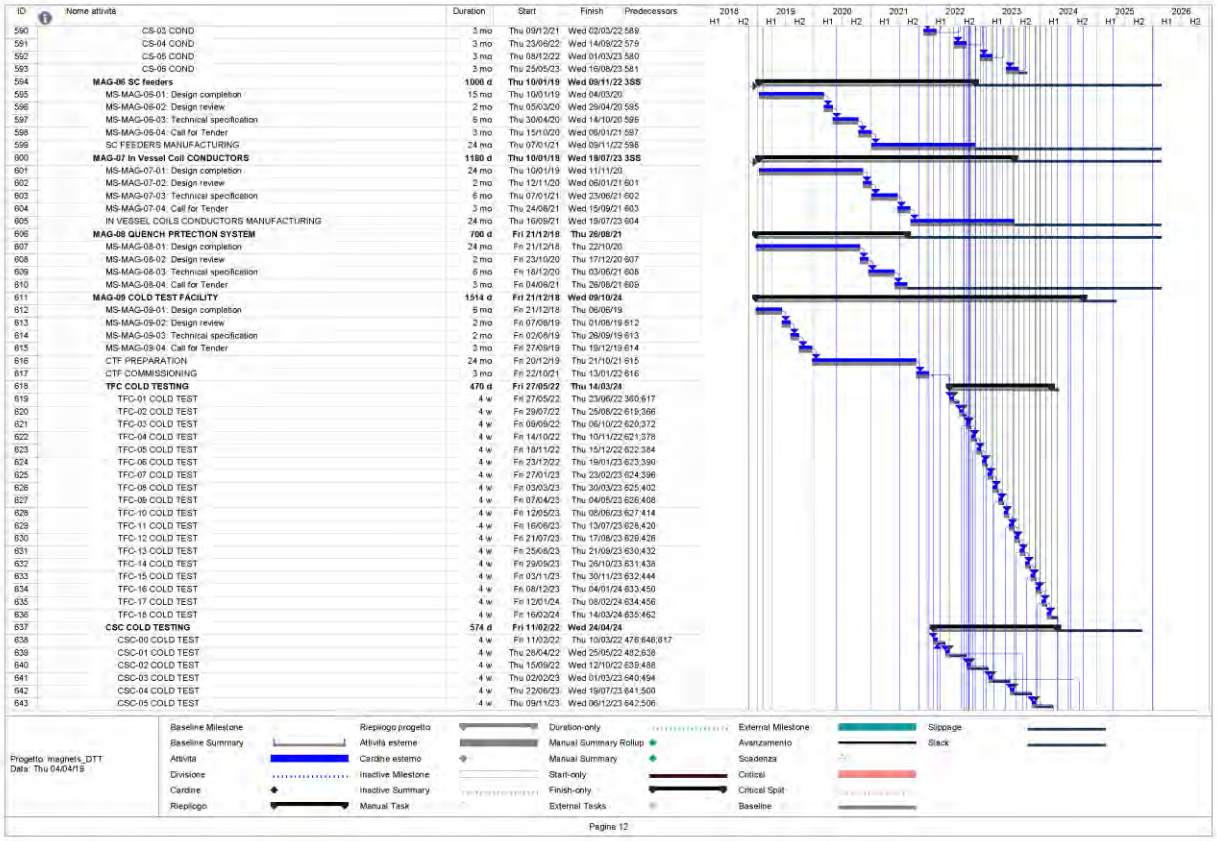
ID
Nome attività
Duration
Start
Finish
Predecessors
2018
2019
2020
2021
2022
2023
2024
2025
2026
H1 H2
560 CS-03 COND 3 mo Thu 09/12/21 Wed 02/03/22 589
561 CS-04 COND 3 mo Thu 23/09/22 Wed 14/09/22 579
562 CS-05 COND 3 mo Thu 08/12/22 Wed 01/03/23 580
563 CS-06 COND 3 mo Thu 25/05/23 Wed 16/08/23 581
564 MAG-06 SC feeders 1000 d Thu 10/01/19 Wed 09/11/22 3SS
565 MS-MAG-06-01: Design completion 15 mo Thu 10/01/19 Wed 04/03/20
566 MS-MAG-06-02: Design review 2 mo Thu 05/03/20 Wed 29/04/20 595
567 MS-MAG-06-03: Technical specification 6 mo Thu 30/04/20 Wed 14/10/20 596
568 MS-MAG-06-04: Call for Tender 3 mo Thu 15/10/20 Wed 06/01/21 597
569 SC FEEDERS MANUFACTURING 24 mo Thu 07/01/21 Wed 09/11/22 598
600 MAG-07 In Vessel Coil CONDUCTORS 1180 d Thu 10/01/19 Wed 19/07/23 3SS
601 MS-MAG-07-01: Design completion 24 mo Thu 10/01/19 Wed 11/11/20
602 MS-MAG-07-02: Design review 2 mo Thu 12/11/20 Wed 06/01/21 601
603 MS-MAG-07-03: Technical specification 6 mo Thu 07/01/21 Wed 23/06/21 602
604 MS-MAG-07-04: Call for Tender 3 mo Thu 24/06/21 Wed 15/09/21 603
605 IN VESSEL COILS CONDUCTORS MANUFACTURING 24 mo Thu 16/09/21 Wed 19/07/23 604
606 MAG-08 QUENCH PRTECTION SYSTEM 700 d Fri 21/12/18 Thu 26/08/21
607 MS-MAG-08-01: Design completion 24 mo Fri 21/12/18 Thu 22/10/20
608 MS-MAG-08-02: Design review 2 mo Fri 23/10/20 Thu 17/12/20 607
609 MS-MAG-08-03: Technical specification 6 mo Fri 18/12/20 Thu 03/06/21 608
610 MS-MAG-08-04: Call for Tender 3 mo Fri 04/06/21 Thu 26/08/21 609
611 MAG-09 COLD TEST FACILITY 1514 d Fri 21/12/18 Wed 09/10/24
612 MS-MAG-09-01: Design completion 6 mo Fri 21/12/18 Thu 06/06/19
613 MS-MAG-09-02: Design review 2 mo Fri 07/06/19 Thu 01/08/19 612
614 MS-MAG-09-03: Technical specification 2 mo Fri 02/08/19 Thu 26/09/19 613
615 MS-MAG-09-04: Call for Tender 3 mo Fri 27/09/19 Thu 19/12/19 614
616 CTF PREPARATION 24 mo Fri 20/12/19 Thu 21/10/21 615
617 CTF COMMISSIONING 3 mo Fri 22/10/21 Thu 13/01/22 616
618 TFC COLD TESTING 470 d Fri 27/05/22 Thu 14/03/24
619 TFC-01 COLD TEST 4 w Fri 27/05/22 Thu 23/06/22 360;617
620 TFC-02 COLD TEST 4 w Fri 29/07/22 Thu 25/08/22 619;366
621 TFC-03 COLD TEST 4 w Fri 09/09/22 Thu 06/10/22 620;372
622 TFC-04 COLD TEST 4 w Fri 14/10/22 Thu 10/11/22 621;378
623 TFC-05 COLD TEST 4 w Fri 18/11/22 Thu 15/12/22 622;384
624 TFC-06 COLD TEST 4 w Fri 23/12/22 Thu 19/01/23 623;390
625 TFC-07 COLD TEST 4 w Fri 27/01/23 Thu 23/02/23 624;396
626 TFC-08 COLD TEST 4 w Fri 03/03/23 Thu 30/03/23 625;402
627 TFC-09 COLD TEST 4 w Fri 07/04/23 Thu 04/05/23 626;408
628 TFC-10 COLD TEST 4 w Fri 12/05/23 Thu 08/06/23 627;414
629 TFC-11 COLD TEST 4 w Fri 16/06/23 Thu 13/07/23 628;420
630 TFC-12 COLD TEST 4 w Fri 21/07/23 Thu 17/08/23 629;426
631 TFC-13 COLD TEST 4 w Fri 25/08/23 Thu 21/09/23 630;432
632 TFC-14 COLD TEST 4 w Fri 29/09/23 Thu 26/10/23 631;438
633 TFC-15 COLD TEST 4 w Fri 03/11/23 Thu 30/11/23 632;444
634 TFC-16 COLD TEST 4 w Fri 08/12/23 Thu 04/01/24 633;450
635 TFC-17 COLD TEST 4 w Fri 12/01/24 Thu 08/02/24 634;456
636 TFC-18 COLD TEST 4 w Fri 16/02/24 Thu 14/03/24 635;462
637 CSC COLD TESTING 574 d Fri 11/02/22 Wed 24/04/24
638 CSC-00 COLD TEST 4 w Fri 11/02/22 Thu 10/03/22 476;646;617
639 CSC-01 COLD TEST 4 w Thu 28/04/22 Wed 25/05/22 482;638
640 CSC-02 COLD TEST 4 w Thu 15/09/22 Wed 12/10/22 639;488
641 CSC-03 COLD TEST 4 w Thu 02/02/23 Wed 01/03/23 640;494
642 CSC-04 COLD TEST 4 w Thu 22/06/23 Wed 19/07/23 641;500
643 CSC-05 COLD TEST 4 w Thu 09/11/23 Wed 06/12/23 642;506
Baseline Milestone
Baseline Summary
Attività
Divisione
Cardine
Riepilogo
Riepilogo progetto
Attività esterne
Cardine esterno
Inactive Milestone
Inactive Summary
Manual Task
Duration-only
Manual Summary Rollup
Manual Summary
Start-only
Finish-only
External Tasks
External Milestone
Avanzamento
Scadenza
Critical
Critical Split
Baseline
Slippage
Slack
Progetto: Magnets_DTT
Data: Thu 04/04/19
Pagina 12

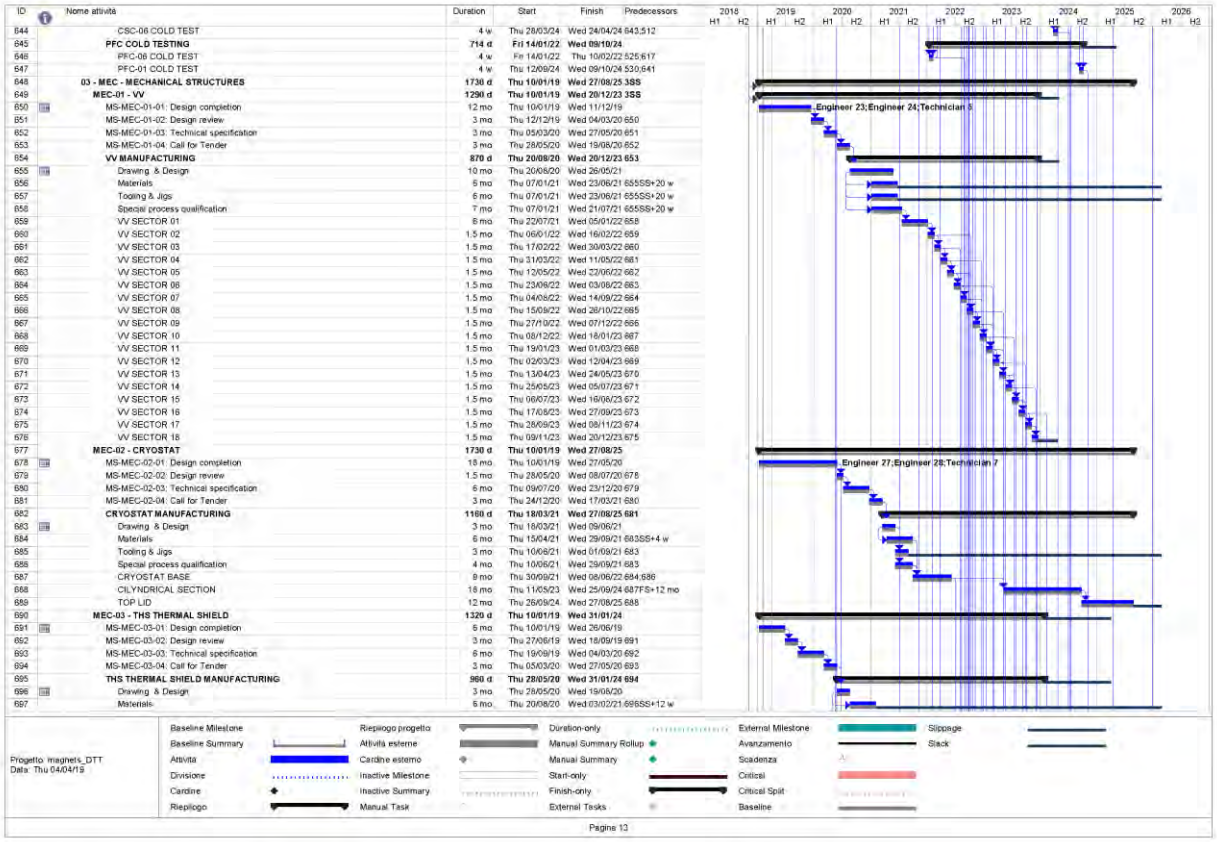
ID
Nome attività
Duration
Start
Finish
Predecessors
2018
2019
2020
2021
2022
2023
2024
2025
2026
H1 H2
644 CSC-06 COLD TEST 4 w Thu 28/03/24 Wed 24/04/24 643;512
645 PFC COLD TESTING 714 d Fri 14/01/22 Wed 09/10/24
646 PFC-06 COLD TEST 4 w Fri 14/01/22 Thu 10/02/22 525;617
647 PFC-01 COLD TEST 4 w Thu 12/09/24 Wed 09/10/24 530;641
648 03 - MEC - MECHANICAL STRUCTURES 1730 d Thu 10/01/19 Wed 27/08/25 3SS
649 MEC-01 - VV 1290 d Thu 10/01/19 Wed 20/12/23 3SS
650 MS-MEC-01-01: Design completion 12 mo Thu 10/01/19 Wed 11/12/19
651 MS-MEC-01-02: Design review 3 mo Thu 12/12/19 Wed 04/03/20 650
652 MS-MEC-01-03: Technical specification 3 mo Thu 05/03/20 Wed 27/05/20 651
653 MS-MEC-01-04: Call for Tender 3 mo Thu 28/05/20 Wed 19/08/20 652
654 VV MANUFACTURING 870 d Thu 20/08/20 Wed 20/12/23 653
655 Drawing & Design 10 mo Thu 20/08/20 Wed 26/05/21
656 Materials 6 mo Thu 07/01/21 Wed 23/06/21 655SS+20 w
657 Tooling & Jigs 6 mo Thu 07/01/21 Wed 23/06/21 655SS+20 w
658 Special process qualification 7 mo Thu 07/01/21 Wed 21/07/21 655SS+20 w
659 VV SECTOR 01 6 mo Thu 22/07/21 Wed 05/01/22 658
660 VV SECTOR 02 1.5 mo Thu 06/01/22 Wed 16/02/22 659
661 VV SECTOR 03 1.5 mo Thu 17/02/22 Wed 30/03/22 660
662 VV SECTOR 04 1.5 mo Thu 31/03/22 Wed 11/05/22 661
663 VV SECTOR 05 1.5 mo Thu 12/05/22 Wed 22/06/22 662
664 VV SECTOR 06 1.5 mo Thu 23/06/22 Wed 03/08/22 663
665 VV SECTOR 07 1.5 mo Thu 04/08/22 Wed 14/09/22 664
666 VV SECTOR 08 1.5 mo Thu 15/09/22 Wed 26/10/22 665
667 VV SECTOR 09 1.5 mo Thu 27/10/22 Wed 07/12/22 666
668 VV SECTOR 10 1.5 mo Thu 08/12/22 Wed 18/01/23 667
669 VV SECTOR 11 1.5 mo Thu 19/01/23 Wed 01/03/23 668
670 VV SECTOR 12 1.5 mo Thu 02/03/23 Wed 12/04/23 669
671 VV SECTOR 13 1.5 mo Thu 13/04/23 Wed 24/05/23 670
672 VV SECTOR 14 1.5 mo Thu 25/05/23 Wed 05/07/23 671
673 VV SECTOR 15 1.5 mo Thu 06/07/23 Wed 16/08/23 672
674 VV SECTOR 16 1.5 mo Thu 17/08/23 Wed 27/09/23 673
675 VV SECTOR 17 1.5 mo Thu 28/09/23 Wed 08/11/23 674
676 VV SECTOR 18 1.5 mo Thu 09/11/23 Wed 20/12/23 675
677 MEC-02 - CRYOSTAT 1730 d Thu 10/01/19 Wed 27/08/25
678 MS-MEC-02-01: Design completion 18 mo Thu 10/01/19 Wed 27/05/20
679 MS-MEC-02-02: Design review 1.5 mo Thu 28/05/20 Wed 08/07/20 678
680 MS-MEC-02-03: Technical specification 6 mo Thu 09/07/20 Wed 23/12/20 679
681 MS-MEC-02-04: Call for Tender 3 mo Thu 24/12/20 Wed 17/03/21 680
682 CRYOSTAT MANUFACTURING 1160 d Thu 18/03/21 Wed 27/08/25 681
683 Drawing & Design 3 mo Thu 18/03/21 Wed 09/06/21
684 Materials 6 mo Thu 15/04/21 Wed 29/09/21 683SS+4 w
685 Tooling & Jigs 3 mo Thu 10/06/21 Wed 01/09/21 683
686 Special process qualification 4 mo Thu 10/06/21 Wed 29/09/21 683
687 CRYOSTAT BASE 9 mo Thu 30/09/21 Wed 08/06/22 684;686
688 CILYNDRICAL SECTION 18 mo Thu 11/05/23 Wed 25/09/24 687FS+12 mo
689 TOP LID 12 mo Thu 26/09/24 Wed 27/08/25 688
690 MEC-03 - THS THERMAL SHIELD 1320 d Thu 10/01/19 Wed 31/01/24
691 MS-MEC-03-01: Design completion 6 mo Thu 10/01/19 Wed 26/06/19
692 MS-MEC-03-02: Design review 3 mo Thu 27/06/19 Wed 18/09/19 691
693 MS-MEC-03-03: Technical specification 6 mo Thu 19/09/19 Wed 04/03/20 692
694 MS-MEC-03-04: Call for Tender 3 mo Thu 05/03/20 Wed 27/05/20 693
695 THS THERMAL SHIELD MANUFACTURING 960 d Thu 28/05/20 Wed 31/01/24 694
696 Drawing & Design 3 mo Thu 28/05/20 Wed 19/08/20
697 Materials 6 mo Thu 20/08/20 Wed 03/02/21 696SS+12 w
Engineer 23;Engineer 24;Technician 3
Engineer 27;Engineer 28;Technician 7
Baseline Milestone
Baseline Summary
Attività
Divisione
Cardine
Riepilogo
Riepilogo progetto
Attività esterne
Cardine esterno
Inactive Milestone
Inactive Summary
Manual Task
Duration-only
Manual Summary Rollup
Manual Summary
Start-only
Finish-only
External Tasks
External Milestone
Avanzamento
Scadenza
Critical
Critical Split
Baseline
Slippage
Slack
Progetto: Magnets_DTT
Data: Thu 04/04/19
Pagina 13

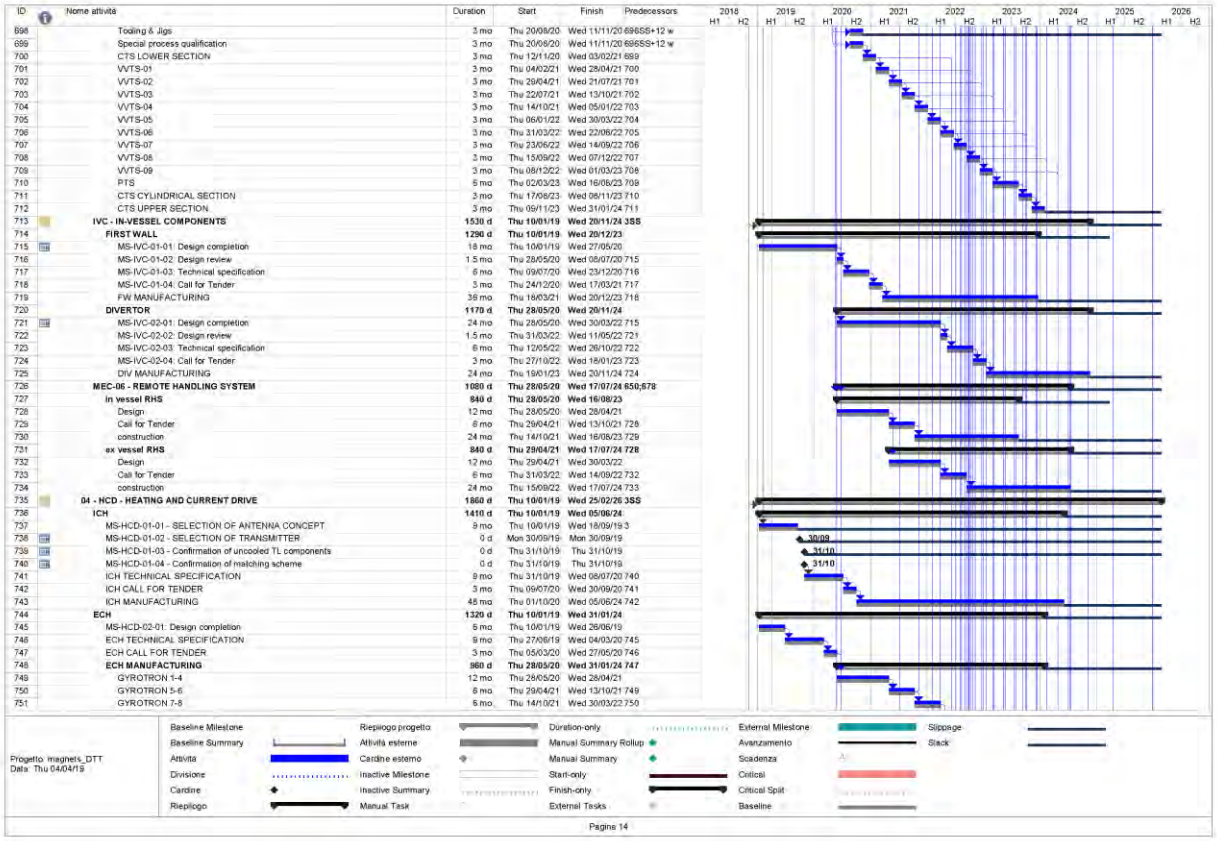
ID
Nome attività
Duration
Start
Finish
Predecessors
2018
2019
2020
2021
2022
2023
2024
2025
2026
H1 H2
696 Tooling & Jigs 3 mo Thu 20/06/20 Wed 11/11/20 695SS+12 w
699 Special process qualification 3 mo Thu 20/06/20 Wed 11/11/20 695SS+12 w
700 CTS LOWER SECTION 3 mo Thu 12/11/20 Wed 03/02/21 699
701 VVTS-01 3 mo Thu 04/02/21 Wed 28/04/21 700
702 VVTS-02 3 mo Thu 29/04/21 Wed 21/07/21 701
703 VVTS-03 3 mo Thu 22/07/21 Wed 13/10/21 702
704 VVTS-04 3 mo Thu 14/10/21 Wed 05/01/22 703
705 VVTS-05 3 mo Thu 06/01/22 Wed 30/03/22 704
706 VVTS-06 3 mo Thu 31/03/22 Wed 22/06/22 705
707 VVTS-07 3 mo Thu 23/06/22 Wed 14/09/22 706
708 VVTS-08 3 mo Thu 15/09/22 Wed 07/12/22 707
709 VVTS-09 3 mo Thu 08/12/22 Wed 01/03/23 708
710 PTS 6 mo Thu 02/03/23 Wed 16/08/23 709
711 CTS CYLINDRICAL SECTION 3 mo Thu 17/08/23 Wed 08/11/23 710
712 CTS UPPER SECTION 3 mo Thu 09/11/23 Wed 31/01/24 711
713 IVC - IN-VESSEL COMPONENTS 1530 d Thu 10/01/19 Wed 20/11/24 3SS
714 FIRST WALL 1290 d Thu 10/01/19 Wed 20/12/23
715 MS-IVC-01-01: Design completion 18 mo Thu 10/01/19 Wed 27/05/20
716 MS-IVC-01-02: Design review 1.5 mo Thu 28/05/20 Wed 05/07/20 715
717 MS-IVC-01-03: Technical specification 6 mo Thu 09/07/20 Wed 23/12/20 716
718 MS-IVC-01-04: Call for Tender 3 mo Thu 24/12/20 Wed 17/03/21 717
719 FW MANUFACTURING 36 mo Thu 18/03/21 Wed 20/12/23 718
720 DIVERTOR 1170 d Thu 28/05/20 Wed 20/11/24
721 MS-IVC-02-01: Design completion 24 mo Thu 28/05/20 Wed 30/03/22 715
722 MS-IVC-02-02: Design review 1.5 mo Thu 31/03/22 Wed 11/05/22 721
723 MS-IVC-02-03: Technical specification 6 mo Thu 12/05/22 Wed 26/10/22 722
724 MS-IVC-02-04: Call for Tender 3 mo Thu 27/10/22 Wed 18/01/23 723
725 DIV MANUFACTURING 24 mo Thu 19/01/23 Wed 20/11/24 724
726 MEC-06 - REMOTE HANDLING SYSTEM 1080 d Thu 28/05/20 Wed 17/07/24 650;678
727 In vessel RHS 840 d Thu 28/05/20 Wed 16/08/23
728 Design 12 mo Thu 28/05/20 Wed 28/04/21
729 Call for Tender 6 mo Thu 29/04/21 Wed 13/10/21 728
730 construction 24 mo Thu 14/10/21 Wed 16/08/23 729
731 ex vessel RHS 840 d Thu 28/04/21 Wed 17/07/24 728
732 Design 12 mo Thu 29/04/21 Wed 30/03/22
733 Call for Tender 6 mo Thu 31/03/22 Wed 14/09/22 732
734 construction 24 mo Thu 15/09/22 Wed 17/07/24 733
735 04 - HCD - HEATING AND CURRENT DRIVE 1860 d Thu 10/01/19 Wed 25/02/26 3SS
736 ICH 1410 d Thu 10/01/19 Wed 05/06/24
737 MS-HCD-01-01 - SELECTION OF ANTENNA CONCEPT 9 mo Thu 10/01/19 Wed 18/09/19 3
738 MS-HCD-01-02 - SELECTION OF TRANSMITTER 0 d Mon 30/09/19 Mon 30/09/19
739 MS-HCD-01-03 - Confirmation of uncooled TL components 0 d Thu 31/10/19 Thu 31/10/19
740 MS-HCD-01-04 - Confirmation of matching scheme 0 d Thu 31/10/19 Thu 31/10/19
741 ICH TECHNICAL SPECIFICATION 9 mo Thu 31/10/19 Wed 08/07/20 740
742 ICH CALL FOR TENDER 3 mo Thu 09/07/20 Wed 30/09/20 741
743 ICH MANUFACTURING 45 mo Thu 01/10/20 Wed 05/06/24 742
744 ECH 1320 d Thu 10/01/19 Wed 31/01/24
745 MS-HCD-02-01: Design completion 6 mo Thu 10/01/19 Wed 26/06/19
746 ECH TECHNICAL SPECIFICATION 9 mo Thu 27/06/19 Wed 04/03/20 745
747 ECH CALL FOR TENDER 3 mo Thu 05/03/20 Wed 27/05/20 746
748 ECH MANUFACTURING 960 d Thu 28/05/20 Wed 31/01/24 747
749 GYROTRON 1-4 12 mo Thu 28/05/20 Wed 28/04/21
750 GYROTRON 5-6 6 mo Thu 29/04/21 Wed 13/10/21 749
751 GYROTRON 7-8 6 mo Thu 14/10/21 Wed 30/03/22 750
Progetto: magnets_DTT
Data: Thu 04/04/19
Baseline Milestone
Baseline Summary
Attività
Divisione
Cardine
Riepilogo
Riepilogo progetto
Attività esterne
Cardine esterno
Inactive Milestone
Inactive Summary
Manual Task
Duration-only
Manual Summary Rollup
Manual Summary
Start-only
Finish-only
External Tasks
External Milestone
Avanzamento
Scadenza
Critical
Critical Split
Baseline
Slippage
Slack
Pagina 14

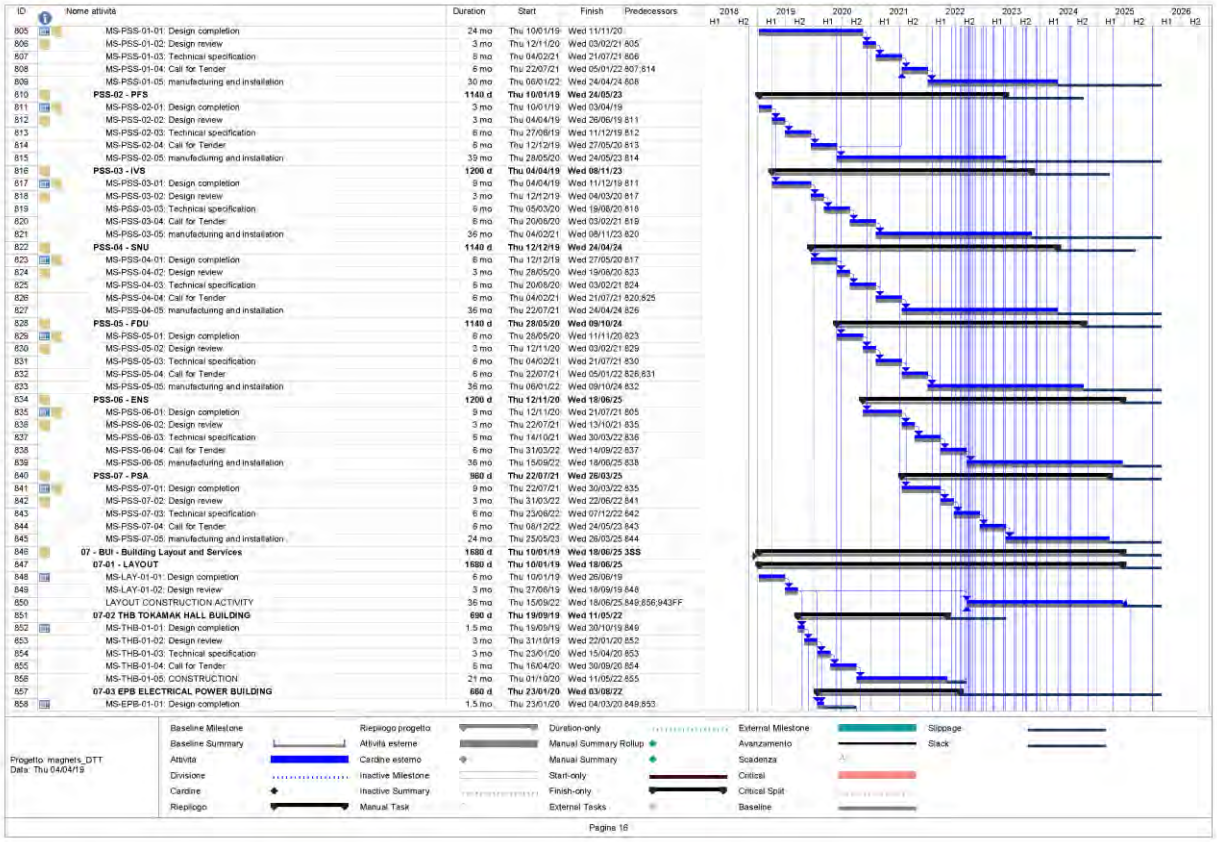
ID
Nome attività
Duration
Start
Finish
Predecessors
2018
2019
2020
2021
2022
2023
2024
2025
2026
H1 H2
805 MS-PSS-01-01: Design completion 24 mo Thu 10/01/19 Wed 11/11/20
806 MS-PSS-01-02: Design review 3 mo Thu 12/11/20 Wed 03/02/21 805
807 MS-PSS-01-03: Technical specification 6 mo Thu 04/02/21 Wed 21/07/21 806
808 MS-PSS-01-04: Call for Tender 6 mo Thu 22/07/21 Wed 05/01/22 807;814
809 MS-PSS-01-05: manufacturing and installation 30 mo Thu 06/01/22 Wed 24/04/24 808
810 PSS-02 - PFS 1140 d Thu 10/01/19 Wed 24/05/23
811 MS-PSS-02-01: Design completion 3 mo Thu 10/01/19 Wed 03/04/19
812 MS-PSS-02-02: Design review 3 mo Thu 04/04/19 Wed 26/06/19 811
813 MS-PSS-02-03: Technical specification 6 mo Thu 27/06/19 Wed 11/12/19 812
814 MS-PSS-02-04: Call for Tender 6 mo Thu 12/12/19 Wed 27/05/20 813
815 MS-PSS-02-05: manufacturing and installation 39 mo Thu 28/05/20 Wed 24/05/23 814
816 PSS-03 - IVS 1200 d Thu 04/04/19 Wed 08/11/23
817 MS-PSS-03-01: Design completion 9 mo Thu 04/04/19 Wed 11/12/19 811
818 MS-PSS-03-02: Design review 3 mo Thu 12/12/19 Wed 04/03/20 817
819 MS-PSS-03-03: Technical specification 6 mo Thu 05/03/20 Wed 19/08/20 818
820 MS-PSS-03-04: Call for Tender 6 mo Thu 20/08/20 Wed 03/02/21 819
821 MS-PSS-03-05: manufacturing and installation 36 mo Thu 04/02/21 Wed 08/11/23 820
822 PSS-04 - SNU 1140 d Thu 12/12/19 Wed 24/04/24
823 MS-PSS-04-01: Design completion 6 mo Thu 12/12/19 Wed 27/05/20 817
824 MS-PSS-04-02: Design review 3 mo Thu 28/05/20 Wed 19/08/20 823
825 MS-PSS-04-03: Technical specification 6 mo Thu 20/08/20 Wed 03/02/21 824
826 MS-PSS-04-04: Call for Tender 6 mo Thu 04/02/21 Wed 21/07/21 820;825
827 MS-PSS-04-05: manufacturing and installation 36 mo Thu 22/07/21 Wed 24/04/24 826
828 PSS-05 - FDU 1140 d Thu 28/05/20 Wed 09/10/24
829 MS-PSS-05-01: Design completion 6 mo Thu 28/05/20 Wed 11/11/20 823
830 MS-PSS-05-02: Design review 3 mo Thu 12/11/20 Wed 03/02/21 829
831 MS-PSS-05-03: Technical specification 6 mo Thu 04/02/21 Wed 21/07/21 830
832 MS-PSS-05-04: Call for Tender 6 mo Thu 22/07/21 Wed 05/01/22 826,831
833 MS-PSS-05-05: manufacturing and installation 36 mo Thu 06/01/22 Wed 09/10/24 832
834 PSS-06 - ENS 1200 d Thu 12/11/20 Wed 18/06/25
835 MS-PSS-06-01: Design completion 9 mo Thu 12/11/20 Wed 21/07/21 805
836 MS-PSS-06-02: Design review 3 mo Thu 22/07/21 Wed 13/10/21 835
837 MS-PSS-06-03: Technical specification 6 mo Thu 14/10/21 Wed 30/03/22 836
838 MS-PSS-06-04: Call for Tender 6 mo Thu 31/03/22 Wed 14/09/22 837
839 MS-PSS-06-05: manufacturing and installation 36 mo Thu 15/09/22 Wed 18/06/25 838
840 PSS-07 - PSA 960 d Thu 22/07/21 Wed 26/03/25
841 MS-PSS-07-01: Design completion 9 mo Thu 22/07/21 Wed 30/03/22 835
842 MS-PSS-07-02: Design review 3 mo Thu 31/03/22 Wed 22/06/22 841
843 MS-PSS-07-03: Technical specification 6 mo Thu 23/06/22 Wed 07/12/22 842
844 MS-PSS-07-04: Call for Tender 6 mo Thu 08/12/22 Wed 24/05/23 843
845 MS-PSS-07-05: manufacturing and installation 24 mo Thu 25/05/23 Wed 26/03/25 844
846 07 - BUI - Building Layout and Services 1680 d Thu 10/01/19 Wed 18/06/25 3SS
847 07-01 - LAYOUT 1680 d Thu 10/01/19 Wed 18/06/25
848 MS-LAY-01-01: Design completion 6 mo Thu 10/01/19 Wed 26/06/19
849 MS-LAY-01-02: Design review 3 mo Thu 27/06/19 Wed 18/09/19 848
850 LAYOUT CONSTRUCTION ACTIVITY 36 mo Thu 15/09/22 Wed 18/06/25 849;856;943FF
851 07-02 THB TOKAMAK HALL BUILDING 690 d Thu 19/09/19 Wed 11/05/22
852 MS-THB-01-01: Design completion 1.5 mo Thu 19/09/19 Wed 30/10/19 849
853 MS-THB-01-02: Design review 3 mo Thu 31/10/19 Wed 22/01/20 852
854 MS-THB-01-03: Technical specification 3 mo Thu 23/01/20 Wed 15/04/20 853
855 MS-THB-01-04: Call for Tender 6 mo Thu 16/04/20 Wed 30/09/20 854
856 MS-THB-01-05: CONSTRUCTION 21 mo Thu 01/10/20 Wed 11/05/22 855
857 07-03 EPB ELECTRICAL POWER BUILDING 660 d Thu 23/01/20 Wed 03/08/22
858 MS-EPB-01-01: Design completion 1.5 mo Thu 23/01/20 Wed 04/03/20 849;853
Progetto: magnets_DTT
Data: Thu 04/04/19
Baseline Milestone
Baseline Summary
Attività
Divisione
Cardine
Riepilogo
Riepilogo progetto
Attività esterne
Cardine esterno
Inactive Milestone
Inactive Summary
Manual Task
Duration-only
Manual Summary Rollup
Manual Summary
Start-only
Finish-only
External Tasks
External Milestone
Avanzamento
Scadenza
Critical
Critical Split
Baseline
Slippage
Slack
Pagina 16

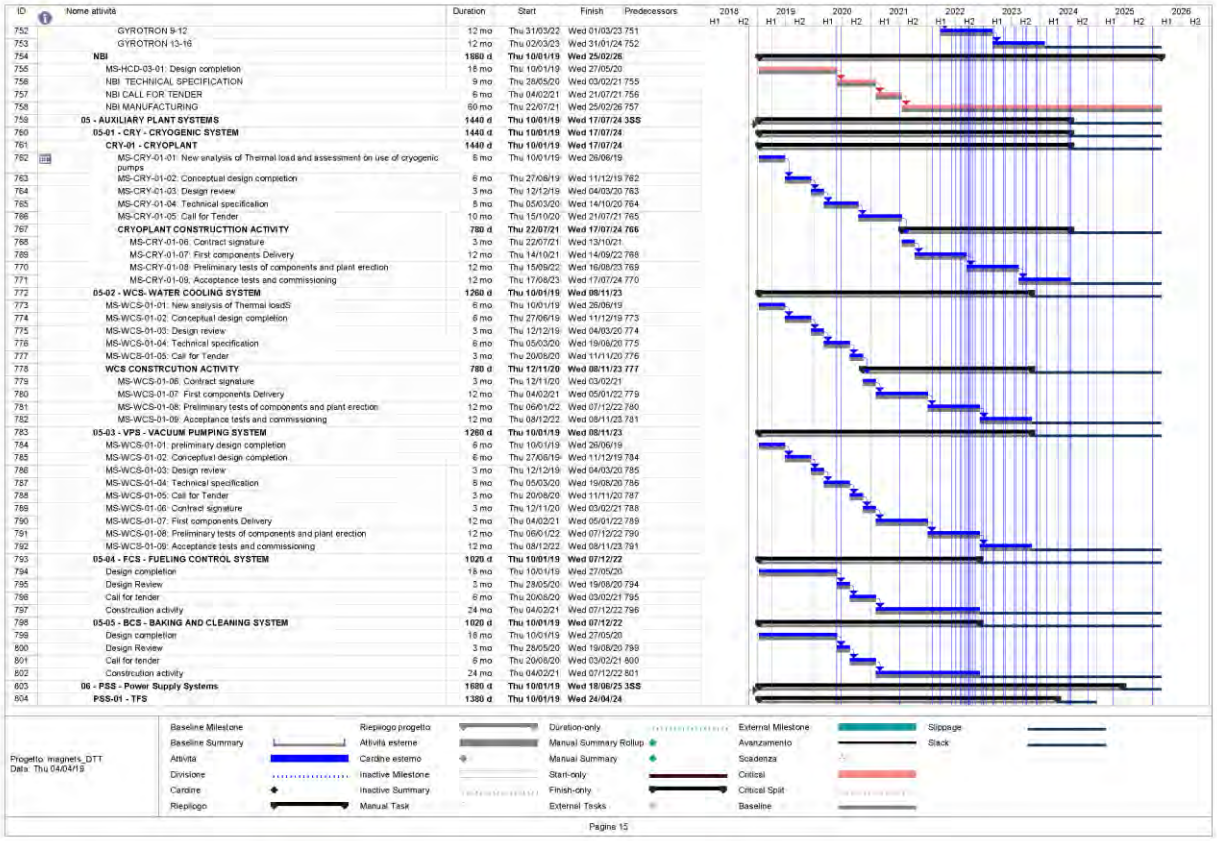
ID
Nome attività
Duration
Start
Finish
Predecessors
2018
2019
2020
2021
2022
2023
2024
2025
2026
752 GYROTRON 9-12 12 mo Thu 31/03/22 Wed 01/03/23 751
753 GYROTRON 13-16 12 mo Thu 02/03/23 Wed 31/01/24 752
754 NBI 1880 d Thu 10/01/19 Wed 25/02/26
755 MS-HCD-03-01: Design completion 18 mo Thu 10/01/19 Wed 27/05/20
756 NBI TECHNICAL SPECIFICATION 9 mo Thu 28/05/20 Wed 03/02/21 755
757 NBI CALL FOR TENDER 6 mo Thu 04/02/21 Wed 21/07/21 756
758 NBI MANUFACTURING 60 mo Thu 22/07/21 Wed 25/02/26 757
759 05 - AUXILIARY PLANT SYSTEMS 1440 d Thu 10/01/19 Wed 17/07/24 3SS
760 05-01 - CRY - CRYOGENIC SYSTEM 1440 d Thu 10/01/19 Wed 17/07/24
761 CRY-01 - CRYOPLANT 1440 d Thu 10/01/19 Wed 17/07/24
762 MS-CRY-01-01: New analysis of Thermal load and assessment on use of cryogenic pumps 6 mo Thu 10/01/19 Wed 26/06/19
763 MS-CRY-01-02: Conceptual design completion 6 mo Thu 27/06/19 Wed 11/12/19 762
764 MS-CRY-01-03: Design review 3 mo Thu 12/12/19 Wed 04/03/20 763
765 MS-CRY-01-04: Technical specification 6 mo Thu 05/03/20 Wed 14/10/20 764
766 MS-CRY-01-05: Call for Tender 10 mo Thu 15/10/20 Wed 21/07/21 765
767 CRYOPLANT CONSTRUCTTION ACTIVITY 780 d Thu 22/07/21 Wed 17/07/24 766
768 MS-CRY-01-06: Contract signature 3 mo Thu 22/07/21 Wed 13/10/21
769 MS-CRY-01-07: First components Delivery 12 mo Thu 14/10/21 Wed 14/09/22 768
770 MS-CRY-01-08: Preliminary tests of components and plant erection 12 mo Thu 15/09/22 Wed 16/08/23 769
771 MS-CRY-01-09: Acceptance tests and commissioning 12 mo Thu 17/08/23 Wed 17/07/24 770
772 05-02 - WCS- WATER COOLING SYSTEM 1260 d Thu 10/01/19 Wed 08/11/23
773 MS-WCS-01-01: New analysis of Thermal loadS 6 mo Thu 10/01/19 Wed 26/06/19
774 MS-WCS-01-02: Conceptual design completion 6 mo Thu 27/06/19 Wed 11/12/19 773
775 MS-WCS-01-03: Design review 3 mo Thu 12/12/19 Wed 04/03/20 774
776 MS-WCS-01-04: Technical specification 8 mo Thu 05/03/20 Wed 19/08/20 775
777 MS-WCS-01-05: Call for Tender 3 mo Thu 20/08/20 Wed 11/11/20 776
778 WCS CONSTRCUTION ACTIVITY 780 d Thu 12/11/20 Wed 08/11/23 777
779 MS-WCS-01-06: Contract signature 3 mo Thu 12/11/20 Wed 03/02/21
780 MS-WCS-01-07: First components Delivery 12 mo Thu 04/02/21 Wed 05/01/22 778
781 MS-WCS-01-08: Preliminary tests of components and plant erection 12 mo Thu 06/01/22 Wed 07/12/22 780
782 MS-WCS-01-09: Acceptance tests and commissioning 12 mo Thu 08/12/22 Wed 08/11/23 781
783 05-03 - VPS - VACUUM PUMPING SYSTEM 1260 d Thu 10/01/19 Wed 08/11/23
784 MS-WCS-01-01: preliminary design completion 6 mo Thu 10/01/19 Wed 26/06/19
785 MS-WCS-01-02: Conceptual design completion 6 mo Thu 27/06/19 Wed 11/12/19 784
786 MS-WCS-01-03: Design review 3 mo Thu 12/12/19 Wed 04/03/20 785
787 MS-WCS-01-04: Technical specification 8 mo Thu 05/03/20 Wed 19/08/20 786
788 MS-WCS-01-05: Call for Tender 3 mo Thu 20/08/20 Wed 11/11/20 787
789 MS-WCS-01-06: Contract signature 3 mo Thu 12/11/20 Wed 03/02/21 788
790 MS-WCS-01-07: First components Delivery 12 mo Thu 04/02/21 Wed 05/01/22 789
791 MS-WCS-01-08: Preliminary tests of components and plant erection 12 mo Thu 06/01/22 Wed 07/12/22 790
792 MS-WCS-01-09: Acceptance tests and commissioning 12 mo Thu 08/12/22 Wed 08/11/23 791
793 05-04 - FCS - FUELING CONTROL SYSTEM 1020 d Thu 10/01/19 Wed 07/12/22
794 Design completion 18 mo Thu 10/01/19 Wed 27/05/20
795 Design Review 3 mo Thu 28/05/20 Wed 19/08/20 794
796 Call for tender 6 mo Thu 20/08/20 Wed 03/02/21 795
797 Construction activity 24 mo Thu 04/02/21 Wed 07/12/22 796
798 05-05 - BCS - BAKING AND CLEANING SYSTEM 1020 d Thu 10/01/19 Wed 07/12/22
799 Design completion 18 mo Thu 10/01/19 Wed 27/05/20
800 Design Review 3 mo Thu 28/05/20 Wed 19/08/20 799
801 Call for tender 6 mo Thu 20/08/20 Wed 03/02/21 800
802 Construction activity 24 mo Thu 04/02/21 Wed 07/12/22 801
803 06 - PSS - Power Supply Systems 1680 d Thu 10/01/19 Wed 18/08/25 3SS
804 PSS-01 - TFS 1380 d Thu 10/01/19 Wed 24/04/24
Baseline Milestone
Baseline Summary
Attività
Divisione
Cardine
Riepilogo
Riepilogo progetto
Attività esterne
Cardine esterno
Inactive Milestone
Inactive Summary
Manual Task
Duration-only
Manual Summary Rollup
Manual Summary
Start-only
Finish-only
External Tasks
External Milestone
Avanzamento
Scadenza
Critical
Critical Split
Baseline
Slippage
Slack
Progetto: Magnets_DTT
Data: Thu 04/04/19
Pagina 15

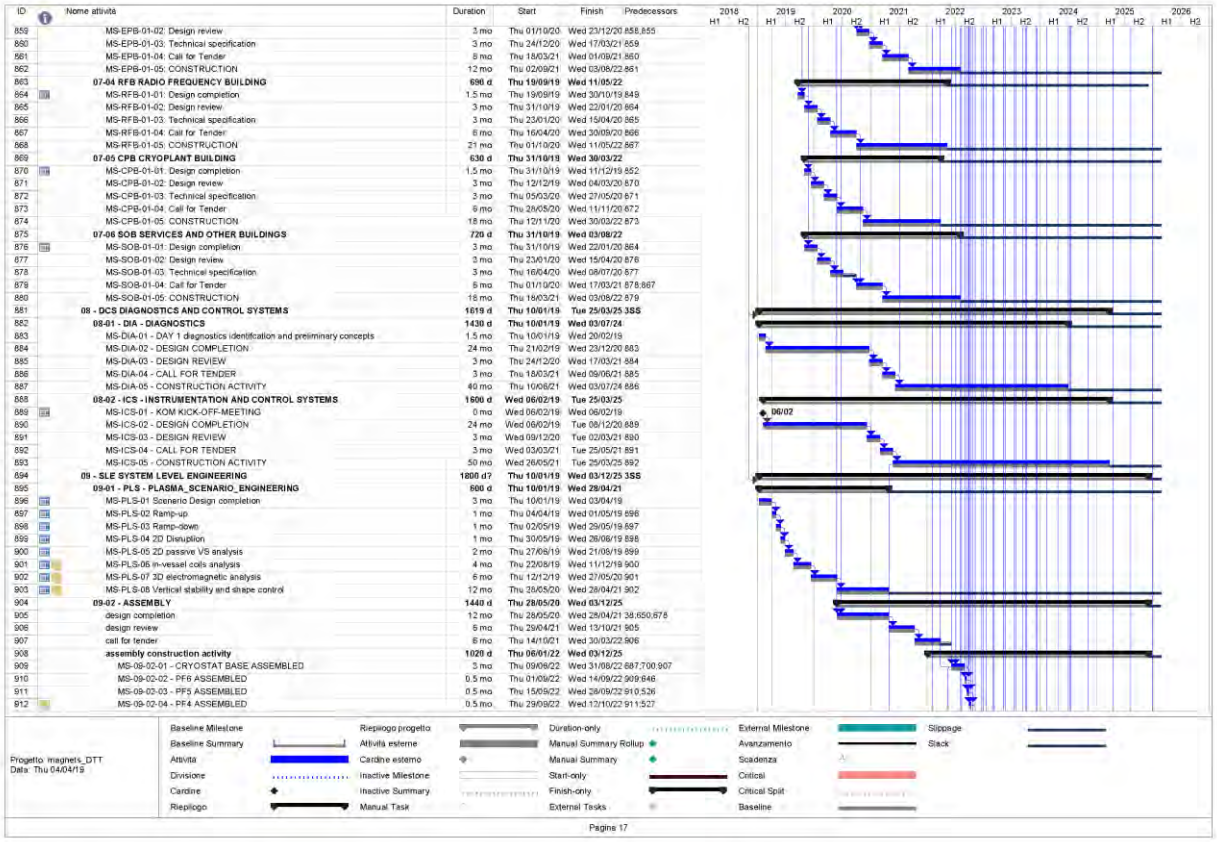
ID
Nome attività
Duration
Start
Finish
Predecessors
2018
2019
2020
2021
2022
2023
2024
2025
2026
859 MS-EPB-01-02: Design review 3 mo Thu 01/10/20 Wed 23/12/20 858,855
860 MS-EPB-01-03: Technical specification 3 mo Thu 24/12/20 Wed 17/03/21 859
861 MS-EPB-01-04: Call for Tender 8 mo Thu 18/03/21 Wed 01/09/21 860
862 MS-EPB-01-05: CONSTRUCTION 12 mo Thu 02/09/21 Wed 03/08/22 861
863 07-04 RFB RADIO FREQUENCY BUILDING 690 d Thu 19/09/19 Wed 11/05/22
864 MS-RFB-01-01: Design completion 1.5 mo Thu 19/09/19 Wed 30/10/19 849
865 MS-RFB-01-02: Design review 3 mo Thu 31/10/19 Wed 22/01/20 864
866 MS-RFB-01-03: Technical specification 3 mo Thu 23/01/20 Wed 15/04/20 865
867 MS-RFB-01-04: Call for Tender 6 mo Thu 16/04/20 Wed 30/09/20 866
868 MS-RFB-01-05: CONSTRUCTION 21 mo Thu 01/10/20 Wed 11/05/22 867
869 07-05 CPB CRYOPLANT BUILDING 630 d Thu 31/10/19 Wed 30/03/22
870 MS-CPB-01-01: Design completion 1.5 mo Thu 31/10/19 Wed 11/12/19 852
871 MS-CPB-01-02: Design review 3 mo Thu 12/12/19 Wed 04/03/20 870
872 MS-CPB-01-03: Technical specification 3 mo Thu 05/03/20 Wed 27/05/20 871
873 MS-CPB-01-04: Call for Tender 6 mo Thu 28/05/20 Wed 11/11/20 872
874 MS-CPB-01-05: CONSTRUCTION 18 mo Thu 12/11/20 Wed 30/03/22 873
875 07-06 SOB SERVICES AND OTHER BUILDINGS 720 d Thu 31/10/19 Wed 03/08/22
876 MS-SOB-01-01: Design completion 3 mo Thu 31/10/19 Wed 22/01/20 864
877 MS-SOB-01-02: Design review 3 mo Thu 23/01/20 Wed 15/04/20 876
878 MS-SOB-01-03: Technical specification 3 mo Thu 16/04/20 Wed 08/07/20 877
879 MS-SOB-01-04: Call for Tender 6 mo Thu 01/10/20 Wed 17/03/21 878,867
880 MS-SOB-01-05: CONSTRUCTION 18 mo Thu 18/03/21 Wed 03/08/22 879
881 08 - DCS DIAGNOSTICS AND CONTROL SYSTEMS 1619 d Thu 10/01/19 Tue 25/03/25 3SS
882 08-01 - DIA - DIAGNOSTICS 1430 d Thu 10/01/19 Wed 03/07/24
883 MS-DIA-01 - DAY 1 diagnostics identification and preliminary concepts 1.5 mo Thu 10/01/19 Wed 20/02/19
884 MS-DIA-02 - DESIGN COMPLETION 24 mo Thu 21/02/19 Wed 23/12/20 883
885 MS-DIA-03 - DESIGN REVIEW 3 mo Thu 24/12/20 Wed 17/03/21 884
886 MS-DIA-04 - CALL FOR TENDER 3 mo Thu 18/03/21 Wed 09/06/21 885
887 MS-DIA-05 - CONSTRUCTION ACTIVITY 40 mo Thu 10/06/21 Wed 03/07/24 886
888 08-02 - ICS - INSTRUMENTATION AND CONTROL SYSTEMS 1500 d Wed 06/02/19 Tue 25/03/25
889 MS-ICS-01 - KOM KICK-OFF-MEETING 0 mo Wed 06/02/19 Wed 06/02/19
890 MS-ICS-02 - DESIGN COMPLETION 24 mo Wed 06/02/19 Tue 08/12/20 889
891 MS-ICS-03 - DESIGN REVIEW 3 mo Wed 09/12/20 Tue 02/03/21 890
892 MS-ICS-04 - CALL FOR TENDER 3 mo Wed 03/03/21 Tue 25/05/21 891
893 MS-ICS-05 - CONSTRUCTION ACTIVITY 50 mo Wed 26/05/21 Tue 25/03/25 892
894 09 - SLE SYSTEM LEVEL ENGINEERING 1800 d? Thu 10/01/19 Wed 03/12/25 3SS
895 09-01 - PLS - PLASMA_SCENARIO_ENGINEERING 600 d Thu 10/01/19 Wed 28/04/21
896 MS-PLS-01 Scenario Design completion 3 mo Thu 10/01/19 Wed 03/04/19
897 MS-PLS-02 Ramp-up 1 mo Thu 04/04/19 Wed 01/05/19 896
898 MS-PLS-03 Ramp-down 1 mo Thu 02/05/19 Wed 29/05/19 897
899 MS-PLS-04 2D Disruption 1 mo Thu 30/05/19 Wed 26/06/19 898
900 MS-PLS-05 2D passive VS analysis 2 mo Thu 27/06/19 Wed 21/08/19 899
901 MS-PLS-06 In-vessel coils analysis 4 mo Thu 22/08/19 Wed 11/12/19 900
902 MS-PLS-07 3D electromagnetic analysis 6 mo Thu 12/12/19 Wed 27/05/20 901
903 MS-PLS-08 Vertical stability and shape control 12 mo Thu 28/05/20 Wed 28/04/21 902
904 09-02 - ASSEMBLY 1440 d Thu 28/05/20 Wed 03/12/25
905 design completion 12 mo Thu 28/05/20 Wed 28/04/21 38,650,678
906 design review 6 mo Thu 29/04/21 Wed 13/10/21 905
907 call for tender 8 mo Thu 14/10/21 Wed 30/03/22 906
908 assembly construction activity 1020 d Thu 06/01/22 Wed 03/12/25
909 MS-09-02-01 - CRYOSTAT BASE ASSEMBLED 3 mo Thu 09/06/22 Wed 31/08/22 887,700,907
910 MS-09-02-02 - PF6 ASSEMBLED 0.5 mo Thu 01/09/22 Wed 14/09/22 909,646
911 MS-09-02-03 - PF5 ASSEMBLED 0.5 mo Thu 15/09/22 Wed 28/09/22 910,526
912 MS-09-02-04 - PF4 ASSEMBLED 0.5 mo Thu 29/09/22 Wed 12/10/22 911,527
Baseline Milestone
Baseline Summary
Attività
Divisione
Cardine
Riepilogo
Riepilogo progetto
Attività esterne
Cardine esterno
Inactive Milestone
Inactive Summary
Manual Task
Duration-only
Manual Summary Rollup
Manual Summary
Start-only
Finish-only
External Tasks
External Milestone
Avanzamento
Scadenza
Critical
Critical Split
Baseline
Slippage
Slack
Progetto: Magnets_DTT
Data: Thu 04/04/19
Pagina 17

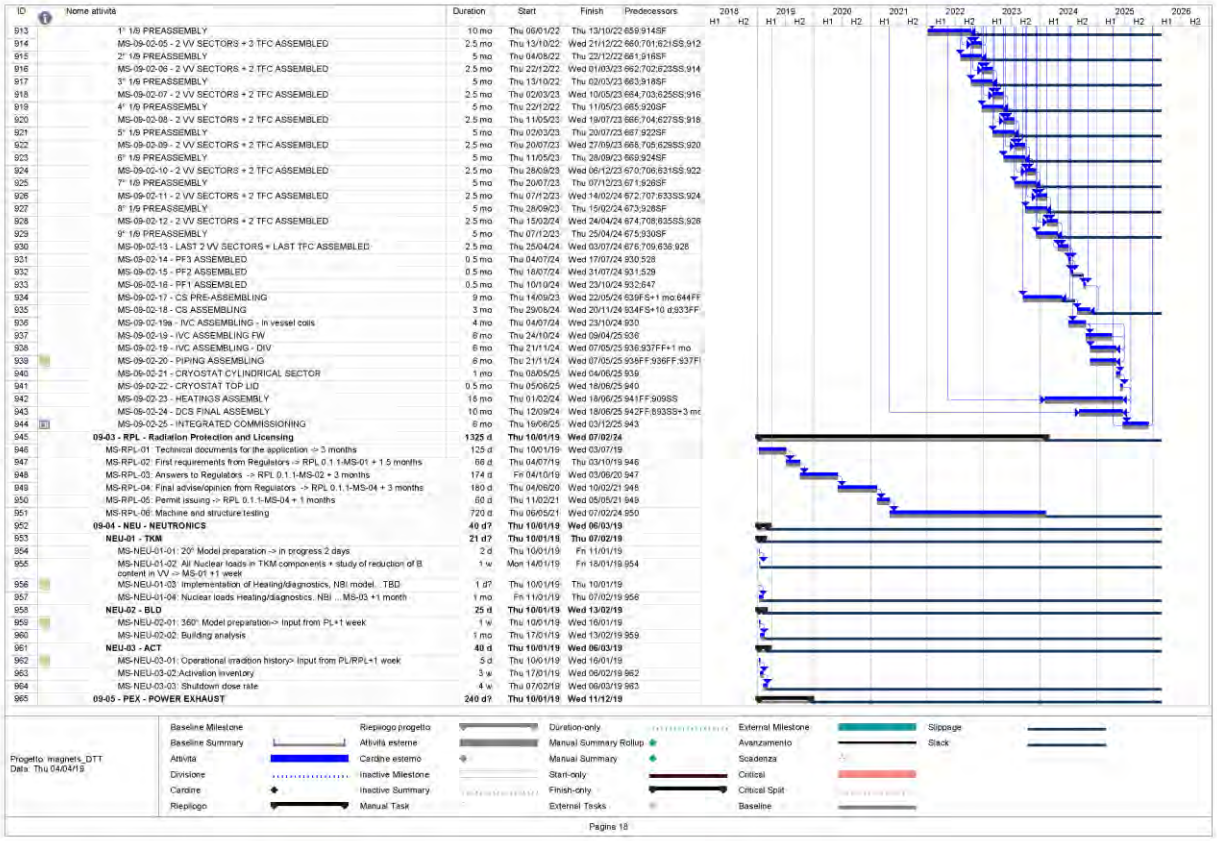
ID
Nome attività
Duration
Start
Finish
Predecessors
2018
2019
2020
2021
2022
2023
2024
2025
2026
913 1° 1/6 PREASSEMBLY 10 mo Thu 06/01/22 Thu 13/10/22 659;914SF
914 MS-09-02-05 - 2 VV SECTORS + 2 TFC ASSEMBLED 2.5 mo Thu 13/10/22 Wed 21/12/22 660;701;621SS;912
915 2° 1/6 PREASSEMBLY 5 mo Thu 04/08/22 Thu 22/12/22 661;916SF
916 MS-09-02-06 - 2 VV SECTORS + 2 TFC ASSEMBLED 2.5 mo Thu 22/12/22 Wed 01/03/23 662;702;623SS;914
917 3° 1/6 PREASSEMBLY 5 mo Thu 13/10/22 Thu 02/03/23 663;918SF
918 MS-09-02-07 - 2 VV SECTORS + 2 TFC ASSEMBLED 2.5 mo Thu 02/03/23 Wed 10/05/23 664;703;625SS;916
919 4° 1/6 PREASSEMBLY 5 mo Thu 22/12/22 Thu 11/05/23 665;920SF
920 MS-09-02-08 - 2 VV SECTORS + 2 TFC ASSEMBLED 2.5 mo Thu 11/05/23 Wed 19/07/23 666;704;627SS;918
921 5° 1/6 PREASSEMBLY 5 mo Thu 02/03/23 Thu 20/07/23 667;922SF
922 MS-09-02-09 - 2 VV SECTORS + 2 TFC ASSEMBLED 2.5 mo Thu 20/07/23 Wed 27/09/23 668;705;629SS;920
923 6° 1/6 PREASSEMBLY 5 mo Thu 11/05/23 Thu 28/09/23 669;924SF
924 MS-09-02-10 - 2 VV SECTORS + 2 TFC ASSEMBLED 2.5 mo Thu 28/09/23 Wed 06/12/23 670;706;631SS;922
925 7° 1/6 PREASSEMBLY 5 mo Thu 20/07/23 Thu 07/12/23 671;926SF
926 MS-09-02-11 - 2 VV SECTORS + 2 TFC ASSEMBLED 2.5 mo Thu 07/12/23 Wed 14/02/24 672;707;633SS;924
927 8° 1/6 PREASSEMBLY 5 mo Thu 28/09/23 Thu 15/02/24 673;928SF
928 MS-09-02-12 - 2 VV SECTORS + 2 TFC ASSEMBLED 2.5 mo Thu 15/02/24 Wed 24/04/24 674;708;635SS;926
929 9° 1/6 PREASSEMBLY 5 mo Thu 07/12/23 Thu 25/04/24 675;930SF
930 MS-09-02-13 - LAST 2 VV SECTORS + LAST TFC ASSEMBLED 2.5 mo Thu 25/04/24 Wed 03/07/24 676;709;636;928
931 MS-09-02-14 - PF3 ASSEMBLED 0.5 mo Thu 04/07/24 Wed 17/07/24 930;528
932 MS-09-02-15 - PF2 ASSEMBLED 0.5 mo Thu 18/07/24 Wed 31/07/24 931;529
933 MS-09-02-16 - PF1 ASSEMBLED 0.5 mo Thu 10/10/24 Wed 23/10/24 932;647
934 MS-09-02-17 - CS PRE-ASSEMBLING 9 mo Thu 14/09/23 Wed 22/05/24 639FS+1 mo;644FF
935 MS-09-02-18 - CS ASSEMBLING 3 mo Thu 29/05/24 Wed 20/11/24 934FS+10 d;933FF
936 MS-09-02-19a - IVC ASSEMBLING - in vessel coils 4 mo Thu 04/07/24 Wed 23/10/24 930
937 MS-09-02-19 - IVC ASSEMBLING FW 8 mo Thu 24/10/24 Wed 09/04/25 936
938 MS-09-02-19 - IVC ASSEMBLING - DIV 6 mo Thu 21/11/24 Wed 07/05/25 936;937FF+1 mo
939 MS-09-02-20 - PIPING ASSEMBLING 6 mo Thu 21/11/24 Wed 07/05/25 936FF;936FF;937FF
940 MS-09-02-21 - CRYOSTAT CYLINDRICAL SECTOR 1 mo Thu 08/05/25 Wed 04/06/25 939
941 MS-09-02-22 - CRYOSTAT TOP LID 0.5 mo Thu 05/06/25 Wed 18/06/25 940
942 MS-09-02-23 - HEATINGS ASSEMBLY 15 mo Thu 01/02/24 Wed 18/06/25 941FF;909SS
943 MS-09-02-24 - DCS FINAL ASSEMBLY 10 mo Thu 12/09/24 Wed 18/06/25 942FF;893SS+3 mo
944 MS-09-02-25 - INTEGRATED COMMISSIONING 6 mo Thu 19/06/25 Wed 03/12/25 943
945 09-03 - RPL - Radiation Protection and Licensing 1325 d Thu 10/01/19 Wed 07/02/24
946 MS-RPL-01: Technical documents for the application -> 3 months 125 d Thu 10/01/19 Wed 03/07/19
947 MS-RPL-02: First requirements from Regulators -> RPL 0.1.1-MS-01 + 1.5 months 66 d Thu 04/07/19 Thu 03/10/19 946
948 MS-RPL-03: Answers to Regulators -> RPL 0.1.1-MS-02 + 3 months 174 d Fri 04/10/19 Wed 03/06/20 947
949 MS-RPL-04: Final advise/opinion from Regulators -> RPL 0.1.1-MS-04 + 3 months 180 d Thu 04/06/20 Wed 10/02/21 948
950 MS-RPL-05: Permit issuing -> RPL 0.1.1-MS-04 + 1 months 60 d Thu 11/02/21 Wed 05/05/21 949
951 MS-RPL-06: Machine and structure testing 720 d Thu 06/05/21 Wed 07/02/24 950
952 09-04 - NEU - NEUTRONICS 40 d? Thu 10/01/19 Wed 06/03/19
953 NEU-01 - TKM 21 d? Thu 10/01/19 Thu 07/02/19
954 MS-NEU-01-01: 2D Model preparation -> in progress 2 days 2 d Thu 10/01/19 Fri 11/01/19
955 MS-NEU-01-02: All Nuclear loads in TKM components + study of reduction of B content in VV -> MS-01 +1 week 1 w Mon 14/01/19 Fri 18/01/19 954
956 MS-NEU-01-03: Implementation of Heating/diagnostics, NBI model... TBD 1 d? Thu 10/01/19 Thu 10/01/19
957 MS-NEU-01-04: Nuclear loads Heating/diagnostics, NBI ... MS-03 +1 month 1 mo Fri 11/01/19 Thu 07/02/19 956
958 NEU-02 - BLD 25 d Thu 10/01/19 Wed 13/02/19
959 MS-NEU-02-01: 360° Model preparation-> Input from PL+1 week 1 w Thu 10/01/19 Wed 16/01/19
960 MS-NEU-02-02: Building analysis 1 mo Thu 17/01/19 Wed 13/02/19 959
961 NEU-03 - ACT 40 d Thu 10/01/19 Wed 06/03/19
962 MS-NEU-03-01: Operational irradiation history> Input from PL/RPL+1 week 5 d Thu 10/01/19 Wed 16/01/19
963 MS-NEU-03-02:Activation inventory 3 w Thu 17/01/19 Wed 06/02/19 962
964 MS-NEU-03-03: Shutdown dose rate 4 w Thu 07/02/19 Wed 06/03/19 963
965 09-05 - PEX - POWER EXHAUST 240 d? Thu 10/01/19 Wed 11/12/19
Baseline Milestone
Baseline Summary
Attività
Divisione
Cardine
Riepilogo
Riepilogo progetto
Attività esterne
Cardine esterno
Inactive Milestone
Inactive Summary
Manual Task
Duration-only
Manual Summary Rollup
Manual Summary
Start-only
Finish-only
External Tasks
External Milestone
Avanzamento
Scadenza
Critical
Critical Split
Baseline
Slippage
Slack
Progetto: Imagine1s_DTT
Data: Thu 04/04/19
Pagina 18

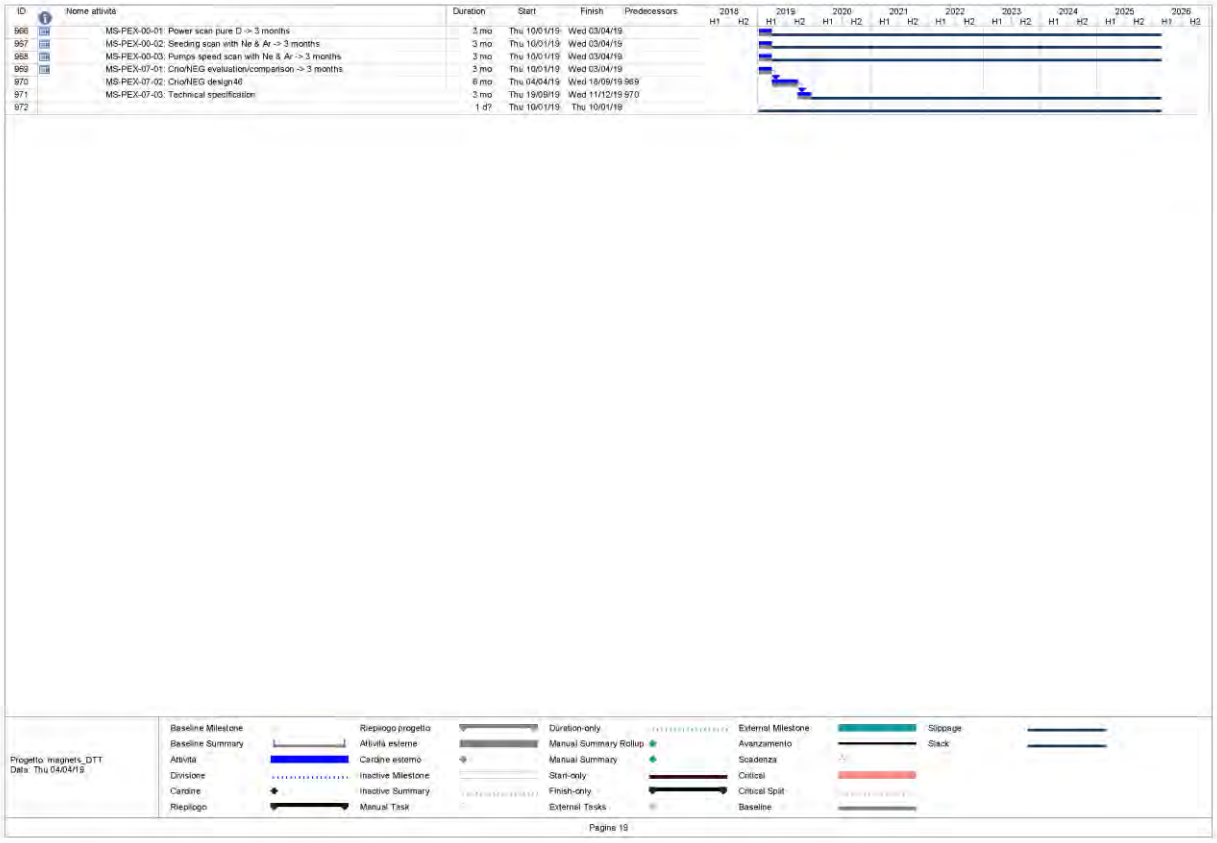
ID
Nome attività
Duration
Start
Finish
Predecessors
2018
2019
2020
2021
2022
2023
2024
2025
2026
966 MS-PEX-00-01: Power scan pure D -> 3 months 3 mo Thu 10/01/19 Wed 03/04/19
967 MS-PEX-00-02: Seeding scan with Ne & Ar -> 3 months 3 mo Thu 10/01/19 Wed 03/04/19
968 MS-PEX-00-03: Pumps speed scan with Ne & Ar -> 3 months 3 mo Thu 10/01/19 Wed 03/04/19
969 MS-PEX-07-01: Cnor/NEG evaluation/comparison -> 3 months 3 mo Thu 10/01/19 Wed 03/04/19
970 MS-PEX-07-02: Cnor/NEG design40 6 mo Thu 04/04/19 Wed 18/09/19 969
971 MS-PEX-07-03: Technical specification 3 mo Thu 19/09/19 Wed 11/12/19 970
972 1 d? Thu 10/01/19 Thu 10/01/19
Baseline Milestone
Baseline Summary
Attività
Divisione
Cardine
Riepilogo
Riepilogo progetto
Attività esterne
Cardine esterno
Inactive Milestone
Inactive Summary
Manual Task
Duration-only
Manual Summary Rollup
Manual Summary
Start-only
Finish-only
External Tasks
External Milestone
Avanzamento
Scadenza
Critical
Critical Split
Baseline
Slippage
Slack
Progetto: Imagine1s_DTT
Data: Thu 04/04/19
Pagina 19

Appendix C

WORK AND TEAM ORGANIZATION

Figure C.1 shows the organizational chart originally illustrated in “DTT - Divertor Tokamak Test facility. Project Proposal”, ISBN 978-88-8286-318-0, ENEA, 2015, also known as “Blue Book”. In 2019 a large part of this organization has been set up, with the nomination of an Interim Project Board, an Interim Responsible for the Project Integration, and the Interim Activity Coordinators of several Tasks.

Suitable human resources have been allocated to each task. Since DTT is in the initial phase for the launch of calls for tender, an administration office is also being set up. As for the foreseen 150 PPY, ENEA and the other organizations involved in DTT has already allocated personnel to the project. In addition, ENEA has recently enrolled a large number of PhD student and permanent staff to be allocated to DTT, also planning further recruitments in the next future.

The team wok has been organized has been organized in the following way.

A Technical Coordination Meeting (TCM) is held every other Tuesday. The Task Coordinators attend these meetings where any progress and/or variation is reported and notified to all the Team.

System Level Engineering (SLE) meetings are called as an output of the TCM or whenever requested by the Task Coordinators or by the Integration Responsible.

A Design Review Meeting (DRM) is called about every 3 months in order to check the overall progress of all the ongoing activities.

A Project Review Meeting (PRM) will be called at the end of any particular activity and in any case before of any tender in order to finally check the results.

A reference living document, the Plant Integration Document (PID) has been prepared. The PID will detail all the main parameters and design choices of DTT during the design phase. It is organized following the Work Breakdown Structure (WBS, Fig. C.2) with two main chapters: the first deals with the physical requirements

of the machine, the second reports the main parameters of each component/system with the use also of hyperlinks to more specific technical notes.

A Document Management System (DMS) has been organized to track changes, issue workflows, identify the responsible for any action and who is giving the necessary approvals. Presently the documentation is archived on a cloud file-sharing platform according to the WBS. Every coordinator is allowed to archive the files and make them available to the others. In the meanwhile another system is being installed. This is a specific platform for document management called “Alfresco”. It will be customized in order to implement most of the features of the IDM system used in the fusion community. Workflows for review and approval process will be installed. Every group will have a dedicated site where the coordinator will have the possibility to report the status of the activities and to create a collaborative working environment.

The site of the project, www.dtt-project.enea.it, is based on a public and a restricted access domains. The restricted access section is designed to provide the team with the information required to interact in the best way in the designing activity. The public section of the site contains the general information of DTT arranged in plain, informative way, in order to share, even with a non-specialized reader, the main characteristic and the mission of the project.

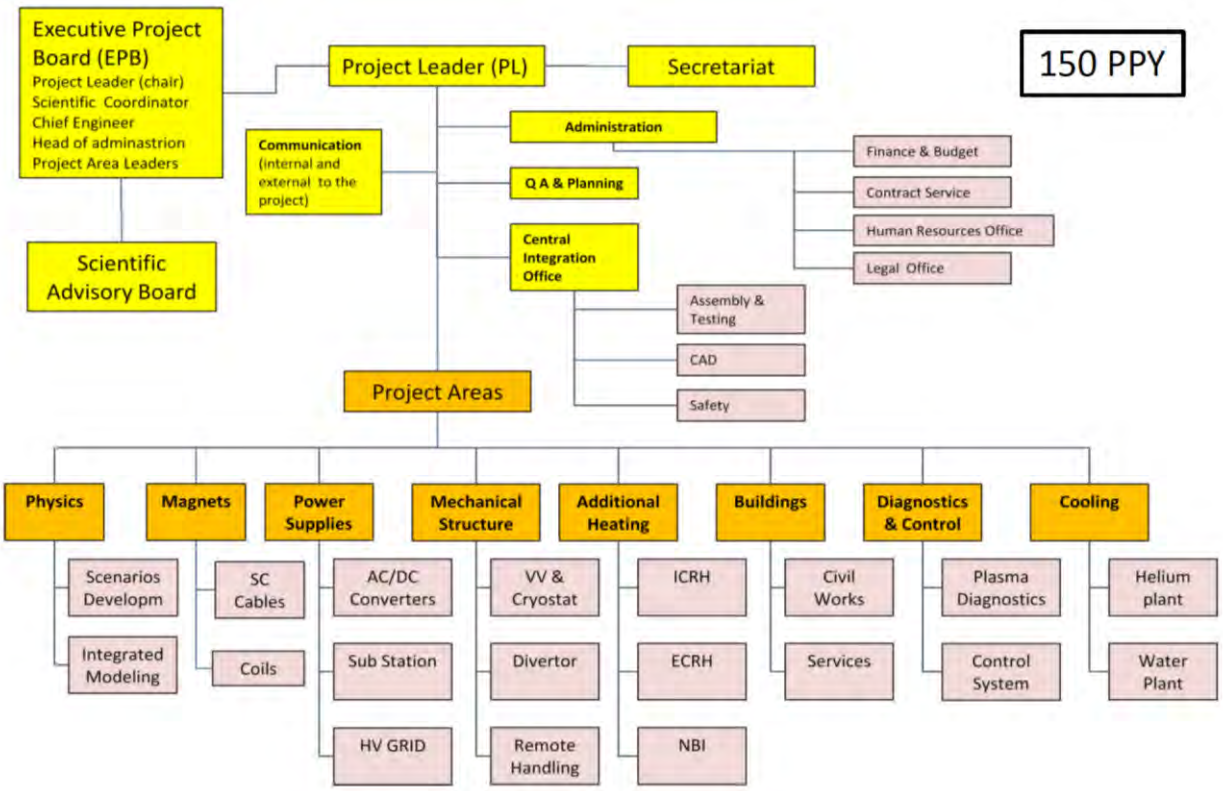

Figure C.1: DTT organizational chart.

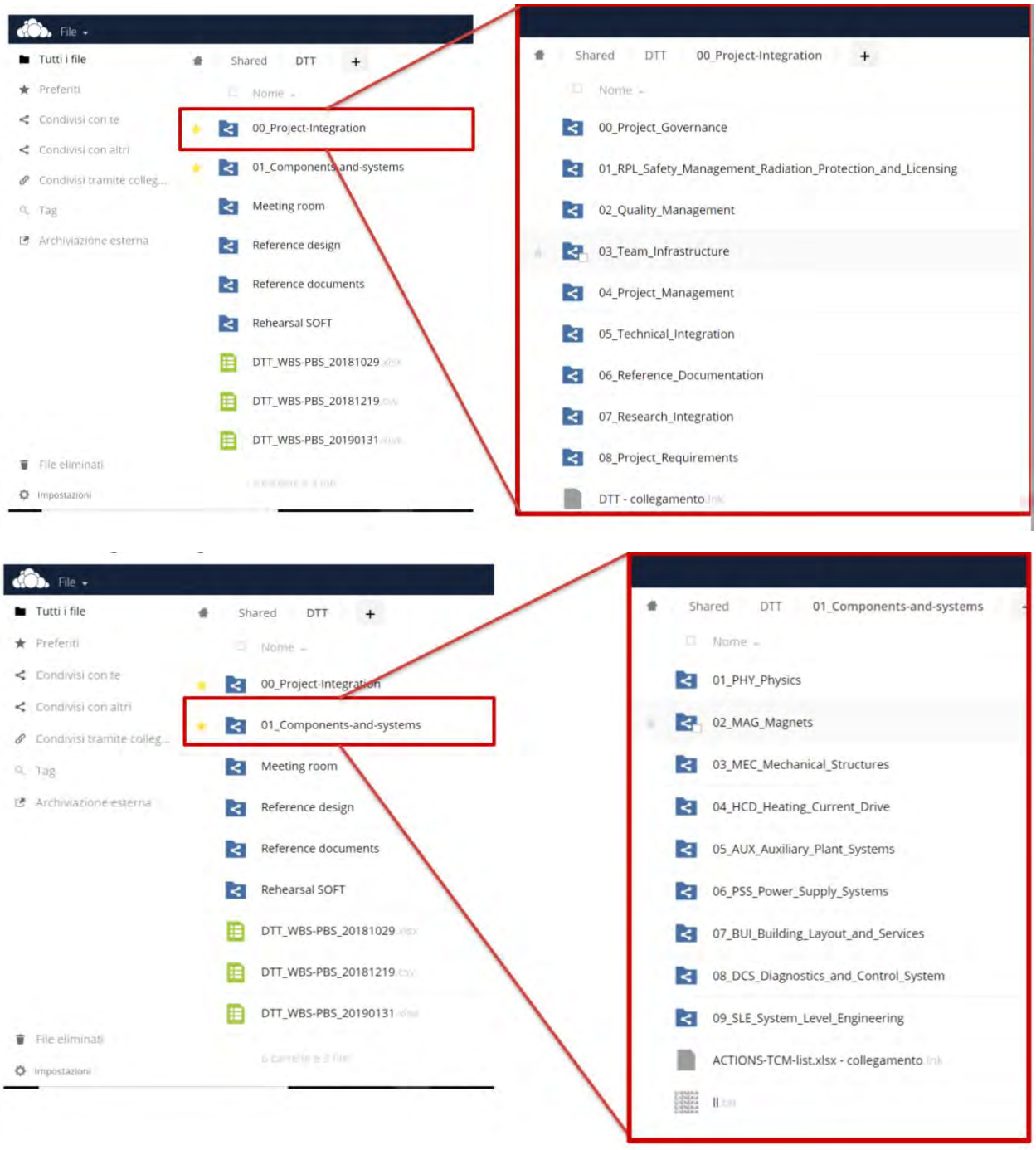

Figure C.2: DTT Work Breakdown Structure.

ENEA
Promotion and Communication Service
www.enea.it

April 2019

ISBN: 978-88-8286-378-4